Mechanical properties of iron hollow sphere reinforced metal matrix syntactic foams

Attila BÁLINT[1, a], Attila SZLANCSIK[1,b]

[1]Budapest University of Technology and Economics Department of Materials Science and Engineering, Hungary

[a]balintattila91@gmail.com (corresponding author), [b]szlana045@gmail.com

Keywords: Syntactic foam, metal matrix composite, pressure infiltration, compressive properties.

Abstract. Metal matrix syntactic foams (MMSFs) were produced by low-pressure inert gas infiltration technique. Matrixes of the produced syntactic foams were Al99.5, AlSi12, AlMgSi1 and AlCu5 respectively, and each was reinforced by pure Fe based hollow. The produced blocks were investigated by optical and scanning electron microscopy. The microstructural investigations revealed proper infiltration with small amount of unwanted voids and an effective and thin interface layer between the matrix materials and the reinforcing spheres. The produced MMSFs were also tested under quasi-static compression loading to get characteristic mechanical properties. The test results showed that the MMSFs with iron spheres have outstanding mechanical properties compared to 'conventional' foams.

Introduction

Metal matrix syntactic foams (MMSFs) are special foams consisting of a metallic matrix and a set of hollow spheres. The matrix material is usually a light-weight alloy (aluminum in most cases), but Fe [1] and Zn [2] are also applied for experiments. Most commonly the hollow sphere inclusions are built up from oxide ceramics (Al_2O_3 and/or SiO_2), but pure iron hollow spheres are also available on the market (Globomet grade spheres from Hollomet GmbH). MMSFs have been investigated in many aspects, but the publications commonly refer to the microstructural and mechanical testing besides the production methods. Regarding the microstructure, the most important part of the MMSFs are the interface layers between the matrix material and the reinforcing hollow spheres, because this layer is the responsible for proper load transfer between the constituents. Due to this distinguished role, the interface layer and the load transfer mechanisms were studied in details [3-6]. The mechanical properties of the MMSFs have been studied in compressive loading mode, most commonly. They have excellent mechanical damping and energy absorbing capability that makes them beneficial as collision dampers or as basement of (vibrating) machines, machine tools. Besides the measurements [7], the compressive properties have been predicted [8] too and the compressive curves were analyzed according to the failure mechanisms of the MMSFs [9]. The tribological properties of MMSFs are also in the focus of interest [10-12]. Dry sliding properties as well as slurry erosive wear and wear in corrosive medium was investigated [10-12]. Due to the promising expected properties the main aim of our paper is to give numerical results about the characteristic properties under compressive loading.

Materials and experimental methods

Production of the composites

Throughout our experiments, pure aluminum (Al99.5) and various aluminum alloys; AlSi12, AlMgSi1 and AlCu5 were used as matrix materials for the synthesis of MMSFs. For all the MMSFs, Globomet grade iron hollow spheres were used as reinforcing material, manufactured by Hollomet GmbH. The reinforcement material was studied in detail, because that should be the main load-bearing component. The diameters of 700 hollow spheres were measured on a stereomicroscope (Fig. 1a), the average diameter of the hollow spheres was found to be 1.9 mm. The density of the hollow spheres was ρ=0.4 gcm^{-3}. Proper surface adhesion of the hollow spheres

is crucial for the production of high quality composites; therefore the surface of the hollow spheres was studied by scanning electron microscopy (SEM). The SEM image (Fig. 1b) clearly shows that the wall of the spheres is porous, which, due to a high surface area, results in excellent contact between the matrix material and the hollow spheres.

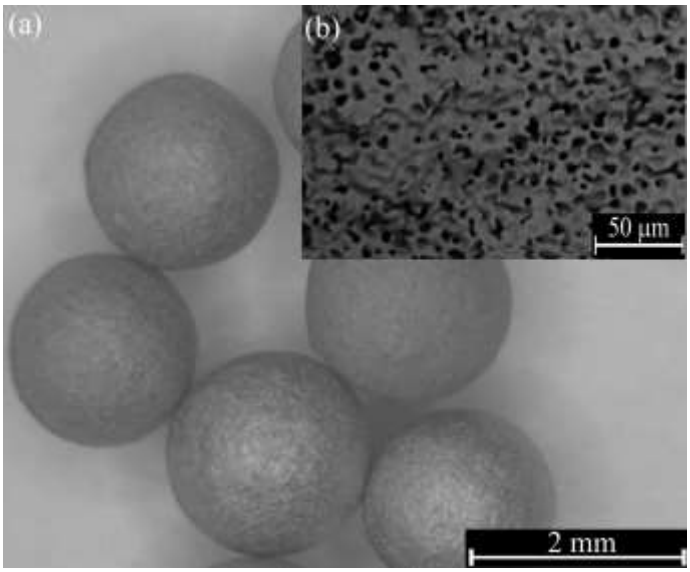

Figure 1. (a) Stereomicroscopic image of the iron hollow spheres (b) SEM image about the wall of an iron hollow sphere

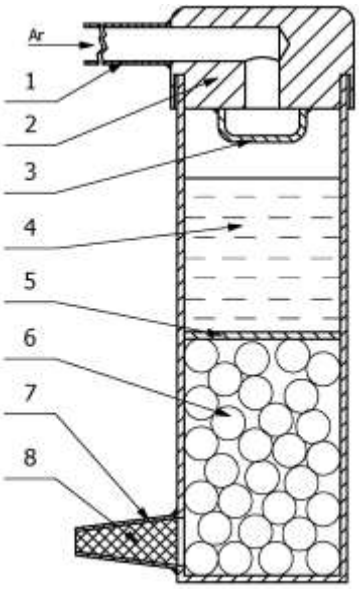

Figure 2. Sketch of the infiltration chamber: 1. gas inlet, 2. closing hatch, 3. gas deflector plate, 4. metal, 5. mesh, 6. hollow spheres, 7. exhaust 8. Al_2O_3 mat

For the synthesis of the low-pressure infiltration was used. The casting mold used throughout the production is shown in Fig. 1. For a casting mold, we utilized a hollow section piece that was closed at the bottom by welding. In addition, an exhaust pipe was welded to the side of the hollow section, which was filled with Al_2O_3 mat in order to prevent the spillage of molten aluminum upon the application of infiltration pressure. The inner side of the mold was coated with graphite spray, and was filled with the iron hollow spheres approximately to the half. The hollow spheres were closely packed by the application of mechanical vibration, and were locked in place by a metal mesh. The casting mold was pre-heated to ~300°C, and was filled with the molten matrix material at ~700°C. Then the mold was sealed and inert gas (Ar) was applied for 30 s at 4 bar pressure. The apparatus was then externally cooled by water. The specimens made with precipitation hardenable alloy matrix materials (AlMgSi1 and AlCu5) were investigated in two different heat treated conditions. First solution heat treatment (specimens marked with O) was applied. According ASTM standard 1 hour of heat treatment at 520ºC, followed by rapid cooling in water. The second was precipitation hardening (specimens marked with T6), whereby additional heating after the solution heat treatment was applied at 170ºC for 14 hour. The specimens were labeled as follows: matrix material-reinforcement (heat treatment if applied). For example, the name AlCu5-GM(O) corresponds to MMSF made by AlCu5 matrix material and a Globomet (GM) reinforcement that was subjected to solution heat treatment (O).

Investigation techniques

Density is an important property of metal foams; it was determined by Archimedes method on the compressive test specimens. The density of the metal foam was also estimated using calculations ($\rho_{calculated}$) by using the average 1.9 mm diameter, 0.4 gcm^{-3} density and ~65% space filling for the reinforcement spheres. The results of the density measurements are shown in Table 1.

The quality of the infiltration was examined by metallographic techniques. For this purpose, a representative piece from the produced sample was cut out and mounted in synthetic resin. The steps for the metallographic sample preparation were as follows: wet grinding with SiC P80, 160, 320, 600, 1200 and 2500 grade grinding papers. Subsequently, automatic polishing steps were applied first with a 3 µm grain size diamond suspension for 40 minutes, followed by polishing with

a 1 μm grain size diamond suspension for 30 minutes, and finally polishing with a 0.05 μm grain size γ-Al_2O_3 suspension for 20 minutes with 15 N force for all the polishing steps respectively.
Molten aluminum is a highly reactive material, and can dissolve the walls of the iron spheres during infiltration; therefore an interface layer was created between the two materials. The thickness of this layer was measured by a Phillips XL-30 scanning electron microscope and linear energy dispersive X-ray spectroscopy (line EDS). For the EDS analysis an EDAX Genesis detector was used with 20 kV accelerating voltage, 35 μs detector amplification time and 15000 ms excitation time for each point along the line respectively. The electron beam spotsize was only approximately 50 nm, therefore it was neglected in the analysis of the transition zones.
Generally, the primary loading mode on MMSFs is compression. Therefore compression tests were done by a hydraulic MTS 810 type universal material testing machine. For the compression tests, cylindrical test specimens of D=14 mm diameter were machined, with height to diameter (H/D) ratios of H/D=1, 1.5 and 2. In total, 18 pieces per composite were compressed (6 per slab). Double lubrication with Loctite anti-size lubricant was applied to the specimens. The test objects were compressed with a constant velocity depending on the H/D ratios. For H/D=1, 1.5 and 2, the compressing speeds were 0.1 mms^{-1}, 0.15 mms^{-1} and 0.2. mms^{-1}, respectively. The measured force – height reduction curves were corrected for alignment error, than the plots were averaged by Origin software, and were converted to stress-strain plots. The evaluation of the diagrams were performed in accordance with the ruling DIN 50134 standards. The monitored properties were the compressive strength, yield strength, plateau strength, structural stiffness, and absorbed energy values.

Results and discussion

The results of the density measurements are shown in Table 1. It is clear that the measured density values were always very close to the calculated vaues. The small difference between them was caused most probably by improper infiltration. In Fig. 3a the white arrow shows a hollow sphere with damaged wall and therefore filled by the matrix material, the black arrow shows the lack of matrix material: an unwanted porosity between the hollow spheres.

Table 1. Theoretical and measured density values of the MMSFs

Sample / MMSF densities (gcm^{-3})	Al99.5-GM	AlSi12-GM	AlMgSi1-GM	AlCu5-GM
Calculated ($\rho_{calculated}$)	1.62	1.60	1.62	1.76
Measured ($\rho_{measured}$).	1.41	1.42	1.60	1.72

As Fig. 3.b shows the spheres had not significant impact on the microstructure of the matrix material. It has polygonal grains, but near to the spheres the number of silicon rich and magnesium rich (in case of AlSi12 and AlMg1 matrix respectively) precipitations had increased. The chemical composition along a line from the matrix was measured perpendicular to the wall of a sphere. For example in Fig. 4, the oxygen content clearly increased in the wall of the spheres, because of the slight oxidation during the preheating process. In the right side of the image the two discursive lines shows the transition layer thickness. This value varies between 4-11 μm for all the samples respectively. In the case of the AlCu5 and AlMgSi matrices a local enrichment of Cu and Mg was detected alongside the spheres. In summary coherent, thin transition layers are present between the matrix and reinforcement material in all samples.
Regarding the compression tests, the more intensively deformable syntactic foams with iron hollow spheres have different shaped compressive curves, compared to more rigid syntactic foams with ceramic hollow spheres. There was no initial stress peak, so they do not have a pronounced compressive strength: the curves constantly step over to the plateau region, because the metal spheres have higher plastic deformation ability, in contrast to the ceramic spheres' rigid behavior. Regarding the characteristic mechanical properties, the structural stiffness (*S*) show higher values when the H/D ratio is higher (Fig. 5). As it is expected, the precipitation hardened alloys showed higher structural stiffness values than the ones with solution heat treatment. The AlSi12-GM(O) and

AlCu5-GM(O) specimens showed higher stiffness values than the specimens of Al99.5(O) and AlMgSi1(O) matrix. The structural stiffness values varied between 1000-7000 MPa. Higher aspect ratios caused also resulted in higher scatters, because there are infiltration errors in the syntactic foams, bigger specimens causing higher probability of serious errors.

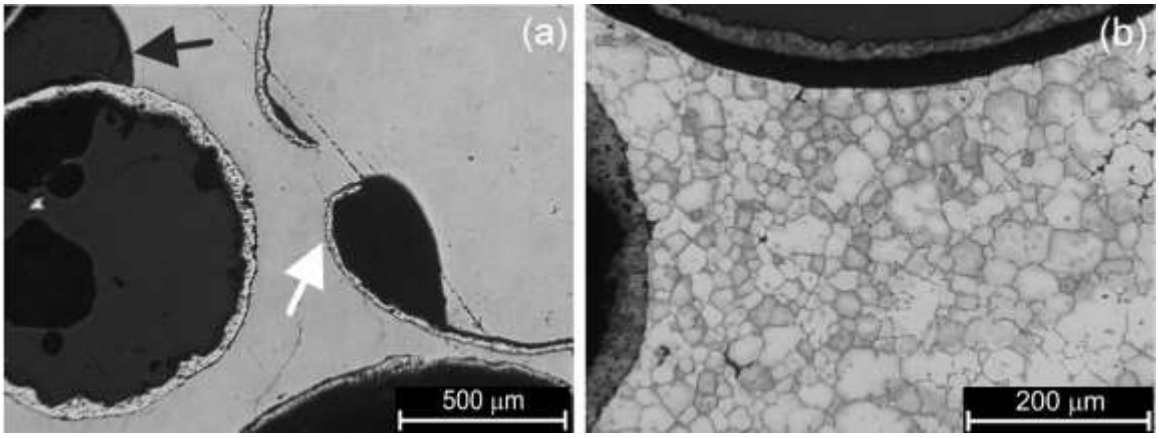

Figure 3. Light microscope images of MMSFs (a) Al99.5-GM(O), polished sample and (b) AlCu5-GM(O), etched sample

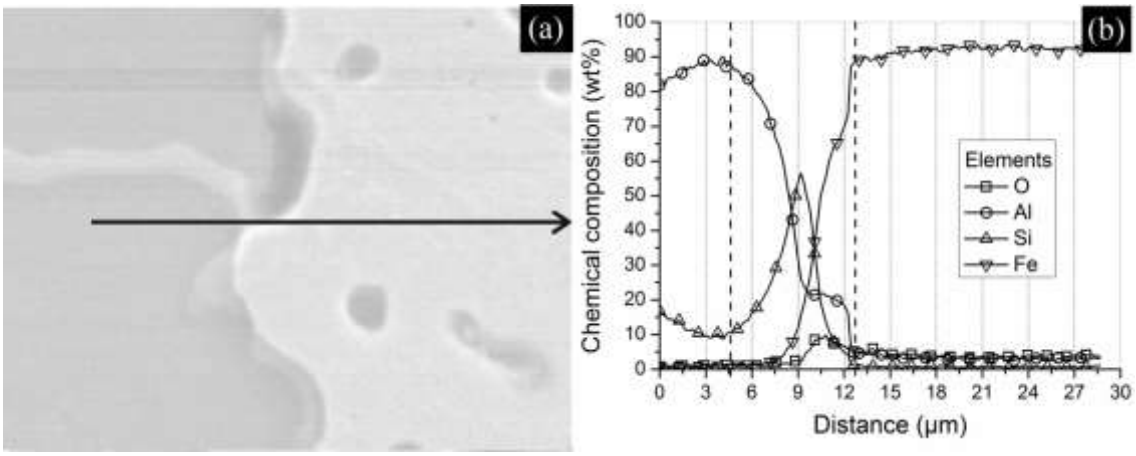

Figure 4. (a) SEM image of a polished AlSi12-GM(O) sample with the line for the EDS measurement, (b) plot of the EDS measurement along the black arrow

In the yield strength (σ_Y) values (Fig. 6) no definitive relation could be found with the aspect ratio; the values within the sample types were within the scatter for each H/D ratio. The T6 heat treated specimens showed significantly higher yield strength values, approximately by 30%, than the specimens with solution heat treatment. Compared to the samples with pure aluminum matrix (~20 MPa) about four times higher yield strength can be achieved with heat treated AlCu5 matrix (~80 MPa). The plateau strength ($\sigma_{plt.}$) values (Fig. 7) had a slight dependence on the H/D ratio, in the case of higher specimen the values were higher (except the AlMgSi1 (O) specimen). The matrix strength also had influence on $\sigma_{plt.}$, and σ_Y, with higher matrix strength, causing higher plateau strength values. The difference can be significant, for example the plateau strength of Al99.5 matrix (~40 MPa) can be tripled by AlCu5 matrix (~120 MPa). As it is expected, the T6 heat treated specimens also had higher plateau strength values then the solution heat treated ones. The mechanical energy absorbed up to 1% plastic deformation ($W_{1\%}$) is the limit value of the maximum energy that the MMSF can withhold without macroscopic fractures. This energy was found to be inversely proportional to the aspect ratio (Fig. 8), but it should be noted that energy values were mostly in the scatter range. The effect of the matrix material and heat treatment on the $W_{1\%}$ and $W_{50\%}$ (overall mechanical energy absorbed up to 50% plastic deformation, Fig. 9) values showed the same trends like the yield strength, plateau strength and structural stiffness respectively. The $W_{50\%}$ values varied within wide ranges from ~2000 MJm^{-3} in the case of Al99.5 matrix up to ~ 6000 MJm^{-3} in the case of AlCu5 matrix with T6 heat treatment. During the compressive tests

different failure mechanisms can be observed in the case of iron spheres reinforced compared to the MMSFs with ceramic spheres, there was no crack plane and the specimens had plastic deformation in all cases. This observation is supported by the metallographic examinations of compressed specimens in Fig. 10. A high level of plastic deformation of the spheres and matrix material can be observed. The spheres crashed (black arrow) because of the pressure, and the matrix tried to follow the deformation of the spheres (white arrow).

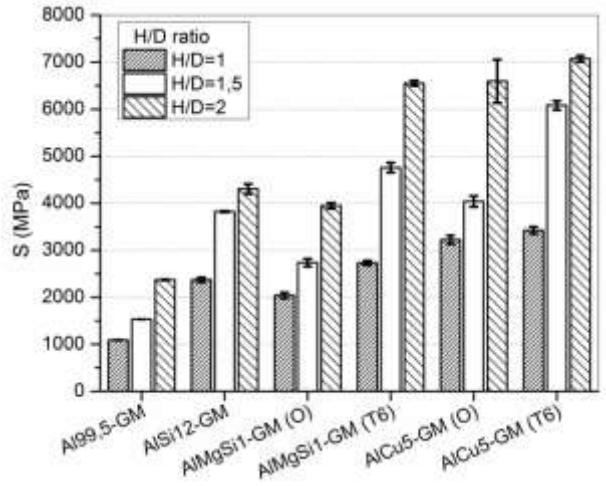

Figure 5. The structural stiffness values

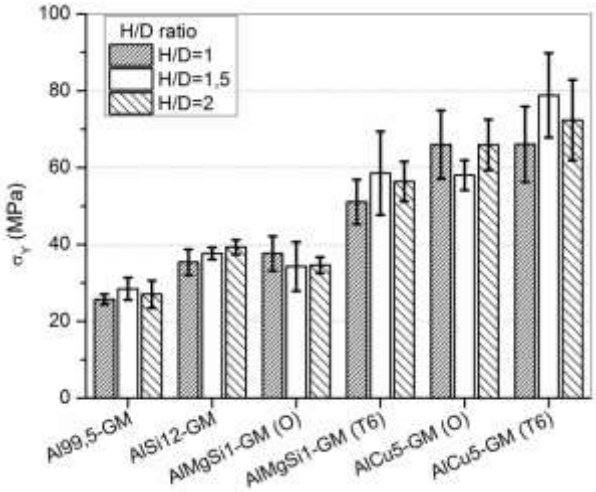

Figure 6. The yield strength values

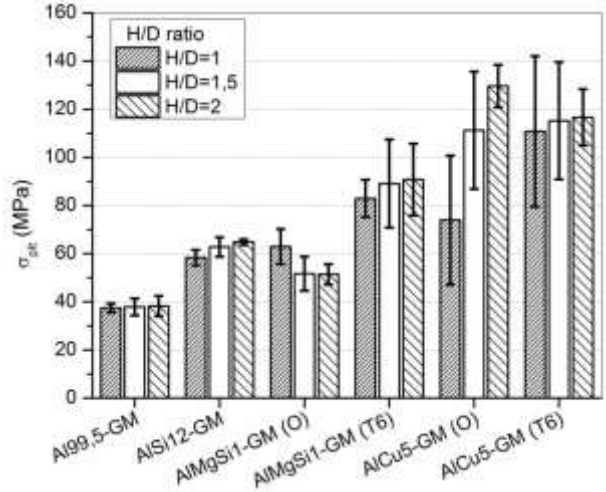

Figure 7. Plateau strength values of the composites

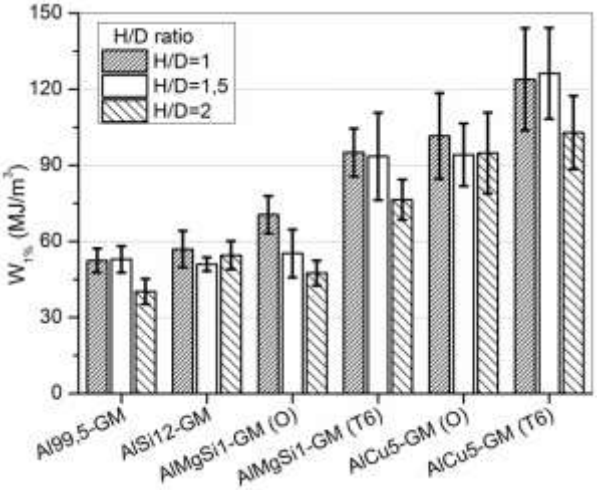

Figure 8. Absorbed energy values (up to 1% plastic deformation)

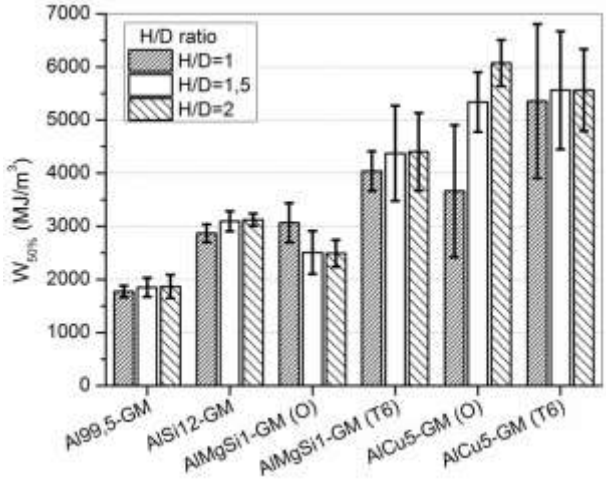

Figure 9. Mechanical energy absorbed up to 50% plastic deformation

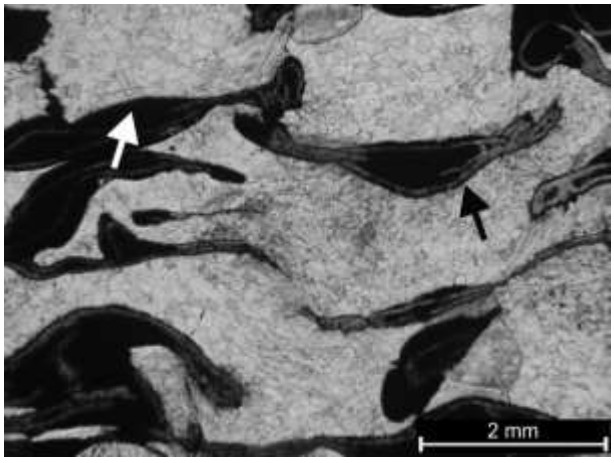

Figure 10. Microscopic image of compressed AlCu5-GM(O) polished and etched specimen

Summary

From the above detailed experiments and investigations the following conclusions can be drawn:
1. Low-pressure infiltration proved to be an effective method for the production of metallic hollow sphere reinforced AMSFs. The produced AMSFs have low unwanted void content, their densities are close to the theoretical ones with small scatter, and the whole procedure is well repeatable.
2. The microstructural investigations showed good cohesion between the matrix material and the hollow spheres that is also confirmed by the presence of a 4-11 μm thick interface layer.
3. The quasi-static compressive tests confirmed outstanding mechanical properties. The structural stiffness and the whole absorbed energy values were in linear relationship with the aspect ratio, while the plateau and yield strength were independent from it. The mechanical energies absorbed up to 1% deformation was inversely proportional to the aspect ratio.
Compared to the data available in the professional literature; the produced AMSFs have significantly better mechanical properties than conventional metallic foams.

Acknowledgments

This work is connected to the scientific program of the " Development of quality-oriented and harmonized R+D+I strategy and functional model at BME" project. This project is supported by the New Hungary Development Plan (Project ID: TÁMOP-4.2.1/B-09/1/KMR-2010-0002).

References

[1] L. Peroni, M .Scapin, M. Avalle, J. Weise, D. Lehmhus, J. Baumeister, M. Busse, Syntactic Iron Foams - On Deformation Mechanisms and Strain-Rate Dependence of Compressive Properties, Adv Eng Mater. 14(10) (2012) 909-918.
[2] A. Daoud, Synthesis and characterization of novel ZnAl22 syntactic foam composites via casting, Mater Sci Eng A. 488(1–2) (2008) 281-295.
[3] DK. Balch, DC. Dunand, Load portioning in aluminium syntactic foams containing ceramic microspheres, Acta Mater. 54 (2006) 1501-1511.
[4] IN. Orbulov, K. Májlinger, Microstructural aspects of ceramic hollow microspheres reinforced metal matrix composites, Int J Mater Res. 104 (2013) 903-911.
[5] IN. Orbulov, K. Májlinger, On the microstructure of ceramic hollow microspheres, Period Polytech Mech Eng. 54 (2010) 89-94.
[6] IN. Orbulov, K. Májlinger, Microstructure of metal-matrix composites reinforced by ceramic microballoons, Mater Techn. 46 (2012) 375-382.
[7] JA. Santa Maria, BF. Schultz, JB. Ferguson, PK. Rohatgi, Al–Al2O3 syntactic foams – Part I: Effect of matrix strength and hollow sphere size on the quasi-static properties of Al-A206/Al2O3 syntactic foams, Mater Sci Eng A. 582 (2013) 415-422.
[8] JB. Ferguson, JA. Santa Maria, BF. Schultz, PK. Rohatgi, Al–Al2O3 syntactic foams—Part II: Predicting mechanical properties of metal matrix syntactic foams reinforced with ceramic spheres, Mater Sci Eng A. 582 (2013) 423-432.
[9] IN. Orbulov, K. Májlinger, Description of the compressive response of metal matrix syntactic foams, Mater Des. 49 (2013) 1-9.
[10] M .Ramachandra, K. Radhakrishna, Synthesis-microstructure-mechanical properties-wear and corrosion behaviour of an Al-Si (12%) – Flyash metal matrix composite, J Mater Sci, 40 (2005) 5989-5997.
[11] M .Ramachandra, K. Radhakrishna, Effect of reinforcement of flyash on sliding werar, slurry erosive wear and corrosive behaviour of aluminium matrix composite, Wear 262 (2007) 1450-1462.
[12] K. Májlinger, IN. Orbulov, Development and evaluation of hybrid aluminium matrix syntactic foams, Mech Eng Lett. 9 (2013) 66-75.

N-alkyl pyrrolidones for plasticizing polyurethane elastomers

András Bánhegyi [1,a], José Trujillo Vilaboy [2, b], Kálmán Marossy [1, 2, c]

[1]Institute of Ceramic and Polymer Engineering, University of Miskolc, Miskolc, Hungary

[2]Borsodchem Zrt., Kazincbarcika, Hungary

[a]andras.banhegyi@gmail.com, [b]jose.trujillo-vilaboy@borsodchem.eu, [c]polkal01@uni-miskolc.hu

Keywords: polyurethane, elastomer, plasticizer, Flexidone

Abstract. Polyurethane (PU) products produced from the reaction of isocyanates and polyols have one of the most extensive consumption of plastics. After the invention in 1937 PU had to wait until the 50's to spread worldwide and since then their development have been continuous. In PU systems are used varied additives, including plasticizers, which are use by several large companies.
In our work a new class of plasticizers, namely N-alkyl-pyrrolidones were used in polyurethane systems. Their trade names are Flexidone® 100, Flexidone® 300 and Flexidone® 500 containing 8, 12 and 18 C-atom long alkyl chain, respectively. These plasticizers showed excellent results in our previous works and the literature has also confirmed their great properties. We supposed that this chemical structure can form a strong interaction with the urethane group.
The effect was monitored by hardness and dynamic mechanical (DMA) measurements. Migration and thermally stimulated discharge (TSD) measurments are in progress.

Introduction

The properties of polyurethane elastomers have been known since the beginning of industrial research on isocyanate chemistry. The properties of PU elastomers can be varied over a wide range through proper choice of raw materials and formulation - properties are determined primarily by the chemical components.

Plasticizers are typical additives in thermoplastics (in particular in PVC) but are not necessary in thermoplastic polyurethanes – are in many books [1, 2], but we know that leader companies use usually several types of plasticizers for polyurethane systems to improve their product's quality.

In the current work we prepared both plasticized cross-linked (CPU) and thermoplastic (TPU) polyurethane elastomers.

In our previous work we compared the properties of two "traditional" plasticizers (DOP and DOA) with Flexidone plasticizers in plasticized PVC [3]. These alkyl pyrrolidons show better properties than DOP and DOA in terms of efficiency, low temperature properties, processing etc. The experiments to understand the differences between the members of the Flexidone family are being in process.

Because of the planar structure of pyrrolidones the oxygen with its high electronegativity can easily send an electron to delocalize, and it produces a strong dipole moment (Figure 1). Chemically binding a flexible non-polar alkyl chain with a compact hydrophilic head makes the alkyl pyrrolidones soluble in both polar and non-polar solvents. It has been found that chain lengths between C8 and C18 are the best types using them as plasticizers. Due to their excellent dissolving power and good compatibility with PVC both gelling temperature and gelling time can be reduced. It leads to highly flexible PVC formulations that even at extremely low temperatures do not lose their flexibility [4, 5].

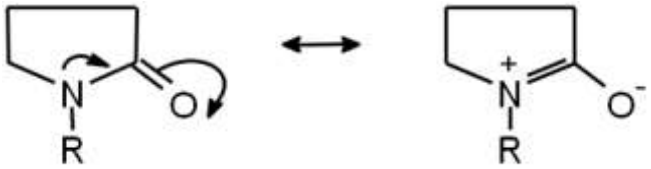

Figure 1:
Electron delocalization in pyrrolidones

Experimental

Materials

Ongronat® 2100 is oligomeric MDI with average functionality of 2.6-2.7. XP-1052 is mid-functionality pre-polymer, produced by reaction of monomeric MDI and 6000 MW polyether triol. As chain extender 1,4-butanediol was used, named BD. In the reaction the catalyst was D33LV®, triethylenediamine as a 33% by weight solution in dipropylene glycol. Finma-Sorb 430 PR molecular sieve pastes made from zeolite in castor oil. Rokopol® D2002 is a high purity polyoxypropylene glycol of molecular weight 2000. Arcol Polyol 1374 is a trifunctional reactive polyether polyol.

Test methods and instruments

Shore A hardness was measured according to ISO 828 standard at 23°C, after 15 s load. Five measurements were carried out and the mean value rounded to whole number.

Dynamic mechanical analysis (DMA) tests were carried out with Rheometric Scientific DMTA MK-III instrument in dual cantilever mode at 1 Hz frequency in the -100 to 150°C temperature range.

Sample preparation

CPU samples were synthesized from previously prepared polyol mixture and from MDI. The mixture was made manually with 0.5% BYK-530 anti-foaming agent to make the samples without bubbles. After mixing the material it was poured into the suitable sized mold.

	A component				B component		Flexidone
	Ar1374	BD	BP	D33LV	XP-1052	Ongronat 2100	
pure CPU	6.82	2.11	0.55	0.08	4.84	5.6	0
10% plasticizer	6.13	1.89	0.49	0.07	4.36	5.04	2
20% plasticizer	5.47	1.7	0.44	0.06	3.87	4.48	4
30% plasticizer	4.78	1.48	0.38	0.06	3.39	3.92	6

Table 1:
Crosslinked polyurethane formulations (Components in grams)

For preparing TPU samples pure MDI was used, which was mixed under N_2 atmosphere at 50°C, with polyether polyol (Rokopol D-2002), and it was mixed for 2 hours at 70°C. Then butanediol as chain extender and the catalyst, as well as plasticizers were added to the previously prepared prepolymer. To complete the reaction, it was carried out in melt by roll-milling at a suitable temperature at 160°C. Rolling-milled felts were compression molded into sheets of 0.5, 1 and 4 mm thickness, respectively.

	prepolymer	BD	D33LV	Flexdione
pure PU	6.82	2.11	0.08	0
10% plasticizer	103.05	10.53	0.22	12.6
15% plasticizer	82.5	8.42	0.18	18.2
20% plasticizer	82.5	8.42	0.18	22.78

Table 2:
Thermoplastic polyurethane formulations (Components in grams)

Results and discussion

Hardness tests

The results show that increasing the concentration of the plasticizer decrease the hardness in all cases. Shore A hardness vs. plasticizer content can be seen in the Figure 2.

The longer alkyl chain in plasticizer results higher efficiency in the thermoplastic PUR elastomers, while in the crosslinked elastomers the shortest alkyl chain gave the best results.

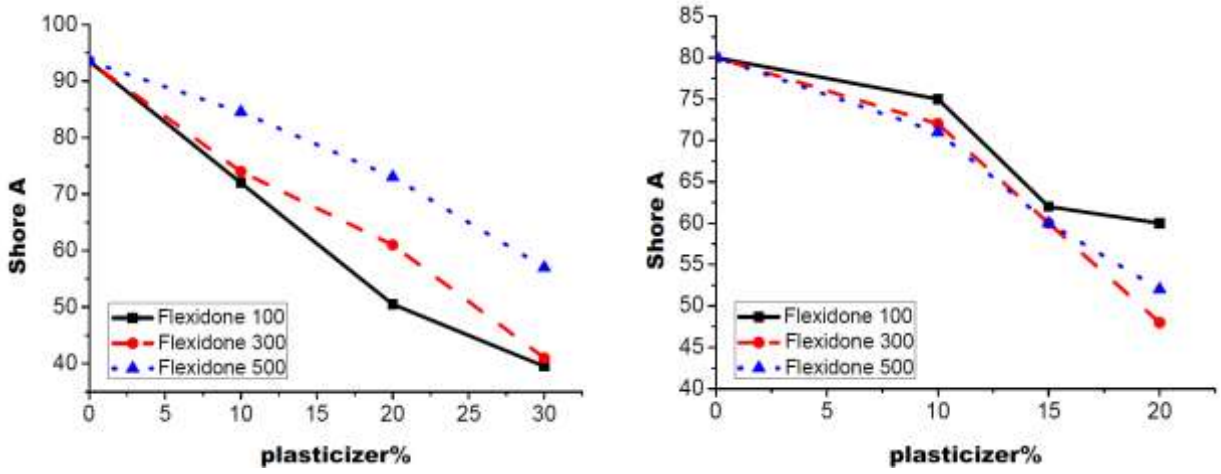

Figure 2:
Comparison of Shore A hardness of crosslinked- (left) and thermoplastic (right) polyurethanes

The standard deviation of Shore A hardness measurements is usually 1 Shore A unit in the 50 - 70 hardness range. There is no explanation for the strange behavior of samples plasticized with Flexidone 100. Because both structural units of the polyurethane are plasticized, other planned structural investigations might answer.

Dynamic mechanical tests

According to our expectancies the glass transition temperature decreases, by increase of plasticizer concentration (shown in Fig. 3) similarly than in case of hardness, Flexidone 100 showed the best results in CPU system.

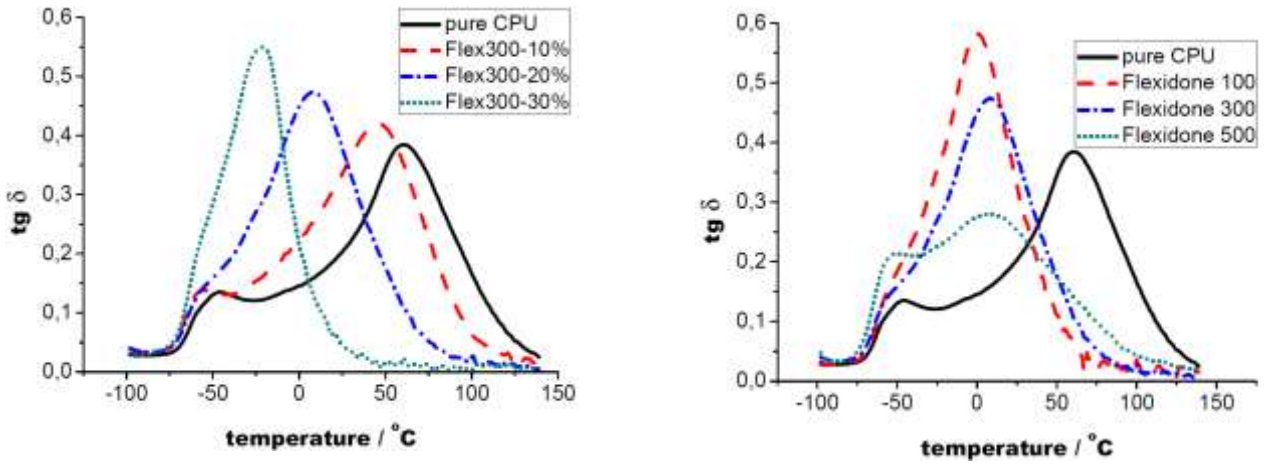

Figure 3:
Mechanical loss factor vs. temperature of crosslinked polyurethane
Plasticizer content varied (left); plasticizer type varied, 20 w/w% (right)

The plasticizers act similarly in thermoplastic elastomers, but the longer alkyl chained plasticizers showed higher efficiency in terms of T_g decrease (Figure 4). Flexidone 300 seems to be optimal.

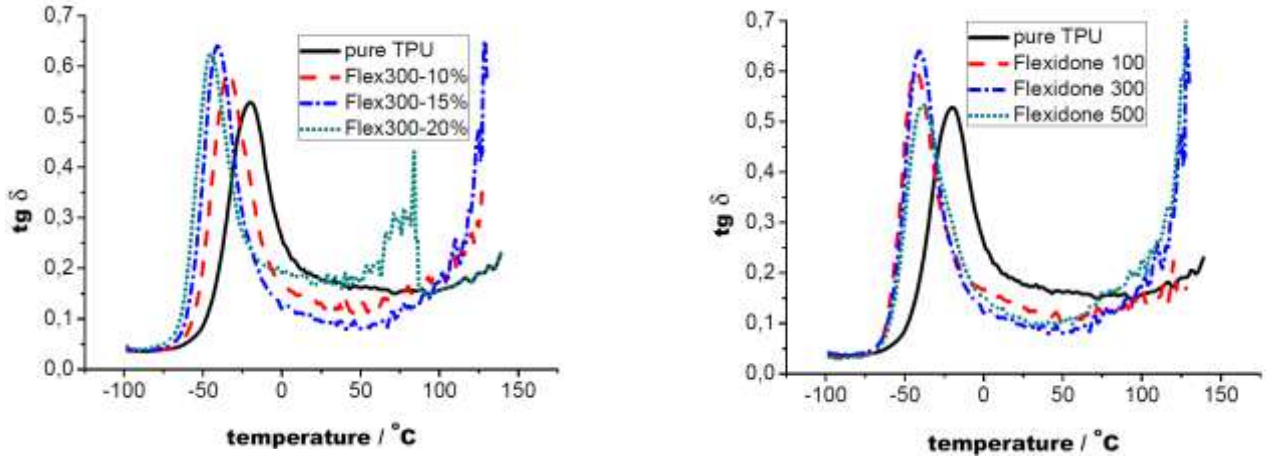

Figure 4:
Mechanical loss factor vs. temperature of thermoplastic polyurethane.
Plasticizer content varied (left); plasticizer type varied, 15 w/w% (right)

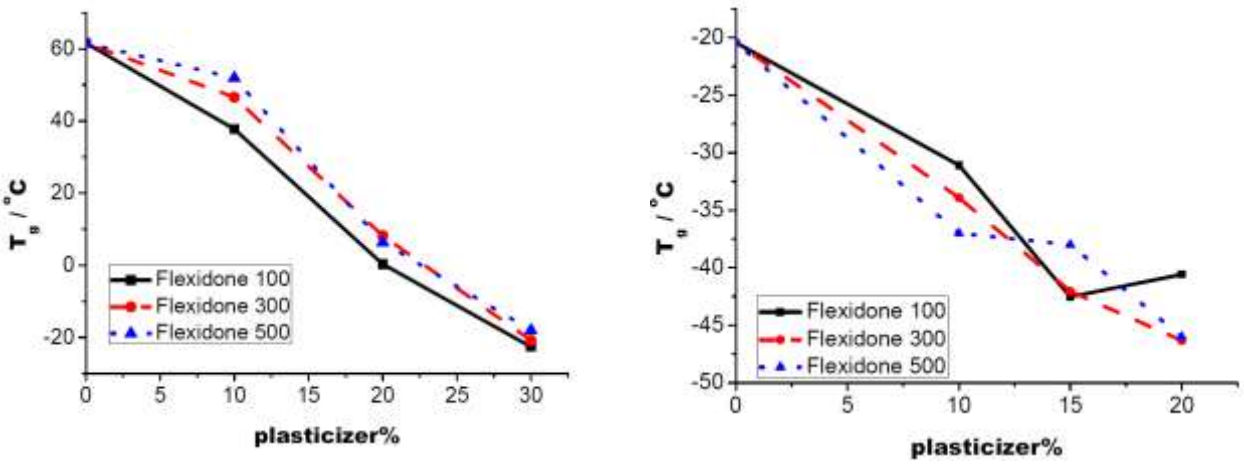

Figure 5:
Glass transition temperature of crosslinked (left) and thermoplastic (right) polyurethanes

Summary

We have tested N-alkyl pyrrolidon plasticizers in polyurethane systems. These materials showed excellent compatibility and efficiency in our previous experiments with PVC [3].

Comparing the samples with different plasticizer concentration Shore A hardness and DMA measurements were carried out.

The results of the experiments show that the previously expected compatibility exists with polyurethane, too; the properties of these plasticized polyurethanes are good and industrially exploitable.

For better understanding of the mechanism of interaction of Flexidone plasticizers and the structure changes we plan further investigations, namely thermally stimulated discharge and Raman imaging.

Acknowledgements

The research was supposed by the TÁMOP 4.2.1.B-10/2/KONV-2010-0001 grant. We would like to thank BorsodChem Isocyanate Technology and the Research Group of Vinyl Technology for their help and professional support.

References

[1] Günter Oertel: Polyurethane Handbook, Hanser, Munich, Germany, 1985

[2] Ferenc Farkas: Polyurethanes, Kémszám Bt., Budapest, 2004

[3] Bánhegyi, A.: Comparative analysis of N-alkyl-pyrrolidone for PVC production, Mechanoplast 2013 Conference in Material Science and Engineering (Miskolc, 20.04.2013.)

[4] Martin Bonnet and Hasan Kaytan (2012) Flexidone® - A New Class of Innovative PVC Plasticizers, Recent Advances in Plasticizers, Dr. Mohammad Luqman (Ed.), ISBN: 978-953-51-0363-9, InTech, Available from: http://www.intechopen.com/books/recent-advances-in-plasticizers/flexidone-a-new-class-of-innovative-pvc-plasticizers

[5] Kaytan, H., Bonnet, M. (2008), New innovative PVC plasticizers: N-alkyl-pyrrolidones, in The 10th International PVC Conference, Brighton, IOM Communications Ltd (2008), p. 305

Prototype of a human spinal disc for medical modeling

Melinda Bozzay[1, a],Martin Reiter[1, b] and Zoltán Major[1, c]

[1]Institute of Polymer Product Engineering, Johannes Kepler University
Altenberger Str. 69, 4040 Linz, Austria

[a]melinda.bozzay@jku.at, [b]martin.reiter@jku.at,[c]zoltan.major@jku.at

Keywords:rapid prototyping, spinal disc, medical modelling.

Abstract. Medical images were generated in computed tomography devices at the medical partner. The medical image format was transformed into engineering data format by the authors and these data were used for printing the macroscopic model of the spine and the spinal disc and subsequently they were assembled. In addition to this macroscopic prototyping process, a novel microstructure based prototyping process was used for generating structure details of the spinal disc. The fiber reinforced and layered structure of the annulus fibrosus was modeled and in a prototype realized using soft and stiff polymeric materials. This method is based on the material microstructure prototyping methodology developed by the research group of the authors.This basic model could be used for medical education, for patient counselling and to support prosthesis development efforts.

Introduction

Neurosurgery is complex and delicate, and it is probably the type of surgery most feared by patients. The brain and spinal cord are two of our bodies most important organs and neither can be replaced with a transplant or artificial device if problems arise. Recently, an interdisciplinary cooperation was established between the research group of the authors and a group of neurosurgeons [1]. Medical biomodels for cerebralaneurysms and spinal discs are generated by converting anatomical data into high quality plastic replicas corresponding to complex anatomical structures. These models can be used for accurate prediction of spine and spinal disc anatomy in medical education, for maintenance of established skills for surgical planning (including emergency situations) and for patient counselling. In addition, these models may be applied for verifying finite element simulations of these structures. Furthermore, the knowledge's generated can be used for the development of improved prostheses.

Rapid prototyping (RPT) technologies are available for engineers for several years, and they allow for transforming 3D computer aided design models to real polymer components. To rapidly manufacture prototypes and models using 3D printing technologies, almost any materials (polymers, ceramics, metals) can be used. With an additive fabrication process any 3D model can be built layer by layer. The variety of materials which are available 3D printed prototypes is increasing.

Rapid prototyping technologies like 3D printing techniques allow for 3D imaging data to be translated into accurate solid plastic replicas of anatomical structures. Today, simultaneous 3D printing of multi-material systems seems to be the most promising rapid prototyping technique to produce biomodels which meet the demands of neurovascular surgery. A novel 3D polyjetprinting system (Objet350 Connex, Stratasys, Minneapolis, USA) was used, which jets multiple materials simultaneously and thus has the ability to print parts and assemblies made of multiple model materials over a wide stiffness and elongation scale. We use this technique to create the bone-like structures made from a stiff material, the cerebral vessels, the aneurysm complex was created using a material with less rigid, flexible properties to simulate the tactile feeling of the real aneurysm when it clipped.

Structure of human spine and spinal disc

The ability of the **human spine** to transfer variable loads and perform a broad range of motion is possible due to the complex structure and function of intervertebral discs which, together with vertebrae, are the basic components of the spine.An intervertebral disc consists of two parts; annulus fibrosus and nucleus pulposus [2-6]. An important role in proper operation of the disc is played by annulus fibrosus located externally and made of 15-25 adjoining, concentric layers – lamellae. The lamellae are made of collagen fibres, lying parallel to each other and tilted at an angle of 30° (the internal lamellae are tilted by as much as ~ 45°). The fibres of successive lamellae are arranged alternately and intersect with each other (right/left-hand alignment as so called cross-ply laminates). The structure of the spinal disc with focus on the annulus fibrosus is shown in figure 1.

The nucleus pulposus contains loose fibers suspended in a mucoprotein gel with the consistency of jelly. The nucleus of the disc acts as a shock absorber, absorbing the impact of the body's daily activities and keeping the two vertebrae separated. The disc can be likened to a doughnut: whereby the annulus fibrosis is similar to the dough and the nucleus pulposus is the jelly. If one presses down on the front of the doughnut the jelly moves posteriorly or to the back. When one develops a prolapsed disc the jelly/ nucleus pulposus is forced out of the doughnut/ disc and may put pressure on the nerve located near the disc. The schematic representation of the spinal disc along with the collagen fibers is shown in figure 1.

The objective of this work is to develop a methodology for the modeling and generative fabrication of spinal disc models. The overall methodology consists of the following steps (see figure 2):

- Transformation of medical data (3D CT images) into corresponding engineering data formats (STL files)
- Visualization of these data in Mimics (Materialise, Leuven, B)
- Improvement and modification of the basic model for fabrication using 3-Matic (Materialise, Leuven, B)
- Development of a collagen fiber reinforced lamina model in a micromechanics software tool
- Prototyping both the macroscopic parts (spine segments) and the spinal disc (fiber/matrix).

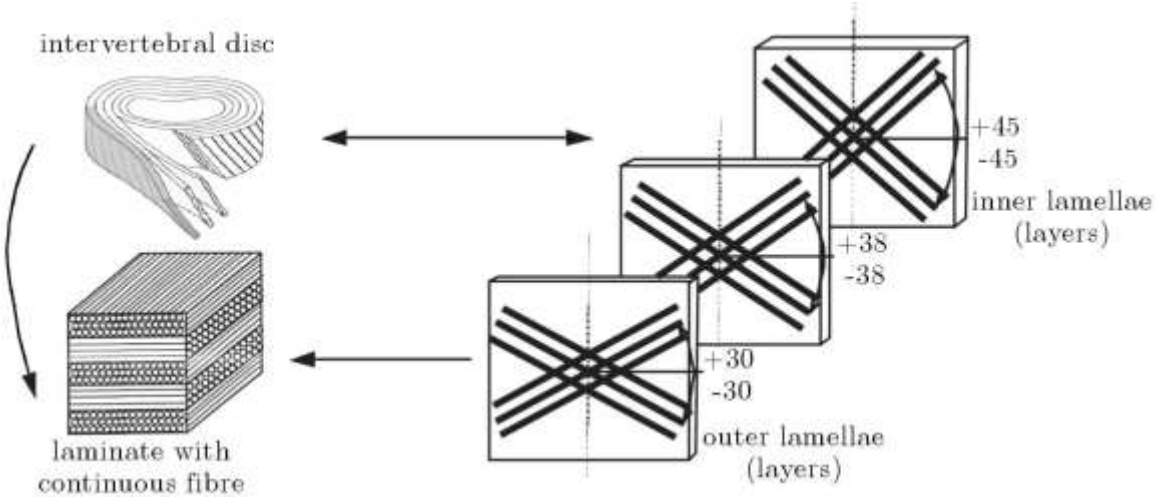

Fig. 1: The changes of collagen fibre angle in subsequent annulus fibrosus lamellae [2].

As it was mentioned above the nucleus pulposus is a fiber reinforced gel-like material. The development of high toughness hydrogels is an objective of another research project of the authors group within cooperation with a Hungarian research partner [7].

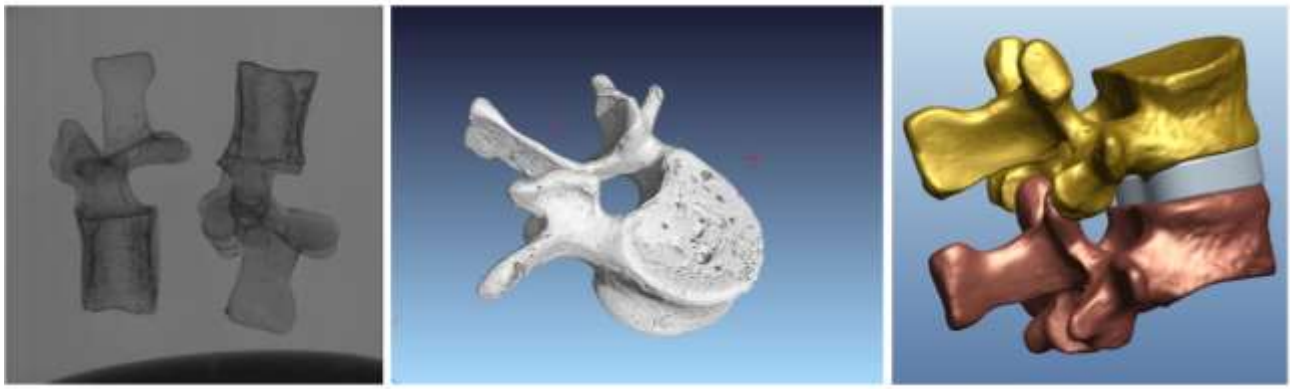

Fig. 2:CT image of a spine segments, the reversed engineered spine segment model, assembly of a spine segment.

Methodology

The microstructure of annulus fibrosus is composed of collagen fibers embedded in the extracellular matrix. Using DigiMat FE software (eXstream engineering, Foetz, LX) we defined the microstructure of matrix and collagen fiber. Fiber and matrix volume fractions were determined to be V_f = 0,15 and V_m = 0,85 based on measurement of collagen content per dry weight (60% dry weight) and water content of 75% [5]. The micromechanics model of single layer including the fibers with predefined orientation is shown in figure 3. The methodology of the micromechanics based structural prototyping was developed by Reiter [8].

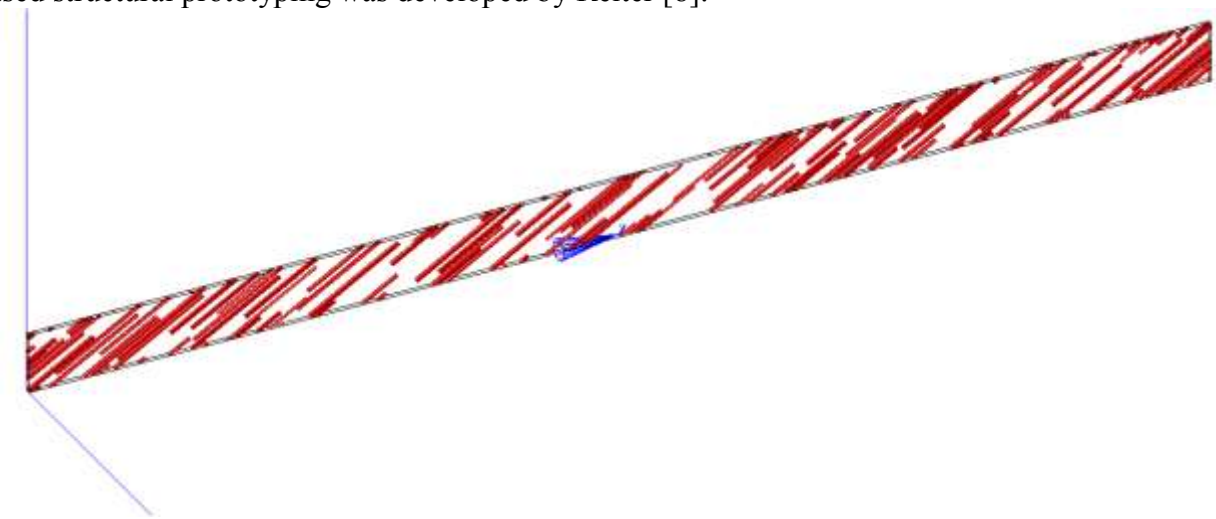

Fig. 3: Definition of a layer including oriented collagen fibersusing by DigiMat FE.

Based on this layer model a corresponding STEP file was generated. After transporting the STEP model to Pro-Engineer, we can bend the collagen fiber models along any type of curve. In this case we defined a half curve of an ellipse. The bending of the layer is shown in figure 4.

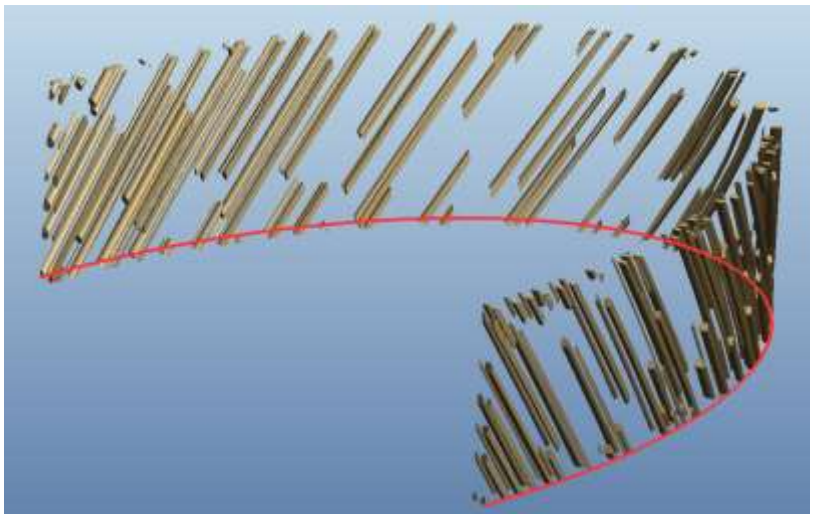

Fig. 4: Bending of layer along a half ellipse curve

Furthermore, all layers were bent around an elliptical curve and the bent layers were assembled. This assembly is containing 7 layers and it is shown in figure 5. The inclination of the fibers and the thickness of the layers were kept constant in all layers. The orientation was changed layer by layer. The outer and inner diameter and the height of the model are in the same range as the corresponding dimensions of an average human spinal disc.

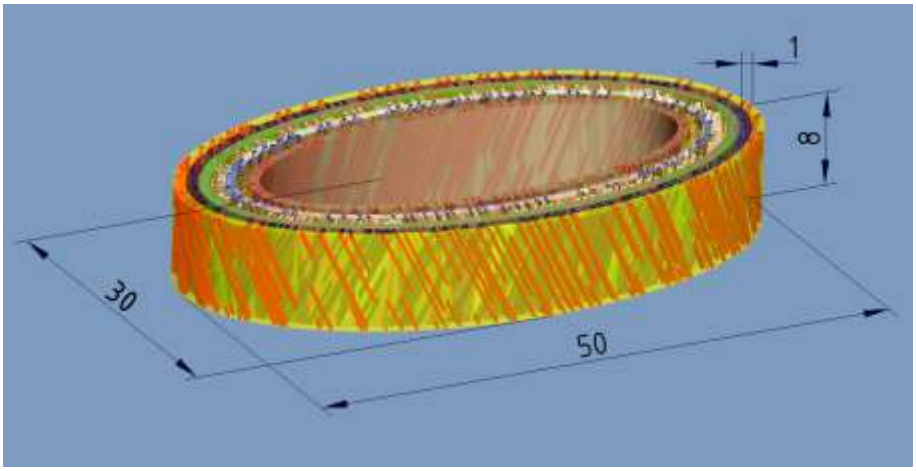

Fig. 5: Final model with 7 layers

Rapid prototyping

The Objet Connex350 (Stratasys, Minneapolis, USA,see figure 6) was used for printing the spinal disc models. To model the extracellular matrix a soft elastomer like material (Tango Black, Objet) was used. The collagen fibers were modeled by a stiffer material (VeroGrey, Objet). The mechanical behavior of these materials was previously characterized and the properties are available in terms of parameters for various material model functions [9].Although, the artificial material properties are far from the real properties of the spinal disc, a model for studying the behavior was generated.

Fig. 6: Objet Connex 3D Printer

A 3D print spine segment, the annulus fibrosus model of the spinal disc and a spine segment assembly is shown in figure 7.

Fig. 7: Prototypes of a spine segment, the annulus fibrosus and an assembly.

In the first step of the future work, this multilayer cross-ply laminate will be modeled in a finite element toll and these results will be verified by proper experiments. A similar procedure as described and used in [8] will be applied. The first step towards this intention was the further development of the basic micromechanics model used for generation of the layer. Based on literature data [5] the real mechanical properties of collagen fibres and extracellular matrix were assigned to the microcell and the mechanical behavior of a single layer was estimated in the linear elastic deformation range. The stress-strain curves of these components are shown in figure 8.

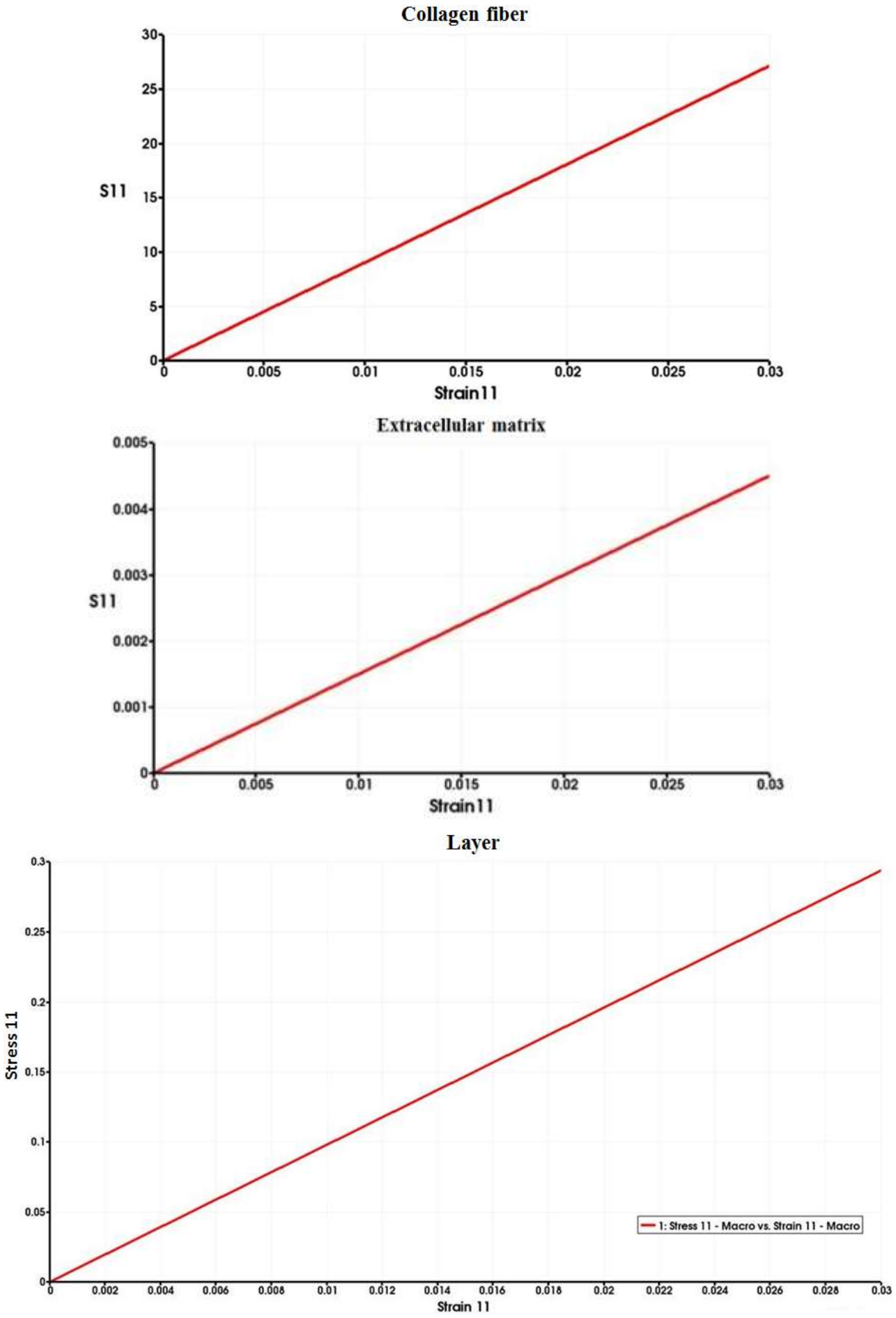

Fig. 8: DigiMat FE Simulation of the linear-elastic behavior of a layer

In further steps, this model will be improvedand the entire layered cross-ply annulus fibrosus structure will be implemented into a finite element tool and the deformation behavior simulated over a wide deformation range while simultaneously considering the inherit viscoelastic behavior of biological tissues.

Summary

Medical models were made from various polymers in a 3D prototyping process. These models can be used for various purposes in the medical praxis. In addition to the medical education in various stages, the surgical planning (including emergency situations) and the patient counselling, these models can be used for verifying numerical simulations of medical structures and organs. Furthermore, based on the comprehensive experience generated by the medical models physical prostheses with improved features can also be developed.

References

[1] G. Wurm, B Tomancok, P. Pogady, K. Holl and J. Trenkler, cerebrovascular stereolithographicbiomodeling for aneurysm surgery, j neurosurg 100:139–145, 2004

[2] C.A. Pezowicz, Analysis of selected mechanical properties of intervertebral disc annulus fibrosus in macro and microscopic scale, Journal of Theoretical and Applied Mechanics 48/4 (2010) 917-932.

[3] F. Marchand, A.M. Ahmed, Investigation of the laminate structure of lumbar disc annulus fibrosus, Spine, 15 (1990) 402-410.

[4] J.J. Cassidy, A. Hiltner, E. Baer, Hierarchical structure of the intervertebral disc, Connective Tissue Res., 23 (1989) 75-88.

[5] J.C. Iatridis, I. A. Gwynn, Mechanisms for mechanical damage in the intervertebral disc annulus fibrosus, Journal of Biomechanics 37 (2004) 1165–1175

[6] D.L. Skaggs, M. Weidenbaum, J.C. Iatridis, A. Ratcliffe, V.C. Mow, Regional variation in tensile properties and biochemical composition of the human lumbar anulusfibrosus. Spine 19 (12) (1994), 1310–1319.

[7] A Szilagyi, K. Sumaru, S. Sugiura, T.Takagi, T. Shinbo M Zrínyi and T. Kanamori, Chem. Mater. 2007, 19, 2730-2732.

[8] Reiter, M. and Major, Z., 2011, A combined experimental and simulation approach for modelling the mechanical behaviour of heterogeneous materials using rapid prototyped microcells, Virtual and Physical Prototyping, Volume 6, Issue, http://www.tandfonline.com/doi/abs/10.1080/17452759.2011.586949.

[9] Z. Major, M. Reiter, E. Hemmeter and F. Hiptmair, Combination of Novel Virtual and Real Prototyping Methods in a Rapid Product Development Methodology (Review article), Polimeri: Plastics and Rubber Journal, Vol. 32 No. 3-4, 2011.

Investigation of the effect of deformation stored energy on the allotropic transformation temperature

Zsolt Csepeli[1,2a *], Péter Bereczki[1,b], Balázs Verő[1,c], Ibolya Kardos[2,d] and Péter János Szabó[3,e]

[1]College of Dunaújváros, Dunaújváros, Hungary

[2]ISD Dunaferr Co. Ltd., Dunaújváros, Hungary

[3]Budapest University of Technology and Economics, Budapest, Hungary

[a]zscsepeli@mail.duf.hu, [b]bereczkip@mail.duf.hu, [c]verob@mail.duf.hu, [d]kardos.ibolya@isd-dunaferr.hu, [e]szpj@eik.bme.hu

Keywords: DIFT, deformation stored energy, austenite transformation temperature, physical simulation, ferrite grain refinement

Abstract. The aim of our investigation was to study the effect of deformation on the start temperature of the austenite-ferrite transformation. The deformation was carried out during cooling before the beginning of the transformation. The transformation start temperature was determined by dilatometric measurement with a Gleeble 3800 thermomechanical simulator. A novel method was developed to study the deformation induced ferrite transformation (DIFT) effect and successful experiments were carried out on S460MC grade steel specimens to determine the effect of the deformation stored energy on the transformation temperature of the austenite. Evaluating the dilatograms a strong relationship was observed between the temperature of the deformation and the austenite transformation start and finish temperatures. Lower deformation temperature resulted finer microstructure after austenite transformation.

Introduction

DIFT process is a promising technology to decrease ferrite grain size at industrial scale. The deformation stored energy increases the A_3 temperature that results in metastable state above the equilibrium transformation temperature and the austenite-ferrite transformation takes place at a larger undercooling than during equilibrium transformation [1,2].

The result of the DIFT process can be an ultra fine grained microstructure with enhanced mechanical properties [3,4]. Using traditional production technologies the smallest attainable ferrite grain diameter is 5 μm, while exploiting the advantages of DIFT process steel strips with 1 μm ferrite grain diameter can be produced [5]. According to the Hall-Petch relationship this grain size reduction results in a significant increase in the yield strength.

The aim of this study was to characterize the effect of the deformation stored energy on the start and finish temperature of the austenite transformation in a Nb microalloyed steel by physical simulation. The effect of the temperature of the deformation on the ferrite grain size was studied by light microscope and scanning electron microscope with EBSD detector.

Experimental procedure

The experiments were carried out on Gleeble 3800 thermo-mechanical simulator equipped with Hydrawedge System. This physical simulator provides a method for simulation of different technological processes even at high temperature on various metals and alloys. Due to the two synchronized hydraulic servo system on each side of the specimen, the applied strain and strain rate can be controlled during the deformation. In addition, the fully integrated mechanical system includes different transducers (for example longitudinal and transversal strain gauges, load cell, dilatometer, etc.), which provides feedback to insure accurate control of the hydraulic compression rams. The heating of the specimen can be realized by a direct resistance heating system. There are

two ways of controlling and monitoring of the temperature of the specimen. One is by thermocouple on four channels and the other is by pyrometer. The thermocouple wires are welded in the middle of the specimen by resistance welding. The testing programs are generated in a Windows-based software. In these programs the mechanical and the thermal systems can be controlled simultaneously in function of time through the specified values of the selected transducer.

In this present examination uniaxial compression tests were performed at high temperature. The cylindrical specimen with 10 mm diameter by 18 mm long was placed between the tungsten carbide anvils. To control the axial strain and strain rate during the compression test, a longitudinal strain gauge was mounted onto the base of the anvils. Moreover, a dilatometer was applied on the cylindrical surface of the specimen in the middle cross section. This transducer with 1 μm resolution ensured the detecting and measuring of the allotropic transition induced changes in the diameter. The dilatometer could roll easily on a bearing in the direction of the deformation. This made possible a fixed contact between the quartz rod of the instrument and the specimen during the complete simulation. The experimental setup can be seen in Fig. 1.

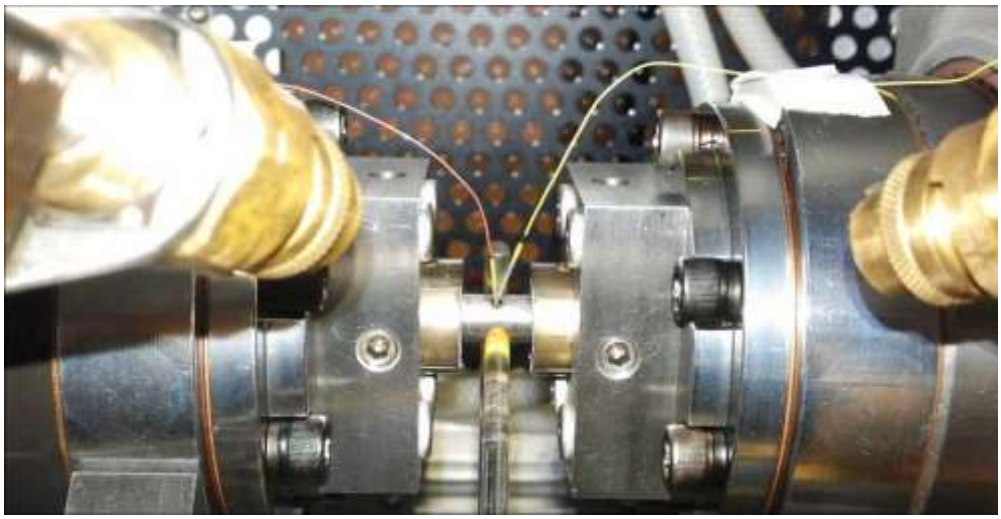

Fig. 1 The experimental setup of the uniaxial compression test

The schematic graph of the testing program is shown in Fig. 2. The specimen was heated up to 950 °C with a rate of 5 °C/s and then was held for 120 s at this temperature for austenitizing the microstructure. After it the specimen was cooled down to the specified temperature of the deformation (T_1) with a rate of 5 °C/s and this temperature was held for 10 s. The characteristic temperatures of the austenite transformation without deformation were determined by JMatPro software and the calculated CCT curve can be seen in Fig 3. During the heat treatment process the thermal expansion was compensated through the control of the mechanical system for zero resultant force. Then the initial height of the specimen was calculated using the axial dilatation. Based on this value, the compression ram deformed the specimen with a rate of 1.0 1/s using the values of the longitudinal strain gauge, until the axial logarithmic strain reached 0.4. The temperature of deformation of the different specimens was 920, 890, 860, 830, 800 and 770 °C.

After the deformation the specimen was cooled down to room temperature in three steps according to the multistep cooling profile in Fig. 2, through the specified intermediate temperatures (T_2, T_3 and 200 °C). The cooling profile was similar to the real cooling pattern of the steel strips. Generally cooling rate after deformation is relatively low until strips reach the water cooling zone, where the cooling becomes more intensive. During the experiments the specimens cooled 175 °C by free cooling and after this intensive cooling the specimens cooled at slower rate again.

During heating and cooling the dilatometer measured the changes of the diameter, so the start and the finish temperature of the allotropic transition could be determined from the dilatograms.

The chemical composition of the investigated HSLA steel is shown in Table 2.

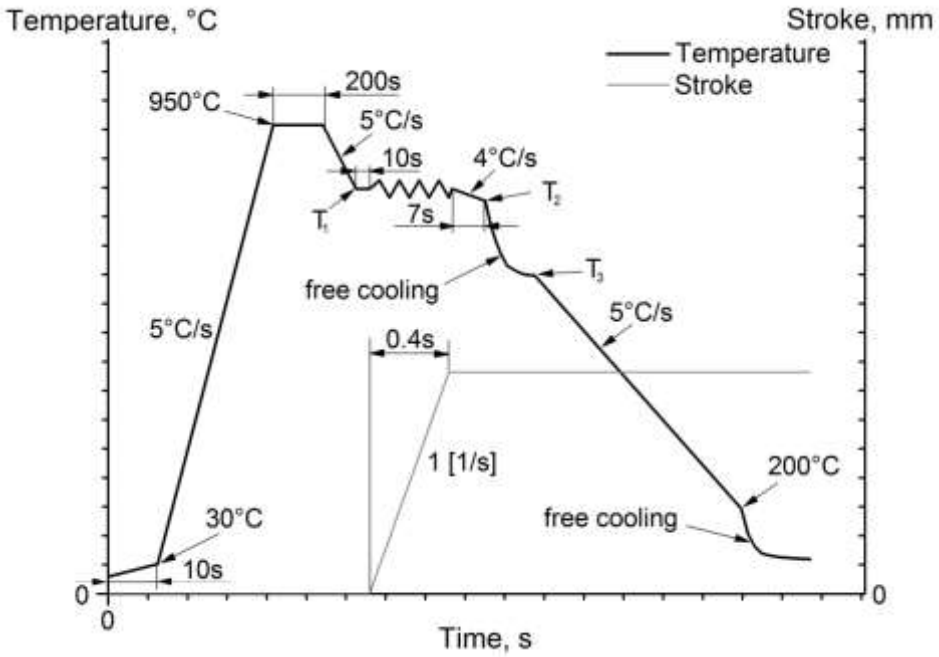

Fig. 2 The schematic drawing of the test program

Table 1. Characteristic temperatures during the experiments

	T_1 [°C]	T_2 [°C]	T_3 [°C]
#1	950	922	747
#2	920	892	717
#3	890	862	687
#4	860	832	657
#5	830	802	627
#6	800	772	597
#7	770	742	567

Table 2. Chemical composition of the investigated steel

Element	C	Mn	Si	S	P	Al	Nb
[mass%]	0.07	1.45	0.016	0.007	0.015	0.076	0.055

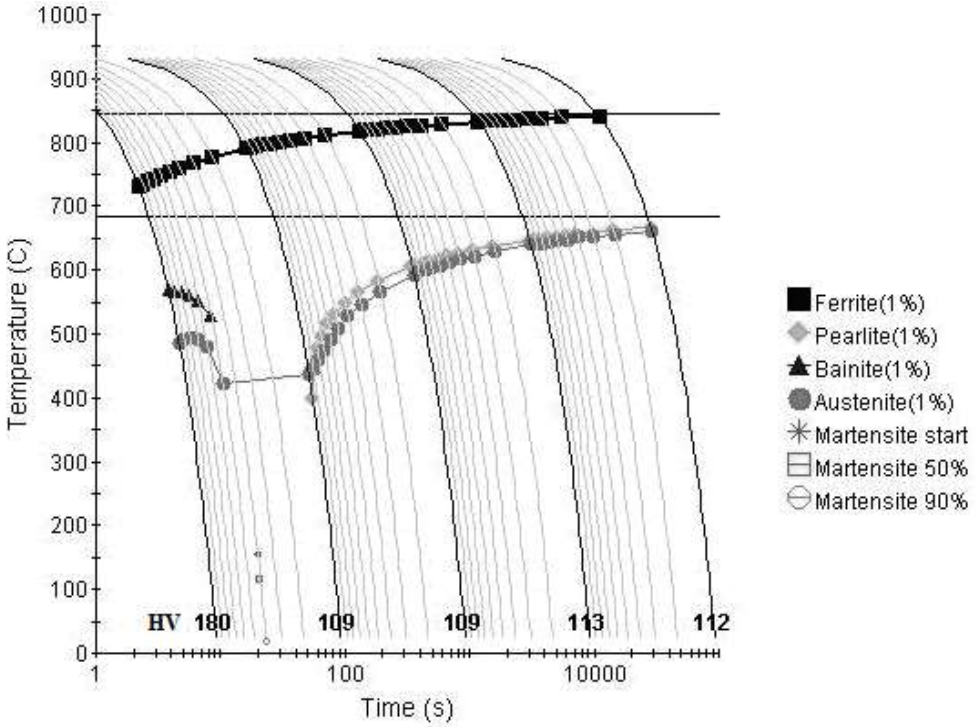

Fig. 3 Continuous cooling transformation diagram of the investigated steel (austenitization temperature = 950.0 °C, austenite grain size : 8.0 ASTM)

Results and Discussion

Typical dilatograms of two experiments can be seen in Fig. 4. The characteristic temperatures of the transformation in the specimen that was deformed at 770 °C could not been determined from the

dilatogram because the transformation started just before or during the deformation and the significant jump in the dilatometric curve during deformation overlaid the effect of the transformation.

The start and finish temperatures of austenite transformation of the other specimens can be seen in Fig. 3. Lower deformation temperature resulted in higher transformation start temperature. When the specimen was deformed at 800 °C the transformation temperature was larger with 23 °C according to the transformation temperature of the specimen deformed at 950 °C. However when the temperature of the deforming was lower, the austenite transformation finished at lower temperature as it is shown in Table 3.

Presumably lower finish temperature is caused by the uneven cooling rate after the deformation. The cooling pattern always included an intensive cooling phase similar to the water cooling of the steel strips in a hot rolling mill. This intensive cooling started always 4 s after the deformation because this is the estimated time that is needed to reach the water cooling zone. When the deformation started at lower temperature, the intensive cooling started at lower temperature as well and this could cause the lower finish temperature of the austenite deformation. In this way the temperature range of the deformation was larger at lower deformation temperature while the rate of the deformation increased as it can be seen in Table 3.

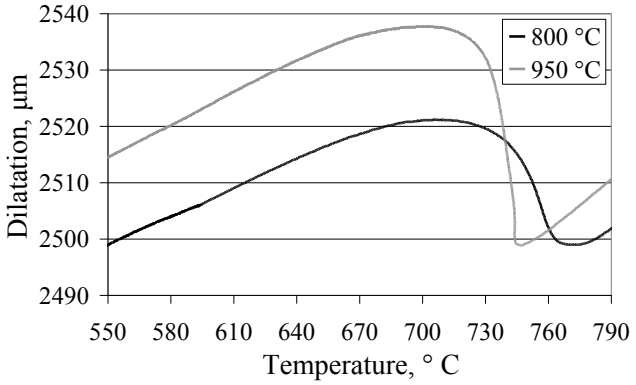

Fig. 4 Dilatation curves of the cooling session after deformation at 800 °C and 950 °C temperatures

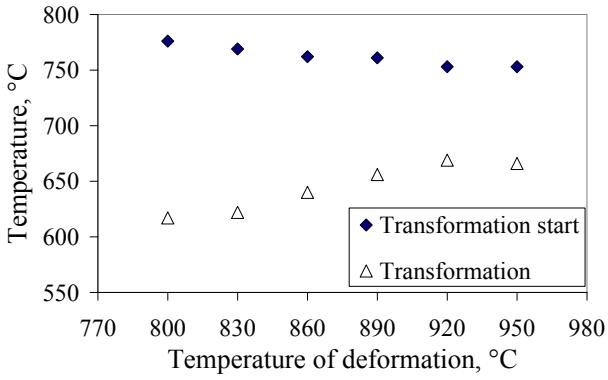

Fig. 5 Start and finish temperatures of the austenite transformation as a function of the deformation temperature

Table 3. Characteristic parameters of the austenite-ferrite transformation after deformation at different temperatures

Temperature of the deformation [°C]	Transformation				
	start temperature [°C]	finish temperature [°C]	temperature range (ΔT) [°C]	time (t) [s]	rate (ΔT/t) [°C/s]
950	753	666	87	84,0	1,0
920	753	669	84	57,3	1,5
890	761	656	105	48,4	2,2
860	762	640	122	39,1	3,1
830	769	622	147	30,7	4,8
800	776	617	159	28,5	5,6

After grinding and polishing, specimens were etched with 2% Nital. Microstructure characterization of all specimens were performed using optical microscopy and two of them were studied in more detail by SEM and EBSD as well to determine their average ferrite grain size. Characteristic microstructure of the specimens can be seen in Fig. 6. Orientation map of the specimens that were formed at the highest and lowest temperatures can be seen in Fig. 7 and their grain size distribution is given in Fig. 8.

In the specimen that was formed at 950 °C the arithmetic average ferrite grain size is 5.6 μm, while in the specimen formed at 800 °C the average ferrite grain size is significantly smaller, 2.2 μm. Taking into account the area that is occupied by the grains the weighted average ferrite grain size is 7.1 μm for specimen formed at 950 °C and 3.8 μm for the one formed at 800 °C.

The pearlite content and size were determined by image analyser on light microscopic images, the measured values were between 3 and 5%. The pearlite content and average area of pearlite decreased with decreasing forming temperature, with the exception of the specimen that was formed at 800 °C.

The specimen that was deformed at the lowest temperature above the transformation start temperature has the same pearlite content and average pearlite size than the specimen formed at the highest temperature that is at 900 °C.

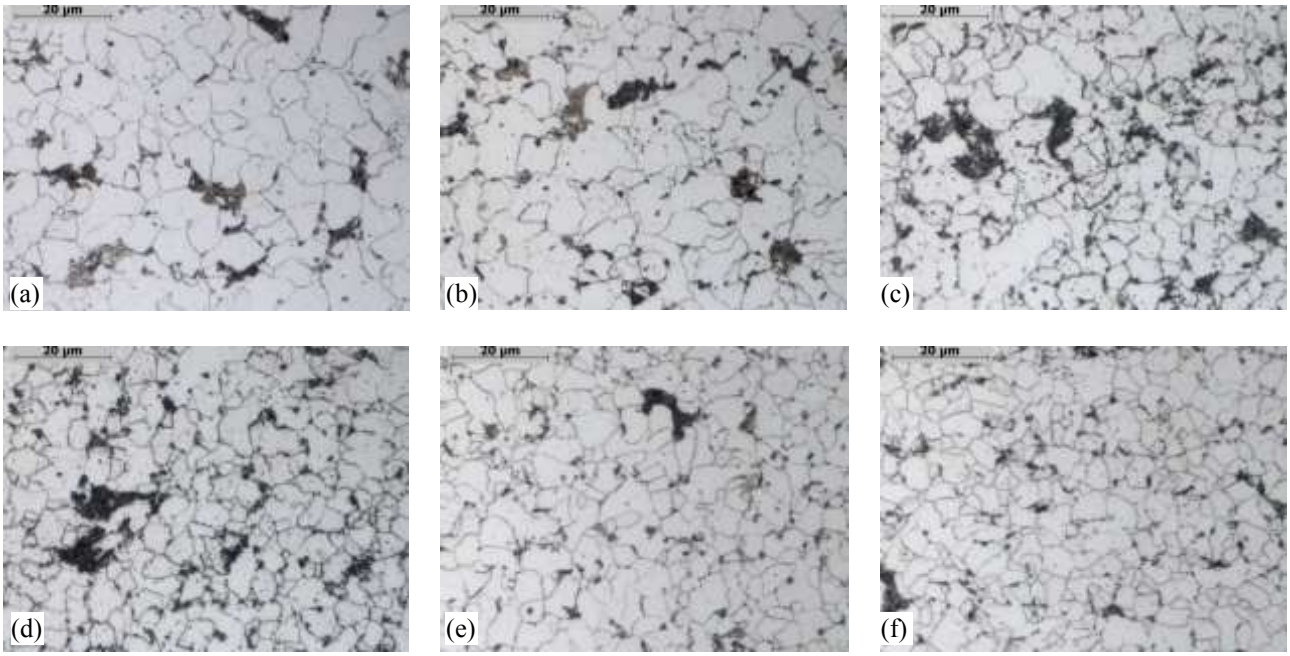

Fig. 6 Micrographs of the specimens deformed at various temperatures. Deformation temperature was (a) 950 °C, (b) 920 °C, (c) 890 °C, (d) 860°C, (e) 830°C, (f) 800°C. (Nital, original magnification: 1000x)

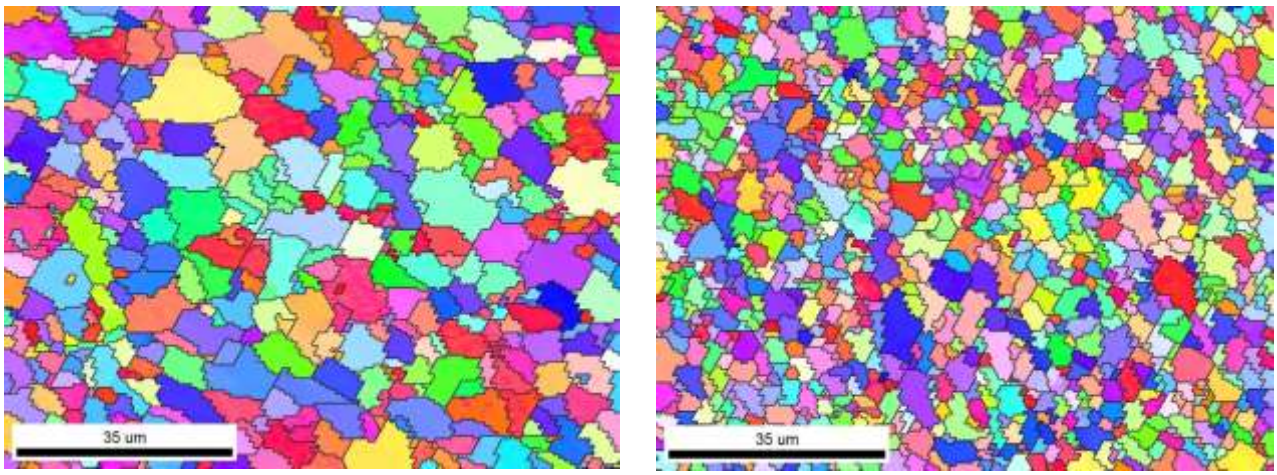

(a) (b)

Fig. 7 Orientation map of two specimens deformed at (a) 950 °C and (b) 800 °C

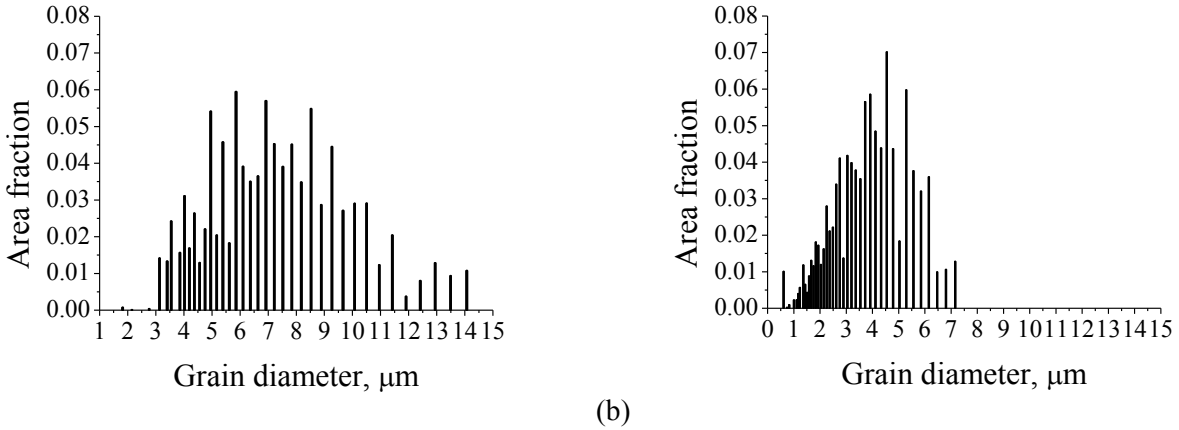

(a) (b)

Fig. 8 Ferrite grain diameter versus area fraction diagram of two specimens deformed at (a) 950 °C and (b) 800 °C

Summary

The effect of deformation stored energy on the austenite transformation temperature and the microstructure was investigated by thermomechanical simulation.

The results of the experiments are as follows:

- A novel methodology was developed to characterize the DIFT effect by dilatometric measurement in physical simulator.
- Based on the dilatograms the start and finish temperature of the austenite were determined after deforming the specimens at nine different temperatures.
- The deformation stored energy during DIFT processing increases the start temperature of the austenite-ferrite transformation and accelerates the transformation.
- Decreasing the deformation temperature a significant grain size reduction was achieved.

The results of the physical simulation experiments can contribute to the development of the industrial production technology of ultra fine grain steels.

Acknowledgement

The work is supported by the TÁMOP-4.2.2.A-11/1/KONV-2012-0027 project. The project is co-financed by the European Union and the European Social Fund.

References

[1] L. Du, C. Zhang, H. Ding, X. Liu, G. Wang, Determination of Upper Limit Temperature of Strain-induced Transformation of Low Carbon Steels, ISIJ International, Vol. 42, No. 10 (2002) 1119–1124.

[2] N. Isasti, D. Jorge-Badiola, M.L. Taheri, B. López, P. Uranga, Effect of Composition and Deformation on Coarse-Grained Austenite Transformation in Nb-Mo Microalloyed Steels, Metallurgical and Materials Transactions A, Volume 42A (2011) 3729-3742.

[3] M. Zhu, G. Xu, D. Luo, J. Wu, F. Luo, Y. Ji, Effect of deformation parameters on austenite transformation and microstructure, Materials Science and Technology (2010) 1336-1341.

[4] J.K. Choi, D.H. Seo, J.S. Lee, K.K. Um, W.Y. Choo, Formation of Ultrafine Ferrite by Strain-induced Dynamic Transformation in Plain Low Carbon Steel, ISIJ International, Vol. 43, No. 5 (2003) 746–754.

[5] Y. Weng, Ultra-Fine Grained Steels, first ed., Springer-Verlag GmbH, Berlin, 2009

Welding properties and fatigue resistance of S690QL high strength steels

Ádám Dobosy[1, a], János Lukács[1,b]

[1]Department of Mechanical Engineering, University of Miskolc, Miskolc-Egyetemváros, 3515, Miskolc, Hungary

[a]metda@uni-miskolc.hu, [b]janos.lukacs@uni-miskolc.hu

Keywords: high strength steels; quenching and tempering; welded joints; high cycle fatigue (HCF); evaluation

Abstract. The objective of this article is to present the first results of our research work. In order to determination and comparison of the fatigue resistance, high cycle fatigue tests (HCF) were performed on RUUKKI OPTIM S690QL quenched and tempered high strength steel. In parallel these; welded joints were made on the same steel using gas metal arc welding (GMAW, MIG/MAG) to preparation of the cyclic investigations of the welded joints. In the article, the performance of the welding experiments will be presented; along with the results of the HCF tests executed on the base material and its welded joints. Furthermore, our results will be compared with different literary data.

Introduction

In our days, the high strength steels play an important role in the welded structures. Under the different claims of applications (e.g. frames, cranes, bridges), complex expectations are evolved with the materials, and the material innovation must follow these tendencies; for example beside the increased strength, preservation of the more deformability. These constructions are often loaded under cyclic stress, so their typical damage form is the fatigue, which means even more complex expectation with the base material.

At the same time, the typical production technology is the welding, which – because of the heat input – modifies the original microstructure of the material. In this way, we achieve totally different mechanical characteristics, which is not allowable in many cases in terms of the construction. Accordingly, there is great significance of testing the welded joints of these steels, and the development of the suitable production technology. On the basis of the complexity of the problems, this article mainly focuses on the fatigue behavior of these steels. We summarized the high cycle fatigue (HCF) examinations, executed both on S690QL quenched and tempered high strength steel base material and its welded joints, and the results of these experiments.

During our experiments, 30 mm thickness base material was used. The main reason for this is, that these steels frequently use in mobile cranes, scrapers, bulldozers structural elements, where the typical thickness is between 60 and 80 mm. The direct examination of this thickness is not practical, but in the terms of the weldability and fatigue features the chosen thickness is just significant.

It is important to note, that the use of the "high strength" attribute, which is featured in the title too, is not unified in the literature, the valid standards do not state the word. At the same time the examined steel group (quenched and tempered steels) is named high strength steels (between 460 and 960 MPa yield strength) by the EN 10025-6 prescription, which is use in Hungary too. But many manufacturers do not use in this way the title.

The authors of the article [1] suggested a possible way to grouping these steels. Accordingly to that steels can be titled as high strength steels (HSS) between 600 and 1200 MPa minimal tensile strength, therefore the S690QL steel group examined by us, too. This grouping can be seen in Fig. 1.

As we can see, the examined steel group belongs to the middle section of the high strength steels, their minimum tensile strength is 770 MPa ($R_{eH} \geq 690$ MPa), but even 850 MPa can be reached. In the marking of the steel, the „L” means that this group can be used at negative temperatures, for

example mobile cranes [2]. Namely, the outstanding strength of these steels can be achieved not only with heat treatment, but with alloying and with using of special production technology. The result is a complex phase: ferrite with tempered martensite and bainite.

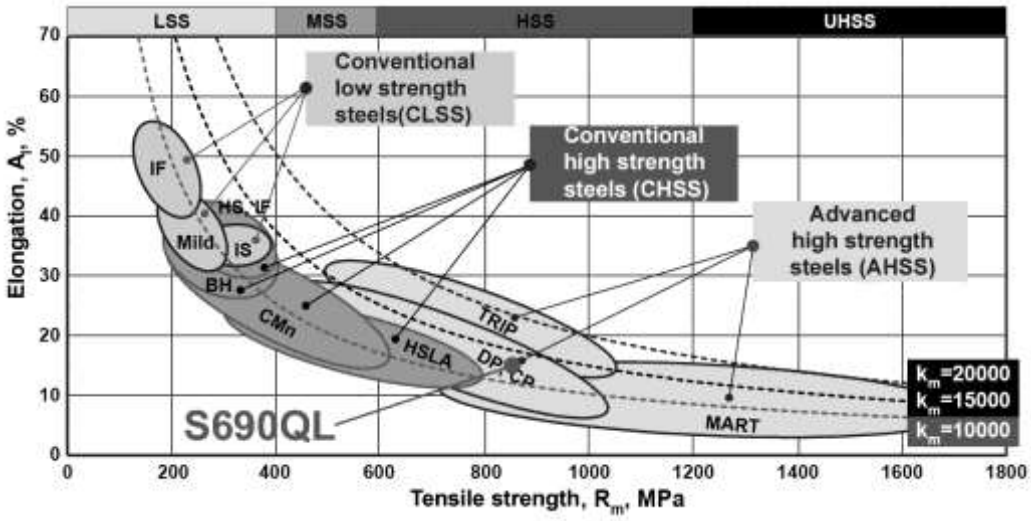

Fig. 1. Different conventional and advanced high strength steels [1].

As we can see, the production of the high strength steels results in nonequilibrium microstructure, which alters the welding process irreversible, hence the original microstructure can be not repositioned after the welding. The heat effected zone can be easily hardened, furthermore in case of too large heat input the heat effected zone can be softened comparing to the base material, which can be caused strength and hardness decreasing. Further undesirable phenomena can be appear: different types of cracks. Primarily the cold cracking, on behalf of avoidance the workpiece must be preheated before the welding, and it is necessary to limit the linear energy, too. At the same time it is necessary to attend to the risk of the appearance of the hot cracking.

Welding experiments

In the case of the S690QL high strength steels, one of the most important features of the successfulness of the weldability is the linear energy. If the value of this is too low, the cooling rate of the welded joint may be too fast, and then cold cracks can be developed. In the opposite case, strong coarse grained microstructure can be evolved in the heat affected zone, which can be caused the decreasing of the strength and toughness features. Therefore, a narrow welding lobe was received; inside this the quality of the joint may be suitable. It is necessary to note that the smaller linear energy is more beneficial based on the experiences, in the case of the welded joint strength, toughness and residual stresses [3]. Beside the linear energy, the preheating and the interpass temperatures are significant too, that the quality of the joint is defined collectively. In the practice, the cooling time ($t_{8,5/5}$) can be used to manage these features, which has a narrow range too, in the case of S690QL steels it is generally 6 – 15 s.

Based on the previous statements, we made welding experiments on S690QL quenched and tempered base metal with 30 mm thickness ($R_{p0,2}$ = 809 MPa, R_m = 850 MPa, A = 17 %). The aim of the welding experiments was to qualify our welding technology, and make usable welded joints for different kind of examinations, mainly for high cycle fatigue tests.

For the welding experiments we chose the gas metal arc welding (GMAW), because these steels are welded mostly with this procedure. Based on industrial experiences too, we chose M21 mixed gas with 18 % CO_2 + 82 % Ar as shielding gas. As filler material, we chose Inefil NiMoCr wire with 1,0 mm diameter, which is a matching filler material in the case of the base material. In the interest of the uniform stress distribution, we designed X joint preparation, and during the welding we rotated the test specimen regularly.

In order to reaching the cooling time between 6 s and 15 s we used the following welding parameters shown in **Hiba! A hivatkozási forrás nem található.**.

Table 1. Welding parameters.

Welding pass	Current type	Current [A]	Voltage [V]	Welding speed [cm/min]	Wire speed [m/min]	Linear heat input [J/mm]
1.	DCEP	130	19	20	5.5	800
2.	DCEP	145	20	20	6	800
3-8.	DCEP	260	29	40	13	1000
9-20.	DCEP	250-260	28-29	35-45	13	1000-1200

For preheating temperature 150 ^{o}C, and for interpass temperature 180 ^{o}C were prescribed. Welding parameters were recorded continuously during the experiments with the help of WeldQAS process monitoring device. Besides all these regulations, the linear energy was between 800 J/mm and 1200 J/mm. The experimental composition is shown in Fig. 2.

Fig. 2. The composition of the welding experiments.

High cycle fatigue tests on base materials

In the interest of the welded joints of the S690QL steels resistance against the cyclic loading, we made experiments on the base material and there welded joints. We performed high cycle fatigue (HCF) experiments on the base material with MTS 810 electro-hydraulic materials testing equipment, at room temperature and on laboratory environment. We used flat test specimens weakened with 92,5 mm radius, the specimen thickness was 6 mm and their width was 24 mm. We applied constant load amplitude during the experiments, with R = 0,1 stress ratio, f = 30 Hz loading

frequency, and sinusoidal loading wave form. The test equipment and the geometry of the test specimens are shown in Fig. 3.

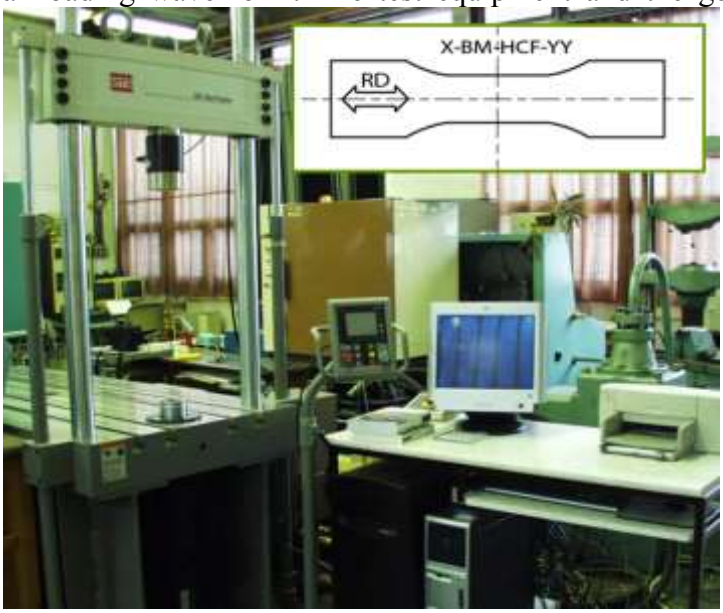

The results of our experiments we compared with some data can be found in the literature [[4][6] and we present these in a common diagram (Fig. 4.). In the case of the steel D38MSV5S (0,384 wt% C, 5,67 wt% Si, 1,23 Mn wt% etc.) the $R_{p0,2}$ = 608 MPa, R_m = 878 MPa, A = 20 % [[4], in the case of the S690 steel the R_{eH} = 733 MPa, R_m = 787 MPa, A = 17 % [[5], while in the case of S690QL steel the $R_y \geq 690$ MPa, R_m = 770-940 MPa, A ≥ 14 % [6].

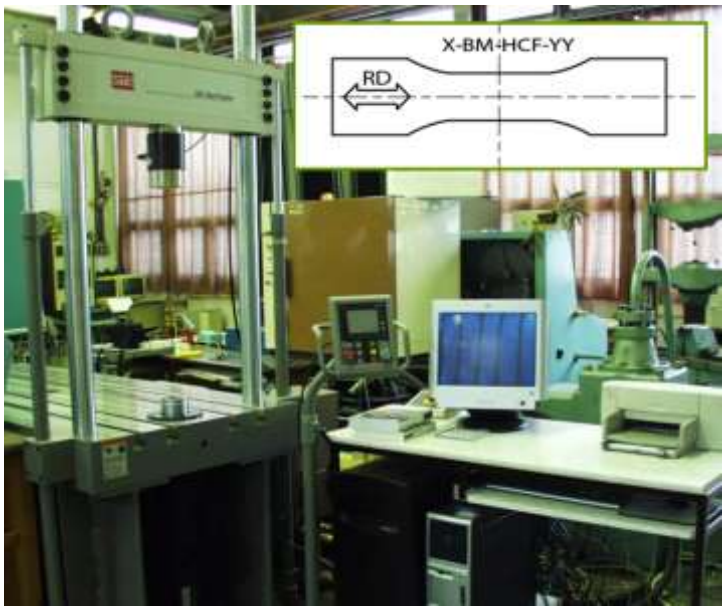

Fig. 3. The test equipment and the specimen geometry of the high cycle fatigue (HCF) experiments.

Based on Fig. 4. we can state that the high cycle fatigue resistance of the examined base material (black squares) is considerable and is in accordance with the data can be found in the literature [4]. The difference compared with the other results probably caused by the different parameters of the experiments, such as the different stress ratio (R) or the different testing frequency (f).

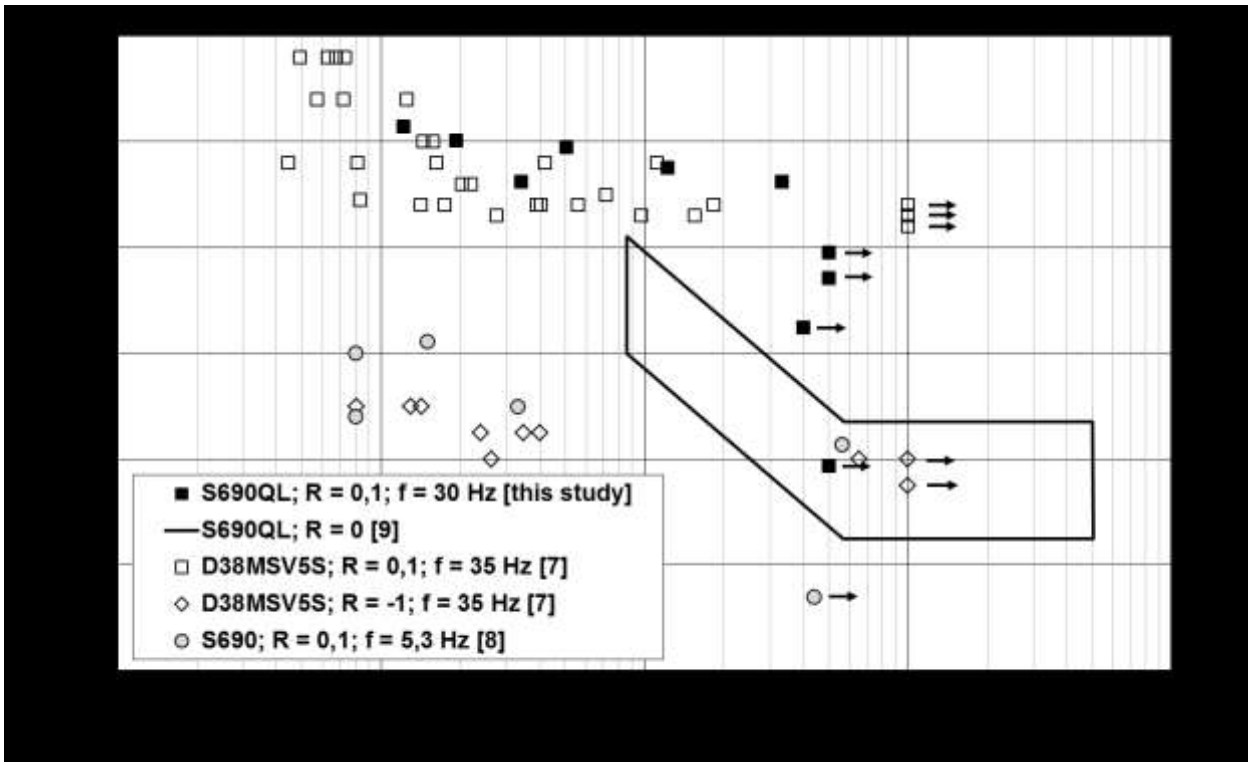

Fig. 4. Results of high cycle fatigue (HCF) tests on base materials.

High cycle fatigue tests on welded joints

After that we finished and evaluated the high cycle fatigue experiments on the base material, we made test specimens from the welded joints, present in the previous point and shown in the Fig. 5. We also made high cycle fatigue experiments on these specimens.

Fig. 5. The welded joint for the high cycle fatigue experiments.

On behalf of comparison we changed nothing on the experiment conditions, only slightly changed the test specimens shape. So, we also used MTS 810 electro-hydraulic materials testing equipment, at room temperature and on laboratory environment. On the test specimens we take into consideration that the welded joint must locate in the center line of the specimens, so the specimens itself must take out from the center of the welded plate, sheer to the surface. Since we used X shape joints the weakest part of the welded joint locate this region. The flat test specimens weakened with 60 mm radius, the specimen thickness was 6 mm and their width was 30 mm, therefore the critical section was a 6x8 mm rectangle section. We also applied constant load amplitude during the

experiments, with R = 0,1 stress ratio, f = 30 Hz loading frequency, and sinusoidal loading wave form.

Just like previously we compared the results of our experiments with some data can be found in the literature [6] and we present these in a common diagram (Fig. 6). In this figure we present our results both on the base material and their welded joints, too. At the same time we had shown the literature [6] results on behalf of comparison; these data also refer to base material and welded joints.

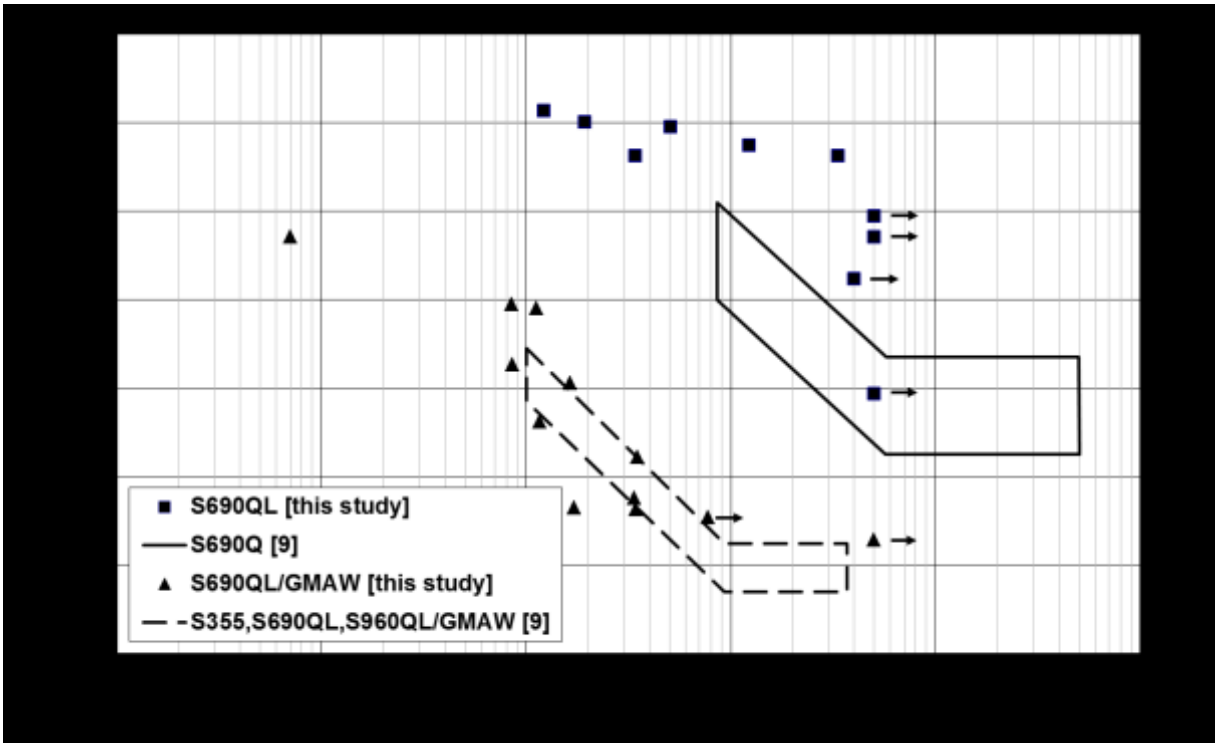

Fig. 6. Results of high cycle fatigue (HCF) tests on base material and welded joints.

It is important to note, that in this article [6] the applied welding process was also gas metal arc welding, but they examined full butt weld joints and we examined test specimens take out from butt weld joints. Even so it is state, that the results of the welded joints are similar, even though the stress ratio is also different. Furthermore it is clearly shown, that the fatigue resistance of the welded joint is less than the base material resistance.

Therefore, the microstructural changes during the welding process affect negatively not only the strength properties, which was examined previously [7], but also the fatigue features as well. But for correct assessment we need more experiments, which we will realize in the future.

Summary

Based on our first investigations and their results the following conclusions can be drawn.

- According to the completed welding joints, the developed welding technology and the determined welding parameters are suitable for making welding joints with an adequate quality.
- Based on the high cycle fatige (HCF) tests on the base material and their welded joints, the fatigue limit of the base material is relatively high (approximately 70% of the R_m value), at the same time the fatique limit of the welded joints is lower.
- The welding cycle effect negatively both on the mechanical properties (see our previous experiments [7]) and the fatigue resistance.
- Our results are in harmony with the results can be found in the literature.

Acknowledgements

The research work presented in this paper/study/etc. based on the results achieved within the TÁMOP-4.2.1.B-10/2/KONV-2010-0001 project and carried out as part of the TÁMOP-4.2.2/A-11/1-KONV-2012-0029 project in the framework of the New Hungarian Development Plan. The realization of this project is supported by the European Union, and co-financed by the European Social Fund.

References

[1] A. Balogh, M. Gáspár and L. Prém, Classification and welding difficulties of conventional and advanced steels for welded structures, Gép. 64 (2013) No. 8 7-12. (In Hungarian.)

[2] R. Wilms, High strength steels for steel constructions, in: Proc. of the Nordic Steel Contruction Conference, Malmö, 2009. pp. 597-604.

[3] Welding Hardox and Weldox, SSAB information on http://www.ssab.com

[4] I. Marines-García, D. Galván-Montiel and C. Bathias, Fatigue life assessment of high-strength, low-alloy steel at high frequency, The Arabian Journal for Science and Engineering. 33 (2008) No. 1B 237-247.

[5] R. J. M. Pijper, et al., Fatigue experiments on very high strength steel base material and transverse butt welds, Advanced Steel Construction. 5 (2007) No. 1 14-32.

[6] U. Hamme, et al., Einsatz hochfester Baustähle im Mobilkranbau, Stahlbau. 69 (2000) No. 4 295-305.

[7] Á. Dobosy and M. Gáspár, Welding of quenched and tempered high strength steels with heavy plate thickness, in: Proc. of the 27th microCAD International Multidisciplinary Scientific Conference, Miskolc, 2013.

Quality control methods of Al_2O_3 based ceramic injection molding raw materials

Ádám Egész[1,2,a] , László A. Gömze[2]

[1] Department of Ceramics and Silicate Engineering, University of Miskolc, Miskolc, Hungary
[2] GE Hungary Ltd., Budapest, Hungary
[a] adam.egesz@ge.com

Keywords: alumina powder, paraffin wax, ceramic injection molding, laser granulometry, thermal analysis, rheological analysis

Abstract. In the illuminant industry, for producing arc tube parts for high intensity discharge lamps the applied method is the ceramic injection molding. The ceramic arc tube parts are made of high purity alumina powder. By producing ceramic parts, one of the most critical step is to optimizing the injection molding process, [1] but first of all we need to know the properties of injection molding raw material, because later the molding process will be optimized for this material, to decrease the amount of cracked ceramics.

For producing ceramic arc tube parts (plugs), there are used two different major components for producing injection molding raw material (feedstock): high purity alumina powder as the main component, and an organic paraffin wax as a binder material. It is expressly important to know the material, physical and chemical properties of these components, since mainly these have affect on the homogenity of feedstock, and therefore on the quality of end product. [3]

In this research, both of the main components and the moldable raw material was investigated by visual, physical, chemical and thermal methods. As most important and main statement, the researchers found that the dynamic viscosity of the injection molding raw material depends on the used mixer equipment and the applied deformation velocity.

Applied analitycal methods were laser granulometry, differential thermal analysis, and rheological analysis.

Introduction

Powder injection molding (PIM) has emerged as a viable method of producing complex shaped parts at a competitive cost. The PIM process, which consists of feedstock preparation, injection molding, debinding and sintering uses a combination of powder metallurgy and plastic injection molding technologies to produce net shape metal, ceramic or hard materials components. Several studies give a guideline as to when to consider PIM as a manufacturing technique. PIM is usually used for complex components, product made of metal, ceramics or other sinterable materials and well usable in mass production. The technology is well established for standard materials, like stainless steel or oxide ceramics. The importance of feedstock homogeneity has been pointed out by both part manufacturers and researchers alike, all agreeing that variations induced in the early process stages cannot be eliminated in the subsequent PIM process steps of molding, debinding and sintering. Therefore, the homogeneity of the feedstock can become a critical characteristic for these later process steps in the PIM process. Inhomogenities can lead to powder/binder separation, defects (e.g. cracks and voids) or increased distortion and eventually to failure of the PIM manufacturing route. [1,2]

Producing the feedstock, the wax is heated in a sigma-blade mixer, and the alumina powder is sequentially dosaged to the molted wax material. The given, properly homogenized mixture is cooled down, and broke in jaw crusher to get granules from it. This granules now is usable for the ceramic injection molding process.

As earlier mentioned, to know the physical, chemical and thermical properties of the given feedstock granules is absolutely necessary, if we would like to set up an efficient injection molding process, which results a quality end product as well. [3,4,5,6]

Experimental
To qualify the alumina powder and feedstock raw material, the following measuring methods were tested:

Laser granulometry. By qualifying the aluminum-oxide powder, absolutely necessary to use the laser granulometry method to determine the grain size distribution of the usable powder. Using this method, it is possible to determine, that the powder in which amount contains the different sizes of grains, and this way, we can predestine the quality of end product. In addition, using this method, if we know the grade of polydispersity, and the given grain distribution, we can conclude to the compaction and volume filling properties of the powder, and thus the density of the end product. [5,6,8.9,10]

Differential thermo analytics. The effect of heat occurring endotherm and exothermic reactions in solid materials can be measured using the well-known differential thermo analytics method. The investigated material heated together with a comparative material (inert material). In the inert material does not occur any endothermic or exothermic transformation in the using temperature range. Using this measurement, the phase transformations – and temperatures - are determinable in different materials, like the melting, evaporation or inflammation temperature. [11,12,13,14,15]

In our case it seems to be very important, when we would like to identify the injection molding work temperature of the used raw material, since the process have to be adjusted to the proper temperature, which is above the melting temperature, but it is under the intensive evaporation temperature, to avoid the material loss during the injection molding process.

Rheological test. By injection molding it is absolutely necessary to know the rheological properties and behavior of raw materials, especially its viscosity. Mainly, this property defines the behavior of the material during injection molding, and identifies the flow behavior in the molding tool, thus it can have effect on the quality of end product. [16,17,18,19]
To define the viscosity of feedstock, dynamical rotation rheometer was used. (Fig. 1.)

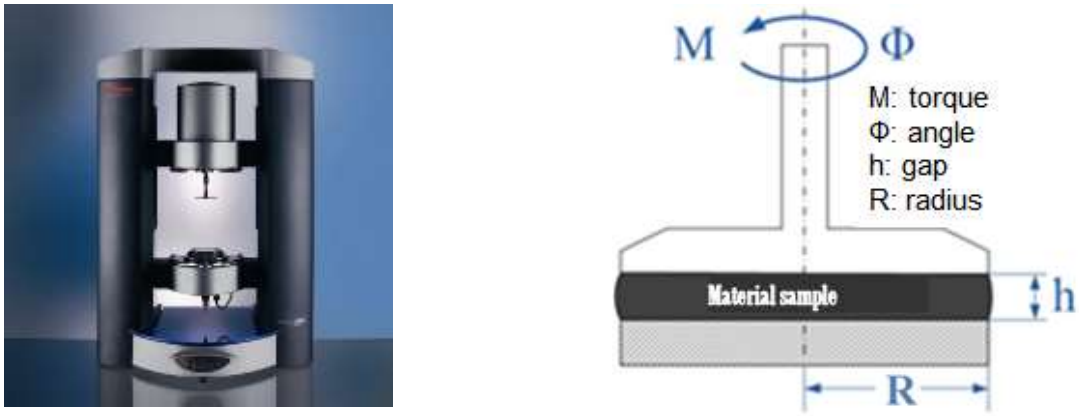

Fig. 1. The applied dynamical rotation rheometer and the principle of operation of rotation rheometer

Besides of the raw material, to know the rheological properties of wax binder material can be also important, since mainly the binder material defines the rheological behavior and viscosity of injection molding raw material. [20,21,22]

Results and discussion

Laser granulometry. The first measurement to qualify the properties of powder is the laser granulometry to investigate grain size distribution. The method is able to determinate the typical grain size and grain distribution of aluminum-oxide powder

In the following, a raw, unmilled and a 10 minutes in vibration ball mill milled alumina powder were compared. On Fig. 2 we can see the grain distribution curve of unmilled powder, where we can observe the two peaks on different grain sizes, which refers to the earlier mentioned polydisperse grain distribution.

The shape of curve of milled powder is clearly different (Fig. 2.). We can see, that the second peak is higher, but closer to the first peak in the smallest grain size range, which refers to the less larger particles and less polydisperse properties of powder, but better compaction properties and higher density, thanks to the more small particles.

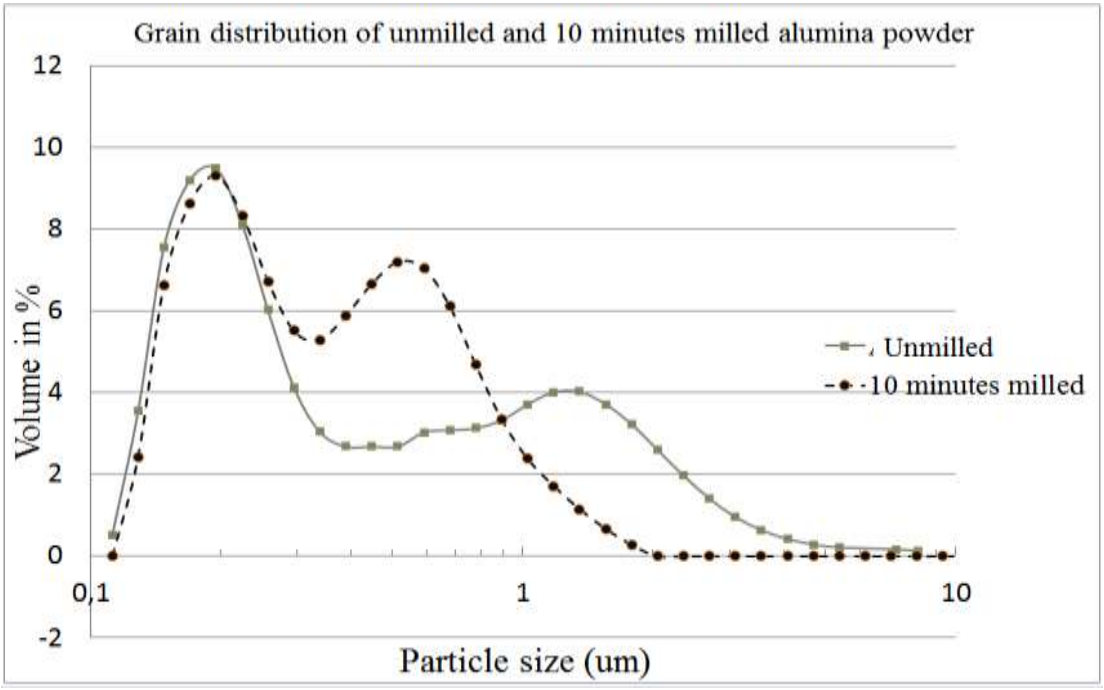

Fig. 2. Grain size distribution of unmilled and 10 minutes milled alumina powder

Differential thermo analytics. The method is usable to investigate the behavior of injection molding raw material in the function of temperature. For the played out processes we can conclude from the weight changing of material. The feedstock material was experimentally tested, the derivatograph of thermal analysis can be seen on the Fig. 3.

We can observe the melting point (T_m) on the first negative peak, the evaporation point (T_e) on the first positive peak and the flashpoint (T_f) on the second positive peak of the material on the DTA curve.

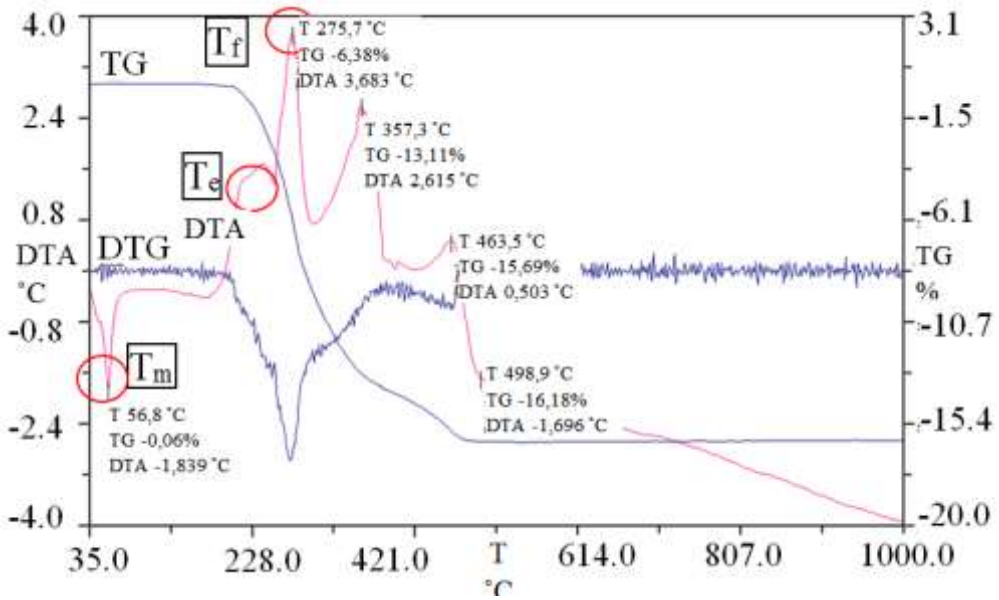

Fig. 3. Derivatograph of injection molding raw material

Rheological test. The reological properties of raw material we can investigate using dynamical rotation rheometer to define the flow properties of material on different shear velocities. This measurement is very important because the flow properties of the material has influence on the injection molding process, and thus on the quality of end product.

In this research, experimentally compared the viscosity of feedstock raw materials made with different types of mixing machines. The applied mixers were the following:

Normal-blade mixer: this type can mix the material the less homogenous due to it's simple formation. (Fig. 4.)

Z-blade mixer: this type of mixer can provide a more homogenous mixing, because the gaps between the blades are more narrow, and in this way, the shear stress - what affect on the material - can be higher. (Fig. 4.)

Fig. 4. The interior of normal-blade mixer and the Z-blade mixer

Shear roll mixer: in this type, the material is mixed between two counter-rotating rolls and move continuously axially, until the mixed material falls in the end of the rolls. One of the rolls is fully spiral, what can bear the material, while the flat roll kneads the material with extremely high shear stress. In this way, theoretically this kind of mixer can provide the most homogenous mixing process. [23,24,25]

The dynamical viscosity of the different mixer made materials were investigated on 65 °C, and can be seen on the Fig. 6.

As we expected, the normal blade mixer made feedstock material has the highest viscosity, since the equipment due it's simple design could not disperse the aluminum powder among the wax material sufficiently. In this case, next to the binder friction, there is still a powder-powder friction in the material, which increases it's viscosity.

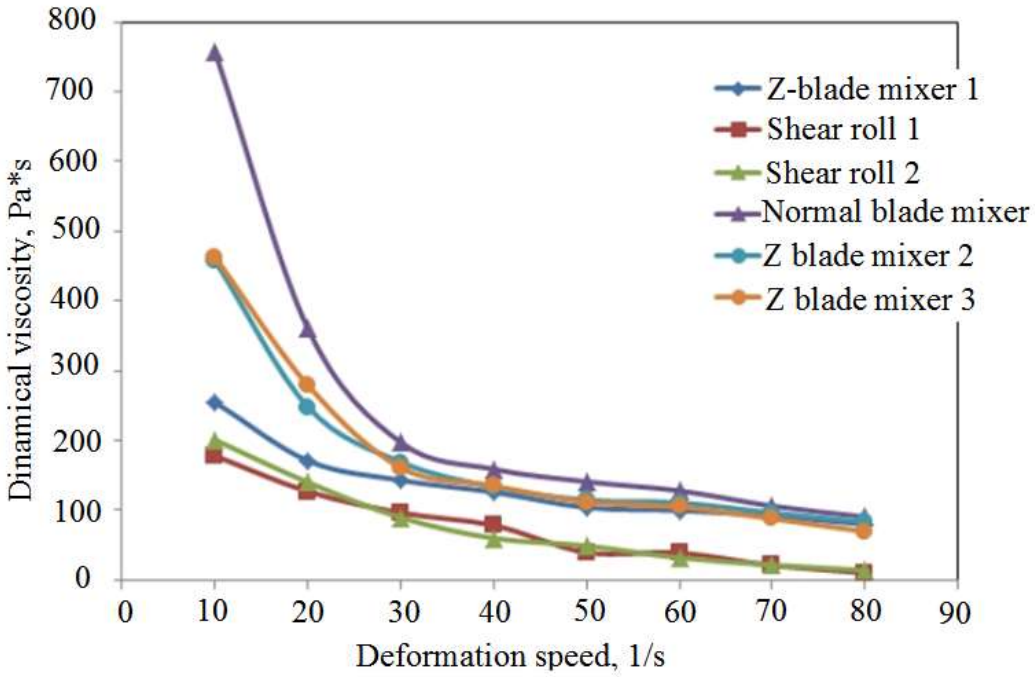

Fig. 6. Dynamical viscosity of the different mixer-made materials

However, we can observe, that the shear roll mixer made material has extremely low viscosity, probably there is no powder-powder friction anymore, the dominant viscosity is the viscosity of wax binder material.

Conclusions

It could be seen, that the investigated measuring methods are able to qualify either the aluminum-oxide powder, or the mixed injection molding raw material. Using these investigations, the quality of the raw materials are determinable, and possible the classification before usage. Testing these methods, very important statements were determined in the optimization of injection molding process point of view.

Measuring the alumina powder using laser granulometry it is possible to determinate the grade of polydispersity of the powder, and in addition, the grade of polydispersity can be reduced in the aluminum-oxide powder using vibration ball mill, to enhance the volume filling.

The injection molding material is well-characterized by DTA, to establish evaporation, melting and inflammation point, and to determinate the temperature work point during injection molding of the usable material .

The dynamic viscosity of the material exponentially decreases with the increasing deformation speed. In addition, it was observed, that the rheological behavior of raw material extremely depends on the applied mixer, the viscosity is decreasing with the increasing applied shear stress.

References

[1] B. C. Matsuddy, Ceramic injection molding**,** Chapman and Hall, 1995.

[2] B. Hausernova, L. Marcanikova, Rheological characterization of powder injection molding using feedstock based on aluminum oxide and multicomponent water-soluble polymer binder, Proceedings of Recent Advances in Fluid Mechanics and Heat & Mass Transfer, (2011) 245-250.
[3] V. A. Krauss, E. N. Pires, A. N. Klein, Rheological properties of alumina injection feedstocks, Materials Research, 8, 2 (2005) 187-189.
[4] Z. S. Rak, New trends in powder injection molding. Powder Metallurgy and Metal Ceramics, 38, (1999) 126-132
[5] W. C. J. Wei, R. Y. Wu, S. J. Ho, Effects of pressure parameters on alumina made by powder injection molding, Journal of the European Ceramic Society, 20 (2000) 1301-1310.
[6] H. Q. Yin, C. C. Jia, X. H. Qu, Micro powder injection molding—large scale production technology for micro-sized components, Science in China Series E: Technological Sci., 51 (2) (2008) 121-126.
[7] W. H. Gitzen, Alumina as a ceramic material, The American Ceramic Society, 11 (1970) 68-78.
[8] G. L. Messing, W. McCauley, K. S. Mazdiyasni, R. A. Haber, Advances in ceramic, ceramic powder science, The American Ceramic Society, 21 (1987) 198-207
[9] F. Filser, L. J. Gauckler, Keramische Werkstoffe, Kapitel 4: 4 Beispiele für strukturkeramische Werkstoffe, ETH-Zürich, Department Materials, 2006
[10] J. Tamásné Csányi, Alumínium-oxid porkerámiák alakadási technológiai paramétereinek optimalizálása, különös tekintettel a mechanikai tulajdonságokra és a mikroszerkezetre, PhD értekezés, Miskolc, 2007
[11] S. Shiegeyuki, Handbook of advanced ceramics, Amsterdam, Elsevier. 1. (2003) 365-369.
[12] J. Enrique, E. Ochandio, M. F. Gazulla, „Chemical analysis," in engineered materials handbook, ASM International, Materials Park, OH. 4 (1997) 125-138.
[13] J. E. Funk, D. R. Dinger, Particle Packing, Part 2. Review of particle packing of polydisperse particle system, Interceram, 41 (3), (1992) 176-179.
[14] F. Stringer, S. Mende, Nanomilling in stirred media mills, Chemical Engineering Science 60 (2005) 4557-4565.
[15] W. Paukert, Material properties in fine grinding, Int. J. Miner. Process. 74 (2004) 3-17.
[16] H. Barth, Modern methods of particle size Analysis, Wiley-Interscience, New York, 1985
[17] T. Allen, Particle size measurement, Wiley-Interscience, New York, 1981
[18] S. Serkowski, M. Müller, Vacuum granulation of ceramic powders – Device and ability, Journal of Materials processing Technology 5 (2005) 458-471.
[19] S. Lowell, J. Shields, Powder surface area and porosity, Chapman and Hall, New York, 1984
[20] L. Cotica, F. Paesano, High energy ball-milled (Fe2O3) (Al2O3) system: A study on milling time effects, Journal of Alloys and Compound, 24 (2005) 45-54.
[21] B. C. Matsuddy, Influence of powder characteristics on the rheology of ceramic injection molding mixtures, Fabrication Sci., 3, Proc. Brit. Ceram. Soc., (1983) 117-137.
[22] M. J. Edirisinghe, J. R. G. Evans, Rheology of ceramic injection molding formulations, Ceram. Trans. J. 86 (1987) 18-23.
[23] T. Tanaka, Injection molding of alumina, Yogyo-Kyokai-shi, 93 (1985) 572-576.
[24] M. J. Cima, J. Lewis, Binder distribution in ceramic greenware during thermolysis, New York, 1989.
[25] J. Csányi, Rheological characteristics of alumina powders in dry pressing technology, Építőanyag, 61 (1), (2009) 6-10

Deposition of nanostructure ZnO with variable morphology by electrochemical and hydrothermal methods onto nonwoven materials

E. Fazakas[1, a], M. Furkó[1, b] E. Takács[2,c] K. Gonter[2,d], M. L. Varsányi[1,e]

[1] Bay Zoltan Nonprofit Ltd. for Applied Research, 1116, Budapest, Fehérvári út 130, Hungary

[2]H A S, Atomic Energy Research Institute,1121 Budapest, Konkoly Thege út 29, Hungary

[a]eva.fazakas@bayzoltan.hu(corresponding author), [b]monika.furko@bayzoltan.hu, [c]erzsebet.takacs@energia.mta.hu, [d]gonter@iki.kfki.hu, [e]magda.lakatos@bayzoltan.hu

Keywords: hydrothermal and electrochemical methods, piezoelectric material, nonwoven material, ZnO nanorod

Abstract. ZnO nanostructures were synthesized by two wet-chemical methods (hydrothermal and electrochemical) featuring low temperature (95°C) and atmospheric pressure onto nonwoven substrates. We investigated a hydrothermal method using reagents $Zn(NO_3)_2.6H_2O$ and hexamethylenetetramine (HMTA) as well as an electrochemical method using $ZnCl_2$, and KCl containing electrolyte with H_2O_2 and/or O_2 bubbling. The surface condition of substrate material and the experimental conditions played a key role in the nanowire formation. The morphologies observed by scanning electron microscopy (SEM) include wurtzit or cabbage-like. These morphologies were found to vary with the method applied.

Introduction

ZnO is a semiconducting and piezoelectric material with a direct wide band gap of 3.37 eV and a large excitation bindingenergy of 60 meV at room temperature [1, 2]. As such, ZnO has been investigated for potential in such diverse fields as optics, optoelectronics, catalysis and piezoelectricity. Among the sophisticated methods hitherto used to create one-dimensional ZnO structures, there are a wide range of techniques, such as wet chemical methods [3], physical vapor deposition [4], metal–organic chemical vapor deposition (MOCVD) [5–7]. These complicated methods require special machinery and expensive conditions such aselevated temperature and pressure.Wet chemical methods are attractive for several reasons: they are cheap, less hazardous, and thus capable of easy scaling up [8]; growth occurs at a relatively low temperature, compatible with flexible organic substrates. There is no need for the use of metal catalysts, and thus it can be integrated with well-developed silicon technologies; in addition, there are a variety of parameters that can tuned to effectively control the morphologies and properties of the final products [9].

Here, in this work, we focused on the 1D ZnO nanostructures that grown by wet chemical methods, although evaluation of ZnO nanostructures was provided in the Ref. [10]. We cover the following aspects. First, we went over the basic hydrothermal synthetic methodologies and growth mechanisms that had been adopted in the literature [10]. Second, we displaid a new method of novel nanostructures of ZnO that achieved by electrochemical method.

Electrodeposition of ZnO at room temperature (RT) was been found difficult due to kinetic constants favorable to zinc hydroxide formation [11]. It was therefore vital to control the nanostructure of ZnO to allow its used in novel applications that may demand a specific morphology to be produced and subsequently utilized on a large-scale, with methods based on the principles presented in this paper potentially contributing to this end. In our research we were systematically studied the effect of concentration of reagent and the nanowire growth time on the pretreated viscose substrate in hydrothermal process.

Experimental

Electrodeposition method

All chemicals were of analytical grade and were used without further purification. Before electrodeposition process, it is necessary to make the viscose material conductive. To achieve this requirement Agor Cu layer was electrolessly deposited onto the substrate material. The thickness of the deposited layers was approximately 2 μm, calculated from the substrate count (weight per unit length) before and after deposition.

In order to perform electroless metal deposition, samples were degreased in alcohol and dipped few minutes into a Sn (II) solution ($SnCl_2$ =10 g/l, HCI = 40 ml/1) then, after rinsed in water, dipped into a palladium solution ($PdCl_2$ =0.5 g/1-1, HCI = 10 ml/1).

This activation step allowed rendering the sample surfaces catalytic for the electroless deposition by the oxide-reduction mechanism. After electroless metal deposition the resistivity of treated substrate materials changed between 2-20 Ω.

Electrodeposition was carried out in a standard three-electrode cell. In this three electrode system, Zn plate and Ag/AgCl were used as acounter-electrode and a reference electrode, respectively. The working electrode was pretreated (silver or copper coated) viscose material. The electrolyte was 5 mM $ZnCl_2$ + 0.1 M KCl + H_2O_2 and/or oxygen bubbling. The temperature was maintained at 85 °C. The electrochemical deposition was conducted at constant potential, -1.5 V for 60 minutes and then – 2 V for 60 minutes. After deposition the samples were rinsed with distilled water then placed to vacuum oven at 100 ^oC for two hours.

Hydrothermal synthesis using viscose substrate

The hydrothermal procedure was carried out by two step process:

1. Pretreatment of the substrates by seed layer deposition:

The process to obtain a colloidal solution to deposit the ZnO nanoparticle seeds on the substrates surface (ZnO seeded substrates). The procedure is based on the sol-gel method [9]. Zinc acetate [$Zn(CH_3COO)_2$] was used as precursor material. Initially 5 mM of zincacetate was dissolved in 2-propanol and magnetically stirred at 60 °C for 1h. Then, sodiumhydroxide was mixed into the solution of Zn/NaOH with molar ratio of 1/5 which resulted in a white opalescent colloid solution. By direct immersion of treated viscose substrates into the colloidal solution, the ZnO nanoparticle seeds were deposited onto the substrate surfaces. Subsequently, the substrates were heated in dry air at 120 °C for 2h.

2. ZnO nanowire growth

Zinc nitrate ($Zn(NO_3)_2.6H_2O$) was used as precursor and hexamethylenetetramine (HMTA), also called methenamine ($(CH_3)_6N_4$) as surfactant and catalysts. The precursor solution was prepared by dissolving equimolar (1-50 mM) of zincnitrate and HMTA in deionized water under vigorous stirring at 50 °C for 1 h to form a colloid solution. Then, the seeded substrates were immersed in this solution in a heat and pressure resistant PTFE flask. The flask was then placed in vacuum oven and kept at 95°C and the reaction was allowed to proceed for different durations of time between 2-30 hours without any stirring.

It was observed that a white ZnO powder precipitated at the flask bottom. Finally, the substrates were thoroughly washed with deionized water and allowed to dry in air at 120 °C.

The surface morphology of the ZnO array films was studied by JEOL JSM-6700F scanning electron microscope (SEM) operating at an accelerating voltage of 5 kV.

Results and Discussion

Electrodeposition method

In the electrochemical deposition process we were used strongly oxidative and chloride containing media as electrolyte. In our experiments we were found, that in the case of oxygen bubbling, mainly the oxidation of electrolessly deposited metal layer occurred, therefore AgO/AgCl or CuO layer formed on the substrate surface instead of ZnO deposition (Fig. 1).

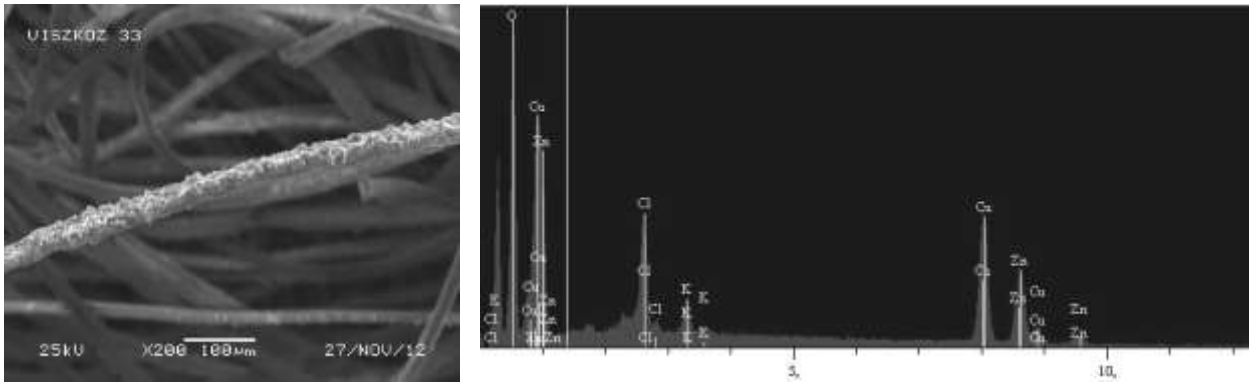

Fig. 1 SEM images and EDX analysis on copper coated viscose material after electrochemical deposition process from 5 mM $ZnCl_2$ + 0.1 M KCl + H_2O_2 with oxygen bubbling

Hence, to avoid this phenomena, we deposited ZnO nanoparticles from the same electrolyte composition but without O_2 bubbling.

Fig. 2 shows a SEM image of ZnO nanostructured array films grown on a conductive viscose substrate. As the large scale field emission SEM image shows, the array consists of the nanolayers and it almost covers the whole substrate. All morphologies produced by the electrodeposition method on viscose substrate were found to deposit primary cabbage-like structures. In this case the ZnO deposition take splace instead of the oxidation of the electroless silver or copper layer.

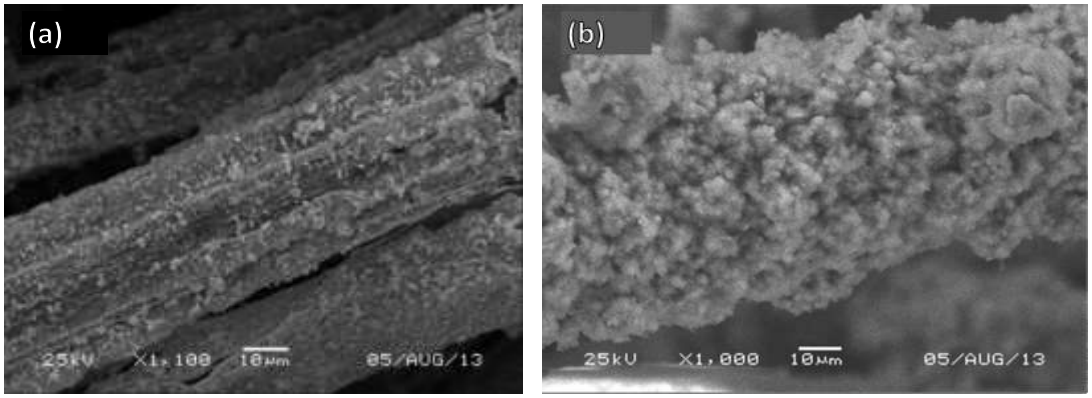

Fig. 2 SEM image of the ZnO nanostructured film (a) deposition onto silver coated viscose (b) deposition onto copper coated viscose from 5 mM $ZnCl_2$ + 0.1 M KCl + H_2O_2without oxygen bubbling.

Hydrothermal synthesis

In this procedure ZnO nanowires (NWs) were grown from ZnO seeds deposited on a substrate immersed in a precursor solution. ZnO seeds in 2-propanol are dropcasted on the substrate to form uniform seeds for ZnO NW growth. NWs were grown by immersing the seeded substrate into aqueous solutions containing equimolar $Zn(NO_3)_2.6H_2O$ and hexamethylenetetramineat 95 °C for different time. After there action was completed, the grown ZnO-NWs were thoroughly rinsed with Milli-Qwater and dried in air to remove residual solvents and precipitations that did not ad here to the surface properly. The aqueous solutions of zinc nitrate and HMTA can be produced the following chemical reactions:

Decomposition reaction of hexamethylene-tetramine:

$$(CH_2)_6N_4 + 6H_2O \longrightarrow 6HCHO + 4NH_3 \quad (1)$$

Formationreaction ofhydroxylion:

$$NH_3 + H_2O \longleftrightarrow NH_4^+ + OH^- \quad (2)$$

Precipitation reaction:

$$2OH^- + Zn^{2+} \rightarrow Zn(OH)_2 \quad (3)$$

ZnOnano-wire growth:

$$Zn(OH)_2 \rightarrow ZnO + H_2O \quad (4)$$

The concentration of HMTA played an important role for the formation of ZnO nanostructure since OH^- is strongly related to the reaction that produces nanostructures. Initially, due to decompositioned of zincnitratehexahydrate and HMTA at an elevated temperature, OH^- was introduced in Zn^{2+} aqueous solution and their concentration increased. The separated colloidal $Zn(OH)_2$in solution was partly as nuclei for the growth of ZnO nanorods. During the hydrothermal growth process, the $Zn(OH)_2$ dissolved with increasing temperature. When the concentrations of Zn^{2+}andOH^-reached the critical value of the supersaturation of ZnO, fine ZnO nuclei formed spontaneously in the aqueous complex solution. When the solution is supersaturated, nucleation began. Afterwards, the ZnO nanoparticles combined together to reduce the inter facial free energy. This was because the molecules at the surface are energetically less stable than the ones already well ordered and packed in the interior.

The nucleation determined the surface-to-volume ratio of the ZnO nanorod. Then incorporation of growth units into crystal lattice of the nanorods by dehydration reaction took place. It was concluded that the growth habit was determined by thermodynamic factor and by concentration of OH as the kinetic factor in aqueous solution growth.

A comparative investigation was conducted on the effect of the precursor solution (HMT and $Zn(NO_3)_2$ concentration and the nanowire growth time in the precursor solution on nanowire morphology and crystallite density.

$Zn(NO_3)_2$ concentration variation

The concentration of zincnitratehexahydrate and the HMTA in the solution were changed from 1 mM to 50 mM.

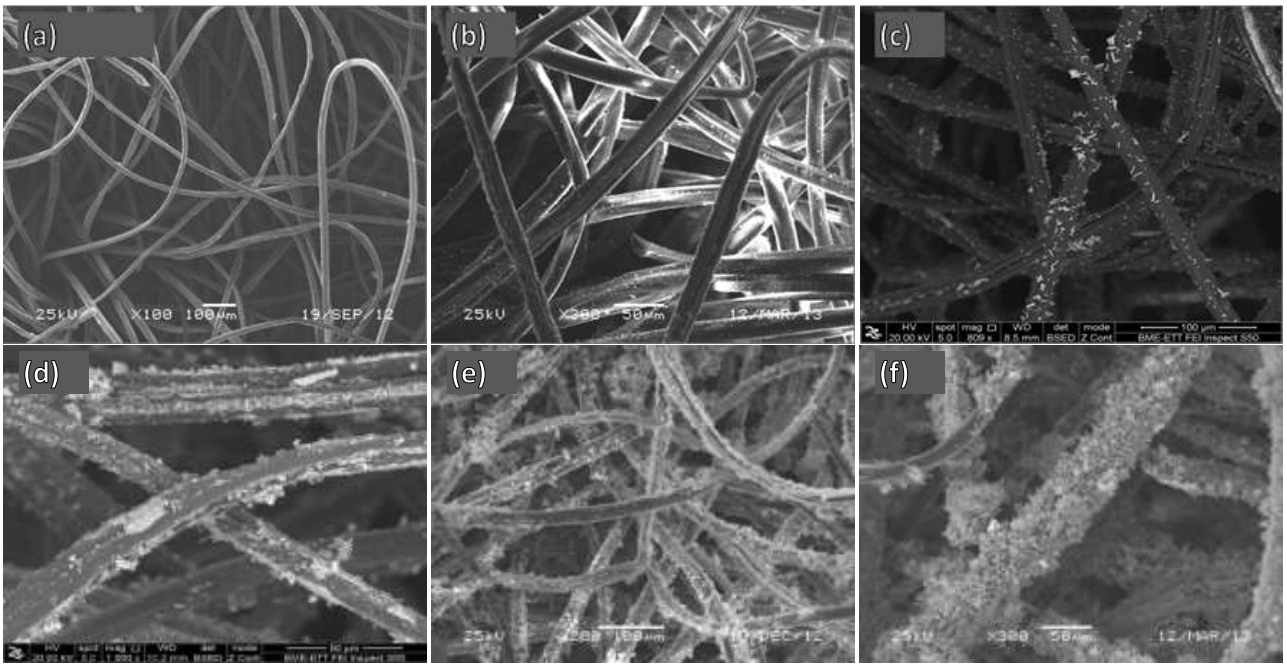

Fig. 3 SEM images on $ZnNO_3$ + HMTA with different concentration growth for 27 hours at 95 °C (a) 0 mM (b) 1 mM - (c) 10 mM - (d) 20 mM - (e) 30 mM - (f) 50 mM precursor solution.

As Fig. 3 shows, there was no ZnO precipitation when the HMT and $Zn(NO_3)_2$ concentrations were less than 10 mM**.** In the case of precursor solution of 10 - 30 mM, the surface coverage was still poor, the ZnO nanowires adhereed only a few unconnected spots, while when the concentration of precursor solution was as high as 50 mM, more dense and continuous ZnO nanowirelayer adheresed to the substrate surface.

ZnO nanowire growth time variation

We have investigated the time dependence of ZnO nanowire growth mechanism in precursor solution of 20 mM. As Fig. 4 indicates, as time elapses, the surface density of ZnO nanowires was increasing.

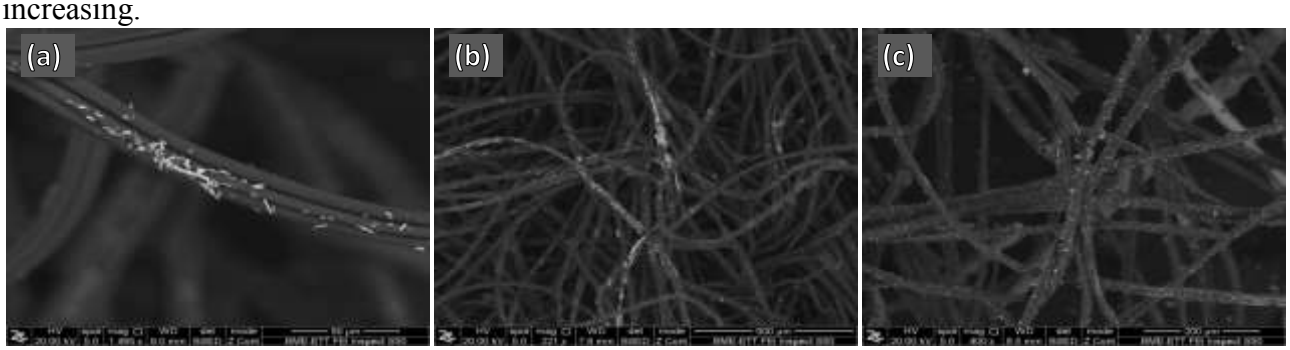

Fig. 4 ZnO nanowire growth in 20mM $ZnNO_3$ + 20 mM HMTA precursorsolution for (a) 6 h, (b) 10 h and (c) 27 h at 95 °C.

Most of the nanowires were perpendicular to the substrate. Fig. 5 reveals a high magnification SEM image of one ZnO nanowire, showing a perfect hexagonally faceted morphology with a diameter of 250 - 500 nm, and lengths of about 3-7 μm. The SEM image indicates that the ZnO product exhibits tubular structure with smooth surface and uniform thicknesses.

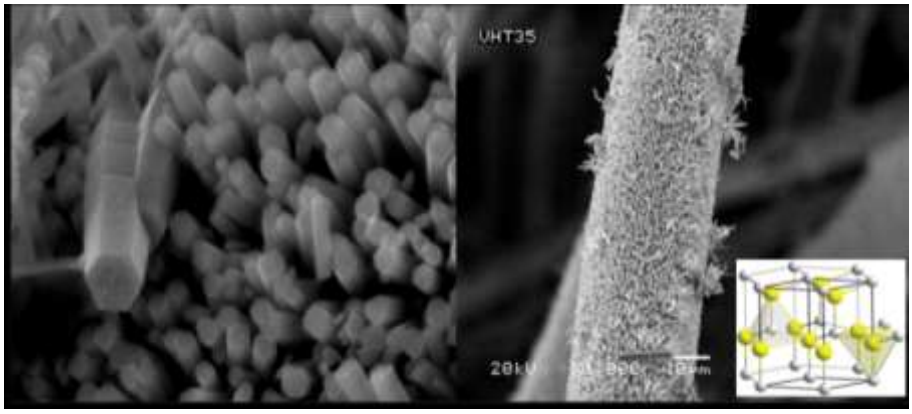

Fig.5 SEM micrographs of samples prepared via hydrothermal synthesis on a viscosesubstrate using, 50 mM $Zn(NO_3)_2$ and 50 mM HMT precursor solution

The ZnO nanoparticles exhibited the nanocrystalline phase and no other impurity such as $Zn(OH)_2$ was observed. Fig. 6 shows the AFM image of the viscos layer of the ZnO nanoparticles and it can be seen that the nanoparticles were uniform, dense and well adhered to the gold-coated viscose substrate which behaved better nucleation centers for the growth of well aligned ZnO nanorods.

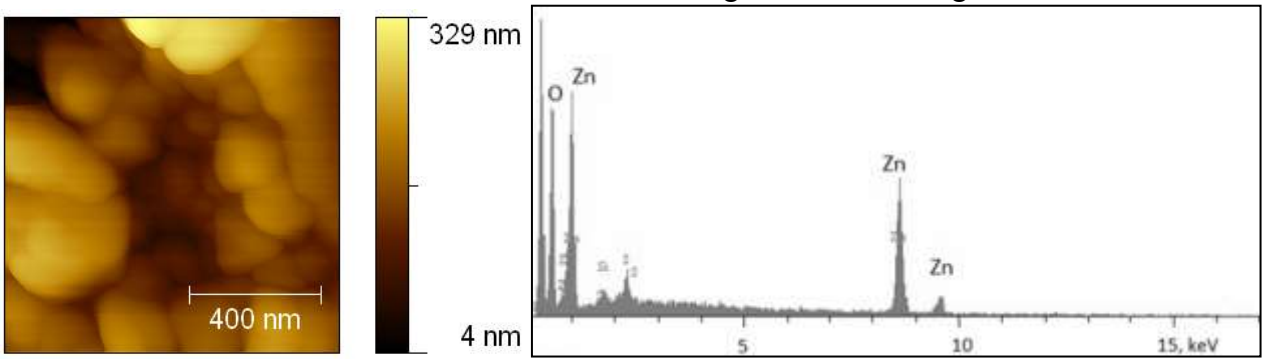

Fig.6 The AFM and EDX image of theviscoselayer of ZnO nanoparticles

Conclusions

Out of nonwoven materials (viscose, polypropylene, Kevlar etc.) we chose viscose because of its higher hydrophilicity compared to other materials. The aim of this work was electrochemical deposition of large-scale single-crystalline ZnO nanotube arrays on the viscose substrate from an aqueous solution.

As the large scale field emission SEM image shows, the array consists of the nanolayers and it almost cover the whole substrate. All morphologies produced by the electrodeposition method on viscose substrate were found to deposit primary cabbage-like structures connected into secondary belt structures.

We have found that the surface coverage was poor in the case of hydrothermal deposition of ZnO nanowire from precursor solution of 1-20 mM. The ZnO nanowires attached to the substrate surface only a few random spots.

According to our extensive research optimum precursor solution turned out to be 50 mM $Zn(NO_3)_2$ and 50 mM HMTA equimolar precursor solution, and the optimum deposition time ranged between 25-30 hours. In this case we were achieved ZnO nanowires with appropriate surface coverage. The nanowires mainly oriented vertically to the substrate surface.

The ZnO nanowires, deposited by hydrothermal method exhibit a perfect hexagonal faceted morphology (wurtzit crystals) with a diameter of 250 - 500 nm, and lengths of about 3-7 μm.

Acknowledgements

This work was supported by Indo-Hungarian project and TÁMOP -4.2.2.A-11/1/KONV-2012-0075 EU- Hungarian project.

References

[1] Z. L. Wang, Nanostructures of zinc oxide, Mat. Today, 7 (2004) 26-33.

[2] G. Gordillo, New materials used as optical window in thin film solar cells, Surf. Rev. and Let., 9 (2002) 1675-1680.

[3] M.D. Driessen, T. M. Miller, V.H. Grassian, Photocatalyticoxidation of trichloroethylene on zinc oxide: characterization of surface-bound and gas-phase products and intermediates with FT-IR spectroscopy, J. of Molec. Cataly. A: Chemical, 131 (1998) 149-156.

[4] S. Music, D. Dragcevic, M. Maljkovic, S. Popovic, Influence of chemical synthesis on the crystallization and properties of zinc oxide, Mater. Chem. and Phys, 77 (2003) 521-530.

[5] A. Erxleben, Structures and properties of Zn(II) coordination polymers, Coord. Chem. Rev., 246 (2003) 203-228.

[6] S-L. Zheng, M-L. Tong, X.-M Chen, Silver (I)-hexamethylenetetramine molecular architectures: from selfassembly to designed assembly, Coord. Chem. Rev., 246 (2003) 185-202.

[7] H. Zhang, D.R. Yang, X.Y Ma, N. Du, J. B. Wu, D.L. Que, Straight and thin ZnO nanorods: Hectogram-scale synthesis at low temperature and cathodoluminescence. J. Phys. Chem. B 110 (2006) 827–830.

[8] S. Xu, et al., Patterned growth of vertically aligned ZnO nanowire arrays on inorganic substrates at low temperature without catalyst, J. of Ameri. Chem. Soci. 130 (2008) 14958–14959.

[9] K. Govender, D. S. Boyle, P.B. Kenway, P. O'Brien, Understanding the factors that govern the deposition and morphology of thin films of ZnO from aqueous solution, J. of Mat. Chem. 14 (2004) 2575–2591.

[10] S. Xu, N. Adiga, S. Ba, T. Dasgupta, C.F. J. Wu, Z. L. Wang, Optimizing and improving the growth quality of ZnO nanowire arrays guided by statistical design of experiments, ACS Nano 3 (2009) 1803–1812.

Low cycle fatigue behavior of VVER-440 reactor pressure vessel steels at isothermal condition

Balazs Fekete[1, a], Peter Bereczki[1,] and Peter Trampus[1]

[1]College of Dunaujvaros, Tancsics Mihaly str. 1/A, Dunaujvaros, Hungary

[a]feketeb@mail.duf.hu

Keywords: reactor, pressure vessel, low cycle fatigue, isothermal fatigue, Coffin-Manson law, energy based prediction

Abstract. The fatigue life of the structural materials 15H2MFA and 08H18N10T of VVER-440 reactor pressure vessel under completely reserved total strain controlled tests were investigated. The measurements were carried out with isothermal condition at 260°C on GLEEBLE 3800 servo-hydraulic thermal- mechanical simulator. The isothermal low cycle fatigue results were evaluated with the plastic strain based Coffin-Manson law, and plastic strain energy based model as well. It was shown that both methods are able to predict the fatigue life of reactor pressure vessel steels accurately.

Introduction

One of the most frequent damage mechanisms in pressurized water reactors (PWRs) is the low cycle thermal- mechanical fatigue caused by simultaneous thermal and mechanical loading, during transient operating processes (e.g. start up, and shut down) and accident conditions. During the thermal fatigue of the PWR structural materials the cyclic heat load (or simultaneous heat and mechanical loads) causes pulsating plastic strain in the materials of the pressurized components as follows:

1. in the near surface layers of the component due to cyclic temperature and pressure loading,
2. in the inside layers of the component due to the inhomogeneous temperature field,
3. in the cross section of the pipes or vessels due to inhomogeneous temperature of the flowing media (e.g. thermal stratification).

The knowledge on low cycle fatigue degradation phenomena became more and more important due to the operation of nuclear power plants beyond their design life.

Experimental Program, Material and Test Procedure

Materials and Specimen Geometry. The test specimens were machined from the base metal (15H2MFA) and the anticorrosive cladding metal (08H18N10T) of the VVER-440/V-213 (Russian designed PWR) reactor pressure vessel. The nominal chemical compositions and mechanical properties are given in Table 1 and Table 2, respectively.

Table 1 Chemical composition of test materials (mass percent, [%])

Material	C	Si	Mn	S	P	Cr	Ni	Mo	V	As	Co	Cu
15H2MFA	0.13-0.18	0.17 - 0.37	0.30 - 0.60	max. 0.025	max. 0.025	2.50 - 3.00	max. 0.040	0.60 - 0.80	0.25 - 0.35	max.0.05	max. 0.02	max.0.015
08H18N10T	≤0.08	≤0.8	≤1.5	≤0.020	≤0.035	17.0 - 19.0	10.0 - 11.0	–	–	–	–	≤0.30

The fatigue specimens used in the tests were cylindrical specimens with gauge length of 7 mm, as shown in Fig. 1. The specimen dimensions were chosen to avoid buckling phenomena under the highest compressive forces anticipated in the test program.

Table 2 Mechanical properties of test materials

	20 °C				350 °C			
Material	Tensile strength [MPa]	Yield strength [MPa]	Elongation [%]	Reduction of area [%]	Tensile strength [MPa]	Yield strength [MPa]	Elongation [%]	Reduction of area [%]
15H2MFA	540	431	14	50	490	392	13	50
08H18N10T	491	215	40	55	353	185	25	40

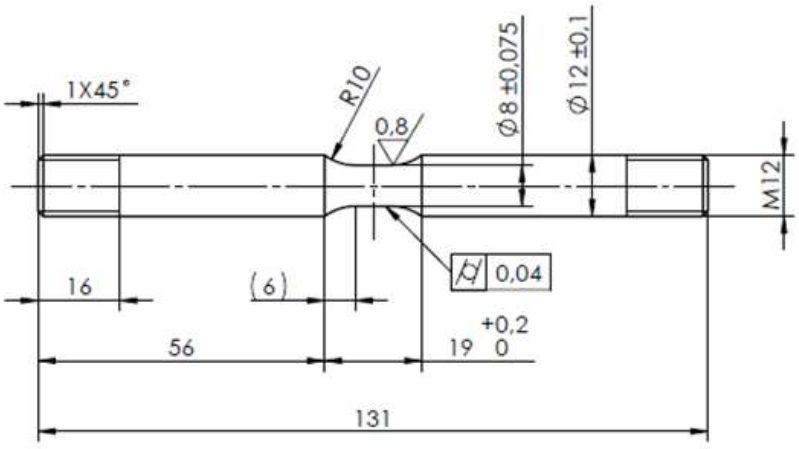

Fig. 1 Geometry of test specimen

The surface of the specimens' gauge was carefully grinded and polished along to the longitudinal direction to avoid the scratches.

Experimental Details and Procedures. The fatigue tests were performed on a servo valve controlled thermal-mechanical testing machine from DSI (model GLEEBLE-3800) at 260 °C. The tests were run under uniaxial tension-compression loading with total strain control. The programmed waveform was triangular for all the fatigue tests with the frequency of 0.08 Hz. The cyclic loading was started from the compressed side. The total strain was measured by a HZT060 type linear displacement transducer which was attached to the specimen. Thermocouples welded in the middle of the gauge length provided signals for accurate feedback control of specimen temperatures. The test machine operated with direct resistance heating (Joule-heating) by copper jaws. The test set-up and the chamber of the GLEEBLE-3800 are shown in Fig. 2.

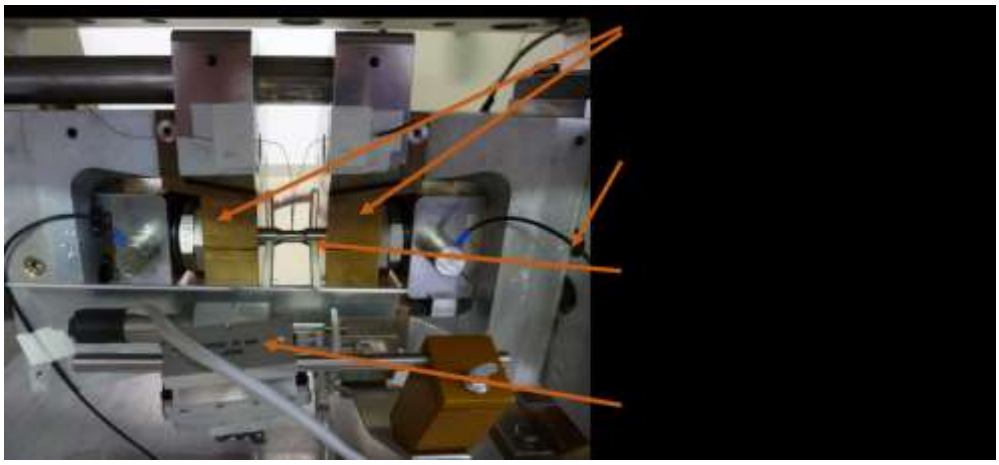

Fig. 2 Work chamber of GLEEBLE with the specimen

In order to investigate the effect of the strain amplitude, four strain amplitudes with strain ratio of -1 were applied. The amplitudes are ±0.6%, ±0.9%, ±1.2%, ±1.5% for the material 15H2MFA and ±0.9%, ±1.2%, ±1.5%, ±2.0% for the 08H18N10T cladding material. Three specimens were tested for each test condition up to 25% drop in load registered in the cycles. This failure criteria results a significant crack on the gauge length of the specimen as shown in Table 3. The sampling frequency of strain, force and temperature data was set to 10 Hz.

Experimental results and analysis

Fatigue Life. Table 3 illustrates the fatigue life of both of the test material during the entire four test condition. A representative stereo-microscopic image of the fatigue crack is shown with respect to each test condition.

Table 3 Summary of the fatigue results

a.15H2MFA

Sample No.	Total mechanical strain ±0.6%	±0.9%	±1.2%	±1.5%
1.	2640	1259	674	442
2.	2749	918	623	470
3.	2308	1001	554	414
Mean:	**2566**	**1059**	**617**	**442**
Deviation:	187.55	145.19	49.17	22.86
				

b. 08H18N10T

Sample No.	Total mechanical strain ±0.9%	±1.2%	±1.5%	±2.0%
1.	2497	1592	851	315
2.	2285	1507	748	351
3.	2605	1375	857	443
Mean:	**2462**	**1491**	**819**	**370**
Deviation:	132.91	89.27	50.02	53.89
				

The obtained fatigue life data with low deviation indicate high in-house repeatability of the developed test configuration.

Strain Based Evaluation of the Experimental Data. The strain based approach is predominantly used to characterize low cycle fatigue behavior of materials operating at elevated temperatures and high levels of stress that observed in power plant during operation and start up or shut down procedures. In these conditions, fatigue damage is generally caused by plastic strain, and can be described by the Coffin-Manson law [1], shown by the power law relation in Eq. 1:

$$\varepsilon_p = \varepsilon'_f \cdot N_f^c . \quad (1)$$

Here ε_p, plastic strain amplitude; ε'_f, fatigue ductility coefficient; N_f, cycles to failure; and c, fatigue ductility exponent.
Based on the Coffin-Manson model, the material parameters are shown in Table 4, which were obtained by fitting to the experimental data.

Table 4 Coffin Manson parameters of the materials

Material	ε'_f	c
15H2MFA	1,0479	-0,7375
08H18N10T	0,2243	-0,4290

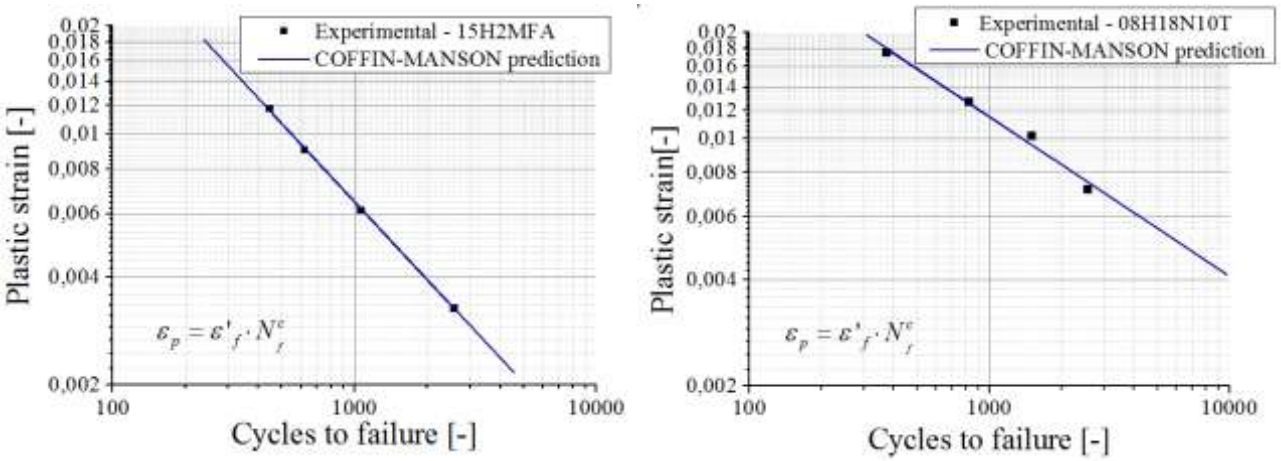

a. b.

Fig. 3 The Coffin-Manson relationship for the tested materials: a. 15H2MFA b. 08H18N10T

We obtain straight lines by plotting in log-log scales the plastic strain amplitude-number of cycle as shown in Fig. 3. It can be seen in Fig. 3 that the fitted lines for both materials are very close to the experimental data, suggesting that the experimental setup and the test program were designed properly.

Evaluation of the low cycle fatigue behavior of the materials based on dissipated energy. During the fatigue process the stress and strain vary in magnitude and cannot be summed. Moreover, within the low-cycle fatigue regime where high cyclic stress and short fatigue lives are encountered, the plastic strain in each cycle is the predominant cause of energy dissipation. Owning the above mentioned reasons an energy based approach using plastic strain energy as a damage parameter may present an alternative to the conventional strain-based approach that has been widely used in characterizing the strain-based fatigue behavior of steels. Plastic strain energy is accumulating per cycles, therefore provides a direct measure of accumulated fatigue damage [2]. It is a measure of the fatigue resistance of materials, which can be characterized by the amount of dissipated energy during the damage process until failure. According to the authors knowledge there has not been yet any research to determine the plastic strain energy based low cycle fatigue behavior of subject materials (15H2MFA, 08H18N10T).

In order to investigate the absorbed energy during the fatigue lifetime of the test materials we calculate the plastic strain energy per cycle after cyclic stabilization by the fiftieth cycle, and the

cumulative plastic strain energy to failure. The calculation were carried out by the numerical integration of the strain-stress data (hysteresis curves) shown in Fig. 4.

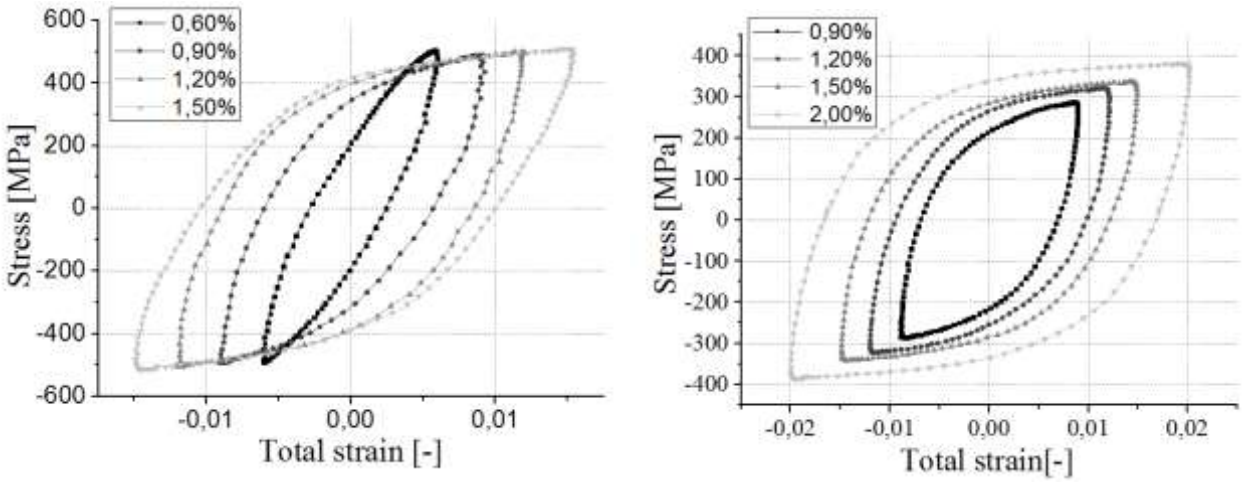

a. b.

Fig. 4 Hysteresis loops plotted in the 50th cycle: a. 15H2MFA b. 08H18N10T

Calculated values of the plastic strain energy are presented in Table 5 and Table 6. We carried out the calculations based on the 50th cycle (Eq. 2 and Eq. 3) and based on all fatigue cycles (Eq. 4).

$$W_p^{50} = \int_{cycle} \sigma \cdot d\varepsilon \,. \tag{2}$$

$$W_f^{50} = W_p^{50} \cdot N_f \,. \tag{3}$$

$$W_f^a = \sum_{i=1}^{N_f} \int_{cycle} \sigma_i \cdot d\varepsilon_i \,. \tag{4}$$

Here W_p^{50}, plastic strain energy for the 50th cycle; σ, uniaxial stress; N_f, cycles to failure; W_f^{50}, accumulated plastic strain energy to failure based on the 50th cycle; W_f^a, accumulated plastic strain energy obtained through all cycles.

Table 5 Calculated plastic strain energy to failure for 15H2MFA

Total strain amplitude	±0.6%		±0.9%		±1.2%		±1.5%	
Sample No.	W_f^{50} (mJ/mm^3)	W_f^a (mJ/mm^3)	W_f^{50} (mJ/mm^3)	W_f^a (mJ/mm^3)	W_f^{50} (mJ/mm^3)	W_f^a (mJ/mm^3)	W_f^{50} (mJ/mm^3)	W_f^a (mJ/mm^3)
1.	8659	11315	8989	8930	8479	8896	8040	8003
2.	12255	12576	11193	10760	8834	8846	7212	7158
3.	10089	12182	8152	8483	7806	7451	8540	8673
Mean:	**10335**	**12024**	**9444**	**9391**	**8373**	**8398**	**7931**	**7945**
Deviation:	1811	645	1571	1206	522	820	671	759

Table 6 Calculated plastic strain energy to failure for 08H18N10T

Total strain amplitude	±0.9%		±1.2%		±1.5%		±2.0%	
Sample No.	W_f^{50} (mJ/mm^3)	W_f^a (mJ/mm^3)	W_f^{50} (mJ/mm^3)	W_f^a (mJ/mm^3)	W_f^{50} (mJ/mm^3)	W_f^a (mJ/mm^3)	W_f^{50} (mJ/mm^3)	W_f^a (mJ/mm^3)
1.	16580	16674	15681	16434	11659	11713	7028	6945
2.	14007	14503	14874	14659	10135	10221	9314	9328
3.	17955	18120	13544	13512	12204	12224	7832	7840
Mean:	**16181**	**16432**	**14700**	**14868**	**11333**	**11386**	**8058**	**8038**
Deviation:	2004	1821	1079	1472	1072	1041	1160	1204

From the obtained fatigue toughness results summarized in Table 5 and Table 6 it can be seen that the difference between the plastic works to failure obtained from the 50th cycle, and that obtained by integrating all of the cycles is very low. This indicates that the 50th cycle can be used as representative value to the calculations for both tested materials.

Summary

Based on the experimental results and analysis presented above, our investigation can be summarized as follows:

1. Isothermal low cycle fatigue experiment was successfully developed to perform tests for 15H2MFA and 08H18N10T reactor pressure vessel steels.
2. The results were evaluated based on Coffin-Manson model and derived the parameters for both material, by curve fitting to the experimental data.
3. The plastic strain energy to failure was calculated and it was concluded that the 50th cycle can be used as representative cycle to the calculations for both tested materials.

Acknowledgement

The publication is supported by the TÁMOP-4.2.2.A-11/1/KONV-2012-0027 project. The project is co-financed by the European Union and the European Social Fund.

References

[1] L. F. Coffin, Fatigue at high temperature – Prediction and interpretation. Proc. Instn. Mech. Engrs. 188 (1974) 109-127

[2] M.D. Callaghan, S.R. Humphries, M. Law, M. Ho, P. Bendeich, H. Li, W.Y. Yeung: Energy-based approach for the evaluation of low cycle fatigue behaviour of 2.25Cr–1Mo steel at elevated temperature. Materials Science and Engineering A 527 (2010) 5619–5623

[3] Mageshwaran Ramesh, Hans J. Leber, Markus Diener, Ralph Spolenak, Conducting thermomechanical fatigue test in air at light water reactor relevant temperature intervals. Journal of Nuclear Materials 415 (2011) 23–30

The effect of thermomechanical treatment on the microstructure and the mechanical behavior of a supersaturated Cu-Ag alloy

J. Gubicza[1,a], K. Sitarama Raju[2,b], V. Subramanya Sarma[3,c], A. Kauffmann[4,5,d], Z. Hegedűs[1,e], M. Peterlechner[6,f], J. Freudenberger[4,7,g] and G. Wilde[6,h]

[1]Department of Materials Physics, Eötvös Loránd University, H-1117, Budapest, Hungary

[2]Centre for Material and Fibre Innovation, Deakin University, Geelong, VIC – 3217, Australia

[3]Department of Metallurgical and Materials Engineering, Indian Institute of Technology Madras, Chennai, 600036 India

[4]IFW Dresden, P.O. Box 270116, 01171 Dresden, Germany

[5]TU Dresden, Institute of Materials Science, 01062 Dresden, Germany

[6]Institut für Materialphysik, Universität Münster, 48149, Münster, Germany

[7]TU BA Freiberg, Institute for Materials Science, 09599 Freiberg, Germany

[a]jeno.gubicza@ttk.elte.hu (corresponding author), [b]sr.raju2003@gmail.com, [c]vsarma.iitm@gmail.com, [d]a.kauffmann@ifw-dresden.de, [e]zoltan885@yahoo.com, [f]martin.peterlechner@uni-muenster.de, [g]J.Freudenberger@ifw-dresden.de, [h]gwilde@uni-muenster.de

Keywords: rolling, thermomechanical treatment, dislocations, strength, ductility

Abstract. Supersaturated Cu-3at.% Ag alloy was processed by cold rolling and short-time annealing in order to achieve a combination of high strength and good tensile ductility. After annealing of the rolled samples a heterogeneous solute atom distribution was developed due to the dissolution of nanosized Ag particles in some volumes of the matrix. In regions with higher solute content, the high dislocation density formed due to rolling was stabilized, while in other volumes the dislocation density decreased. The heterogeneous microstructure obtained after annealing exhibited a much higher ductility and only a slightly lower strength than in the as-rolled state.

Introduction

The combination of plastic deformation and annealing (referred to as thermomechanical treatment) is generally used for tailoring mechanical properties of metallic materials. In the last decades, different severe plastic deformation (SPD) procedures were developed in order to increase the mechanical strength of metals and alloys by introducing large density of lattice defects, such as dislocations and grain boundaries, into the workpieces [1]. However, it was revealed that the increase of the strength in these ultrafine-grained (UFG) materials was accompanied by a reduction of the tensile ductility due to the lost of strain hardening capacity of the samples [2]. Moderate heat-treatments after SPD were successfully applied in order to increase the ductility considerably while retaining the high strength [3]. In the annealing step of these thermomechanical treatments usually heterogeneous structural relaxation (i.e. recovery and recrystallization) occurs. In the relaxed volumes the dislocation density can increase again during tensile test, leading to a considerable strain hardening capacity which results in an improved ductility of the material. In pure metals, the heat-treatments often yield bimodal grain structures with coarse recrystallized grains embedded in an UFG matrix. In the present study, the effect of a moderate annealing after rolling at room and liquid nitrogen temperatures (denoted by RT and LNT, respectively) on the microstructure and the tensile performance of a supersaturated Cu-3at.% Ag alloy is investigated.

Experimentals

Cu-3at.% Ag alloy was prepared by induction melting in Ar atmosphere from high purity (99.9%) elements and casting them into 15 × 15 × 150 mm^3 graphite moulds. The alloy was homogenized at 750 °C for 5 h, then it was quenched in water. The homogenized plates were subjected to rolling at RT and LNT (~77 K) to a strain of ~2. Former differential scanning calorimetry measurements at a heating rate of 10 K/min showed that recovery and recrystallization in the RT and LNT rolled samples start at about 400 and 375 °C, respectively [4]. Isothermal annealing at these temperatures for 5 min resulted in 5-10% hardness reduction, indicating that this heat-treatment yielded only a moderate structural relaxation [4]. The effect of this annealing on the microstructure and the tensile performance was investigated in the present work. The microstructure of the Cu matrix in the as-rolled samples as well as in the RT and LNT rolled specimens annealed for 5 min at 400 and 375 °C, respectively were studied by X-ray diffraction (XRD). The X-ray diffraction patterns were measured by a high-resolution rotating anode diffractometer (Nonius, FR591) with $CuK\alpha_1$ radiation (wavelength: λ = 0.15406 nm). The lattice constant was determined by extrapolating the lattice parameters obtained from the different reflections to $2\Theta = 180°$ by the Nelson–Riley method [5]. The X-ray diffraction line profiles were evaluated for the microstructure by the Convolutional Multiple Whole Profile (CMWP) fitting method [6]. In this procedure, the diffraction pattern is fitted by the sum of a background spline and the convolution of the instrumental pattern and the theoretical line profiles related to the crystallite size, dislocations and twin faults. As an example, the fitting for the LNT rolled specimen is shown in Fig. 1. The theoretical profile functions used in this fitting procedure were calculated on the basis of a model of the microstructure, where the crystallites have spherical shape and log-normal size distribution. The following parameters of the microstructure were obtained from the CMWP fitting procedure: the area weighted mean crystallite size ($\langle x \rangle_{area}$), the dislocation density (ρ) and the twin boundary probability (β). The twin boundary probability is defined as the fraction of twin faults among the {111} lattice planes. The uniaxial tensile performance of the as-rolled and the annealed samples were investigated by a mechanical testing machine (model 3367 of Instron, UK) at an initial strain rate of 10^{-3} s^{-1}. The specimens were machined as per ASTM E8 sub-size specifications with the gauge length along the rolling direction.

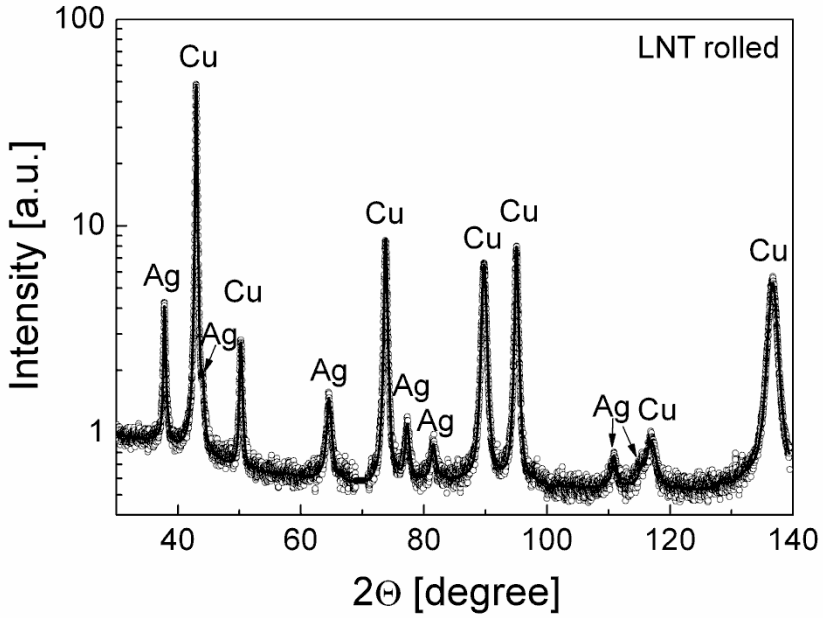

Fig. 1. The CMWP fitting for the LNT rolled Cu-3at.% Ag. The open circles and the solid line represent the measured data and the fitted curves, respectively. The intensity is in logarithmic scale.

Results and discussion

The phase composition and the microstructure of the rolled and the subsequently annealed samples. The Ag solute content in the Cu matrix was determined from the lattice parameter measured by XRD. The Ag concentrations in the Cu matrix of RT and LNT rolled samples were estimated to be 1.3 ± 0.1 at.% and 1.0 ± 0.1 at.%, respectively (see Table 1). As the total concentration of Ag in the base alloy is 3 at.%, about 1.7 and 2 at.% Ag is expected to be present as secondary Ag phase in RT and LNT rolled alloys, respectively. Ag peaks were indeed observed in the XRD patterns of the as-rolled samples (see Fig. 1). According to the equilibrium phase diagram of the Cu-Ag system, the solubility limit of Ag in Cu is 4 at.% at 750 °C, therefore during the homogenization heat-treatment all Ag atoms were dissolved in the Cu matrix. The Ag precipitates observed in the as-rolled samples might form during quenching to RT and/or subsequent rolling processes at RT and LNT. Nevertheless, the Cu matrices with ~1-1.3 at.% solute Ag concentration after rolling are supersaturated since the equilibrium solubility limit of Ag in Cu is practically zero at RT. The microstructural parameters of the Cu matrix in RT and LNT rolled samples obtained by X-ray line profile analysis are presented in Table 1. It is revealed that the crystallite size is smaller and the dislocation density is higher in the LNT rolled sample when compared to the RT rolled specimen. Considerable twinning was not detected in the specimen rolled at RT while significant twin boundary probability was measured in the LNT rolled sample. The practically zero value of the twin boundary probability for the sample rolled at RT does not mean definitely the lack of twinning as the lowest detection limit of twin boundary frequency is about 0.05 % in the present analysis. Indeed, former TEM study showed that deformation twins also formed in some locations of both specimens [4]. It is noted that the crystallite size obtained by XRD corresponds rather to the subgrain size which is smaller than the grain size determined by TEM (100-200 nm for both rolled materials [4]).

Table 1: The solute Ag concentration (c_{Ag}) and the parameters of the microstructure for the Cu matrix in the Cu-3at. % Ag alloy in RT rolled, RT rolled + annealed, LNT rolled and LNT rolled + annealed conditions: $\langle x \rangle_{area}$: area-weighted mean crystallite size, ρ: dislocation density, β: twin boundary probability.

Sample	Region	c_{Ag} [at.%]	$\langle x \rangle_{area}$ [nm]	ρ [10^{14} m^{-2}]	β [%]
RT rolled		1.3 ± 0.1	36 ± 4	32 ± 3	<0.05
RT rolled + annealed	1	1.3 ± 0.1	32 ± 4	14 ± 2	<0.05
	2	2.7 ± 0.2	41 ± 6	24 ± 3	<0.05
LNT rolled		1.0 ± 0.1	30 ± 3	48 ± 5	0.49 ± 0.07
LNT rolled + annealed	1	1.0 ± 0.2	27 ± 3	8 ± 1	<0.05
	2	2.6 ± 0.2	55 ± 8	30 ± 4	<0.05

Following annealing of the RT and LNT rolled samples, each diffraction peak of the Cu matrix splits into two components (see Fig. 2). This phenomenon is believed to be caused by the development of an inhomogeneous solute atom distribution in the Cu matrix during annealing resulting in a variation of the lattice parameter of the Cu matrix. Each line profile was evaluated by fitting it with the sum of two profile components having different Bragg-angles which correspond to two distinct regions of the matrix having different average lattice parameters. It should be noted that most probably the description of the distribution of the solute concentration by only two distinct solute contents is a simplification. Nevertheless, this procedure characterizes the inhomogeneity of the chemical composition of the matrix. The Ag solute concentrations in the two regions of the matrix have been determined and listed in Table 1. Region 1 has the same Ag content as for the Cu matrix after rolling but before annealing. Region 2 has significantly larger lattice parameter indicating an increase in Ag solute concentration. The partial dissolution of the Ag phase is also confirmed by the decrease of the relative intensity of its XRD peaks. The equilibrium solubility limit of Ag in Cu at the temperature of annealing (375-400 °C) is ~0.4 at.%, therefore a decrease of the solute atom concentration from 1.0-1.3 at.% during annealing of the rolled samples would have

been expected. Our experiments revealed an opposite tendency, i.e. an increase of the solute Ag content in a part of the Cu matrix (referred to as region 2). This phenomenon could be caused by the large specific interface energy between Ag nanoparticles and Cu grains which yielded an enhanced equilibrium solubility limit of Ag in Cu. This solubility limit depends on the size of Ag dispersoids as expressed by the Gibbs–Thomson formula (also referred to as Ostwald–Freundlich equation) [7,8]:

$$c_r = c_\infty \exp\left(\frac{2A\gamma V_m}{dRT}\right), \qquad (1)$$

where d is the diameter of the spherical Ag precipitates, T is the temperature of annealing (about 670 K), c_∞ (0.4 at.%) and c_r are the equilibrium solute Ag concentrations in the Cu matrix with Ag precipitates having infinitely small curvature (large radius) and radius of r, respectively, γ is the interface energy (~1.5 J/m^2 [9]) between the Cu matrix and the Ag precipitates, R is the molar gas constant, V_m is the molar volume of Ag (10^{-5} m^3/mole) and A is a constant with the value of 2 or 3, depending on the assumptions made in the derivation of eq. (1). For instance, in the case of the LNT rolled sample at the temperature of annealing (648 K) and with A=3, for precipitate sizes smaller than 18 nm the value of c_r obtained from eq. (1) is higher than the solute Ag concentration measured before annealing (1 at.%). Therefore, the smaller Ag nanoparticles in the size distribution were dissolved during annealing which is in accordance with the increase of the average size of Ag crystallites from ~20 nm to ~30 nm in the annealing process as observed by XRD. In the region where dissolution occurred the solute Ag concentration in the Cu matrix increased and this volume was denoted as region 2. The solute Ag content in region 2 of the annealed samples is ~2.7 at.% which is only slightly smaller than the nominal Ag concentration of the base alloy, suggesting that the majority of precipitates in region 2 were dissolved during annealing.

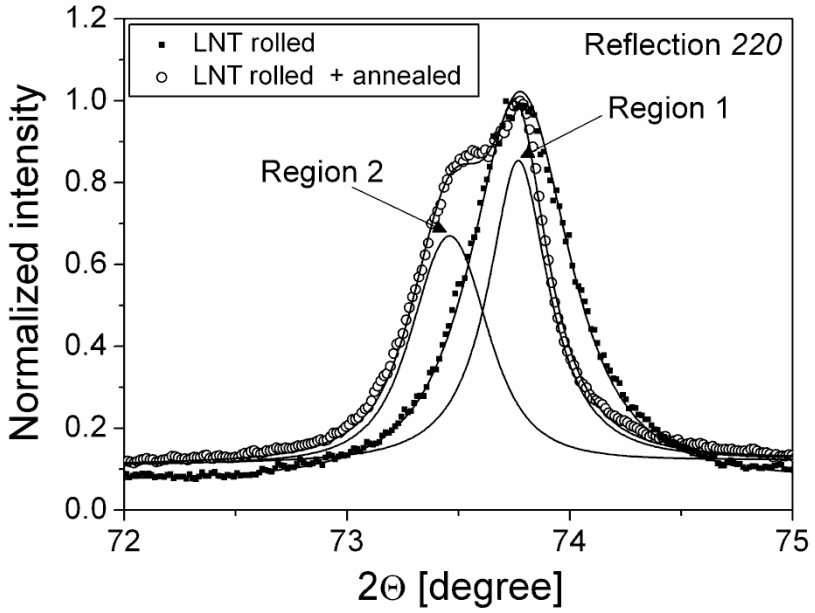

Fig. 2. The CMWP fitting for *220* reflection of the Cu-3at.% Ag samples for LNT rolled, and LNT rolled and annealed conditions. The symbols and the solid lines represent the measured data and the fitted curves, respectively. The diffraction peak in the annealed condition is a sum of two reflections related to regions 1 and 2 having different average lattice parameters.

Regions 1 and 2 with different Ag contents obtained after annealing of RT and LNT rolled samples were investigated by X-ray line profile analysis. In the fitting of the experimental patterns, each theoretical line profile consisted of two peaks corresponding to the two regions. The microstructural parameters for regions 1 and 2 of the Cu matrix were determined from the fitting

and are listed in Table 1. The results reveal that in region 1 the crystallite size did not change significantly while the dislocation density decreased by a factor of 2-4 after annealing the RT and LNT rolled specimens. In region 2 the crystallite size increased slightly and the dislocation density decreased only by ~ 25-40 %. In the volumes where the dissolution of the precipitates was negligible (region 1), the solute Ag content remained low and the dislocation density decreased due to recovery. However, the increased concentration of solute Ag atoms in region 2 hindered the recovery, resulting in the retention of the high dislocation density. The increase of the average size of Cu crystallites in region 2 can be explained by the growth of Cu crystallites into the volumes occupied formerly by the Ag precipitates which were dissolved during annealing.

The tensile behavior of the specimens. Figure 3 shows the engineering stress-strain curves for RT rolled, LNT rolled and annealed samples. The RT and LNT rolled samples exhibit high ultimate tensile strengths (UTS) with negligible uniform elongation (~1 %). The strength of the LNT rolled sample (~710 MPa) is ~20 % higher than that for the RT rolled sample (~575 MPa) which can be attributed to the larger dislocation density and twin boundary frequency. After annealing of the RT rolled sample, the UTS decreased only slightly (by ~20 MPa) with significant improvement in the uniform elongation (from 1 to 10 %). Similarly, annealing of the LNT rolled sample resulted in a decrease in the UTS by ~60 MPa and the ductility improved from 1 to 8 %. The increased strain hardening capacity for the annealed samples compared to the rolled samples could be attributed to the formation of a heterogeneous microstructure as revealed by XRD. It should be noted that the heterogeneous microstructure in the present alloys refers to both the varying solute content and dislocation density. The improvement of ductility was most probably caused by the decrease of the dislocation density in region 1, which yielded a considerable work hardening in this region during subsequent tension, thereby increasing the uniform elongation, as compared to the rolled specimens. At the same time, in region 2 the increase of the solute Ag concentration during annealing hindered the annihilation of dislocations, therefore the strength was only slightly reduced in comparison with the rolled samples.

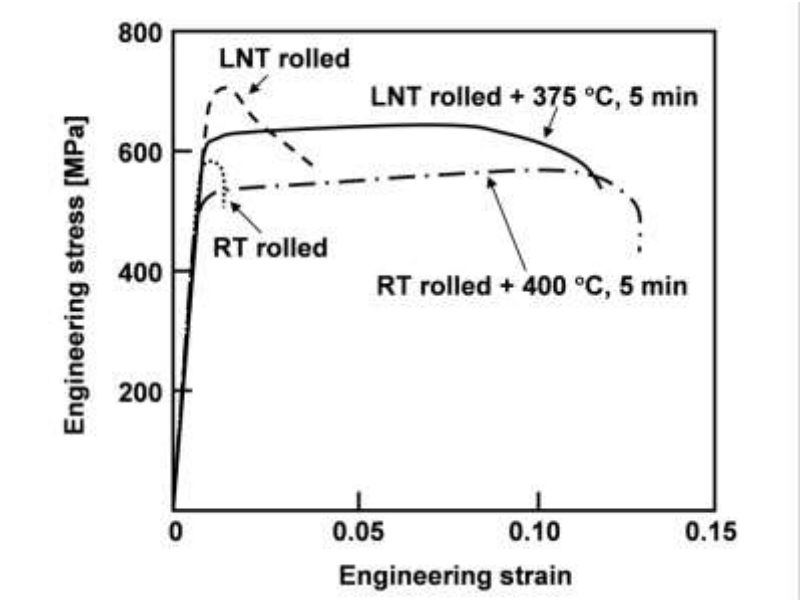

Fig. 3. Engineering stress-strain curves for the RT and LNT rolled as well as the annealed Cu-3at.% Ag alloys.

Summary

1. Supersaturated Cu-3at.% Ag alloy was subjected to thermomechanical treatment including short-time annealing after cold rolling at RT or LNT. In the annealed samples an inhomogeneous solute

atom distribution developed in the Cu matrix due to the dissolution of the smaller Ag nanoparticles in the size distribution. In the region where the solute concentration increased, the dislocation density developed during rolling was retained in the Cu matrix even after annealing, while in the region where the Ag solute content did not increase, significant decrease in dislocation density was observed. Therefore, in the rolled and annealed samples heterogeneous microstructures were developed where both the dislocation density and the solute concentration varied considerably.
2. The as-rolled samples exhibited high ultimate tensile strengths close to 600-700 MPa with negligible uniform elongation (~1%). After short-time annealing the strength decreased only by ~5-10%, while the uniform elongation increased by about one order of magnitude. The improvement of the ductility is attributed to the heterogeneous microstructure in the Cu matrix since the reduction of the dislocation density in some regions increased the strain hardening capacity of the material.

Acknowledgements

This work was supported by the Hungarian Scientific Research Fund, OTKA, Grant No. K-109021.

References

[1] R.Z. Valiev, I.V. Alexandrov, Y.T. Zhu, T.C. Lowe, Paradox of Strength and Ductility in Metals Processed by Severe Plastic Deformation, J. Mater. Res. 17 (2002) 5-8.

[2] N. Tsuji, Y. Ito, Y. Saito, Y. Minamino, Strength and ductility of ultrafi ne grained aluminum and iron produced by ARB and annealing, Scripta Mater. 47 (2002) 893-899.

[3] Y. Wang, M. Chen, F. Zhou, E. Ma, High tensile ductility in a nanostructured metal, Nature, 419 (2002) 912-915.

[4] K. Sitarama Raju, V. Subramanya Sarma, A. Kauffmann, Z. Hegedűs, J. Gubicza, M. Peterlechner, J. Freudenberger, G. Wilde, High strength and ductile ultrafine-grained Cu–Ag alloy through bimodal grain size, dislocation density and solute distribution, Acta Mater. 61 (2013) 228-238.

[5] J. Nelson, J.D. Riley, An experimental investigation of extrapolation methods in the derivation of accurate unit-cell dimensions of crystals, Proc. Phys. Soc. Lond. 57 (1945) 160-177.

[6] G. Ribárik, J. Gubicza, T. Ungár: Correlation between strength and microstructure of ball milled Al-Mg alloys determined by X-ray diffraction, Mater. Sci. Eng. A 387-389 (2004) 343-347.

[7] M. Perez, Gibbs–Thomson effects in phase transformations, Scripta Mater. 52 (2005) 709-712.

[8] G. Kaptay, Nano-Calphad: extension of the Calphad method to systems with nano-phases and complexions, J. Mater. Sci. 47 (2012) 8320-8335.

[9] F. Delogu, Free Energy Differences between Ag-Cu Nanophases with Different Chemical Order, J. Phys. Chem. C 114 (2010) 19946-19951.

Development of cellulose-reinforced Poly(Lactic Acid) (PLA) for engineering applications

Sándor Hajba[1,a], Tibor Czigány[1,2,b], Tamás Tábi[1,2,c],

[1] Department of Polymer Engineering, Faculty of Mechanical Engineering, Budapest University of Technology and Economics, Muegyetem rkp. 3., H-1111 Budapest, Hungary

[2] MTA–BME Research Group for Composite Science and Technology, Muegyetem rkp. 3., H-1111 Budapest, Hungary

[a]hajbasanor4@gmail.com, [b]czigany@pt.bme.hu, [c]tabi@pt.bme.hu

Keywords: Biocomposites, biodegradable polymers, natural fibers, cellulose, Poly(Lactic Acid)

Abstract. The renewable resource based polymers and composites, especially the Poly(Lactic Acid) (PLA) and natural, plant fiber reinforced composites are one of the most important research fields of biocomposites. Due to the mechanical properties of PLA, it stands out of the other biodegradable polymers, but in order to be able to use PLA in engineering application, reinforcing of PLA is needed. PLA can be reinforced with natural plant fibers, however their high moisture content can degrade PLA through hydrolysis during processing of PLA and the fibers into biocomposites. In this paper the effect of pre-process drying was analyzed on the mechanical properties of 30 weight% flax, cotton, and jute fabric reinforced PLA biocomposites. The results of pre-process drying tests showed that the optimum drying temperature was 100°C for the PLA and 120°C for the plant fabrics. It was demonstrated that the drying temperature of PLA and the fabrics has significant effect on the mechanical properties of the biocomposites.

Introduction

Poly(Lactic Acid) is a renewable natural resource based biodegradable thermoplastic polymer, which belongs to the family of aliphatic polyesters [1]. PLA is one of the main representatives of the biodegradable polymers due to its good mechanical and optical properties. It has low density (1,26 g/cm^3), while its tensile strength is about 65 MPa and tensile modulus is about 3 GPa. According to its mechanical properties, it is comparable to the conventional synthetic polymers such as poly(styrene) (PS) and poly(ethylene terephthalate) (PET). PLA has two stereoisomers, namely PLLA and PDLA which affect both the thermal and mechanical properties. PLLA is a semi-crystalline polymer, while PDLA is amorphous. In a commercial PLA the L:D ratio is usually around 9:1 [2-5]. PLA is considered the most promising biopolymer, thus it is a good choice for producing biocomposites by using natural, plant fibers. With cellulose based natural plant fibers the biodegradability and the environment-friendly features of PLA can be kept. Unfortunately both PLA and natural plant fibers have hygroscopic characteristic, so it is critical to dry the raw materials before the production, because the presence of both remaining water and high processing temperature cause PLA to degrade through hydrolysis [6]. Since there is no universally accepted drying parameters used for the drying of PLA and its reinforcements [7-10], thus in our research, the effect of pre-process drying of PLA and plant fabrics as reinforcements was analyzed on the mechanical properties of natural plant fabric reinforced PLA biocomposites.

Experimental

NatureWorks PLA type 4032D biopolymer was chosen as matrix material with a density of 1.24 g/cm^3, and a melting temperature of 155-170°C. The jute, flax and cotton woven fabrics were supplied by Dél-Alföldi Műszaki Konfekció Ltd (Hungary). The main properties of the fabrics are shown in

Table 1.

Table 1. Main properties of woven fabrics

Type	weave type	surface weight [g/m^2]
jute	plain weaved	400
flax126	plain weaved	126
flax200	plain weaved	200
cotton P695	plain weaved	120
cotton 9/10	plain weaved	375
cotton 350h/P	plain weaved	480

Before composite production drying tests were performed to determine the optimal drying conditions for the PLA and the natural fabrics. Three different temperatures were used namely 80, 100 and 120°C. After the pre-process drying, 30 weight% fiber content biocomposites were made with film-stacking technology by laying plant fabrics and thin PLA films on each other and compression molding this multilayer structure. The effect of processing temperature was also investigated as both PLA, and moreover the plant fabrics are highly susceptible to thermal degradation. According to the melting temperature of PLA 4032D 190, 210, and 230°C processing temperatures were analyzed. Finally, the effect of pre-process drying was analyzed on the mechanical properties of the biocomposites by using tensile, flexural and impact (Charpy) tests.

Results and discussion

The presence of water and high temperature causes hydrolysis in PLA during the biocomposite preparation thus, the drying characteristics were determined (Fig. 1).

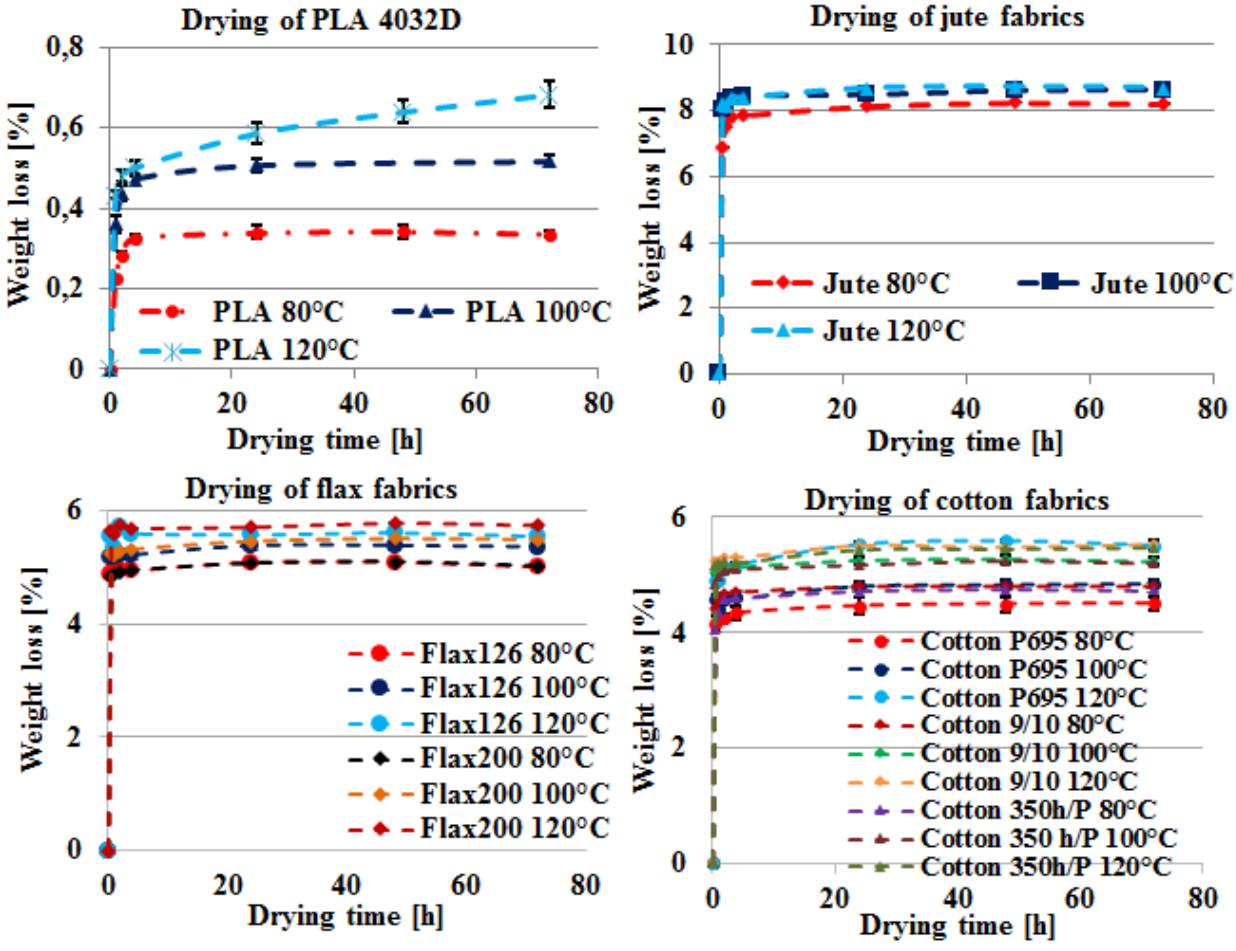

Fig. 1. The drying characteristics of the materials

From the investigated temperatures the optimal drying conditions for PLA was 100°C for about 6 hours. The 120°C drying temperature is not acceptable because most probably hydrolysis occurred due to the high drying temperature and the remaining moisture in the pellets as indicated by the continuously increasing weight loss. For the natural fabrics the optimum drying temperature was 120°C for around 24 hours. The maximum weight losses were 8-9% for jute and 5-6% for both cotton and flax fabrics.

Based on the literature data, the moisture content of PLA should be kept below 250 ppm [1, 6] to avoid any kind of degradation. This means that only 10 minutes are available after the drying for biocomposite preparation. Some biocomposites were prepared to determine the optimal processing temperature (Fig. 2, Fig. 3). It can be seen that at higher processing temperatures, the components of the natural fabrics such as lignin and hemicellulose start to decompose and this resulted in a decrease of mechanical properties.

Fig. 2. Composites produced at 190, 210 and 230°C

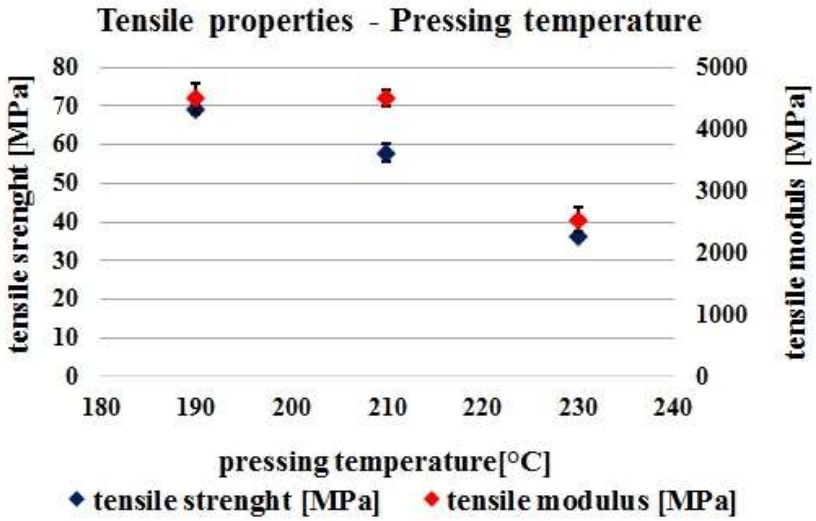

Fig. 3. The effect of processing temperature on the mechanical properties

Accordingly 190°C processing temperature was chosen for further biocomposite production. The biocomposites for the final investigation were prepared with various pre-process drying temperatures to determine its effect on the mechanical properties (Fig. 4-Fig. 6).

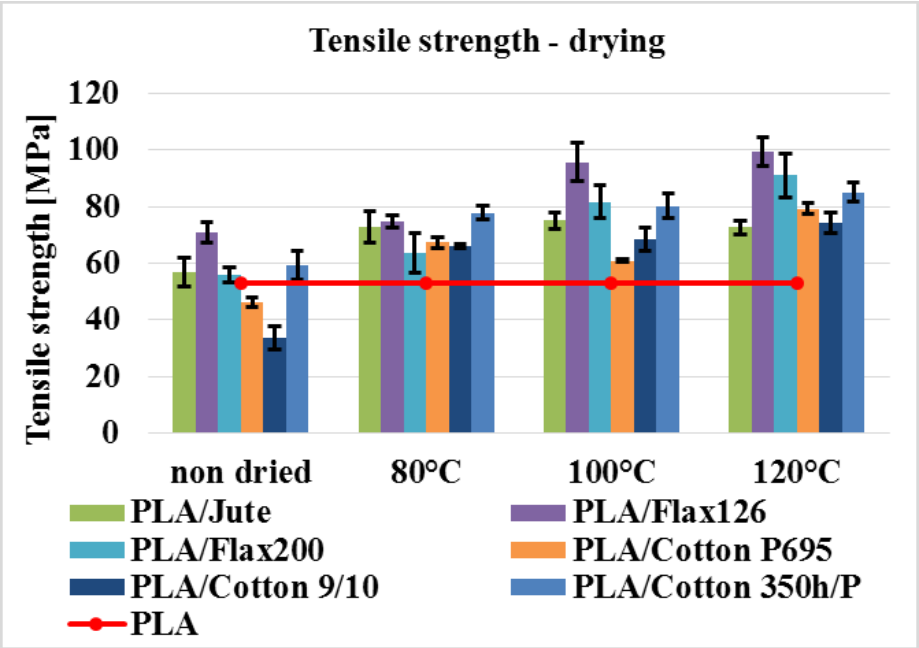

Fig. 4. Tensile strength of the biocomposites

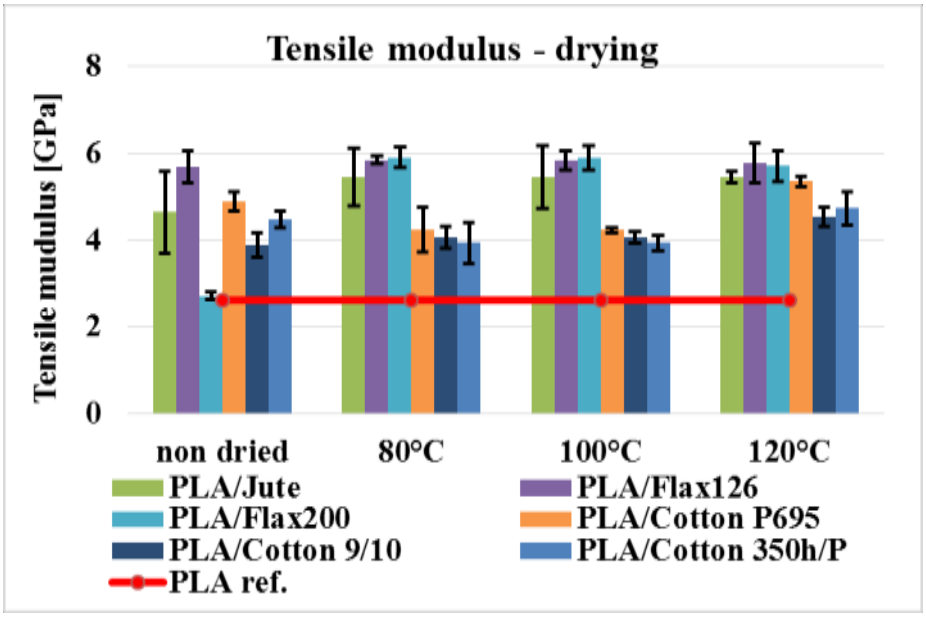

Fig. 5. Tensile modulus of the biocomposites

As it can be seen the pre-process drying was found to have very significant effect on the mechanical properties of the biocomposites. 20-40 MPa improvements can be seen in the tensile strength of the biocomposites only by increasing the drying temperature from 80 to 120°C. Accordingly, the tensile strength of the Flax200 reinforced PLA biocomposite increased from 63.6 MPa to 91 MPa only by increasing the pre-processing drying temperature from 80 to 120°C. The highest tensile strength was found in case of Flax126 fabrics reinforced PLA biocomposite, where the fabric was dried at 120°C. Accordingly, compared to the reference PLA the tensile strength has increased from 62 MPa to 99 MPa and the tensile modulus has increased from 2.69 GPa to 5.67 GPa. In case of the flexural properties (data not shown) jute reinforced biocomposites proved to have the highest strength and modulus. Its flexural strength was 110 MPa and the flexural modulus was 8.03 GPa, while the reference flexural strength of PLA was 58 MPa and the flexural modulus was 3.41 GPa respectively. The impact tests show (Fig. 6) that the pre-process drying had also an effect on the impact strength, however, this effect was not as significant as in the case of tensile and flexural strengths. Nevertheless, the relatively small impact strength of neat PLA of around 15 kJ/m^2 was enormously increased with Cotton 350h/P fabric reinforcement to 60 kJ/m^2.

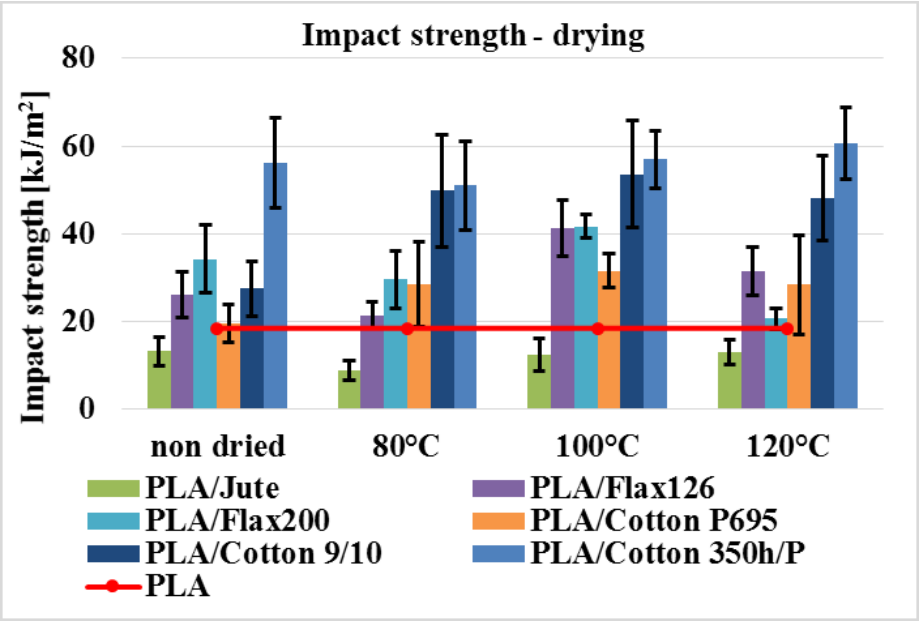

Fig. 6. Impact strength of the biocomposites

Summary

In our work the effect of pre-process drying was analyzed on the mechanical properties of fully renewable resource based biodegradable polymer biocomposites based on Poly(Lactic Acid) (PLA) and flax, jute and cotton fabrics. The reinforcements were dried at various temperatures (80, 100, 120°C), and the mechanical properties of the 30 weight% plant fabric reinforced biocomposites prepared by using film-stacking method was determined. For the natural plant fabrics the optimum drying temperature was found to be 120°C for around 24 hours, while for PLA it was found to be 100°C for around 6 hours. During moisture uptake tests it was demonstrated that only around 10 minutes are available after the drying of the components for biocomposite preparation to be able to avoid any hydrolitical degradation in PLA during processing due to the quick moisture uptake of the fabrics after drying. The investigation of the mechanical properties of the biocomposites revealed that pre-process drying temperature of PLA and the fabrics has significant effect, since 20-40 MPa improvements were found in the tensile strength of the biocomposites only by increasing the pre-process drying temperature from 80 to 120°C. Accordingly, the tensile strength of the Flax200 reinforced PLA biocomposite increased from 63.6 MPa to 91 MPa only by increasing the pre-processing drying temperature from 80 to 120°C. The tensile strength and modulus of the neat PLA increased from 62 MPa and 2.69 GPa to 99 MPa and 5.67 GPa respectively, by using flax fabric as reinforcement. Also, flexural strength and modulus of the neat PLA increased from 58 MPa and 3.41 GPa to 110 MPa and 8.03 GPa respectively, by using jute fabric as reinforcement. Finally, impact tests showed that the pre-process drying had also an effect on the impact strength, however, not as significant as in the case of tensile and flexural strengths. Nevertheless, the relatively small impact strength of neat PLA of around 15 kJ/m^2 was enormously increased with Cotton fabric reinforcement to 60 kJ/m^2.

Acknowledgement

This paper was supported by the János Bolyai Research Scholarship of the Hungarian Academy of Sciences. This publication was supported by the Italian-Hungarian and the Mexican-Hungarian bilateral agreement of the Hungarian Academy of Sciences. This work was supported by the Hungarian Scientific Research Fund (OTKA K105257, PD105995). This work is connected to the scientific program of the "Development of quality-oriented and harmonized R+D+I strategy and functional model at BME" project. This project is supported by the New Széchenyi Plan (Project ID: TÁMOP-4.2.1/B-09/1/KMR-2010-0002). The authors thank Arburg Hungária Kft. for the

Arburg Allrounder 370S 700-290 injection moulding machine, Lenzkes GmbH for the clamping tool system and Piovan Hungary Kft. for their support.

References

[1] D. Garlotta: A Literature review of poly(lactic acid), J. Polym. Environ 9 (2001) 63-84.

[2] A. Södergard, M. Stolt: Industrial production of high molecular weight poly(lactic acid), in: R. Auras, L.-T. Lim, S.E.M. Selke, H. Tsúji (Eds), Poly(lactic acid) synthesis, structure, properties and applications. John Wiley & Sons Inc., New Jersey 2010, pp. 27-41.

[3] L.-T. Lim, R. Auras, M. Rubino: Processing technologies for poly(lactic acid), Prog. Polym. Sci. 35 (2008) 338-356.

[4] R.M. Rasal, A.V: Janorkar, D.E. Hirt: Poly(lactic acid) modifications, Prog. Polym. Sci. 35 (2010) 116-125.

[5] F. Carrasco, P. Pages, J. Gámez-Pérez, O.O. Santana, M.L. Maspoch: Processing of poly(lactic acid): Characterization of chemical structure, thermal stability and mechanical properties, Polym. Degrad. Stabil. 96 (2010) 116-125.

[6] L.-T. Lim, K. Cink, T. Vanyo: Processing of poly(lactic acid), in: R. Auras, L.-T. Lim, S.E.M. Selke, H. Tsúji (Eds), Poly(lactic acid) synthesis, structure, properties and applications. John Wiley & Sons Inc., New Jersey 2010, pp. 191-215.

[7] N. Graupner, A.S. Hermann, J. Müssig: Natural man-made cellulose fibre-reinforced poly(lactic acd) (PLA) composites: An overview about mechanical characteristic and application areas, Compos. Part A-Appl. S. 40 (2009) 810-821.

[8] M. Jonoobi, J. Harun, A.P. Mathew, K Oksman: Mechanical properties of cellulose nanofiber (CNF) reinforced polylactic acid (PLA) prepared by twin screw extrusion, Comp. Sci. Technol. 70 (2010) 1742-1747.

[9] M. Kowalczyk, E. Piorkowska, P. Kulpinski, M. Pracella: Mechanical and thermal properties of PLA composites with cellulose nanofibers and standard size fibers, Compos. Part A-Appl. S. 42 (2011) 1509-1514.

[10] N. Graupner, J. Müssig: A comparison of mechanical characteristic of kenaf and lyocell fibre reinforced poly(lactic acid) (PLA) and poly (3-hydroxybtyrate) (PHB) composites, Compos Part A-Appl. S. 42 (2011) 2010-2019.

Styrene-butadiene rubber/graphene nanocomposites: Effect of co-milling with cyclic butylene-terephthalate

István Halász[a], Tamás Bárány[b]

Department of Polymer Engineering, Faculty of Mechanical Engineering
Budapest University of Technology and Economics
H-1111 Budapest Műegyetem rkp. 3, Hungary

[a]halaszi@pt.bme.hu, [b]barany@pt.bme.hu (corresponding author)

Keywords: elastomer, nanocomposite, dispersion, milling, CB, graphene nanoplatelets, SBR

Abstract. Graphene nanoplatelets (GnP) reinforced styrene-butadiene rubber (SBR) nanocomposites were produced by two different methods. For reference purpose carbon black (CB) reinforced formulations served. In the first method the components were mixed on a two roll open mill directly. In the second method, GnP was subjected to milling in an attritor mill together with cyclic butylene-terephthalate oligomer (CBT) powder prior to the mixing on two roll mill. Samples were cured in a hot press. The rubber sheets were characterized by tensile and tear tests, and their fracture surfaces inspected in scanning electron microscopy (SEM). Results showed that GnP outperformed CB with respect to reinforcing effect. Previous co-milling of GnP with CBT caused a slight decrease in mechanical properties. SEM images proved, that the co-milling process did not affect significantly the dispersion of GnP, its particles were shredded into smaller pieces, which caused the slight decrease in the mechanical properties.

Introduction

Research to explore possibilities of rubber reinforcement by various fillers is dating back to the beginning of rubber industry. The role of fillers became particularly emphatic with the appearance of synthetic rubbers (such as SBR), because most of their properties are poor in their raw, unfilled state. It was discovered in the early years, that mechanical and wear properties of rubbers can greatly be improved by adding carbon black (CB) to the mixture. Note that CB can be considered as a nanofiller, because the average particle size of CBs is in nanometer scale [1-3].

In the past two decades novel allotropes of carbon was discovered, such as graphene and single- or multiwalled carbon nanotubes (SWCNT and MWCNT). Due to their extraordinary mechanical, physical, electrical and thermal properties they became objects of strong interest [3, 4]. Their outstanding specific surface area accompanied by excellent mechanical properties and the potential presence of reactive or functional groups makes them ideal for preparation of composite structures. The reason why they did not became widely used is linked with the difficulty of adequate dispersion of these fillers. This dispersion problem arises from the anisotropy of particles (wide, closely stacked layers, or very thin fibrous structure, which can form a heavily entangled network of nanotubes) along with the Van der Waals interactions acting between them. To increase the dispersion of carbonaceous nanofillers is a key issue of nanocomposites' production [5].

Cyclic butylene terephthalate oligomer (CBT) is a cyclic compound, its rings are composed of 2-7 monomer units. The melting temperature of CBT ranges from 120 to 160°C. In the presence of a suitable catalyst it can be polymerized into polybutylene-terephthalate (PBT). Due to the difference in the average molecular weight and crystallinity compared to the traditional polycondensation PBT, the ring-opening polymerized version is denoted by pCBT in the literature. The very low melt viscosity (0.02 Pas at 190°C) makes CBT particularly suitable as in situ polymerizable matrix

material for composites. Furthermore it can be used as a processing aid to improve the processability of a broad range of thermoplastic resins. Flow properties can be significantly improved by adding only a few wt.% of CBT and it hardly affects other properties of the material [6]. Previous studies showed that rubber/CBT hybrids have outstanding mechanical and wear properties, so CBT seems to be able to act as an active filler in rubbers [6-8]. Another noteworthy work demonstrated, that using CBT powder and high-energy ball milling (HEBM) the strongly entangled MWCNT agglomerates can be efficiently broken up, and well dispersed MWCNT reinforced nanocomposites can be prepared [9].

Based on the above mentioned properties and results the goal of this work was to investigate the effect of graphene nanoplatelets (GnP) and CBT for the properties of sulphur-cured styrene-butadiene rubber (SBR). Attempt was also made to check whether or not a preliminary co-milling of GnP with CBT is beneficial.

Materials and Testing

As matrix material Plioflex 1502 SBR was used with 23.5 wt.% bound styrene content supplied by Goodyear Chemical (Akron, Ohio, USA). The activator, antioxidant and curing agents were commercially available materials. Cyclic butylene-terephthalate oligomer, grade CBT100 (without polymerization catalyst), was provided by Cyclic Corporation (Schwarzheide, Germany) in a powder form. Carbon black was a commercial grade high abrasion furnace (HAF) N330 CB. Graphene nanoplatelets powder was xGnP H grade, supplied by XG Sciences Inc. (Lansing, Michigan, USA). CBT-GnP dry blends were milled in a Union Process 01HD laboratory attritor (Union Process Inc., Akron Ohio, USA) for 3x10 minutes with 600 rpm. The weight of the steel balls was 1000 g and the balls were 5 mm in diameter. A schematic illustration of the attritor is given in Fig. 1.

Figure 1. Schematic build-up of the attritor

Preparation of the rubber blends were carried out on a laboratory two roll mill (Labtech Scientific LRM-SC-110, Labtech Engineering Co., Ltd., Samut Prakarn, Thailand), friction was set to 1.3, the temperatures of the front and back rotor were 70°C and 50°C, respectively. The compositions of the samples are listed in Table 1.

Mixtures

		Sample No.									Samples	
		1	2	3	4	5	6	7	8	9	Sample No.	Abbreviation
SBR 1502	**[phr]**	100									1	Reference
ZnO		5									2	CB
Stearic acid		1									3	
TMQ		1									4	GnP
CBS		1									5	
Sulphur		2									6	GnP+CBTh
N330 CB		0	1	5	0						7	
CBT100		0					4	20	4	20	8	GnP+CBTa
xGnP H		0			1	5	1	5	1	5	9	

Table 1. Recipes of the sample, and their abbreviation. Designations: TMQ - 2,2,4-trimethyl-1,2-dihydroquinoline CBS - Cyclohexyl-2-benzothazolesulfenamide phr-part per hundred part rubber

The samples were cured in a Collin Teach-Line Platen Press 200E laboratory press (Dr. Collin GmbH, Edersberg, Germany) at 170°C for 20 min with 2 MPa pressure producing sheets with ca. 2 mm thickness. Specimens (DIN 53504 Type 1 for tensile and ASTM D624 Type C for tear tests) were punched from the sheets. Tensile and tear tests were performed on a Zwick Z250 universal testing machine equipped with a 20 kN load cell (Zwick GmbH & Co. KG, Ulm, Germany) with a crosshead speed of 500 mm/min at room temperature.

Results and Discussion

Mechanical characterizations. Fig. 2-4 shows the tensile strength, strain at break and modulus (M-100, stress at 100% strain) values of the composites as a function of the filler (CB and GnP) content. GnP+CBTa represents the previously milled sample, GnP+CBTh samples were mixed only on the two roll mill. It can be seen, that GnP has superior reinforcing effect than CB even at lower filler content. Tensile strength was affected negatively by the milling process. CBT itself has a reinforcing effect in SBR. Recall that the reinforcing effect of CBT was already presented earlier by us [6].

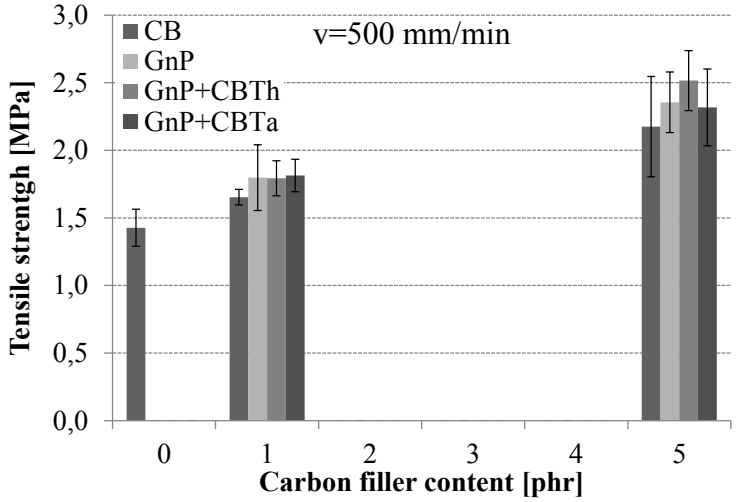

Figure 2. Tensile strength values as a function of filler (CB or GnP) content

Similar tendency can be noted for the strain at break values. At lower filler contents the difference between the effects of fillers and co-milled and non-milled GnP-CBT systems are less notable. However, at higher filling it can be seen that non-milled GnP-CBT improves the strain at break compared to the sample with co-milled GnP-CBT.

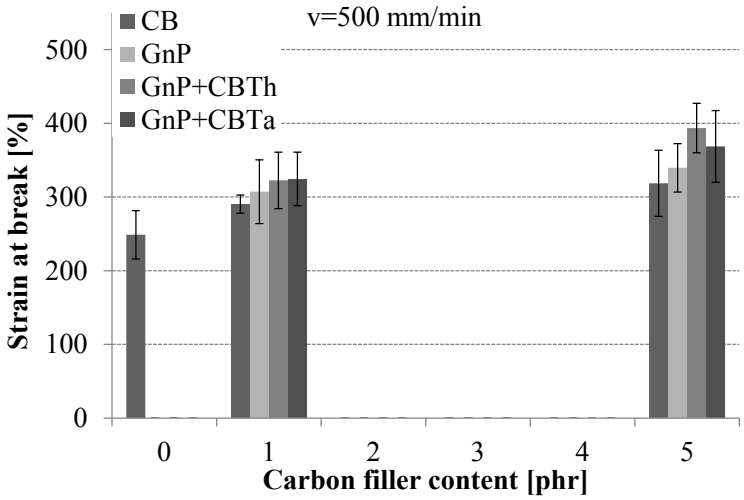

Figure 3. Strain at break values as a function of filler (CB or GnP) content

Analyzing the M-100 values of the composites containing 5 phr carbon filler content, it can be concluded, that the difference caused by the milling is increasing with increasing filler content.

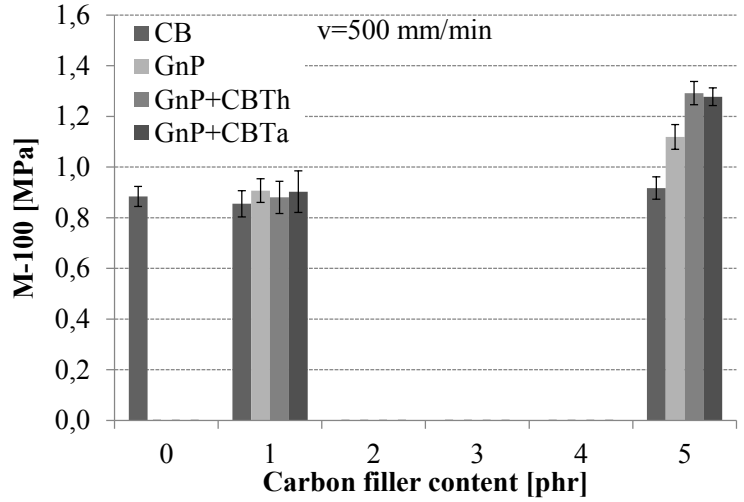

Figure 4. M-100 values as a function of filler (CB or GnP) content

Fig. 5 shows the tear strength values of the samples as a function of the filler (CB and GnP) content. Similarly to M-100, tear strength is only minimally affected by the fillers, if their content is only 1 phr. If the content is increased, a remarkable increment can be noticed, and the values of the non-milled samples were the highest.

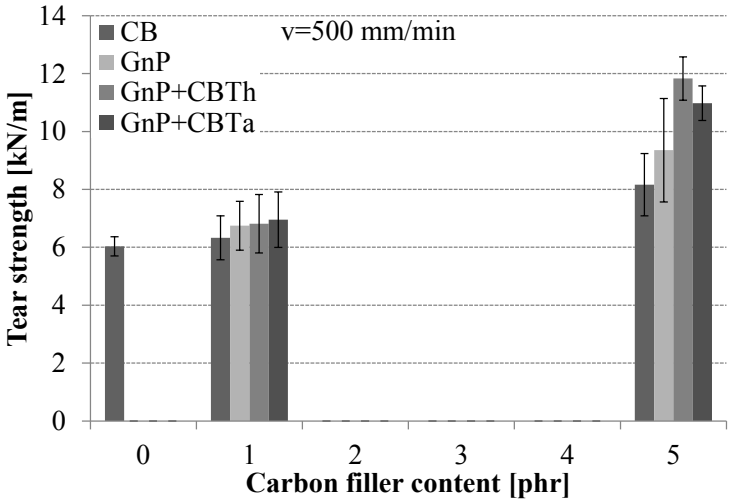

Figure 5. Tear strength values as a function of filler (CB or GnP) content

Morphology. Fig. 6 shows the torn surface of a specimen after tear test. It can be clearly observed, that the GnPs were shredded during the milling. Not only their lateral (thickness), but also their longitudinal (width) dimensions were reduced. Note that the white arrows mark the GnPs. Consequently the dispersion of the GnP filler was improved. On the other hand, these smaller particles could not reinforce the rubber as effectively as the original larger ones.

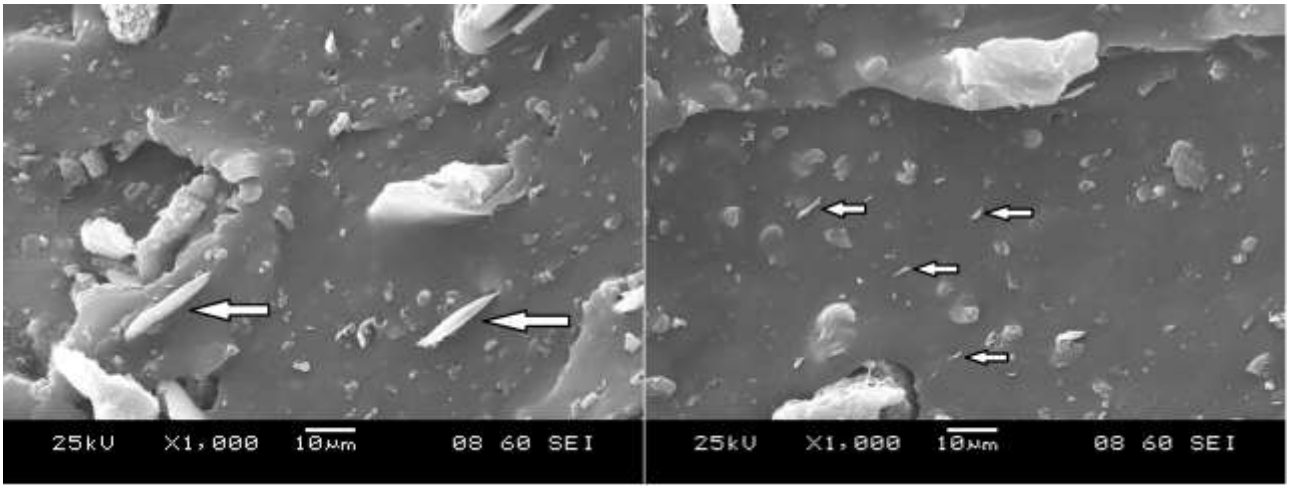

Figure 6. SEM images taken from the torn surface of tear specimens (*GnP+CBT left, GnP+CBTa right)*

Summary

The aim of this study was to investigate the effect of a previous milling of the nanofiller with a "carrier" powder on the dispersion of the nanofiller. This carrier in this case was a cyclic butylene terephthalate oligomer (CBT) in powder form GnP. Rubber samples were prepared by different methods: including a preliminary milling and without it. To compare the effects of GnP, carbon black (CB) filled samples were also produced. Tensile and tear tests showed, that GnP has a slightly stronger reinforcing effect compared to traditional CB. Incorporation of CBT alone also improved thermomechanical properties. SEM pictures showed, that the milling reduced the GnP particle size, thereby improving the dispersion of the platelets. This had, however, a negative effect on the mechanical properties. Nonetheless, the method introduced in this work is very promising for the production of rubber nanocomposites containing high filler contents. Next, co-milling with CBT will be adapted to disperse other nanofillers, such as carbon nanotubes (CNTs), silica in rubbers. Milling parameters, mostly the milling time is that parameter which should be optimized for better results.

Acknowledgements

This work was supported by the Hungarian Scientific Research Fund (OTKA K100294).

References

[1] C. Sirisinha, N. Prayoonchatphan, Study of carbon black distribution in BR/NBR blends based on damping properties: Influences of carbon black particle size, filler, and rubber polarity, J. Appl. Polym. Sci. 81 (2001) 3198-3203.

[2] S. Dankers, S. Schraml, S. Will, A. Leipertz, Application of laser-induced incandescence for the determination of primary particle sizes of nanoparticles demonstrated using carbon blacks, Chem. Eng. Technol. 25 (2002) 1160-1164.

[3] M. Dresselhaus, G. Dresselhaus, P. Eklund. Science of Fullerenes and Carbon Nanotubes: Academic Press; 1996.

[4] A.K. Geim, K.S. Novoselov, The rise of graphene, Nat. Mater. 6 (2007) 183-191.

[5] D. Feldman, Elastomer Nanocomposite; Properties, J. Macromol. Sci. A 49 (2012) 784-793.

[6] J. Karger-Kocsis, D. Felhős, T. Bárány, T. Czigány, Hybrids of HNBR and in situ polymerizable cyclic butylene terephthalate (CBT) oligomers: properties and dry sliding behavior, Express Polym. Lett. 2 (2008) 520-527.

[7] D. Xu, J. Karger-Kocsis, Rolling and sliding wear properties of hybrid systems composed of uncured/cured HNBR and partly polymerized cyclic butylene terephthalate (CBT), Tribol. Int. 43 (2010) 289-298.

[8] D. Xu, J. Karger-Kocsis, A.A. Apostolov, Hybrids from HNBR and in situ polymerizable cyclic butylene terephthalate (CBT): Structure and rolling wear properties, Eur. Polym. J. 45 (2009) 1270-1281.

[9] G. Romhány, J. Vigh, R. Thomann, J. Karger-Kocsis, I.E. Sajó, pCBT/MWCNT nanocomposites prepared by in situ polymerization of CBT after solid-phase high-energy ball milling of CBT with MWCNT, Macromol. Mater. Eng. 296 (2011) 544-550.

The examination of the cutting capacity of different aluminium alloys with statistical methods, using different edge material non-conventional (Wiper) edge geometry diamond tools

Richard Horvath*[1,a], Gyula Mátyási[2,b] and Ágota Drégelyi-Kiss[1,c]

[1]Óbuda University Donát Bánki Faculty of Mechanical and Safety Engineering, H-1081 Budapest 8 Népszínház Street

[2] Budapest University of Technology and Economics, H-1111 Budapest, 1 Egry József Street

[a]horvath.richard@bgk.uni-obuda.hu, [b]matyasi@manuf.bme.hu, [c]dregelyi.agota@bgk.uni-obuda.hu,

Keywords: fine turning, surface roughness measurement, design of experiments, RSM method, statistical analysis, cutting capacity

Abstract. The aluminium alloys are used by the automotive, aerospace industries increasingly because of their numerous advantageous mechanical and chemical properties. Surface roughness measurements are essential in characterization of the features of a machined surface. The most widespread aluminium alloy used in cutting is the die-cast type, alloyed with silicon. Industries prefer using two types of such alloys, the so-called eutectic and hypereutectic alloys reinforced with silicon. In this article the cutting capacities of two die-cast aluminium alloys are examined. The cutting experiments were carried out with design of experiment – DOE (the so-called central composite design – CCD). In the course of the examination three factors were altered (cutting speed – v_c, m/min; feed – f, mm; depth of cut – a, mm), and the main surface roughness parameters used in the industries were taken as output parameters. The parameters of the manufactured surface roughness and their deviation in case of different workpiece-materials, tool-materials and edge-materials were analysed with statistical methods. Besides minimizing surface roughness, another important criterion of the manufacturing system (machine – tools – chuck – workpiece) is its surface roughness maintaining capacity, which was analyzed with coefficient of variation (CV).

Introduction

Surface roughness measurements are essential in characterization of the features of a machined surface. To examine the effect of cutting parameters on surface roughness thoroughly, a huge number of experiments are needed, depending on the number of parameters. By utilizing the method of design of experiments (DOE), the number of experiments can be reduced in such a way that the effect of parameters could be assessed appropriately. If linear effects of cutting parameters are considered, then fractional factorial design is sufficient, but to examine the quadratic term, RSM method has to be utilized [1].

DoEs are often employed in cutting research. Aouchi et al. [2] and Noordin et al. [3] examined hard turning with a CBN and hard metal tool and the resulting surface with the help of DoE. Asiltürk et al. [4] examined stainless steel turning with coated hard metal tools. Dry, wet, and MQL turning was examined with the help of DoE by Hwang [5]. Harničárová et al. studied the the topography of laser-cut surfaces [6]. Lazarevic et al. examined the surface roughness of engineering polymers by using Taguchi method [7].

Horvath et al. examined the fine-turning of aluminium with the help of DOE, they set up empiric equations to estimate the roughness producing capacity of the examined tools (*Ra, Rz*) [8], as well as they defined surface roughness and productivity target functions and they looked for optimal parameters [9].

During this research cutting experiments were made in order to determine the connection between cutting parameters and surface roughness values in case of non-conventional (Wiper) edge geometry diamond tools and different workpiece materials. The two chosen aluminium alloys are described in detail. Besides minimizing surface roughness, another important criterion of the

manufacturing system (machine – tools – chuck – workpiece) is its surface roughness maintaining capacity, which was analyzed with coefficient of variation (*CV*).

Subject and Methods

Workpiece and tool materials

The increased silicon content means difficulties in the course of aluminium cutting. The prime silicon crystals found in the aluminium matrix make the chip break more easily, but their presence leads to faster tool-wear (which can be most often observed in case of hardmetal tools) and leads to the increase in difficulties during cutting.

The workpiece material were AS12 (eutectic) and AS17 (hypereutectic), which are frequently used in automotive, aerospace and defence industries. The advantage of the eutectic workpiece material is its perfect cast capacity while the benefits of hypereutectic alloy are their larger endurance limit and their better abrasion-resistant. The chemical composition (in wt.%) and hardness of the workpiece were: for AS12 the Al content is 88.43%, the Si content is 11.57%, and the hardness is 64±2 $HB_{2,5/62,5/30}$. For AS17 the Al content is 74.35%, the Si content is 20.03%, the Cu content is 4.57%, the Fe content is 1.06%, and the hardness is 114±3 $HB_{2,5/62,5/30}$.

The examined part was a cylinder with a diameter of 110 mm. The experimental runs were made in every 10 mm. The two metallographic specimen of the workpiece material (machined surface) are shown in Fig. 1. In the figures the difference between the eutectic and hyper-eutectic fabrics can be clearly seen.

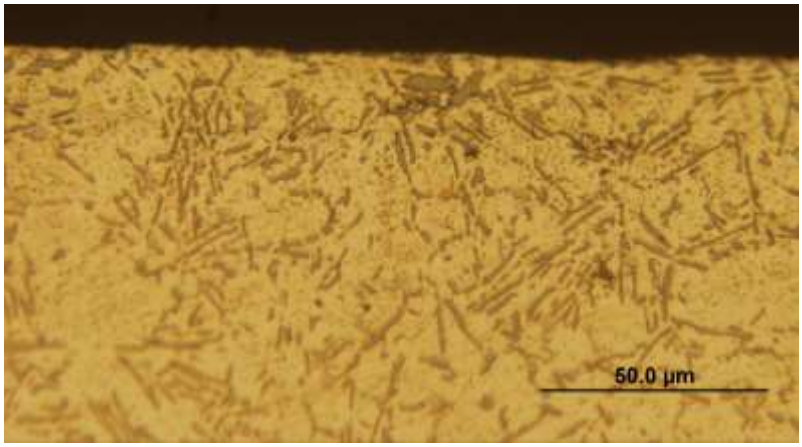

a)

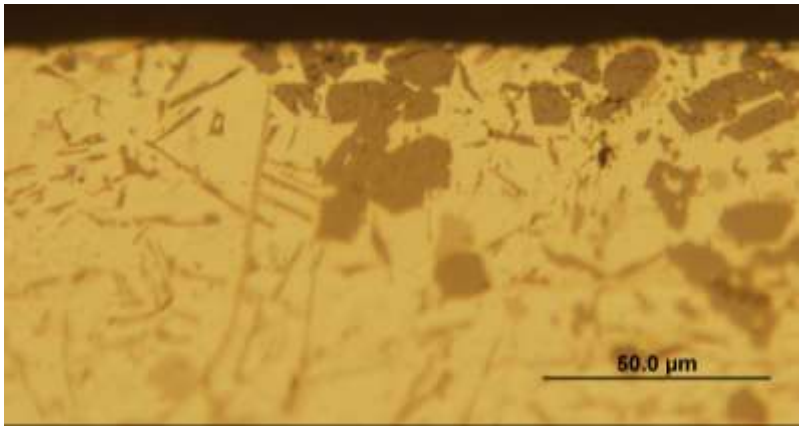

b)

Fig 1. The metallographic specimens of the workpieces

a) Material: AS12 material; cutting parameters: v_c = 1833 m/min, f = 0.118 mm, a = 0.733

mm; tool material: CVD-D, tool geometry: Wiper

b) Material: AS17 material; cutting parameters: v_c = 1833 m/min, f = 0.118 mm, a = 0.733 mm; tool material: CVD-D, tool geometry: Wiper

The standard designation of the tools selected were DCGW 11T304 with non-conventional (so-called Wiper) edge geometry. The edge geometry of the tools are shown in Fig. 2. The edge materials were PCD, CVD-D, and they were manufactured by TiroTool. The holder of the tool was codified as SDJCR 1616H 11. The average surface roughness (*Ra*) and maximum height values (*Rz*) were measured by a Mitutoyo SJ-301 surface roughness tester. Parameters related to surface roughness measurement were: *l=4 mm,* λ_c*=0.8, N=5*. The measurements were repeated at twelve reference lines equally positioned at 30° and the result was the average of these values.

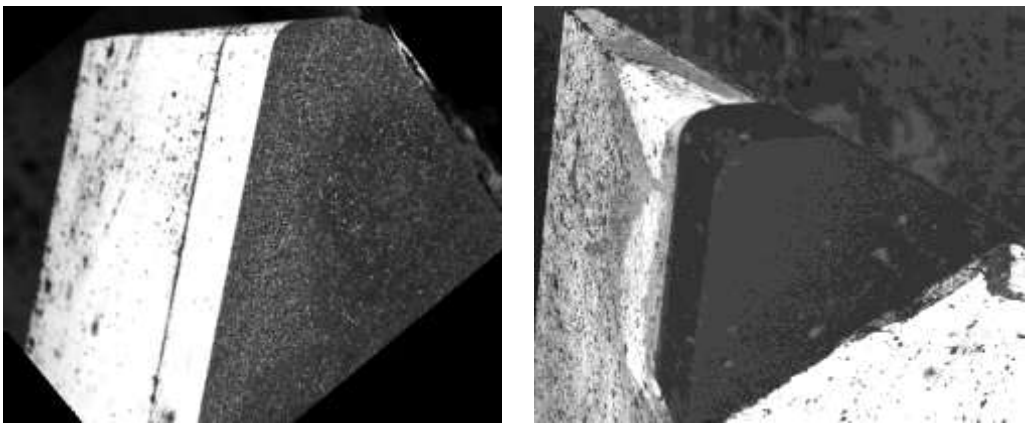

a) b)

Fig 2. SEM photo of nose radius (Wiper) of examined tools (magn.: 20x)

a) non-convetional – Wiper geometry (edge material: PCD)

b) non-convetional – Wiper geometry (edge material: CVD-D)

Experimental design

Response surface methodology (RSM) is a procedure which is able to determine a relationship between independent input process parameters (e.g. cutting parameters) and output data (process response, e.g. *Rz, Ra*). In the course of design of experiments, a response surface method was chosen, the central composite design (CCD) method. CCD was set up for three controllable factors: cutting speed (v_c), feed rate (f) and depth of cut (a). Each factor had 5 different levels. The number of experimental runs was 16, in which two trials were examined in the centre of the design (Table 1).

Table 1: Design of experiments with the levels of factors

2^3 central composite design			
Runs	v_c	f	a
1	-1	-1	-1
2	-1	-1	1
3	-1	1	-1
4	-1	1	1
5	1	-1	-1
6	1	-1	1
7	1	1	-1
8	1	1	1
9	-1.28719	0	0

10	1.28719	0	0
11	0	-1.28719	0
12	0	1.28719	0
13	0	0	-1.28719
14	0	0	1.28719
15 (C)	0	0	0
16 (C)	0	0	0

The limits of the studied cutting parameters are set so that they meet the values used by industries currently and so that they should meet the requirement of high speed cutting (HSC) applications as well. The minimum and maximum values of the cutting parameters applied in the examination can be seen in Table 2.

Table 2: The limits of used cutting parameters

v_{cmin} =500 m/min	v_{cmax} = 2000 m/min
f_{min}= 0.12 mm	f_{max} = 0.24 mm
a_{min} = 0.2 mm	a_{max}= 0.8 mm

Results and statistical analysis

The experiments were made for two types of tools and two types of workpiece-materials in the range of the examined cutting parameters. During the experiments made with Wiper tools the average values of the *Ra* and *Rz* parameters can be seen in Fig. 3. Comparing the experiments carried out with two types of Wiper geometry tools it is stated that in case of both tools the means of the surface roughness values are lower when AS17 workpiece-material is cut.

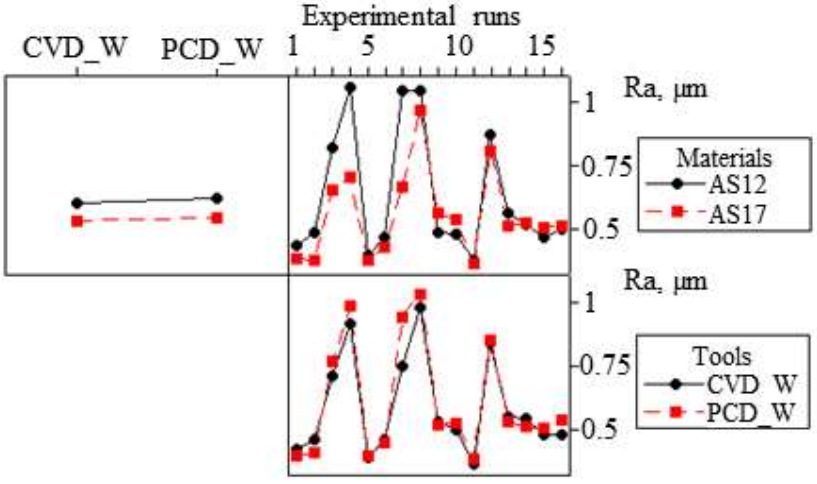

a)

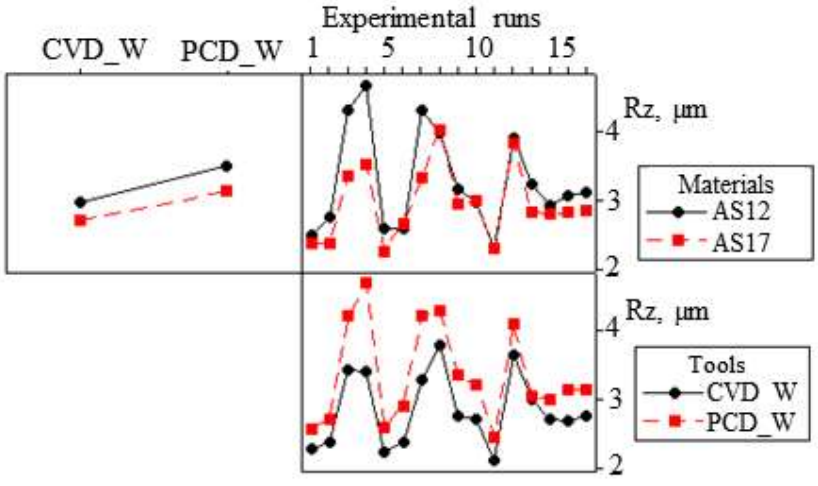

b)

Fig 3. The means of *Ra* and *Rz* values in case of different experimental runs

a) The means of the average surface roughness values regarding different workpiece materials and different tools

b) The means of the maximum height surface roughness values regarding different workpiece materials and different tools

The index-number of the surface roughness measured on the cylinder (twelve times, every 30 degrees) may be the value of the coefficient of variation (*CV*) which is the quotient of the measurement deviations and the average of the measured values. The *CV* values of the examined tools can be seen in Fig 4. It is clear that the deviations of surface roughness are significantly smaller in case of AS17 workpiece-material.

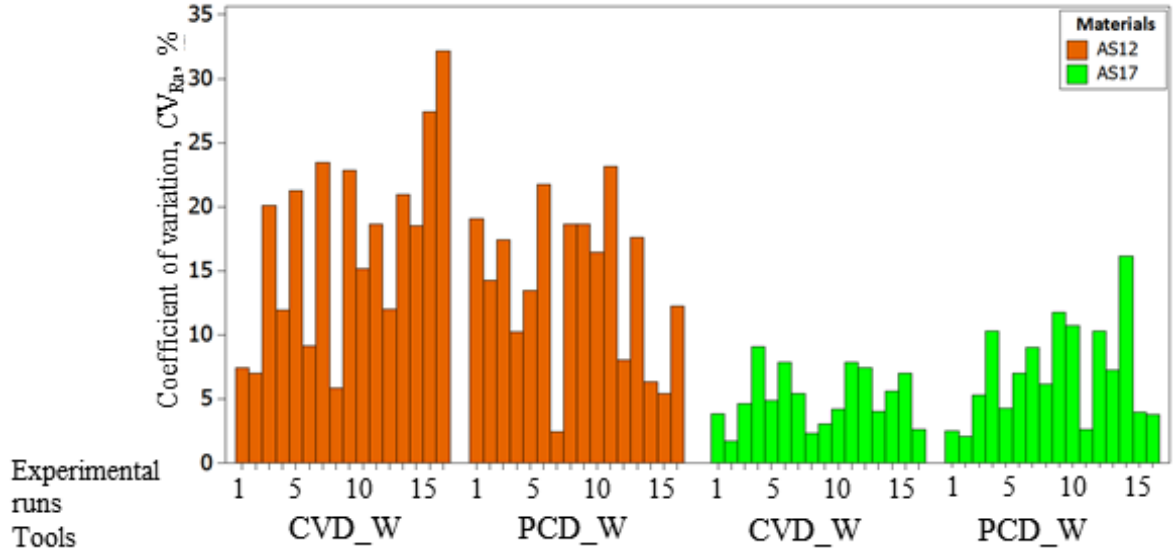

a)

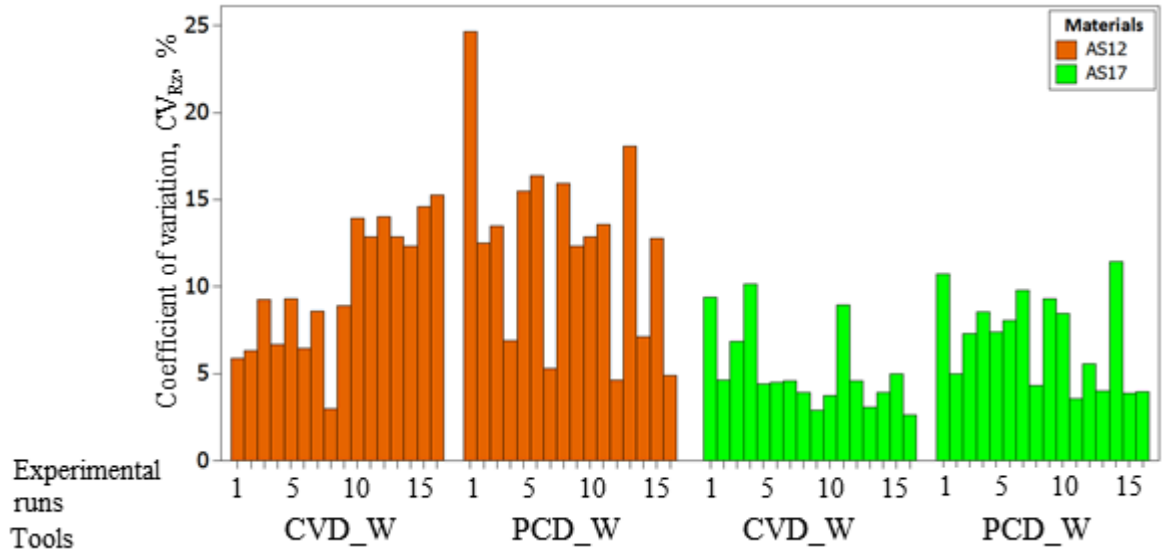

b)

Fig 4. Analysis of coefficient of variations

a) *CV* values in case of *Ra*

b) *CV* values in case of *Rz*

Summary

In this article it was examined the cutting capacity of two types die-cast aluminium alloys and different edge-material diamond tools. The results of the examinations are as follows:

- the tools produced significantly smaller surface roughness in case AS17 workpiece-material,
- the statistical analysis showed that AS17 workipece-material has smaller deviation in case of all tools,
- the standard deviation of the machined surface roughness only depends on the examined workpiece-materials, it is independent from the tool.

Acknowledgement

The project was realised through the assistance of the European Union, with the co-financing of the European Social Fund, TÁMOP-4.2.1.B-11/2/KMR-2011-0001 Research on Critical Infrastructure Protection.

References

[1] Á. Drégelyi-Kiss, R. Horváth, B. Mikó, Design of experiments (DOE) in investigation of cutting technologies, Development in Machining Technology/Scientific-Research Reports vol.3, Krakow University, 2012

[2] A. Hamadi, A. Y. Mohamed, C. Kamel, M. Tarek, R. Jean-François, Analysis of surface roughness and cutting force components in hard turning with CBN tool: Prediction model and cutting conditions optimization, Measurement 45 (2012) 344-353.

[3] M. Y. Noordin,, D. Kurniawan, Y. C. Tang, K. Muniswaran, Feasibility of mild hard turning of stainless steel using coated carbide tool, Int J Adv Manuf Technol (2012) 853–863.

[4] I. Asiltürk, S. Neseli, Multi response optimisation of CNC turning parameters via Taguchi method-based response surface analysis, Measurement 45 (2012) 785–794.

[5] Y. K. Hwang, C. M. Lee, Surface roughness and cutting force prediction in MQL and wet turning process of AISI 1045 using design of experiments, Journal of Mechanical Science and Technology 24 (2010) 1669-1677.

[6] M. Harničárová, J. Valíček, M. Kušnerová, R. Grznárik, J. Petrů, L. Čepová, A New Method for the Prediction of Laser Cut SurfaceTopography, Measurement Science Review 12 (2012) 195-204.

[7] D. Lazarević, M. Madić, P. Janković, A. Lazarević, Surface roughness minimization of polyamide pa-6 turning by Taguchi method, Journal of Production Engineering 15 (2011) 29-32.

[8] R. Horváth, Á. Drégelyi-Kiss, Analysis of surface roughness parameters in aluminium fine turning with diamond tool, Measurement 2013 Conference, Smolenice, Slovakia, (2013) 275-278.

[9] R. Horváth, Á. Drégelyi-Kiss, Gy. Mátyási, Application of RSM method for the examination of diamond tools, Acta Polytechnica Hungarica 11 (2014) 137-147.

Ceramic reinforced metal matrix nano- and micro-composite layers produced by combined laser melt injection technology and thermochemical surface treatment

Viktória Janó[1,a]

[1]Bay Zoltán Nonprofit Ltd. for Applied Research, Institute for Materials Science and Technology (BAY-ATI), Hungary, 1116 Budapest, Fehérvári út 130.

[a]viktoria.jano@bayzoltan.hu

Keywords: in-situ metal matrix composite, ferritic nitrocarburizing

Abstract. In-situ synthesized Nb(C,N) reinforced metal-ceramic composite layers were fabricated on nitridable (16MnCr5) and non-nitridable (S235J) steel surface by combined laser melt injection technology and ferritic nitrocarburizing treatment. The feasibility of processing composites layer by an in situ reaction using laser beam were carried out. Beside that the hardness of the treated layers increases up to 1000-1170 HV0.5 in the diffusion zone and after it the hardness of the samples reach 300-450 HV0.5, which is related the Nb alloying depth (1200-1400 μm). The results of the composite layer are presented in this paper.

Introduction

Metal matrix composites that are reinforced by ceramic particles result in various feature combinations, but they are significantly more expensive than conventional alloys. In some cases, however, it is enough to improve only surface properties of the part. One of the recent possibilities for production of metal matrix composites, was discovered 35 years ago [1,2], which is known today as LMI (Laser Melt Injection) technology. During LMI hard ceramic or metal particles are injected by a gas stream with the size range of 10–100 μm into a liquid metal, which is melted by a laser beam. In this case, between the layer and the base material some cohesive connection is established, thus parts and tools of increased lifetime – with optimal property combination in respect of volume and surface stress – can be produced economically. In case of LMI it should be noted that the impulse energy required by ceramic particles for successful engulfment depend on the temperature and the quality of the steel melt [3]. The impulse energy is resulted from the mass and from the speed of the particle, which overcomes the buoyancy force caused by the difference of density. On the other hand it should cover the interfacial energy as well.

In our earlier studies [4] we found that direct LMI of TiC particles results a lot of semi -melted and undissolved particles because of the solubility of ceramic phase in liquid steel is very poor, however the metal component of the ceramic phase dissolves quite well, for example: Al, Nb, Ti, Zr etc. This limit can be solved if the second phase (reinforcing phase) is established by way of controlled in situ reaction in the melt. In situ creation of the reinforcing phase allows to affect the size and quantity of the particles and thereby the character of connection to the matrix by parameters of applied technology, which establishes possibility for production of nano- and micro-composite layers.

In this study the ceramic particles (carbonitrides) were created in the steel matrix by ferritic nitrocarburizing of the surface layer alloyed by ferro-niobium. Ferritic nitrocarburizing is a thermochemical surface treatment involving the simultaneous diffusion of nitrogen and carbon into a steel surface at, 570–580ºC. It is performed primarily to improve the wear resistance and fatigue strength of ferrous components. Compared with other treatments, ferritic nitrocarburizing stands out as simple, cheap and offering improvements over a range of properties. Studying of the novel method has several reasons. According to my experience of more than one decade, surface alloying by laser beam has no special difficulties, it can be performed with high safety and good controllability. Ferritic nitrocarburizing can be performed at relatively low temperature, without

considerable distortion of the part to be treated and without significant change of the texture, and the result is determined only by the content of the object to be treated and by the parameters of the treatment. This method can be applicable for the establishment of ferritic nitrocarburized layers even on non-nitridable steels, or for regeneration of worn surfaces of objects that were originally nitridable, because alloying with niobium will improve ability to ferritic nitrocarburizing as well, and it will substitute material removed by wear. This method offers promising options for local modification of surfaces of parts of machine (vehicle) industry according to a specified target.

Experiments

Nitridable (16MnCr5) and non-nitridable (S235J) steel samples were used as a substrate in our experiments. The chemical compositions of the steels are seen in Table 1. The particle size of ferro-niobium (68 m/m% Nb, 32 m/m% Fe) to be injected was from 45 to 75 μm as a carbonitride-forming alloying element. The particles were blown on the surface of the laser melted sample under the angle of 67,5º using the argon carrier gas, with a flow rate of 8 liter/min.

Table 1. Chemical compositions of the steels

Marking	C %	Mn %	Si %	Cr %
16MnCr5	0,14-0,19	1,00-1,31	max. 0,40	0,80-1,10
S235J	max. 0,17	max. 1,4	-	-

Table 2 shows the parameters of the Nd:YAG laser beam and the heat treatment. The laser beam was moved relative to the steel substrate with a linear speed of 400 mm/min. On each run, 8 parallel laser tracks were melted, overlapping each other by 50%. After the laser treatment, samples were ferritic nitrocarburized by using the parameters shown in *Table 2*. The microstructure of the 1 mm laser treated composite layer was characterized using optical microscope, and scanning electron microscope (SEM).

Table 2. The parameters of the experiments

Sample Nr.	Parameters of the laser treatment			Additional material: ferro-Nb [g/min]	Ferritic nitrocarburizing
	Laser power [kW]	Laser spot diameter [mm]	Speed of laser beam [mm/min]		
1.5S5	1,5	3	400	0.32	T=560°C duration: 12 h composition of the gas: 250 l/h NH_3, 10 l/h CO_2, 50 l/h N_2
1.5S10	1,5	3	400	0.68	
2S5	2	3	400	0.32	
2S10	2	3	400	0.68	
S	-	-	-	-	
1.5N5	1,5	3	400	0.32	
1.5N10	1,5	3	400	0.68	
2N5	2	3	400	0.32	
2N10	2	3	400	0.68	
N	-	-	-	-	

Results and discussion

Sample S235J (S) and 16MnCr5 (N) without ferro-niobium alloying, were characterized in order to study the effect of Nb nitriding element on the properties of the ferritic nitrocarburized steel layers.

Microstructure of the composites layers. The optical micrographs of the S and N samples are shown in Fig. 1 with the micro hardness curves as a function of the layer depth. On both top of the steel surface, white layer depth of 10-30 μm can be clearly seen and also the diffusion zone below the white layer. The white layer is known to be very hard and brittle and comprises two intermixed

phases that support the results of the hardness data. The maximum hardness of the nitridable steel is 650 HV0.5 and in case of non-nitridable steel it is 480 HV0.5.

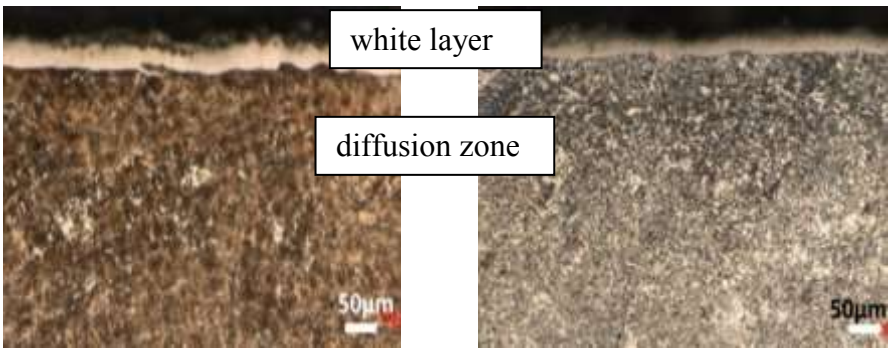

a) *b)*

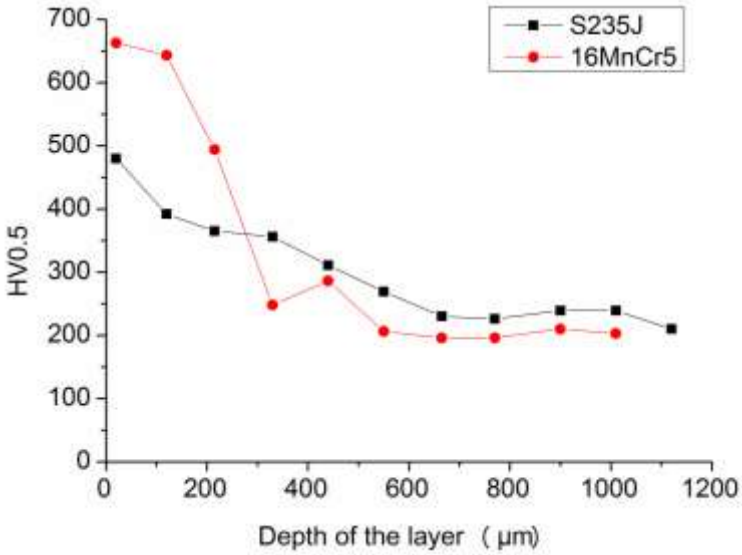

c)

Fig. 1. Optical micrographs of a) N and b) S samples (etching Nital 2%) c) micro hardness curve as a function of the layer depth

Fig. 2 shows the microstructure and the Nb-map of the ferro-niobium alloyed samples indicated 2N10 (a) and 2S10 (b). Nb map shows that there is a direct relation between the microstructure and the Nb content. The flow shape of the layer drawn through the Nb content is the effect of the Marangoni-flow effected the laser treatment.

Beside the micrograph, the content of Nb and N as a function of depth can also be seen. The curves show that the nitrogen penetration of samples (2N10, 2S10) is around 200µm. The maximum content of Nb is 7m/m% and the depth is 1200-1400µm, which is seven times more than the depth of the N diffusion. This means that the ferritic nitrocarburized layer is held by a strength layer containing Nb, which is favourable for the bearing of the material.

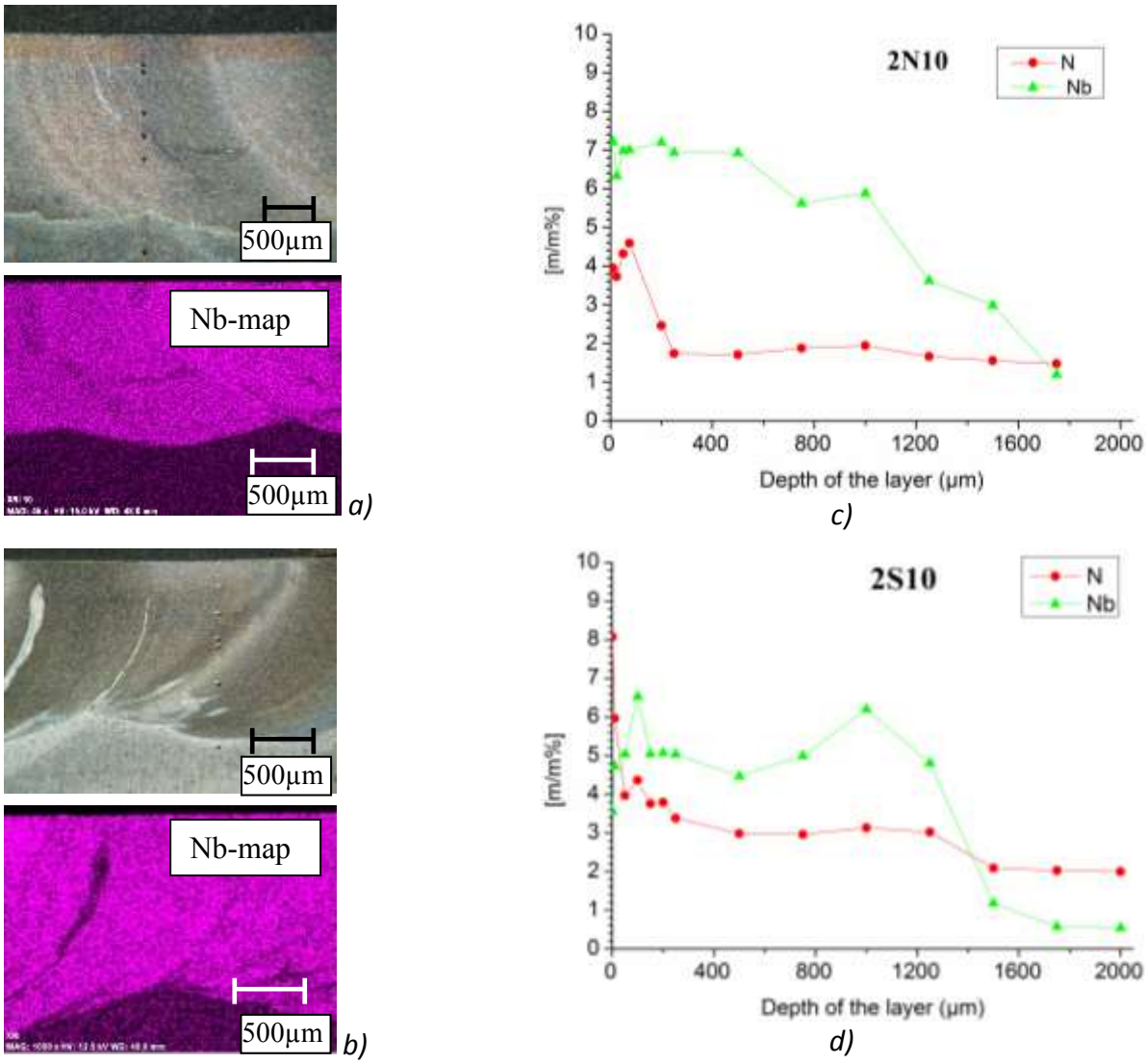

Fig. 2. Optical micrographs of a) 2N10 and b) 2S10 samples (etching: Nital 2%) and the Nb and N content of c) 2N10 sample d) and of 2S10 sample

Fig. 3 shows the microstructure of the samples (2N10, 2S10) with a higher magnification. The table indicates the analysis of the elements from 6 to12 points. In case of 8, 9 and 11 points, the Nb, N and C value are higher than in the middle of the grains (point 10), which are assumed to be Nb(C,N). The presence of Fe at the points 8, 9 and 11 is provided from the environment of the precipitates. The SEM images confirm that the carbonitrides are precipitated at the ferrite grain boundaries as it follows the crystallite shape of the base material.

Table 3. The element analysis of the points

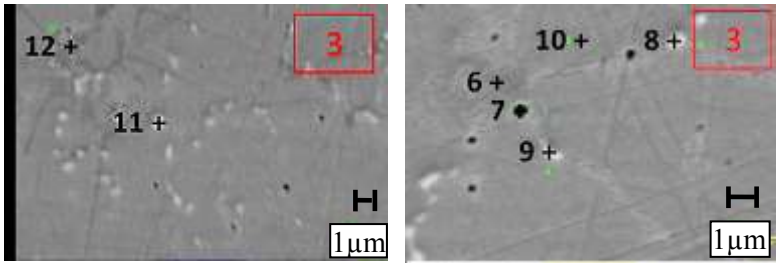

Points	Fe	N	Nb
	[m/m%]		
6	74.67	6.13	12.65
7	41.78	5.85	15.99
8	33.74	4.94	43.69
9	19.28	1.63	58.14
10	89.92	1.08	2.50
11	47.71	0.61	35.24
12	87.07	5.88	1.79

Fig. 3. The precipitates around the ferrite grain boundaries can be seen in the SEM images of the sample 2S10 (a) and 2N10 (b)According to the analysis of the nitridable steel, which contains 0,8-1,1m/m% Cr, Cr(N) and Cr(C) were not indicated. It means that by reason of Nb presence, the C

and N elements form nitrides and carbides with Nb. This statement is supported by the data of the *table 2*. The data shows that the standard entalphy of the Nb is more negative then the Cr for nitrides and carbides as well [5].

Table 2. The standard enthaphy (kJ/mol) of the Nb-, and Cr- nitride and -carbide at room temperature, 298 K [5]

Element	Nitride	Carbide
Nb	-235	-139
Cr	-117	-55

Advantage of laser beam alloying by Nb is clearly demonstrated by the fact that in diffusion zone of ferritic nitrocarburized layer of nitridable steel no Cr(C, N) but Nb(C, N) particles were formed. This is in accordance with data concerning forming standard free enthalpy of the mentioned phases.

Mechanical properties of the composites layers. Fig. 4 shows the micro hardness of the samples (1,5S5, 1,5S10, 2S5, 2S10, 1,5N5, 1,5N10, 2N5, 2N10) as a function of the layer depth. The hardness of the base nitridable steel is 261 HV0.5, which increase to 1000-1170HV0,5 at the depth of 100-150 µm in the composite layer. This parameter for non-nitridable steel is: 233HV0.5, which increase to 900-1000HV0.5. One can also see from the curves, that after 100-150 µm, the hardness of the samples is 300-400 HV0.5, which is in accordance with Nb alloying depth (1200-1400 µm). This more strength layer, than the base core serves as a support for the ferritic nitrocarburizing layer.

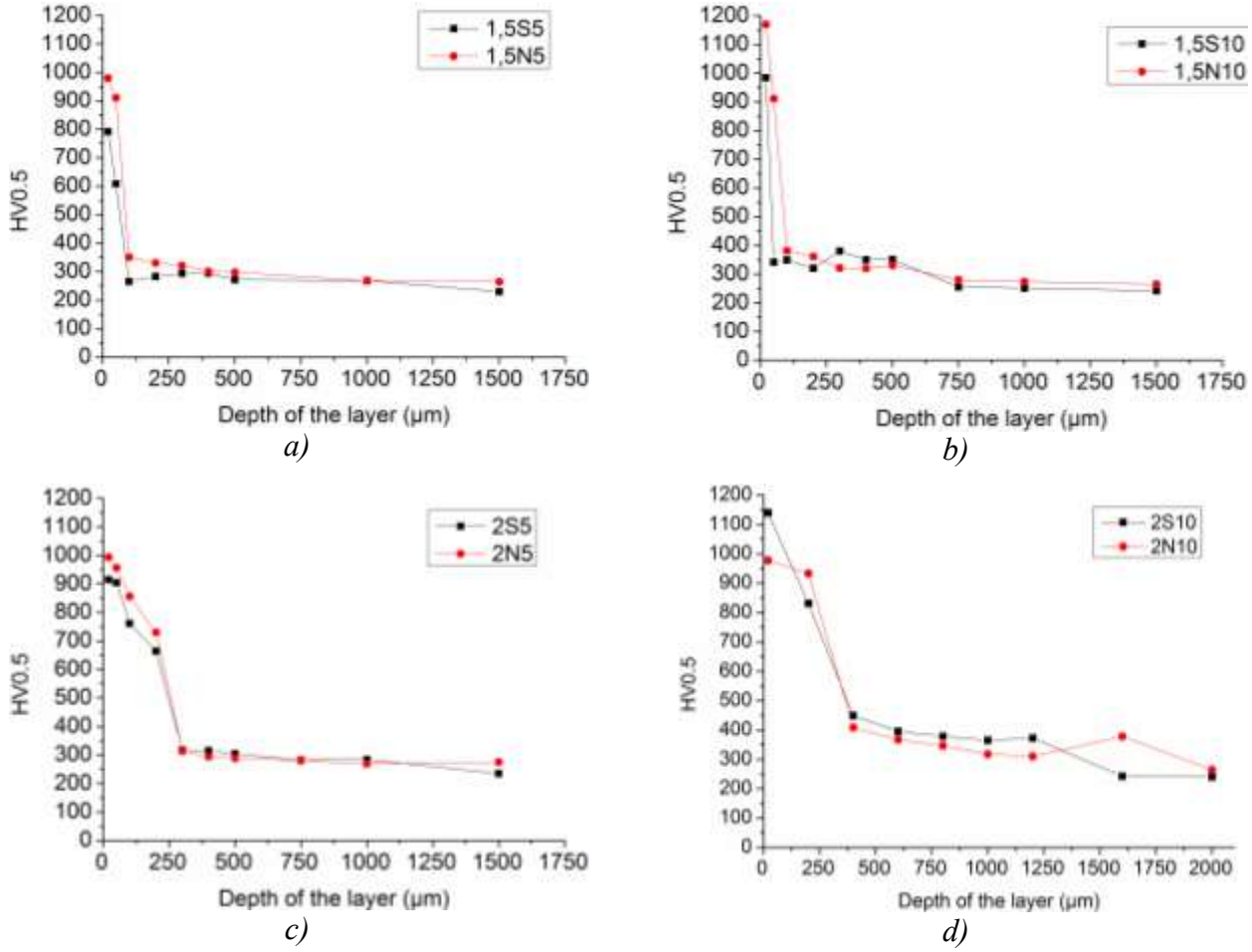

Fig. 4: The hardness of the samples as a function of the depth a) 1.5S5 and 1.5N5 b) 1.5S10 and 1.5N10 c) 2S5 and 2N5 d) 2S10 and 2N10

Results of the wear tests. The tribological properties of the composite surface were tested using new, special equipment, which is fit to examine the local wear processes [6]. This device is a modified and enhanced tribometer using a ball. The system is allowed to on-line measure the wear depth. Moreover, the ball does not suffer wear during the test, because it moves not on defined track but perform a stochastic movement. *Fig. 5* shows the wear trace of the sample 2N10 and 210. During the wear test it was realized that the steel ball worned in a major degree as the composite layer so the results was just considered as an indication. Pin-on-disc device will be used to caracterize the wear properties of the layer.

a) *b)* *c)*

Fig. 5: The wear trace of the sample a) 2N10 and b) 2S10 c) The steel ball using for the wear test

Summary

I proved experimentally that the surface of structural steels, without nitride-forming elements, by a complex treatment consisting of surface alloying by ferro-niobium and gas ferritic nitrocarburizing, turn into nitridable. I showed that depth extension of the alloyed layer that contains about 3-5m/m% Nb is bigger than that of the nitrided layer consisting of the compound layer and diffusion zone, thus the zone alloyed with Nb having greater hardness than the base material. The alloyed zone serves as supporting for the ferritic nitrocarburized layer.
Based on energy-dispersive microanalysis results I proved experimentally that precipitation of max. 200-300 nm size that are present in diffusion zone formed during laser beam surface alloying performed by ferro-niobium on steel of type 16MnCr5 and gas ferritic nitrocarburizing – according to forming standard enthalpy values for Nb(C, N) and Cr(C,N) – are considered as Nb(C, N).

Acknowledgement

This project has been financed by OTKA (nr.: 82064) and NiobelCon bvba. The author wish to thank for Prof. Balázs Verő and Prof. George Kaptay for their encouragement and discussions during this work.

References

[1] R. J. Schaefer and J. D. Ayers: USA patent 4,200,669, (1980)
[2] R. J. Schaefer and J. D. Ayers, T. R. Tucker: USA patent 4,299,860, (1981)
[3] R. J. Schaefer and J. D. Ayers: USA patent 4, 200,669, (1980)
[4] O.Verezub, P.Boross, Z.Kálazi, B.Verő, A.Grabchenko and G.Kaptay: Possibilities to Obtain W-alloyed, TiC-reinforced Composite Surface Layers on Carbon Steels by Laser Melt Injection. A theoretical Analysis. Proc. of microCAD 2003 Conference, Section Metallurgy, University of Miskolc, (2003), p. 59-64.
[5] Kaptay Gy., Bolyán L.: Kerámiával erősített fémmátrixú kompozitanyagok gyártásának határfelületi vonatkozásai, BKL, 131, 9-10, (1998)
[6] Kovács Tünde Anna: Acélok szövetszerkezetének hatása a lokális kopásra, ph.d. Értekezés, Budapest (2007)

Degradation Behaviour of Zeolite Filled Polyurethanes under In Vitro Aging Process

Peter Kaali[1, a],György Czél[2,b]

[1]Nynas AB, Raffinaderivägen, Nynashamn, Sweden SE-149 82

[2]Institute of Ceramic and Polymer Engineering, University of Miskolc, Miskolc-Egyetemvaros, Hungary, HU-3515

[a]peter.kaali@nynas.com, [b]femczel@uni-miskolc.hu (corresponding author)

Keywords: zeolite filled TPU, mechanical degradation, aging process, SEM analysis.

Abstract

In this study the degradation and ion/zeolite release processes of in vitro aged zeolite loaded polyurethane composites were evaluated. Two in vitro artificial aging solutions were used; artificial lysosomal fluid (ALF) and Gamble´s solution and the total exposure time was 12 weeks. Periodically, SEM micrographs were taken of the surface of polyester type polyurethane-zeolite composites. After exposure to ALF solution the samples showed round holes and a rougher surface in general over time. Micrographs of the samples immersed in Gamble's solution exhibited different signs of degradation with damage features on the surfaces, understood as black holes and a rougher surface pattern. In addition varying amount of salt was also observed on the surfaces that might influence the ion/zeolite release. Furthermore, the zeolite filler caused remarkable changes in mechanical properties after the aging process, which could not be discerned.

Introduction

Zeolite filled polyester type polyurethanes (TPU) are commonly used in biomedical applications [1,2]. Zeolite is filled with antimicrobial metallic ions (i.e. silver) that are slowly released during the whole service time [3]. It has been reported by our previous studies [4] that silver-zeolite expresses very good antimicrobial properties. However, there are other metallic ions (i.e. Cu, Zn) that show antimicrobial effect and can be used to treat zeolites in order to make them applicable for antimicrobial purposes [5]. To estimate the service time (mechanical degradation effect) of the antimicrobial zeolite polyester type polyurethane, artificial aging process was carried out. The current study aimed to characterize the surface degradation and the mechanical strength stability of single, binary and ternary ion-exchanged zeolite systems in TPU matrix after in vitro aging process. The presently published stability results support the author's thin layer injection moulding technology research.

Materials and Sample preparation

A-type zeolite was used as antimicrobial agent, which was loaded with different metallic ions during the experiments. In the current study the zeolite was ZEOMIC AJ10D inorganic antimicrobial agent (Ag content 2.5%) supplied by Sinanen Zeomic Co., Ltd.). It was then modified and filled with Ag, Cu and Zn ions [4]. Single, binary and ternary ion-exchanged zeolite samples were prepared by ion-exchange reactions. In case of binary and ternary systems the procedure identical to single metallic ions, where the ion-exchange reactions were performed with Ag-Zn, Ag-Cu, Zn-Cu and Ag-Zn-Cu nitrate solutions. Due to the limited content space of the present article only some results could be published referring to binary and ternary ion filled zeolite systems. Laripur 5725 polyester type polyurethane was used as

matrix material for the preparation of polyurethane-zeolite composites. The preparation of the composites was performed according to the following procedure. The polyurethane was mixed with different multi-ionic zeolites in 1% in a Haake-Polylab System equipped with a Rheomix 600 mixer (Thermo Fisher Scientific Inc., Karlsruhe, Germany). The mixing temperature was 210 °C at 100 rpm and the duration of constant mixing was 5 minutes. After mixing the composite samples were ground into pellets and were injection moulded on a Krauss Maffei KM80/C1 type injection moulding machine. The obtained dimensions of these samples were 100x100x1.5 mm.

In vitro aging process

Two synthetic body fluids were chosen to simulate different *in vivo* conditions, see in Table 1. Both fluids have been previously identified to cause degradation of plastic implant materials. Artificial Lysosomal Fluid (ALF) simulates the immunological reaction of the body while Gamble's solution is similar to the interstitial fluid of the deep lungs. SEM micrographs were taken from the surface of the samples after aging that was performed on a Hitachi S-4800 Ultra-High Resolution Field Emission Scanning Electron Microscope (FE-SEM) at different magnifications. SEM investigation aimed to study the possible surface alterations and degradation signs on the polymers and composites. Prior to the SEM anaylsis the samples were coated with Au/Pa layer with a thickness of approximately 10 nm. The initial and aged surface morphology was examined and compared. Typically the surfaces were smooth and significant alterations were not observed prior exposure to ageing solution.

Table 1. Chemical composition of the artificial body fluids (g/l).

Chemicals	**ALF**	**Gamble**
$MgCl_2$	0.050	0.095
NaCl	3.21	6.019
KCl	-	0.298
Na_2HPO_4	0.071	0.126
Na_2SO_4	0.039	0.063
$CaCl_2 \cdot 2H_2O$	0.128	0.368
$C_2H_3O_2Na$	-	0.574
$NaHCO_3$	-	2.604
$C_6H_5Na_3O_7 \cdot 2H_2O$	0.077	0.097
NaOH	6.00	-
$C_6H_8O_7$	20.8	-
H_2NCH_2COOH	0.059	-
$C_4H_4O_6Na_2 \cdot 2H_2O$	0.090	-
$C_3H_5NaO_3$	0.085	-
$C_3H_3O_3Na$	0.086	-
pH	4.5	7.4

Appearance and pH control

Samples from both pure and zeolite filled composites were cut to a dimension of 30x10 mm and placed into acid-cleaned (1 % HNO_3 for 24 h) glass vessels that were filled with 10 ml of either ALF or Gamble's solution, and thoroughly sealed with Parafilm®. Subsequently, the samples were placed in an incubator and stored under static and dark conditions at 37°C for 84 days. Total duration of the test series was 3 month. Each week, samples were taken out from the conditioning cabinet and were dried. The pH of the solutions was randomly checked using a pH indicator paper. Besides, the appearance of the samples was carefully compared with the unaged material in order to detect any optical changes on the immersed samples as a function of time. Samples were withdrawn from the solution on a weekly basis were thoroughly cleaned with deionised water and alcohol and dried.

Surface morphology

Parallel lines as a result of the mould surface pattern were observed. Besides, the zeolite particles could be determined inside the polymer matrix. SEM micrographs of the surface structure of the samples were taken in order to study changes in them due to the aging

immersion. As it can be seen in Figure 1.a-c, micrographs taken of the TPU-Reference samples immersed in the ALF solution indicated slightly signs of degradation over time. The surface was not as smooth as on the unaged sample. It seemed to have increased roughness and irregular, small cracks and ridges appeared. The changes observed in the micrographs taken of the rest of TPU-zeolite composites were significant. A general behaviour between samples immersed in the ALF solution could be discern (Fig.1b), while samples immersed in the Gamble's solution showed different characteristics (Fig.1c).

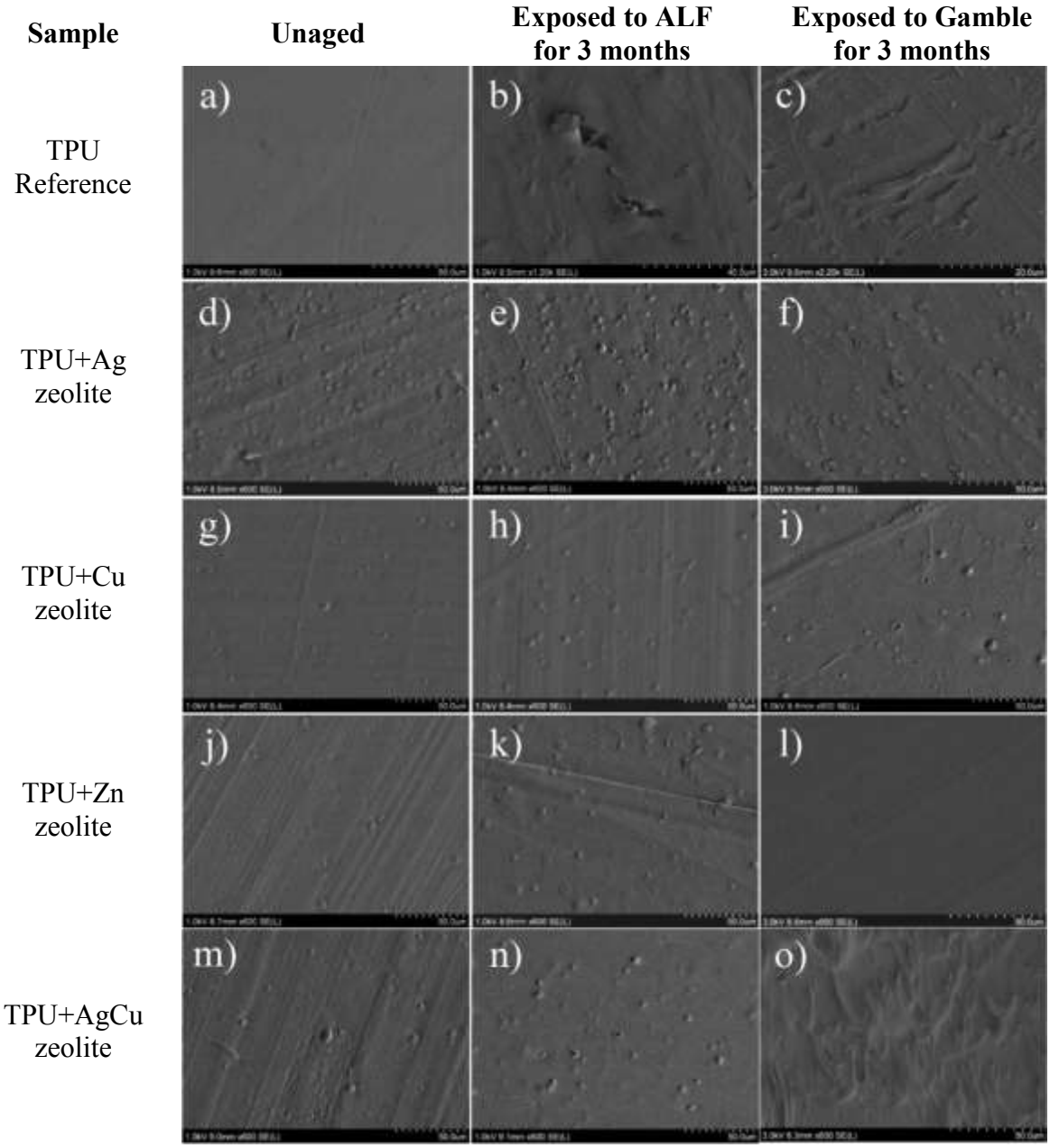

Figure 1. Microstructure evolution of TPU-reference (a-c), TPU-Ag zeol. (d-f), TPU-Cu zeol(g-i), TPU-Zn zeol.(j-l), TPU-AgCu zeol.(m-o) samples after in vitro aging process: unaged (a, d, g, j, m), exposed to ALF for three month (b, e, h, k, n), exposed to Gamble for 3 months (c, f, i, l, o).

The main feature showed by samples immersed in the ALF solution was the appearance of small round holes. The number of these holes increased over time, which thought to be the way out of the zeolite particles from the polymer matrix into the aging solution. TPU-Ag was the sample which exhibited more holes of this kind, as can be appreciated in Fig.1.e. Besides,

large quantities of salt from the aging solution were observed on the surface. Examining the SEM micrographs taken of the TPU-Cu (Fig.1.h.) and TPU-Zn (Fig.1.k.) samples, the same round holes found in TPU-Ag were observed on the samples immersed in the ALF solution, but in a lower quantity and appearing later, only during the second month, in case of the TPU-Zn and during the third month for the TPU-Cu. Micrographs taken of TPU-AgCu samples immersed in the ALF solution exhibited the same behaviour as the rest: round holes and a surface with increased roughness, in general, over time (Fig.1. n).The rest of surfaces (TPU-AgZn, TPU-ZnCu and TPU-AgZnCu samples) showed the same characteristics and deviation from the unaged surface. Those immersed in the Gamble's solution only exhibited surface signs of degradation (migration of zeolite particles leaving black holes behind, some ridges and surface roughness) and in some cases salt adhered to the surface also (Fig.1.o). Several conclusions can be drawn from the previously discussed SEM figures. First of all, the ALF solution seemed to be a better media for the release of zeolite particles since many holes formed on the surface of those samples. Therefore, a higher concentration of released ions is expected in ALF solutions than in Gamble's solutions. In addition, the large amount of salt adhered to the surface which might have affected the ion-release of samples immersed in Gamble's solution to some extent. Perhaps this salt layer acted as an obstacle, preventing ions to be released from the polymer matrix. Finally, the rate of deterioration observed in the SEM micrographs was not extreme enough to conclude that the TPU-zeolite composites underwent severe degradation processes. This is favourable in the case of practical thin layer applications.

Mechanical test results

Mechanical testing was carried out to determine the influence of ion loading on the mechanical and long term properties of the composites. The test was performed on an Instron 5560 tensile tester (Instron, High Wycombe, United Kingdom) according to EN-ISO 527 standard before and after aging process. Mini standard sized test specimens were cut out of polyurethane zeolite samples. The test temperature was 23 °C with 50 % of humidity. The specimens were conditioned under these conditions for at least 24 hours prior to the test. The tensile velocity was 10mm/min. The mechanical properties of the unaged samples are summarized in Table 2. The properties shown are values for tensile strength (MPa), tensile strain (%) and Young´s modulus (MPa).

Table 2. Mechanical test results for the unaged TPU-zeolite composites.

Sample	Tensile strength [MPa]	Tensile strain [%]	Young´s modulus [MPa]
Reference	53.7 ± 9.0	331.7 ± 45.6	322.6 ± 36.9
Ag	49.2 ± 3.8	420.9 ± 103.4	291.3 ± 51.3
Cu	56.4 ± 5.8	556.2 ± 31.9	281.6 ± 18.9
Zn	50.1 ± 5.8	531.6 ± 27.1	263.6 ± 31.4
AgCu	68.8 ± 8.3	522.2 ± 88.6	366.8 ± 52.0
AgZn	57.1 ± 4.6	536.5 ± 44.5	322.8 ± 65.8
ZnCu	53.2 ± 2.2	539.0 ± 47.6	304.3 ± 18.1
AgZnCu	59.9 ± 2.6	564.4 ± 33.5	377.1 ± 14.0

Tensile strength values were approximately the same for all the samples. Tensile strain results increased for all the TPU-zeolite composites in comparison with the TPU-reference. However, the modulus for the TPU-reference was a bit higher than for the rest of the composites (except in the case of TPU-AgCu and TPU-AgZnCu filled zeolite). Standard deviations were high in some cases since only three samples were tested and if one of them

had a clearly different behaviour with respect to the rest, the values were sensibly affected. As it is stated in the literature [3], there would be an improvement in the mechanical properties of the TPU due to the incorporation of zeolites, increasing the resistance of the polymer versus deformation. However, this could not be clearly seen in the results presented above since all the mechanical parameters were similar between the TPU-reference and the TPU-zeolite composites. This may be ascribed to the zeolite content being only 1%. Thus, the impact of the presence of zeolite on the mechanical properties could not be discerned. The mechanical performance of the TPU-zeolite composites at different immersion times and in both aging solutions was evaluated in order to see any possible changes (Table 3). The mechanical properties were relatively affected by aging time. The stress-strain relation for some of the TPU-Zn filled zeolite composites is displayed in Figure 2. This mechanical parameter is related to the swelling effect, which explains the differences between unaged and aged samples. The degree of mechanical deterioration can be related to the water content of the composite.

Table 3. Tensile stress at 200% strain values of the aged TPU-zeolite composites.

Sample	**ALF**	**Gamble**	**Sample**	**ALF**	**Gamble**
TPU-Reference	T.stress at 200% [MPa]	T.stress at 200% [MPa]	**TPU-Ag**	T.stress at 200% [MPa]	T.stress at 200% [MPa]
Unaged	39.2	39.2	Unaged	35.8	35.8
4 weeks	34.7	32.6	4 weeks	25.0	26.9
8 weeks	31.1	33.1	8 weeks	25.9	26.9
12 weeks	30.1	30.3	12 weeks	26.4	25.9
Reduction	**23.3%**	**22.6%**	**Reduction**	**26.2%**	**27.8%**
TPU-Cu			**TPU-Zn**		
Unaged	33.2	33.2	Unaged	27.1	27.1
4 weeks	27.1	25.7	4 weeks	23.6	24.7
8 weeks	27.7	25.2	8 weeks	24.0	24.0
12 weeks	24.1	25.7	12 weeks	23.3	22.8
Reduction	**27.5%**	**22.7%**	**Reduction**	**14.1%**	**15.8%**

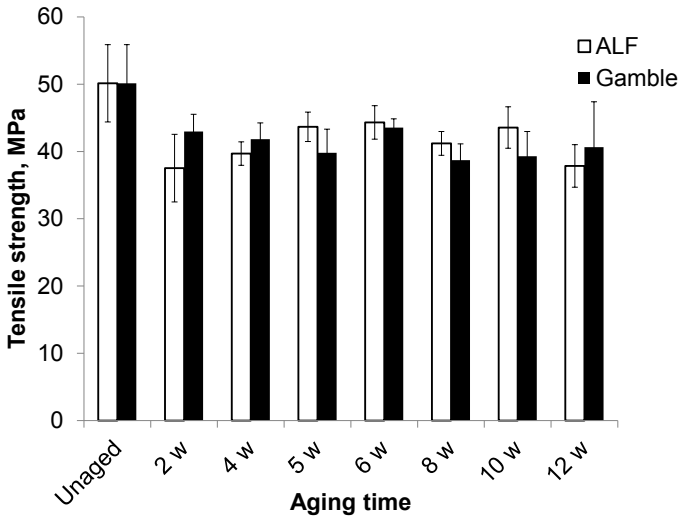

Fig. 2: Change in tensile strength of TPU-Zn as a function of aging time.

Besides, the Young's modulus was also reduced, while the tensile stress and the tensile strain remained basically constant for all the TPU-zeolite composite samples over time with some exceptions. Their tendencies are collected in Table 3.and Figure 2-3 illustrates some of the before mentioned behaviours. The Young's modulus was one of the mechanical parameters most affected by aging time and its total reduction varied from 50% for the TPU-AgCu to 25% in case of the TPU-Zn composite at week 12 (Table 4). TPU-Ag and TPU-Zn showed the lower reduction values. Variation of the change in modulus shows nearly the same scatter over the time. A reduction in the Young's modulus involves that the material softens and can deform easier than before if the same stress is applied. Figure 3. the evolution of Young's modulus for the TPU-AgCu and for the TPU-Zn is compared.

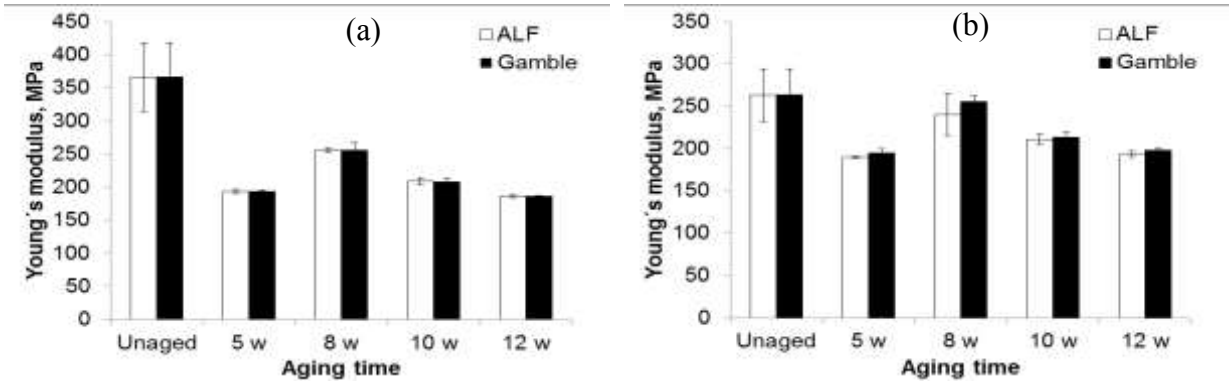

Figure 3. Change in Young's modulus of TPU-Reference (a) and TPU-Zn (b) as a function of aging time.

Table 4. Reduction in Young's modulus of the aged TPU-zeolite composites.

Sample	5 weeks		8 weeks		12 weeks	
	ALF	GAMBLE's	ALF	GAMBLE's	ALF	GAMBLE's
Reference	42.0%	41.4%	35.2%	34.5%	47.7%	46.8%
Ag	26.4%	28.4%	25.1%	27.9%	30.0%	30.32%
Cu	31.0%	32.5%	28.2%	16.6%	34.8%	33.2%
Zn	28.0%	26.1%	8.7%	3.0%	26.6%	24.9%
AgCu	48.5%	47.2%	45.7%	30.2%	49.7%	49.2%
AgZn	39.6%	38.9%	35.9%	22.0%	40.7%	42.0%
ZnCu	36.1%	36.2%	33.0%	27.6%	35.9%	35.6%
AgZnCu	49.8%	50.4%	43.9%	35.4%	50.9%	46.6%

Summary

After in vitro aging process the zeolite–polyurethane composite material was used as experimental material in degradation evaluation. Micrographs taken of TPU-zeolite samples immersed in the ALF solution exhibited round holes and a rougher surface, in general, over time. However, in this case, micrographs of the samples immersed in the GAMBLE's solution exhibited different signs of degradation with damage features on its surface, understood as black holes and a rough surface. Mechanical parameters were similar between the TPU-Reference and the TPU-zeolite composites, which may be ascribed to the zeolite content, only 1%. Thus, the impact of the zeolite presence into the mechanical properties could not be discerned.

References

[1] D.Papaioannou et al., The role of natural and synthetic zeolites as feed additives on the prevention and/or the treatment of certain farm animal diseases: A review, Microporous and Mesoporous Materials 84(1-3) (2005) 161-170.

[2] J. L. Flowers, S.A. Lonky and E.J. Deitsch, Clinical evidence supporting the use of an activated clinoptilolite suspension as an agent to increase urinary excretion of toxic heavy metals, Nutrition and Dietary Supplements 1 (2009): 11-18.

[3] M. A. S. D. Barros, Binary ion exchange of metal ions in Y and X zeolites, Brazilian Journal of Chemical Engineering 20 (2003) 413-421.

[4] P. Kaali and Gy. Czel, Single.Binary and Ternary ion Exchanged Zeolite as an Effective Bioactive Filler for Biomedical Polymer Composites, Mat. Sci. Forum 729 (2013) 234-239

[5] Y. Inoue and Y. Kanzaki, The mechanism of antibacterial activity of silver-loaded zeolite, Journal of Inorganic Biochemistry 67(1) (1997) 377-377.

Analysis of a NiTi shape memory alloy

László Kálmán[1,a], István Mészáros[2,b]

[1,2] Budapest University of Technology and Economics (BUTE),

Department of Materials Science and Engineering

H-1111 Bertalan Lajos st. 7, Budapest, Hungary

[a] MSc student of Mechanical Engineering Faculty

[b] Associated professor, meszaros@eik.bme.hu

Keywords: Shape memory alloy, nitinol, flexinol, NiTi, one-way effect, austenitic-martensitic transformation, hysteresis of shape memory.

Abstract

This work demonstrates particularly the basic properties of shape memory alloys and gives a brief review about their basic crystallographic processes. The attributes of shape memory alloys will be presented through the NiTi alloys. The crystallographic principles of three unique properties were investigated and the functional mechanism described. One of the three essential mechanisms, the one-way effect was demonstrated through an experiment. The change of length depending temperature was tested and documented. The hysteresis behavior of shape memory alloys was recorded.

Introduction

The shape memory alloys are metallic materials which are able to acquire pre-defined size and shape, determined by heat treatment. The austenitic-martensitic phase transformation and its reverse result the unique shape memory effect of these alloys. Properties are not characterized from stress-strain point of view, but by thermo-mechanical properties which can be illustrated by the phase transformation diagram. These diagrams are not linear, a wide hysteresis loops (temperature difference between contraction and elongation curves, ΔT) can be observed in each case among the measured temperature and stress data points.

In the case of pseudo elasticity, the investigated alloys are able to be reversible deformed slightly above the transition temperature. Under stress or temperature load the austenitic phase gets into martensitic phase, and after the termination of the load, due to the fixed parameter, the alloy returns to the austenitic phase. The pseudo elasticity can not only be found in shape memory alloys, however, it can reckon among shape memory phenomenal due to the distinctive occurrence of the progress.

In case of two-way shape memory effect, the shape memory alloy acquires a predefined shape not only under heating, but also under cooling. The setting of various formats is attainable through cyclical phase transformations (cyclical training).

In case of one-way shape memory effect, the shape memory alloy under shaping and after relief, suffers permanent deformation. However, during the subsequent heating above the transformation temperature, it will regain shape, or optionally can be shortened. The resulting shape after the refrigeration to the initial temperature is fixed. It returns to the original state both in terms of temperature and stress. The phenomenon is considered to be one-way because only the initial state can be reached perfectly; the mechanically modified form depends on the loading.

Nowadays the shape memory alloys are applied in more and more areas, such as actuator technologies, control systems, security, automotive, dentistry and medicine. They are capable of producing high specific force, low-noise operation, safe and clean, well absorb vibration, the friction losses are small and they function in the absence of gravitational field [1], [2], [3].

Experimental

Investigated material. Among the different types of NiTi alloys the study was performed on a Flexinol wire. The Flexinol is also an alloy of nickel and titanium having high flexibility. The heat causes contraction that can be compared to human muscle contractions. In applications where linear motion or servo motors are required, Flexinol can perform the actuation. The technical features of Flexinol were provided by the manufacturer:

Diameter [mm]	Activation temperature [°C]	Resistance [Ω/m]	Recommended current [mA]	Length [mm]	Recommended pull force [g]	Recommended deformation [%]
0.5	90	4	4000	1000	3560	3-5

Table 1 Features of Flexinol wire

The Flexinol wire was examined by energy-dispersive X-ray spectroscopy (EDS). The result revealed that the flexinol consisted of 50 % nickel and 50 % titanium. The study required no further preparation of the wire.

Design of measurement and measuring equipment. The purpose of the measurement was the analysis of the one-way shape memory effect of the Flexinol wires by slow warming under different constant loads, while recording the temperature values during the process. In the course of measurement the length change of nitinol wire was recorded for every temperature point and the resulting points were shown in the graph illustrated in heating and cooling that took place during the process. The other important consideration was the recording of the small-scale foreshortenings and extensions. It was necessary to create measuring equipment which provides the required sensitivity. The base of the measuring equipment gives a U-section that had plug plates at both ends. In this way an open container was built where the test wire was fixed in the longitudinal direction. The wire was attached to one end and the other end connected via a fixation part to a cable, which was draped over a pulley system. The pulley system provided the gravitational load of wire, with different masses. The clamped length of the test wire was *485* mm in each case. The heating was accomplished by water that provided a slow warm-up and cool-down. The low speed made easy to document the results. The container and the water were electrically heated. The temperature measurement was provided by a mercury-in-glass thermometer. The displacement was recorded by a linear potentiometer, which was fixed to the axis of rotations, with the swing of shaft the resistance of potentiometer changed so that gave a measurable voltage change. The power for the operation of the potentiometer was supplied by a 24 V power source. The voltage drop documentation was performed with a DMM. A schematic diagram of the measuring equipment can be seen in Figure 1.

Forces applied during the measurement do not exceeded the limit of plastic deformation. Errors from inaccurate readings of the thermometer and the potentiometer were relatively small.

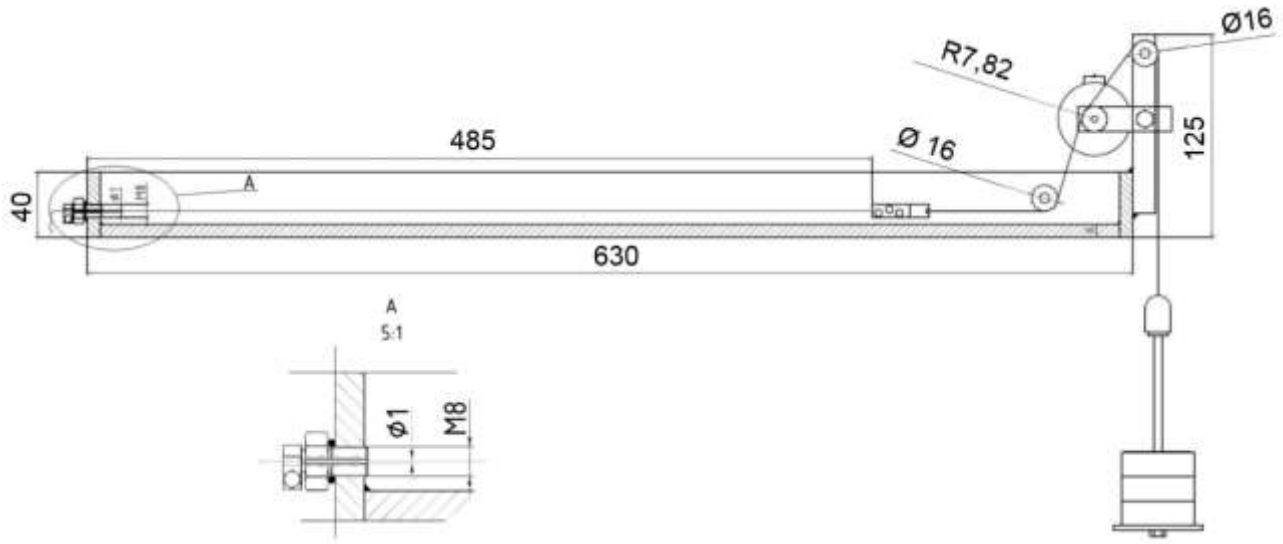

Figure 1 Schematic diagram of the measuring equipment

Results

The wires ability to one-way shape memory had been checked before starting the test. For that, a heating electric current was used at a constant load. The wire was originally in austenitic phase. Thus the martensitic phase was generated by constant mechanical load. The austenitic phase was reached by heating, and under cooling, the mechanical load produced the martensitic phase transformation. The measurement points were recorded at three different loads. The following weight values and load values were applied:

- m_1 = 1001 [g], small load case
  The plotted values clearly show the most regular hysteresis curve, the resulting contraction and elongation in this case had the maximum value (Figure 2).
- m_2 = 2642 [g], medium load case
  During the evaluation, there were no significant differences in the expected values. A similar figure resulted like in the case of small load measurement. During the contraction and elongation time, the voltage values changed more quickly, than in the previous case.
- m_3 = 3144 [g], large load case which resulted in moderate overloading
  The load was chosen close to the maximum of the load limit. According to the previous results, the contraction is smaller and the phase transformation hysteresis gave a less regular curve. It was unexpected that after contraction, stress values were slightly higher than the initial values. One explanation of this behavior may be that the wires were likely to have been slightly overloaded. It is supposed that the irregular hysteresis is caused by the elastic contraction of the wire. It can be concluded that in case of overloading, the lifetime of the wire could be shortened.

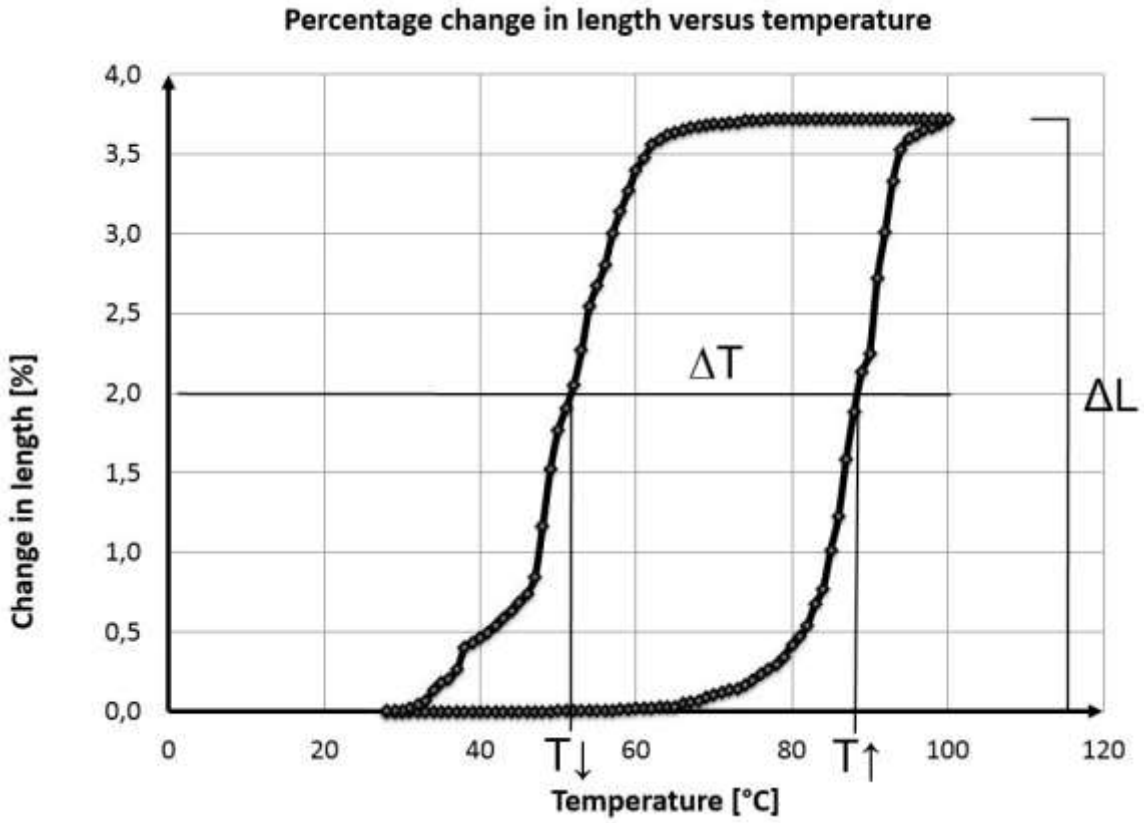

Figure 2 Small load case (1001 g) hysteresis curve with the indicated up and down activation temperatures.

In each case the hysteretic behavior was detected as wire length vs. temperature. The obtained up (T↑) and down (T↓) activation temperatures, the load-dependent activation temperatures [Austenite start (A_s), Austenite finish (A_f), Martensite start (M_s), Martensite finish (M_f)] summarized in Table 1.

Load value (m)	A_s [°C]	A_f [°C]	M_s [°C]	M_f [°C]	ΔL [mm]
1001 g	66	97	73	32	18,045
2642 g	69	100	75	26	12,837
3144 g	76	100	71	38	4,542

Table 1. The activation temperatures

The width of the hysteresis loop (ΔT) and elongation (ΔL) at different load cases summarized in Table 2.

Measurement (ΔL)	T↑ [°C]	T↓ [°C]	ΔT [°C]	ΔL [mm]
1. (9 mm)	88	51	37	18.045
2. (6.4 mm)	95	58	37	12.837
3. (2.2 mm)	94	56	38	4.542

Table 2. Up (T↑) and down (T↓) activation temperatures, width of the hysteresis loop (ΔT) and elongation (ΔL) data obtained at different load cases.

Conclusions

The one-way shape memory operation has been tested and verified in a Nitinol wire. It was found that the length vs. temperature shows hysteretic behavior.

It was obtained that the one-way shape memory effect can produce the same elongation and contraction. However, the contractile capability (ΔL) of the wire decreases significantly with increasing loading. The increase of loading increases both (up and down) activation temperatures. In other words the hysteresis loop is shifted parallel along temperature scale by the change of the applied loading. Therefore the width of the hysteresis loop was found to be independent of the applied load. This phenomenon makes easier to create memory shape alloy hysteresis curves. After a few exact measurements, ΔT can be determined. The determination of ΔT value allows drawing the hysteresis curve in any load cases, without measurement. Only the four characteristic points (A_s, A_f, M_s, M_f) and the ΔT value can define the approximate hysteresis curve. Moreover this phenomenon is significant for each application, when the shape memory alloy used during any load.

Acknowledgement

This work is connected to the scientific program of the " Development of quality-oriented and harmonized R+D+I strategy and functional model at BME" project. This project is supported by the New Hungary Development Plan (Project ID: TÁMOP-4.2.1/B-09/1/KMR-2010-0002).

References

[1] J. Ginsztler, B. Hidasi, L. Dévényi: Alkalmazott anyagtudomány, Műegyetemi Kiadó, 2000.

[2] E. Hornbogen: Review Thermo-mechanical fatigue of shape memory alloys, J. of Materials Science 39 (2004) pp. 385– 399

[3] J. Prohászka: A fémek és ötvözetek mechanikai tulajdonságai, Műegyetemi Kiadó 2001.

[4] Nanoscale Science, Engineering & Technology, Teacher's preparatory guide, Shape memory alloys - Smart materials (www.nnin.org)

[5] Wolfgang Predki, Adam Knopik, Björn Bauer: Engineering applications of NiTi shape memory alloys (2006. December)

[6] Marek Novotny - Juha Kilpi: Shape Memory Alloys (SMA)

[7] Manfred Kohl: New materials for micro-scale sensors and actuators (An engineering review, 2007. June)

[8] G. Costanza, M.E. Tata, C. Calisti: Nitinol one-way shape memory springs; Thermomechanical characterization and actuator design (2009. November)

[9] Dr. Savas Dilibal: General applications of NiTi shape memory alloys (2008. May)

[10] K. Otsuka, X. Ren: Physical metallurgy of Ti–Ni-based shape memory alloys (2004)

[11] Káldor Mihály - Hidasi Béla: A martensites átalakulás szerepe az alakemlékezés jelenségében (1997)

[12] Dobránszky János, Magasdi Attila: Az alakemlékező ötvözetek alkalmazása napjainkban (2001. December)

Development of ceramic feedstock for Powder Injection Molding

Zs. KARÁCSONY[1, a], A. ERŐS[1], E. ANDERSEN[1], Gy. BÁNHEGYI[1]

[1]Bay Zoltán Nonprofit Ltd. for Applied Research, Institute for Materials Science and Technology, Budapest, 1116 Budapest, Fehérvári street 130. Hungary

[a]zsuzsa.karacsony@bayzoltan.hu (corresponding author)

Keywords: alumina, feedstock, DTA/TGA, Powder Injection Molding

Abstract. As part of our technology development program we started to prepare for introducing ceramic injection molding technology. The technology consists of the following steps: 1. feedstock preparation (mixing the ceramic powder with binding agent), 2. injection molding (green body production), 3. thermal or solvent debinding (brown body production), 4. sintering of the brown body. To make alumina ceramic parts essential to know the properties of all raw materials which are used during the PIM process. That is why this article is focused on the thermogravimetric studies of potential raw materials. These thermogravimetric studies helped to optimize the debinding experiments at specimens with high alumina content. First of all the measured curves of the feedstock were compared with calculated curves from the single raw materials. This comparison helped us to understand the processes in the feedstock during the sintering. Then thermogravimetric experiments in air atmosphere were made to optimize the sintering process. These experiments resulted good structural properties at the sintered parts.

Introduction

Powder Injection Molding is a commonly used method to make small alumina parts with complex geometry and with good quality [1-3]. Figure. 1. shows the shematic steps of the PIM process. The first step is the preparation of the feedstock by mixing the raw materials: the ceramic and the binder materials. The base of the binder is the polyolefin which is liable for the strength of the molded specimens. Additional materials can be the copolymers which can improve the wettability of the polyolefins and the adhesion to the inorganic components. Waxes and fatty acids decrease the viscosity to promote the injection moldability, and the fatty acids are against the segregation of the inorganic and organic components [4]. The second step is the injection molding of the pelletized compound. The injection molded specimen is called green body. The third step is the debinding process: the organic binder is removed from the green body by a thermal treatment which results the brown body [5]. The last step is the sintering of the brown body to obtain the ready ceramic product [6].

Our aim is to develop proprietary feedstock and processing technology for producing alumina based sintered bodies of various densities. The feedstock should contain 80-90 wt% mineral filler (alumina and/or alumina trihydrate, ATH), the rest is organic material consisting of a polyolefin, a polyolefin copolymer and a wax component. The quality of the feedstock is determined by the surface treatment and size distribution of the mineral additive and the parameters of compounding. In our laboratory scale trials we used a Brabender Plastograph (Brabender, Germany) for producing the feedstock which was compression molded first for debinding studies. The main thermal decomposition processes were identified by simultaneous DTA-TGA measurements (using a Setsys 16/18 apparatus, Setaram, France) in Ar atmosphere, which was followed by scanned + isothermal debinding studies in the same apparatus and by oven debinding studies performed on compression molded samples [7].

In this article we focus on the thermogravimetric studies to analyze the binder components' burn-out properties. This work helps to understand the mechanism of sintering process and to find the ideal binder burn-out strategy. The pending work is the injection molding of specimens and comparison of properties of samples made by different methods.

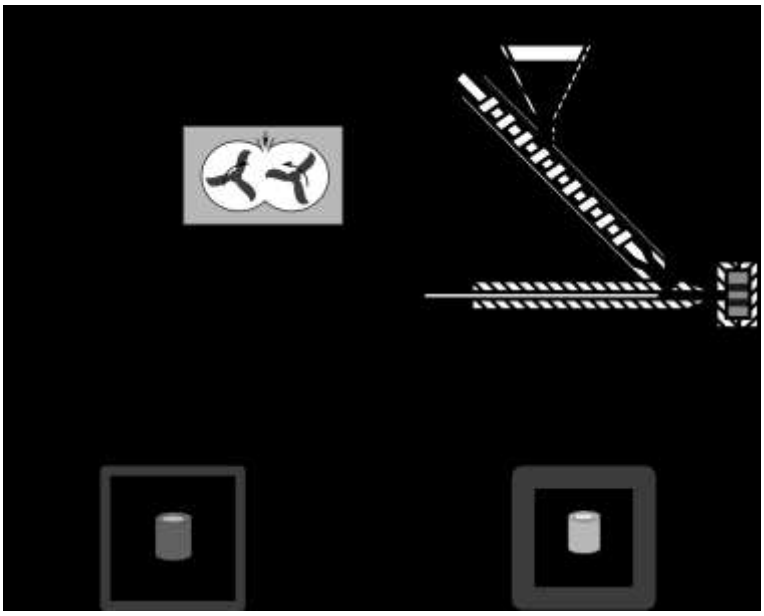

Figure 1. The technological steps of the Powder Injection Molding process (*modified from* [8])

Materials and methods

To make ceramic injection moldings alumina (ALO-G4-4G, MAL, Hungary) was used with d_{50}=4-7 µm particle size, specific surface 1.3 m^2g^{-1}. Different types of binder systems were used. The main components of binders were polyolefin, copolymer, fatty acid and wax. Aluminum hydroxide (ATH, $Al(OH)_3$) was also used. The polyolefins were the backbone polymers. The ceramic loading in the feedstock (including the ATH content) was 85-90 w%. The different feedstocks were mixed by a heated kneader (Brabender-Plasti Corder). Table 1. shows the composition of the studied feedstocks.

Table 1. Composition of the feedstock of the samples*

Number of the sample	Polyolefin [w%]	Copolymer [w%]	Wax [w%]	Fatty acid [w%]	Al_2O_3 [w%]	ATH [w%]
1	9,3	-	2,9	0,6	87,2	-
2	9,5	-	0,6	0,6	89,2	-
3	-	9,3	2,9	0,6	87,2	-
4	-	9,3	2,9	0,6	58,1	29,1

*The exact grades are not given for proprietary reasons.

The feedstock to the sintering studies were die pressed into a 5cm×5cm×5mm pressing mold. The samples to the thermogravimetric experiments were cut out from these pressed specimens.

The DTA/TGA measurements were made by a Setaram Setsys 16/18 equipment in argon and synthetic air atmospheres. 10°C/min linear heating rate was used between 20°C and 900°C in argon and between 20°C and 600°C in air. The decomposition properties were measured in argon and the burning properties were followed in air.

Results and discussions

Figures 2. and 3. show the heat flow and mass change curves of the binder components in argon atmosphere. The melting points of wax and polyolefin are 95°C and 142°C respectively. The main decomposition temperatures are also marked on the heat flow curves. The fatty acid starts the decomposition at the lowest temperature in the binder components. The degradation of fatty acid takes place in two stages between 250 and 450°C. The wax has a wide decomposition range from

300°C to 500°C and the polyolefin has a narrow debinding range between 450 and 490°C. It can be seen that at 500°C all the binder components were completely removed. ATH (aluminum hydroxide) is used as an additional source of alumina. The ATH transforms into alumina at 320°C while the chemically bonded water is evaporated.

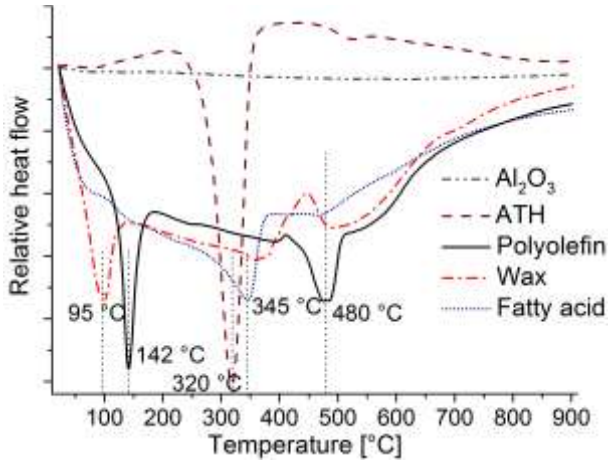

Figure 2. Heat flow curves of the binder components and ceramic components in argon

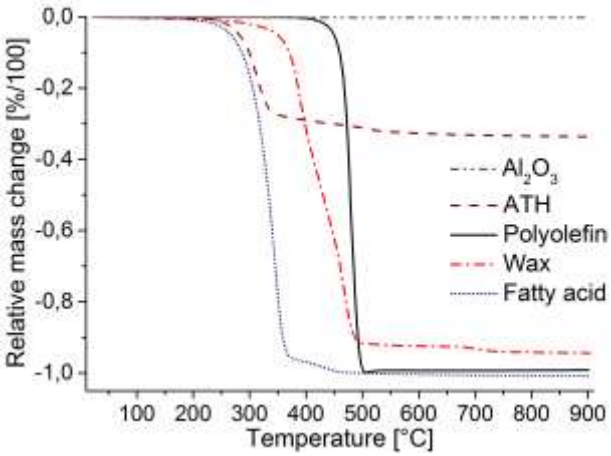

Figure 3. Weight loss curves of the binder and ceramic components in argon

After the raw materials we made further measurements from the different feedstocks and we analyzed the DTA/TGA curves. The measured curves were compared with the calculated curves which were created from the weighted single raw material curves. In this review only one example will be shown in Figure 4. The main components are the ATH and polyolefin in addition to the alumina. The curves show the main characteristics of these materials. The wax and the fatty acid have a slight effect on the decomposition of ATH, the measured curve alludes to complex processes. These components also have an effect on the polyolefin's burnout. An interesting thing is, that the theoretically calculated weight loss is higher than the measured mass change. The changes in the feedstock during the preparation can cause the difference between the two curves.

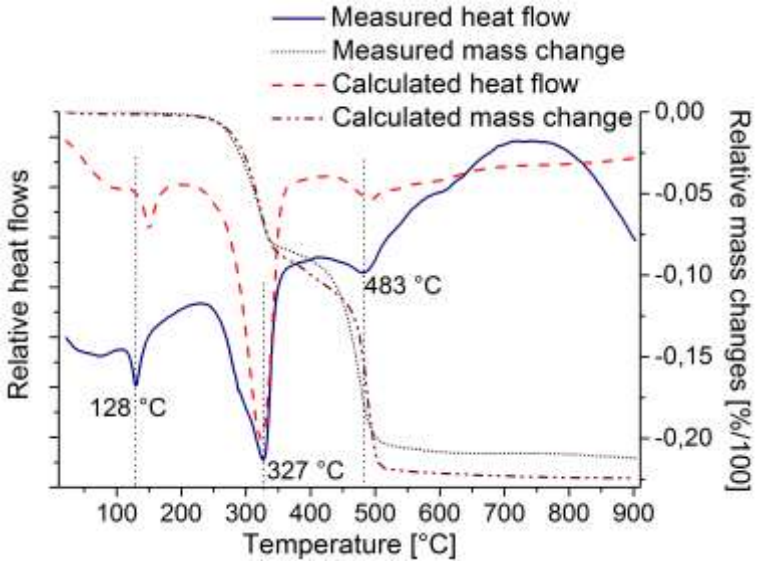

Figure 4. The measured and the calculated heat flow and mass change curves of the chosen feedstock in argon

Table 1. shows the composition of feedstock of the chosen samples. The samples listed in Table 1. were measured both in argon and air atmospheres. Measurements in air atmosphere can simulate the ongoing processes in the furnace. Figs 5. and 6. show the curves in argon and air atmospheres

respectively. The typical decomposition temperature range of the polyolefin can be identified on the heat flow curves in argon. The total weight loss at the samples corresponds to their alumina content. The processes in air are more complex than in argon. The burning of the binder in air causes these changes. The total burnout of the binder is finished at higher temperatures in air.

Based on the literature and the DTA/TGA measurements successful debinding and sintering experiments were made on the die pressed specimens. The debinding temperature was 550°C and the sintering temperature was 1600°C. The sintered parts with higher than 85 w% alumina content had favorable structural properties.

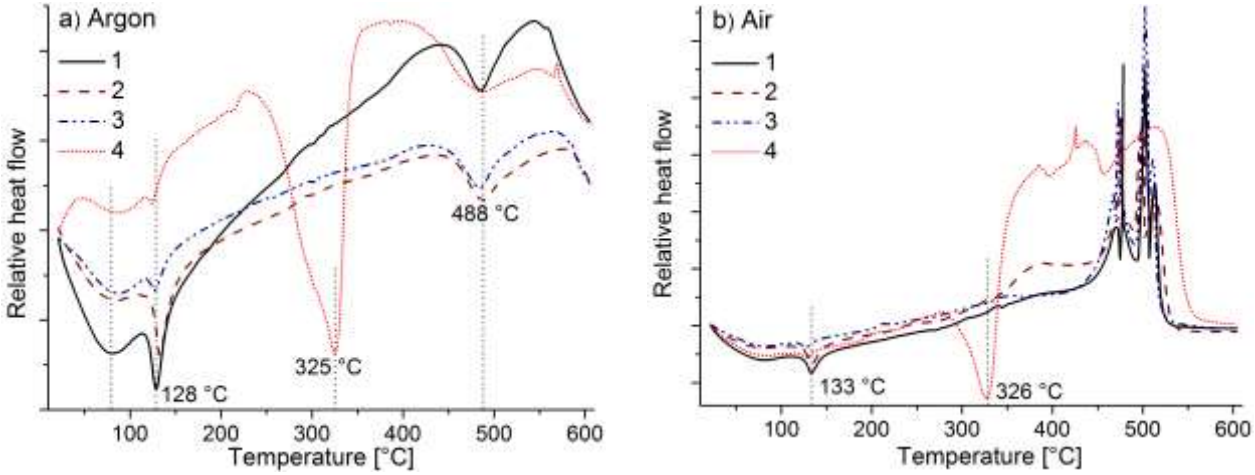

Figure 5. Heat flow curves in Ar (a) and Air (b) atmospheres

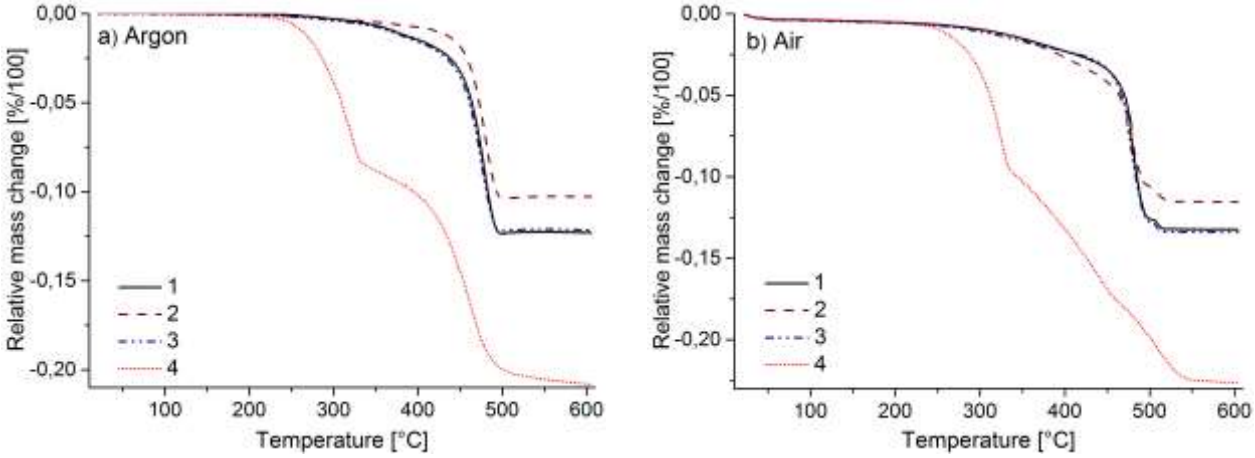

Figure 6. Weight loss curves in Ar (a) and Air (b) atmospheres

Conclusions

Compounds with higher than 90 w% of alumina content were prepared. These compounds after die pressing and sintering have favorable structural properties, so the experiments were successful. The thermogravimetric studies helped to optimize the debinding experiments. The injection molding process of these materials is under development.

References

[1] Z. S. Rak, New Trends in Powder Injection Moulding, Powder Metallurgy and Metal Ceramics. 38 (1999)

[2] B. S. Zlatkov, E. Griesmayer, H. Loibl, O. S. Aleksic, H. Danninger, C. Gierl és L. S. Lukic, Recent advances in PIM technology I, Science of Sintering. 40 (2008) 79-88.

[3] B. C. Mutsuddy és R. G. Ford, Ceramic Injection Molding, first ed., Chapman&Hall, London, 1995.
[4] K.M. Achikita és S. A. Ohtsuka, U.S. Patent 5,135,977. (1992)
[5] M. Trunec és J. Cihlar, Thermal removal of multicomponent binder from ceramic injection mouldings, Journal of European Ceramic Society. 22 (2002) 2231-2241.
[6] T. Moritz és R. Lenk, Ceramic injection moulding: a review of developments in production technology, materials and applications, Powder Injection Moulding International. 3 (2009) 23-34.
[7] S. T. Lin és R. M. German, Interaction between binder and powder in injection moulding of alumina, Journal of Material Science. 29 (1994) 5207-5212.
[8] U. M. Attia és J. R. Alcock, A review of micro-powder injection moulding as a microfabrication technique, Journal of Micromechanics and Microengineering. 21 (2011) 043001.

UHMWPE modified sodium alginate

Mariann Kollár[1], Gabriella Zsoldos[2], Tamás Szabó[3]

[1,2,3] University of Miskolc, Institute of Ceramic and Polymer Engineering, Hungary

[1] femmaja@uni-miskolc.hu

[2]femzsgab@uni-miskolc.hu

[3]polsztam@uni-miskolc.hu

Keywords: : Ultra High Molecular Weight Polyethylene (UHMWPE), sodium alginate, DSC, FTIR, SEM

Abstract: Aim of our experiments was to modify prosthetic material UHMWPE powder using sodium alginate. The sodium alginate has an important property that the appropriate chemical reagent could exchange its Na^+ ions to Ca^{2+} ions. The Ca has important role in the healing process, so modifying this substance the UHMWPE material helps patients healing. In the first step we examined that the raw material UHMWPE powder is necessary to be treated in order to adhere alginate at the surface of the UHMWPE powder. In a second step, we examined that insoluble Ca alginate coating left at the surface of UHMWPE powder after the exchange of Na ions. The treated powders were analyzed by Fourier Transformed Infrared Spectroscopy and Diffential Scanning Calorymetry methods. SEM investigations were carried out on the prepared samples moreover energy-dispersive X-ray spectroscopy (EDAX) measurements were performed,-for detection of the presence of small amounts of Na and Ca ions. It has been found that the complex and complicated Caro's acid chemical treatment is unnecessary in order to prepare alginate coated substrates. The best results were achieved by selecting the correct order of surface layer preparation; first coating the substrate with alginate solution then treating with aqueous $CaCl_2$.

Intorduction

The ultra high molecular weight polyethylene (UHMWPE) is the most important artificial hip implant base material which is widely used in orthopedics over the past 45 years for processing artificial joints cup. The lifetime of plastic cups period specified. The most important problems are fracture wear and creep. As the wear of the cup also increases the oxidation of the plastic and the leaving particles (debris) so researchers have begun work on an alternative method that is blended the raw material with antioxidants. One of such an antioxidants is α-tocopherol known as vitamin E. It is the most efficient antioxidant being present in the human body. Vitamin E has a recognized antioxidant, anti-inflammatory property and plays an important role in the fight against free radicals.

Sodium alginate is the sodium salt of alginic acid. Sodium alginate is most well known for its use in culinary spherification. The spherification technique was introduced to modernist cuisine by Ferran Adrià in 2003. It consists of a controlled jellification of a liquid which forms spheres when submerged in a bath. The spheres can be made of different sizes and have been given names like caviar when they are small, eggs, gnocchi and ravioli when they have larger size. The resulting spheres have a thin membrane and are filled with the flavored liquid.

Sodium Alginate is a natural polysaccharide product extracted from brown seaweed. As soon as sodium alginate is added to a solution of calcium chloride, a gel forms as the sodium ions (Na^+) are replaced with calcium ions (Ca^{2+}) and the polymer becomes crosslinked and insoluble (Fig.1). The polymer has special properties; it behaves like an egg box, trapping Ca

ions. The basis of the idea presented here, came from the modification of UHMWPE with vitamin-E. We believe that applying as a special preparation onto the surface of UHMWPE powder the sodium alginate could form a layer, which traps calcium ions from solutions. UHMWPE's main medical application is for hip joint cups. If we could introduce calcium ions by using alginate, the calcium may reduce the risk of rejection, and help bone growth.

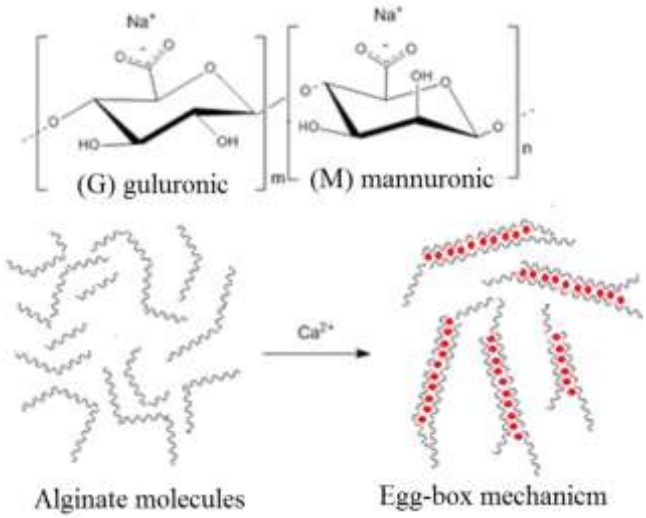

Figure. 1. Sodium alginate egg-box mechanism

Many problems were faced during the preparation of the samples. The first was to work out how the coating can be applied on the surface of the UHMWPE, since the polymer is a very stable and inert material. The second was that at higher temperatures the alginate might decompose or could not withstand the sterilizing 20 kGy gamma radiation.

Materials and Modification

The used UHMWPE is GUR 4120 (Average molecular weight: 5×10^6 g/mol (Mw)) powder. In the first stage the surface of the polymer powder was etched by Caro's acid (1:1 ratio of H_2SO_4 and 30 v/v % aqueous solution of H_2O_2.). The surface was modifying for different durations (1 min, 20 min, 180 min). The surface of the polymer particles was observed using SEM.

After treatment, it was found that there is no significant difference between the surfaces of the polymer powders (Fig. 2.). Thin net-like structures inside the polymer powder particles remained without thinning. Therefore eroding of the surface of the polymer particles can not be detected.

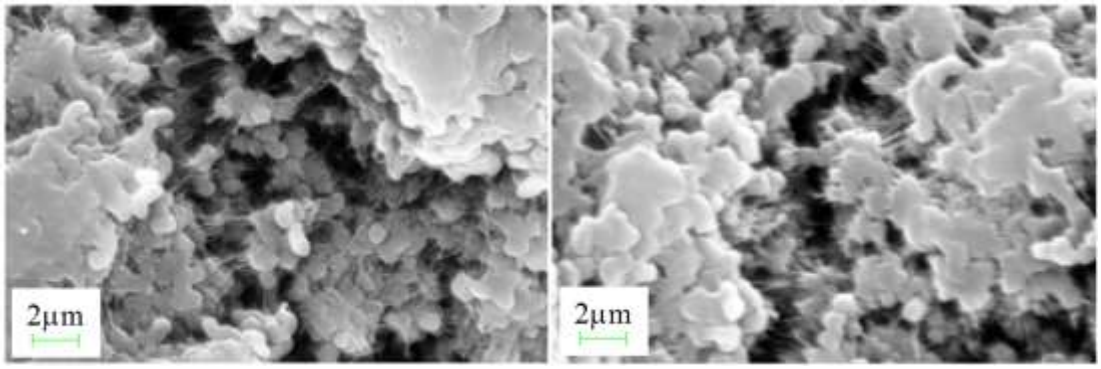

Figure. 2. Surface of the untreated (left) and treated(right) UHMWPE

The sodium alginate (ISP Alginates) alcohol solution (0,5 wt% aqueous solution with alcohol) and calcium chloride and calcium carbonate (commercial product) (20 wt% aqueous solution) sprayed onto the modified and non modified UHMWPE powder. The treatment is performed in the reverse. The samples were heated 50°C for 1 hour. Then the samples cooled and controlled with Scanning Electron Microscopy EDAX, FTIR analysis, and DSC analysis.

Experiments

The goal of the experiments was to check the adhesion of alginate to the substrate using different coating methods. From the results of the tests we could select the most optimal method of binding Ca on the surface of UHMWPE powder.

Infrared spectroscopic measurements

The tests were carried out on a Bruker Tensor 27 FTIR instrument. From first set of Caro's acid treated and untreated samples it was established that, - since the oxidation peak (1730cm^{-1}) was always absent, - the surface modification did not occur, or was with a very low efficiency, what is not detectable.

In latter tests, when the eroded and non eroded samples were analyzed after coating with $CaCl_2$ + alginate, it has been found that for both cases the results are the same. This indicates that there is no need for chemical pre-treatment, which is preferred in terms of that there is no extra treatment step (Fig.3.).

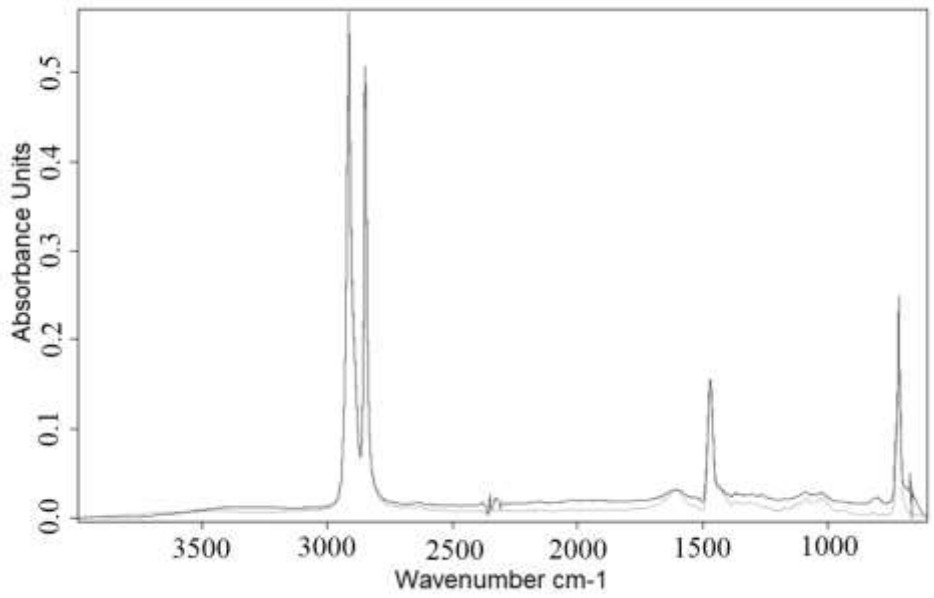

Figure. 3. IR absorption curve of the treated UHMWPE (black) and untreated UHMWPE (grey) powder after $CaCl_2$ + alginate coating

On a second series of samples the effect of spraying order was examined. First, the sodium-alginate solution and later the $CaCl_2$ solution was sprayed to the UHMWPE powder, and then on a separate sample, the order was reversed (Fig.4.)

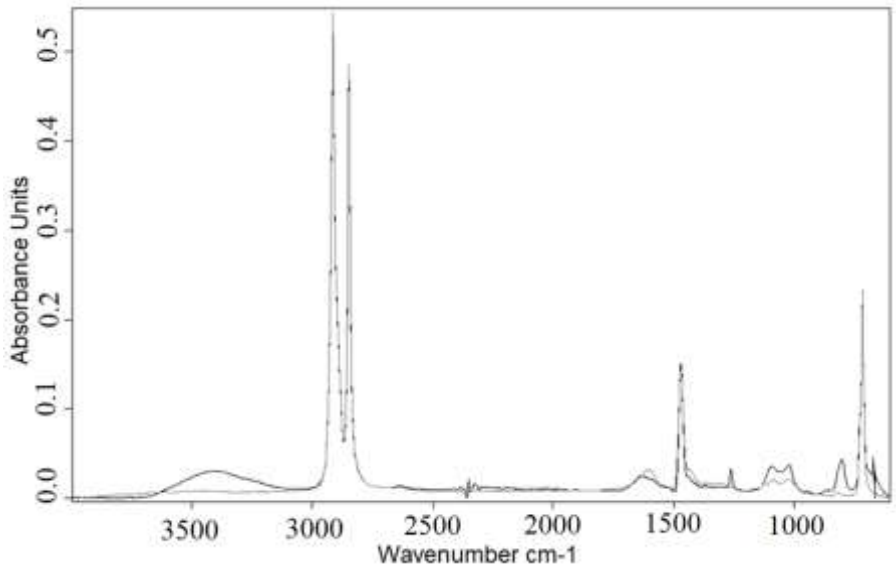

Figure. 4. IR spectra of the UHMWPE powder after treatment 1. $CaCl_2$ solution 2. alginate coating (black) and after 1. alginate 2. $CaCl_2$ solution coating (grey)

If after washing with distilled water, the alginate absorption peaks appear on the sample's spectrum,it also means that the calcium alginate is present in the powder what was our intent. Since the sodium alginate is water soluble but the calcium alginate is not. The two curves which we got are very similar, but in the case of the 1. $CaCl_2$ 2. alginate sequence has shown higher water absorption from the air.

Differential Scanning Calorimetric **method**

Differential Scanning Calorimetry (DSC) is a thermo-analytical technique in which the difference in the amount of heat required to increase the temperature of a sample and a reference is measured as a function of temperature. This investigation was used to determine if any structural change happened to the UHMWPE.

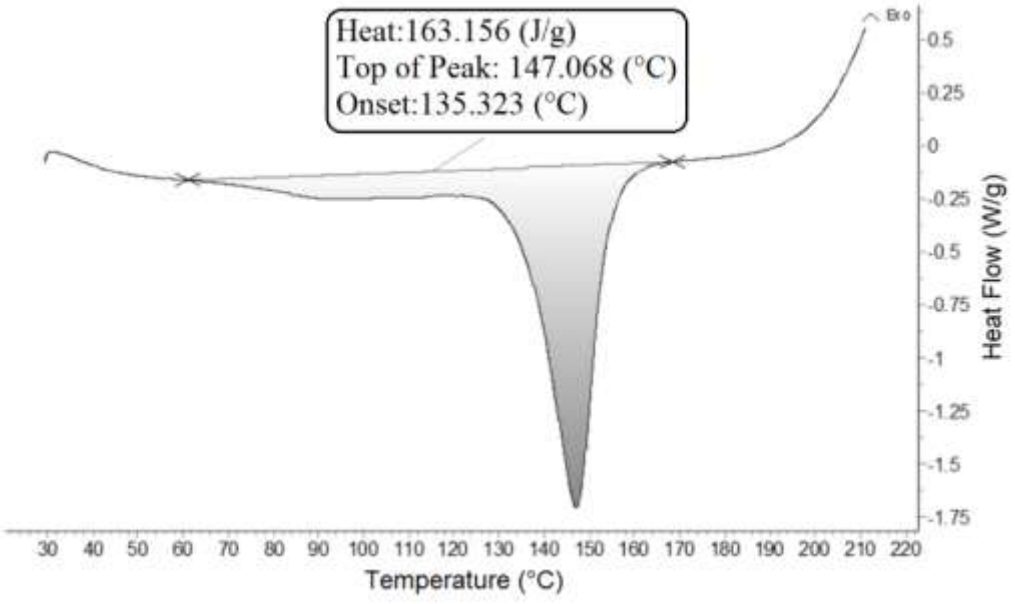

Figure. 5. Thermogram of the UHMWPE+alginate +$CaCl_2$ system

The alginate has a wide melting peak at 130°C, which endothermic peaks don't appear in the thermograms Fig.5. shows that the melting temperature was shifted to 147.1°C as the effect of these substances. The T_m for most samples became larger than the pure dusts' of UHMWPE, thus proven that alginate complexes are present because the alginate's calcium salts have a melting temperature above 300°C.

Scanning Electron Microscopy – Energy Dispersive X-ray Microprobe

With SEM Microanalysis it was verified that even after washing; the Ca remained on the surface of the UHMWPE powder; proving that the water soluble Na alginate was transformed into water insoluble Ca alginate. The Na peek refers to the presence of unchanged alginate the Ca peek to the presence of Ca ions.

Water absorption and swelling

The determination of water absorption and swelling is important to learn how the treated UHMWPE will behave under wet/humid conditions. Compression molded sheets were made from the treated UHMWPE powder. From the results of sessile drop surface tension measurements it has been found that those UHMWPE sheets which were taking up less moisture from the air have a greater contact angle to water.

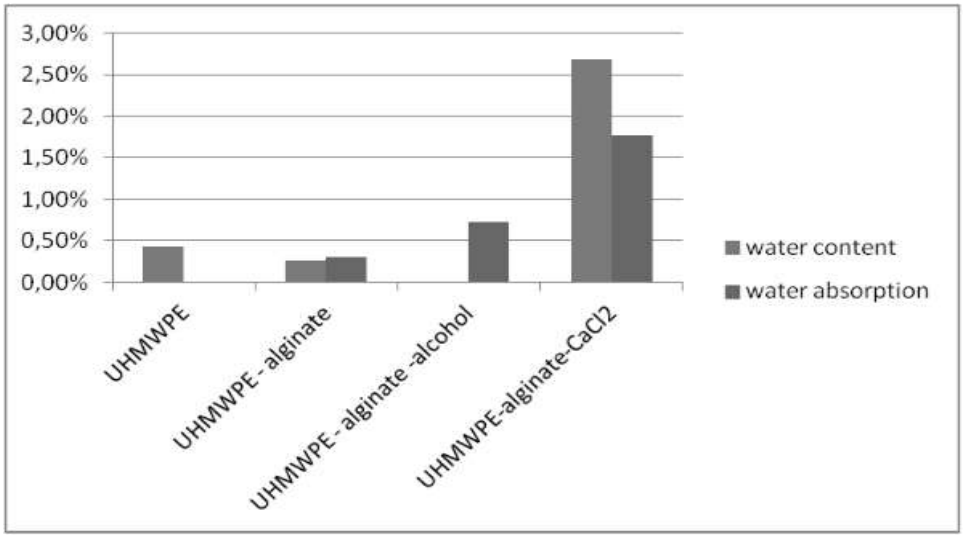

Figure. 6. Results of the Sessile drop surface tension measurements

Summary

Our goal was to find a solution to incorporate calcium in the hip prosthetic material UHMWPE, similarly to the well known vitamin-E containing products. The reagent of choice was Na-alginate. When the Na^+ ions were exchanged to Ca^{2+} ions in the alginate it formed a water insoluble compound. Ensuring that the calcium remained on the UHMWPE's surface. The first experiments were aimed to evaluate the need of surface treatment of the UHMWPE powder. The SEM Microanalysis showed that alginate adsorption on treated and untreated powders resulted in the same (or a very similar) alginate surface layer. After treatment, SEM experiments and DSC measurements were carried out to observe any structural changes. The UHMWPE powder's structure was unchanged in respect of the different treatment methods. The number of different treatment trials (16 types) were too many, so FTIR analysis was used to select the most suitable method for providing the best amount of alginate to remain after washing the surface with distilled water. We have found that the best results were obtained

when the surface was first sprayed with an alcoholic solution of Na-alginate, and after with with the aquious solution of $CaCl_2$.
Water absorption and swelling are important properties of the alginate treated UHMWPE powders and the results shows that the samples which were made from UHMWPE-alginate-$CaCl_2$ have a higher water content and water absorption. The water absorption of non reacted sodium alginate may be up to 200%. Such a high water uptake with a large increase in volume is not favorable in a material for implantation. We think, that if the swelling is limited, this Ca carrying layer could function well on the surface of the implant, as the remaining swollen Na alginate can work as a lubricant layer.

Acknowledgement
This research work was supported by TÁMOP-4.2.1.B-10/2/KONV-2010-0001

References

[1] J. Wang, X. Zhang, X. Wang, Preparation, characterization and permeation of calcium alginate macro-capsules containing shape- stabilize phase change materials, Renewable Energy, 36 (2011) 2984-2991.
[2] I. A. Kapandji, Physiology of the Joints: Volume 2 Lower Limb, 6e, Churchill Livingstone, London, 2010.
[3] Czvikovszky T., Nagy P., Polimerek az orvostechnikában, Műegyetemi, Budapest, 2003.
[4] Zsoldos G. ,UHMWPE-biopolimer felületének módosítása polimerizációs technológiákkal, PhD thesis, 2013.
[5] S. M. Kurtz, UHMWPE Biomaterials Handbook – A Primer on UHMWPE, Academic Press, 2009.
[6] S. M. Kurtz, UHMWPE Biomaterials Handbook – Highly Crosslinked UHMWPE Doped with Vitamin E, Academic Press, 2009.
[7] Information on http://www.molecularrecipes.com/modernist-cuisine ingredientshydrocolloidsstarches/sodium-alginate-alginate-algin/
[8] Information on http://www.willpowder.net/sodiumAlginate.html
[9] Information on http://molecule-r.com/en/content/29-sodium-alginate

Surface Hardening of Austenitic Stainless Steel by Explosive Treatment

Tunde Kovacs-Coskun[1, a], Peter Pinke[2,b]

[1]Óbuda University, Bánki Donát Faculty of Mechanical Engineering, Department of Material Sciences, 1081 Budapest Népszínház u. 8. Hungary

[2]Faculty of Materials Science and Technology Trnava, Slovak University of Technology Bratislava, Paulínska 16, 917 24 Trnava, Slovak Republic

[a]kovacs.tunde@bgk.uni-obuda.hu, [b]peter.pinke@stuba.sk

Keywords: surface hardening, phase transformation, microstructure, stainless steel

Abstract. Specimens of austenitic stainless steel hardness changing were tested. The used hardening technology was a modified explosive treatment. During the hardening tests the explosive exploded different distance from surface. Same setup was tested with 2, 3 and 4 mm holder. The hardness improving and the plastic deformation were different as function of the holder size. The hardness was measured by Vickers hardness tester. The amount of strain induces martensite was detected magnetically. It can suppose that the microstructure changed during high rate strain. Results showed that the strain rate and result hardness depend on the holder size. We found that the bigger holder size in case of the tested setup provoke higher hardening. To determine the hardness properties it's important to use an optional setup.

1. Introduction

Surface hardening, a process that includes a wide variety of techniques is used to improve the wear resistance [1]. Surface hardening of steels traditionally industries use heat treating or coatings technologies. It can use cold working surface hardening too. The austenitic stainless steels have great ductility and low hardness. In case of this steel it can't use any heat treating technology because of the special microstructure.

Explosive hardening is a process which for many applications cannot be performed by conventional methods. In addition, usually it is a relatively quick and simple operation, and one which can be performed in remote locations without heat treating furnaces or heavy-duty deformation processing equipment. It can be used for sizes and configurations of parts which are inappropriate for conventional methods and, if desired, the process can be applied to only specific areas of the workpiece [2].

To improve hardness properties we have to use optional setup. The parameter optimization in case of explosive hardening technology isn't well understood yet. It means practically that to determine parameters we need to do tests. Explosive-hardening is an operation in which an explosive charge is detonated in contact with a metal, creating a very strong short pulse which travels through it. Hardening due to local deformation in the region of loading is generally expected with changes in the mechanical properties of the metal. The hardness values and the depth of the hardened layer are dependent on the initial properties of the metal and the intensity of the impulse delivered by the explosive [3].

It knows that the metals properties change under high energy rate forming. The austenitic steel has a face centered cubic structure and under explosion shock wave this structure change. The effect of strain rate on the ϒ-α' transformation in stainless steels has been of interest for a number of years. The early work simply noted that an increase in rate decreased the amount of martensite [4].

The aim of this study is to report the results of the hardness improving of an austenitic stainless steel treated using explosive treatment. Among the treatments intended to improve the surface properties of materials, shocks are known to induce an important hardening, either by flyer plate impact [5, 6].

2. Experimental procedure

2.1 Experimental procedures

The explosive substances for surface treatment Permon 10T (parameters show in Table1), it was applied like powder layer thickness deposited on the flayer plate (see Figs. 1 and 2) was in the range 30 mm. The thickness of the explosive powder was optimized on base of practice. It knows that it needs a minimal amount of explosive, that about 0,017 (g/mm^2) Permon 10T [7]. The shock characteristics (pressure) have been estimated to be close to 31 GPa respectively for the Permon 10T. The detonator located in the middle axe of the samples.

Table 1. Explosive parameters

Explosive	**PERMON 10T (powder)**
Volume of the gas	928 dm^3/kg
Detonation rate (v_D)	3200 m/s
Density (ρ)	850 kg/m^3
Distance between the plates	2, 3, 4 mm
Thickness of the explosive	30 mm
Weight	319 g

The average pressure calculated by (1), where ρ explosive density and v_D is the detonation rate (Table 1).

$$P = 0{,}25 \cdot \rho \cdot v_D^2 \tag{1}$$

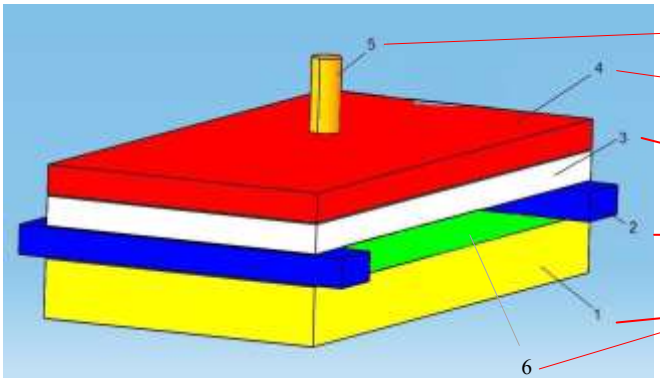

Fig.1. Setup of indirect hardening (1base material, 2 holder, 3flayer plate, 4 explosive, 5 detonator, 6 plastic isolation)

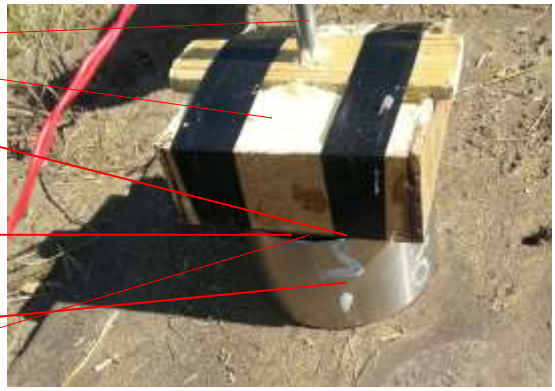

Fig.2. Setup of the hardening (1base material, 2 holder, 3flayer plate, 4 explosive, 5 detonator, 6 plastic isolation)

On the base material surface we used an isolation layer (Fig. 1. /6) (thin plastic film) because we didn't want do a cladding, we used the flayer plate only like holder. In case of experiments the holders were 2, 3 and 4 mm.

2.2. *Material*

The studied material was an austenitic stainless steel, chemical composition shows in Table 2, the type of this steel about Hungarian standard MSZ4360-80 KO33, DIN X5CrNi1810, EN 1.4301, AISI 304. Average hardness of the samples 215 HV.

Table 2. Chemical composition of samples (weight %)

Type	C	Si	Mn	Cr	Ni	N_{max}	P_{max}	S_{max}
KO33	0,07	1	2	18,25	9,25	0,11	0,045	0,015

The cylindrical geometry (diameter 80 mm x 40,5±1 mm) specimens were first polished before the explosive treatment and the cross section of the samples were polished again before hardness tests. The size of the samples shows the Table 3.

2.3. *Characterization of the induced effects in the material*

The effects induced in the material by the explosive treatment were investigated by different methods. Simple empirical test by a permanent magnet, base of the ferromagnetic behavior of the martensite (austenite is paramagnetic). Plastic deformation shows the deformation rate and the reduction of the samples. It's only a comparison of the original and treated samples sizes. Vickers hardness tests with a load of 30 kg on the surface and at different depths were performed. Measuring points showed in the Fig. 3.

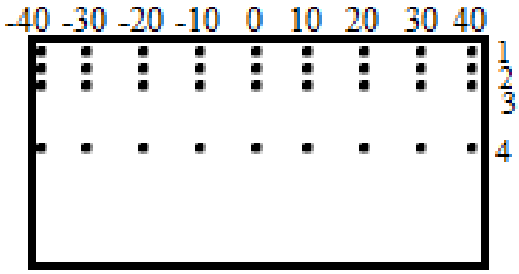

Fig.3. Vickers hardness measuring points

Fig. 4. The flayer plate and the hardened sample

3. **Results and discussion**

3.1. Magnetic behavior

Magnetic test results in case of every samples that the surface behavior changed and shows ferromagnetic property. We have to establish also, that feature can observe only on the surface and in the nearby layers of the surface.

3.2. Plastic deformation

The plastic deformation shows very small difference between the samples. Also the highest deformation is also 2,39% (Table 3). This deformation rate in case of work hardening can't cause significant hardness increasing. On the surface of the sample and the flayer plate (Fig.4) can see the detonation wave lines and the deformation.

Table 3. Plastic deformation

Number of the sample	original height (mm)	height after hardening (mm)	reduction (mm)	reduction (%)
2. (2 mm)	41,32	40,5	0,82	1,98
1. (3 mm)	40,39	39,6	0,79	1,95
3. (4 mm)	40,98	40	0,98	2,39

3.3. Hardness results

Vickers hardness tests show many interesting results. It's clear that the hardness highest on the surface. Between the explosion distance (holder size) and the surface hardness find a strong relationship. It has to establish that on the surface as function of the location the hardness are different. The lowest hardness find in case of all sample in the middle axe. The results show also the hardness far from the surface decrease us function of the distance. The results are accomplished in the Table 4.

Table 4. Vickers hardness results

	Vickers hardness (HV_{30})	**Distance from the middle axe (mm)**								
	Measuring point	0	10	20	30	40	-10	-20	-30	-40
	Sample 1.									
1	surface	217	219	249	254	329	225	260	255	331
2	depth 2 mm	202	204	228	240	317	205	226	247	325
3	depth 4 mm	200	203	223	229	302	201	213	240	304
4	depth 20 mm	183	184	197	200	258	187	190	202	249
	Sample 2.									
1	surface	222	216	234	234	320	219	234	232	325
2	depth 2 mm	200	203	218	225	311	202	217	218	311
3	depth 4 mm	201	199	206	220	307	200	209	210	304
4	depth 20 mm	177	183	191	196	280	172	190	190	297
	Sample 3.									
1	surface	243	223	241	252	348	232	249	250	321
2	depth 2 mm	220	211	226	240	341	208	224	234	320
3	depth 4 mm	208	203	219	227	328	206	215	224	287
4	depth 20 mm	181	184	191	198	300	183	194	191	252

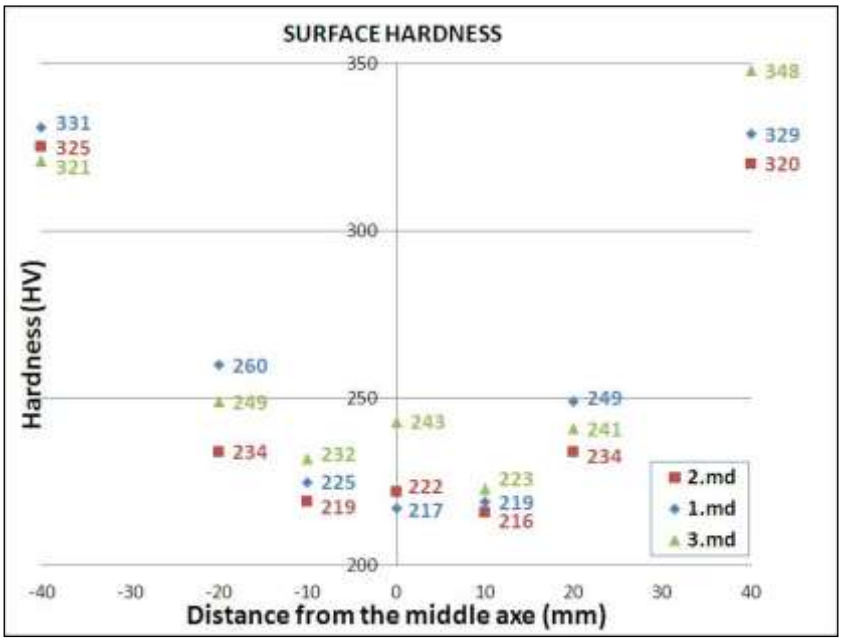

Fig.5. Hardness on the surface

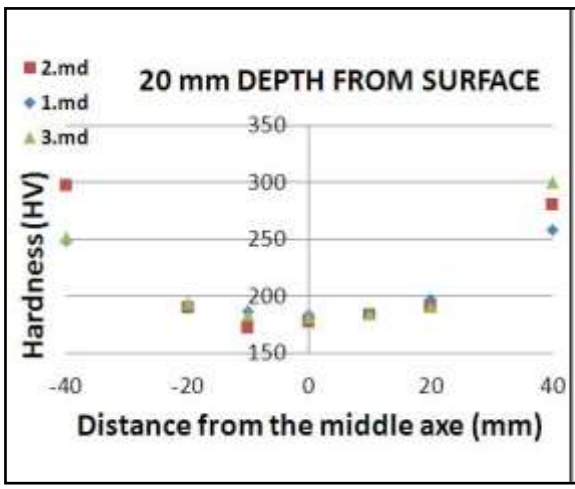

Fig.6. Hardness 4 mm depth from the surface

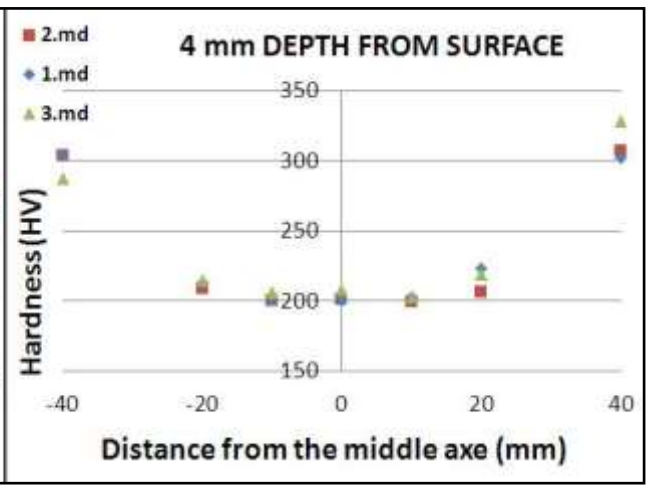

Fig.7. Hardness 20 mm depth from the surface

The hardness increasing is different in case of different setup (holder size) shows Fig.8. The plastic deformation rate and the hardness shows also relationship.

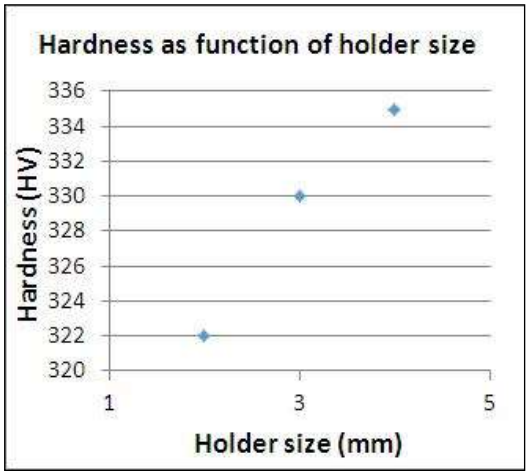

Fig.8. Hardness as function of holder size

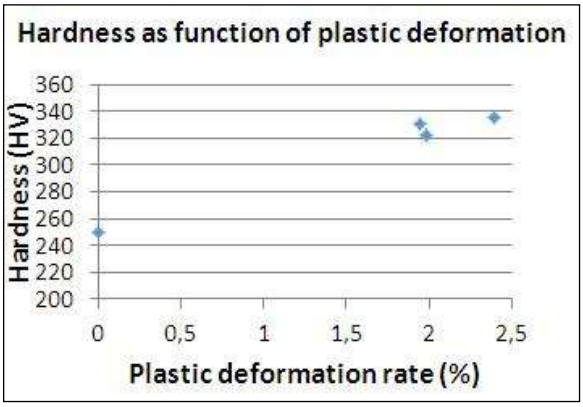

Fig.9. Hardness as function of plastic deformation rate

4. Conclusion

We observed the next thesis on base the results.

I. The hardness increasing on the surface depends on the distance from the detonator. We can explique this phenomenal with the behavior of the detonation. The detonator starts the detonation, but the nascent pressure rate is lower than the average explosion pressure. The pressure increasing needs an incubation way to reach the maximal pressure rate. It's a strong relationship between the pressure rate and the result hardness.
II. Also the same cause of the relationship between the hardness and the holder size. In case of bigger holder size the collision velocity of the flayer pate is also higher than in case of small holder size.
III. We found also some relation between the plastic deformation and the hardness increasing but it's not so strong.
IV. The surface magnetic behavior of the sample changed, we suppose that the austenitic microstructure changed and under the explosive treatment shape a martensite structure.

References

[1] J.R. Davis: Surface Hardening of Steels, ASM International (2002) pp. 1-16.

[2] T.Z. Blazynski, Explosive welding forming and compaction, Elsevier Science Publishing Co., Inc. (1983) pp. 94-103.

[3] S. A. Meguid, On the explosive hardening of one end of a metallic block Int. J. mech. Sci. Pergamon Press. Vol. 18, Printed in Great Britain (1976) pp. 351-355.

[4] M. A. Meyers, L. E. Murr, Shock Waves and High-Strain-Rate Phenomena in Metals, International Conference on Metallurgical Effects of High-Strain-Rate Deformation and Fabrication, Albuquerque, N.M., (1980) pp. 91-111.

[5] L. Fouilland-Paill, M. Gerland, P. Violan, Cyclic behavior of a 3 16L stainless steel hardened by an explosive Materials Science and Engineering A201 (1995) pp. 32-39.

[6] K.P. Staudhammer, C.E. Frantz and S.S. Hecker, in M.A. Meyers and L.E. Murr (eds.), Shock Waves and High Strain Rate Phenomena in Metals, Plenum, New York, (1981) pp. 91-l12

[7] Kovacs-C.T.,Volgyi B.,Sikari-N.I., Investigation of aluminum-steel joint formed by explosion welding, IC-RMM1 Conference Hungary, Lillafüred, (2013)

Comparing two examination methods for measuring metal to artery ratio of coronary stents

Miksa Kovács[1,a], Dóra Károly[1,b] László Dévényi[1,c]

[1]Department of Materials Science and Engineering, Faculty of Mechanical Engineering, Budapest University of Technology and Economics, 1111 Budapest Bertalan L. u. 7., Hungary

[a]miksa.kovacs@gmail.com, [b]karoly.dora@gmail.com, [c]devenyi@eik.bme.hu

Keywords: coronary stent, metal to artery ratio (MAR), metallic surface area (MSA), stent pattern, cell size, maximum achievable cell diameter, examination method.

Abstract. This article shows two examination methods to measure the metal to artery ratio of stents. Our goal was to further develop the previously used measuring method in order to make it suitable for the integration into the quality control process of endovascular stent manufacture to provide more realistic data. The previous method was performed manually using rotating equipment under a stereomicroscope. The new method is an automatic method using an integrated scanner and a rotating engine. Both methods aimed at converting the cylindrical stent into a flattened two-dimensional image in order to enable the measurement of stent surface area by imaging software. From the image we can determine the cell sizes, the maximum achievable stent diameter, and the structure of the stent pattern. Each measurement process was tested on different types of stents. Our findings showed that the methods gave similar results, the largest differences are speed and accuracy.

Introduction

In the public mind the most feared disease is probably cancer, while there is a much more devastative group of diseases; the cardiovascular diseases, which are responsible for one third of the mortalities in the world. In Hungary cardiovascular diseases affect more than 50 percent of the population, as well as lead the cause of morbidity and mortality. So the prevention of these diseases is a high priority. Coronary artery disease is the most common reason of death in this group of diseases [1,2].

During the formation of the disease the organic and inorganic (such as cholesterol or minerals) are deposited on the inner wall of the blood vessel, thus forming the so-called plaque. Stent implantation is an angioplasty method for the treatment of atherosclerosis. A stent is a small bio- and hemocompatible tubular mesh, which is mounted on a balloon catheter to reach the narrowed section of the vessel. After dilating and removing of the balloon catheter (Fig. 1), the stent compresses the plaque and supports the artery, thus ensures the free flow of blood, so the blood flow of the closed area is restored [2,3]. Coronary stents are made usually by laser beam cutting of 316L stainless steel, L605 type cobalt-chromium alloy or platinum-chromium alloy high-precision tubes. After cutting out the stent the first step is etching to get rid of burrs, then electropolishing to smooth the surface. [4-7].

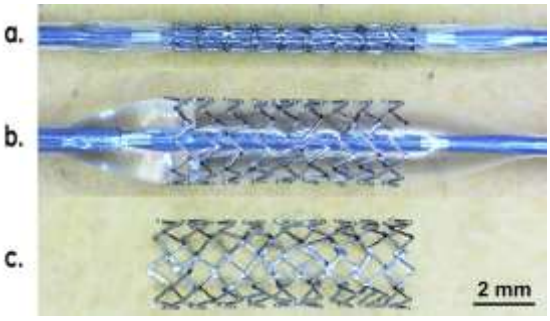

Figure 1 Dilation of the 2.75×8 mm (A) stent system; a. crimped stent, b. dilated balloon and stent, c. dilated stent without balloon.

Metallic surface area (MSA) or metal to artery ratio (MAR). According to the standard, stent outer surface area (SOSA) is the contact area between the stent and the vessel and stent-free surface area (SFSA) is a percentage of surface area of cylinder formed by the implant frame, which is not covered by implant material [8]. Metallic surface area (MSA) and metal to artery ratio (MAR) is a rate which describes a ratio (in percentage) between the stent outer surface and the covered vessel inner surface (Eq. 1). The MSA is inversely proportional to SFSA but the MSA value of stents has become a more practical parameter that is commonly referred by manufacturers. Complying with the industrial needs we keep on giving the MSA value of stents beside SFSA.

$$MSA = \frac{A_{stent}}{A_{vessel}} \cdot 100\,[\%] \tag{1}$$

A_{stent}: outer surface of the stent
A_{vessel}: surface of the covered vessel

The favourable effects of MSA values are not clearly defined yet. Considering strength, the high ratio is the best because in this case the stent can support the vessel wall more securely. On the other hand, the high ratio is bad because the large metallic surface raises the possibility of thrombosis and restenosis [9].

Restenosis. The narrowing of expanded blood vessels (restenosis) is perhaps the major complication associated with endovascular stent implantation. It is believed to be caused by inadequate MSA in stents. Shortly after the implantation the stent surface is in direct contact with the blood, and due to the extraneous surface acute thrombosis can occur, leading to in-stent restenosis. This undesirable process can be influenced with coatings and reducing the metallic surface area of the stent. Analysis of the literature suggests that a more efficient selection of functional properties of bare metal stents can reduce the probability of the re-narrowing of the vessel. Stents deployed in small arteries have a higher metal-to-artery ratio; this may increase the risk of sub-acute thrombosis or restenosis. Various studies have shown that stent design, stent coating, and stent strut thickness may all influence event-free survival. Dedicated stents for small vessels with less metal (so a smaller metallic surface area), appropriate expansion properties and cell morphology, may further improve the results from stenting in this setting [10-13].

From the image of the flattened stent other functional stent properties can be determined, such as the largest and the smallest cell sizes, the maximum achievable stent diameter or stent pattern. The smallest and the largest cell sizes, and the overage cell area were measured. Maximum achievable stent diameter is a useful feature when the stent needs to be placed into a side branch of a vessel and the physic has to get through one of the stent cells with another stent or a balloon catheter. From the evaluated image we get information of the main structure of the stent pattern. Stent pattern influences many other functional stent properties such as flexibility, foreshortening or side branch access. The visibility of the stent is determined by the material of the stent or its density, the thickness and width of the strut and the stent pattern [9,14].

Materials and methods

Five stent systems were investigated (Fig. 2). Table 1 shows the investigated stent systems' nominal properties. The stents were dilated at nominal pressure. All measurements correspond to the MSZ EN ISO 25539-2 standard.

Table 1 The main nominal sizes of the stents.

Stent	Nominal length (mm)	Nominal diameter (mm)	Nominal pressure (bar)	Material
(A)	8	2.75	11	PtCr
(B)	8	3	9	CoCr L605
(C)	12	3	9	CoCr L605
(D)	12	3	9	CoCr L605
(E)	19	3	9	CoCr L605

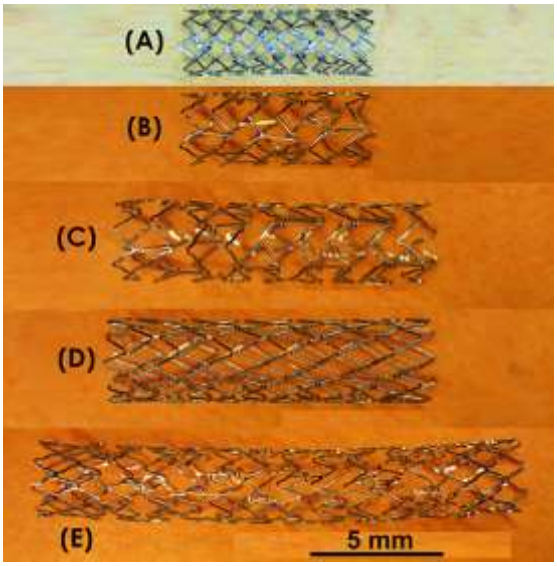

Figure 2 The investigated stents after dilation.

Manual method. The first method was performed by manual stereo-microscopy. High-resolution digital images were taken of each segment of the stents' mantle. The pictures were taken with a Olympus SZX16 stereo microscope fitted to a precision rotary unit. The stents were rotated by increments of 15° from the starting 0° position to 360°. The 24 pictures were then joined to each other, and examined with image analysis software.

Automatic method. The second method was done in an automated manner by a new configuration. The stents were pulled up to a shaft connected to a motor, so that the stents were rotating during the scanning process. In this case we get one whole picture of the stent pattern. The rotational speed and direction can be changed using the buttons of the control panel. Pictures were taken at a resolution of 4800 DPI. The Canon CanoScan LiDE 700F scanner that we used has a 9600 DPI resolution, so the images have far better quality than required.

Both (the manual and the automatic) methods aimed at converting the cylindrical stent into a flattened two dimensional image in order to analyse the stent pattern with imaging software. With the stent pattern the properties were determined by an image analysis program.

Results

Table 2 MSA and the according properties of stents with the manual method.

Stent	Num (pc)	MSA (%)	A_{LC} (mm^2)	D_{LCmax} (mm)	A_{SC} (mm^2)	D_{SCmax} (mm)	A_{AC} (mm^2)	σ_C (mm^2)
(A)	16	16.48	3.69	0.75	2.56	0.63	3.10	0.31
(B)	15	15.38	4.12	1.25	2.72	0.89	3.33	0.42
(C)	24	16.65	3.58	1.08	2.41	0.94	3.00	0.32
(D)	24	18.80	3.88	0.83	1.61	0.68	3.15	0.67
(E)	74	20.19	2.67	1.07	0.52	0.56	1.59	0.79

Table 3 MSA and the according properties of stents with the automatic method.

Stent	Num (pc)	MSA (%)	A_{LC} (mm^2)	D_{LCmax} (mm)	A_{SC} (mm^2)	D_{SCmax} (mm)	A_{AC} (mm^2)	σ_C (mm^2)
(A)	16	18.81	3.39	0.79	2.28	0.61	2.86	0.31
(B)	15	14.51	4.03	1.25	2.70	0.91	3.31	0.39
(C)	24	17.33	3.62	1.07	2.22	0.89	2.94	0.47
(D)	24	20.32	3.88	0.86	1.77	0.71	3.26	0.64
(E)	74	18.15	2.92	1.11	0.58	0.55	1.69	0.79

The measurement results are given with the following markings and units in Table 2 and Table 3.
- Number of cells: Num (pc)
- Metallic surface area: MSA (%)
- Largest cell area (marked in yellow in Fig. 3): A_{LC} (mm^2)
- Maximum diameter of the circle in the largest cell (marked in red in Fig. 3.): D_{LCmax} (mm)
- Smallest cell area (marked in green in Fig. 3): A_{SC} (mm^2)
- Maximum diameter of the circle in the smallest cell (marked in red in Fig.3.): D_{SCmax} (mm)
- Average cell area: A_{AC} (mm^2)
- Deviation of cell area: σ_C (mm^2)

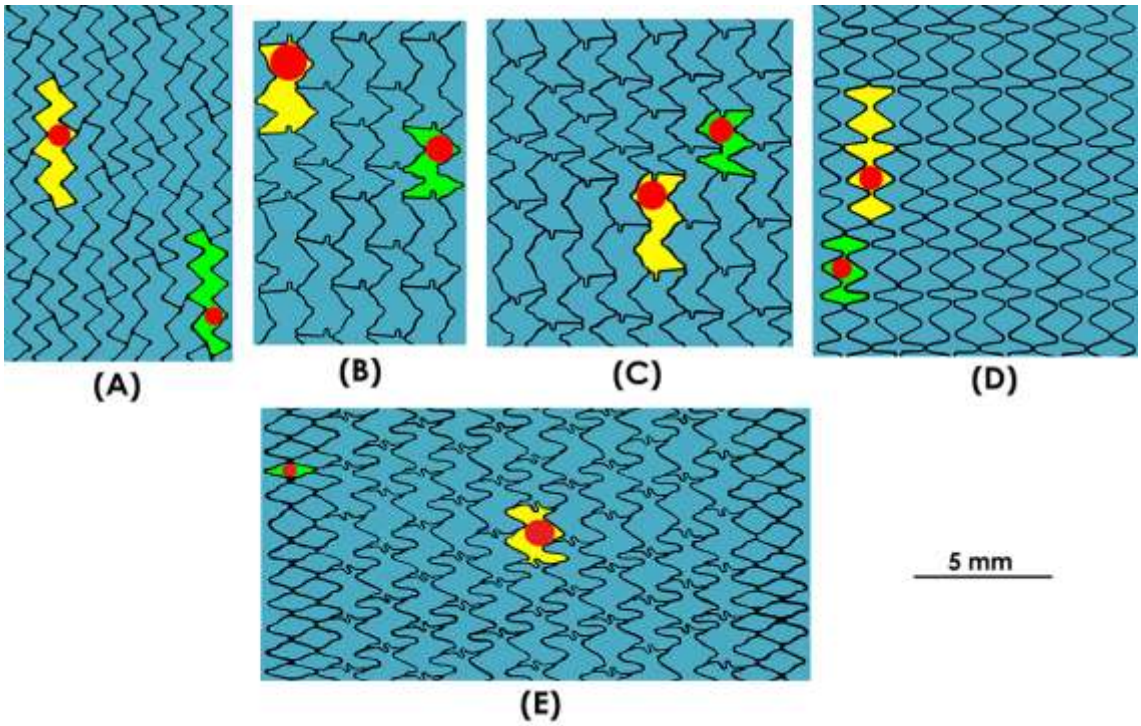

Figure 3 The evaluated images of the stents with the automatic method; The largest cells are yellow, the smallest cells are green, and the circles with the maximum achievable diameter are red.

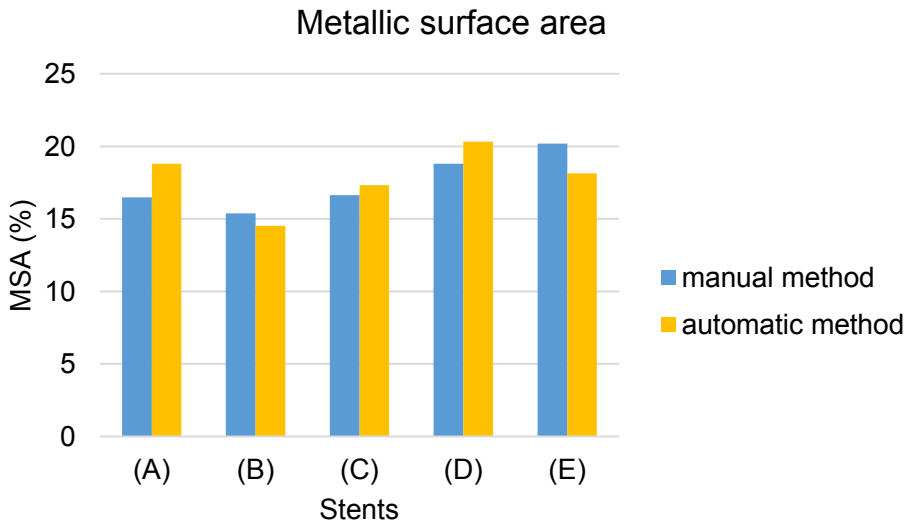

Figure 4 Metallic surface area values with the two methods.

Metallic surface area. MSA only depends on the stent pattern and the strut width. We can say that all the stents have MSA with medium coverage (15-20%). This is appropriate for the re-formation of the intima cell layer. Our findings showed that the first and the second methods gave similar results in MSA (Fig. 4). The maximum deviation is about 2 %.

Cell sizes. The location of the largest and smallest cells are the same with the manual and the automatic method, except in the case of (A) stent. Since the difference between the largest and the second largest cell was negligibly small, the error might be due to inappropriate joining of images. Because of the special pattern of (E) stent there are two types of cell in the pattern.

Stent pattern. The investigated stent patterns can be divided to 3 groups. (A) and (D) stent has homogeneous pattern, so the entire surface of the stent is made of nearly identical elements. (B) and (C) stent have repetitive cyclic pattern, so the rings are connected with bridges in the longitudinal direction of the stent. Most of the commercial stents have this kind of pattern. (E) stent has individual pattern, which includes both kind.

Comparing the methods. Though, the manual method to determine the MSA value of stents is reliable but the measurement takes long time. The automatic method needs less time (the difference is in hours), because the pictures did not need to be joined together. This is an important factor when the stent is too long to fit in the microscopic field. In that case separate images are taken of both ends of the stent, and then 48 images have to be joined up to create one big image (like in the case of (E) stent). Resulting errors are multiplied during image editing, and the needed time also increases.

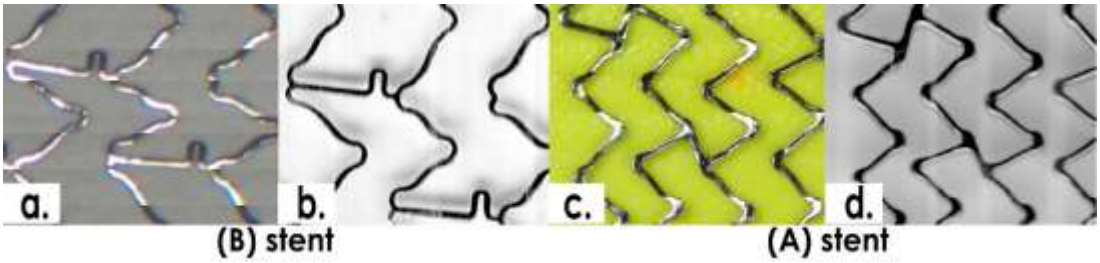

Figure 5 Image of (B) stent with a. manual, b. automatic method; image of (A) stent with c. manual, d. automatic method.

In addition, Figs. 5 a and c clearly shows that the struts reflect light in the microscope pictures of the metal stent surface. We used a Nikon SMZ-2T stereomicroscope to measure the stents except (A) stent, when an Olympus SZX16 stereomicroscope was used. The difference between the images can see in Figs. 5 a and c. The Olympus microscope is much better, but the reflections also appear here. Because of the reflections, bright and dark parts seem to have different strut widths which need to be corrected during evaluation. This takes more time and causes inaccuracy. In contrast, reflective glare is eliminated in the images taken by scanner (Figs. 5b and d). In case of external light source, the rotating shaft should be made of transparent material that guides the light to the stent. This solution eliminates the contour errors caused by shadows.

Summary

We used two methods to measure MSA values. These results favour the automatic method, which on the basis of this study seems to give the information about the MSA most accurately, in the shortest time. The collected experience and results of this study provide a basis for further research. We plan to use the obtained image data to create a three-dimensional stent models and run finite-element simulations to predict mechanical properties of stents with given defined patterns. Our plans also include investigating the reproducibility of the measurements with the automatic method. The actuality of the topic determined by the requirements of the development in modern medicine. The section of medical area, connected with stents, develops very fast. New geometries, materials and methods appear, so there is plenty to investigate in this field. The research and development of

the devices helping and supporting the function of the human organism are (beyond the innovation) evolutionary question for the society and the individual.

Acknowledgement

This work is connected to the scientific program of the " Development of quality-oriented and harmonized R+D+I strategy and functional model at BME" project. This project is supported by the New Hungary Development Plan (Project ID: TÁMOP-4.2.1/B-09/1/KMR-2010-0002).

References

[1] E.A. Ashley, J. Niebauer, Cardiology Explained, Chapter 5: Coronary artery disease, Remedica, London, 2004.

[2] M.J. Stampfer, F.B. Hu, J.E. Manson, E.B. Rimm, W.C. Willett Primary, Prevention of Coronary Heart Disease in Women through Diet and Lifestyle, The New England Journal of Medicine, 343 (2000) 16-22.

[3] Peter Lanzer, Mastering Endovascular Techniques: A Guide to Excellence. Lippincott Williams & Wilkins, 2007.

[4] Gy. Meszlényi, P. Nagy, Sz. Bella, J. Dobránszky, Laser beam cutting and welding of coronary stents, Welding & Material Testing, 14:2 (2008) 17-26.

[5] B. Katona, P. Nagy, E. Bognár, K. Hirschberg, Development of nitinol stents: etching experiments, Materials Science Forum, 729 (2013) 240-245.

[6] Á. Lengyel, P. Nagy, E. Bognár, K. Hirschberg, Development of nitinol stents: electropolishing experiments, Materials Science Forum, 729 (2013) 436-441.

[7] B. Katona, E. Bognár, B. Berta, P. Nagy, K. Hirschberg, Chemical etching of nitinol stents, Acta of Bioengineering and Biomechanics, 15:4 (2013) 2-8.

[8] MSZ EN ISO 25539-2: Cardiovascular implants. Endovascular devices. Part 2: Vascular stents. (ISO 25539-2:2013)

[9] Gy. Ring, E. Bognár, Zs. Bálint-Pataki, J. Dobránszky, Different properties of coronary stents, Anyagok világa, 7:2 (2007) 1-7.

[10] T. Takács, E. Bognár, J. Dobránszky, Az újraszűkülést befolyásoló műszaki paraméterek vizsgálata coronariastenteken, Lege Artis Mediciane, 20 (2010) 227-233.

[11] T. Balázs, E. Bognár, E. Zima, J. Dobránszky, Mechanical properties of coronary vein – in vitro evaluation of longitudinal and transversal samples, Biomechanica Hungarica 3:1 (2010) 24-32.

[12] H. Hara, M. Nakamura, J.C. Palmaz, R.S. Schwartz, Role of stent design and coatings on restenosis and thrombosis, Advanced Drug Delivery Reviews, 58 (2006) 377-386.

[13] A. Roguin, E. Grenadier, Stent-based percutaneous coronary interventions in small coronary arteries, Acute Card Care, 8:2 (2006) 70-74.

[14] Gy. Ring, E. Bognár, J. Dobránszky, J. Ginsztler, L. Major, Mechanical behaviours of coronary stents. Advances in Science and Technology, 49 (2006) 91-96.

Influence of internal leakage in hydraulic capsules on dynamic behavior of Hydraulic Gap Control system

Attila Kovari [a,b]

[a]ISD Dunaferr Co. Ltd., Directorate of Investment, Vasmű tér 1-3. Dunaujvaros, H-2400, Hungary

[b]College of Dunaujvaros, Institute of Informatics, Táncsics M. út 1/A, Dunaujvaros, H-2400, Hungary

[a]kovari.attila@isd-dunaferr.hu, [b]kovari@mail.duf.hu

Keywords: gauge control, AGC, hot rolling mill, hydraulic capsule, leakage.

Abstract. In hot rolling mills the plastic deformation of the strip is realized at high force and plastic strain speed controlled by electro-hydraulic servo actuators. These hydraulic servo actuators - hydraulic capsules – are capable to adjust the rolling gap at great rolling force dynamically. The dynamic behaviour of the rolling mill's AGC (automatic gap adjustment) system mainly depends on the correct operation of hydraulic actuators and servo valves. These equipments are great value, planned maintenance is essential for reliable correct operation. The maintenance includes the refurbish of damaged, worn surfaces inside the cylinder and replacement of worn out seals. In the study a laboratory hydraulic positioning system was used to examine the effect of hydraulic actuator internal leakage to dynamic behaviors of the positioning system. Because the laboratory test system is similar to the hydraulic gap adjustment system therefore the laboratory test results can be extended to the rolling mill's Hydraulic Gap Control system.

Introduction

Hot Strip Mill includes finishing mills, which reduce the thickness of the transfer bar down to the gauge required by the customer or the next process. Hot rolling is a hot metalworking process where large pieces of metal, such as slabs, are heated above their recrystallization temperature and then deformed between rollers to form thinner cross sections. In a hot rolling mill stand the slab is passed between a set of work rolls and this type of rolling permits large deformations of the metal to be achieved with some rolling cycles (Fig. 1). [1]

Hot rolling is primarily concerned with manipulating material shape and geometry rather than mechanical properties. This is achieved by heating the slab and then applying controlled load to adjust the gap between the work rolls which form the material to a desired size. Automatic Gauge Control (AGC) is a commonly used position control in modern strip rolling mills to adjust the gap between the work rolls. Nowadays hydraulic gap control (HGC) is relevant because of it good dynamic performance at high load (Fig. 2). With regard to the very high rolling forces present in the rolling mill stand, the fine-tuning of the roll gap can be precisely controlled by a hydraulic system.

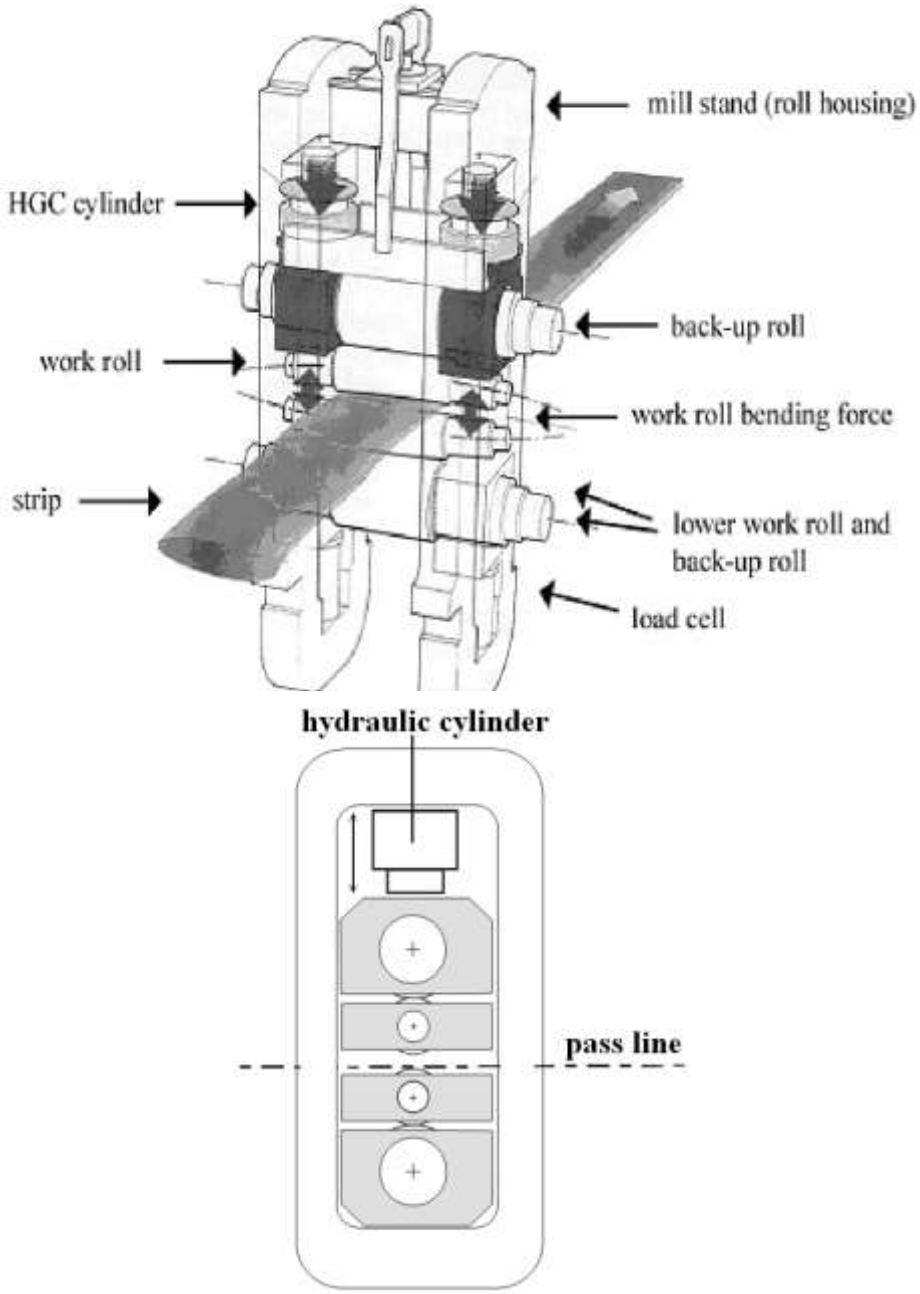

Fig. 1. Hot rolling mill stand [1]

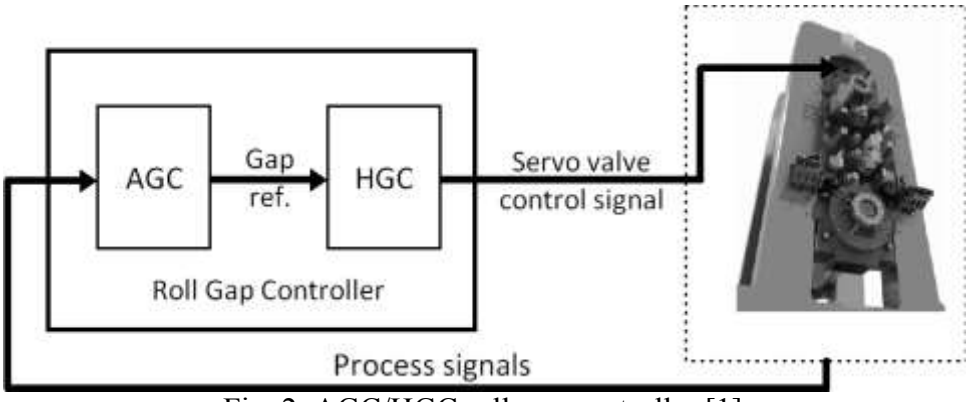

Fig. 2. AGC/HGC roll gap controller [1]

The hydraulic gap adjusting cylinders are located under bottom back-up roll chocks or on the top back-up roll chocks (Fig. 1). The load forces are directly controlled by a hydraulic gap controller (HGC) using HGC hydraulic cylinder/capsule driven by an electro-hydraulic servo system (Fig. 3).

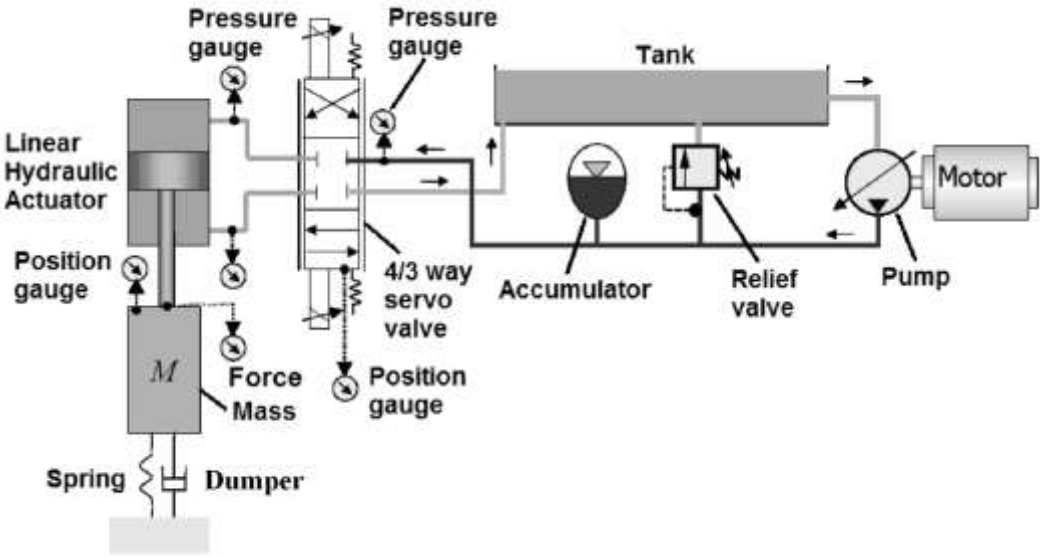

Fig. 3. Electro-hydraulic servo system [2]

Load Model of the Hydraulic Gap Control System

The mathematical model of the hot rolling mill stand is described in [1], [2]. The upper and lower rolls, bearings, work-roll and back-up-roll chocks, the strip, the mill stand and the adjustment system form a complex system of springs, dampers and masses [5, 6] (Fig. 4). The dynamic deformation model of this complex mechanical system can be determined using this model [1]:

$$F_{roll} = -M \cdot (a+g) + B_P \cdot v + K_S \cdot x + sign(v) \cdot F_f \tag{1}$$

where M is the total mass of the mill; g: gravity; F_f: frictional force; v: speed, a: acceleration and x: position of the piston, K_S: spring with stiffness coefficient; B_P: damping ratio.

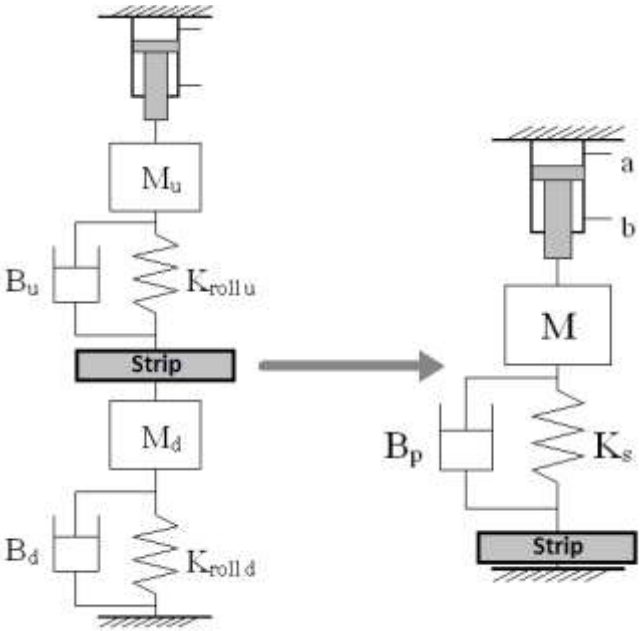

Fig. 4. Model of the hot rolling mill stand [2]

Sims' approximation [5,6] is applied to calculate the strip rolling force [2]:

$$F_{strip} = 2 \cdot k \cdot b_m \cdot l_d \cdot Q_P = \frac{2}{\sqrt{3}} \cdot Y_m \cdot b_m \cdot l_d \cdot Q_P \tag{2}$$

here b_m denotes the strip mean width, l_d is the contact arc length, Q_p is a complex function of the roll gap, Y_m is the plane strain yield strength of the strip. The strip rolling force can be approximated as a spring with spring coefficient Y_m.

According to Eq. 1. and Eq. 2. the load of the Hydraulic Gap Control system can be approximated as a mass-spring system with a small damping factor [2].

Laboratory Test System

A laboratory hydraulic positioning system at Obuda University Donat Banki Faculty of Mechanical and Safety Engineering (Fig. 5) was used to examine the effect of internal leakage to the dynamic behavior of the positioning.

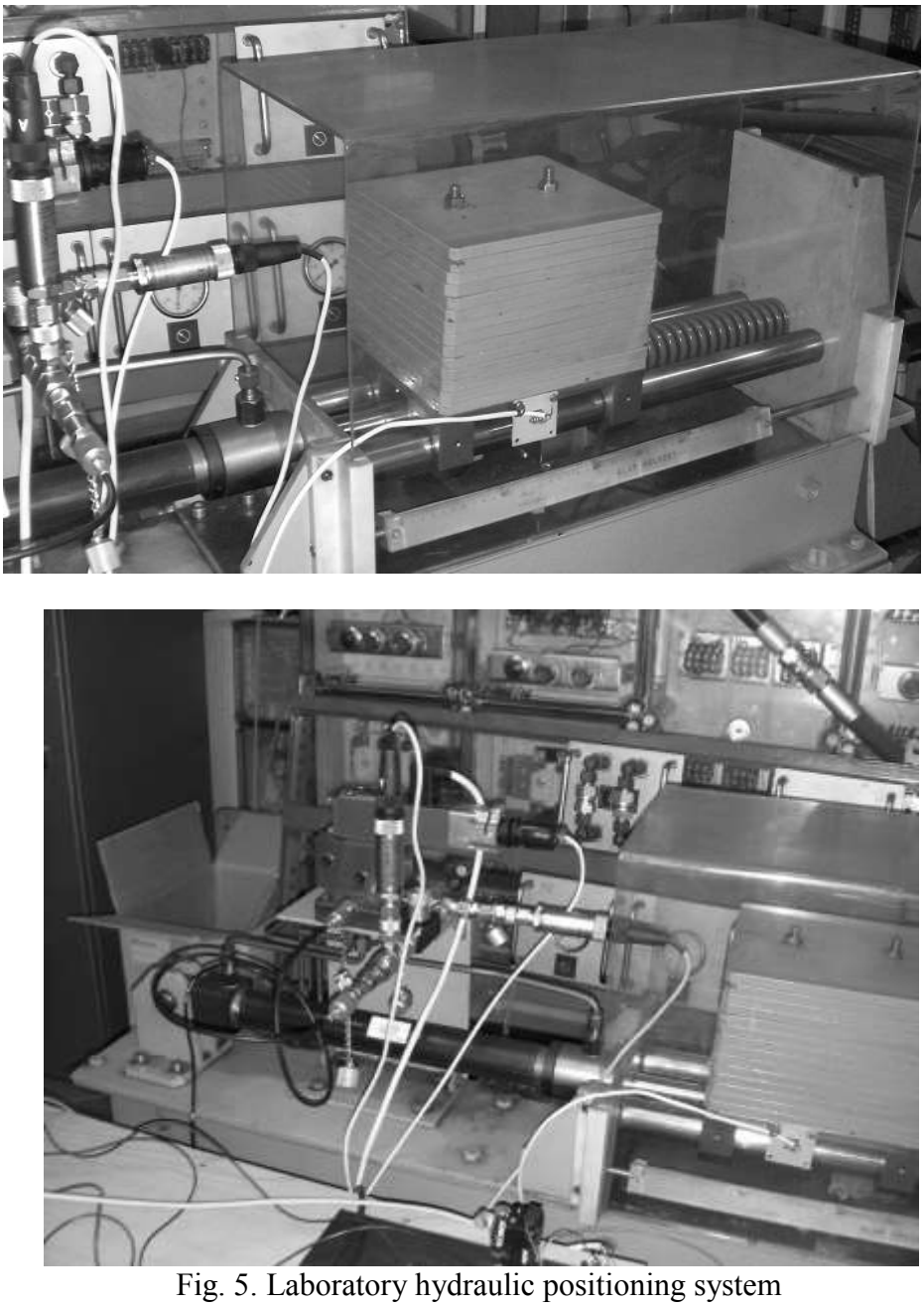

Fig. 5. Laboratory hydraulic positioning system

The hydraulic positioning system consists of an asymmetric hydraulic actuator, a proportional valve, and a mass-spring load. The internal leakage of the hydraulic actuator was simulated by a precision adjustable throttle connected parallel to the actuator (Fig. 6).

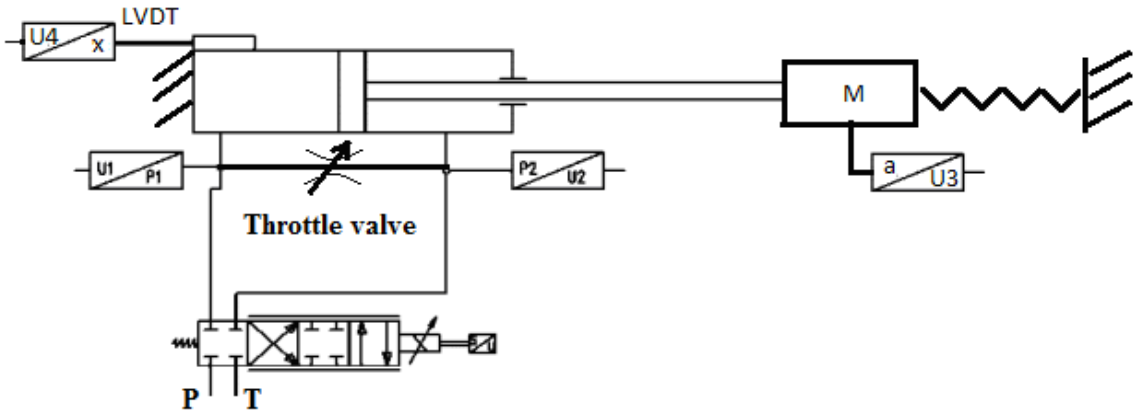

Fig. 6. Hydraulic positioning system

An accelerometer was used to measure the dynamic movements of the positioning system. Pressure transducers were used to examine the pressure change in the actuator chambers. The mechanical oscillations were examined at quick valve closing using the accelerometer signal with different throttle valve values, so in case of different hydraulic leakage resistance. The settling time, at ε_a=0,1 m/s^2 error band, was calculated and can be seen in Table 1 at different throttle values/internal hydraulic leakage resistance. [7]

Table 1.

Ri [10^{10} Ns/m^5]	Settling time [s]
>5	0,35
5	0,34
1,32	0,29
0,22	0,23

Correlation can be observed between the internal leakage resistance and damping ratio of position oscillation. It can be also observed that transient oscillation of the electro-hydraulic positioning system mainly depends on the hydraulic cylinder's internal leakage resistance.

Conclusion

According to the results, when the leakage resistance decreases - so consequently, the leakage flow increases - the settling time of the system is reduced. This impact refers to the increased dumping factor in the positioning system. When the damping factor of the hydraulic positioning system increasing the speed and dynamic behavior of the system will be degraded. This effect of leakage is similar to the Hydraulic Gap Control system where hydraulic capsules are used in Hot Rolling Mills. The wrong sealing or surface defects can decrease the internal leakage resistance and consequently the increasing internal leakage oil flow inside the hydraulic capsule. According to Table 1. the settling time and consequently the transient response of the gap adjustment system is decreasing when the internal leakage is increasing, so the dynamic behavior of the Hydraulic Gap Control system fails.

References

[1] A. Kovari, Dynamic Model of Rolling Mill's Electro-Hydraulic Gap Adjustment System, Materials Science Forum 659 (2010) 411-416.

[2] A. Kovari, D. Fodor, ARX model based Fault Detection of Rolling Mill's Automatic Gauge Control System, Proc. of 15th International Power Electronics and Motion Control Conference (2012) DS1d.6-1-DS1d.6-6.

[3] Meehan P.A., Edwards W.J., Wallace G.A., Modeling and Simulation of Vibration Phenomena in Rolling Mills, Proceedings of the 7th International Conference on Steel Rolling (1998) 166-172.

[4] Tlusty J., Chandra G., Critchley S., Paton D., Chatter in Cold Rolling, CIRP Annals - Manufacturing Technology 31 (1982) 195-199.

[5] Sims R. B., The calculation of roll force and torque in hot rolling mills, Proc. Institute of Mechanical Engineers 168 (1954) 191-200.

[6] Rudkins N., Evans P., Mathematical modelling of set-up in hot strip rolling of high strength steels, Journal of Material Processing Technology 80–81 (1998) 320 -324.

[7] A. Kovari, D. Fodor, Identification Based Leakage Detection of Hydraulic Capsules, Proc. of 14th IEEE International Symposium on Computational Intelligence and Informatics (2013) 419-422.

Real-Time Test Environment for Hydraulic Gap Adjustment System in Hot Rolling Mill

Attila Kovari [a,b]

[a]ISD Dunaferr Co. Ltd., Directorate of Investment, Vasmű tér 1-3. Dunaujvaros, H-2400, Hungary

[b]College of Dunaujvaros, Institute of Informatics, Táncsics M. út 1/A, Dunaujvaros, H-2400, Hungary

[a]kovari.attila@isd-dunaferr.hu, [b]kovari@mail.duf.hu

Keywords: hot rolling, hydraulic gap control, real-time, simulation.

Abstract. Hardware-in-the-Loop (HIL) test is an effective platform for developing and testing complex real-time systems and allows the engineer to examine units or equipments with greater test coverage compared to physical testing alone. Expensive and unique electro-hydraulic servo systems, which are applied in Hydraulic Gap Adjustment Systems in Hot Rolling Mills, are hard to test in different operating conditions, but a HIL test system can provide this examinations. In this paper a HIL test environment is presented which can be used to observe the dynamic behavior of the Hydraulic Gap Adjustment System.

Introduction

The hydraulic rolling gap adjustment system in a hot rolling mill stand is a complex and nonlinear system, which can be controlled or observed properly by complicated methods.
To develop for example a hydraulic control unit, or to examine the prototypes in a testing environment as close to reality as it can be is required in most cases. To carry out the necessary testing phases of these developments, the establishment of a real-time testing environment well approximated to the behavior of hot rolling mill roll stands would be of great help, where research with distinct parameters could be done and the real-time observation of ongoing changes would be ensured. Such a testing environment i.e. a system in which sub-elements are induced in one loop and to which their behavior is well approximated is called hardware-in-the-loop (HIL) system (Fig. 1). [1]

The advantages due to the HIL-based testing environments could be determined as follows:

- the real progress or its copy is not needed to do tests;
- the real system should be repeatedly operated several times during testing, which is very expensive and difficult; however, in a HIL-based testing environment, it would be simple and cost-efficient;
- injuries may happen in real progress, but not in the case of the HIL unit;
- automatic test runs could be easily done;
- states out of the operating range of the real system could also be tested;
- as a result of the previously mentioned facts, developing time and costs could be reduced.

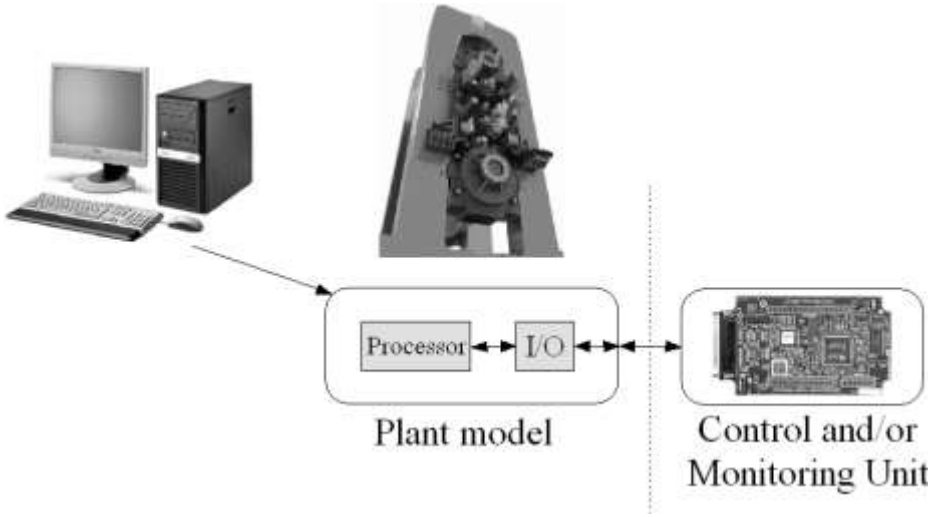

Fig. 1. Hardware-In-The-Loop System [1]

To be able to apply a PC in the HIL-based testing environment, i. e. to exchange it for a real unit, the followings are required:

- the HIL system should operate as the real system regarding its inputs and outputs;
- to receive and implement the signals of the real system, it should contain an analog/digital or digital/analog converter;
- it should also contain suitable computing power to compute with the determined sampling time of the mathematical model of the real system;
- a kernel ensuring real-time running.

Real-Time HIL Test Environment for Hydraulic Gap Adjustment System

By applying the complex mathematical model determined in [2, 3, 4], a well approximating to the behavior of the roll stand, parameterized, real-time testing environment could be established. In the mathematical model, the roll stand was taken into consideration as a mass-spring-damping vibratory system, while in the electro-hydraulic servo system apart from the exact description of the dynamic features, the effect of the inner leakage was also considered. The model of the roll stand and the electro-hydraulic servo system could be seen in Figure 2 and 3.

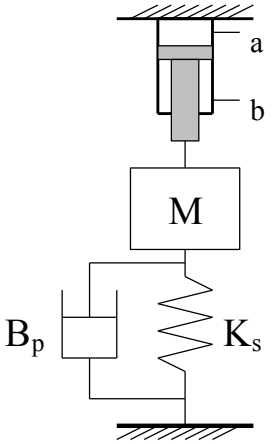

Fig. 2. Mechanical model of the rolling mill stand
(M: load mass, Ks: spring stiffness coefficient, Bp: damping ratio)

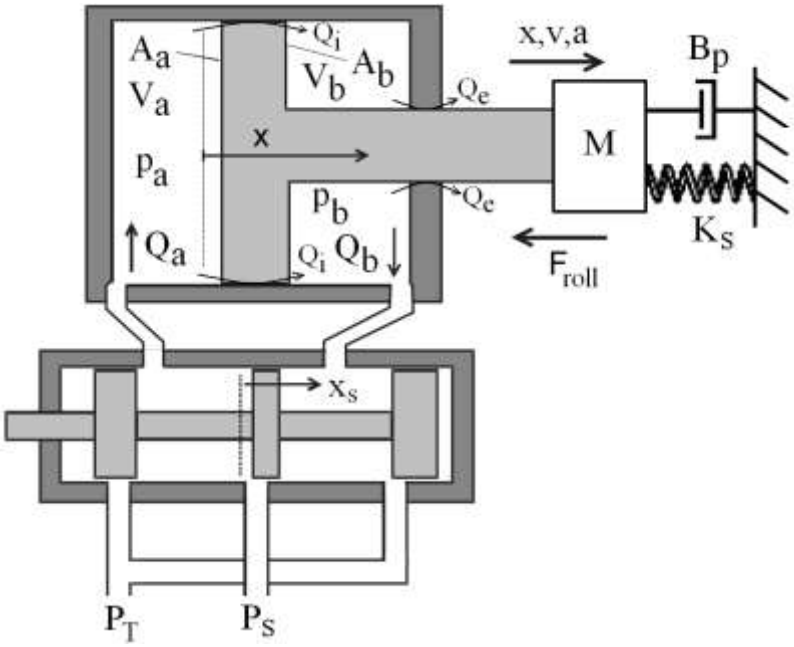

Fig. 3. Model of the electro-hydraulic servo system
(A_a, A_b: active area of the piston annulus, V_a, V_b: internal fluid volume, p_a, p_b: the load and return pressure, Q_a, Q_b: load and return oil flow, Qi, Qe: internal and external cylinder's leakage oil flow, P_S, P_T: supply and tank pressure)

To achieve our purpose, a PC containing a modern four-kernel processor, a PCI-6259 data acquisition card produced by National Instruments and the MATLAB xPC Target real-time software environment were used. A Target PC was used to simulate the mill stand together with the hydraulic gap control system in real-time and a Simulink based Host PC to program, supervise and manage the Target (Fig. 4.).

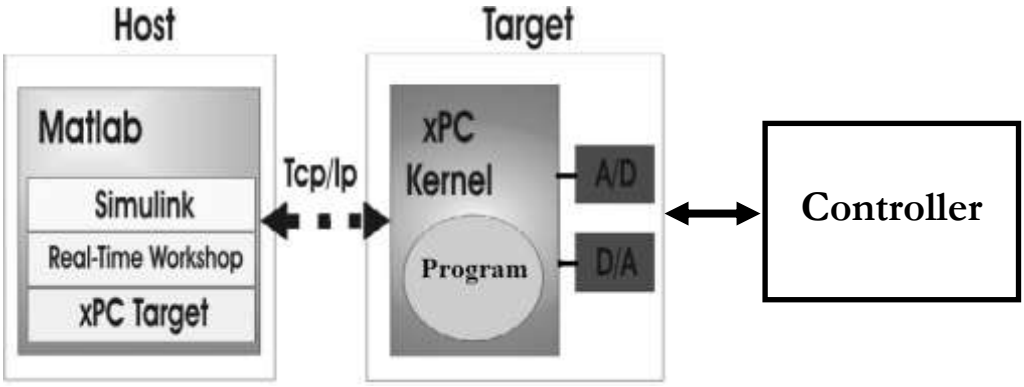

Fig. 4. MATLAB xPC Target

The code running on the xPC Target was prepared on the so-called Host PC using MATLAB. The computer running the xPC Target kernel, also called as Target PC, was connected to the Host PC on network. The data acquisition card was placed in the Target PC. The established system can be seen in Figure 5. The system is configurable, controllable and observable real-time by the Host PC easily. The modification of the parameters can be done simply and the save and post processing of the system signals can be easily carried out.

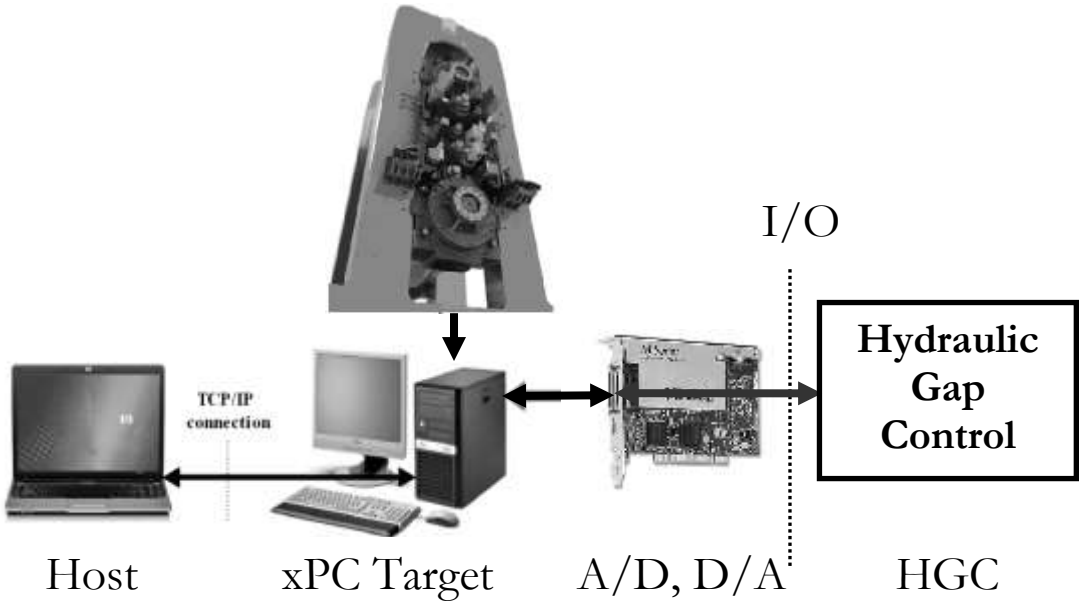

Fig. 5. HIL based test environment

In order to approximate the testing environment to the real system properly, besides a properly detailed mathematic model, the sampling time determining the period of time of calculation / computing should also be low. The oscillations of the hydraulic gap adjustment system are primarily determined by the mechanical oscillating system. The thickness-dependent counterforce explicated against the rolling power of the hot rolled band, the friction force as well as the subject of investigation in this dissertation, the internal leakage of the hydraulic capsule, have a dampening effect on the oscillations. In comparison to the frequency of the undamped mechanical oscillation, while considering the above-listed other dampening effects as well, the frequency of the occurring real oscillations will be lower, so the frequency of the undamped oscillation refers to the upper estimation of the frequency occurring in the real system. Based on the oscillating time of the mechanical undamped harmonic oscillating motion and the Shannon sampling thesis [5], in an M=80t moving mass, k_h=4,8•109 N/m spring constant system, the maximum sampling time T_{smax}, minimum sampling frequency f_{smin} magnitude, in case of enough samples:

$$T_{rezg} = 2 \cdot \pi \cdot \sqrt{\frac{M}{k_h}} = 0{,}0256s = 25{,}6ms\,,\ f_{rezg} = \frac{1}{T_{rezg}} = 39Hz \tag{1}$$

$$T_{s\max} = \frac{T_{rezg}}{2} = 12{,}8ms \tag{2}$$

$$f_{s\min} = \frac{1}{T_{\max}} = 78Hz \tag{3}$$

In engineering practice, considering the finite number of available samples, usually one magnitude higher sampling frequency should be chosen than the significant frequency components of the investigated signal, so in case of the investigated system, it should be 400-500 Hz.

HIL Test Results

Plant model runs on a PC using xPC Target real-time kernel and a laptop with MATLAB to generate the code from the mathematical model of the electro-hydraulic servo system. The PCI-6259 A/D card voltage input is used to control the servo valve and voltage outputs to examine the acting force and position/speed of the hydraulic cylinder.

The test execution time was 0.25s and step response was examined. Time functions of the electro-hydraulic gap adjustment system are shown in the next figure (Fig. 6).

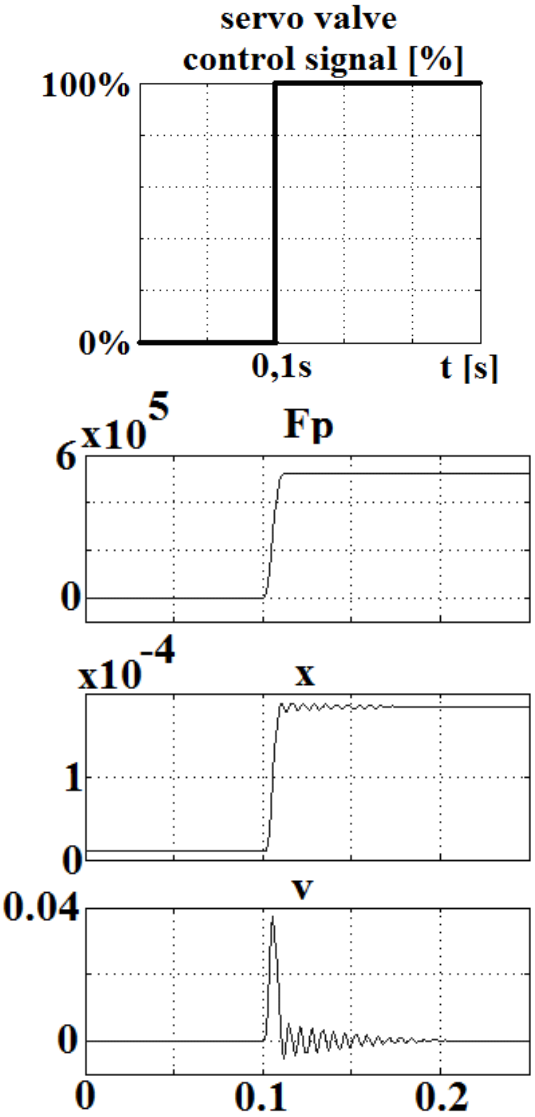

Fig. 5. HIL test results
(Fp [N]: acting force, x [m],v [m/s]: position and speed of hydraulic cylinder)

Conclusion

The presented HIL based real-time test environment can be used to examine Hydraulic Gap Adjustment System which is applied in Hot Rolling Mills to precisely control the roll gap. The developed test environment is an effective platform for developing and testing such complex units in real-time same conditions as the real physical system. The Hydraulic Gap Adjustment HIL test environment is suitable to observe the dynamic behavior and oscillations of the roll gap and hydraulic control system which information is very useful for further developments to improve the quality of the roll gap control and the hot rolled strip properties.

References

[1] A. Kővári, Real-Time HIL Closed Loop System of Rolling Mill's Electro-Hydraulic Gap Adjustment, Materials Science Forum 659 (2010) 417-422.

[2] A. Kovari, Dynamic Model of Rolling Mill's Electro-Hydraulic Gap Adjustment System, Materials Science Forum 659 (2010) 411-416.

[3] A. Kovari, D. Fodor, ARX model based Fault Detection of Rolling Mill's Automatic Gauge Control System, Proc. of 15th International Power Electronics and Motion Control Conference (2012) DS1d.6-1-DS1d.6-6.

[4] A. Kovari, D. Fodor, Identification Based Leakage Detection of Hydraulic Capsules, Proc. of 14th IEEE International Symposium on Computational Intelligence and Informatics, (2013) 419-422.

[5] Luka H. D., The origins of the sampling theorem, IEEE Communications Magazine 37, (1999) 106-108.

In-situ Al_3Nb formation in liquid Al by Nb particle addition

Sundaram Kumar[1,a], Sam Agarwal[2,b] and Keyna O'Reilly[3,c]

[1,2,3]Department of Materials, University of Oxford, Parks Road, Oxford, OX1 3PH, United Kingdom
and The EPSRC Centre for Innovative Manufacturing in Liquid Metal Engineering.

[a]kumar.sundaram@materials.ox.ac.uk, [b]samridh.agarwal@materials.ox.ac.uk,
[c]keyna.oreilly@materials.ox.ac.uk

Keywords: master alloy; Al-Nb; Al_3Nb; casting; microstructures; extraction; intermetallics.

Abstract. Master alloys are used in the metals industry to control chemical composition and to help to achieve a particular mi**c**rostructure or promote growth of desired phases. This study reports on making a Al_3Nb containing aluminium (Al) - niobium (Nb) master alloy by solid-liquid reaction processing, where solid Nb particles are added to the liquid Al. Nb react with Al to form in-situ Al_3Nb. The in-situ formed Al_3Nb particles were facet and polygonal in shape. The three dimensional analysis revealed that the outer surface of the partially reacted Nb was covered with faceted Al_3Nb particles. The different nature and morphologies of the in-situ phases that were produced were determined using SEM, EDX, XRD and extraction techniques. A mechanism for the observed microstructural difference is discussed.

Introduction

Al represents the second largest metals industry in the world today [1]. Sectors such as housing, aerospace and automotive are rapidly growing in developing countries because of the increased demand due to the increasing population, which is one of the driving forces for the supply need and growth of light-weight high-strength materials like Al [2]. The grain size of primary Al plays an important role in the final properties of the casting. It is common practice in industries to add grain refiner particles to the liquid metal in the form of a master alloy, in-order to get a sound product by having a fine microstructure and uniform chemical composition [3]. It has been observed that addition of peritectic elements such as titanium (Ti), vanadium (V), zirconium (Zr) and Nb, in the form of pure metal or master alloy, influences the formation of solidifying microstructure such as Al grains [4]. It has also been experimentally observed that pre-peritectic particles are observed in these peritectic alloys specifically when the addition level is above the maximum solid solublity in Al. Therefore it has been suggest that the grain refinemet in these peritectic element added alloys is due to the presence of pro-peritectic particles which acted as potent substrate to nucleat Al [4]. For the grain refiner master alloy to act as an effective dopant, the physical nature (shape, size morphology or number density) of the pre-existing phases in the master alloy play a key role in the microstructural development during casting [5]. The physical nature of pre-existing phases can be tailored during the master alloy production process [3,6]. However there is little literature available on the production of Al-Nb based master alloys with a defined physical nature of the pre-peritectic Al_3Nb particles for this purpose [7,8]. Therefore in this study, an attempt was made to produce Al_3Nb particle containing master alloys by a solid-liquid reaction process with the processing conditions being varied systematically in-order to understand the mechanism involved in the phase formation. The nature of the Al-Nb intermetallic particles that form during this casting process is investigated using two dimensional (2D) metallographic analysis and three dimensional (3D) morphological analysis. A phase extraction technique is used to facilitate observation of the 3D nature of the intermetallic particles by dissolving the Al matrix.

Experimental details

The Al-Nb master alloy with 5 wt.% Nb was prepared as a fresh batch each time. About 500 grams of commercially pure Al (CP Al) was melted in a boron nitride coated ceramic crucible using

a mini constrained rapid induction-melting furnace (mini-CRIM). The required amount of Nb powder was wrapped in Al foil and pre-heated to 250°C before adding into the melt. When the temperature of the liquid reached 750°C the wrapped niobium powder was added, after which the temperature of the melt was raised to 850°C and held for different holding times (5, 30 and 60 min). Throughout the experiment the melt was frequently stirred to reduce particle settling. The melt was then cast into a pre-heated (720°C) boron nitride coated TP1 mould. Once the melt was poured, the mould was subsequently lowered vertically in the retaining ring of the quench tank with water flow rate fixed at one gallon (3.8 litres) per minute. The samples were sectioned at 38 mm from the bottom for microstructural analysis. Intermetallic extraction apparatus (IEA) was used to extract the intermetallic particles from the cast samples. IEA uses anhydrous boiling butan-1-ol (butanol) to dissolve the Al matrix of the alloy while keeping the intermetallic phases intact. The intermetallics are then collected on a poly-tetrafluoroethene (PTFE) filter membrane (47 mm diameter, pore size of 0.2µm). The phases were identified using a Philips 1700 X-ray diffractometer (XRD) with Cu-K_α (λ=1.54Å) source at 35KV, 50 mA and 0.05° step size. Scanning electron microscopy (SEM) analysis was carried out on both the mounted and extracted samples using JEOL 840F and JEOL 840A SEMs. The initial Nb particle size was analysed using a Malvern Mastersizer 2000 particle size analyser attached with a large volume sample dispersion, Hydro 200MU, unit.

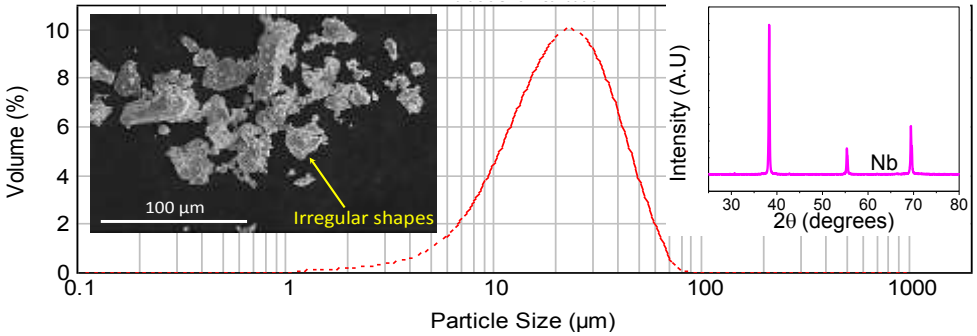

Fig. 1 The particles size distribution, SEM image and XRD pattern of Nb.

Results

The Nb particles which were used for this study (Fig. 1) had a wide particle size distribution with mean particle size of 25 µm. The particles had non-uniform shapes and morphologys.

Two dimensional analysis (2D)

The BSE-SEM 2D metallographic analysis (Fig. 2) of the master alloy revealed the presence of two different types of particles with different contrast: light-gray (A) and dark-gray (B). In all cases the light-gray particles were surrounded by a layer of dark-gray particles. The interface between the light and dark-gray particles was smooth when compared to the interface between the dark-gray particles and the Al matrix. In addition, there were dark-gray particles randomly distributed away from the light-gray particles. It is interesting to note that the size of these light-gray particles decreased with as increase in time melt holding. The EDS analysis of the metallographic samples revealed different ranges of Al:Nb ratio within these particles. Among these particles, the dark-gray particles were rich in Al and Nb and the light-gray particles had only Nb. This suggests that the light-gray particles were un-reacted Nb and the dark-particles were in-situ formed Al-Nb intermetallic phases which were the reaction product of Nb and liquid Al.

Three dimensional analysis (3D)

In-order to understand the 3D nature of these intermetallics it is essential to remove the Al matrix and analyse the extracted particles. It is very interesting to note that these extracted intermetallic particles were facet, polygonal (Fig. 3) and they were less than 7 µm in size, which

could not be ascertained from the 2D observations made of the metallographic samples. EDX analysis of the extracted samples confirmed that individual polygonal particles were rich in Al and Nb which suggests Al-Nb based intermetallics, but could not detect any un-reacted niobium. Interestingly, the EDS analysis on the 2D metallography samples showed un-reacted niobium surrounded by the Al-Nb based intermetallic reaction layer. This difference is because the extracted particles reveal only their outer surfaces which consist of Al-Nb based intermetallics fully encasing any residual Nb. On the other hand the 2D analysis helps by cross-sectioning the intermetallics, revealing the inner residual Nb. Therefore it is important to characterise the intermetallics using both metallography samples and extracted particles. Based on the 2D and 3D analyses, the following conclusions can be drawn, (a) the dark-gray particles seen in 2D around the un-reacted Nb particles were observed to be small, faceted, (Fig. 3a) pologinal particles in the 3D analysis and (b) the dark-gray particles seen separately in 2D were observed to be individual polygonal shaped particles in 3D. XRD analysis of the extracted particles revealed the presence of Al_3Nb phase. Based on the XRD and EDS analysis it is concluded that most of the pologonal particles were Al_3Nb. Inaddition, $Al_{13}Fe_4$, Al_6Fe and Nb traces were also observed (Fig. 4a). Presence of Fe bearing intermetallics are due to use of the CP Al (Al-0.14Fe-0.02Si) for this investigation. The large sized in-situ formed intermetallics were observed in the long holding time sample (Fig. 4b).

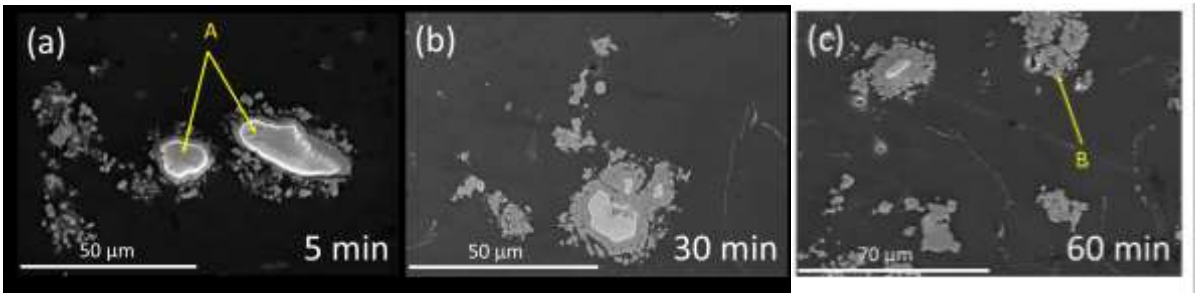

Fig. 2. Back scattered (BSE) SEM images of the samples held for (a) 5, (b) 30 and (c) 60 min.

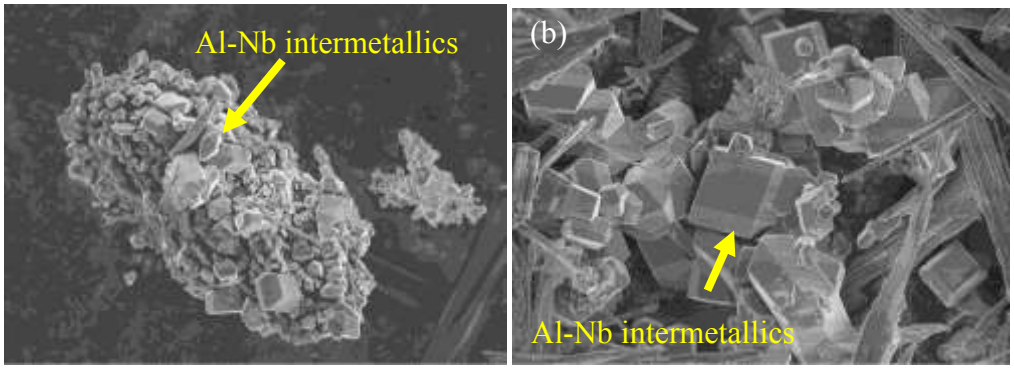

Fig. 3. SEM images of extracted particles, where (a) represents the reacted surface of a Nb particle, from the 5 min holding sample and (b) represents the in-situ formed Al-Nb based intermetallics particle from the 60 min holding sample.

Discussion

From present results it can be suggested that when Nb particle come in contact with liquid Al, the surface of the particle immediately undergo following reaction,

$$3Al_{liq} + Nb_{solid} \rightarrow Al_3Nb_{solid}. \quad (1)$$

The XRD analysis of the extracted particles confirms the presence of Al_3Nb. These in-situ formed Al_3Nb particles were fine and polygonal in shape (Fig. 3). The formation of Al_3Nb in the solid-liquid reaction process is mainly due to a diffusion controlled dissolution process [9]. It has been observed that the diffusion controls the dissolution process when most refractory metals

(including Nb) contact with liquid Al. This can be well described by the following Nernst-Shchukarev equation [9],

$$\ln \frac{C_s - C_o}{C_s - C} = k \frac{st}{v}. \quad (2)$$

where C is the concentration of dissolved (Nb) solute element in the melt, C_s is the saturation concentration of Nb in the melt, C_o is the initial concentration of Nb in the melt, k is the dissolution rate constant, s is the particle surface area, t is the time for dissolution and v is the melt volume. Equation (2) suggest that for a constant volume of Al melt (v), an increase in holding or reaction time (t) increases the Nb concentration (C) in the melt which inherently reduces the Nb dissolution rate (k). If the dissolution is by diffusion controlled transfer of atoms, then it is also influenced by melt stirring or agitation and melt temperature. It is important to note that the mini-CRIM used in this study induces forced convection, with similar effect to mechanical stirring, which might also contribute to an increase in dissolution rate by either dispersing the Nb particles or fragmentation of the intermediate layer. This can be explained using the relation below [9],

$$k = 0.554 I^{-1} D^{\frac{2}{3}} o^{\frac{-1}{6}} w^{\frac{1}{2}}. \quad (3)$$

where D is the diffusion co-efficient of Nb in the Al melt, o is the kinematic viscosity of the melt, w is the angular rotation speed of the Nb and I=f(Sc), where Sc is Schmidt number. Equation (3) suggests that increase in angular velocity of the Nb increase the diffusion coefficient which intern increase the dissolution rate. In this study Nb are added in the form of particles with wide size distribution which also contribute to the viscosity factor of the melt.

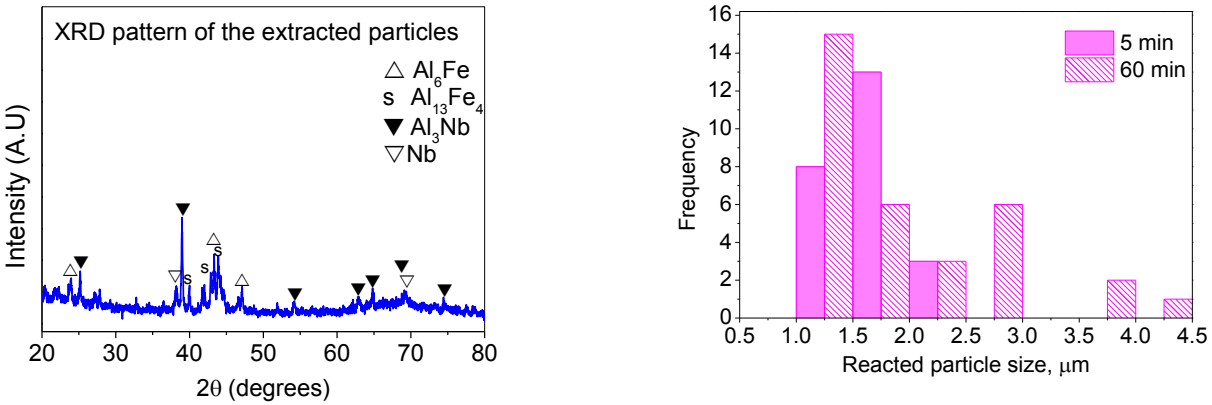

Fig 4. (a) XRD spectra of the extracted particles from 5 min holding sample and (b) intermetallic particle size distribution.

Fig. 5 describes the different stages of the proposed mechanism, from the time the Nb particles are added to the melt to the time it was cast. In this mechanism it is assumed that the Al melt is unsaturated with Nb solute at all studied times. Consider the time, t=0, when the Nb particles were added to the Al melt. At t=1, the Nb particles have reached the same temperature as the molten Al and the reaction starts to take place at the Nb/Al interface through a diffusion controlled dissolution process. At this initial stage dissolution of Nb in to the melt will be relatively rapid. Nucleation of fine polygonal intermetallic (Al_3Nb) particles occurs on the Nb particle surface (Fig. 3a) i.e. at the Nb/Al interfaces and coats the Nb particles, so ceasing the direct contact between solid Nb and liquid Al. According to the Al-Nb binary phase diagram, Al_3Nb should form at ~1300°C on cooling, but the observance of Al_3Nb at this lower temperature (850°C) in the present study is attributed to dissolution. Further dissolution of Nb is now controlled by the intermediate layer.
Further growth of this layer occurs predominantly on the Nb/Al_3Nb or Al_3Nb/Al interface depending on whether Al or Nb diffuses fastest through Al_3Nb. Al_3Nb has a DO_{22} crystallography

structure, as shown in Fig. 6, with Nb atoms surrounded by Al atoms. Ogurtani [10] and Slama et al [11] proposed that the growth of Al_3Nb is controlled by the diffusion of Al atoms.

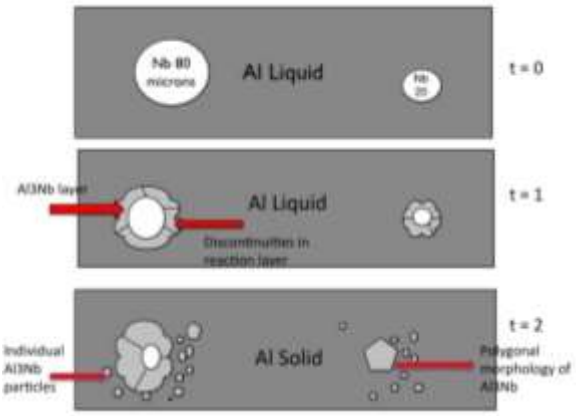

Fig. 5 Schematic illustration showing the formation of the Al_3Nb particles, where t is holding time.

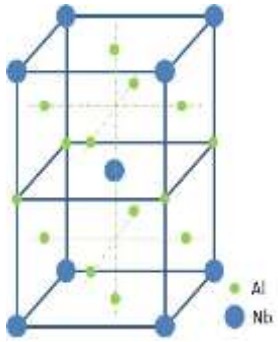

Fig 6. Al_3Nb unit cell (DO_{22})

This is because if the Nb atoms to diffuse, they have to exchange only with the Al vacancies as they are surrounded by Al. If this happens, then the symmetry of the Al_3Nb structure is destroyed. However for Al atoms to diffuse, they can easily replace the nearest neighbouring Al vacancy without disturbing the crystal structure (one third of Al neighbour are Nb atoms and two third are Al). In-addition, the activation energy required for the Al to diffuse into Al_3Nb (185.56 KJ/mol) is lower than that for the diffusion of Nb (427 KJ/mol) [12]. Thus the growth of the layer occurs predominantly by Al diffusing into the Al_3Nb layer. The thickness of the reaction layers was measured as 2.1, 4 and 4.8 μm for Nb particle holding times of 5, 30 and 60 minutes. The overall thickness of this layer is purely governed by the growth rate of the advancing layer front and dissolution of layer in contact with unsaturated melt. This can be expressed as [9,12]

$$\frac{dx}{dt} = \frac{k_2}{x} - \frac{\rho_l c_s k}{\rho_{imc}\varphi} exp\left(\frac{-kstc}{v}\right). \quad (4)$$

Where x is the thickness of the reaction layer, k_2 is the layer growth rate constant, ρ_l is the density of the liquid, ρ_{imc} is the density of the reaction compound, φ is the content of Nb in the reaction compound and c is a correction factor. On the right hand side of equation (4) the first term expresses the layer growth rate and the second term expresses the dissolution rate of the layer.

In Fig. 5, at t=2, small Nb particles have completely transformed into Al_3Nb (Fig. 3b) particles, but when there has been coarse sized Nb particles the reaction layer continues to grow until the layer starts to experience stress that make it rupture or completely transform. This stress can be due to changes in volume and/or thermal state. Niobium has a BCC crystal structure with a unit cell volume of 0.036 nm^3 and Al_3Nb which has a DO_{22} tetragonal crystal structure with a unit cell volume of 0.128 nm^3 [14]. The DO_{22} and BCC structure have 8 and 2 atoms per unit cell, respectively. Therefore a change in volume due to expansion due to the transformation could build-up stress that could cause rupture. In addition, the difference in molar volumes gives rise to stresses in the reaction layer when the ratio of the volume of reaction layer to the volume of the original Nb particle is not equal to 1 [7]. The thermal stress between the product and reaction layer can occur if there is a difference in coefficient of thermal linear expansion. Al_3Nb has 18% higher thermal expansion than Nb [13] hence peeling is possible. Thus these stresses induced cracks in the reaction layer leaving fine channels for further liquid Al to come in contact with residual Nb and the process continue till the residual Nb is consumed.

It is important to note that the formation of other Nb based intermetallics ($AlNb_2$ or $AlNb_3$) layer as observed in Al-Nb binary phase diagram between Nb and Al_3Nb are favourable if the Al melt is saturated with Nb or the saturated melt is completely consumed by the Al_3Nb [12].

Conclusions

The polygonal shaped in-situ formed Al_3Nb particles were produced using a solid-liquid reaction process. The dissolution of solid Nb is a diffusion controlled process. This method of adding Nb powder into the liquid metal can be used to produce Al-Nb master alloys and Al-Al_3Nb in-situ composites. The 3D analysis played a critical role in understanding the factors controlling the intermetallic phase formation and in particular the intermetallic morphology at the interfaces. While 2D sections showed systematic variations in intermetallic compound size and shape, they completely failed to reveal the true highly facet and clustered nature of the intermetallics at the interface observed in 3D.

Acknowledgement

The authors acknowledge the financial support of EPSRC and SAPA.

References

[1] G. Rombach, Raw material supply by aluminium recycling – Efficiency evaluation and long-term availability, Acta Mat., 61 (2013) 1012-1020.

[2] Information on http://www.aluminiumleader.com/en/serious/industry/ last assessed 26/01/2014.

[3] B.S. Murty, S.A. Kori, M. Chakraborty, Grain refinement of aluminium and its alloys by heterogeneous nucleation and alloying, Int. Mater. Rev. 18 (2002) 2–29.G.

[4] F. Wang, Z. Liu, D. Qiu, J.A. Taylor, M.A. Easton, M.X. Zhang, Revisiting the role of peritectics in grain refinement of Al alloys, Acta Mat. 61 (2013) 360–370.

[5] M.A. Easton, D.H. StJohn, An analysis of the relationship between grain size, solute content, and the potency and number density of nucleant particles, Metall Mater Trans A, 36A (2005), 1911-1920.

[6] K. Venkateswarlu, M. Chakraborty, B.S. Murty, Influence of thermo-mechanical processing of Al–5Ti–1B master alloy on its grain refining efficiency, Mater Sci Eng A, 364 (2004), 75–83.

[7] M.H. Robert, S.L. Filho, Investigations on the production of Al-NbAl3 composites, Mat. Sci. Forum, 217-222 (1996) 359-364.

[8] H.B. Nadendla, M. Nowak, WO2012110788 A2 (2013).

[9] V.N. Yeremenko, Y.V. Natanzon, V.I. Dybkov, Interaction of the refractory metals with liquid aluminium, J. Less Common Met., 50 (1976) 29-48.

[10] T. Ogurtani, Kinetics of Duffusion in the Nb-Al System, Metall. Trans., 3 (1972) 42-425.

[11] G. Slama, A. Vignes, Diffusion dans les aluminiures de niobium, J. Less-Common Metals, 29 (1972), 189-2012.

[12] N. Tunca, R.W. Smith, Intermetallic Compound layer Growth at the Interface of Solid Refractory Metals Molybdenum and Niobium with Molten Al, Metall. Trans. A, 20 (1989) 825-835.

[13] A. Robin, H.R. Sandim, Degradation behavior of niobium in molten aluminium, Int. J. Refractory Met. and Hard Mat., 20 (2002) 221-225.

[14] JCPDS file 13-146 and 35-789, International Center for diffraction data, Powder diffraction file, 2008.

Effect of equal channel angular pressing on different face center cubic (FCC) metals

Gábor Ladányi[1, a], Judit Pázmán[1,b] and Balázs Verő[1,c]

[1]College of Dunaújváros, 2400, Dunaújváros, Táncics M. u. 1/a., HUNGARY

[a]ladanyi@mail.duf.hu, [b]pazman@mail.duf.hu, [c]verob@mail.duf.hu

Keywords: FCC metals, Severe Plastic Deformation (SPD), macroscopic materialparameters.

Abstract. Equal channel angle pressing (ECAP) of commercial purity aluminum (1050), oxygen free high conductivity copper (OFHC Cu) and high purity tin (99,99% Sn) were conducted using C processing route. The variation of microstructure, of micro-Vickers hardness and of macroscopic material parameters with number of pressings was documented up to ten passes. Tensile tests were used to evaluate post ECAP deformation response. Optical microscope was used to obtain statistical information on the microstructure developed during ECAP. The present results showed that, as it can be found in the literature, first ECAP pass has resulted in enhancement of mechanical properties. Further ECAP processing, as original observation, has resulted in slight improvement and after ~7 pressing decreasing of hardness can be observed. The true stress–strain curve for ECAP-ed specimens tested under tension showed the evolution of macroscopic material properties is similar. This behavior can be connected with the deformation microstructure of the specimen, grain deformation and fragmentation.

Introduction

Severe plastic deformation (SPD) procedures are well known methods to procedure bulk ultrafine-grained metals. During last decade several severe plastic deformation (SPD) technologies were investigated. The most relevant of them produce large deformation without volumetric strains. This requirement is satisfied in methods, where plastic deformation is induced by shear stress. The most popular similar methods are the High Pressure Torsion (HPT), Equal Channel Angular Extrusion (ECAE), or recently 3D deformation, Accumulative Roll Bonding, Constrained Groove Pressing, Repetitive Corrugation and Straightening, Twist Extrusion (TE) and Multiaxial Forging (MF).

To predict the effect and quality of produced ultrafine grained metals understanding the mechanism of SPD methods is necessary. One of the best developed and wide spread SPD process is the equal channel angular pressing (ECAP) method [1]. During the ECAP process the cross section of the deformed specimen is unchanged, consequently the process can be repeated. Multiple processes can be used to refine the grain size and mechanical properties. With appropriate configuration the homogeneity of the specimen can be guaranteed [2].

The ECAP die consists of two channels equal in cross section, intersecting at an angle ϕ that is a subject of research in ECAP, usually ranging from 90° to 157°, and taking the higher side for hard materials. Researches pointed out, lower angle leads higher deformation force and more intense shear effect on the specimen. There is also an additional angle Ψ, which defines the arc of curvature at the outer point of intersection of the two channels, and also it has been a subject of research. It is believed that during ECAP, only simple shear is introduced into the specimen [3].

The value of the two angles, ϕ and Ψ, determine the equivalent strain in specimen after n number of pressing:

$$\varepsilon = \frac{n}{\sqrt{3}} \cdot \left[2 \cdot cot\left(\frac{\phi}{2} + \frac{\psi}{2}\right) + \psi \cdot cosec\left(\frac{\phi}{2} + \frac{\psi}{2}\right) \right] \quad (1)$$

Most homogeny material properties can be reached using B_C route pressing. Using C route, the end angle of specimen increases in each pressing step. C route is more practical, because on this way the end angle stay lower than 45°.

The present work focuses on processing 1050 commercial purity aluminum, oxygen free high conductivity copper (OFHC Cu) and high purity tin (99,99% Sn) by ECAP through the C and document the enhancement of the mechanical properties and provide an interpretation of results through microstructural investigation using optical microscope.

Experimental procedures

The ECAP die was manufactured with angles $\psi = 90°$ and $\phi = 90°$, see on Fig 1. Using equation (1) the equivalent strain in our work is $\varepsilon \approx 0.9069$. Type C route was adopted in present work which means samples were rotated 180° between subsequent pressings. Forming speed and temperature were $v = \sim 0.5\ mm/s$, $T = 25℃$. Three type of materials were used in this study, commercial 99.5% purity aluminum (Al1050), oxygen free high conductivity copper (OFHC Cu) and high purity tin (99,99% Sn).

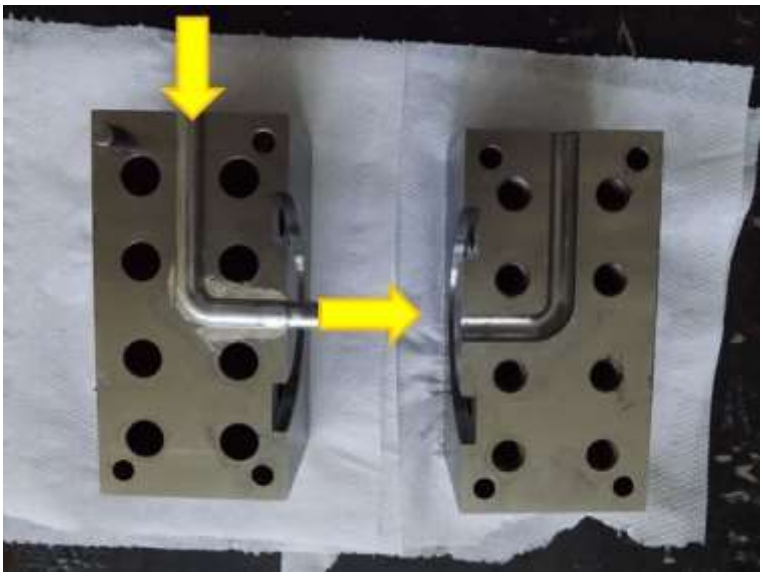

1. Figure 8mm diameter ECAP die used in 50kN hydraulic press

All the materials were supplied as cold rolled plates of $10mm$ thickness. Cylindrical samples of $8mm$ diameter and $55mm$ in length were machined parallel to the rolling direction. Al1050 and copper test specimens were heat treated, homogenized and softened on $T_{Al1050} = 450℃$ for $1hour$ and $T_{Cu} = 450℃$ for $3hour$, respectively.

The micro-Vickers hardness (HV0.2/10) was measured using Ernst Computest SC Vickers machine. Hardness samples were cut at the middle plane of the ECAP specimen (and the middle plane of the die). Five tests were measured along the length of each specimen. Average and variance of the hardness were calculated.

Testing mechanical properties micro-tensile specimens were machined in direction of the ECAP body. The draft of the test specimen is shown on Fig. 2. Instron 3366 type tensile test machine was used. Test speed and temperature were $v = 1\ mm/min$ and $T = 25℃$, respectively.

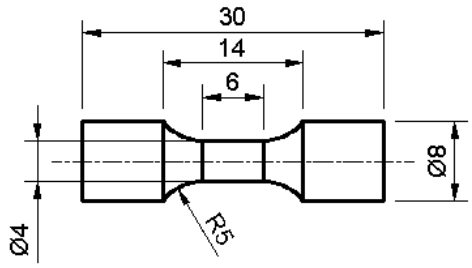

2. Figure Draft of micro-tensile specimen

Length and cross section of the specimen were observed in optical microscope (Zeiss Axiovert 40 Mat). Section samples were polished and prepared with appropriate chemical liquid. To sense the grain size and orientation $50x$ and $1000x$ magnification were used with CDIC image correction process.

Results and discussion

Fig. 3 depicts different situations during a single pass in an equal channel angle die, the upper sample shows a status where it is just entering the outlet channel, the middle sample shows the state where the sample is about to go completely in the outlet channel. The third sample shows the state when it is completely pushed out of the outlet channel. Also shown is the fixed ECAP die axes system xyz, whose axes coincide with the ED (extrusion), ND (vertical) and TD (transverse) directions. The billet deforms by simple shear along the x′ direction on the channel intersection plane. In addition, the simple shear reference axes x′y′z′ are indicated.

Microstructure. Aqusition of data in optical microscope images could be done only on OFHC Cu specimens. Fig. 3 shows the $50x$ and $1000x$ magnitude images made in half plane parallel with the extrusion direction of the specimens. The average grain size was too small to measure with optical microscopy, but trends of the grain deformation and orientation are well observable on the pictures.

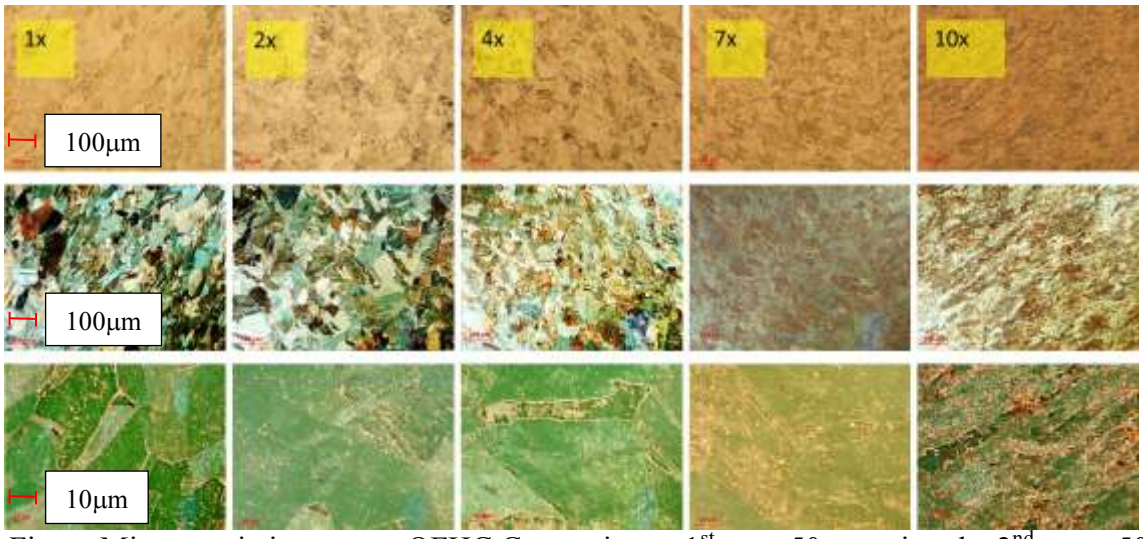

3. Figure Microscopic images on OFHC Cu specimen: 1st row: 50x magintude, 2nd row: 50x magnitude/CDIC, 3rd row: 1000x magnitude/CDIC

In Fig. 3 one can observe, increasing number of ECAP extrusions the orientation of the grains rotate into the direction of shear (x′). Above seven extrusions the grain size decreases and grains seem to be broken. Sharpness of the grain boundaries decreases with increasing pressing number. It refers the increasing diffusivity of the grain system.

Tensile characteristics. Using micro-tensile specimen the true stress-true strain relationship were determined on ECAP specimens. In Fig. 4 the tensile diagrams of Al1050 test specimens are shown after 1X, 4X and 10X ECAP pressing.

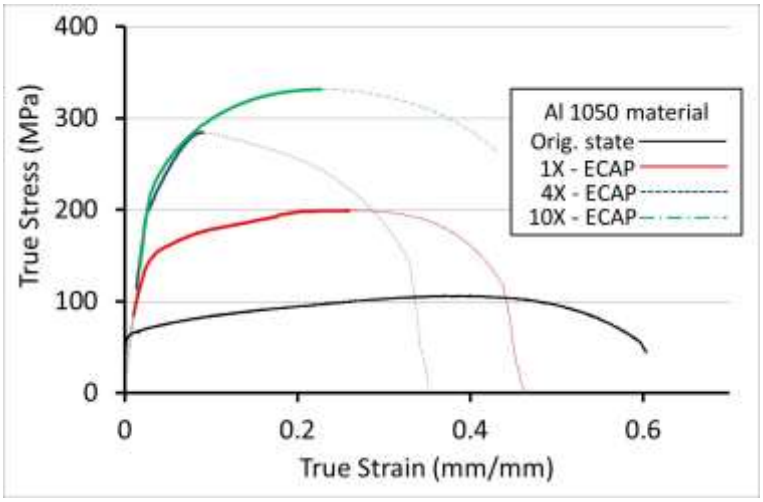

4. Figure Stress-strain curve of Al1050 test specimens after 1X, 4X and 10X ECAP pressing.

By Holomon relationship the conventional power-law of large plastic deformation is

$$\sigma = \sigma_0 + K \cdot \varepsilon^n \quad (1)$$

where σ_0, K and n are fitting parameters, yield stress, strength coefficient and strain hardening exponent, respectively. These parameters can be dependent of microstructural parameters of different dislocations [5].

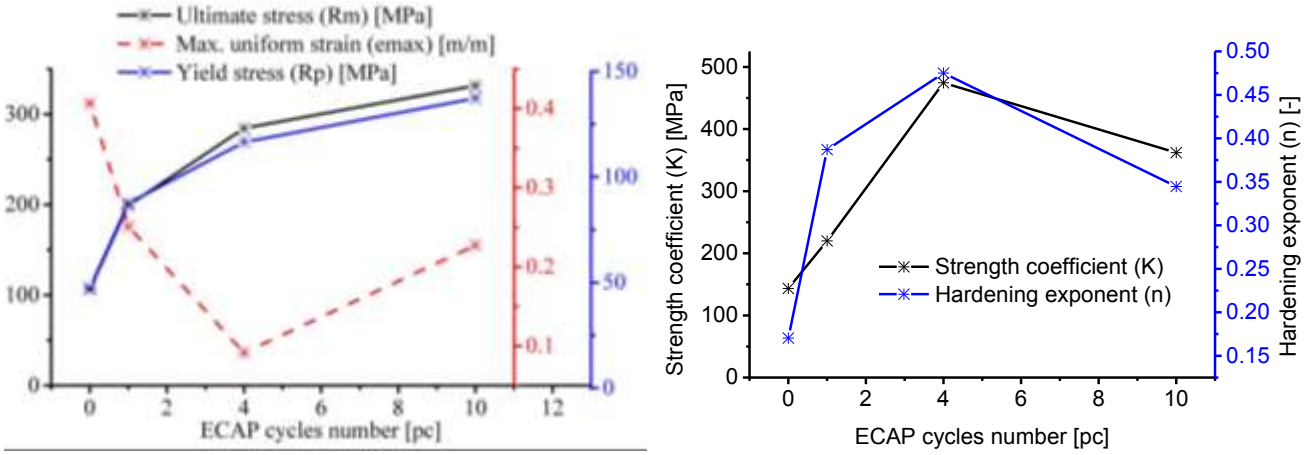

5. Figure Effect of ECAP forming on a.) Ultimate stress, Maximum uniform strain and. Yield stress, b.) Strength coefficient (K) and Hardening exponent (n)

In case of above Al1050 material specimens the macroscopic parameters were determined with least square method. Observing Fig.5 and Fig.6 one can consider the dependency of material parameters and number of ECAP cycles. Similar behavior of yield stress (σ_0), ultimate stress (R_m) and maximal uniform elongation (ε_{max}) can be found in the literature [5], [6].

Similar results were found in case of OFHC Cu and HP Sn materials. In each case, above seven times ECAP forming the strength coefficient (K) and strain hardening exponent (n) starts to decrease.

1. Table Macroscopic parameters of ECAP pressed Al1050 specimens

Number of ECAP pressing	Ultimate stress $R_m[MPa]$	Max. Uniform Elongation $[mm/mm]$	Yield stress $\sigma_0[MPa]$	Strength coeff. $K[MPa]$	Strain hardening exp. $n[-]$
Original state	106.5	0.4064	47.37	143.45	0.1704
1	199.3	0.2511	87.53	219.99	0.3871
4	284.4	0.0913	116.55	474.47	0.4750
10	331.6	0.2271	137.33	361.90	0.3446

Micro-Vicker hardness. The variation of Vickers hardness with the number of pressings, up to ten passes, using route C and shown in Fig. 7. Hardness measurements were taken in the half of the sample on a plane parallel with the extrusion direction. Hardness values on both planes were very much comparable. The reported hardness values are the average of 5 readings, and the variations were within ±5% of the average value. Micro-Vicker hardness of the observed materials can be seen in Fig. 5 as function of pressing number. Hardness of the Al1050 material increases with the number of ECAP forming and after seven pressing seems to be saturated. The hardness of the OFHC Cu material increases until fourth pressing in ECAP die. Higher number of pressing caused decreasing in hardness. Similar to this, the hardness of the HP Sn material increases until fourth pressing in ECAP die. Higher number of pressing caused decreasing in hardness.

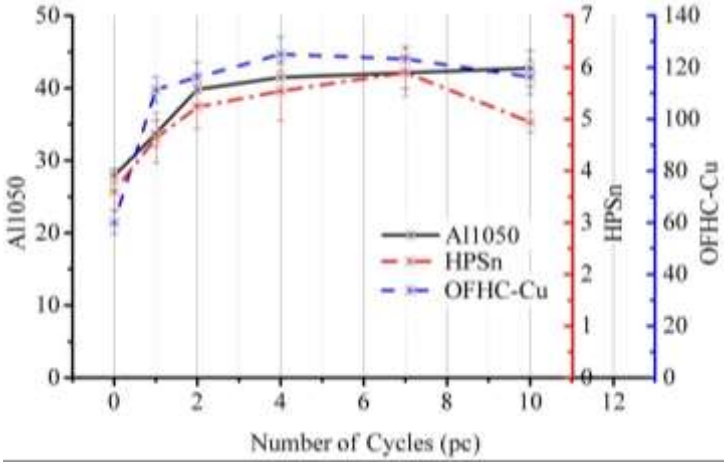

6. Figure Micro-Vicker hardness of different material as function of pressing number

Summary

In recent study effect of equal channel angular pressing (ECAP) process was observed on three different materials: Al1050 commercial aluminium, oxygene free high conductivity copper (OFHC Cu) and high purity tin (Sn 99.99%). ECAP process was applied circular test specimen 1, 2, 4, 7 and 10 times in C route configuration.

Tensile test, micro-Viskers hardness and optical microscopy were used to observe the extruded specimens. Summary our results:

- In the observed FCC metal specimens the severe plastic deformation process caused increasing hardness. As new observation, above four time passes in ECAP die, this trend returned back and the hardness started to decrease. The highest increases of HV/0.2 were 53%, 109% and 64% in Al1050, OFCH Cu and Sn samples, respectively.
- The pressing force, micro-Vickers hardness and the diffusivity of grain boundaries are strongly correlated. The shattering of grains led decreasing of the mechanical properties.
- Macroscopic material parameters of tested specimens are correlated to equivalent strain after ECAP pressing. Results are similar to former documented parameters in the literature. Similar to micro-Vickers hardness, as new result, after beginning increase they saturate and above 7 times pressing decreasing of them could be observed.

- Similar tests are planned using body centered cubic (BCC) and hexagonal close packed (HCP) structure materials.
- It seems to be interesting to test effect of other severe plastic deformations. Application of Twist extrusion (TE) and Simple Shear Extrusion (SSE) processes are under introducing on our product floor.

Acknowledgements

The work/publication is supported by the TÁMOP-4.2.2.A-11/1/KONV-2012-0027 project. The project is co-financed by the European Union and the European Social Fund.

References

Reference an article:

[1] R. Z. Valiev, T. G. Langdon, Principles of equal-channel amgular pressing as a processing tool for grain refinement, Progress in Materials Science 51 (2006) 881-981.

[2] P. Sun, P. Kao, C. Chang, Effect of deformation route on microstructural development in aluminum processed by equal channel angular extrusion. Metall. Trans. A 35 (2004) 1359–1368.

[3] M.A. Meyers, A. Mishra, D.J. Benson, Mechanical properties of nanocrystalline materials, Progress in Materials Science 51 (2006) 427–556.

[4] T. Csanádi,, N. Q. Chinh, J. Gubicza, T. G. Langdon, Plastic behavior of fcc metals over a wide range of strain: Macroscopic and microscopic descriptions and their relationship, Acta Materialia 59 (2011) 2385-2391.

[5] E.A. El-Danaf, M.S. Soliman, A.A. Almajid, M.M. El-Rayes, Enhancement of mechanical properties and grain size refinement of commercial purity aluminum 1050 processed by ECAP, Materials Science and Engineering A 458 (2007) 226–234.

[6] Mahmoud S. S, Ehab A., El-Danafa A., Abdulhakim A., Effect of Equal-Channel Angular Pressing Process on Properties of 1050 Al Alloy, Materials and Manufacturing Processes Vol.27, Issue 7, (2011) 746-750.

Influence of sintering time on properties of alumina-based ceramic composite

Dóra Lipusz[1,a], Ákos Isztli[2,b] and László A. Gömze[1,c]

[1] Department of Ceramic and Silicate Engineering, University of Miskolc, Hungary

[2] Kerox Ltd. Diósd, Hungary

[a] lipuszdora@gmail.com , [b]isztliakos@gmail.com, [c]femgomze@uni-miskolc.hu

Keywords: Alumina based ceramic, sintering time, properties, microstructure

Abstract. The authors have investigated the influence of sintering time at 1600 °C on microstructure, shrinkage, density, surface hardness and bending strength of Al_2O_3 based ceramic composites. From the ceramic powder mixes, the specimens were compacted by uniaxial pressing and during sintering the heating gradient was 100 °C/h. The experiments have shown that at 1600°C of sintering temperature, the specimen densifications have almost finished within 5 hours, meanwhile the crystal grows processes were continued for up to 9 hours of sintering. The authors have found that the maximum values of hardness and mechanical bending strength of specimens were obtained at 5 hours of sintering and these values have slowly decreased with increasing the sintering times.

Introduction

The most of single lever water tap ceramic cartridges in Europe are produced from aluminium-oxide atomizer powders [1, 2]. These ceramic powders are mixes of different oxides (Table 1.) having different values of elastic modulus. In this hetero-modulus powder composite system, the content of Al_2O_3 was about 94% and the volume of SiO_2 was approximately 4%. The components of this ceramic powder mix have different values of melting point and elastic modulus as it is shown in Fig. 1.

Table 1. Component of Martinswerk KMS-94

Component	w/w%
Al_2O_3	~ 94
CaO	~ 0,3
Na_2O	< 0,1
SiO_2	~ 4
Fe_2O_3	< 0,1
MgO	~ 1

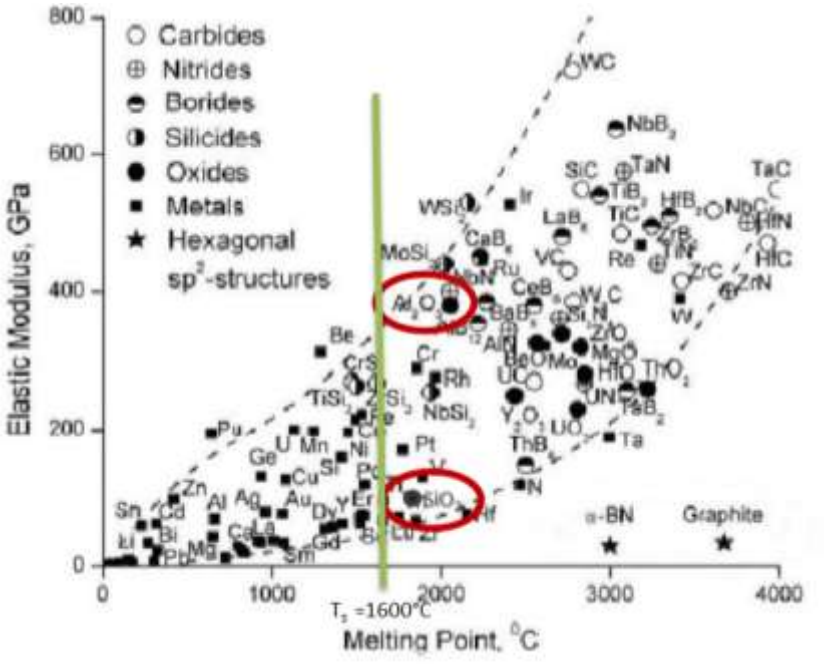

Figure 1. Melting points and elastic modulus of advanced technical materials [3]

In Fig. 1, it can be seen clearly that the T_s=1600°C sintering temperature is much lower than the melting point of Al_2O_3, SiO_2, MgO, and CaO components. In spite of the fact that Na_2O (<0,1%) and Fe_2O_3 (<0,1%) have lower melting temperature, the most of phase transformations have occurred in solid-phase stage during sintering of this kind of ceramic composites at 1600°C. The properties of alumina-based hetero-modulus material systems [4-6] created at this temperature depend on the occurrences of the heat treatment times [7-10]. Therefore, the aim of this research work is the examination of microstructure, shrinkage, density, surface hardness, bending strength of alumina based hetero-modulus ceramic composites depending on the occurrences of sintering times at 1600°C.

Materials and experiments

In this research work, aluminium-oxide spray dried powder was used for ceramic disc specimens. This powder is the same alumina powder from which the single-lever water tap ceramic cartridges are produced. The oxide-content of this ceramic powder mix is described in Table 1. To do this research work, 1200 pieces of ceramic disc specimens were compacted by bilateral uniaxial pressing at pressure values of 400 MPa. During sintering, the heating gradient was 100°C/h up to 1600°C in a laboratory chamber kiln. At this temperature, the sintering times were 0, 1, 3, 5, 7 and 9 hours and 200 pieces of ceramic discs were sintered in each case. The sintering time means, that we held the maximum 1600 °C temperature for the defined hours. Thus the 0 hour means that the cooling started immediately after the heating curve. After sintering the geometrical sizes (shrinkage), densities, hardness, and mechanical bending strengths of the specimens were measured and determined.

Results and discussions

To determine the sintering shrinkage, 20-20 pieces of specimens were selected randomly by each sintering time. The average shrinkage in diameters at different sintering times (Fig. 2.) were determined as follows:

$$S_d = \frac{\sum_{i=1}^{20} \frac{D_{g_i} - D_{s_i}}{D_{g_i}}}{20} * 100 \ [\%] \qquad (1)$$

Where:
S_d: the average shrinkage in diameter [%]
D_{gi}: the diameter of the i-th green specimen [mm]
D_{si}: the diameter of the i-th sintered specimen [mm]

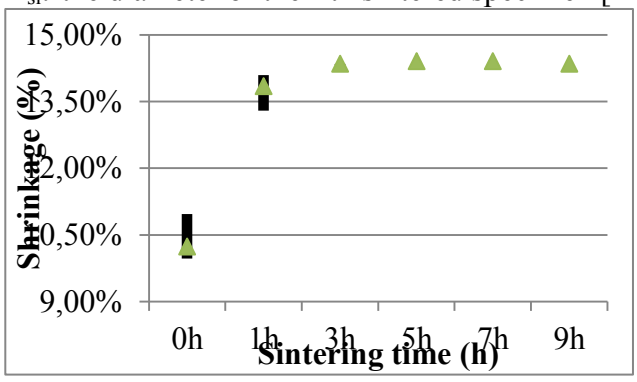

Figure 2. Shrinkages of the ceramic specimens depending on the sintering times

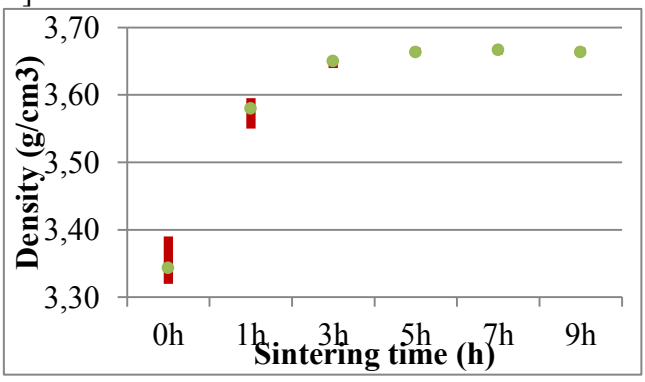

Figure 3. Densities of the ceramic specimens depending on the sintering times

The mean sintered densities (Fig. 3.) were determined by Archimedes method on the same specimen samples as the diameter shrinkages. The mean values in Fig. 2. and 3. have similar characters and show that the ceramic disc specimens after 3 hours of sintering at 1600°C provide almost the same values as after 5, 7, or 9 hours of sintering.

To determine the Vicker hardness, 5-5 pieces of sintered alumina ceramic specimens were selected randomly by each sintering times. The surface hardness was measured on Instron Tukon 2100B Hardness tester at 300N load.

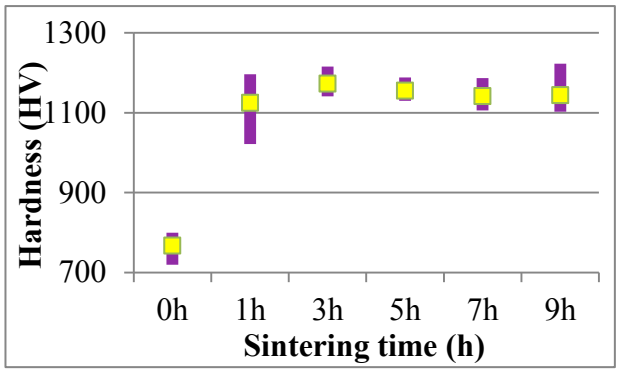

Figure 4. Vicker-hardness of the ceramic specimens depending on the sintering times

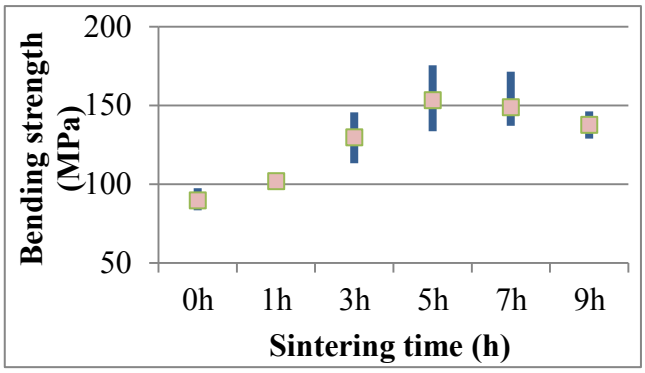

Figure 5. Bending strength of the sintered ceramic samples depending on the sintering times

As it is shown in Fig. 4., the contours of mean values of Vicker hardness have similar shape as shrinkage and density had. It is obvious from the data that the ceramic specimens have obtained the best surface hardness after 3 hours of sintering. This is essential technological information in all cases where surface hardness is important.

The bending strength of the alumina-based ceramic composite specimens was determined by standard three-point bending test [4]. The measurement results, the standard deviation, and the mean values are shown in Fig. 5. The bending strength has achieved the maximum value only after 5 hours of sintering at 1600°C. After this, the bending strength of specimens has decreased with increasing the sintering time. This is essential technological information for alumina matrix ceramic composites in all cases where bending strength is important.

For morphology test of the sintered hetero-modulus ceramic specimens, Hitachi TM-1000 Tabletop Scanning Electron Microscopy was used. The typical microstructures of the sintered ceramic items are shown in Figure 6 depending on sintering times at 1600°C.

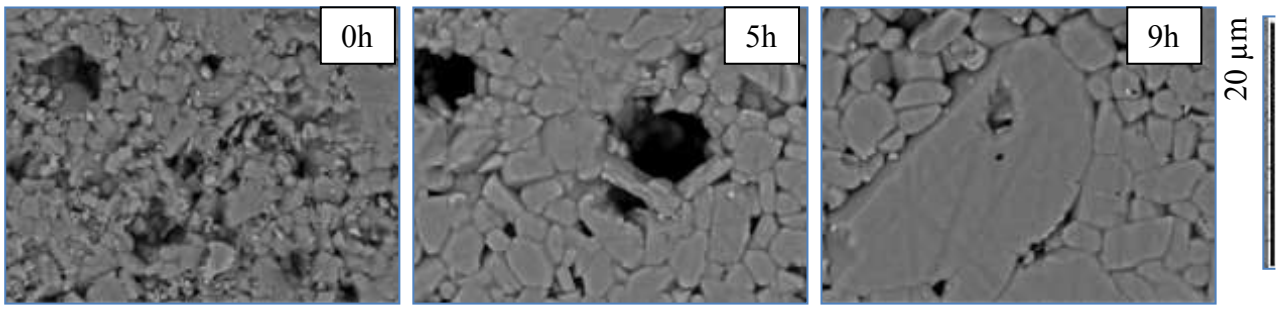

Figure 6. The morphology of the ceramic plates after 0, 5, and 9 hours of sintering time

As it is shown in Fig. 6., at 0 hour of sintering time at temperature of 1600°C, there are many pores and gaps between the particles. After 5 hours of sintering time, an essential crystal grows and bonds between particles can be observed. After 9 hours of sintering at the above temperature, the geometrical sizes of particles had grown considerably, meanwhile the size of pores and gaps between them decreased.

Finally, we compared (Table 2.) the shrinkage, density, hardness, and bending strength of our sintered specimens with the ceramic discs (sample 2) we have received from ceramic plant of Kerox Ltd. These ceramic discs of Kerox Ltd. were uniaxial compacted also at 400 MPa pressure and sintered in a 27 m long tunnel kiln for 48 hours. In the tunnel kiln, the maximum temperature was 1650°C and at this temperature, the ceramic discs have spent 5 hours.

Table 2. The examined properties of our specimens and industrial sample 2 (discs of Kerox Ltd.)

Sintering time (h)	Shrinkage (%)	Sintered density (g/cm^3)	Hardness (HV)	Bending strength (MPa)
0	10,24	3,34	846,24	89,53
1	13,84	3,58	852,82	101,76
3	14,35	3,65	849,08	129,58
5	14,40	3,66	971,71	153,24
7	14,40	3,67	961,62	148,67
9	14,35	3,66	858,14	137,61
sample2	14,48	3,67	888,56	125,00

Reviewing the data in Table 2, it is obvious that the mechanical and physical properties of specimens sintered in laboratory chamber kiln at 1600°C are similar to ceramic discs of Kerox sintered in the industrial tunnel kiln with sintering cycle of 48 hours. Therefore, usage of laboratory chamber kilns can help to predict and estimate the expected properties and qualities of alumina composite items produced and sintered under industrial circumstances. This can be very important when a company plans to use new raw material receipts or plans to change the technological conditions.

Conclusion

After the examination of microstructure, shrinkage, density, surface hardness, bending strength of the alumina-based hetero-modulus ceramic composite specimens compacted at 400MPa uniaxial pressing and sintered at 1600°C, the following statements can be made:

- The thermal shrinkage of hetero-modulus ceramic items prepared from raw material mix described in Table 1 have obtained their maximum values within 3 hours, meanwhile the maximum density could be obtained only after 5 hours of sintering in the laboratory chamber kiln.
- 3 hours sintering of these composite ceramics at temperature of 1600°C is enough to reach the maximum values of Vickers hardness, meanwhile the maximum values of bending strength can be obtained only within 5 hours of sintering.
- With regards to the microstructure, an essential crystal grows and bonds between the particles can be obtained only after 5 hours of sintering.

Acknowledgments
This research was supported by TÁMOP 4.2.1.B-10/2/KONV-2010-0001.

References

[1] J. Csanyi, L. A.Gömze, Néhány nagy tisztaságú Al_2O_3 műszaki kerámia hajlítószilárdsági vizsgálata, Építőanyag 53 (2001) 103-108.

[2] J. Csanyi, L. A.Gömze, Impact of nitrogen atmosphere on sintering of alumina ceramics, Építőanyag 60 (2008) 15-18.

[3] L. A. Gömze, L. N. Gömze, Hetero-modulus alumina matrix nanoceramics and CMCs with

extreme dynamic strength, Materials Science and Engineering 18 (2011).

[4] L. A. Gömze, L. N. Gömze, Alumina-based hetero-modulus ceramic composites with extreme dynamic strength – phase transformation of Si3N4 during high speed collisions with metallic bodies, Építőanyag 61 (2001) 38-42.

[5] L. A. Gömze, L. N. Gömze, Hetero-modulus nanoparticles reinforced corundum matrix CMC with extreme wear and thermal shock resistances,Material Science Forum 659 **(**2010),165-170

[6] L. A. Gömze, L. N. Gömze, Advanced Hetero-Modulus and Hetero-Viscous Complex Materials Material Science Forum 729 **(**2013) 43-48.

[7] W. H. Gitzen, Alumina As A Ceramic Material, The American Ceramic Society, 1970.

[8] S. N. Kulkov, M. V. Grigoriev, Sintering of Al_2O_3 ceramics based on different sizes powders, Építőanyag 62 (2010) 66-69.

[9] W. Kollenberg, Technische Keramik, Vulkan-Verrag Essen, 2004.

[10] E. Rocha-Rangel, D. Hernandez-Silva, E. Terres-Rojas, E. Martinez- Franco, S. Diaz-De La Torre, Alumina-based composites strengthened with titanium and titanium carbide dispersions, Építőanyag 62 (2010) 75-78.

Role of the Physical Simulation for the Estimation of the Weldability of High Strength Steels and Aluminum Alloys

János Lukács[1, a], László Kuzsella[1,b], Zsuzsanna Koncsik[1,c]
Marcell Gáspár[1,d], Ákos Meilinger[1,e]

[1]University of Miskolc, Faculty of Mechanical Engineering and Informatics, Institute of Materials Science and Materials Processing, H-3515 Miskolc-Egyetemváros, Hungary

[a]janos.lukacs@uni-miskolc.hu, [b]femkuzsy@uni-miskolc.hu, [c]metkzs@uni-miskolc.hu, [d]gasparm@uni-miskolc.hu, [e]metakos@uni-miskolc.hu

Keywords: physical simulation, weldability, Nil-Strength Temperature (NST), hot tensile test, high-strength low-alloy (HSLA) steel, aluminium alloy, Heat Affected Zone (HAZ) test, Rykalin-3D model

Abstract. The physical simulation is an ultimate innovative way to develop the welding processes. The paper introduces the connection between weldability and physical simulation, hot-cracking sensibility, the Gleeble 3500 thermo-mechanical physical simulator, respectively. Four kinds of materials were investigated and different kinds of physical simulation test methods were made such as, identification of the Nil-Strength Temperature (NST), hot tensile tests (on heating and on cooling parts of the welding simulation curve are also investigated). Furthermore, Heat Affected Zone (HAZ) tests are being introduced. The future approaches of the research are also exposed.

Introduction

It is a complex task to determine the weldability either on an overall or a specific level. A high number of semi-empirical and empirical approaches, technological investigations and tests, as well as the computer simulation facilitate to find the answer to the complex questions. The scope of such facilities has been widened through the possibilities offered by physical simulation. The paper aims are, on the one hand, describing the connection between weldability and physical simulation as well as the issue of hot crack sensitivity; on the other hand, the first tests and their results are being introduced.

Weldability and physical simulation

The technological investigations and tests regarding weldability date back to the development of different welding technologies. Not only the diverse qualities of materials, but the different welding processes as well as the high variety of these processes have resulted in the elaboration of further tests [1]. They are specified by their variety, applicability within limits, as well as their limited comparability. Considering the complex issue of weldability (such as material quality, technology, structure, etc.) [2, 3], there is not one single test which would allow evaluating the problem, it is not and would not be sensible either, consequently weldability cannot be determined with a single characteristic. The underlying reasons are to be examined separately under specific conditions, which then will enable us to rank the different materials based on the given results. The order of ranking depends on the requirements, i.e. it is not considered constant. The complex correlations between the factors do not allow defining other properties (e. g. mechanical properties) through characteristics. Besides the investigations and tests, semi-empirical and empirical investigations are given an ever increasing emphasis in order to avoid limitations [4].

There is at least double contradiction in the investigations and tests. On the one hand, the actual processes can only be performed on small parts and in small volumes, which means that there are only small-size specimens available to define the data belonging to the materials and/or technologies [5]. This fact, due to the aspect of size effect, will decrease the reliability of the results. On the other hand, the technological investigations are reflected within limits as regards the real processes and physical simulations.

The mathematical (computational) simulation may contribute to cancelling the limitations of investigations and tests, as well as those of the different approaches, which are not to be considered in the current study. However, the other consideration is the physical simulation. Physical simulation applied in metallurgy dates back to the mid-20th century. The basic purpose of the first physical simulators was to provide reproducibility for the welding Heat Affected Zone (HAZ).
The specifications of the physical simulation and simulators can be summarised as follows [6, 7]: a physical simulator is not considered as „reduced" production system; a physical simulator is not a target equipment; the physical simulation is always a real time process; the effects on the specimens being applied in a physical simulator are determined by the specification of the concerned industrial process; specimens treated in a physical simulator must be suitable for further tests as well; the physical simulation is definitely closer to an industrial process considering mathematical (numerical and computational) and physical simulations.

Hot-cracking sensitivity

Hot cracks occur at high temperatures during a welding process. The hot cracks formed in the weld metal are the solidification cracks, while the hot cracks occurring beside the seam, on the transition between the seam and the base material, on the fusion line or in the base material, are the liquation cracks [2, 3]. The deformation theory of the occurrence of hot cracks described as follows in Fig. 1.

Plasticity of a metal alloy (P) varies between the liquidus (T_L) and solidus (T_S) temperatures according to the curve, while the deformation capability required for avoiding hot cracks is P_{th}. In BTR (Brittleness Temperature Range) where plasticity will not reach the required (threshold) deformation capability, hot cracks may be formed. During the crystallisation process tensile strains – due to unequal heating and cooling as well as to restrained shrinkage – exert effect on the weld metal, which will cause deformation. If the deformation of the weld metal exceeds the deformation capability, cracks will occur (ε_1), while in the case of more minor deformation (ε_2), cracks will not be formed. The report [8] expressed the reserve deformation (ε_z) with strain caused by thermal cycle (ε_s) and shrinkage strain (ε_k), between the real strain (ε_1') and the deformation limit (ε_1) (Fig. 2.).

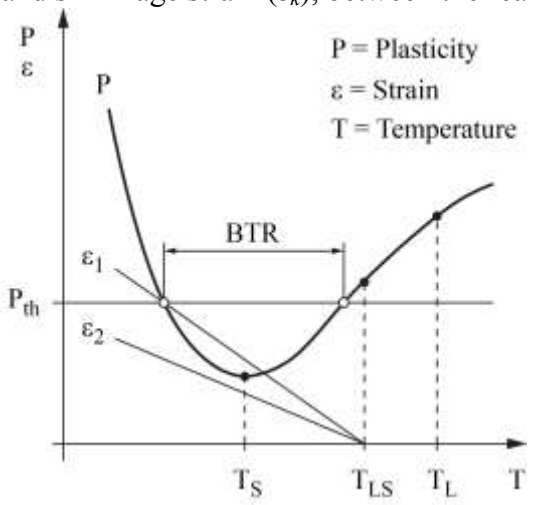

Fig. 1. A sketch to the theory of hot crack occurrence concerning to the strain.

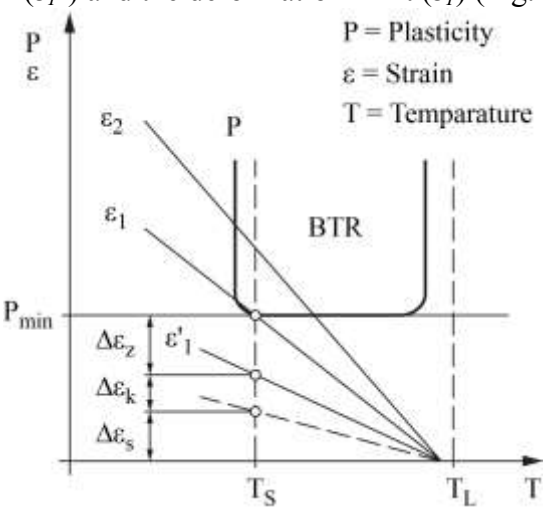

Fig. 2. Deformations in the theory of hot crack occurrence [8].

Measuring based on the physical simulation of hot cracking sensitivity and the comparison of the sensitivity of different materials (more exactly that of welded joints made by means of different welding technologies) various measures are used, depending partly on the material quality as well.

These are presented in Fig. 3 [1, 9] based on tests performed on heating and on cooling which are aiming at defining hot-tensile and nil-strength temperatures. The values considered in Fig. 3 are as follows: Nil-Strength Temperature (NST); Nil-Ductility Temperature (NDT); Ductility Recovery Temperature (DRT); Brittleness Temperature Range (BTR); Nil-Ductility Range (NDR); Ductility Recovery Rate (DRR); Ratio of Ductility Recovery (RDR).

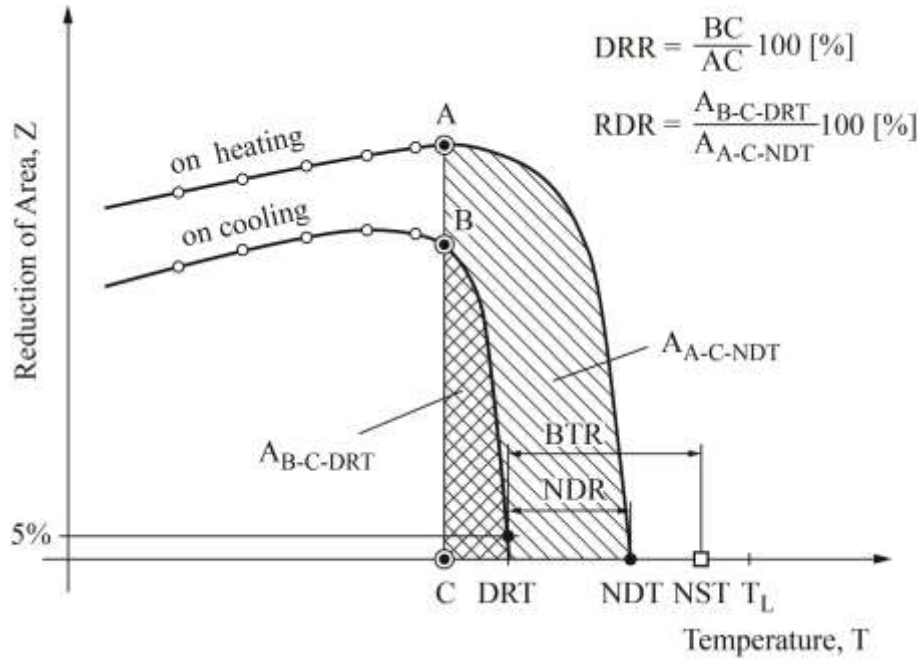

Fig. 3. Possibilities for expressing hot cracking sensitivity characteristics by physical simulation (based on [9]).

Measurement of the Nil-Strength Temperature

Nil-Strength Temperature (NST) is the temperature which causes the specimen under the effect of even some minor load to tearing. Most of the materials testing equipment are not suitable for precisely defining the NST of steels. There are double reasons for this fact: firstly, the specimen has to be heated in a well-controlled way up to a temperature which is close to the melting point of steel, at a low heating rate close to the testing temperature (*1-2 K/s*); on the other hand, the device is to provide the minimum pre-strained state, the maintenance of which, due to thermal expansion, causes serious problems in control techniques. During the tests a specific pneumatic system keeps the permanent value of the minimum load required to define NST. The diameter of the cylindrical specimens applied in the tests was *6 mm*, with a length of *80 mm*, and the testing length was *25 mm*. The load must be as low as possible; however, too low pre-load will decrease the reproducibility of the test and increase uncertainty in defining NST. Considering all this as well as the geometry of the specimen, 80 N pre-load was applied in the tests. NST is a value close to the solidus temperature (T_S) of the tested material. In order to define it precisely, the heating rate prior to the solid temperature must be as low as possible. Two different heating rates are to be applied during the test. In the starting phase of the test, i.e. from room temperature up to below the solidus temperature, approximately *100-150 °C*, the heating rate may be relatively high (*20 °C/s*), while in the phase afterwards this rate must be decreased (*1-2 °C/s*).

Two types and four kinds of materials were investigated. One type is high-strength low-alloy steel (HSLA), the material grades are S960QL and S690QL. The other types are aluminium alloys 5754 (AlMg3) and 6082-T6.

Table 1. Results of the NST examinations.

Material grade	Number of specimens	Average, °C	Standard deviation, °C	Standard deviation coefficient, %
S690QL	9	1421.5	19.15	1.35
S960QL	11	1408.0	30.46	2.16
5754 (AlMg3)	10	602.6	1.81	0.30
6082-T6	10	616.6	7.15	1.16

Hot ductility tests on HSLA steel grade S690QL

Hot tensile tests were made only on HSLA steel grade S690QL and were carried out using on heating and on cooling specimens. The smooth, cylindrical specimens applied in the tests have a diameter of *10 mm*, a length of *116.5* mm, and a testing length of *80 mm*.

In a given material the definition of NST is always prior to the definition of strength on heating and on cooling since the maximum temperature of the tests is to be below NST at least by *20-30 °C*. In the case of the tested material NST was below the average *1403.8 °C*, this was the reason why *1380 °C* was chosen as peak temperature.

The actual testing temperatures in accordance values of the determined tensile strength (R_m) and reduction of area (Z) are shown in Table 2. Rounded data of the reduction of area values were summarized in the table, which also show minor differences between the results. The values are in compliance with the data can be found in the literature [9].

Table 2. Actual temperatures and results of hot tensile tests.

Thermal cycle	$T_{testing}$, °C	R_m, MPa	Z, %
on heating	800	292.8	93.05
	1000	146.0	99.82
	1200	84.4	99.99
	1380	52.8	100.0
on cooling	1200	82.5	99.93
	1000	160.5	96.43
	800	252.0	92.73
	500	446.7	83.98

Heat Affected Zone tests on HSLA steel grade S960QL

Aim of HAZ Tests. When weldability of quenched and tempered steels is investigated, welding engineers need to have knowledge about the effect of welding parameters on heat affected zone, which can be critical in terms of the success of technology [10]. This chapter aims to present the properties of HAZ of (Q+T) high strength steel joints by the use of physical simulation, while the effect of welding parameters ($t_{8.5/5}$ cooling times) on the different HAZ zones is also investigated. Optimal $t_{8.5/5}$ cooling time intervals, getting tighter by the application of higher strength categories, can be specified for high strength steels. According to the recommendation of SSAB steel producer, the optimal cooling time range is *5-15 s* for WELDOX 960. Approaching to the lower limit, the risk of cold cracking increases, in case of long cooling times the reduction of toughness and strength properties can be expected. When single run welds are used, the typical HAZ of a (Q+T) high strength steels includes:

- coarse grained zone, CGHAZ (*1100 °C…T_{liq}*),
- fine grained zone, FGHAZ (*A_3…1100 °C*) ,
- intercritical zone, ICHAZ (*A_1…A_3*),
- subcritical zone, SCHAZ (*500 °C…A_1*).

Heat cycle parameters. Due to the limited extension of HAZ, the above mentioned zones cannot be deeply examined by real welding experiments; therefore Gleeble HAZ test module was used. Heat cycles were defined by the use of Rykalin-3D model in Quicksim software, developed for the simulator. The model can be generally used for thick plates, and independent from plate thickness.

On the basis of real welding experiments (where EN 1011-2 was applied for the determination of preheating temperature), preheating temperature was selected to *200 °C*. Hold time at peak temperature was set to *1 s* and heating rate was *500 °C/s* for all tests. Three peak temperatures, *1350 °C*, *950 °C* and *800 °C*, were used for the simulation of CGHAZ, FGHAZ and ICHAZ (SCHAZ was not simulated in the course of these experiments). The highest peak temperature was selected slightly under than the NST temperature of the investigated steel (*1408 °C*), which can result the largest grains expected in real welded joints. The simulation of this zone can be critical due to the mechanical load, caused by the thermal expansion, which can be detrimental for the specimens, heated close to the NST. Preliminary simulations, including optical microscopic tests, were made

for the selection of other two peak temperatures, since A_1 and A_3 temperatures move up (A_{c1} and A_{c3}) due to the intensive heating rate. In terms of the heat input, *1015 J/mm* was selected to result $t_{8.5/5} = 5$ *s* and *3046 J/mm* was given to result the upper limit (*15 s*) of the optimal cooling time range. Fig. 4 demonstrates an example for the applied heat cycles during the simulation of CGHAZ.

Execution of tests. Specimens with the size of *10×10×70 mm* were used, in order to realize the planned Charpy-V tests after the simulations. Four specimens were prepared per each zone and cooling times, one for microscopic and hardness tests, the other three for impact tests. NiCr-Ni thermocouples were welded to their surface before the simulation.

Hardness. One specimen from each set was etched by *2%* nital, then microscopic and hardness tests were performed. Tests were evaluated according to EN 15614-1 standard which permits maximum *450 HV10* for S960QL, belonging to the third steel group of CR ISO 15608.

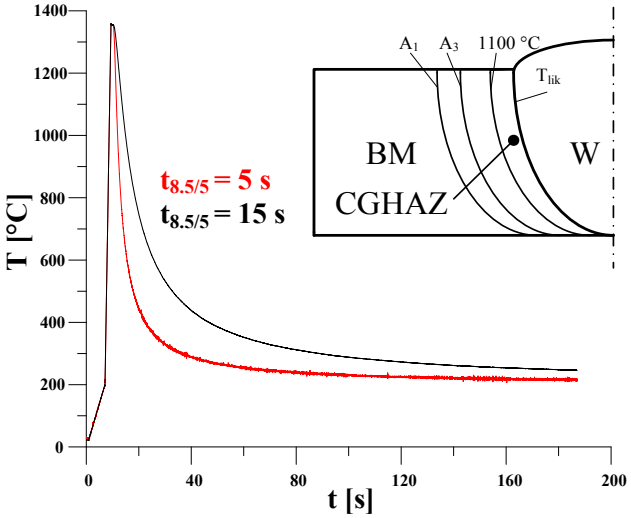

Fig 4. Example for the applied heat cycles during the simulation of CGHAZ.

Measured hardness values are summarized in Table 3, which is including the average hardness of 5 measured values per each zone. Conclusion can be drawn that all tests fulfilled the requirements of the governing standard, although significant differences can be noticed between the several zones and cooling times.

Table 3. Average hardness of HAZ.

HAZ	T_{max}, °C	Hardness, HV10	
		$t_{8.5/5} = 5$ s	$t_{8.5/5} = 15$ s
Coarse grained (CGHAZ)	1350	417	385
Fine grained (FGHAZ)	950	418	363
Intercritical (ICHAZ)	800	348	351

With regards to cold cracking, CGHAZ is the most critical, in the welded joint peak hardness values are generally measured in this zone. By the use of longer cooling time the hardness significantly decreased in CGHAZ and FGHAZ, although this difference was not measured in case of ICHAZ. When $t_{8.5/5} = 5$ *s* was used the hardness of CGHAZ and FGHAZ were almost the same. Micro hardness tests were performed for the deeper analysis of ICHAZ, where the hardness of the austenized parts were close to the values, measured in CGHAZ and FCHAZ, belonging to the shorter cooling time. The other element of ICHAZ, the tempered original microstructure, softened, therefore values in Table 3 can be considered as the average hardness of the austenized and tempered parts of this zone.

Conclusions

On the basis of the above described facts, the following conclusions can be drawn.

- Physical simulation (particularly in Hungary) is an innovative and effective way to be applied in understanding and developing the details of welding processes.
- Nevertheless, physical simulation is not and cannot be considered the only way in this field. The possibilities offered by physical simulation and the results to be achieved by its means may fully be explored through the common application of technological investigations and tests, semi-empirical and empirical experience as well as numerical simulations.
- The reliability of the NST tests made on four kinds of materials is regarded satisfactory.
- The results of hot tensile tests of S960QL steel carried out on heating and on cooling specimens are satisfactory, considering their tendencies as well. Further investigations are

required in two or even three directions to define further data (see Fig. 3) and to draw further conclusions. It seems essential to reduce the difference between the actual temperatures (one direction), as well as to change the heating and cooling rates of the heating period (another direction). After we have had the results of the further tests, we may decide whether it is necessary to increase the number of specimens when performing tests with one parameter respectively (third direction).

- Using the Gleeble 3500 thermo-mechanical physical simulator the critical zones of S960QL HAZ can be reproduced. The technology planning for GMAW, based on the HAZ tests, can be performed and the joint quality can be guaranteed. Hardness values of simulated CGHAZ and FGHAZ are significantly different at the two $t_{8.5/5}$ cooling times, while the average hardness of ICHAZ can be considered as the same. All hardness values are safely lower than the maximum permitted hardness according to EN 15614-1 standard.

Acknowledgements

The installation of the Gleeble 3500 thermo-mechanical physical simulator was supported by the TIOP 1.3.1-07/1-2F-2008-0005 project on the summer of 2012.

The investigated S960QL material was accorded by the Ruukki Tisza Zrt. (Jászberény).

The research work presented in this paper based on the results achieved within the TÁMOP-4.2.1.B-10/2/KONV-2010-0001 project and carried out as part of the TÁMOP-4.2.2/A-11/1-KONV-2012-0029 project in the framework of the New Széchenyi Plan. The realization of this project is supported by the European Union, and co-financed by the European Social Fund.

References

[1] C. Pohle, Zerstörende Werkstoffprüfung in der Schweisstechnik, Deutscher Verlag für Schweisstechnik DVS-Verlag GmbH, Düsseldorf, 1990.

[2] K. E. Easterling, Introduction to the Physical Metallurgy of Welding, Butterworths Monographs in Materials (BMM), Butterworths & Co (Publishers) Ltd., 1983.

[3] U. Boese, D. Werner, H. Wirtz, Das Verhalten der Stähle beim Schweissen, Teil II: Anwendung. Deutscher Verlag für Schweisstechnik (DVS) GmbH, Düsseldorf, 1984.

[4] B. Buchmayr, Computer in der Werstoff- und Schweisstechnik: Anwendung von mathematischen Modellen, Deutscher Verlag für Schweisstechnik DVS-Verlag GmbH, Düsseldorf, 1991.

[5] B. Yuan, W. N. Sharpe, Fatigue testing of microspecimens, in: G. Lütjering, H. Nowack (Eds.) Proceedings of the Sixth International Fatigue Congress (FATIGUE'96), Pergamon, 1996. Vol. III. pp. 1943-1948.

[6] B. Verő, A fizikai szimuláció helye és szerepe a műszaki anyagtudományban, ISD DUNAFERR Műszaki Gazdasági Közlemények. 47 (2007) Issue 4 (148) 167-172. (In Hungarian.)

[7] B. Verő, A fizikai és matematikai szimuláció helye és szerepe a vaskohászati kutatás-fejlesztésben. ISD DUNAFERR Műszaki Gazdasági Közlemények. 48 (2008) Issue 3 (151) 114-116. (In Hungarian.)

[8] J. Adamiec, M Kalka, Brittleness temperature range of Fe-Al alloy, Journal of Achievements in Materials and Manufacturing Engineering (JAMME). 18 (2006) Issues 1-2, September-October 2, 43-46.

[9] S. T. Mandziej, Physical Simulation of Metallurgical Processes, Materiali in technologije / Materials and technology. 44 (2010) Issue 3, 105-119.

[10] R. Laitinen, D.A. Porter, L.P. Karjalainen, P. Leiviskä, J. Kömi, Physical Simulation for Evaluating Heat-Affected Zone Toughness of High and Ultra-High Strength Steels, Materials Science Forum. 762 (2013) 711-716.

Behaviour of AlMg3 base material and its friction stir welded joints under cyclic loading conditions

János Lukács[1, a] and Ákos Meilinger[1, b]

[1, 2]Department of Mechanical Engineering, University of Miskolc
H-3515 Miskolc-Egyetemváros, Hungary

[a]janos.lukacs@uni-miskolc.hu, [b]metakos@uni-miskolc.hu

Keywords: friction stir welding (FSW), aluminium alloy, high cycle fatigue (HCF), fatigue crack propagation (FCG), limit curve.

Abstract. The friction stir welding (FSW) is a dynamically developing version of the pressure welding processes. Nowadays, the knowing of the properties and the behaviour of the welded joints is an important direction of the investigations, especially under cyclic loading. The research work aimed (i) to demonstrate the behaviour of the FSW welded joints under cyclic loading conditions; (ii) to confirm the applicability of the used friction welding technology. Experiments were performed on 5754-H22 aluminium alloy and its welded joints; both high cycle fatigue (HCF) and fatigue crack propagation (FCG) tests were executed. HCF limit curves were determined based on staircase method. Statistical behaviour of the base material and the welded joints under FCG was represented by the cutting of the specimens, in other words by the using of different crack paths. FCG limit curves can be determined by own developed six step method. The investigations and their results were compared with each other and with the results can be found in the literature.

Introduction

The role of aluminium alloys in structural applications has become unquestionable nowadays. Different aluminium alloys are used in more and more amount and with more and more purpose in the field of aircraft, automotive [1], marine and rail industries, and bridge structures [2]. The effort of different material development (e.g. [3]) is to allow a wider application range and to satisfy the most various demands of users. Technological developments are also needed in addition and in close contact with material developments at least the reason of satisfactory of user's requirements – inside the safety requirements – and economy. The situation is similar in the field of welding technology, where the friction stir welding (FSW) is one of the more dynamically developing pressure welding process [4] since its invention (1991) [5]. The material developments and the application requirements induce technological developments and we can find examples of its inverse, too [6-9]. In case of different structural applications the loading condition has frequently cyclic aspects, among the damages (failures), the high cycle fatigue (HCF) and the fatigue crack growth (FCG) are occurring. Regarding to significant importance of damages and failures during cyclic stresses, these stresses should be set to the focus of investigations.

The purpose of this article is to present the resistance of the AlMg3 or 5754-H22 aluminium alloy and its FSW joints against cyclic stresses (HCF and FCG). Own considerations and results are also compared with literature data; furthermore we also refer the possibility of derivation and determination of limit curves against cyclic stresses (HCF and FCG).

Materials, welded joints and testing conditions

Examinations were performed on AlMg3 or 5754-H22 of aluminium alloy, both base materials (BM) and FSW joints (WJ) were tested. Table 1 and Table 2 show the chemical composition, thickness (t) and basic mechanical properties (R_y = yield stress, R_m = tensile stress, A = elongation) of the examined and comparative materials, respectively. (W/B means WJ/BM in Table 2.)

Table 1. Chemical composition of the examined and comparative materials (wt%).

Material	Mg	Si	Zn	Cu	Mn	Fe	Cr	Ti	Reference
5754-O	3,3	0,19	0,08	0,03	0,34	0,2	–	–	[10]
5754	2,854	0,095	–	0,028	0,316	0,239	0,011	–	[11]
AlMg3	2,95	0,179	0,044	0,022	0,277	0,301	0,043	0,04	this study
5754-H22	2,8	0,26	0,06	0,04	0,32	0,31	0,05	0,03	this study

Table 2. Thickness and mechanical properties of the examined and comparative materials.

Material	t	R_y			R_m			A			Reference
		BM	WJ	W/B	BM	WJ	W/B	BM	WJ	W/B	
	mm	N/mm^2		–	N/mm^2		–	%		–	
5754-O	3	170	72	0,424	253	217	0,858	12,3	10,1	0,821	[10]
5754-H22	3	–	–	–	235	93	0,397	15,0	0,6	0,042	[12]
5754	4	165	–	–	252	–	–	17,6	–	–	[11]
AlMg3	12	128	–	–	218	–	–	–	–	–	this study
5754-H22	6	190	–	–	239	223	0,933	14,5	–	–	this study

FSW joints were made with an own designed tool on a conventional milling machine. Table 3 and Table 4 summarize the parameters of the FSW technology made from comparative and examined materials.

Table 3. FSW technological parameters of comparative and examined materials I.

Material	Thickness	Welding speed	Rotational speed	Shoulder diameter	Tool tilt angle	Reference
	mm	mm/min	rpm	mm	°	
5754-O	3	13	700; 1100	15	2	[10]
5754-H22	3	15; 20; 25	2000; 3000	18	–	[12]
5754-H22	6	100	400	16	2	this study

Table 4. FSW technological parameters of comparative and examined materials II.

Material	Thickness	Pin diameter	Pin length	Pin geometry	Reference
	mm	mm	mm	–	
5754-O	3	5/2	2	taper, threaded	[10]
5754-H22	3	6	2	threaded	[12]
5754-H22	6	8/4	5,7	staggered	this study

As the data of Table 3 and Table 4 show our applied technological parameters partially differ from published data of other authors. This fact confirms the experience that the sufficient quality of welded joints can be reached with several parameter combinations on FSW process.

Figure 1 shows the geometry of the flat specimens for HCF tests, executed on 5754-H22 material. The applied specimen geometries were same for base materials and FSW joints, post-weld heat treating and cutting were not applied after the welding on FSW joints (as-welded condition). The examinations were performed with tensile stress, $R = 0,1$ stress ratio, sinusoidal loading wave form, at room temperature and on laboratory air, using MTS type electro-hydraulic testing equipment. The loading frequency was $f = 30$ *Hz*.

The FCG tests were executed on AlMg3 and 5754-H22 base materials and 5754-H22 FSW joints, on CT specimens ($W = 50$ *mm*), the positions of the notches were different and correlated with the rolling direction and the centreline of the welded joint. The different cases, in other words the statistical approach, are shown in Figure 2.

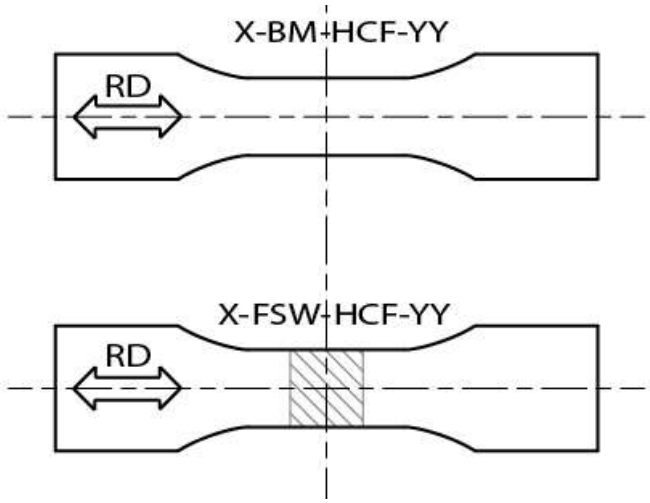

Fig.1. Flat specimen geometry for the HCF tests (X = aluminium group, in this case 5; YY = line number of specimen).

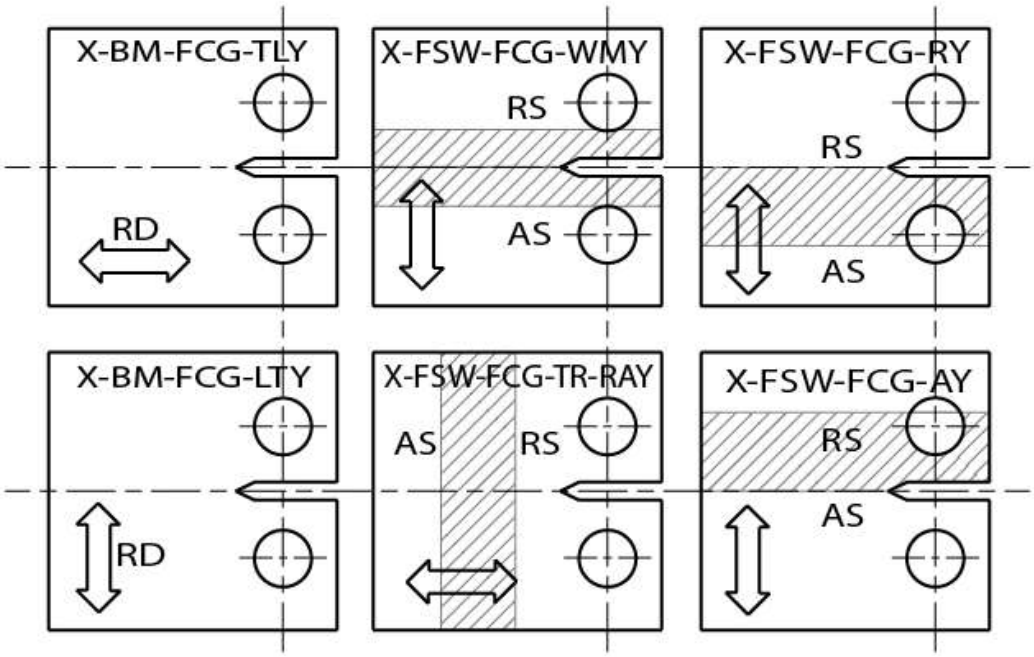

Fig.2. CT specimen geometry and notch locations for the FCG tests (X = aluminium group, in this case 5; YY = line number of specimen).

As the Figure 2 shows the positions of the notches and the crack paths represent the most important and the most typical directions (RS = retreating side, AS = advancing side). Post-weld heat treating and cutting were not applied after welding on FSW joints (as-welded condition). FCG examinations were executed same circumstances as HCF tests ($R = 0,1$ stress ratio, sinusoidal loading wave form, room temperature, laboratory air, MTS type electro-hydraulic testing equipment). The loading frequency was different, it was $f = 20$ *Hz* at the two-thirds of crack growth, and it was $f = 5$ *Hz* at the last third. The propagating crack was registered with compliance method.

Results of examinations

Numbers of cycles to failure were recorded during HCF tests. The fracture was happened on the weld centre at 5754-H22 material. Our examinations were evaluated according to the staircase method [13]. Figure 3 summarizes the test results (measured data and determined S-N curves) and the comparative test results (only measured data).

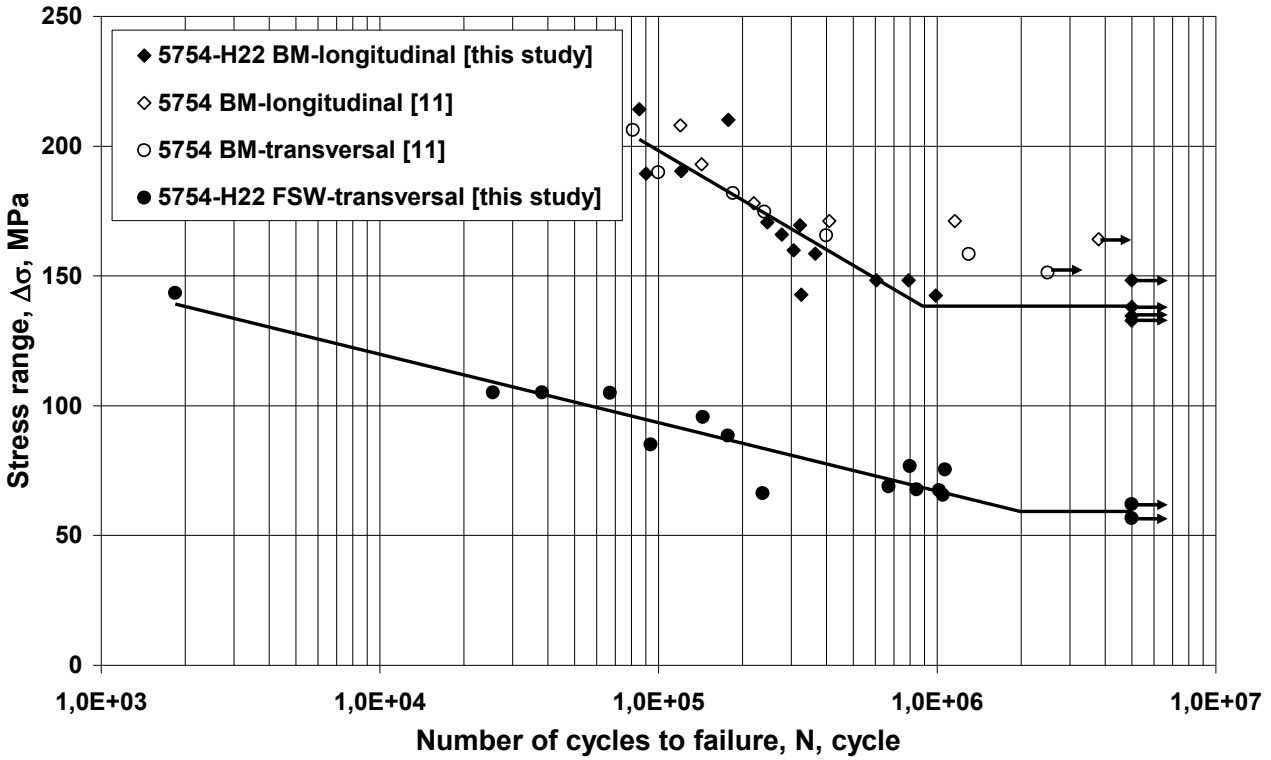

Fig.3. Results of HCF tests and the determined S-N curves.

Seven point incremental polynomial method (ASTM E 647) was used to evaluate the fatigue crack growth data. The constants (*C* and *n*) of the Paris-Erdogan relationship [14] were calculated. Figure 4 shows the kinetic diagrams determined on AlMg3 and 5754-H22 base materials on different orientations (T-L and L-T). The determined kinetic diagrams of the propagating cracks on different orientation and joint parts of 5754-H22 FSW joints are shown in the Figure 5.

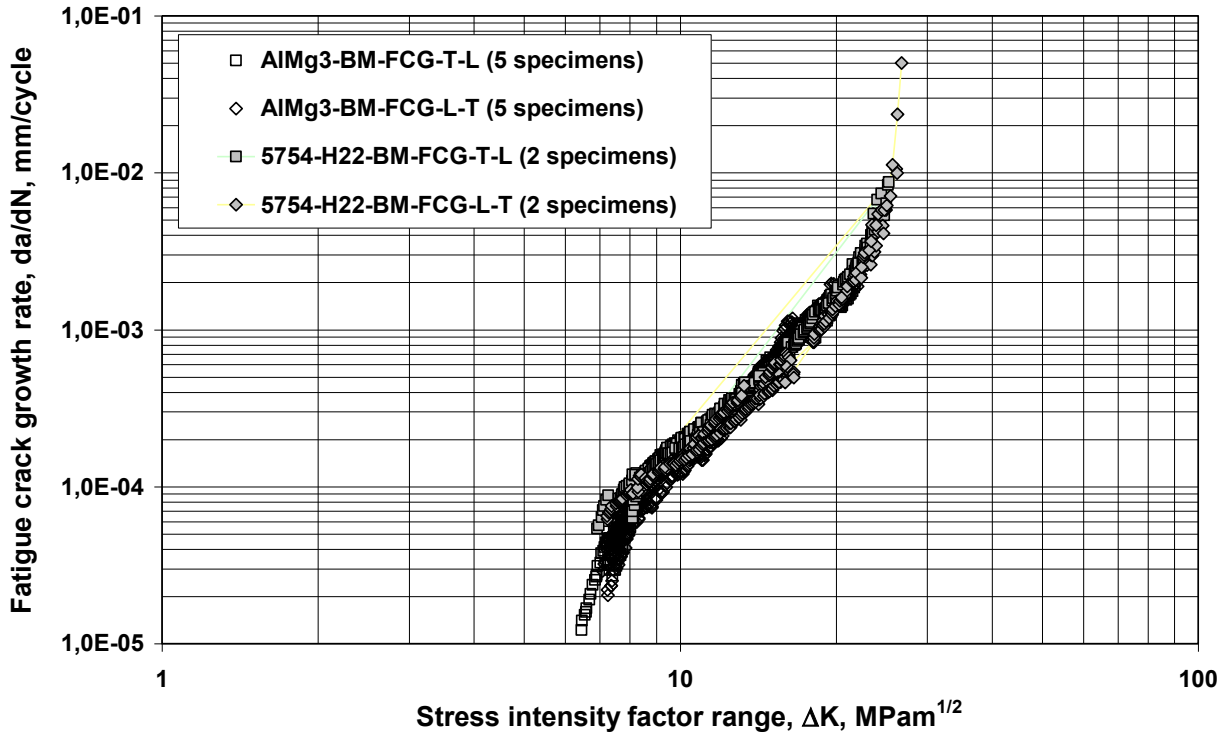

Fig.4. Results of FCG tests executed on base materials (AlMg3, 5754-H22).

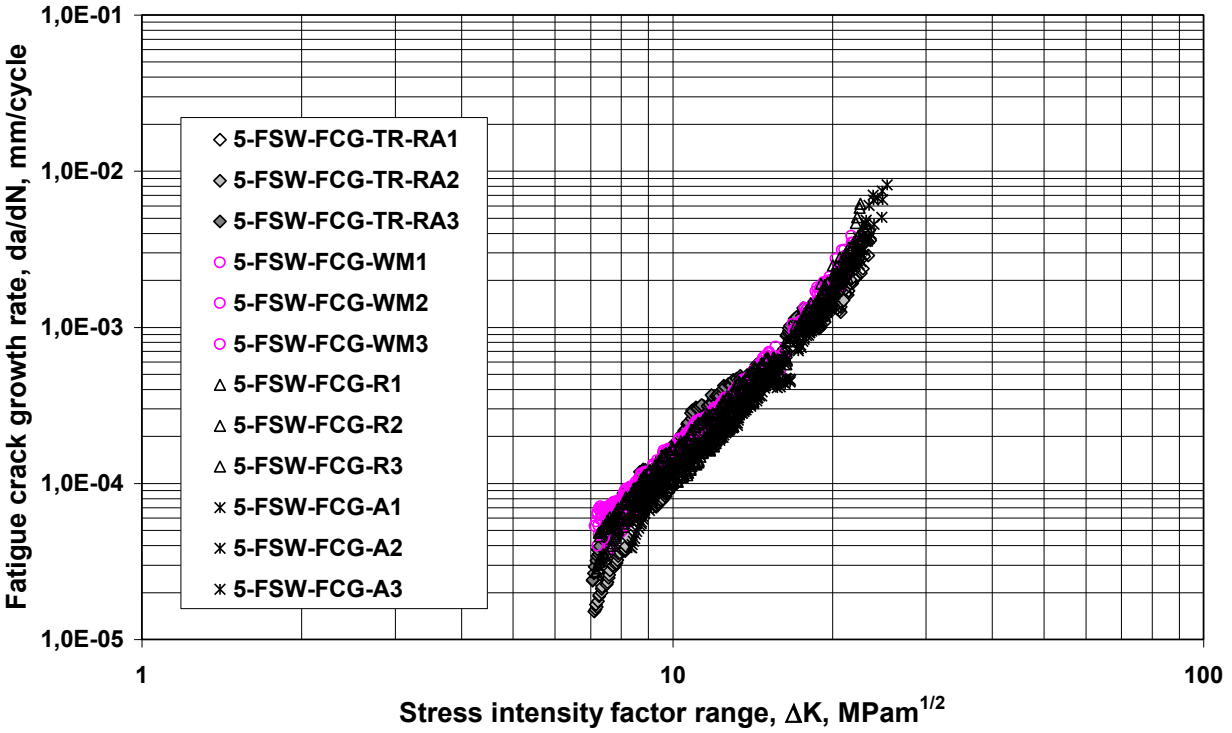

Fig.5. Results of FCG tests executed on 5754-H22 FSW joints.

Table 5 summarizes the Paris-Erdogan constants which determined from the certain kinetic diagrams. In that case when the kinetic diagram can be written with more straight section in the domains, then only the constants of the relationship which describes the greatest (middle) part of the diagram were announced in the Table 5.

Table 5. Paris-Erdogan constants (*C* and *n*, *MPam*$^{1/2}$*-mm/cycle*) and the correlation coefficients (*r*).

Specimen ID	C	n	r	Specimen ID	C	n	r
AlMg3-BM-FCG-TL1	1,55E-07	3,06	0,994	Transversal direction (TR-RA, see Fig.2.)			
AlMg3-BM-FCG-TL2	1,61E-07	3,03	0,993	5-FSW-FCG-TR-RA1	1,00E-07	3,16	0,997
AlMg3-BM-FCG-TL3	1,52E-07	3,05	0,993	5-FSW-FCG-TR-RA2	1,12E-07	3,97	0,995
AlMg3-BM-FCG-TL4	1,06E-07	3,20	0,993	5-FSW-FCG-TR-RA3	1,00E-07	3,25	0,994
AlMg3-BM-FCG-TL5	1,62E-07	3,03	0,993	Parallel directions (WM, R, A, see Fig.2.)			
AlMg3-BM-FCG-LT1	7,08E-08	3,32	0,997	5-FSW-FCG-WM1	1,49E-07	3,00	0,995
AlMg3-BM-FCG-LT2	1,78E-08	3,84	0,996	5-FSW-FCG-WM2	1,19E-07	3,15	0,997
AlMg3-BM-FCG-LT3	1,07E-07	3,22	0,993	5-FSW-FCG-WM3	2,19E-08	3,80	0,998
AlMg3-BM-FCG-LT4	1,11E-07	3,21	0,988	5-FSW-FCG-R1	5,00E-08	3,50	0,997
AlMg3-BM-FCG-LT5	7,69E-08	3,34	0,996	5-FSW-FCG-R2	4,69E-08	3,47	0,993
5-BM-FCG-TL1	1,76E-07	3,04	0,996	5-FSW-FCG-R3	1,96E-08	3,73	0,993
5-BM-FCG-TL2	9,37E-08	3,25	0,995	5-FSW-FCG-A1	1,61E-08	3,80	0,993
5-BM-FCG-LT1	1,10E-07	3,16	0,996	5-FSW-FCG-A2	3,98E-08	3,50	0,998
5-BM-FCG-LT2	3,24E-07	2,67	0,989	5-FSW-FCG-A2	2,39E-08	3,66	0,987

Summary and conclusions

Based on the performed tests and their results the following conclusions can be drawn.

- The determined results refer to reliable (see the correlation coefficients) and reproducible tests.
- The results of the HCF tests on FSW joints confirm the applicability of the welding technology. The fact that the resistance against HCF of the FSW joints on 5754-H22 material is barely half of the base material suggests the possibility of the improvement of the applied welding technology.

- The results of the FCG tests on the two essentially equal base materials (AlMg3 and 5754-H22) can be considered equal per orientations (T-L and L-T). The size effect ($t = 12$ *mm* and $t = 6$ *mm*) is not detectable significantly. All of these allow the more general applicability of these results.
- The fatigue crack propagation on the FSW joints of 5457-H22 material consider significantly different, it depends on these growth on weld centreline, edges or perpendicular to the centreline.
- The results of our experiments have good correspondence with the literary results.
- Further examinations required to statistically more establish conclusions.

Acknowledgements

The research work presented in this paper based on the results achieved within the TÁMOP-4.2.1.B-10/2/KONV-2010-0001 project and carried out as part of the TÁMOP-4.2.2.A-11/1/KONV-2012-0029 project in the framework of the New Széchenyi Plan. The realization of this project is supported by the European Union, and co-financed by the European Social Fund.

References

[1] W. S. Miller, et al., Recent development in aluminium alloys for the automotive industry, Materials Science and Engineering. A280 (2000) 37–49.

[2] P. Tindall, Aluminium in bridges, ICE Manual of Bridge Engineering, Institution of Civil Engineers. (2008) 345-355, doi: 10.1680/mobe.34525.0345.

[3] C. B. Fuller, et al., Microstructure and mechanical properties of a 5754 aluminum alloy modified by Sc and Zr additions. Materials Science and Engineering A338 (2002) 8-16.

[4] R. S. Mishraa and Z. Y. Ma, Friction stir welding and processing, Materials Science and Engineering. R 50 (2005) 1–78.

[5] Friction Stir Welding. http://www.twi.co.uk/technologies/welding-coating-and-material-processing/friction-stir-welding/

[6] A. Kostrivas and J. C. Lippold, Weldability of Li-bearing aluminium alloys, International Materials Reviews. 44 (1999) No. 6 217-237.

[7] P. F. Mendez and T. W. Eagar, Welding processes for aeronautics, Advanced Materials and Processes. (2001) May 39-43.

[8] S. K. Chionopoulos, et al., Effect of tool pin and welding parameters on friction stir welded (FSW) marine aluminium alloys, in: K.-D. Bouzakis (Ed.) Proc. of the 3rd ICMEN, EEDM and PCCM, Thessaloniki, 2008. pp. 307-316.

[9] Á. Meilinger and I. Török, Formation and microstructure of friction stir welded joint, Hegesztéstechnika. 24 (2013) No. 4 35-38. (In Hungarian.)

[10] Z. Barlas and U. Ozsarac, Effects of FSW Parameters on Joint Properties of AlMg3 Alloy. Welding Journal, 91 (2012) January 16-s-22-s.

[11] J. Li, The effect of microstructure and texture on high cycle fatigue properties of Al alloys, University of Kentucky, Doctoral Dissertations, Paper 522 (2007).

[12] M. Vural, et al.,On the friction stir welding of aluminium alloys EN AW 2024-0 and EN AW 5754-H22, Archives of Materials Science and Engineering. 28 (2007) Issue 1, January 49-54.

[13] H. Nakazawa and S. Kodama, Statistical S-N testing method with 14 specimens: JSME standard method for determination of S-N curves, in: T. Tanaka, S. Nishijima, M. Ichukawa (Eds.), Statistical Research on Fatigue and Fracture. Current Japanese Materials Research, Vol. 2. Elsevier Applied Science, London-New York, 1987. pp. 59-69.

[14] P. Paris and F. Erdogan, A critical analysis of crack propagation laws, Journal of Basic Engineering, Transactions of the ASME. (1963) 528-534.

Characteristics of Martensitic Transformations Induced by Uni-axial Tensile Tests in a FeMnCr Steel

Valeria Mertinger[1,a], Erzsebet Nagy[2,b] , Marton Benke[2,c] , Ferenc Tranta[2,d]

[1]Institute of Physical Metallurgy, Metalforming and Nanotechnology, University of Miskolc, Miskolc-Egyetemvaros, Hungary 3515

[2] MTA-ME Materials Science Research Group, University of Miskolc, Miskolc-Egyetemvaros, Hungary 3515

[a]femvali@uni-miskolc.hu (corresponding author), [b]femzsofi@uni-miskolc.hu,

[c]fembenke@uni-miskolc.hu, [d]femtran@uni-miskolc.hu

Keywords: martensitic transformation, TRIP steel, TWIP steel.

Abstract. Austenitic FeMnCr steels have high strength, high toughness and formability because of the stress- and strain-induced γ→α and γ→ε martensitic phase transformations. These are the so-called TRIP (Transformation Induced Plasticity) and TWIP (Twining induced Plasticity) effects. TWIP steels deform by both glide of individual dislocations and mechanical twinning [1]. The type and mechanism of the austenite→martensite transformation depends on the composition, deformation rate and temperature. The ratio and quantity of the resulting phases determine the properties of the product. It is known that austenitic steels can transform into α and/or ε martensite phases during plastic deformation The characteristics of the martensitic transformations induced by uni-axial tensile tests between room temperature and 200°C in a FeMnCr steel with 2,26 w% Cr content were examined. Mechanical properties as, yield stress were determined from tensile tests. Metallographic examinations, quantitative and qualitative phase analysis by X-ray diffraction were carried out on the uniformly elongated part of the samples (cross, longitudinal sections).

Introduction

Austenitic steels which perform TRIP/TWIP effect are attractive for automobile applications including press-formed parts due to their high energy absorption and structural reinforcement. Steels consisting of duplex austenite and ε martensite structures can exhibit multiple TRIP effects from deformation-induced phase transformation of austenite to ε martensite as well as ε martensite to α martensite. Chemical composition [2,3] and temperature [4] are known to be the main factors in controlling stacking fault energy (SFE) and consequently, determining the operative deformation mechanisms in high-Mn TWIP steels [5,6]. In general, deformation behavior becomes transformation-induced plasticity (TRIP) when the SFE is below 20 mJm^{-2}, twinning-induced plasticity when the SFE is 20–40 mJm^{-2}, shear-band-induced plasticity or microband-induced plasticity when the SFE is near 100 mJm^{-2} and slip when the SFE is above 100 mJm^{-2} [7,8,9]. Finally, the occurring deformation mechanisms determine the mechanical properties of the TRIP/TWIP steels. The effect of individual alloying elements on the SFE depends on the chemical composition of the steel. Because of this and the lack of the insufficient experimental data inconsistent conclusions can be found in the literature regarding the effect of individual alloying elements on SFE.

The aim of the present manuscript is to examine the mechanical properties of FeMnCr steels at different temperatures above room temperature, the resulting microstructures and the volume fractions of the stress/strain/temperature induced phases.

Experimental

Table 1. shows the composition of examined alloy. It was casted and hot rolled to 10 mm in diameter at the Freiberg University of Mining and Technology. The transformation temperatures austenite start-A_s, austenite finish-A_f, martensite start-M_s, martensite finish-M_f of the alloy were determined by dilatometric and Differential Scanning Calorimetric (DSC) methods (Table 2.).

Cylindrical tensile test specimens (length: 15 mm, diameter 8 mm) were machined from the ingots. The specimens were solution heat treated at 1000°C in Nitrogen atmosphere for 30 minutes and subsequently quenched in room temperature water.

Uni-axial tensile tests were performed between room temperature and 200°C with an Instron 5982 universal testing machine equipped with a climate chamber to obtain multiple TWIP/TRIP effects. The mechanical properties were characterized through tensile strength, yield stress and elongation data determined from the tensile tests. During the tensile tests the specimens were heated up to 300°C (holding temperature) then cooled down to the test temperature (isothermal treatment) than were loaded up to the fracture. The test temperatures were 25, 110, 125, 140, 160, 180, 200°C. After the fracture the specimens were cooled down to room temperature. Samples were cut from the longitudinal and cross section of the uniformly elongated part of the test specimens. Metallographic examinations by light microscopy (LM) and X-ray diffraction technique (XRD) were used to describe the characteristics and volume fractions of the phases, respectively. A Zeiss Axio Imager m1M optical microscope and a Bruker D8Advance dirfractometer equipped with an Eulerian cradle and Co radiation were used. The volume fractions were calculated by the APX 63 software based on the 2θ: 45°….130°scan. The specimens were mechanically polished and Beraha and nitric acid solution etchants were used.

[w%]	C	Mn	Cr	S	P	S
Steel 1	0,026	17,7	2,26	0,1	0,0051	0,029

Table1. The composition of the examined alloy

[°C]	A_s (ε→γ)	A_f (ε→γ)	M_s (γ→ε)	M_f (γ→ε)
Dilatometric	180	221	131	46
DSC	188	218	142	112

Table 2. The transformation temperatures of the examined alloy

Results and discussion

Table 2 shows the ε↔γ transformation temperatures of the alloy (thermally induced α does not form in this temperature range). The results of the two methods show good agreements except the M_f temperature. This effect is caused by the character of the γ→ε forward transformation and the large time constant of the applied heat flux DSC [10,11] Because of these effects the results obtained by the dilatometric measurements were considered. It is clear that the all of the samples were in austenitic state at the holding temperature (300°C) before the isothermal tensile test treatment. If the test temperature was lower than the M_s than thermally induced ε martensite formed before the tensile test. During the tensile test if the temperature was below the M_d, (stress/strain induced martensite start temperature) stress and/or train induced martensites (ε and/or α) could form. In the thermodynamic sense, if the M_f temperature was below the test temperature, an increase of the volume fraction of the thermally induced ε martensite was possible during the cooling from the test temperature to room temperature.

Figs 1 and 2 represent the metallographic features of the cross and longitudinal sections of the samples fractured at different temperatures, respectively. The microstructure is quite complex in both sections, but only the longitudinal sections show a deformed, curved structure. Two or three phases, twins and large-angle grain boundaries can be distinguished in the samples fractured at 25, 110, 125 and 140°C. At higher temperatures (180 and 200°C) the structure is simpler and the twins

are dominant. The XRD result of the cross and longitudinal sections can be seen in Figs. 3 and 4, respectively. These results confirm the LM observations. The "initial" data was obtained from the solution heat treated and quenched samples. It shows that the thermally induced ε martensite is dominant and only a few amount of austenite (12%) could be measured.

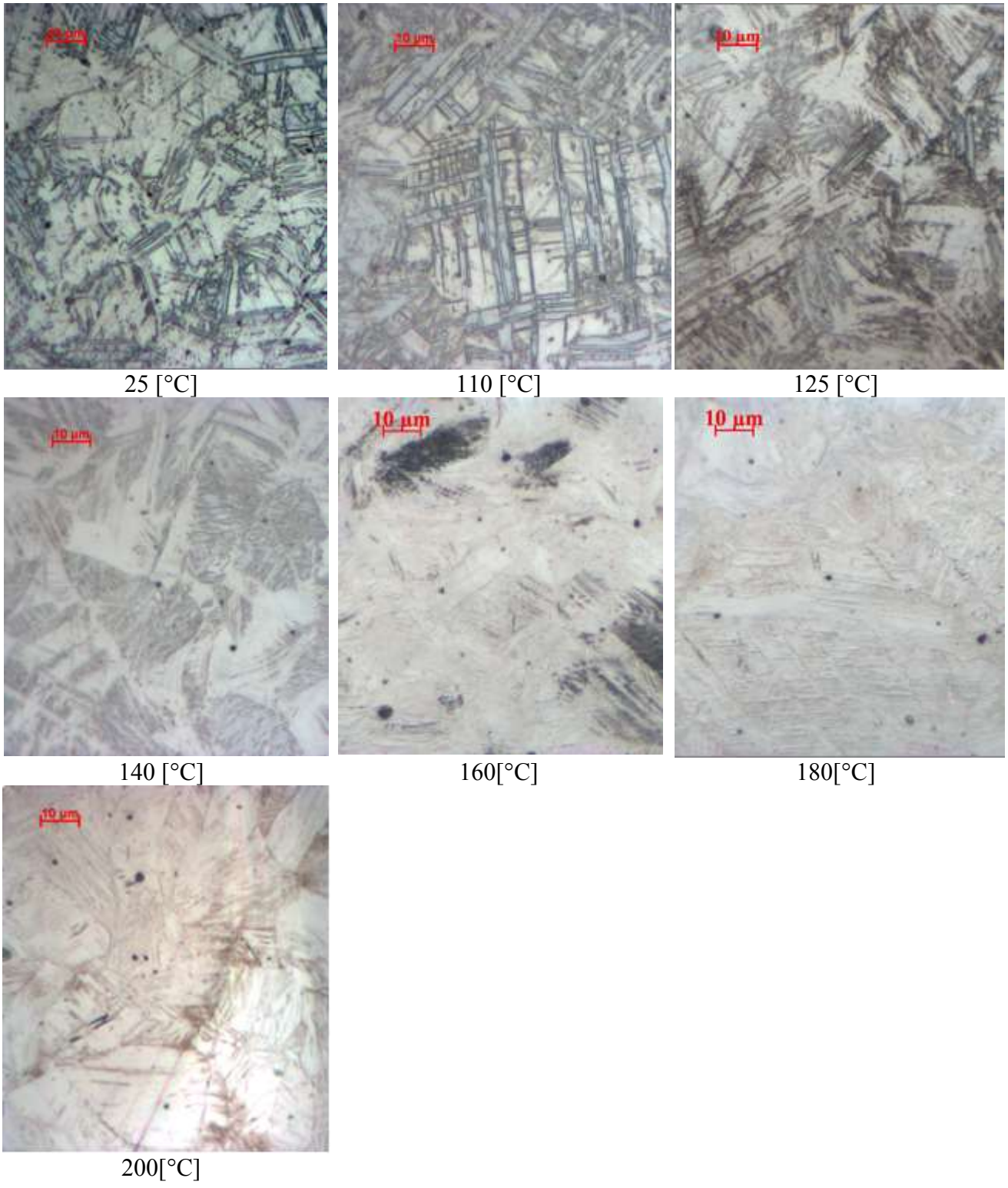

25 [°C] 110 [°C] 125 [°C]

140 [°C] 160[°C] 180[°C]

200[°C]

Fig. 1. LM pictures from the cross sections of the samples fractured at different temperatures

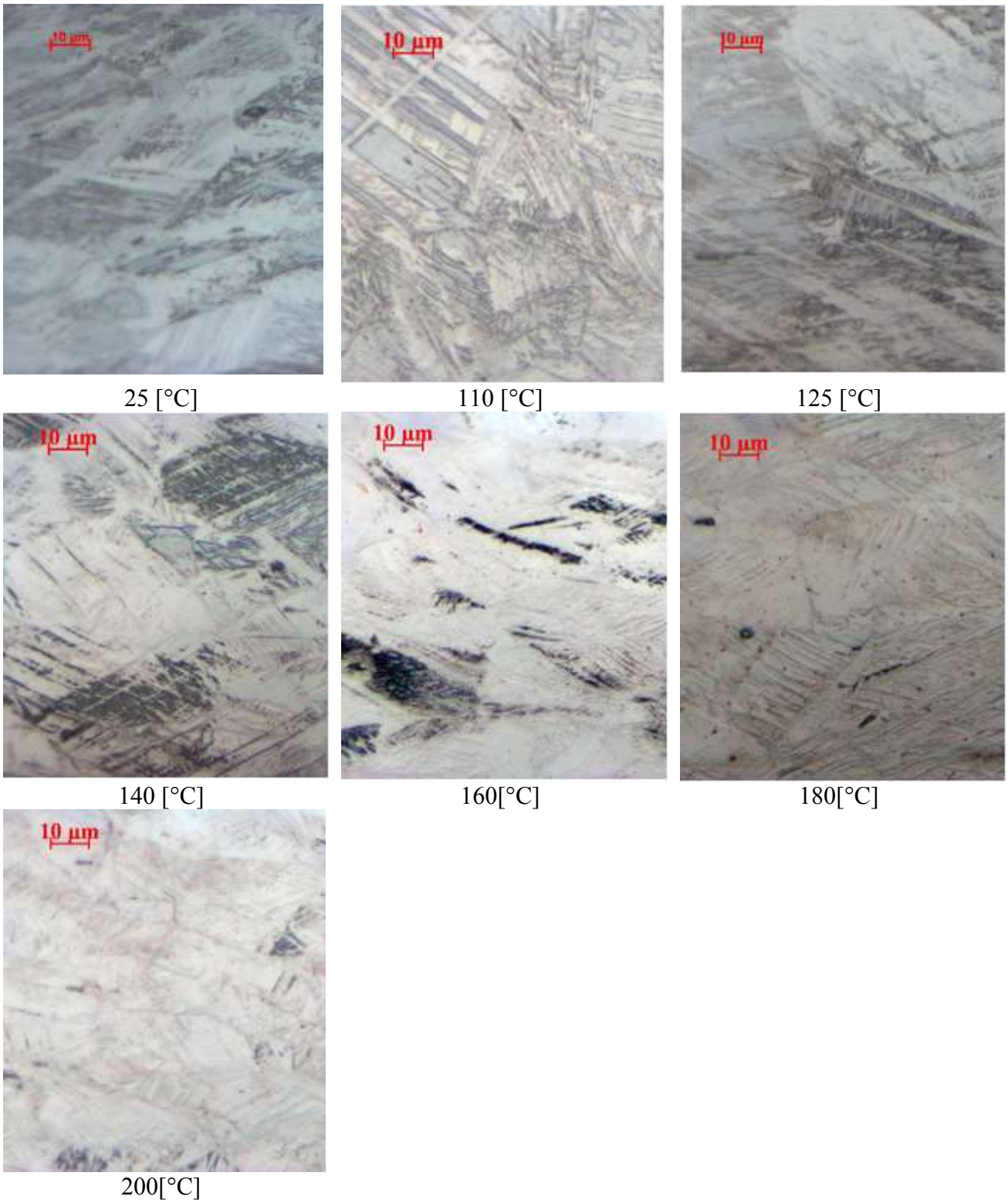

Fig. 2. LM pictures from the longitudinal sections of the samples fractured at different temperatures

During the tests at lower temperatures (25, 110, 125 and 140 °C.) untransformed austenite was present and both ε and α martensites were formed. The volume fraction curve of α martensites goes through a maximum as a function of the test temperature. At the higher temperatures thermally and mechanically induced ε martensite formed from the austenite phase. The M_d temperature for the α martensite is very close to 160°C.

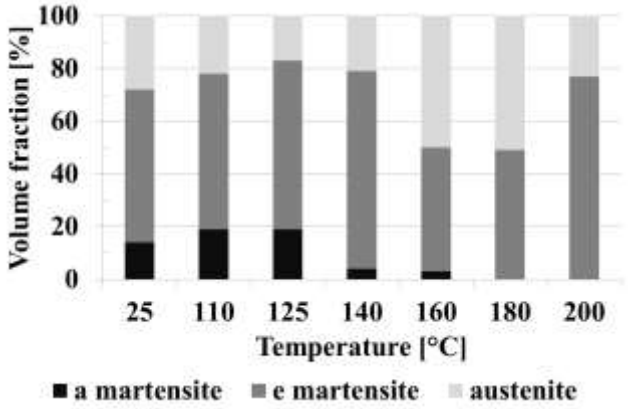

Fig. 3. Volume fraction measured at the longitudinal section.

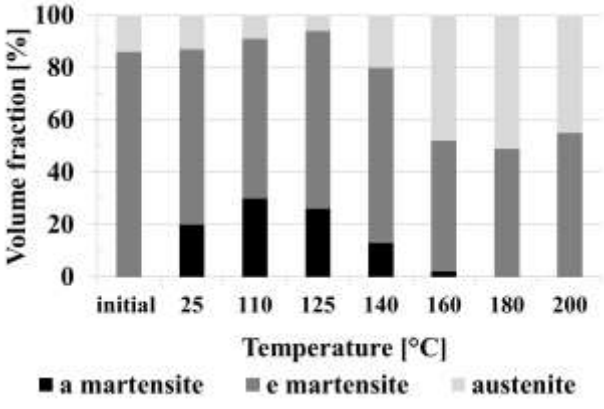

Fig. 4. Volume fraction measured at the cross section.

The true strain- true stress diagrams and the stress, strain parameters as a function of test temperatures determined from the tensile test diagrams can be seen in Figs. 5 and 6. These results have a good demonstration about the advantages of these types of alloys: the true stress exceeds the 1000 MPa even at 125 and 140 °C and the elongation exceeds the 60% at the same time. This high strength is associated with the maximum volume fraction of α martensite and the highest elongation is due to the ε martensite and austenite dual phase structure. Because the volume fraction of α martensite goes through a maximum, the tensile strength and elongation parameters also go through a maximum as function of temperature. Contrarily, the yield strength has a different character. The presence of α martensite drastically decreases the yield strength. If only the dual (austenite and ε martensite) structure is present the yield strength is nearly unchanged, not even if the temperature reaches the 200°C. The tensile curves loaded at 110, 125, 140°C show serrated phenomenon, which also associated the presence of α phase. This is what is called DSA-dynamic strain aging. During tensile testing, continuous jumps in the stress-strain curves are the consequence of the attractive interaction between diffused solute atoms in the alloys and mobile dislocations [12,13].

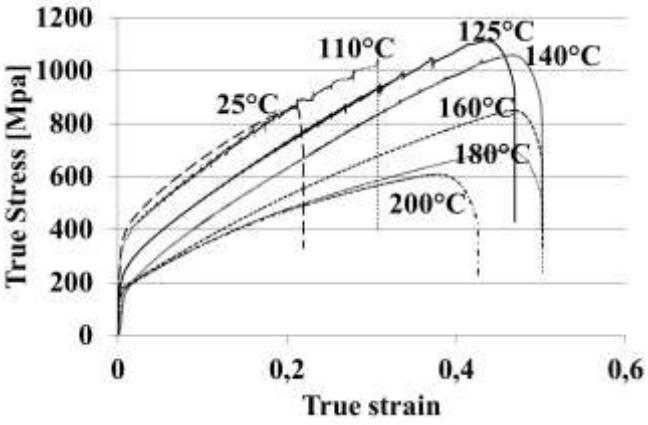

Fig. 5. The true stress-true strain curves at different tests temperatures

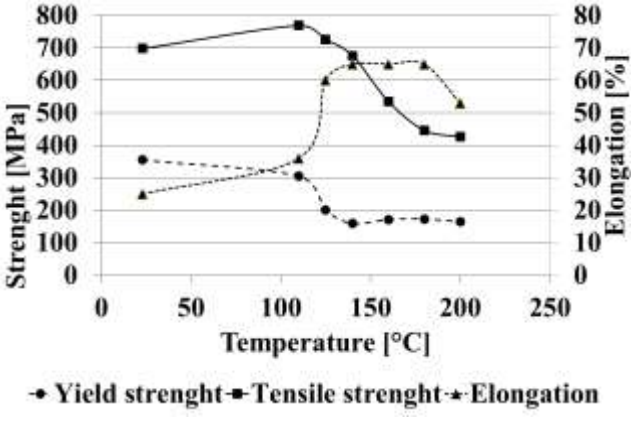

Fig. 6. Yield strength, tensile strength and elongation at different temperatures.

Summary

The characteristics of the martensitic transformations induced by uni-axial tensile tests between room temperature and 200°C in a FeMnCr steel with 17,7 Mn and 2,26 w% Cr contents were

examined. Mechanical parameters as tensile strength yield stress, elongation, true stress-true strain curves were determined from the tensile test. Metallographic examinations, quantitative and qualitative phase analysis by X-ray diffraction were carried out on the uniformly elongated part of the samples (cross, longitudinal section). It was shown that the presence of mechanically induced α martensite causes an increase in tensile strength but decrease in yield strength and the DSA-dynamic strain aging effect also can be observed. The maximum elongation was reached when the austenite and thermally and mechanically induced ε martensite dual structure was formed.

Acknowledgement
This work has been carried out as part of the OTKA K 84065 and the TÁMOP-4.2.1.B-10/2/KONV-2010-0001 projects within the framework of the New Hungarian Development Plan. The realization of this project is supported by the European Union, co-financed by the European Social Fund. The authors say thanks for Mr. Michael Hauser for the data of the transformation temperatures.

References

[1] H. Bhadeshia, R. Honeycombe, Steels, Microstructure and Properties, Third edition, Butterworth-Heinemann publications, Great Britain, 2006
[2] L. Mosecker, A.S.Akbari, Nitrogen in chromium–manganese stainless steels: a review on the evaluation of stacking fault energy by computational thermodynamics, Sci. Technol. Adv. Mater.14 (2013) 033001 (14pp)
[3] A. Dumay, J.-P. Chateau, S. Allain, S. Migot, O. Bouaziz, Influence of addition elements on the stacking-fault energy and mechanical properties of an austenitic Fe–Mn–C steel, Materials Science and Engineering A 483–484 (2008) 184–187
[4] L. Remy, A. Pineau, Temperature dependence of stacking fault energy in close-packed metals and, materials Science and Engineering, 36 (1978) 47 – 63
[5] S.Allain, J.-P. Chateau, O.Bouaziz, S.Migot, N.Guelton, Correlations between the calculated stacking fault energy and the plasticity mechanisms in Fe-Mn-C Alloys, Mat. Sci. Eng. A 387-389 (2004) 158-162
[6] L. Remy, A. Pineau, Twinning and strain-induced F.C.C. - H.C.P. transformation in the Fe-Mn-Cr-C system, Mater. Sci. Eng. 28, (1977) 99-107
[7] K. H.Kwon, B-C. Suh, S.Baik, Y-W. Kim, J-K. Choi, N.J. Kim, Deformation behavior of duplex austenite and ε martensite high-Mn steel, Sci. Technol. Adv. Mater. 14 (2013) 014204 (8pp)
[8] A.S. Hamada, L.P. Karjalainen, Hot ductility behaviour of high-Mn TWIP steels, Materials Science and Engineering A 528 (2011) 1819–1827
[9] O. Bouaziz, N. Gu, Modelling of TWIP effect on work-hardening, Materials Science and Engineering A319–321 (2001) 246–249
[10] Benke M, Tranta F, Barkóczy P, Mertinger V, Daróczi L, Effects of heat flux features on the differential scanning calorimetry curve of a thermoelastic martensitic transformation, Mat. Sci. Eng. A-Structural Materials Properties Microstrucure and Processing 481: pp. 522-525. (2008)
[11] M. Benke, F. Tranta, P. Barkóczy, V. Mertinger, L. Daróczi, Supplement on "Effects of heat-flux features on the differential scanning calorimetry curve of a thermoelastic martensitic transformation, Mat. Sci. Eng. A-Structural Materials Properties Microstrucure and Processing 527:(9) pp. 2441-2443. (2010)
[12] L. Bracke Steels, Microstructure and Properties, Deformation behaviour of Austenitic Fe-Mn
[13] L. Chen, H.S. Kim, S.K. Kim, B. C. de Cooman, Localized Deformation due to Portevin–LeChatelier Effect in 18Mn–0.6C TWIP Austenitic Steel, ISIJ International, Vol. 47 (2007), No. 12, pp. 1804–1812

Necklace Formation During Dynamic Recrystallization of 5182 Aluminium Alloy Under Isothermal Compression

Tamás Mikó

PhD Student, Institute of Physical Metallurgy, Metal Forming & Nanotechnology, University of Miskolc, H-3515, Egyetemváros, Miskolc, Hungary

femmiko@uni-miskolc.hu

Keywords: DRX, necklace, grain refinement, hot compression test, aluminium alloy

Abstract

Dynamic recrystallization (DRX) characteristics of an 5182 Al alloy was investigated at temperatures ranging from 673 K- 773 K and constant strain rates of 0.01 s^{-1}, 0.1 s^{-1}, 1 s^{-1}, 10 s^{-1}, and 50 s^{-1}. The average grain size of the as-casted alloy was 160 μm and was refined to 20 μm via deformation at 773 K, 50 s^{-1} to a strain level of 0.5 (40%). The true stress-strain curves were determined and divided into two main groups based on the temperatures and strain rates. The activation energy of the DRX in the examined aluminum alloys was calculated, being 175,87 kJ/mol. During the crystallization process compound phases were crystallized along the border of initial grains due to the great content of Mg, Mn and Fe. It was deduced from the metallography examination that most of the new grains formed via necklacing mechanism from the mentioned borders during the DRX.

Introduction

Discontinuous dynamic recrystallization (dDRX) is an important phenomenon for controlling the microstructure and mechanical properties during hot working. If this softening process is operating, the aluminum grains are refined [1]. The evolution of the dynamically recrystallized microstructure is specifically different from microstructure development during static recrystallization after cold working. The nucleation of DRX in poly-crystals predominantly proceeds from prior grain boundaries and expands into the unrecrystallized volume. The reason of this the dislocation density is bigger near by the grain boundary than inside the grains. The activation energy of nucleation is smaller along the original grain border and therefore at the first period of DRX the new grains occurs along to the deformed original grain boundaries. This newly created microstructure is called a necklace structure. In Fig.1 the microstructure development according to the necklacing mechanism is shown schematically [2].

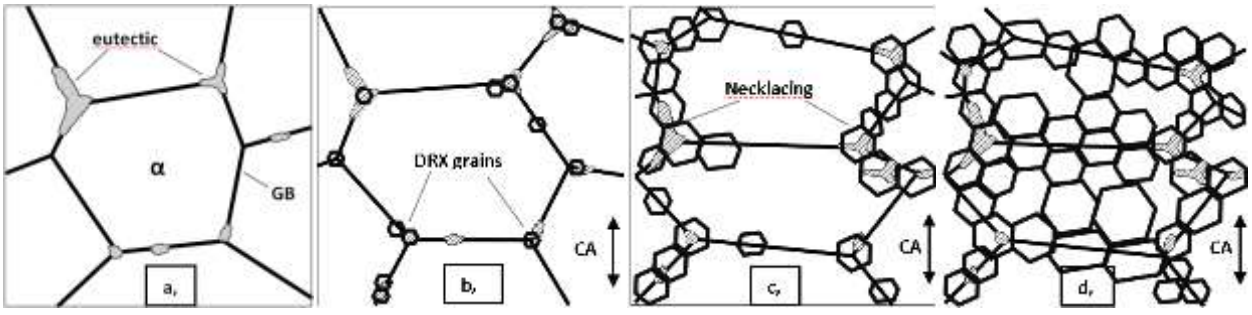

Fig. 1. Microstructure evolution by the necklacing mechanism in 5182 Al alloy.

Almost all in the alloys used in practice, compound phases can be found in the high-angle grain boundaries Fig 1(a). When reaching the critical deformation, the energy required for the nucleation of new grains is usually reached at these areas due the high magnitude of stored energy Fig 1(b) [3]. With the constant raising of the deformation more and more new grains appear and the so called necklace structure forms Fig 1(c). This structure fills different extent of available space depending on the strain, temperature, and the strain rate Fig 1(d). Increasing the hot working temperature and the applied strain rate the driving force of this mechanism is raises. The carried out examinations proved this phenomenon.

1. Test material

Aluminum 5182 alloy is a wrought alloy type with a good corrosion resistance. It is mainly used in sheet or plate form but can be obtained as extrusions as well. The chemical compositions of these alloys are (wt.%) 4.3 Mg; 0.25 Mn; 0.3 Fe; 0.15 Si; 0.1 Cu; 0.1 Cr; 0.1 Zn; 0,1Ti; Al (balance). The state of experimented material was as-cast. Two types of compounds solidify during cooling besides the alpha solid solution according to the performed DSC examinations. The first compound crystallizes at 877 K, the second one at 846 K, on the grain boundaries of the alpha solid solution. The approximate compositions were determined by scanning electron microscopy. Al6MnFe and Mg2Si compounds were found at the grain boundaries Fig. 2.

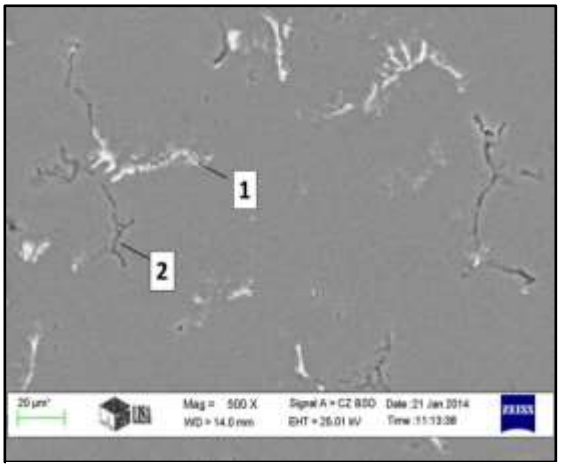

Fig. 2. SEM image of the as-casted sample

2. Experimental procedure

Firstly, cylindrical specimens were machined with a diameter of 10 mm and a height of 15 mm from the as-cast ingots. Grooves on both sides of each specimen were machined and filled with glass powder as lubricant to reduce the friction between the dies and specimen. A Servotest 500 kN servo hydraulically equipment was used for warm compression tests. The specimens prior to isothermal compression were preheated with induction heating and held for 40 sec at the deformation temperature to obtain a uniform deformation temperature Fig. 3. Then these were overheated with 25 K and moved with a manipulator into the furnace where the testing was performed. All the thirteen specimens were compressed to true strain of 0.5 (height reduction of 40%) in a furnace at the temperatures of 673 K, 723 K, and 773 K, and the strain rates of 0.01 s^{-1}, 0.1 s^{-1}, 1 s^{-1}, 10 s^{-1} and 50 s^{-1}.

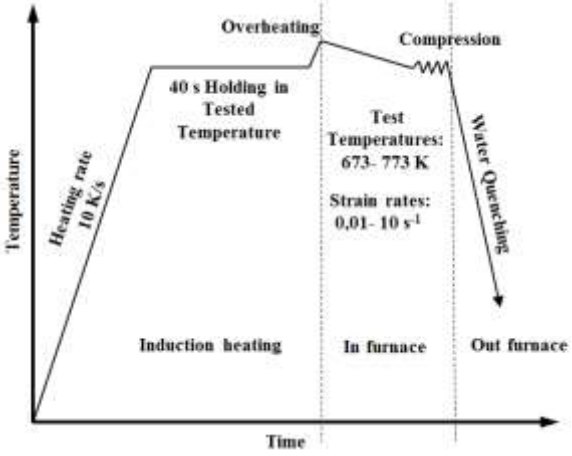

Fig. 3. Experimental procedure for hot compression tests

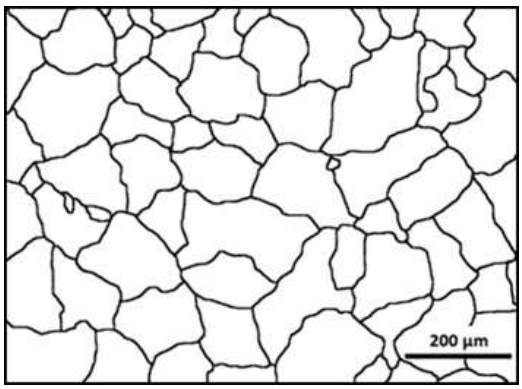

Fig. 4. The initial casted microstructure (100X)

The samples were quenched immediately after deformation to investigate the DRX microstructure. All the specimens were sectioned perpendicular to the longitudinal compression axis for metallographic examination. The sections were polished and etched with Barker reagent. The new structures of the crystallites were investigated with optical microscopy. Five photos were taken from each specimen in same scale. The grains visible under polarized light were contoured and transformed to binary images Fig. 4. A Leica software was used for the image analysis [4]. The number of grains, the diameter of the grains, and the boundary interface were measured by the image analyzer software. All the thirteen tested specimens were investigated with these procedures.

3. Results and discussion

3.1. Flow curves

The microstructure evolution and deformation mechanism during hot working are closely related to the flow stress. [5] Flow curves obtained at different temperatures and strain rates are shown in Figs. 5 and 6. Looking at the stress-strain curves it can be seen that the effect of the temperature and strain rate on the flow stress are significant. Lower strain rates and higher temperatures will decrease the flow stress, while higher strain rates and lower temperatures will increase the flow stress of the 5182 aluminum alloy. The effect of strain rate is much more significant than the effect of deformation temperature.

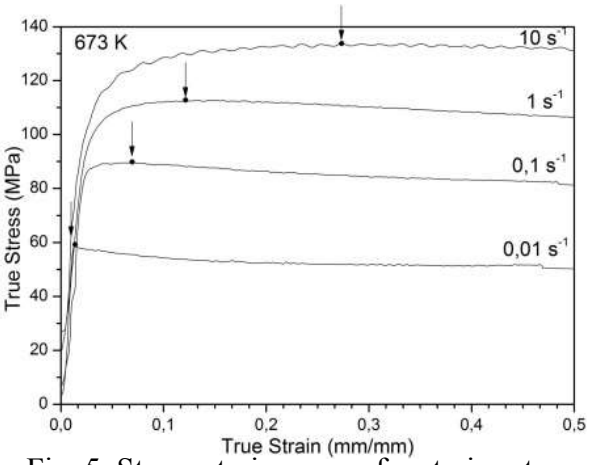

Fig. 5. Stress-strain curves for strain rates 0.01- 10 s^{-1} at 673 K

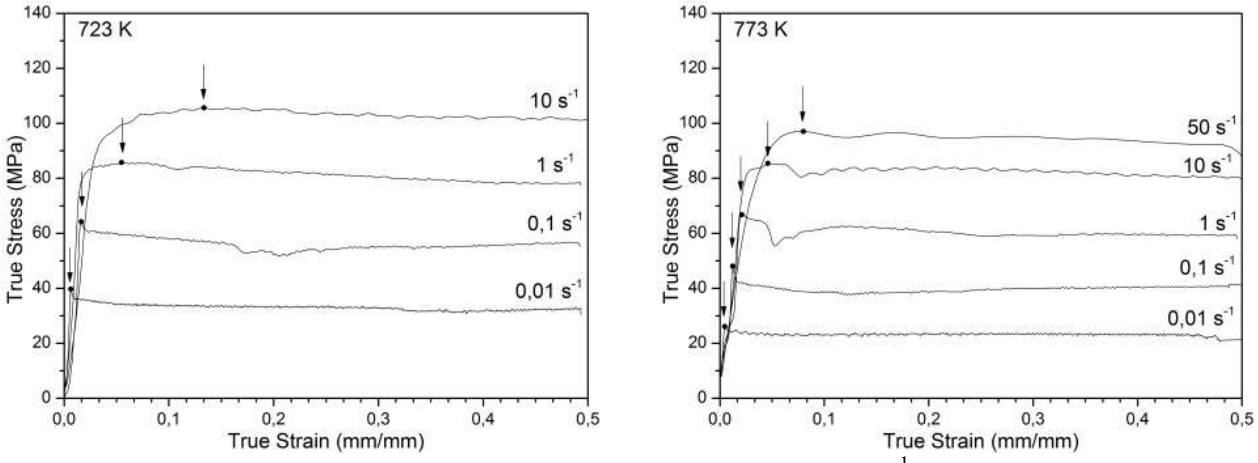

Fig. 6. Stress-strain curves for strain rates 0.01- 50 s^{-1} at 723- 773 K

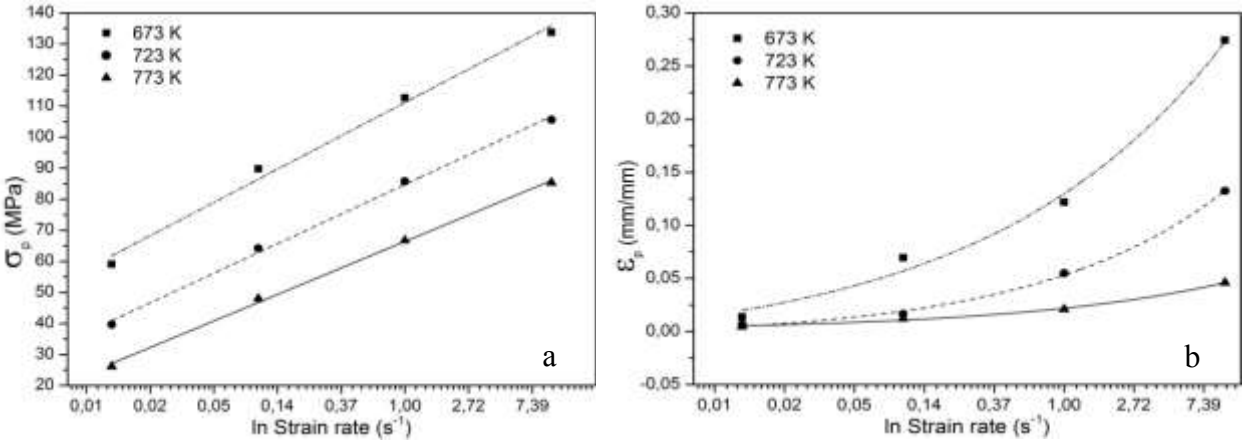

Fig. 7. The peak stress and peak strain dependence on the temperature and strain rate

As shown in Fig. 7(a), the mentioned effect can be clearly seen. There is a linear relationship between the value of peak stress and strain rate. For higher strain rates the peak strain increases in a non-linear way Fig. 7(b).The flow curves can be divided into two main groups. One of them exhibit typical DRX behavior with a single peak stress followed by a gradual fall towards a steady state stress Fig.8(a). These peak stresses belong to a minor peak strains. These samples were deformed with at 573 K strain rate ($0.01s^{-1}$) at 623 K strain rates (0.01-0.1 s^{-1}) and at 773 K strain rates (0.01-1 s^{-1}). For the case of the other groups of flow curves the peak stresses are not too sharps, and the gradual fall after them can not to be seen. The peak strains are much greater on these curves. These samples were deformed with typically high strain rates in the case of all the investigated temperatures. If the grain structures corresponding to the flow curves are checked, it can be stated, that although recrystallized grains are found in all samples, but significant recrystallization is only present in the samples of b-type flow curves.

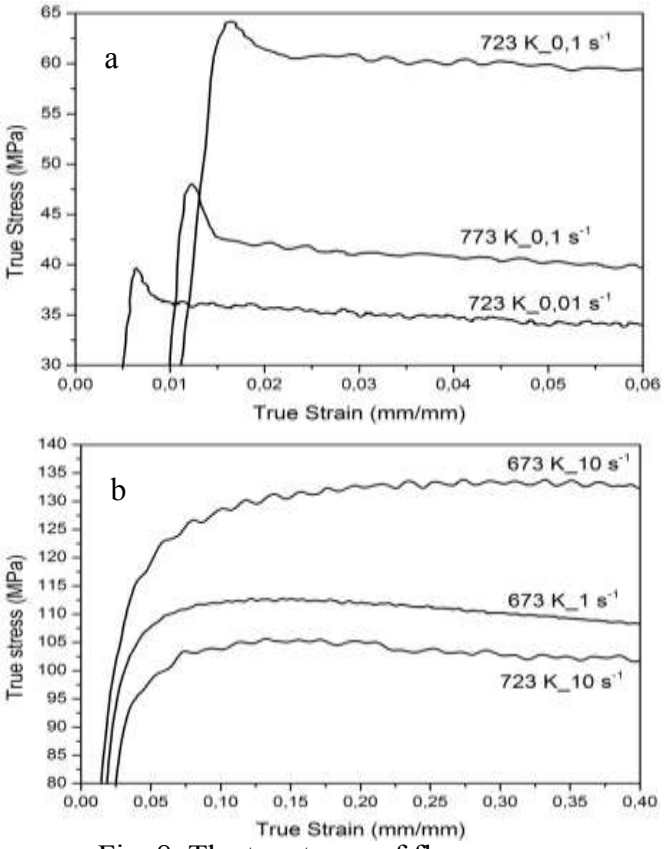

Fig. 8. The two types of flow curves

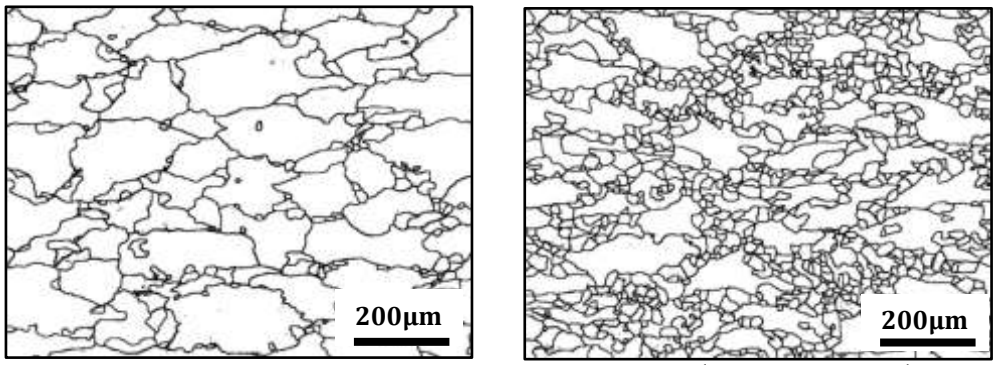

Fig.9. Typical microstructural at: (a) 773 K 0,01 s^{-1}(b) 773 K 10 s^{-1}

3.2. Grain refinement during DRX

As shown in Fig. 10 the mentioned necklace mechanism occur during hot working. Where is eutectic along the grain boundary there are much more new grain. The initial and DRX grain structures can be seen in the Fig. 11. The grain size distribution charts shows that the average grain size of the as-cast material is 160 μm. In contrast that the average grain size of the hot worked material is 20 μm. It is clearly seen that the sample which was deformed with maximal strain of 0.5 temperature of 773 K and 50 s^{-1} strain rate contained parent grains, but already the half microstructure was recrystallized during hot working. In order to distinguish the non-deformed original grains from the DRX grains, the recrystallized grains are defined as grains having an average diameter of <50 μm and the volume fraction of fine grains V_f is defined as follows [6]:

$$V_f = \frac{\text{Total area of individual fine grains } \sum A_f}{\text{Total sampling area } \sum A_i}$$

The amount of DRX grains increased with temperature and strain rate as seen in Fig. 12. The recrystallized volume fraction increases significantly when the strain rate is greater than 1 s^{-1} and the temperature is 773 K. The maximum volume of new grains is 48 %.

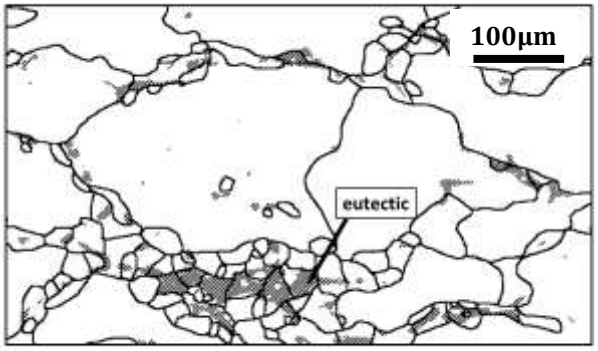

Fig. 10. The necklaced structure along to the original grain boundary and the eutectic

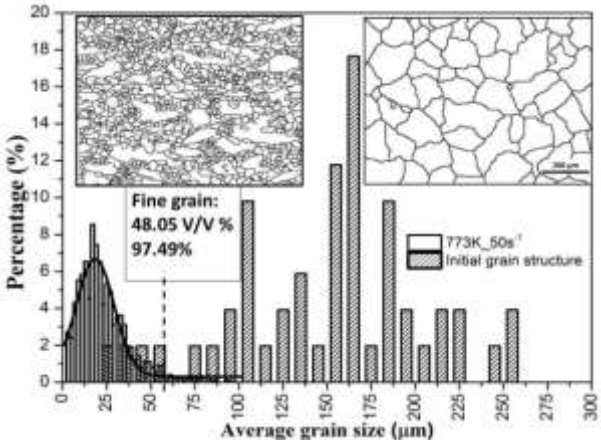

Fig. 11. The initial and hot formed grain structure and grain size distribution charts

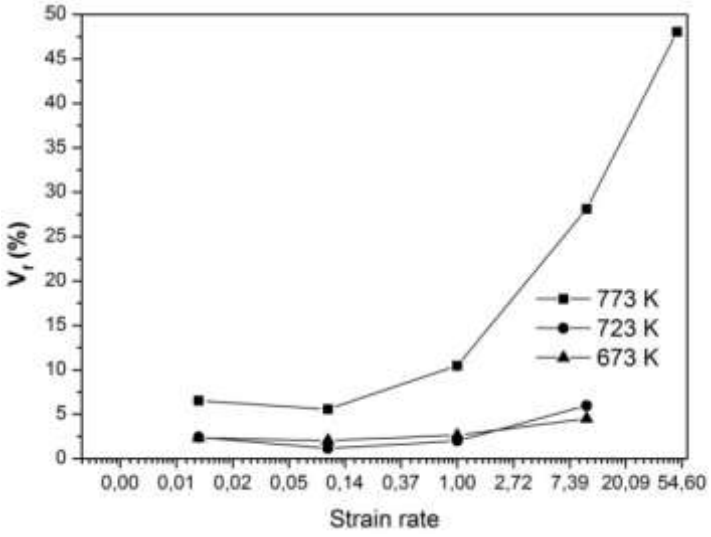

Fig. 12. The amount of DRX grains increased with temperature and strain rate

4. Conclusion

The structure of the investigated as-cast material has a great impact on the DRX process. The nucleation and grain grow of recrystallized grains occur along the eutectic phase. This is because these phases inhibit the free movement of dislocations, and the strain degree is much greater at the grain boundary where compound phases are also present. The flows curves can be divided into two main groups depend on the temperatures and strain rates. The used 0.5 maximum strain was not sufficient for the total recrystallization of the as-cast structure. The used strain rate has the biggest effect to the volume of DRX grains. The recrystallized volume fraction increases significantly when the strain rate is greater than 1 s^{-1} and the temperature is 773 K.

Acknowledgments

The author acknowledges with gratitude the assistance of the Chair of Metal Forming at Montan Universität Leoben, for the hot compression tests and for the metallographic preparation.

The research work presented in this paper based on the results achieved within the TÁMOP-4.2.1.B-10/2/KONV-2010-0001 project and carried out as part of the TÁMOP-4.2.2.A-11/1/KONV-2012-0019 project in the framework of the New Széchenyi Plan. The realization of this project is supported by the European Union, and co-financed by the European Social Fund.

References

[1] M. Jafari, A. Najafizadeh, Comparison between the Methods of Determining the Critical Stress for Initiation of Dynamic Recrystallization in 316 Stainless Steel, J. Mater. Science, Vol. 24, (2008) 840-844.

[2] D. Ponge, G. Gottstein, Necklace formation during dynamic recrystallization: mechanism and impact on flow behaviour, Acta Mater.*,* Vol. 46, (1998) 69-80.

[3] Sakai, T., Belyakov, A., Kaibyshev, R., Miura, H., Jonas, J.J., Dynamic and Post-Dynamic Recrystallization under Hot, Cold and Severe Plastic Deformation Conditions, Progress in Materials Science*,* 2013.

[4] Csaba Póliska, Zoltán Gácsi, Péter Barkóczy, The Effect of Melt Flow on the Dendrite Morphology, MATERIALS SCIENCE FORUM 508 (2006) 169-174.

[5] R. Ebrahimi, S. Solhjoo, Characteristic Points of Stress-Strain Curve at High Temperature, International Journal of ISSI, (2007) 24-27,

[6] J. C. Tan, M. J. Tan, Dynamic continuos recrystallization characteristics in two stage deformation of Mg-3Al-1Zn alloy sheet, Materials Science and Engineering, A339, (2003) 124-132.

Optimizing steel-making secondary metallurgy slag at ISD DUNAFERR Zrt.

Róbert MÓGER*, Mihály RÉGER, Alfred ENDER**, Róbert JÓZSA*, Krisztián WIZNER***
***ISD Dunaferr Co. Ltd., Dunaújváros, Hungary,**
****Óbuda University, Budapest, Hungary**

Introduction

ISD DUNAFERR Co. Ltd., formerly named as Dunai Vasmű (Danube Ironworks), has a history of over half a century. Currently it is the only factory in Hungary that is operated by integrated steel-making technology and has a hot metal production capacity of 1.7 million tons (**Figure 1**). The metallurgical combine includes coke production, hot metal production, steel-making, hot and cold rolling, profiling and manufacturing of galvanized products too. Steel is produced by 2 BOFs with the capacity of 135 tons each.

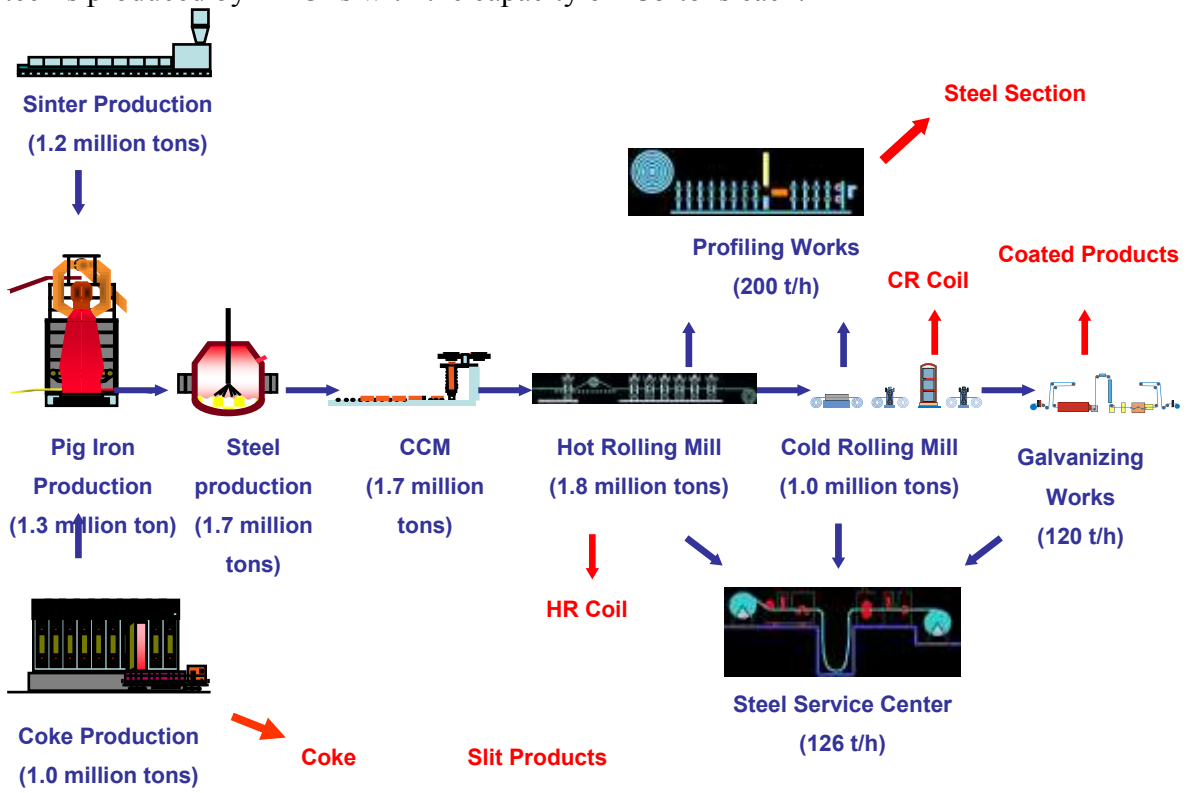

Figure 1 Production process of ISD DUNAFERR Co. Ltd.

Produced steel heats are metallurgically treated at a 3-position ladle metallurgical station, where composition and temperature parameters can be monitored, heats can be flushed with inert gas, corrected by alloying additions (wires or pieces), inclusion modifying agent can be added (Ca-cored wire), as well as the temperature of steel heat can be decreased in a controlled way. There is no heating possibility at the metallurgical station.

The formation of slag of adequate quantity and consistency is of special importance during steel-making. The main function of primary slag in BOF is to bond the sulphur and phosphorus content of steel, however this slag is disadvantageous from the point of view of its treatment following steel tapping, primarily due to its high FeO content.

During tapping the primary slag with high oxygen content, flowing from BOF increases alloying addition burn-off, as well as the additional quantity of deoxidizing agent used for bonding additional oxygen represents inclusion input in steel, which definitely has adverse effect on the quality of steel. Floating ball method is applied to decrease primary slag flowing through.

Instead of the primary slag retained in the BOF a new active secondary metallurgy slag is formed in the casting ladle during tapping. The function of secondary metallurgy slag is to bond the impurities content of steel and developed deoxidation products, thermal insulation and protection of the steel bath from reoxidation.
The secondary metallurgy slag has to be of adequate composition and consistency so as to be capable of performing adequate metallurgical work. It is often experienced during secondary metallurgy slag forming technology used at DUNAFERR that the slag does not have adequate properties for the performance of required metallurgical work.
The problem is that the physical condition of secondary metallurgy slag - in many cases - is such that does not facilitate the optimal taking place of metal-slag boundary processes. For the above reasons we set the aim of forming a secondary metallurgy slag by using the possible least solid slag-forming additions, which acts as a homogeneous system during the metallurgical activity (has adequate viscosity and melting point) and adequately performs its tasks, as well as it is cost-effective. ISD DUNAFERR Co. Ltd. launched a research project together with Óbuda University with the aim of forming secondary metallurgy slags of adequate properties (tender no. TÁMOP4.2.1. B11/2/KMR-2011-0001).
Detailed physical and thermodynamic analytical principles were presented in a former publication [1].

Statistical analyzes and modelling
The consistency of slags - formed during the production of mild steels - included in the test was considered subjectively, in a former test, by visual inspection. Based on this slags were classified in non-fluid and fluid categories. Composition of slags was analysed by significance test (95% significance level, Student-test [2]) (**Table 1**).

Table 1 Statistical basic data and the result of significance test in the group of „fluid“ and „non-fluid“ slags

Changing	„fluid” slag (n=206) average and standard deviation	„non-fluid” slag (n=124) average and standard deviation	Probability level > 95%
FeO SLES	9.8 $\pm$ 2.4	9.6 $\pm$ 3.0	„fluid” = „non-fluid”
CaO SLES	55.8 + 2.8	57.8 + 3.2	„fluid” < „non-fluid”
SiO_2 SLES	8.2 + 2.2	9.3 + 2.9	„fluid” ~ „non-fluid”
Al_2O_3 SLES	18.9 + 4.5	16.2 + 5.2	„fluid” > „non-fluid”

CaO and SiO_2 content of secondary metallurgy slag is also significantly different in the two slag classes, the increasing quantity of these has "non-fluid" slag forming effect. CaO increase results in higher liquidus temperature, thereby higher solid phase ratio at a given temperature. Higher value of Al_2O_3 content of secondary metallurgy slag is favourable for the forming of "fluid" slag.

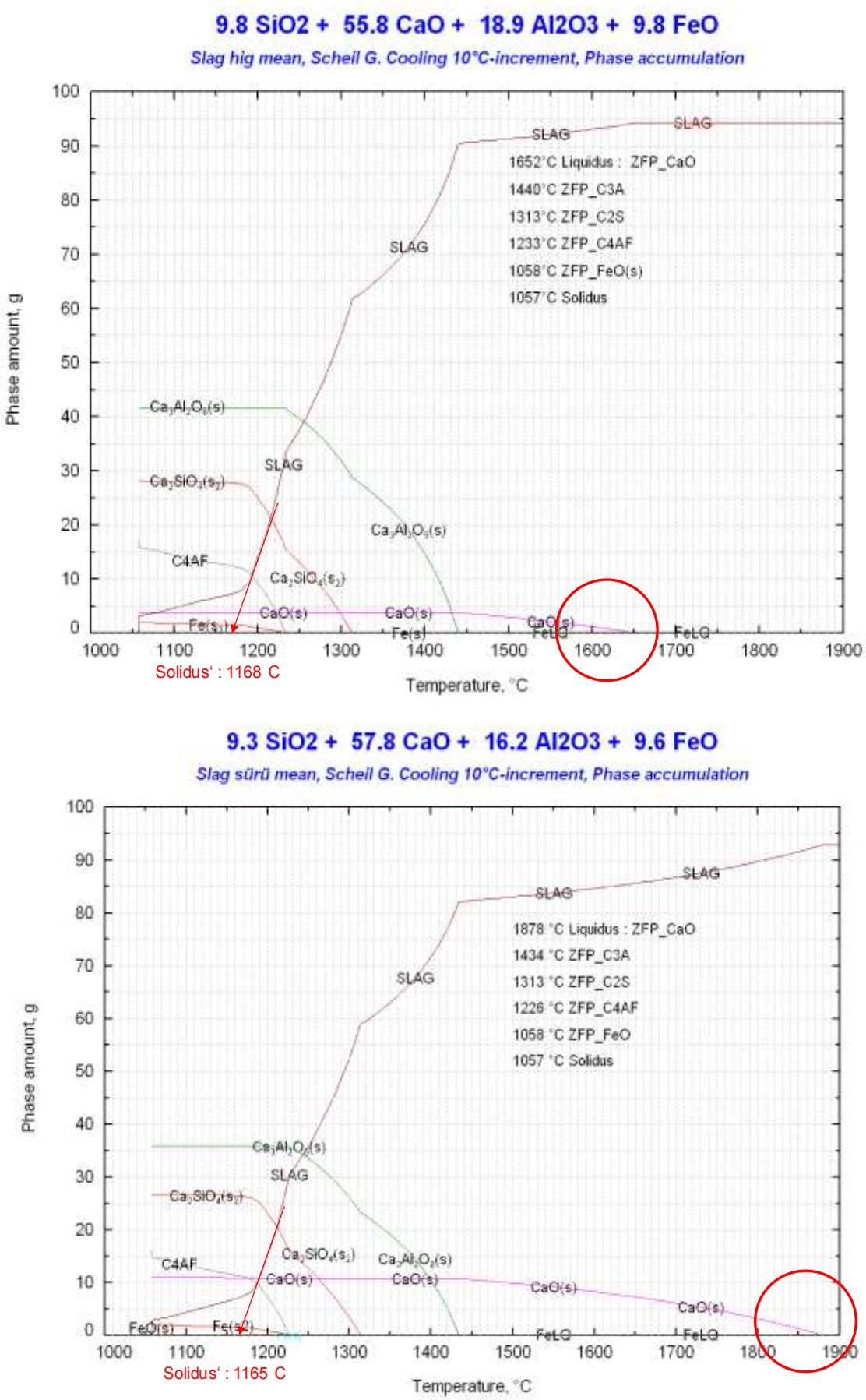

Figure 2 Initial freezing temperatures of "fluid" and "non-fluid" slags during the equilibrium freezing process

So it can be stated that small differences in average CaO, SiO_2 and Al_2O_3 contents of "fluid" and "non-fluid" secondary metallurgy slags represent significant difference between the two classes.

Equilibrium freezing processes of "fluid" and "non-fluid" slags were compared by using FactSage-5.5 version [3], „Equilibrium”-module, the result of which is presented by **Figure 2**.

The composition of melt parts was modelled with the help of the same software during the freezing process. The research stated that the most important difference between "fluid" and "non-fluid" slags is in CaO saturation. CaO content is 65% in case of "non-fluid" slags, while this value was 59% in case of "fluid" slags.
We studied the solid fraction of "fluid" and "non-fluid" slags, as well as the viscosity of slag of suspension kind, and the conclusion was that there is more solid fraction in the case of "non-fluid" slags (**Figure 3**). The relative viscosity rise of "fluid" slag is 14%, while it is about 50% for "non-fluid" slag group as an effect of CaO-C3A precipitation transition at about 1440°C.

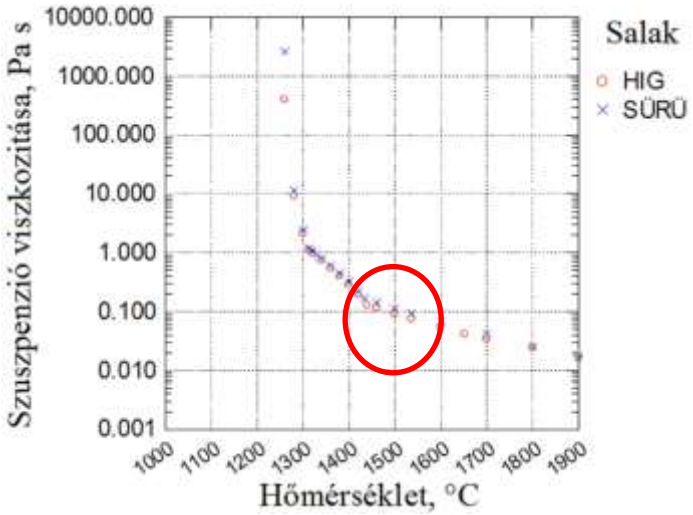

Figure 3 Change in the viscosity of "fluid" and "non-fluid" slag of suspension kind in relation to temperature

A research program was launched [4] in order to optimize the physical and metallurgical properties of secondary metallurgy slag by changing its composition.
The field marking the initial composition of secondary metallurgy slag is indicated on the magnified $CaO\text{-}Al_2O_3\text{-}SiO_2$ ternary diagram (**Figure 4)**.

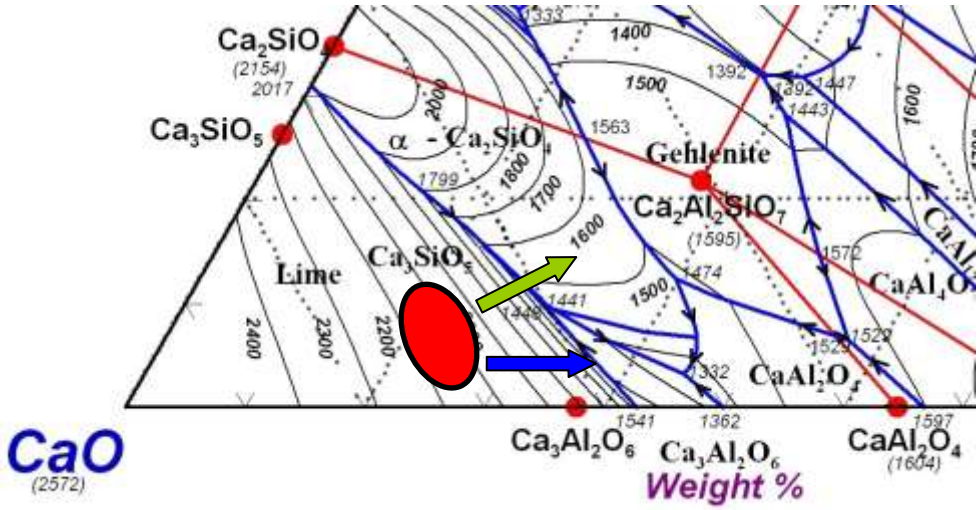

Figure 4 Magnified CaO peak of $CaO-Al_2O_3-SiO_2$ ternary diagram

We wanted to decrease the melting point of the studied slag in two different ways: one solution was to increase Al_2O_3-content, while another was to increase SiO_2- and Al_2O_3-content together. These two solutions are presented by the arrows indicated on **Figure 4**.
Thermomechanically rolled, fine grained structural steels (S355MC, S420MC, etc.) became the subject of the research. Calculations regarding the review of the relations between slag composition and viscosity were made with FactSage- 5.5 version, „Equilibrium"-module. Thermodynamic database [5] was used in relation to $CaO-Al_2O_3-SiO_2-FeO-Fe_2O_3$ system.

Performed tests

In the first series of researches we studied the effect of aluminate slag (aluminium metallurgical by-product) charged in various quantities on slag properties. Having various aluminate slag consumptions (50 kg, 100 kg, 150 kg) we studied the properties of developed secondary metallurgy slag based on the processing of various parameters of almost 27 steel heats.
Based on plant observations, slag analyses and final samples of steels it was stated that the highest degree of desulphurization could be realized by charging 100 kg/heat aluminate slag (ΔS=0.0035%). Fluidity of slag showed the most favourable values also in the case of charging 100 kg/heat aluminate slag. As a result of plant observations it was stated that granulometric composition of charged aluminate slag (dust) is not adequate, as high extent of dust emission could be experienced during its usage. It has to be used in some way during further research in the form of briquette.
In the second series of researches Al_2O_3- and SiO_2-content of slag was increased by adding fireclay. Al_2O_3 and SiO_2 have the ratios of 40-40% in the composition of fireclay.
During the research we want to change the quantity of fireclay in test heats in the quantities of 50, 100, 150, 200 kg/heat. Up to the time of presentation fireclay was charged into secondary metallurgy slag in the quantities of 50 kg for production of 15 heats and 100 kg for production of 15 heats.
Based on theoretical model tests the effect of fireclay changes the melting point of the melt in the way presented by Figure (**Figure 5**), in case of various charged quantities thereof.

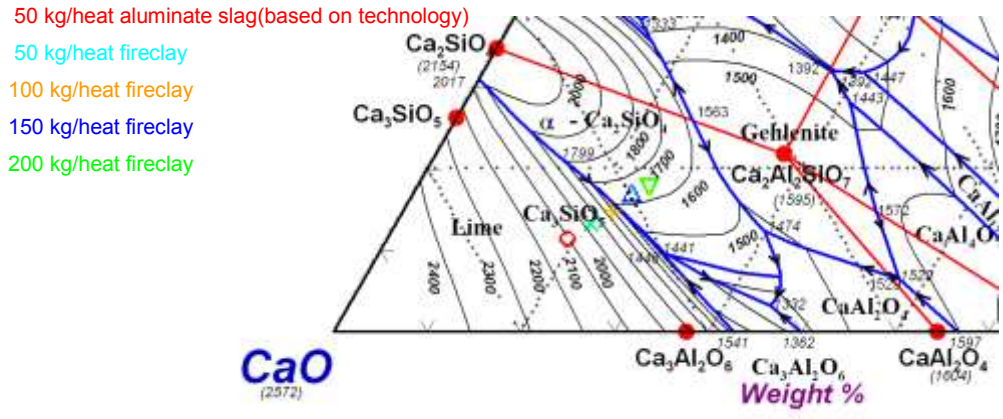

Figure 5 Effect of fireclay on the melting point of the slag system

The above ternary diagram and the model test performed by the FactSage software (**Figure 6**) both proved that the liquidus temperature of slag can be significantly decreased by increasing the quantity of fireclay.

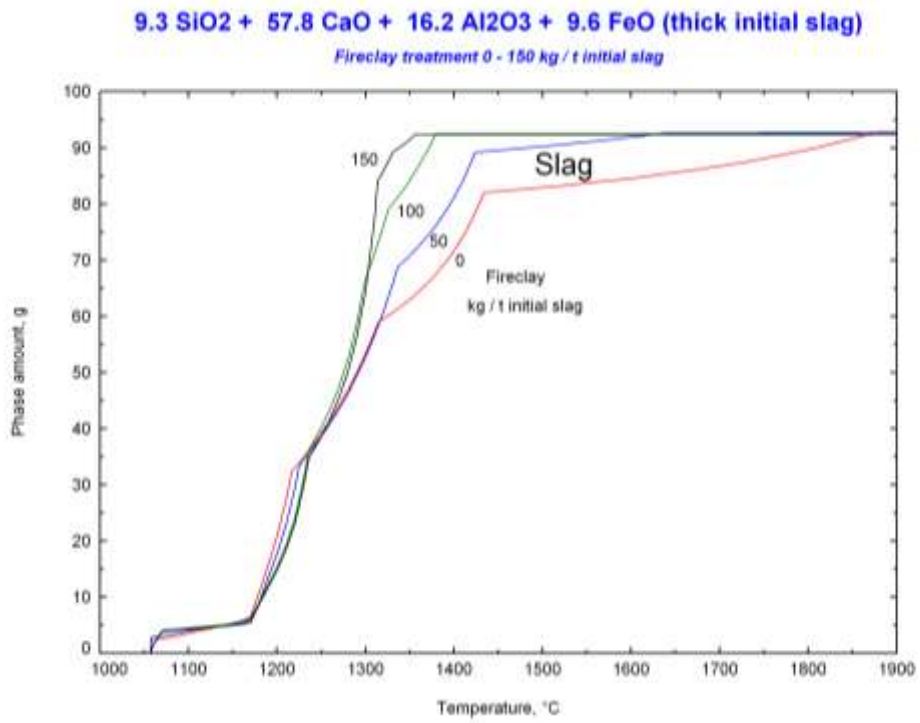

Figure 6 Initial temperature of solid phase precipitation in case of charging various quantities of fireclay

As it definitely turns out from **Figure 6**, the precipitation of the greater quantity of solid phase happens at lower temperatures. This temperature is 1440 °C in case of the charging of 0 kg/heat fireclay, while decreases to 1330 °C in case of the usage of 150 kg/heat.

The results of tests performed on suspension kind slag show that the viscosity of slags is decreased to a small extent by the charging of 0 and 50 kg/heat fireclay, while to significant degree by the addition put in secondary metallurgy slag in the quantities of 100 as well as 150 kg/heat (**Figure 7**).

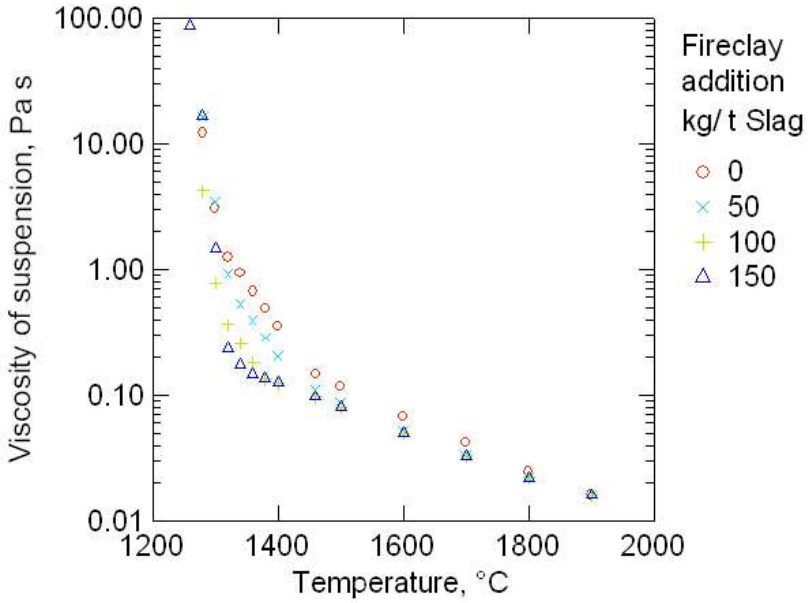

Figure 7 Testing of the viscosity of slag melt in case of adding various quantities of fireclay

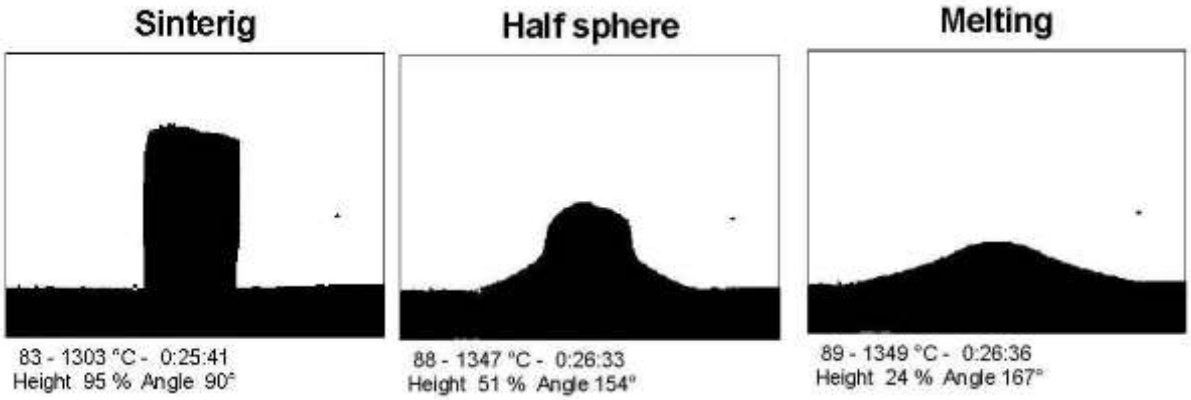

Figure 8 Typical temperatures of the melt microscopic test of secondary metallurgy slag

The tests with the latter fireclay were started, at first by using the quantities of 50 kg/heat and 100 kg/heat. We subjected secondary metallurgy slag samples of test heats to melt microscopic test in cooperation with the Department of Ceramic and Silicate Engineering of the University of Miskolc. During the tests with the melt microscope the deformation in the test piece form is examined by continuously heating the furnace. Easily interpretable photos are taken of the changes, which are assessed by software. **Figure 8** shows the melt microscopic images of the typical conditions of test secondary metallurgy slag sample taken upon using the fireclay.

Summary

The steel-making secondary metallurgy slag used at ISD DUNAFERR Co. Ltd. has extremely high CaO-content, and by precipitation of solid phases the viscosity of developed suspension causes problem during production.

Conducted researches and model tests showed that the metallurgical-physical characteristic of secondary metallurgy slag can be improved by modifying its composition.

Secondary metallurgy slag parameters can be optimized by increasing the ratio of Al_2O_3-content and SiO_2- and Al_2O_3-content, as well as by decreasing its CaO-content.

Further optimizing of the metallurgical characteristics of secondary metallurgy slags would be greatly supported, if the ladle metallurgical equipment applicable for the heating of the steel heat was constructed, as well as if stopping of the primary slag from the BOF could be made more reliable at ISD DUNAFERR Co. Ltd.

References

[1] Réger, M.; Ender, A.; Józsa, R.: Viscosity Problems of Secondary Ladle Metallurgy Slag at ISD Dunaferr Co. Ltd, ISD Dunaferr, Műszaki Gazdasági Közlemények 168 (2013) No. 1, p. 17 – 27

[2] Retzlaff, G.; Rust, G.; Waibel, J. (1978): Statistische Versuchsplanung, Planung naturwissenschaftlicher Experimente und ihre Auswertung mit statistischen Methoden, 2. verbesserte Auflage, ISBN 3-527-25799-9, Verlag Chemie, Weinheim, New York

[3] Bale, C.W. et al. (2009) : FactSage thermochemical software and databases – recent developments, CALPHAD: Computer Coupling of Phase Diagrams and Thermochemistry 33, p. 295 – 311

[4] ISD-Dunaferr Zrt, Research program 13/2012 assessment

[5] Decterov, S.A.; Kang, Y.-B.; Jung, I.-H. (2009) : Thermodynamic Database for the Al-Ca-Co-Cr-Fe-Mg-Mn-Ni-Si-Si-O-P-S System and Applications in Ferrous Process Metallurgy, Journal of Phase Equilibria and Diffusion Vol. 30, No. 5, p. 443 – 461

Adjusting the flexibility of fabric reinforced composite laminates using experimental design

T. Molnar*, V. Baranyai*, S. Kemény**, Gy. Bánhegyi*, J. Szabó*

* Bay Zoltán Nonprofit Ltd. for Applied Research Institute for Materials Science and Technology (BAY-ATI), H-1116 Budapest, Fehérvári út 130

** Budapest University of Technology and Economics, Chemical and Environmental Process Engineering, H-1521 Budapest, Budafoki út 8

tibor.molnar@bayzoltan.hu, viktor.baranyai@bayzoltan.hu, kemeny@mail.bme.hu, gyorgy.banhegyi@bayzoltan.hu, jozsef.t.szabo@gmail.com

Keywords: design of experiments, fiber reinforced composite, flexural modulus, tensile modulus

Abstract

The objective of our work is to improve the mechanical stiffness of fiber reinforced laminates. The stiffness can be characterized by flexural and tensile moduli or their derivation. We applied design of experiments (DOE) to achieve our goals, because to solve the existing analytical and numerical models is complicated.

We examined the effects of the following parameters: a) composition of reinforce materials (solely carbon, or carbon and glass combination), b) modulus of resin, c) mass ratio of resin-reinforcement, d) order of layers.

The samples manufactured on the basis of DOE were investigated mechanically (flexural and tensile moduli measurements) and morphologically (scanning electron microscopy). We compared the measured modulus results to calculated values.

Introduction

The fiber reinforced composites are modern sort of the technical construction materials. They were designed under the inspiration of the fact that the loads of various constructional parts are not equal in all direction of space [1, 2]. Frequently the required strength along the force lines is greatly bigger compared to other directions [3-6].

Composites are multiphase materials consisting of reinforcement and matrix material. Essentially the adhesive connection between the high strength and modulus fibrous reinforcement material and the lower strength but tough matrix material is outstanding, remains durable in case of high level deformation and load [7-9].

Design of experiments (DOE) is part of the survey process, with the aim of designing the circumstances of observation based on the preliminary model. In case of DOE the function of mathematical statistics is dual, active and passive. The roles of the experiment are determined by mathematics via DOE which are preparing the program, evaluating the results, correcting the roles if it is needed and at last determining the consequences. An important part of DOE is the determination of the objective function, whose optimal value is desired. After processing the results of the carried out experiment, the significance of the effects of the factors on the objective function are evaluable. There are analytical and numerical models (for example: FEM) for calculating mechanical properties of fiber reinforced composites, but it is difficult to calculate with them [10-12]. We have chosen the tensile and flexural moduli as the objective function. Consequently we investigated the effect of the factors on the moduli.

Experimental

Materials

The composite laminates were made of two types of reinforcement materials. One of them is carbon fiber 2/2 twill weave the other is glass fiber weave with areal densities of 240 g/m^2 and 220 g/m^2, respectively. The matrix materials were two component epoxy resin systems. The mixture of Ipox MR 3010 and Ipox MH 3124 components constituted resin with higher strength, while the combination of Ipox MR 3010 - Ipox MH 3124 and Ipox ES 61 A - Ipox ES 61B systems resulted a more flexible resin. All of the resin components were manufactured by the Ipox Chemicals Kft., Hungary.

Manufacturing of the samples

Manufacturing of the samples was performed via manual laminating, which is one of the most widespread technologies. We applied a square flat wooden plate (length of edges: 1 200 mm) for mold. The bottommost layers were resin followed by the reinforcement. Rectangular specimens (length: 100 mm, width: 20 mm) were cut off from the finished composite plates with thickness of 2.5- 5 mm.

Testing methods

Tensile and flexural moduli of the composite samples were measured by Instron 8874 testing machine. All of measurements were performed at room temperature. Circumstances of the tensile modulus test were the following:

- original gauge length: 25mm,
- distance between clamping heads: 65 mm,
- crosshead speed: 3.5 mm/min.

Change of length was detected by bonded strain gauge.
Three point flexural tests delivered the flexural modulus results. The test conditions are listed below:

- support span: 80 mm,
- crosshead speed: 6 mm/min,
- pusher and support radius: 5 mm,
- measurement of flexural deformation: Epsylon 3540 – 012M-LHT.

SEM images were made via Hitachi TM 1000 scanning electron microscope for the observation of the goodness of impregnation, degree of lining, nature of resin-fiber clinging.

Simplest analytical model

The following equation is the simplest analytical model for computing elastic modulus of more layered composites:

$$E_c = \eta_\theta \cdot E_f \cdot V_f + E_m \cdot V_m \quad (1)$$

where:

- E_c: calculated modulus of composite
- η_θ: proportionally factor of fiber orientation,
- E_f, E_m: moduli of fiber and matrix,
- V_f, V_m: volumetric ratio of fiber and matrix.

The equation assumes unidirectional overplacement of layers, but the texture of real weave is more difficult.

Factors

We have chosen the following factors of the experiment:

- modulus of the resin (rigid or flexible),
- nature of reinforcement material (only carbon or carbon + glass),
- ratio of reinforcement material and resin (40 % or 60 %),
- order of reinforcement layers (a or b; only in the case of carbon + glass fibers). Order of layer type a: 2 carbon, 1 glass, 2 carbon, 2 glass, 2 carbon 1 glass, 2 carbon; order of layer type b: 4 carbon, 4 glass, 4 carbon.

Experimental matrix is summarized at Table 1. Sample 9 and 10 possess the same attributes as sample 1. The results of reproduced samples indicate the adequateness of sample fabricating process.

Sample number	Modulus of resin	Ratio of resin	Reinforcement material/order of layers
1	High	40%	C
2	High	40%	C/G a
3	High	40%	C/G b
4	Low	40%	C
5	Low	40%	C/G a
6	Low	40%	C/G b
7	High	60%	C
8	Low	60%	C
9	High	40%	C
10	High	40%	C
11	High	60%	C/G a
12	Low	60%	C/G a
13	High	60%	C/G b
14	Low	60%	C/G b

Table 1. Matrix of experimental factors

Results and discussion

Relation between measured and calculated moduli

The comparison of measured tensile modulus to the calculated results is seen at Fig 1. The calculation based on the following characteristic data: modulus of carbon fiber: 242 GPa; density of carbon fiber: 1.8 g/cm^3; modulus of glass fiber: 79 GPa; density of glass fiber: 2.54 g/cm^3; density of resins: 1.25 g/cm^3; moduli of resins: 20 GPa (high modulus) and 2 GPa (low modulus). The results are corresponding in order of magnitude but, expectedly, the model denied the bowing the fibers overestimates the absolute values of modulus. The correlation between the data is significant, but relatively low (R^2=0.66)

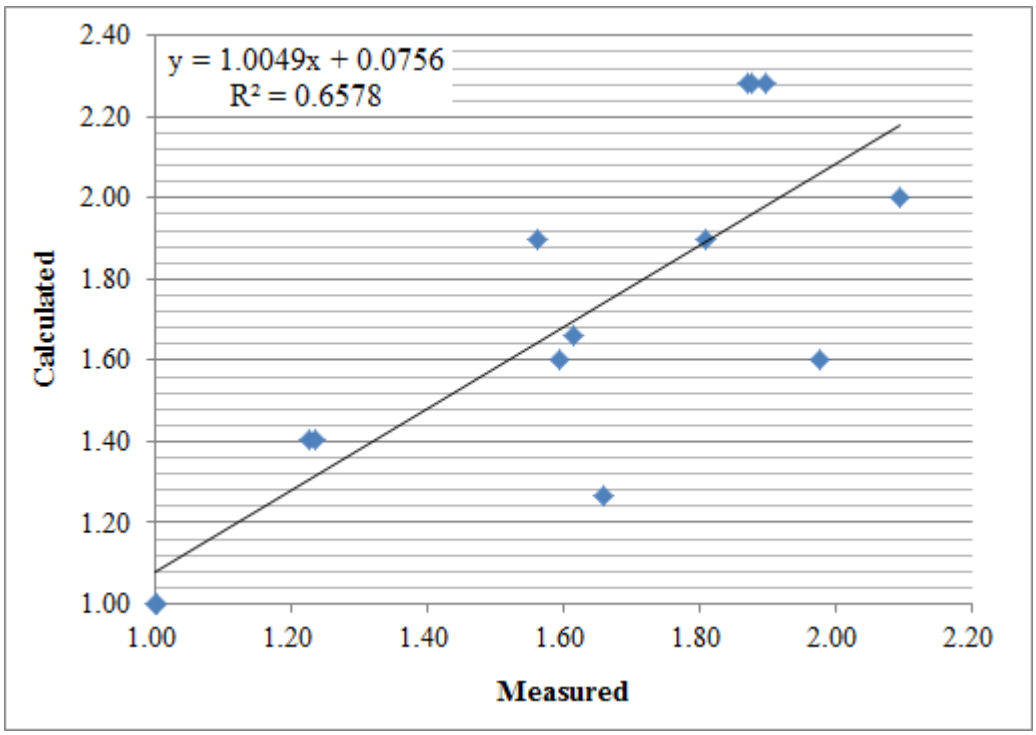

Figure 1. Measured and calculated relative modulus values (basis of relative moduli: measured: 26.86 GPa; calculated: 31.315 GPa)

Relation between tensile and flexural moduli

Fig. 2 shows the connection between tensile and flexural moduli. There is correlation between the data at significance level 99 % (R^2=0.44). The results suggest that increase of tensile modulus to unity causes on the flexural modulus increase to 0.5 times unity. The axial intercept considerably deviates from zero.

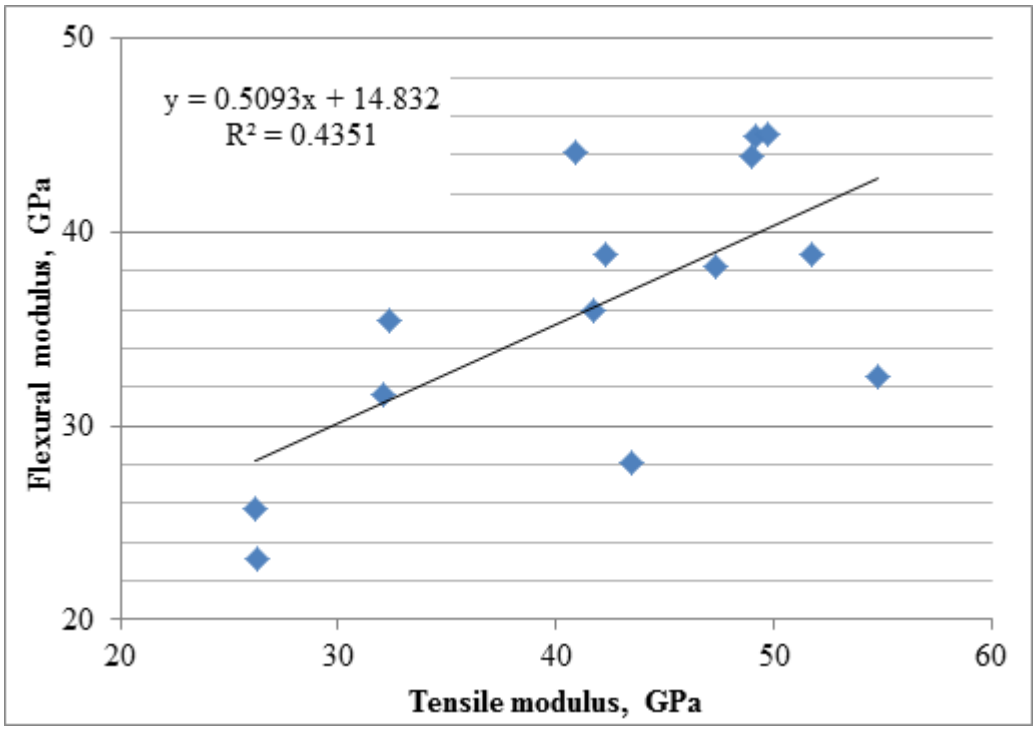

Figure 2. Flexural modulus as a function of tensile modulus

Results of modulus measurements

Fig. 3 and 4 show the distribution of test results of tensile and flexural moduli. The values are derived from five parallel measurements from every single sample. The first sample is two times reproduced (sample number 1, 9 and 10), which were separately investigated, so we can characterize the reproducibility of the manufacturing process. The difference between the results are irrelevant, the manufacturing process is good reproducible. It is worth to notice, that the deviation values of flexural modulus are lower compared to the tensile modulus.

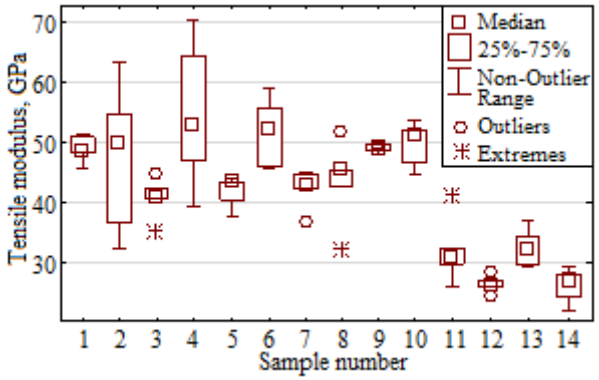

Figure 3. Distribution of tensile modulus

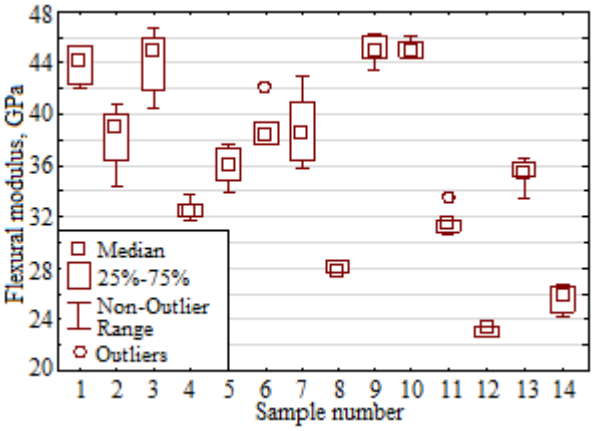

Figure 4. Distribution of flexural modulus

We examined the impacts of the factors on the moduli. Not only the effects of solely factors were analyzed but the derived affection of more factors was investigated. The effect on tensile modulus of the order of reinforcement layers (exclusively carbon; carbon + glass A; carbon + glass B) and of the ratio of resin are significant, while influences of two derivative factors (modulus of resin X order of layers and of modulus of resin X ratio of resin) are reduced. Effects of factors are illustrated in Fig. 5 and 6. The moduli of resin and reinforcement are different in order of magnitude, therefore the great influence of the ratio of resin is intelligible. The order of layers is in case of solely carbon/carbon+glass relationship is important, the composites with solely carbon reinforcement had always higher tensile modulus compared to C+G materials. Nevertheless the order of glass and carbon layers had not caused definite differences. The tensile modulus was not influenced by the modulus of resin, what is explainable by the strong resin-fiber interactions. The good resin-fiber adhesion allows the transmission of forces to the high modulus fibers.

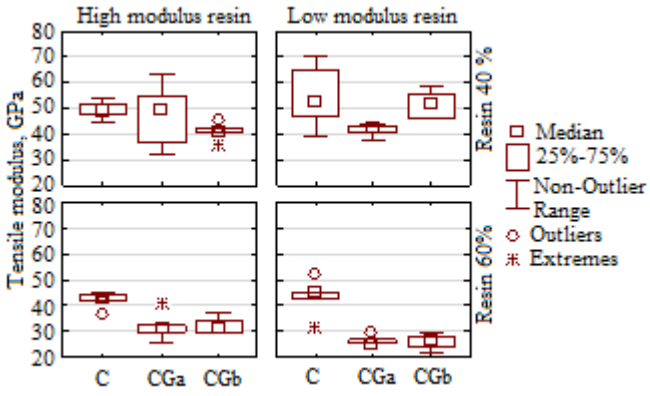

Figure 5. Analysis of tensile modulus

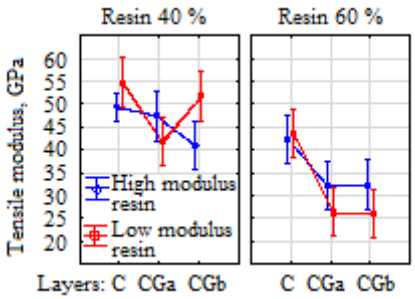

Figure 6. Tensile modulus and resin% interaction

All factors had significant effect on the flexural modulus (Fig. 7 and 8). We assume that the role of fibers is not as unequivocal as in case of tensile test. The not longitudinal forces emphasize the importance of resin modulus, or the order of layers.

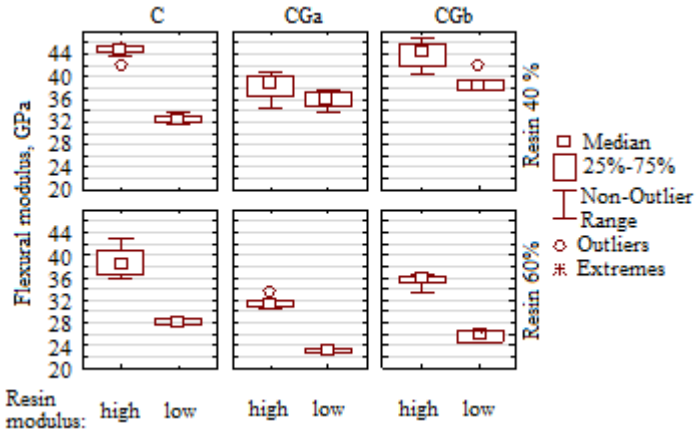

Figure 7. Analysis of flexural modulus

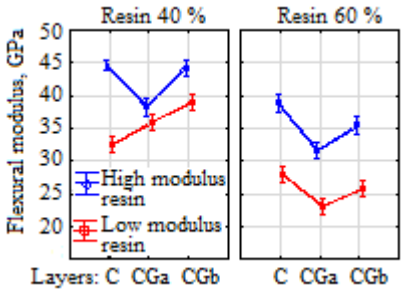

Figure 8. Flexural modulus and resin% interaction

SEM images

Broken surfaces were investigated via scanning electron microscope (SEM). It can be observed, that the fiber-resin adhesion was adequate, we have not found bunch of fiber without resin residue. Pulled-out carbon fibers were less typical compared to glass fibers. On the glass fibers pulled out are traces of resin observable, but the bigger areas of the fibers were free of resin (Fig. 9).

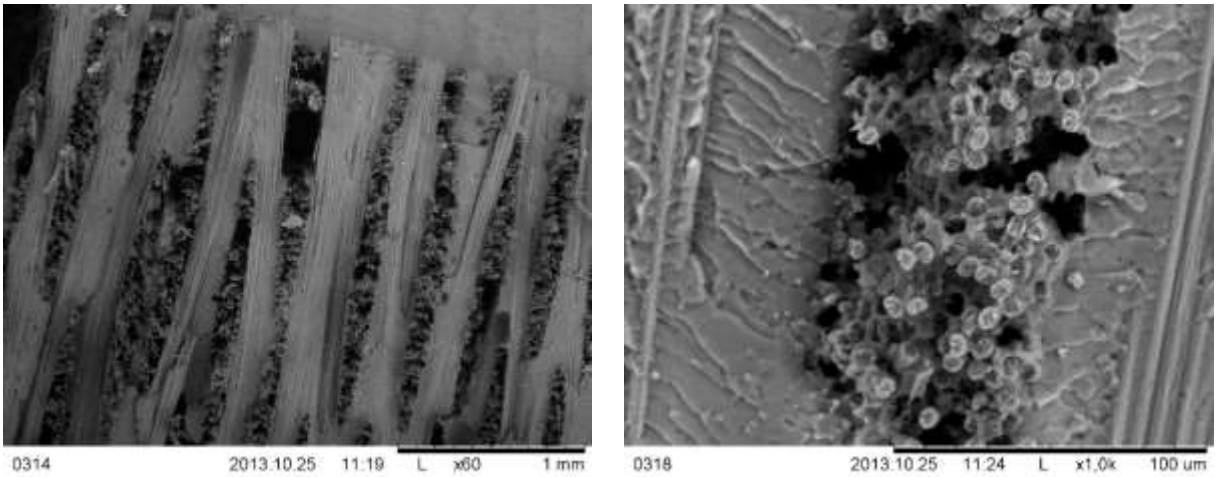

Figure 9. SEM photographs of composites: curved structure of the fibers (left), adhesion between carbon fiber and resin (right)

Conclusions

Correlation between measured and calculated (via simplest analytical model) tensile moduli is significant, but relatively low (R^2=0.66). It is attributable to phenomena denied by the model (e. g. bowing of fibers). Correlation between tensile and flexural moduli is significant, but low (R^2=0.44). Flexural modulus show half of growth compared to tensile modulus.

Two factors have largest effect on tensile modulus: type of layers (solely carbon or C+G) and ratio of resin. Order of C+G layers and modulus of resin has negligible importance. Flexural modulus is influenced not only by the two factors above, but all of examined factors have considerable effect on it.

References

1. David R., The Fundamental Principles of Composite Material Stiffness Predictions, University of the West of England, Bristol, 2006
2. Evgeny V. Morozov, Mechanics and Analysis of Fabric Composites and Structures, AUTEX Research Joumal, Vol. 4 No. 2, South Africa, 2004
3. W. D. Callister, Fundamentals of Materials Science and Engineering, fifth ed., John Wiley and Sons, New York, 2001.
4. J. W. Martin, Materials for Engineering, third ed., Woodhead, Cambridge, 2006.
5. M. F. Ashby, D. R. H. Jones, Engineering Materials 1, second ed., Butterworth-Heinemann, Oxford, 1996.
6. C.S. Verma, V.M. Chariar, Development of layered laminate bamboo composite and their mechanical properties, Composites Part B 43 (2012) 1063-1069
7. C. Dong, I. J. Davies, Flexural and tensile moduli of unidirectional hybrid epoxy composites reinforced by S-2 glass and T700S carbon fibres, Materials and Design 54 (2014) 893-899
8. C. Dong, I. J. Davies, Flexural and tensile strengths of unidirectional hybrid epoxy composites reinforced by S-2 glass and T700S carbon fibres, Materials and Design 54 (2014) 955-966
9. H. He, J. Wangb, K. Li, J. Wanga, J. Gu Mixed resin and carbon fibres surface treatment for preparation of carbon fibres composites with good interfacial bonding strength, Materials and Design 31 (2010) 4631-4637
10. R. Rikards, A. Chate, Identification of Elastic Properties of Composites by Method of Planning of Experiments, Composite Structures 42 (1998) 257-263
11. R. Rikards, A. Chate, G. Gailis, Identification of Elastic Properties of Laminates Based on Experiment Design, International Journal of Solids and Structures 38 (2001) 5097-5115
12. R. Rikards, A. Chate, W. Steinchen, A. Kessler, A.K. Bledzki, Method for identification of elastic properties of laminates based on experiment design, Composites Part B 30 (1999) 279–289

Measuring of fiber/matrix adhesion in thermoplastic polymer composites: A preliminary study

Bálint MORLIN[1, 2 a], Tibor CZIGÁNY[1, 2 b]

[1] Department of Polymer Engineering, Faculty of Mechanical Engineering, Budapest University of Technology and Economics, Muegyetem rkp. 3, Budapest 1111, Hungary

[2] MTA–BME Research Group for Composite Science and Technology, Muegyetem rkp. 3, Budapest 1111, Hungary

[a]morlin@pt.bme.hu (corresponding author), [b]czigany@eik.bme.hu

Keywords: adhesion test, micromechanical method, cylinder test

Abstract. The possibilities of the application of microbond test and cylinder tests for determining the interfacial shear strength at the fiber-matrix interface in thermoplastic matrix polymer composites were investigated. Possibilities of test specimen preparation were also investigated. Finally the applicability of the method to make high precision measurement of interfacial shear strength was evaluated.

Introduction

Fiber reinforced polymer composites can be found nowadays everywhere in practically all niches of life. This exceptionally important role is due to their controllable anisotropy, high strength and low density. The reason for these properties lays in the high strength of the fibers and toughness of the matrix, as well as the excellent adhesion between them, ensuring proper cooperation between the phases. In order to qualify and design composite structures the knowledge of adhesion relations is of primary importance, especially in short fiber reinforced (e.g. injection molded) systems. The application of the so-called microbond (or microdroplet) test is very good for this purpose (Fig. 1.a). Several tests were performed to qualify reinforced thermoplastic materials and to develop the most suitable sample preparation method [1-7]. When preparing the test specimens the first step is the application of the matrix onto the reinforcing fiber, for which several possibilities are available: for example fibers are made of the thermoplastic and a knot is placed onto the fiber, or a slit piece of polymer film is placed onto the fiber (see Fig. 1.b). In the next step the matrix is melted in order to form the interfacial interaction and the droplet. In course of the test specimen preparation it is of decisive importance that the matrix solidifies symmetrically, possibly in nearly perfect spherical shape with homogeneous material properties. The next step is the microscopic investigation of the test samples in order to eliminate specimens unfitting for tests because of shape deformity or size probblems and to determine size parameters necessary for evaluation (fiber diameter, embedded length etc.).

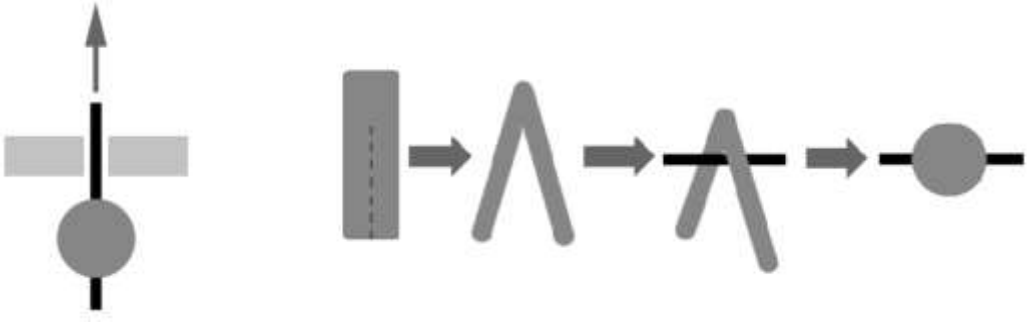

a) b)

Fig 1. Scheme of the microbond test (a), and sample preparation according to the literature [7] (b)

The droplet size is very important with respect to the test results. The lower limit of the diameter (D) is the size which can be still practically applied onto the fiber, but it influences the stress state in the droplet, therefore the resulting shear strength value. Much more important, direct role is played by the embedded length (L). The maximum value of this parameter is determined by the tensile strength of the fiber. It should be lower than the critical failure length as if it not true, the fiber will break and the test will be unsuccessful. The goal is the achievement of the technically possible shortest length. For testing the prepared reinforcing fiber is first clamped into the test equipment, the blades used to remove the droplet are adjusted according to the size of the droplet so that they just touch the surface of the droplet, then the test is performed usually by pulling out the fiber. As a last step the data obtained are processed by one of the many available mathematical models [8]. The disadvantage of the results obtained is that their scattering, i.e. the uncertainty of the test is high – due to the relatively ill-defined droplet shape and to the widely varying geometrical parameters.
In our earlier works [9, 10] cylinder test developed form the microbond test has been introduced (Fig. 2.), which is devoid of the aforementioned disadvantages, the advantages and disadvantages of this method have been so far tested by thermoset matrices.

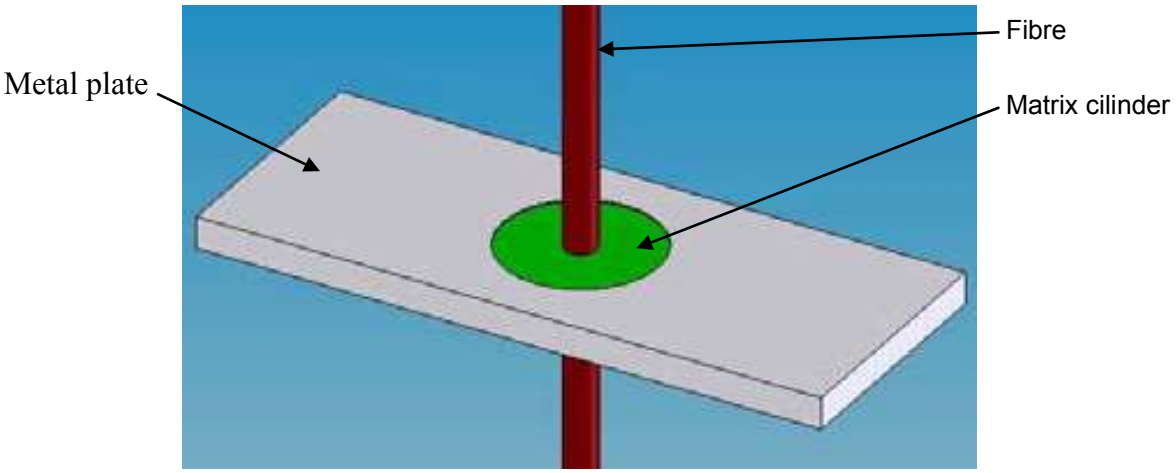

Fig. 2. Test sample of the cylinder test

The essence of this method is the single fiber embedded centrally in a borehole prepared in a metal sheet, which provides favorable conditions for load transfer between the fiber and the matrix. When preparing the test specimen the sheet is fixed by fork shape part of a special instrument which ensures simultaneously the proper centeredness and concentric position. When performing the test the sheet is fixed and the fiber can be pulled out by a tensile tester, based on the geometrical size and the recorded force the interfacial shear strength can be reliably calculated using the simplest methods used so far (Eq. 1):

$$\tau = \frac{F}{\pi * d_f * L}. \qquad (1)$$

where τ is the interfacial shear strength, F is the pull-out force, d_f is the fiber diameter, L is the embedded length. The advantage of the method is the high precision which can be explained by the concentric and uniaxial positioning of the fiber and the matrix cylinder, i.e. by the simple, circularly symmetric stress state, and by the elimination of the effect of variable size of the test specimens. Repeatability also improves and the dependence on operator and sample preparation skills decreases. All this greatly improves the reliability of the tests. A droplet (cylinder) placement method was designed and built for this purpose.
The goal of this article is to apply the method proven for thermosets also for thermoplastic matrices, in comparison to the traditional microbond test.

Materials and Methods

The matrix used is Copolyester GN071, Natural PET-G of Eastar (processing temperature 249-271°C). The reinforcing fiber is RT310 0001 100 glass fiber of Saint-Gobain.

Preparation of thermoplastic specimens

Microbond test: The fiber to be tested was always glued onto a paper test window. According to our experience the methods described in the literature are not expedient, e.g. certain parts of the thin polymer films become easily burnt while at other places the material does not even melt, therefore the shape and material properties of the droplets will not be uniform, which precludes exact measurements. Preparing knots from matrix material fibers yields good results but it requires high concentration on the part of the operator and there are several possibilities of error [7]. We used the following method for microbond tests: matrix was applied from a matrix melted on a heated plate. From the melted pellets a fiber was formed on the tip of a needle, and before it was frozen the matrix fiber was bent over the reinforcing fiber placed into the test window. The amount of the applied resin could be regulated by the thickness of the matrix fiber. One can prepare even very small droplets this way, sometimes so small that they could not be clamped during the droplet removal. After some practice it can be achieved that the thermoplastic fiber does not cool down exceedingly and adheres to the reinforcing fiber and there is no need for further attachment procedure. Fig. 3 shows the process of droplet application used by us.

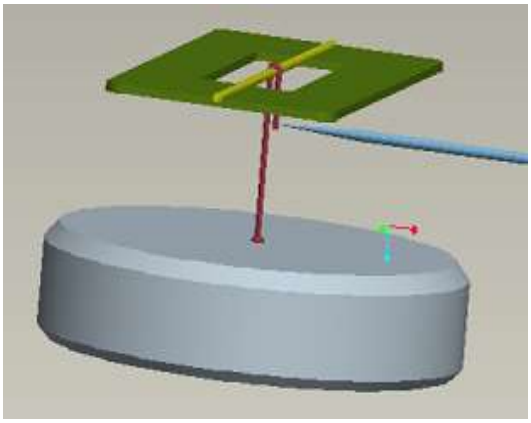

Fig 3. The method used by us for droplet application

Cylinder test: In the cylinder test the thermoplastic material should fill in the narrow gap between the reinforcing fiber and the adjacent wall of the concentric borehole. For this a fairly low melt viscosity is needed. In order to achieve this, a proper temperature should be reached as soon as possible in a small area to avoid heat losses. Another important requirement is the exact maintenance of the set temperature to avoid the degradation of the material at excessive temperatures.

Taking into account these requirements a soldering iron of SOLDER01 type with controllable temperature was modified and used. The head of the solder iron is exchangeable (with screw) and a properly shaped copper heating element was placed here (Fig. 4/a). When applying the droplet the fork holding the sheet with the borehole fits well the wall of the heating element because of their conical shape, therefore the heat transfer is good. The fiber is placed in the central vertical groove. In order to prepare the test specimens a version of the forks fitting the shape of the heating element was also necessary. This consisted of two copper sheets, the sheet with the borehole was fixed by a screw pressing the two halves together (Fig. 4/b and c). The proper fitting between the fork and the solder iron peak was ensured by the conical shape of the mating surfaces.

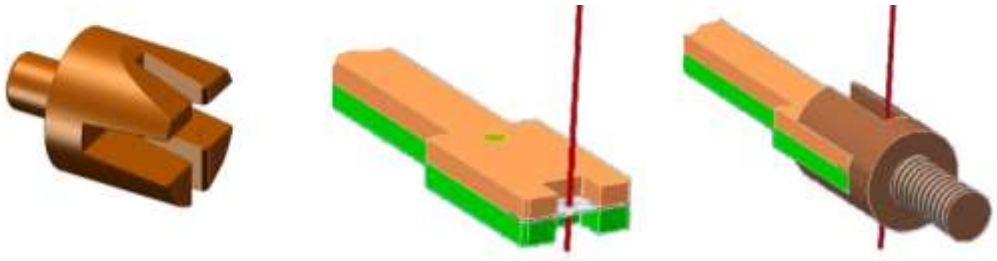

a) b) c)

Fig. 4. The heating element (a) used to prepare the test samples in the thermoplastic cylinder test, the corresponding fork (b) and its application (c)

The preparation of the test specimens is only a little bit modified as compared to those of thermoset samples: the sheet with the borehole was fixed in the fork, then the reinforcing fiber in inserted and centered. The heating element was screwed onto the controllable soldering iron and the necessary temperature was set (according to the controller of the soldering iron between 350 and 400 °C, depending on the material). Thereafter a proper amount of the matrix to be applied is placed near the fiber onto the sheet and finally (while taking care of the fiber) the soldering iron is pressed to the fork. After a proper time (usually 20-30 seconds) the matrix melts and fills the borehole. Of course the temperature of the sheet (due to the limitations of heat transport) is much lower than that of the soldering iron and was enough only for the melting of the matrix. For this reason and because of the short dwelling time the degradation of the polymer is improbable. Then the soldering iron is removed and the ready specimen is removed from the droplet application equipment similarly as before. This method yields acceptable results in the case of certain low viscosity matrices (as e.g. CBT).

Thermoplastic polymer matrices usually exhibit too high viscosity to fill the borehole from the surface of the sheet without external pressure. If a polymer pellet is placed onto a heated plate and is melted, then the sheet with the borehole is pressed onto it, the melt usually fills completely the borehole. Afterwards on one side of the sheet the excess matrix is removed down to the surface of the sheet and the matrix cylinder is drilled with a borer of 0.15 mm diameter. The position of the borehole can be checked by microscopy. Thereafter the sheet is fixed into the fork and placed into the droplet application equipment and so the reinforcing fiber can be inserted into the borehole of the matrix. Finally the sheet is heated up by the solder iron, under the effect of heat the drilled matrix cylinder melts and fills in the borehole of the sheet, but this time it contains the inserted reinforcing fiber. The drilled volume is replaced by the material remaining on the surface of the sheet, no material shortage was observed (Fig. 5.). Finally the side ensuring the excess material is planed to the sheet surface before the droplet removal, so the reinforcing fiber is surrounded only the matrix cylinder with a thickness identical to that of the metal sheet.

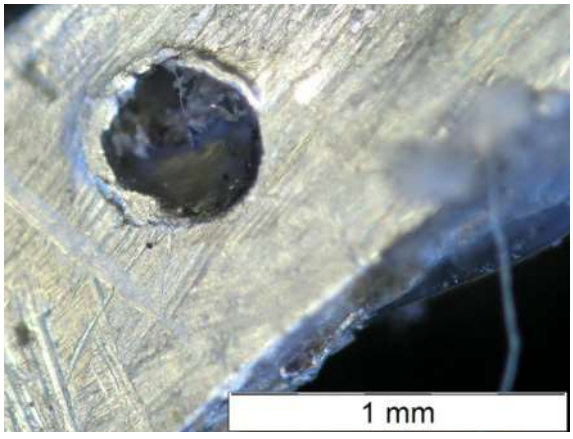

Fig. 5. Micrograph of the test specimen used in the cylinder test

Results and Discussion

The test results are shown in Table 1. The relative scattering calculated as a ratio of the scattering of the measured values and the shear stresses is much lower than in the case of the paper-window method, i.e. the reliability of the test improved considerably also for thermoplastic materials, due to the uniform size and shape used in the cylinder test. Earlier, in the case of thermoset matrices the cylinder test yielded 7-14% relative scattering [11], which can be explained by the simpler test specimen preparation. It is conspicuous, however, that about 50% lower shear stresses were obtained using this method, as compared to the microbond test. This is probably due to the large temperature difference and to the consequent heat expansion. The matrix initially fills out the borehole but it is conceivable that during the second heating-cooling cycle microcracks appear in the matrix, which may lead to a reduced adhesion. According to our microscopic observations these are microscopic in size or do not even reach the surface of the material (see Fig. 5.). The slight worsening of the relative scattering with respect to those of thermosets may also be explained by the aforementioned cracks.

Method	**d_{fiber} [µm]**	**D [µm]**	**L [µm]**	**τ [MPa]**	**Relative scattering**
Microbond test	13.19±1.41	61,3±13,7	93.89±16,88	24.92±7.38	29.65%
Cylinder test	12.94±0,87	400	200	12.43±2.37	19.03%

Table 1. Results obtained on glass fiber - PETG material pair

Based on our results, therefore, a further development of cylinder method seems necessary to determine exactly the fiber/matrix interfacial properties in thermoplastic matrix systems. This may prove to be useful taking into account the special technological characteristics of processing (e.g. high pressures and fast cooling during injection molding, etc.) as the molecular structure evolving in the matrix around the fiber influences considerably the interfacial shear strength.

Conclusions

Methods of using the cylinder test and the microbond test and the methods of sample preparation were investigated for determining the interfacial shear strength of the fiber/matrix interface in composites with thermoplastic matrices. We proposed a new method for preparing test samples for the microbond test and performed experiments to apply the cylinder test to high viscosity, thermoplastic materials. We concluded that it is possible to prepare cylindrical test specimens amenable to testing even form these materials. Their usefulness is, however, limited to deter mine the interfacial hear strength with high precision as, in spite of the more advantageous stress sate the measured shear strength values are smaller than those measured in the traditional microbond test, presumably due to the microcracks developing because of the thermal expansion of the test specimen.

References

[1] X. Y. Liu, G. C. Dai, Surface modification and micromechanical properties of jute fiber mat reinforced polypropylene composites. Express Polym. Lett. 1 (2007) 299-307.

[2] S. Yalvac, J. J. Jakubowski, Y. H. So, A. Sen, Improved interfacial adhesion via chemical coupling of cis-polybenzobisoxazole fibre-polymer systems. Polymer. 37 (1996), 4657-4659.

[3] T. Czigány, Special manufacturing and characteristics of basalt fiber reinforced hybrid polypropylene composites: Mechanical properties and acoustic emission study. Compos. Sci. Technol. 66 (2006), 3210-3220.

[4] L. Yang, J. L. Thomason, Interface strength in glass fibre-polypropylene measured using the fibre pull-out and microbond methods. Compos Part A-Appl. S. 41 (2010), 1077-1083.

[5] J. L. Thomason, L. Yang, Temperature dependence of the interfacial shear strength in glass-fibre polypropylene composites. Compos. Sci. Technol. 71 (2011), 1600-1605.

[6] L. J. Thomason, Y. Liu, Temperature dependence of the interfacial shear strength in glass–fiber polypropylene composites investigated by a novel single fiber technique. ANTEC 2012 Conference, (2012) Orlando, Florida p.5.

[7] Természetes nyersanyagbázison alapuló és/vagy biológiailag részlegesen vagy teljesen lebomló, társított anyagokból készült termékek előállítása és alkalmazása című NKFP 3A/0036/2002 pályázat, 1. részjelentés. Budapest, (2003).

[8] P. Zinck, H. D. Wagner, L. Salmon, J. F. Gerard, Are microcomposites realistic models of the fibre/matrix interface? I. Micromechanical modelling. Polymer. 42 (2001), 5401-5413.

[9] B. Morlin, T. Czigány, Cylinder test: Development of a new microbond method. Polym. Test. 31 (2012) 164-170.

[10] B. Morlin, L. M. Vas, T. Czigány, Investigation of fiber/matrix adhesion: test speed and specimen shape effects in the cylinder test. J. Mater. Sci. 48 (2013) 3185-3191.

[11] B. Morlin, Development of a new method and process to determine the fiber/matrix adhesion (in Hungarian). Ph.D thesis. BME (2013).

Recrystallization of boron containing and boron-free low carbon steels investigated by thermoelectric power and hardness measurements

András Mucsi[1, a], László Dévényi[1,b]

[1] Budapest University of Technology and Economics, Department of Materials Science and Technology, 1111 Budapest, Bertalan Lajos street 7., Hungary
Tel.: (+361) 463-1234
Fax: (+361) 463-1366

[a]mucsia@eik.bme.hu, [b]devenyi@eik.bme.hu

Keywords: recrystallization, low carbon steel, boron steel, thermoelectric power

Abstract. The measurement of thermoelectric power is a powerful method to investigate the metallurgical processes occurring in steels. In this study, four low carbon cold rolled steel sheets having different composition were investigated. The cold rolled sheets were heated up at heating rate 20 °C/hour up to different temperatures, whilst the change of thermoelectric power and hardness have been measured at room temperature after slow cooling. The thermoelectric power of steels increases with temperature until the recrystallization finishes. The raise of thermoelectric power during recrystallization is ranging between 50 and 160 nV/K, depends on the composition of the sheet. Specimens consist of boron exhibit lower thermoelectric power after recrystallization than the steel without any boron, probably due to metastable borocarbide dissolution. This fact could be a good starting point to investigate the effect of boron on thermoelectric power of steels.

Introduction

The thermoelectric power of materials reveals the raise of electric potential due to thermal activation. The usual equipment for measuring thermoelectric power (Fig. 1) consists of two large heat capacity blocks, which provide the temperature difference for the sample [1,2]. In our case, the blocks are made of copper. The sample is placed between the two blocks having different temperature.

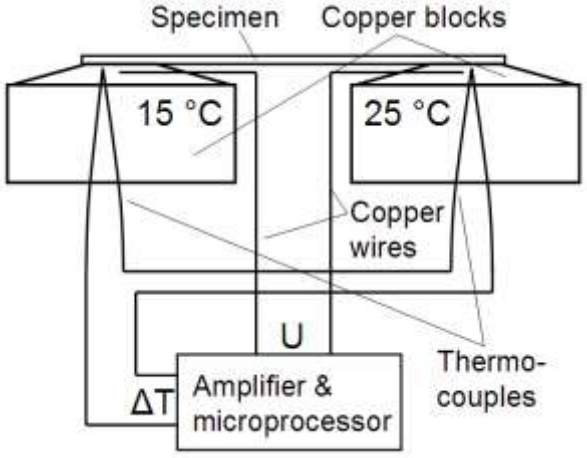

Figure 1: The general assembly of the thermoelectric power measuring device

The temperature difference induces voltage difference between the blocks. The thermoelectric power (S) of the specimen is defined as the ratio of the thermoelectric voltage (U) and temperature difference (ΔT) [2]:

$$S = U / \Delta T \quad (1)$$

The measured thermoelectric voltage depends not only on the properties of the sample, but on the reference as well. The electrical wires between the connection pins of the amplifier and copper blocks contribute to the voltage measured by the amplifier; therefore the thermoelectric power defined by Eq. 1 is a relative value. However, the reference wires between the copper blocks and amplifier do not change their properties; consequently, a possible alternation in S is caused by the change of some microstructural property of the sample.
As it was mentioned, the thermoelectric power of metals depends on a plenty of microstructural properties. If the distortion of the crystal lattice increases, then the value of S will decrease; whist a possible reduction in the distortion of the crystal lattice will increase the thermoelectric power. So, recovery, recrystallization and precipitation of substitutionals or interstitials from solid solution increase the value of S; in contrast to this, cold working and dissolution will decrease the value of thermoelectric power [3-5]. The effect of elements in solid solution on thermoelectric power is proportional to the amount of element in solid solution, and expressed by the so-called Nordheim-Gorter law [6].

$$\Delta S = \sum K_i \cdot x_i \qquad (2)$$

where x_i is the amount of the element i in solid solution, K_i is a coefficient linking the content of the given element in solid solution with its contribution to the thermoelectric power.

K_C	K_N	K_{Al}	K_{Cu}	K_{Mn}
-45	-24	-30	-2	-3

Table 1. Numerical values of coefficients K_i in Nordheim-Gorter law, expressed in μV/(K·wt%) [1,10]

The effect of cold working or recovery and recrystallization on thermoelectric power is hard to define quantitatively, such as the effect of boron in solid solution.
The aim of this study is to investigate the evolution of thermoelectric power of cold rolled steels during slow heating. In order to compare the change of thermoelectric power with the effect of recrystallization, hardness measurements have been performed.

Materials and methods

For the experiments, low carbon steels having different composition have been used. The steels have been received in hot rolled state, and they have been cold rolled to 70 % thickness reduction. The composition of the steels is given in Table 2.

Steel	C	Mn	Si	P	Cu	Cr	Ni	Al	N	B
A	0.024	0.224	0.011	0.007	0.01	0.056	0.031	0.026	0.006	0.003
B	0.110	0.614	0.015	0.01	0.094	0.049	0.04	0.06	0.005	0.000
C	0.024	0.195	0.008	0.005	0.012	0.090	0.021	0.032	0.005	0.003
D	0.035	0.207	0.009	0.008	0.009	0.051	0.045	0.032	0.006	0.003

Table 2: The composition of the steels investigated

Specimens with size of 75x5x1 mm have been prepared from the centerline of the cold rolled sheet. For investigating recrystallisation, the specimens were heated from room temperature up to different temperatures at 20 °C/h heating rate, after that they have been cooled down at 10 °C/min cooling rate to room temperature. The thermoelectric power of the specimens denoted by S_T as well as the hardness (HV5) of them has been measured after cooling. Since S_T is a relative value, its change (S*) has been calculated using the thermoelectric power of the specimens at 20 °C (S_{20}):

$$S^* = S_T - S_{20} \tag{3}$$

Results and discussion

The hardness of specimens does not change up to 300 °C. In temperature range 300…500 °C the hardness of the specimens increases by about 10-12 HV5, probably due to the aluminium-nitride precipitation process [7,8]. The standard empirical deviation of hardness measurements has also been calculated as:

$$\sigma_{HV} = \sqrt{\frac{\sum_{i=1}^{N}(HV - HV_a)^2}{N-1}} \tag{4}$$

where N=5 is the number of parallel hardness measurements performed on a sample. The average standard empirical deviation of hardness measurements was found to be 4.8 HV5, as indicated in Fig. 2.

In temperature interval 500…600 °C recrystallization occurs. In the case of Steel B, the hardness after heating up to 550 °C is about 220 HV5 (early stage of recrystallization), whilst the hardness of Steel C at this temperature is lowered by the recrystallization to about 150 HV5 (~ 50% recrystallized fraction). This fact can be explained by the effect of impurities on the rate of recrystallisation. At 580 °C, all of the steels are in a similar (almost completely recrystallised) state; however, their hardness decreases further up to 650 °C.

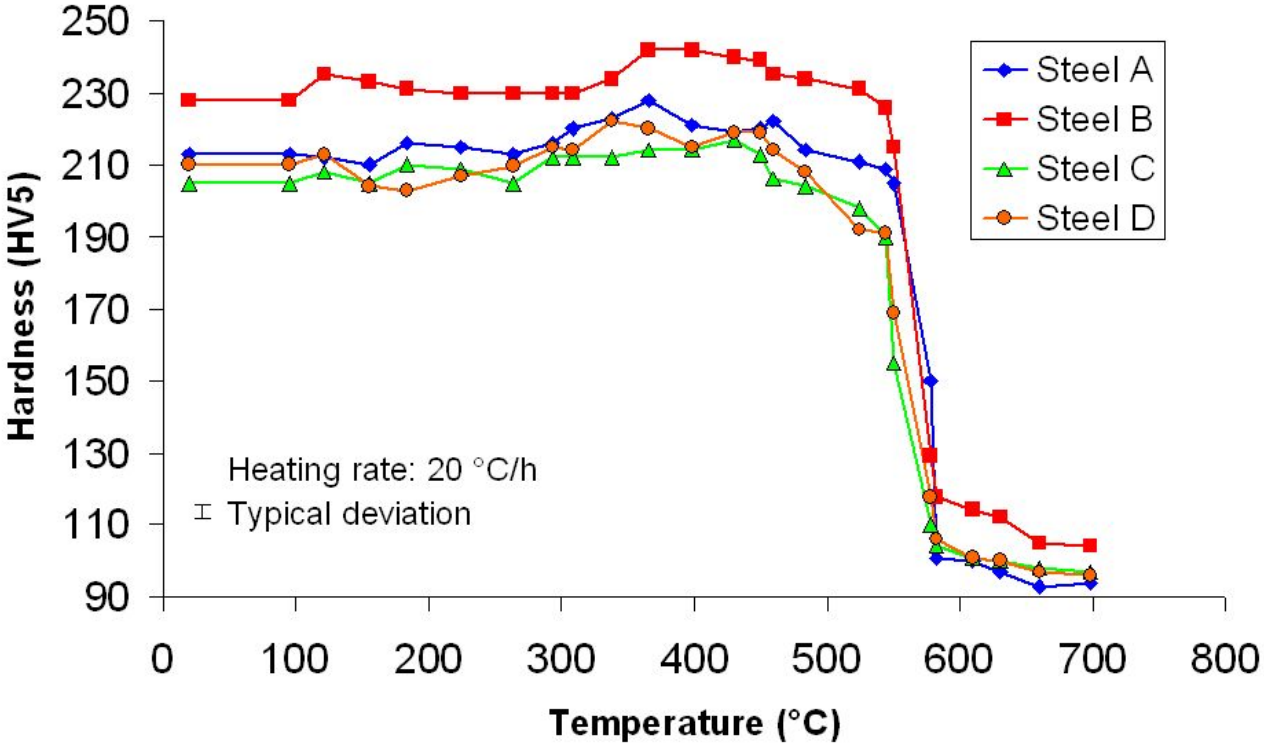

Figure 2: The evolution of hardness during heating up the cold rolled specimens

The thermoelectric power of the specimens increases in the same manner up to the beginning of the recrystallization. The recrystallization has different effect on the thermoelectric power of the steels. In the case of Steel B, the increase of S* is about 200-300 nV/°C during recrystallization; in contrast to this the thermoelectric power of Steel C increases only 50 nV/°C.

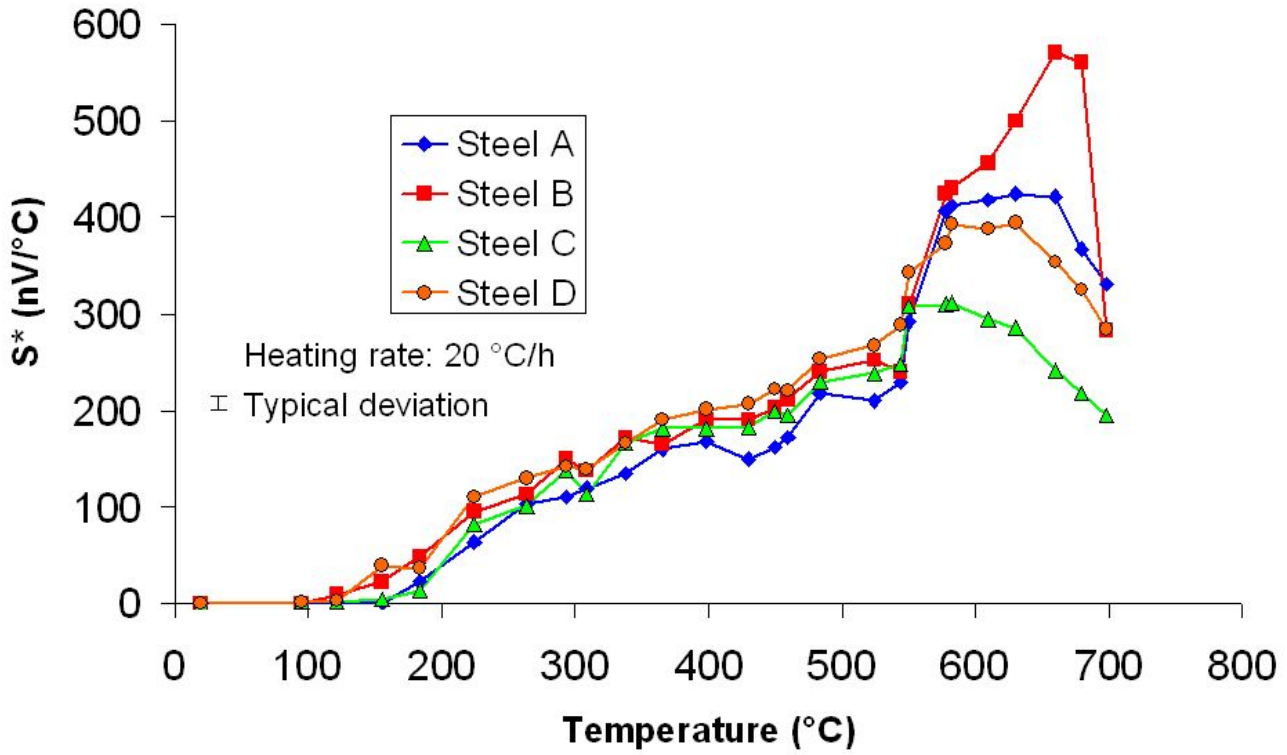

Figure 3: The change of the thermoelectric power of cold rolled low carbon steels

The standard empirical deviation of thermoelectric power test results has been also calculated from four parallel measurements, in the similar way as for hardness measurements (Eq. 4). There is a remarkable difference in the evolution of thermoelectric power among the steels after recrystallization as well. In the case of Steel B (which has the largest carbon content, but does not contain boron) the thermoelectric power increases by ~ 150 nV/°C above 600 °C, however, the thermoelectric power of the other (boron-free) steels decreases in this range. Since there is not cold working or such crystal lattice distorting effect after recrystallization, the presence of elements in solid solution can cause the decrease of the thermoelectric power.
The solubility limit of boron in steel is quite low, the solubility limit in austenite is approx. 45 ppm by weight at 1100 °C, which decreases to 10 ppm at 900 °C. In the ferritic range, at 710 °C, only 4 ppm boron is dissolved. At temperatures lower than 600 °C, metastable Fe3BC borocarbide could be present [9]. The decrease of thermoelectric power of boron steels above 600 °C is probably associated with the dissolution of metastable borocarbides. The same conclusions were drawn from computer simulations. According to JMatPro simulation software, boron is present in steel A, C and D in the vicinity of carbides below 600 °C, but it starts to dissolve above that temperature. During the experimental work introduced above, after cooling down of the specimens from temperatures above 600 °C, probably a little boron remains in solid solution and cause decrease in thermoelectric power. At temperatures above 680 °C, a possible massive precipitate (for example iron-carbide) dissolution can cause a strong decrease in thermoelectric power by all of the steels [2].

Summary

In this paper, the evolution of thermoelectric power and hardness of cold rolled low carbon steels during heating was studied. The effect of recrystallization on the thermoelectric power is remarkable, but it changes with the composition of the steel. The difference in the thermoelectric power before and after the recrystallization is ~ 200-300 nV/°C in the case of the steel without boron, whilst by the steels having boron this value is ranging between 50…200 nV/°C. Experimental investigations and computer simulation results show that boron containing metastable

precipitates start to dissolve into ferrite above 600 °C, which could cause the decrease of thermoelectric power of steels containing boron after recrystallization.

Acknowledgements

This work is connected to the scientific program of the "Development of quality-oriented and harmonized R+D+I strategy and functional model at BME" project. This project is supported by the New Hungary Development Plan (Project ID: TÁMOP-4.2.1/B-09/1/KMR-2010-0002). The authors are also indebted to Gedeon Richter Talentum Foundation for its financial support.

References

[1] V. Massardier, V. Guétaz, J. Merlin, M. Soler, “Kinetic and microstructural study of aluminium nitride precipitation in a low carbon aluminium-killed steel”, Mat. Sci. Eng. A 355 (2003) 299-310.

[2] J. P. Ferrer, T. de Cock, C. Capdevila, F. G. Caballero, C. G. de Andre´s, omparison of the annealing behaviour between cold and warm rolled ELC steels by thermoelectric power measurements, Acta Mat. 55 (2007) 2075–2083.

[3] A. Brahmi, R. Borrelly, Study of aluminium nitride precipitation in pure Fe-Al-N alloy by thermoelectric power measurements, Acta Mat. 45 (1997) 1889-1897.

[4] S. Carabajar, J. Merlin, V. Massardier, S. Chabanet, Precipitation evolution during the annealing of an interstitial-free steel, Mat. Sci. Eng. A 281 (2000) 132–142.

[5] R. Rana, S.B. Singh, O.N. Mohanty, Thermoelectric power studies of copper precipitation in a new interstitial-free steel. Scr. Mat. 55 (2006) 1107–1110.

[6] L. C. Nordheim, J. Gorter, “Bemerkungen über Thermokraft und Widerstand”, Physica 2 (1935) 383-390.

[7] S. S. Satyam, B. J. Kishor, Heating rate effects during non-isothermal annealing of AlK steel, J. Mat. Eng. Per. 12 (2003) 157-164.

[8] F. G. Wilson, T. Gladman, Aluminium Nitride in Steel, Int. Mat. Rev. 33, (1988) 223-286.

[9] R. C. Sharma, Principles ofHeat Treatmet of Steels, New Age International, New Delhi, 1996.

Chemical etching of dental implant material

Lilla Nádai[1,a], Bálint Katona[1,b], Eszter Bognár[1,2,c]

[1] Budapest University of Technology and Economics, Department of Materials Science and Engineering, H-1111 Budapest, Bertalan Lajos u. 7. Hungary

[2]MTA–BME Research Group for Composite Science and Technology, H-1111 Budapest, Műegyetem rkp. 3. Hungary

[a]nadai.lilla@gmail.com, [b]katona@eik.bme.hu, [c]eszter@eik.bme.hu

Keywords: surface treatment, chemical etching, dental implant material, Grade 2 titanium, Grade 5 titanium

Abstract. In this article we dealt with the development of a new method of chemical etching on dental implant materials, Grade 2 and Grade 5 titanium. Certain process creates reproducible homogenous and microrough surface, furthermore improves the reproducibility and productivity for industry appliance. During the research we modified the surface roughness of 2 mm thick samples in a single step of acid etching with a mixture of HF, HNO_3 and distilled water varying the etching time (15-600 seconds). After the surface treatment we obtained the changes of mass and the surface roughness on both sides of every sample. The resulting surface was examined with stereo- and electron microscopy. Based on our results we can determine a parameter setting where the homogenous and microrough surface is reproducible.

Introduction

Most of the dental implants are constructed from metals or alloys. The base material can be titanium or tantalum, the alloys are aluminium, vanadium, cobalt, chromium, molybdenum and nickel. The most commonly used material type in dentistry is titanium [1]. Titanium and its alloys have low density compared to other metals of similar mechanical and thermal properties. Furthermore they have excellent biocompatibility and corrosion-resistance in many environments because of the formation of a protective oxide surface film [1][2]. The ASTM Committee F04 on Materials for Surgical Implants distinguishes four Grades of commercially pure titanium (Grade 1, Grade 2, Grade 3 and Grade 4) and two titanium alloys (Ti-6Al-4V and Ti-6Al-4V extra low interstitial). These materials are used as dental implants [3][4]. Titanium surface modifications are employed to fabricate implant surfaces in order to promote osseointegration, faster healing time, higher bone-to-implant contact ratio, and longevity of titanium implants [5].

Commercially available etched implants from implant systems were investigated by S. Szmukler-Moncler and his colleagues. According to the study on Osseotite implants (manufactured by 3i) are used after dual thermo-etching. The implant surface is successively immersed in a 15% HF bath to remove the native titanium oxide layer and then etched in a mixture of H_2SO_4/HCl acids (ratio of 6:1), and heated at 60–80 °C for 180–600 seconds to create the surface texture. After the treatment the surface roughness was 0.46±0.06 μm (Ra). SLA-ITI implant (manufactured by Straumann AG) is sandblasted and etched in a boiling mixture of HCl/H_2SO_4. Etching temperature was between 125–130°C and the etching time was 300 seconds. The resulted surface roughness was 1.56±0.27 μm (Ra). This study revealed that the industrial process is not fully reproducible and treating titanium surfaces with acid does not create a standard topography [6]. Several parameters affect the topography of etched implants, including the surface roughness or roughening procedure prior to etching, acid mixture, acid bath temperature and etching time [6][7][8].

C. N. Elias et al. modified the surface of Grade 4 titanium discs and dental implants by acid etching with a mixture of HNO_3, HCl and H_2SO_4. The surface roughness after acid etching was 0.51±0.10 μm (Ra). The results show that surface morphology, topography, roughness and chemical composition were changed by the treatments and these changes have a significant influence on

osseointegration [9]. Furthermore they determined that the removal torque of acid etched implants is higher than that of machined implants, which means that the osseointegration mechanisms are faster in acid treated implants than machined implants [10].
G. Juodzbalys and his team did experiments by acid etching the surfaces of implants. Titanium Grade 5 discs and implants were etched using different acids (HCl, H_2SO_4, H_3PO_4) and their combinations with variable time exposures at +20 °C. The conclusion was, the titanium surface etched with H_2SO_4 and HCl according to its topography combines the main properties of roughened titanium surface: glossily micro rough and large waviness. In general, the experimental surface was rougher when compared to commercially available implants [11].
According to the study of H. Garg et al acid etching can be done by using a HCL/H_2SO_4 mixture or by pickling in 2% HF/10%HNO_3. These processes leave pits and craters [12]. In addition to the surface roughness, sand blasting and acid etching with 1% HF and 30% HNO_3 can remove the surface contaminants and the morphologic irregularities could improve initial cell anchorage, providing better osseointegration [13]. Immersion of titanium implants for several minutes in a mixture of concentrated HCl and H_2SO_4 heated above 100 °C (dual acid-etching) is employed to produce a microrough surface. This type of surface promotes rapid osseointegration [14].
Strong acids such as HCl, H_2SO_4, HNO_3 and HF are used often for roughening titanium dental implants. Acid-etching produces micro pits on titanium surfaces with sizes ranging from 0.5 to 2 μm in diameter. At the same time, it cleans the surface of the implant [15][16]. Etching has been shown to greatly enhance osseointegration and improve the stability of the titanium dental implant at an early stage [16][17][18]. During treating titanium dental implants in fluoride solutions created both a surface roughness and fluoride incorporation favorable to the osseointegration of dental implants [15][19].
The manufacturer Struers recommends the most common chemical etchant for titanium, namely Kroll's reagent. This consists of 100 ml water, 1-3 ml hydrofluoric acid and 2-6 ml nitric acid. The concentration can vary depending on the alloy and can be adjusted individually [21].
In this article we uncover a new method of chemical etching on implant materials, Grade 2 and Grade 5 titanium in order to modify the surface roughness of the samples. The aim of our research was to create the same surface roughness, 0.5-2 μm, as stated in the references above in order to reinforce osseointegration, however replacing the two introduced steps (sand blasting and dual etching) by one unified treatment. We researched parameter settings, where the homogenous and microrough surface is reproducible, which is a major factor for industry appliance.

Materials and methods

For our experiments we used Grade 2 and Grade 5 titanium samples, which are often used for manufacturing of dental implants. Dental implants are formed by turning in industry. 2 mm thick discs were turned from bar shaped row materials. The disc shaped samples were sliced with a Buehler Isomet 1000 diamond cutter into 4 pieces creating a total of 24 samples in order to have enough samples for the research. During surface treatment we applied same parameter settings for quarter disc shaped samples from both materials therefore we could compare the results and make conclusions. Furthermore we were looking for a parameter combination (etching solution, etching time, temperature) which create reproducible microrough surface on samples for both materials. These could provide productivity for industrial production. During the experiment we used an etching solution consisting of 9 V/V% HF, 12 V/V% HNO_3 and distilled water selected on Struers' recommendation and on the basis of preliminary experiments. We carried out the chemical etching of samples in an ultrasonic cleaner in order to increase the efficiency of the reaction. Fig. 2 shows a schematic illustration of the treatment.

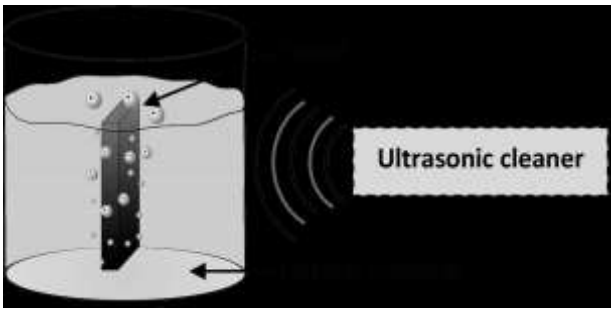

Figure 1: The chemical etching process of Grade 2 and Grade 5 titanium samples

Etching is an exothermic process, so the system heats up. Since the etching solution intensity depends closely on temperature, we had to keep it at an optimal level of 30 °C based on measurements. Chilled acetone cooled the reaction environment to keep the temperature of the etching solution at 30±1°C.
During the process the reaction between the samples and the etching solution causes material lost from the treated samples. Chemical etching is affected by material composition, the etching solution, the temperature and the treatment time.
As the time of chemical etching is an important parameter for surface quality, we analyzed samples with various treatment times. For both materials (Grade 2 and Grade 5 titanium) we applied the times shown in Table 1.

Sample No.	1	2	3	4	5	6	7	8	9	10	11	12
Etching time (sec)	15	30	60	120	180	240	300	360	420	480	540	600

Table 1: Etching time of the samples

Before the treatment we measured with a Denver-Instrument APX-200 analytical balance mass and the surface roughness with Mitutoyo Surftest 211 on both sides of titanium samples. As a single measurement is not reproducible and cannot provide reliable results, we defined the mass of every sample from the average of three measurements, and the surface roughness on both sides of every sample from the average results measured of five different surface area. We carried out these measurements also after chemical etching, obtaining data on the surface quality and loss of material plotted against etching times. We examined the samples with Olympus SZX16 stereo microscopy and Philips XL 20 electron microscopy.

Results of chemical etching

From the etching treatment we expect that longer etching time causes greater material loss. This thesis cannot be confirmed simply on the basis of the results, because on the surface of the samples there are different amount of burr and contaminations after turning. Moreover during the treatment the mass of the precipitates can be different as well. For example Figure 2 shows that extremely high mass loss occurred on sample 8 from Grade 2 titanium. Furthermore it can happen that the etching solution gets expended. In addition, measurement errors may occur such as at sample 9 from Grade 2 titanium showed by Figure 2.
Mass distribution of Grade 5 titanium samples before and after etching covers a smaller range than for the Grade 2 titanium samples. The least material loss for Grade 5 samples happened at sample 4 (2%). In case of Grade 2 samples, the least material loss was 2% as well which occurred on sample 2 without the outlier sample 9. Furthermore taking into account the standard deviations at both, materials show almost similar mass loss at the 15-180 seconds etched samples. The greatest material loss at Grade 2 is 5% if the sample 8 is not taken into account. For Grade 5 titanium samples the same values occurred at sample 9. The samples from both materials etched 420-600 seconds showed 4-5% material loss. This is not a significant difference compared to the less time etched samples, but the treatment takes longer.

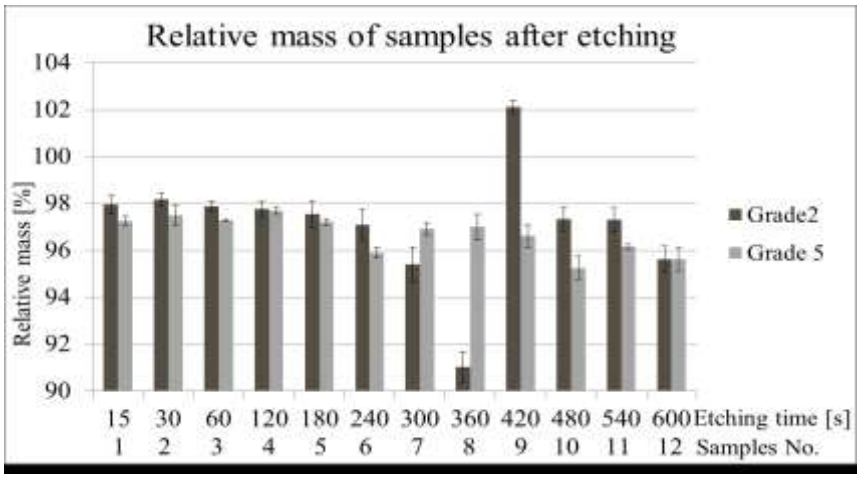

Figure 2: Masses of Grade 5 titanium samples

Figure 3 shows the average surface roughness of the titanium samples in the function of etching time. The dark colored bars represent the surface roughness of Grade 2 samples and the light colored bars are the Grade 5 samples. Comparing the roughness of the Grade 2 and Grade 5 samples after etching, we determined that the Grade 5 samples got lower surface roughness than the Grade 2 samples. The surface roughness distribution in the function of time at the Grade 5 samples covers a smaller range 0.19-0.31±0.04 μm than for the Grade 2 titanium samples 0.34-0.59±0.05 μm. At the Grade 2 samples the maximum surface roughness (0.59±0.07 μm) was achieved by sample 4. Taking into account the standard deviations, similar surface roughness (0.5±0.06 μm) was evolved on the first three samples (etching time of 15-60 seconds) as well. The smoother surface roughness (0.34±0.03 μm) was achieved by sample 6. Considering the standard deviation the surface roughness values (0.34±0.03 μm) were similar at samples with longer etching time. Nevertheless the surface of sample 7 and 9 is rougher (0.45±0.06 μm) which may arise from measurement inaccuracies. For the Grade 5 samples the maximal surface roughness (0.31±0.04 μm) is observed at sample 3. This value is smaller than the smoother surface roughness achieved at Grade 2 sample after etching. From 15 to 30 seconds etching samples have similar surface roughness value (0.31±0.04 μm). The smoother surface roughness (0.19±0.04 μm) at Grade 5 samples are indicated by the samples 11 and 12. Taking into account the deviation the samples from 4 to 10 are in a similar surface roughness range. From the results it can be concluded that by increasing etching time the surface roughness was not significantly smoother.

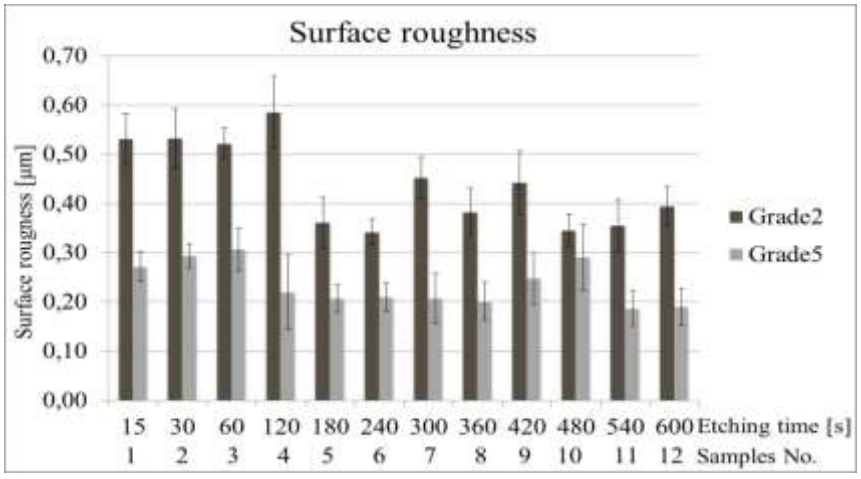

Figure 3: Surface roughness of Grade 2 and Grade 5 titanium samples after etching

We examined the samples with stereo- and electron microscopes. Figure 4 shows electron microscope images. In the upper photos can be seen the grooves on a turned Grade 2 and Grade 5 sample. On the chemical etched surfaces of Grade 2 sample can be observed that the surface became homogeneous and detached the grooves formed during the turning. The electron microscope image of Grade 5 titanium sample shows that the surface is rougher than at Grade 2

titanium sample. Nevertheless contaminants, burr and deep grooves disappeared and the surface became homogenous.

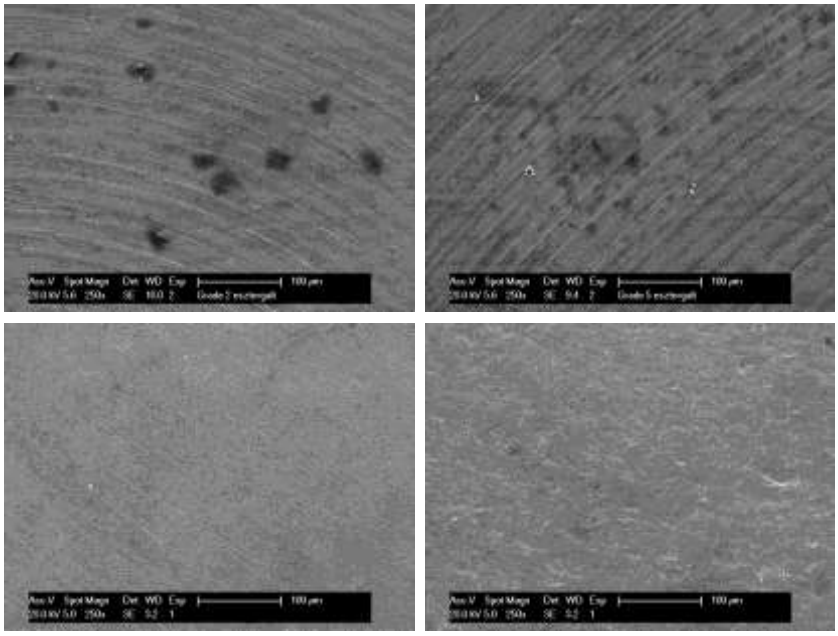

Figure 4: Scanning electron microscope images about Grade 2 (upper left) and Grade 5 (upper right) images after turning and about 30 seconds etched Grade 2 (bottom left) and Grade 5 (bottom right) samples

Summary

In our research we modified the surface roughness of implant materials, Grade 2 and Grade 5 titanium by chemical etching with HF, HNO_3 and distilled water. We carried out the surface treatment in a single step, thus we did not use either sand blasting or dual etching.

During our research we found that the chemical etching of 2 mm thick quarter disc-shaped samples of Grade 5 has an average mass loss in the interval of 2-5 % and the Grade 2 as well without the outliers. Mass distribution of the Grade 5 titanium before and after etching covers a smaller range than for the Grade 2 titanium samples.

Comparing the surface roughness of the Grade 2 and Grade 5 samples, we found after acid etching the Grade 5 samples got smoother surface roughness than the Grade 2 samples. The surface roughness distribution in the function of time at the Grade 5 samples covers an interval from 0.19 µm to 0.31µm and at the Grade 2 titanium samples from 0.34 µm to 0.59 µm.

Major factors for industry appliance are the reproducibility and productivity; therefore, we took into account at the surface treatment the low material decrease and shortest etching time. Based on our result we can determine that the homogenous and microrough surface on both materials became at the following parameter settings: etching time of 30 seconds, etching solution of 9 V/V% HF, 12 V/V% HNO_3 and distilled water with temperature of 30°C.

The images made with scanning electron microscopy show that the surface of both materials became homogenous after 30 seconds acid etching. In fact, on the Grade 2 samples the grooves completely disappeared.

Based on our result we can determine that we created homogenous and microrough surface on Grade 2 and Grade 5 titanium As stated in the literature at the beginning this surface has a significant role to enhance osseointegration and improve the stability of the titanium dental implant at an early stage [17][18].

Acknowledgements

This work is connected to the scientific program of the " Development of quality-oriented and harmonized R+D+I strategy and functional model at BME" project. This project is supported by the New Hungary Development Plan (Project ID: TÁMOP-4.2.1/B-09/1/KMR-2010-0002).

References

[1] B.C. Muddugangadhar, G.S. Amarnath, S. Tripathi, S. Dikshit, Biomaterials for dental implants, International Journal of Oral Implantology and Clinical Research 2 (2011) 13-24.

[2] Information on http://www.britannica.com/EBchecked/topic/597135/titanium-Ti 27.01.2014

[3] M. McCracken, Dental Implant Materials: Commercially: Pure Titanium and Titanium Alloys, Journal of Prosthodontics 8 (1999) 40-43.

[4] ADA Council on scientific affairs, Titanium applications in dentistry, Journal of the Dental Association 134 (2003) 347-349.

[5] K. Subramani, R.T. Mathew: Emerging Nanotechnologies in Dentistry, Chapter 6: Titanium Surface Modification Techniques for Dental Implants - From Microscale to Nanoscale, William Andrew Publishing, ISBN: 978-1-4557-7862-1 2011, pp. 85-102.

[6] S. Szmukler-Moncler, T. Testori, J. P. Bernard: Etched Implants: A Comparative Surface Analysis of Four Implant Systems, J Biomed Mater Res Part B: Appl Biomater 69 (2004) 46–57.

[7] S. Szmukler-Moncler, D. Perrin, V. Ahossi et al, Biological properties of acid etched titanium implants: effect of sandblasting on bone anchorage, J. Biomed. Mater. Res. 68 (2004) 149-159.

[8] S.Anil, P.S. Anand, H. Alghamdi, J.A. Jansen, Dental Implant Surface Enhancement and Osseointegration, Implant Dentistry - A Rapidly Evolving Practice, InTech (2011) ISBN: 978-953-307-658-4

[9] C.N. Elias: Titanium dental implant surfaces, Revista Matéria 15 (2010) 138-142.

[10] C. N. Elias, Y. Oshida, J. H. C. Lima, C. A. Muller, Relationship between surface properties (roughness,wettability and morphology) of titanium and dental implant removal torque, Journal of the Mechanical Behavior of Biomedical Materials 1 (2008) 234-242.

[11] G. Juodzbalys, M. Sapragoniene, A. Wennerberg, New Acid Etched Titanium Dental Implant Surface, Stomatologija, Baltic Dental and Maxillofacial Journal 5 (2003) 101-105.

[12] H. Garg, G. Bedi, A. Gargmost, Implant Surface Modifications: A Review, Journal of Clinical and Diagnostic Research 6 (2012) 319-324.

[13] G. Orsini, B. Assenza, A. Scarano, M. Piatteli, A. Piatteli, Surface analysis of machined versus sand blasted and acid etched Ti implants, Int. J. Oral Maxillofac. Implants 15 (2000) 779-784.

[14] S.A. Cho, K.T. Park, The removal torque of titanium screw inserted in rabbit tibia treated by dual acid etching, Biomaterials 24 (2003) 3611–3617.

[15] L. Le Gu´ehennec, A. Soueidan, P. Layrolle , Y. Amouriq, Surface treatments of titanium dental implants for rapid osseointegration, Dental Materials 23 (2007) 844-854.

[16] C.Y. Guo, A.T.H. Tang, J.P. Matinlinna, Insights into surface treatment methods of titanium dental implants, Journal of Adhesion Science and Technology 26 (2012) 189-205

[17] M. Wong, J. Eulenberger, R. Schenk, E. Hunziker, Effect of surface topology on the osseointegration of implant materials in trabecular bone, J. Biomed. Mater. Res. 29 (1995) 1567–1575.

[18] R. B. Parekh, O. Shetty, R. Tabassum, Surface modifications for endosseous dental implants, International Journal of Oral Implantology and Clinical Research, 3 (2012) 116-121.

[19] J.E. Ellingsen, Pre-treatment of titanium implants with fluoride improves their retention in bone, Journal of Materials Science: Materials in Medicine 6 (1995) 749–758.

[20] J.E. Ellingsen, C.B. Johansson, A. Wennerberg, A. Holmen, Improved retention and bone-to-implant contact with fluoride-modified titanium implants, International Journal of Oral and Maxillofacial Implants 19 (2004) 659–66.

[21] B. Taylor, E. Weidmann, Struers Application Notes: Metallographic preparation of titanium (2008)

Surface properties of lightweight aggregate concrete and its correlation with durability

Rita Nemes[1, a]

[1]Budapest University of Technology and Economic, Department of Construction Materials and Engineering Geology, 1111 Budapest, Műegyetem rkp. 3. HUNGARY

[a]nemes.rita@epito.bme.hu

Keywords: lightweight aggregate concrete (LWAC), durability, abrasion resistance, frost resistance, frost scaling, expanded clay, expanded glass.

Abstract Durability is one of most important requirements of concrete design. From this aspect is arising the required minimal compressive strength class of conventional concrete in order to ensure durability. The porosity of cement mortar matrix and consequently the liquid and gas permeability of concrete may be reduced. But the strength of lightweight aggregate concrete depends primarily on the crushing resistance of lightweight aggregate (LWA). With low strength LWA may be achieved higher concrete strength by high strength cement mortar matrix. Therefore we can not consider durability simply on the basis of the compressive strength of concrete. The most important durability factors are closely related to the porosity and strength of the cement mortar matrix but for example the abrasion resistance depends more significantly on the aggregate type. Lightweight aggregates usually do not have high abrasion resistance, but they can be advantageous in case of restoration of bridge pavement. The most important factors of durability regarding pavements are frost scaling and abrasion resistance. These parameters (especially abrasion resistance) are not available in the literature when using LWA.

Introduction

Lightweight aggregate concrete (LWAC) can be determined as a type of special, high performance concrete made with porous aggregates with low particle density. Due to the increasing air pollution and using deicing salts in winter, durability of urban structures made of LWAC is an important research topic in Middle Europe [1]. Chemical effects reduce the lifetime of reinforced concrete structures, by to chloride corrosion [2], carbonation, frost-thaw cycles, etc. Usage of LWAC can be advantageous in urban structures, e.g. bridges, because of its lower density and through that the lower dead load, but it should be able to resist frost and chemical effects too [3]. Many properties of LWAC influence the durability of concrete structures. Mechanical parameters of concrete are determinative [4], but to compare durability of different concrete types, water permeability is also very important. Permeability of LWA is higher and frost resistance of LWA is lower than normal weight aggregate (NWA). Liu, Chia and Zhang [5] made an experimental study to evaluate the effect of LWA content on water absorption, water permeability, and resistance to chloride-ion penetration in LWAC [6]. They found that diffusion coefficient of LWAC was not significantly different to normal weight concrete (NWC) made with the same water-cement ratio (w/c-ratio). This means that cement type and w/c-ratio determined durability of LWAC; although the volume of the aggregate is higher than cement mortar. We tested different LWAs in “weak” cement mortar (a mortar having high w/c-ratio). In certain cases, abrasion and frost resistance are not preliminary requirements while a density limit is given, and the concrete will be subjected to these effects. A Hungarian example was the concrete of the temporary pavement of Margaret Bridge in Budapest, which was under reconstruction, where most important requirements were low density, and the strength was also limited. The original stress value was not to be exceeded during reconstruction [7]. The required strength class of this concrete was low (LC20/22) in terms of durability requirements (frost resistance and abrasion resistance). This was reduced due to the expected life time (one year) of the pavement.

Lightweight Aggregate

LWAC is mixed with LWAs (e.g. expanded clay, expanded glass, expanded perlite, crashed ceramic brick, and crashed volcanic tuff) which are serving as a substitution of the coarse aggregate fraction of ordinary concrete. The aim is to reduce the density of concrete (through which the reduction of the dead load can be achieved). In the typical internal load bearing mechanism of LWAC, the main load bearing part of the material is the cement mortar matrix. The aggregate has high porosity, mostly with open-pores, with high water absorption capability. LWAC with adequate strength needs high cement content and low water-cement ratio. The internal structure and the rate of open and closed surface pores of LWA is little affected by the compressive strength, but are very important in the aspect of durability. The internal structure of expanded glass aggregate is very different to expanded clay and natural light density stone. This difference can be seen on the scanning electron microscope (SEM) images (Fig. 1, Fig. 2). The internal pore structure of expanded glass is hemispherical and closed surfaced in many places. (This expanded glass is aggregates, not same with crushed or ground glass [8].) The internal pore structure of expanded clay is cannel-like, whereupon it has high and fast water absorption capability. The pores on the surface of LWA can be closed (blocked) during manufacturing, and so the durability can be increased; the possibility of production technologies may further be developed.

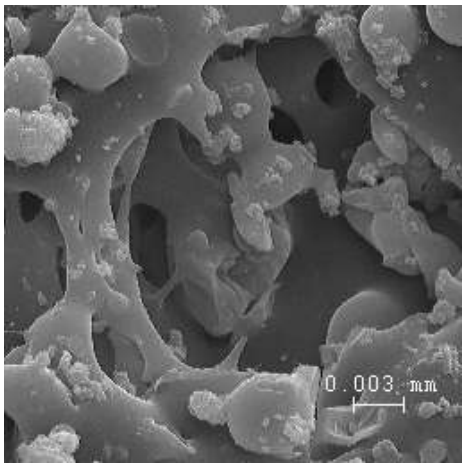

Fig. 1 SEM image of the cut surface of an expanded glass particle

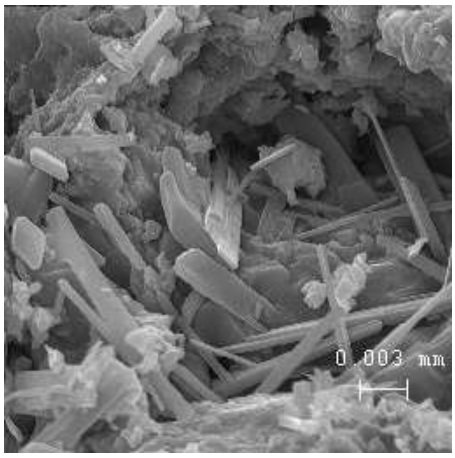

Fig. 2 SEM image of the cut surface of an expanded clay particle

Durability

Regarding concretes, durability is an equivalent requirement in construction as load bearing capacity and serviceability [9]. The high targeted strength class of conventional concretes increases durability due to the physical and chemical changes in concrete which happen as a result of liquids and gases penetrating the material. These processes can be reduced by keeping the porosity at a lower value. Similarly is important that, what kind of pore structure is in LWA and where it is concentrated. Detailed test results can be found in the literature regarding the cement paste porosity to achieve an appropriate material. But there are no data for aggregates, except where the regulations prescribe the usage of certain aggregates, by excluding many other options. When using lightweight aggregates it is common, that other conditions (which were worked out for conventional concretes) are not true.

Laboratory Tests

Different LWAC mixtures and a reference one (with quartz gravel aggregate) were made in laboratory with different coarse lightweight aggregate types (expanded glass and two types of

expanded clay). The mortar composition and volume were constant parameters, differences were only in the type of coarse aggregates. The applied water-cement ratio was high (0.61), consequently the porosity of the cement mortar matrix was also high. So differences between the aggregates can be detected easily. Frost scaling and abrasion tests were performed. We focused at first on surface properties. The test specimens were prepared to allow the investigation of all type of surfaces: against formwork, inner (cut), and cast (top) surface (Fig. 3).

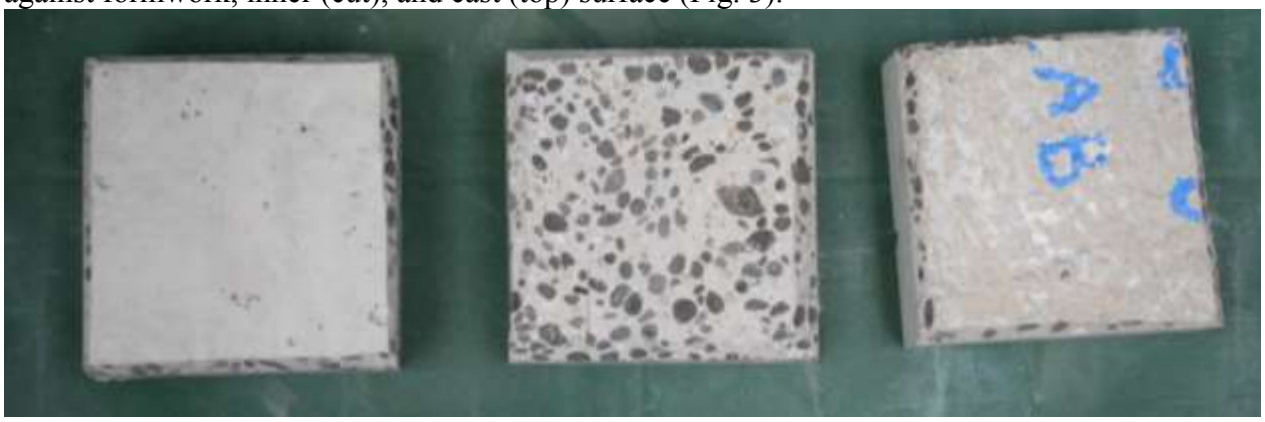

Fig. 3 Tested surfaces of concretes: against formwork, inner (cut), and cast (top) surface before further testing

Frost Scaling

The frost resistance tests were carried according to CEN/TS 12390-9:2006 [10] standard. The frost scale test is more sensitive to the aggregate type than conventional frost-thaw test on cube specimens. The main cause of low frost resistance is the highly porous cement stone (water-cement ratio = 0.61). Normal weight concrete can be seen on (Fig. 4), its behavior similar to expanded clay aggregate (Fig. 6, Fig. 8). The difference between the composition of the concretes on Fig. 4, 5, 6 is only the type of the coarse aggregate. The expanded clay behaves similarly to quartz gravel, but the resistance against frost scaling of the measured expanded glass concrete (Fig. 5) is better than quartz gravel or expanded clay. Expanded glass aggregate concrete has very low strength (f_{cm}=15.6 N/mm^2), but it has a good frost resistance. This can be explained by the featuring internal structure of expanded glass (Fig. 1). With the tested expanded clay aggregate mixture can be achieved enough frost resistance when the water-cement ratio is not higher than 0.5 (Fig. 7, 9). Such was the actual concrete mixture of temporary pavement during Margaret Bridge reconstruction.

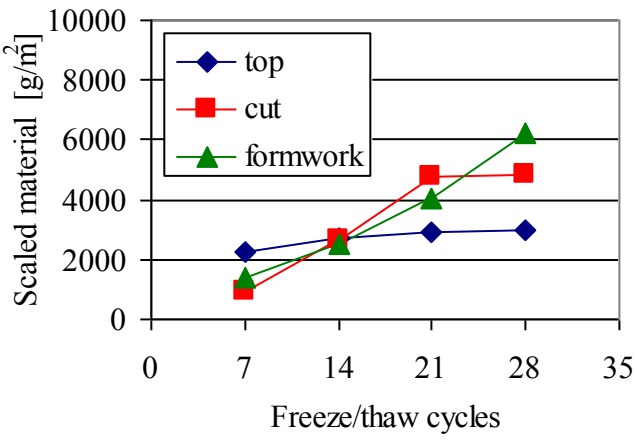

Fig. 4 Frost scales of quartz gravel aggregate concrete (w/c=0.61)
ρ_b=2365 kg/m^3 f_{cm}=44.4 N/mm^2

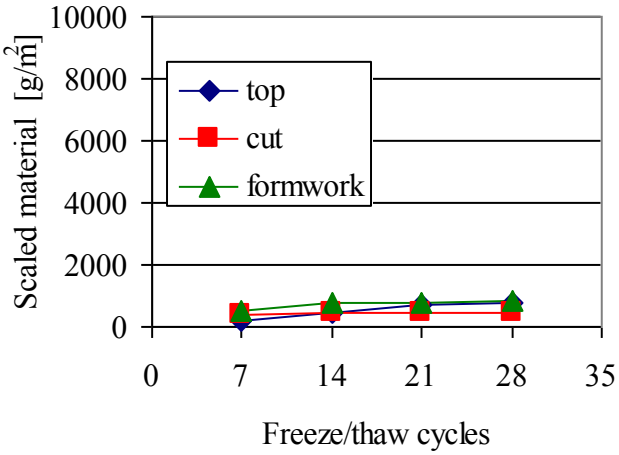

Fig. 5 Frost scales of expanded glass aggregate concrete (w/c=0.61)
ρ_b=1647 kg/m^3 f_{cm}=15.6 N/mm^2

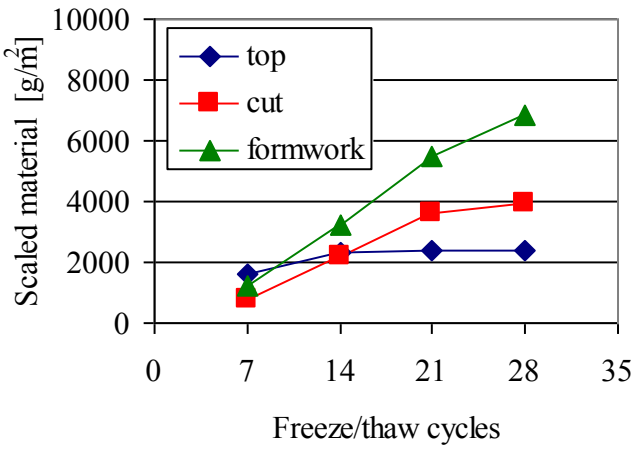

Fig. 6 Frost scales of expanded clay aggregate concrete (w/c=0.61)
ρ_b=1907 kg/m^3 f_{cm}=35.5 N/mm^2

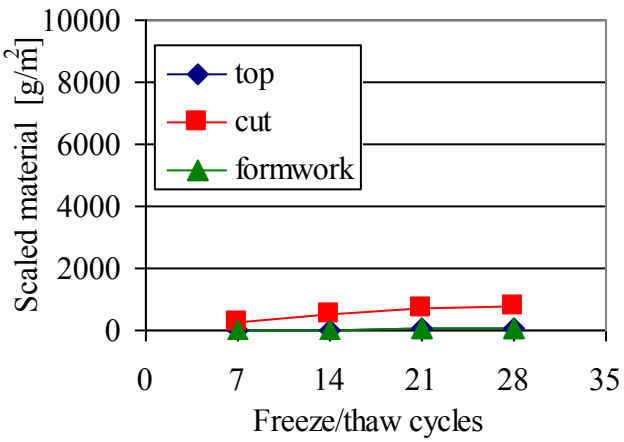

Fig. 7 Frost scales of expanded clay aggregate concrete of Margaret bridge (w/c=0.5)
ρ_b=1680 kg/m^3 f_{cm}=29.9 N/mm^2

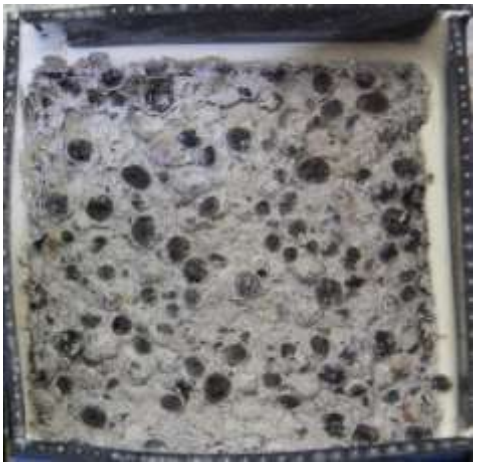

Fig. 8 Surface of specimen after the test (expanded clay aggregate, w/c=0.61)

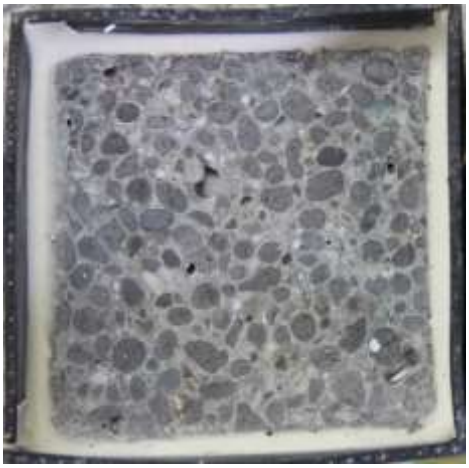

Fig. 9 Surface of specimen after the test (expanded clay aggregate, w/c=0.5)

Abrasion Resistance

The abrasion resistance was studied by the Böhme test according to EN 1338:2003 Annex H [11] on cube specimens (70x70x70 mm), by the dry surface method, on the same composition concretes as the frost resistance tests (Table 1) were carried out. Before testing, the density of the specimens was determined by measuring the mass and determining the volume. Based on the Böhme method, normalized abrasive powder is spread on the steel test track and the specimen is positioned in the Böhme Abrasion Test instrument. The apparatus rotates the grinding plate, submitting the specimen to the abrasive load of 294 N for a given number of cycles. The standard test is performed for 4x4 cycles composed of 22 turns each, but we performed 5x4x22, and recorded the measured quantities after every 4x22 cycles. At the end of the test, the abrasion value is calculated as an average loss in volume and mass.

The average of the abrasion loss of lightweight aggregate concretes was about three times larger then the reference quartz gravel aggregate concrete.

Abrasion resistance on cast (top) surface (blank shapes and interrupted lines in Fig. 10) increased if the density of concrete was increased. It is practically equal to the expected results. In the first series of abrasion (after 4x22 cycles) the abrasion volume loss was 25-65 % higher than the

difference between 4th and 5th series (after 4x4x22 and 5x4x22 cycles). In case of lower particle density of LWA this difference was higher.

Table 1 Density and compressive strength of concrete for abrasion test

Type of aggregate	Density of concrete [kg/m^3]	Compressive strength of concrete [N/mm^2]
Expanded glass	1367	22.4
Expanded clay	1862	35.5
Quartz gravel	2266	44.4

The results, which were measured on cut surfaces (full shapes and solid lines in Fig. 10) are different from the ones measured on cast surfaces. There was no significant difference between two various LWAC in respect of abrasion. The measured values of abrasion on cast surfaces were in all cases higher than on cut surfaces.

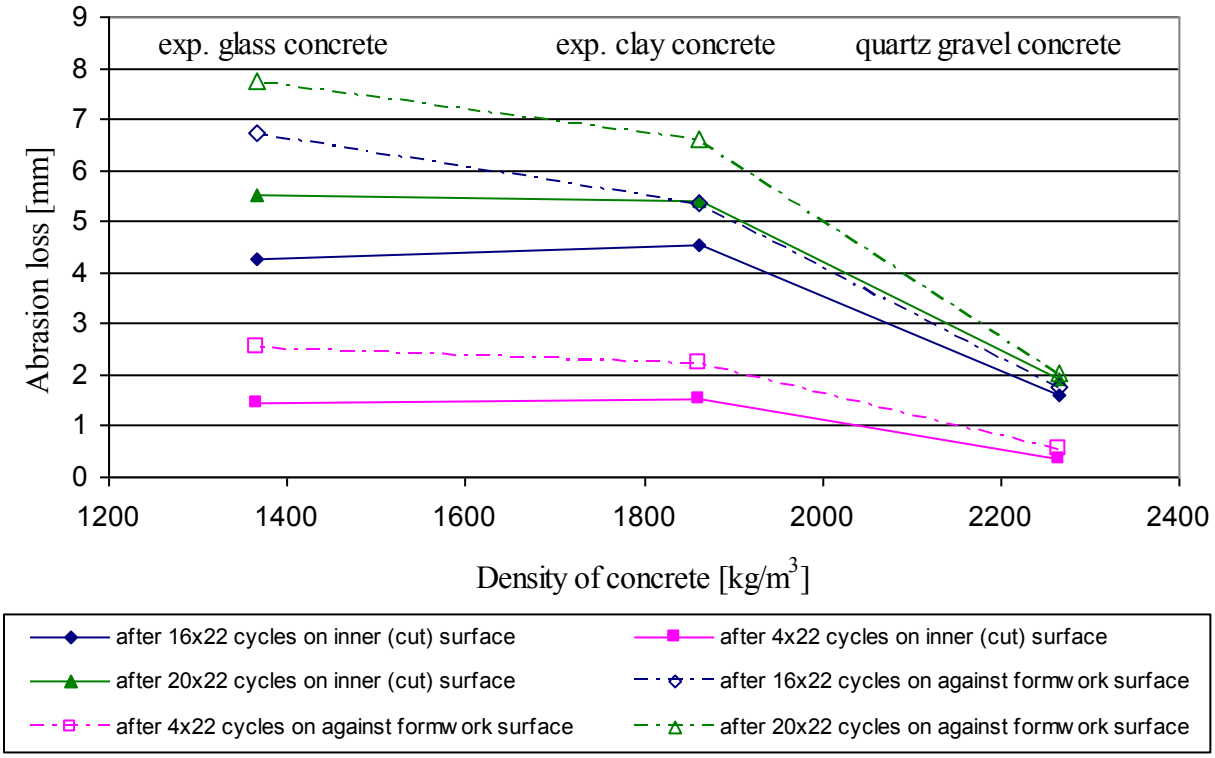

Fig. 10 Abrasion losses of measured concretes in case of different density

Summary

Different LWAC mixtures and one reference (NWC) mixtures were tested in laboratory with different coarse lightweight aggregate types (expanded glass, expanded clay). We found that, in the aspect of durability of LWAC the surface properties are more important then compressive strength and conventional frost-thaw resistance. This is especially true in case of outdoor and horizontal structure elements, for example a bridge pavement.

The higher porosity of cement stone (higher w/c ratio) causes a lower frost resistance, so the porosity of cement stone has greater impact on this property then the type of the lightweight

aggregate. At the same time expanded glass aggregate concrete had a high frost scale resistance, which can be the result of the pore structure of this aggregate type, but further researches should be carried out to investigate this phenomenon. If the porosity of cement mortar matrix is lower (w/c-ratio is 0.5 or less) the frost scale might be low enough to satisfy the requirements (e.g. a bridge pavement).

In terms of abrasion resistance the tested LWACs are unfavorable. Their abrasion losses are three times higher as the abrasion loss of quartz gravel aggregate concrete, when the cement mortar has a high (0.61) water-cement ratio. The abrasion loss in case of different types of LWA may only be characterized by cut surface measurements, which is an important factor for further testing. In the future we intend to test this property with other LWAs (for example LWA with closed surface pores and low water absorption) and by the application of better cement mortar matrixes.

Acknowledgements

Author wishes to express her gratitude to the Duna-Dráva Cement Kft., Biotech Hungária Kft. and Liabau Kft. which companies supported present research and provided the tested materials.

References

[1] J. L. Vítek, Sustainable Engineering Structures, In J. Radič, M. Kušter (Eds.) Durability of Concrete Structures CCC 2012 Plitvice Lakes, Croatia 4-6 Oktober 2012
[2] Gy. Balázs, K. Kopecskó Chloride Binding in Concrete, Concrete Structures 3: pp. 47-51. 2002
[3] R. Nemes, O. Fenyvesi, Frost Resistance of LWAC Made with Different Lightweight Aggregate in Urban Enviroment, in: J. Biliszuczuk, J. Bień, P. Kawryszków, T. Kmaiński (Eds.), Concrete Structures in Urban Areas, CCC 2013, Wrocław, Poland, September 4-6, 2013, pp. 394-397.
[4] T.Y. Lo, H.Z. Cui, Z.G. Li, Influence of aggregate pre-wetting and fly ash on mechanical properties of lightweight concrete, Waste Management Vol. 24 (2004) 333-338. doi:10.1016/j.wasman.2003.06.003
[5] X. Liu, K. S. Chia, M. Zhang, Water absorption, permeability, and resistance to chloride-ion penetration of lightweight aggregate concrete, Construction and Building Materials Vol. 25 (2011) 335-343.
[6] M-J Lee, M-G Lee, J-Y Chen, et al. Strength and Freeze-Thaw Testing of Lightweight Aggregate Concretes Chang, JR; Yang, SR (Eds.) Conference: 8th International Conference on Road and Airfield Pavement Technology (ICPT) Taipei, Taiwan Jul 14-18, 2013
[7] Zs. Józsa, R. Nemes, O. Fenyvesi, Lightweight Aggregate Concrete Pavement on Margit Bridge in Budapest In: L. Gy. Balázs, É. Lublóy (Eds.) Innovative Materials and Technologies for Concrete Structures: CCC2011 Hungary, Balatonfüred 22-23 Sept. 2011 pp. 81-84.
[8] A. Al-Sibahy, R. Edwards, Mechanical and thermal properties of novel lightweight concrete mixtures containing recycled glass and metakaolin, Construction and Building Materials. 31 (2012) pp.157-167.
[9] O. Fenyvesi, Affect of lightweight aggregate to early age cracking in concrete. Periodica Polytechnica-Civil Engineering 55:(1) (2011) pp. 63-71.
[10] CEN/TS 12390-9:2006 Testing hardened concrete – Part 9: Freeze-thaw – Scaling
[11] EN 1338:2003 Concrete paving blocks. Requirements and test methods

Analysing the suitability of C16/20-X0v(H)-24-F3 concrete for pumping

Alexandra Kitti Németh[1,a], Mária B. Maros[1,b]

[1]University of Miskolc, Institute of Material Science and Materials Processing,
H-3515 Miskolc-Egyetemváros, Hungary

[a]xandra.nemeth@gmail.com; [b]maria.maros@uni-miskolc.hu

Keywords: ready-mix concrete, pumping, composition, fine-particle content, qualification

Abstract. The current paper introduces a case study dealing with the problem of pumpability of the ready-mix concrete of grade of C16/20-X0v(H)-24-F3 [1]. During solving a practical industrial problem we have worked out a modified composition of the related concrete material in order to improve the pumpability. After describing some possible theoretical and practical methods the authors give suggestion for a practical solution. The characteristic feature of the method consists in modifying the recipe of the given grade of concrete without altering the additive structure, and to assure the pulp saturation. The paper reports the results of standardised physical and mechanical tests, executed on the novel concrete material. Based on these results it has been proved, that besides solving the original practical problem of pumpability, the new concrete material possesses better application and technological performance, and is more economical to produce.

Preliminaries and Objectives

The domestic concrete industry often faces the problem that costumers do not indicate certain – occasionally very important – technical requirements, like e.g. the demand for pumpability. This shortcoming may lead to serious damages, furthermore may cause extra costs and loss of time. In the current paper authors introduces a case study originated from a similar problem. The grade of the concrete is C16/20-X0v(H)-24-F3, a widely used, low grade concrete in Hungary, with a well-known quality. The problem happened after it was transported to the construction site and started to be pumped when a concrete bogging in the transporting pipe happened and led to the shutdown of the pump. Analysing the case, it became clear soon, that the problem have been caused by the costumer, who missed to indicate during ordering that he is intended to pump the concrete. Consequently, the manufacturer supplied the concrete of the ordered grade, however without the extra feature of pumpability. The current paper aims at introducing some possible solutions for the problem, and presenting the practically realized case that involves the development of a modified composition of the concrete material. The various qualification tests executed on the modified concrete material and their consequences will also be reported.

Finding the root of problem: analysis of the original recipe

In order to find the cause of the problem the original composition should be analysed. Under the term of recipe of the concrete its composition is understood. We can define the fine particle content of the concrete knowing the recipe, based on which we can draw the conclusion whether the concrete is suitable for transportation with concrete pump or not (see Table 1).This quantity is defined in the Swiss issue of the European concrete-standard [2], which sets out directives regarding the fine particle content of 1 cubic meter of concrete, that is equal to 350 kg/m^3 for the given grade. According to the original recipe – as it can be seen from Table 1. – the fraction of 0.125 mm grain size cannot be found among the additives, therefore the fraction of 0.25 mm grain size should be considered, as fine particle. Thus the content of the fine particle can be determined by summarizing the amount of the various additive grains being smaller than 0.25 mm, i.e. the amount of cement and the lime-flour. This amount is 273 kg/m^3, which is less than it is required by the standard (350 kg/m^3). It is obvious, that this concrete material cannot be transported with a concrete pump [3, 4].

Table 1. The original recipe (refers to 1 m^3 of concrete)

Total amount of additive, admixture and auxiliary materials	1820 kg
Amount of fraction with grain size less than 0.25 mm	18 kg
Cement	255 kg
Lime fume	0 kg
Total fine particle content (fraction with grain size $\leq$0.25mm + cement + complementary materials)	273 kg
Admixture (Plasticiser SIKA BV-40)	1.53 kg

Potential solutions

One of the possible solutions is to modify the recipe of the certain grade of concrete to assure the pulp saturation of the concrete in order to provide pumpability, without altering the structural additives. Another solution is represented by using further components, like plasticizer, stabilizer, etc. Their application brings about increase of the consistency, strength and density of concrete, furthermore the adhesive force among the grains increases in spite the reduced water content. Some additives directly improve pumpability: these increase the viscosity of the mixture, but they are expensive. Mixtures of different greasing materials are also available which reduce friction between concrete and the pipe wall [5]. These lubricants must be applied before starting the pumping process [6, 7, 8. The most frequently used mixtures for facilitating pumping are the cement-water mixture or carboxymethyl-cellulose (CMC) solution in water. Application of the silica powder as additive, is very similar to that of the lime fume. However it is less prevalent in Hungary, and in spite of its advantageous feature of possessing higher fine particle content, better strength and tightness, it is very expensive and therefore it is not a realistic alternative to solve the current problem [4, 9].

From the listed solutions our choice was to work out a modified recipe that assures the pumpability of the concrete without altering the structure-additives of the concrete material. In the following sections proposals for modified recipes fulfilling this requirement are presented.

Proposal No.1: Recipe with lime fume

The addition of lime fume is one of the most obvious solutions for varying the original recipe. This material can be found in a concrete factory in relatively high amounts, furthermore it is a widely used and well-known complementary material in the concrete manufacturing, not to mention that its price is favourable compared to other additional materials. An important aspect of the recipe alteration was, not to modify the composition of the structural additives (see Table 2.).

Table 2. Recipe modified with lime fume (refers to 1 m^3 of concrete)

Total amount of structural additives and auxiliary materials	1820 kg
Amount of fractions under 0,25 mm	18 kg
Cement	260 kg
Lime fume	75 kg
Total fine particle content ($\leq$0.25+cement+fine components)	353 kg
Admixture (Plasticiser SIKA BV-40)	1.70 kg

Main element of the alteration was the additional lime fume, which increased the fine particle ratio of the concrete. When calculating the fine-parts content of the concrete we still have to take into consideration the additives with grain size below 0,25 mm, i.e. the used cement and lime fume [10]. The prescribed fine-particle content according to the Swiss standard still remains 350 kg/m^3. After some simple calculations we can conclude, that adding 75 kg lime fume to the original composition, the fine particle content (353 kg/m^3) of the recipe exceeds the recommended value, so this sort of concrete can be regarded, as pumpable.

In this case we increased the amount of the plasticiser additive too, which as a side effect increases the costs. However, it is necessary to assure the consistency of the fine particles (i.e. cement and lime fume) since consistency is decreasing with increasing fine particle content [3, 4].

Proposal No. 2: Recipe with fly-ash added

Fly ash is a complementary material which creates fine-parts in the concrete, thus whole amount of lime fume is possible to be substituted with it. – It is also an important aspect that it has a favourable price. – Since consequently there will be no any lime fume in this concrete material, in order to get the amount of the fine particle to be supplemented we should subtract the amount of the cement from the prescribed limit values of the fine particle. This method shows that the necessary amount of the fly ash is 95 kg. In the modified recipe, containing fly ash, the required amount of structural additives should be decreased with the amount of the complementary fine particle, i.e. fly ash. Thus the total amount of additives reaches 1820 kg, while the amount of fine particle is 17 kg. The amount of the plasticiser additives should be increased, as well. The composition of this material is presented in Table 3. [3, 4]. This proposal results in a cheaper concrete than the first one, besides it is still proper from the viewpoint of pump-technology.

Table 3. Recipe upgraded with fly ash (refers to 1 m^3 concrete)

Total amount of structural additives and auxiliary materials	1820 kg
The amount of cement	255 kg
The amount of admixture (plasticiser SIKA BV-40)	1.53 kg
The prescribed min. amount of fine particle	350 kg
Amount of the complementary fine particle	95 kg
Amount of modified additive	1725 kg
Fine particle content in case of the modified amount of additives	17 kg
Amount of fly ash equals to amount of the complementary fine particle minus fine particle content of the modified additives	78 kg
Amount of additional materials	2.1 kg

Proposal No. 3: Recipe designed with adding sand of "0-1 fraction"

Sand of "0-1 fraction" possesses fine particle structure as well. Sand is many times cheaper compared to the other additives mentioned so far, and easy to procure, consequently the missing fine particle can be complemented with such type of sand, as well. We established – after executing a sizing test of the sand available at the company in question –that the certain sand of "0-1 fraction" contained insufficient amount of fine particle. Therefore using this sand would end up in using such high amount of – in order to supply the missing fine particles –, which would almost equal to the total amount of the additives to be complemented. Its application would cause a further problem, namely, more additives, i.e. cement, water and plasticiser would be required to apply – to counter balance its negative effects – , that would increase the costs. This solution should not be neglected, even the tested sand, available for us at the company would alter unfavourably the grain distribution of the mixture from the viewpoint of pumpability, since sand of "0-1 fraction" with higher fine particle content may be found in other mines. The favourable price of the sand of "0-1 fraction" also justifies to consider this solution [3, 4, 11].

The chosen solution

Since we aimed at accomplishing a trial test of the suggested recipe of the modified concrete material, i.e. realizing an experimental production, the final selection was basically influenced by the availability of the raw materials on stock at the manufacturer.

- Lime fume, constituent of the first concrete recipe, can be found in almost every concrete plant, furthermore, the other materials are also quite common, where the production process was planned to try out.
- The second solution was ousted, since fly ash, recommended it was not available unfortunately, in addition the quality of the sand of the required "0-1 fraction" was not proper, i.e. its fine material content was insufficient.

Taking into account the availability of the necessary components, as well as the aspects of productivity and cost efficiency – for solving the pumpability problem of the

C16/20-X0v (H)-24-F3 grade concrete-mix – we decided to start the experimental production and qualification procedure of the concrete material described by the first solution, i.e. recipe modified by the lime fume addition. It should also be noted, that moreover it was the cheapest solution. The chosen type of concrete was subsequently manufactured and the most common standardized qualification tests for concrete materials have been accomplished in order to judge the application and technological characteristics – i.e. pumpability –of the concrete. These tests are described in detail in works [12], hereby we only summarize and evaluate the most important test results.

Flow table test

The aim of this sort of test is to characterize the consistency of the fresh concrete. The measuring tool of this test is the so called flow table, satisfying the standard of EN 12350-5. Performing the test according to the MSZ EN 12350-5:2009 standard the result of the test is the size of the concrete pie, that is: $d = (d_1+d_2)/2$ (see Fig. 1.) The concrete satisfied the consistency class of F3 according to MSZ EN 206-1: 2002 standard, which means, that the characteristic *d* size of the pie should fall into the range of 420-480 mm. The higher spread value belonged to the modified recipe and could be attributed to the higher level of pulp saturation and higher content of the fine particles that resulted in easier spreading of the concrete and better flow in the pipe [4, 9, 1, 13].

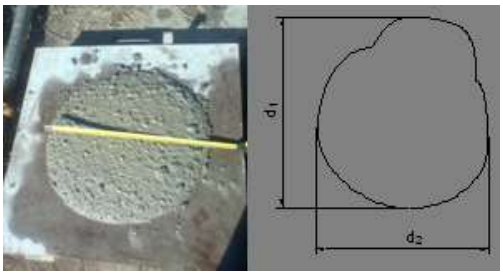

Fig. 1. *Flow table test of a fresh concrete*

Air-content of the concrete

The air-content is limited to achieve high density of the concrete material. The test procedure is regulated by the MSZ EN 12350-7 standard. The applied measuring tool was an air-content measuring device of type B2020, produced by FORM+TEST, according to standard: DIN 1048.
In accordance with MSZ EN 206-1: 2002 NAD (2003) the air-content of these type of concrete materials can be maximum 1,6%. Our measurements resulted in the following results: concrete of the original recipe had 1,6% air content, while that of the modified recipe was 1,4%. Thus both concrete materials fulfilled the requirements of the standard.
It can be also concluded that the concrete material with the higher consistency had lower air-content, since its increased fine particle content resulted in a lower viscosity of concrete, that can be aired sooner. Altogether, the modified concrete had more favourable consistency [4, 9, 13].

Compressive strength

To control of the fracture strength is very important from the viewpoint of both the manufacturer and the costumer. Notation of a concrete material refers to features being the most important ones for costumers in general. One of them is the compressive fracture strength. The first letter of the notation of C16/20-X0v(H)-24-F3 is 'C', which defines the class of the compressive strength of the concrete. This letter is followed by two numbers. They represent the standard strength characteristics measured on cylindrical and cubic samples. The device used for the strength test was an ALPHA 3-3000S type crushing machine (Fig. 2.), which fits the EN 12390-4 standard and manufactured by the FORM+TEST. The test samples were standard cubes with 150 mm edge length, according to MSZ EN 12390-1:2006.

Fig. 2. *The test cube in the crushing machine before and after the test*

Three pilot samples of the concrete materials were used to define the compressive strength according to both the original, and the modified recipe. The tests were carried out in two different conditions: on the one hand immediately after, on the other hand 21 days after the samples have been stored in water for 7 days. Further on these tests will be called "7 days strength test" and "28 days strength test" respectively. The results can be summarized as follows:
In case of the 7 days strength test the required minimum prescribed compressive strength is 12 N/mm^2 according to MSZ EN 206-1: 2002 standard. In case of the 28 days strength test, the related minimum strength is 22 N/mm^2 according to the prescriptions of the NAD (National Application Document). Fig 3. illustrates that the strength characteristics were satisfactory for concrete materials both of the original, both of the modified recipe, however in both conditions the strength of the modified concrete material was the higher – i.e. by 12 %, in case of the "7 days strength", and by 15% in case of the "28 days strength". The increased strength values could be attributed to the lower air content of the concrete material of the modified recipe.
As mentioned formerly, the increased fine particle content is accompanied by a lower air-content, which – as a positive side effect – results in a more solid structure, consequently in an increase of the strength of the concrete material [4, 9, 12, 13, 14].

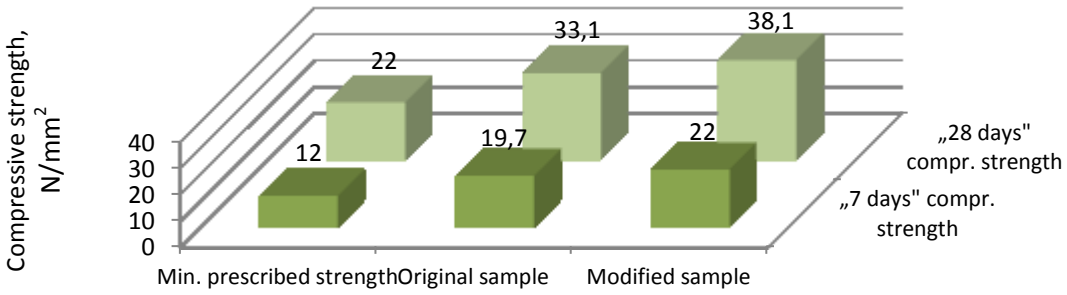

Fig 3. *Results of the strength tests on the original and modified concrete material*

Here should be mentioned that prescriptions of standards for the minimum strength data and composition (namely water/cement ratio) are occasionally in contradiction [15].

Summary

To improve the pumpability of the C16/20-X0v(H)-24-F3 type concrete 3 different novel alternative concrete recipes have been worked out, with the intention to modify the composition of the concrete without altering its additive-structure. Based on the test results of the original and one of the proposed novel concrete materials, the following conclusions can be drawn:

- It is impossible to produce a concrete suitable for transporting with pump without assuring the necessary amount of "fine particle" content of the basic mixture. The standards define the minimum required value of the fine particle content. Though a concrete with excess fine particle content can easily be transported with pump, additives that are required to compensate the accompanying strength reduction may cause significant increase in the

costs. During the calculation of proper fine particle content, both factors have to be taken into consideration.

- To assure the necessary portion of the "fine particle" content various complementing materials, additives and additional materials are available, among which we examined the cases of adding lime fume, fly ash or sand of "0-1 fraction".
- Recipe containing high amount of lime fume was tested in practice, with the following observations: application and technological characteristics of the new concrete material were qualified as satisfactory, moreover, on occasion they exceeded those of the original material.

Based on the presented industrial practical problem and the suggested solution, we can conclude that we worked out a possible modified concrete recipe of a cheap, widely used concrete material of grade of C16/20-X0v(H)-24-F3. Beside the basic goal - to assure appropriate pumping characteristics – we could also improve certain application properties, e.g. strength characteristics as well. Moreover this material is even cheaper to produce.
The direction of the future work is a more detailed analysis of certain phenomenon of hydrodynamics during pumping occurring in the concrete material, and separation of composition elements. Authors also consider other solutions (e.g. application of additives and other complementary materials) promising for the improvement of the pumping characteristics.

Acknowledgement

The research work presented in this paper based on the results achieved within the TÁMOP-4.2.1.B-10/2/KONV-2010-0001 project and carried out as part of the TÁMOP-4.2.2/A-11/1-KONV-2012-0029 project in the framework of the New Széchenyi Plan. The realization of this project is supported by the European Union, co-financed by the European Social Fund.

References

[1] MSZ 4798-1:2004, Beton. 1. rész: Műszaki feltételek, teljesítőképesség, készítés és megfelelőség, valamint az MSZ EN 206-1 alkalmazási feltételei Magyarországon
[2] Schweizer Norm (SN) EN 206-1:2000: Beton - Teil 1: Festlegung, Eigenschaften, Herstellung und Konformität, Nationaler Anhang, Begriffe, Erläuterungen, nationale Regelungen
[3] Sika® Beton Kézikönyv, Sika Hungária Kft., 2009. pp1-115.
[4] MSZ 4798-1:2004, Beton. 1. rész: Műszaki feltételek, teljesítőképesség, készítés és megfelelőség, valamint az MSZ EN 206-1 alkalmazási feltételei Magyarországon
[5] Asztalos, I.: A folyósítók technológiájának fejlődése-Új lehetőségek a betoniparban, Beton, 2008. 16. évf. 2. sz., pp7-11.
[6] Jolin, M., Burns, D., Bissonnette B., Gagnon, F., Bolduc, L-S.: Understanding the pumpability of Concrete, 2009. ECI Conference on Shotcrete for Underground Support XI.
[7] Dyer, R.M.: An Investigation of Concrete Pumping Pressure and the Effects of Pressure ont he Air-Void System of Concrete, Master Thesis, University of Washington, pp223.
[8] Kaplan, D.: Pompage des bétons, Doctorete Thesis l'École Nationale des Ponts et Chaussées, pp225.
[9] Kojics, A., Pluzsik, T., Szegőné Kertész, É.: Betonpraxis, Holcim Hungária Zrt., 2011. 1-140.old. (zsebkönyv)
[10] Asztalos, I., Jankó, A., Kausay, T., Korcsák, E., Liptay, A., Tariczky, Zs., Sulyok, T.: MSZ 4798-1 Beton szabvány alkalmazási segédlet, Magyar Betonszövetség, ISBN: 963 217 748 7, 2004. pp1-93.
[11] MSZ EN 933-1:2012, Kőanyaghalmazok geometriai tulajdonságainak vizsgálata. I. A szemmegoszlás meghatározása. Szitavizsgálat
[12] Németh, A.: Betonok szivattyúzhatóságának vizsgálata, BSc szakdolgozat, ME-GÉIK, Miskolc, 2012.
[13] Asztalos, I., Jankó, A., Kausay, T., Korcsák, E., Liptay, A., Tariczky, Zs., Sulyok, T.: MSZ 4798-1 Beton szabvány alkalmazási segédlet, Magyar Betonszövetség, ISBN: 963 217 748 7, 2004. 1-93.old.
[14] MSZ EN 12390-1:2006, A megszilárdult beton vizsgálata. 1. rész: A próbatestek és sablonok alak-, méret- és egyéb követelményei
[15] Troli, R., Collepardi, M.: Technical contradictions in the European Norm EN 206 for concrete durability, http://www.inti.gob.ar/cirsoc/pdf/tecnologia_hormigon/europeNorm206.pdf

Characterisation of hybrid metal matrix syntactic foams

Imre Norbert ORBULOV [1,2,a], Kornél MÁJLINGER[1,b]

[1]Budapest University of Technology and Economics Faculty of Mechanical Engineering Department of Materials Science and Engineering, Bertalan Lajos u. 7., 1111 Budapest, Hungary

[2]MTA-BME Research Group for Composite Science and Technology, Műegyetem rkp. 3-11., H-1111 Budapest, Hungary

[a]orbulov@eik.bme.hu (corresponding author), [b]vmkornel@eik.bme.hu

Keywords: Metal matrix syntactic foams, hybrid syntactic foams, hollow sphere reinforcement, compressive properties.

Abstract. High quality aluminium matrix syntactic foams (AMSFs) were produced by pressure infiltration. This method can ensure the maximal volume fraction of the reinforcing hollow spheres and very low amount of unwanted or matrix porosities. By this method hybrid MMSFs with mixed metal and ceramic hollow spheres were also produced. The matrix material was AlSi12 alloy and two different types – produced by Hollomet GmbH in Germany – of hollow spheres were used: Globomet (GM) and Globocer (GC). The geometrical properties of the hollow spheres were similar (average outer diameter), but their base material was pure iron and Al_2O_3+SiO_2 in the case of GM and GC hollow spheres respectively. The volume fraction of the reinforcing hollow spheres were maintained at ~65 vol%, but the ratio of them was altered in 20% steps (100% GM + 0% GC, 80% GM + 20% GC…). The results of the compression tests showed, that the compressive strength, yield strength, plateau strength, structural stiffness and the absorbed mechanical energy values increased with higher ceramic hollow sphere reinforcement ratio. The fracture strains of the investigated MMSFs decreased with the higher GC ratio. Generally the strength values also increased with higher diameter to height (H/D) ratio from H/D=1 to H/D=1.5 and 2.

Introduction

Metal matrix syntactic foams (MMSFs) are special composites that consists different size and material hollow spheres as reinforcement. Due to the hollow structure and beneficial strength of the spheres these composites behave like strong metallic foams, with at least two times higher compressive strength and energy absorbing capacity, than conventional ones. In MMSFs, the matrix material is usually some kind of aluminium alloy, but Fe matrix variants [1, 2] and Mg [3, 4], or Zn [5, 6] based versions are also known.

Nowadays MMSFs are investigated more and more intensively. Most of the published papers focus on the production and/or mechanical properties of the foams [7, 8]. Some of the works gives overall review on the investigated MMSF systems that are most important, for example Santa-Maria et al. and Fergusson et al. investigated the microstructure and quasi-static compressive mechanical properties of Al-A206/Al_2O_3 MMSFs. They found that the peak strength, plateau strength and toughness of the foams were increased with increasing wall thickness to diameter ratio [9-10]. The expected mechanical properties were also predicted by mathematical model [10]. The mechanical response of the MMSFs is also important in the case of high strain rate loading too. In the case of collision damping or other, energy absorbing applications high loading speeds can occur. Luong et al. [11-13] investigated the MMSFs in this point of view and found that while the matrix alloy does not show any appreciable strain rate sensitivity, the composite shows higher strength at higher strain rates. The energy absorption capability of MMSFs is found to be higher at higher strain rates.

In the published papers, the MMSFs usually have a simple reinforcement that means only one grade of well-defined hollow spheres are applied. However there is a possibility to use for example bimodal reinforcement [14] or different grade reinforcement to produce hybrid MMSFs. Due to this our main goal was to produce such hybrid MMSFs and report their properties.

Materials and methods

Constituents and production method

As matrix material near eutectic AlSi12 alloy (Al4047) was used due to its low melting point (~575°C) and low viscosity. Besides Al the material contained 12.83 wt% Si and about 0.2 wt% other elements (Fe, Cu, Mn, Mg, Zn). This composition is in the range of the nominal values. The reinforcement consists of two different types of hollow spheres (one ceramic and one metal) manufactured by Hollomet GmbH. The ceramic hollow spheres (Globocer, GC) had the average diameter of Ø1450 μm and average wall thickness of t=60 μm. Their density was ρ=0.816 gcm^{-3}. The hollow sphere's wall material was built up from ~30 wt% Al_2O_3, ~50 wt% SiO_2 and ~20 wt% $3Al_2O_3 \cdot 2SiO_2$. The metallic hollow spheres (Globomet, GM) had the similar average diameter and wall thickness, while their density was ρ= 0.4 gcm^{-3}. The ratio of the hollow spheres was varied from 100% GM and 0% GC to 0% GM and 100% GC, in 20% steps. The hybrid ASFs were produced pressure infiltration technique (Fig. 1). The mechanically mixed hollow spheres were put into a ~360 mm height, graphite coated carbon steel mould (cross section: ~40×60 mm) to the half and they were densified by gentle tapping to get ~65 vol% volume fraction, that corresponds to randomly closed packed structure. Subsequently, a layer of alumina mat was placed on the hollow spheres and a block of matrix material was inserted on the mat. The mould was put into the infiltration chamber; the furnace was closed and evacuated by a vacuum pump to a rough vacuum.

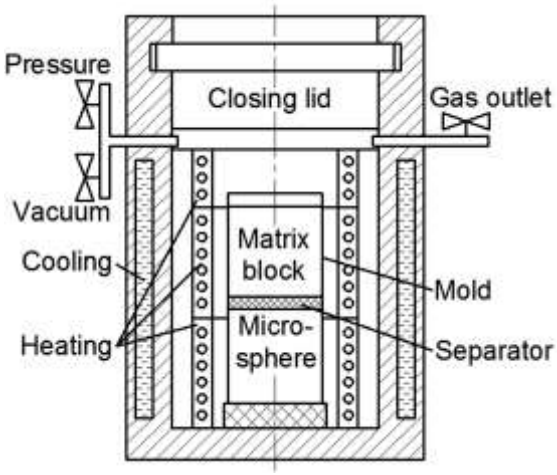

Figure 1. Schematic sketch of the infiltration setup

Table 1. Measured density values of the AMSFs

Reinforcement	Measured density, ρ_m (gcm^{-3})
100GM-0GC	1.327
80GM-20GC	1.639
60GM-40GC	1.649
40GM-60GC	1.694
20GM-80GC	1.743
0GM-100GC	1.833

During the heating the temperatures of the matrix block and the hollow spheres were monitored by two thermocouples. After melting of the matrix material the fluid sealed the mould above the separator layer. Subsequently, Ar gas was let into the chamber at 400 kPa to perform the infiltration. After slow cooling and solidification the mould was removed from the chamber and further cooled to room temperature in water. Then the AMSF block (~40×60×180 mm) was removed from the mould. The blocks were designated after their constituents, for example 80GM-20GC stands for an AMSF block with ~65 vol.% of hollow spheres that is mixed from 80% GM and 20% GC hollow spheres respectively. The measured composite densities (ρ_m) are listed in Table 1.

Experimental

Scanning electron microscopy (SEM) investigations and line EDS (energy dispersive spectroscopy) were done on a Phillips XL-30 type electron microscope and its EDAX Genesis EDS attachment on polished surfaces. The measurements started from the matrix and crossed the wall of the hollow sphere. Along each line thirty points were evaluated. The points were excited for 15 s with 35 μs amplification time.

The compressive properties were determined in quasi-static conditions on Ø14 mm cylindrical specimens. The aspect ratio (H/D) of the specimens was varied and was set to1, 1.5 or 2. The compression tests were done on a MTS 810 type hydraulic testing machine in a four column tool at room temperature. The surfaces of the tool were polished and lubricated. The speed of the test was

set to 0.01 s^{-1}. From each specimen group five specimens were compressed up to 25% engineering strain (in summary 90 tests were done). The recorded curves were evaluated in accordance with the ruling standard DIN50134. The investigated properties were: compressive and flow strength, fracture strain, structural stiffness and absorbed energies.

Results and discussion

Microstructural investigations

The quality of infiltration was investigated by optical microscopy and SEM. The observations showed almost perfect infiltration, the cavities between the hollow spheres were fulfilled by the AlSi12 matrix. The uninfiltrated void content between the hollow spheres remained minimal, below 3%. Some hollow spheres were broken and therefore infiltrated. Most of the infiltrated spheres were GM grade, because the molten AlSi12 can dissolve pure Fe from the wall it was weakened and lead to the infiltration of the hollow spheres. The molten matrix can react with the reinforcement according to Eq. 1 and Eq. 2-4 in the case of GC and GM spheres respectively.

$$4Al_{(liquid)} + 3SiO_{2(solid)} \rightarrow 2Al_2O_{3(solid)} + 3Si_{(liquid\ solution)} \quad \text{(Eq. 1)}$$

$$Fe_{(solid)} + Al_{(liquid)} \rightarrow Fe\text{-}Al_{(liquid\ solution)} \quad \text{(Eq. 2)}$$

$$Fe_{(solid)} + 3Al_{(liquid)} \rightarrow Al_3Fe_{(solid)} \quad \text{(Eq. 3)}$$

$$Fe_{(solid)} + Si_{(liquid\ solution)} \rightarrow FeSi_{(solid)} \quad \text{(Eq. 4)}$$

The diffusion reaction described in Eq. 1 was induced by the Si concentration mismatch between the material of the hollow spheres and the matrix. However, this exchange reaction was constrained by the high Si amount in the matrix. The properties of the interface layer between matrix and reinforcements were investigated by EDS along distinguished lines perpendicular to the wall of the spheres. A typical site of 40GM-60GC AMSF is shown in Fig. 2. The SEM micrograph of a GM (left) and GC (right) hollow spheres near to each other and the path of the line EDS analysis (arrow) are shown in Fig. 2a, and the chemical composition along the investigated line in Fig. 2b. The SEM image shows unharmed hollow spheres and the less than 100 μm gap between the GM and GC hollow spheres and the matrix prove the good infiltration.

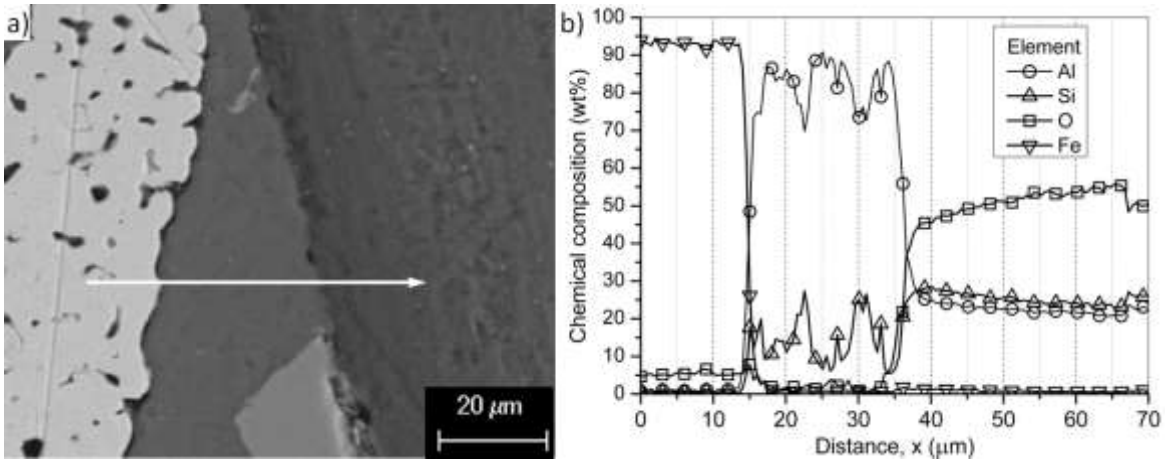

Figure 2. a) SEM image of 40GM-60GC sample of a GM (left) and GC (right) hollow spheres and the line of the EDS analysis (arrow), b) the chemical composition along the investigated line

The chemical composition along the analysis line follows the actual composition of the wall, the interface and the matrix respectively. The first couple of micrometers measured in the GM hollow sphere showed Fe and some O due to the oxidization of the specimen's surface. Between the spheres Si peaks can be detected beside the dominant Al, because of the eutectic matrix material. In the GC hollow spheres the Al-Si-O ratio followed the composition of the ceramic wall. Because of the interface layers between the hollow spheres and the matrix material sudden changes can be observed in the chemical composition. These narrow zones indicate thin interface layers. The thickness of these layers can be estimated from the slope changes of the differentiated Fe and O curves and it was between 5 μm and 7 μm in the case of GM and GC hollow spheres respectively.

Compressive properties

The compression tests were evaluated according to the standard (DIN50134) about the compression tests of cellular materials. The strength of MMSFs was characterised by (i) the first stress peak (compressive strength, σ_c), (ii) the strength at a given plastic deformation (similar to yield strength, σ_y) and (iii) the plateau strength (σ_p, the average stress level in the second half of the compressive curve). The deformation capability can be described by is the fracture strain (ε_c), that is the strain at σ_c. The elastic behaviour of the AMSFs can be characterised by the slope of the initial part of the stress – strain curve, called structural stiffness (S). The fracture energy (the absorbed energy up to the fracture strain, W_c), and the area under the stress-strain curve as the whole absorbed energy (W) were further monitored properties. The energies can be determined by the numerical integration of the stress-strain curves up to the fracture strain or up to 25% in the case of fracture energy and the overall absorbed energy respectively.

Fig. 3 plots the measured compressive strength values as the function of aspect ratio and the ratio of the hollow sphere types. (In the case of pure GM reinforcement, pronounced compressive strength could not be determined; therefore the yield strength was plotted for comparison). There are some notable trends in the measured values: the smaller specimens were stronger and the compressive strength also increased with the amount of the GC grade reinforcement. The gradient of this increment was rather moderate: as the amount of the weaker, plastically deformable GM fraction decreased, the compressive strength increased proportionally. In the case of pure GC reinforcement a higher increment was observed: the stronger GC spheres and the lack of plastically deformable GM hollow spheres ensured higher strength niveaus and altered the fracture mechanism. Identical behaviour can be concluded from the yield strength values (Fig. 4).

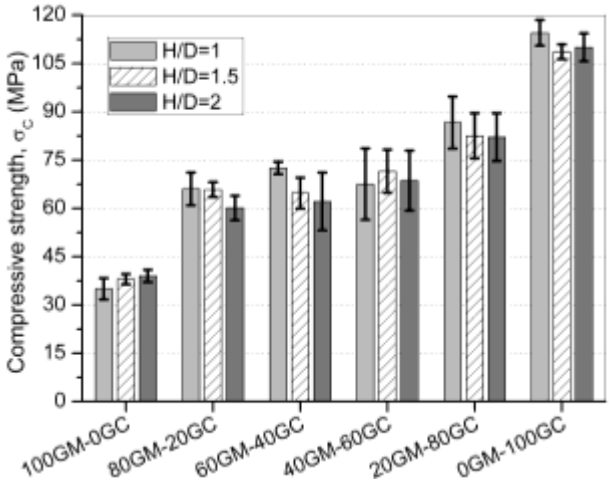

Figure 3. Compressive strength values

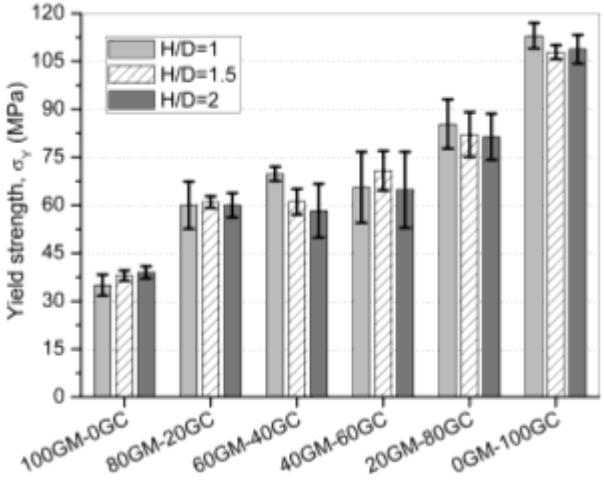

Figure 4. Yield strength values

The AMSFs with GM type reinforcement had no pronounced compressive strength, but a long and almost constant plateau region with completely plastic deformation (like 'conventional' metallic foam). Due to the unique built up and deformation of each sample the scatter of the plateau were somewhat larger (Fig. 5). By the gradual increment of the GC fraction, the compressive strength became more pronounced and the failure mechanism also turned to brittle mode with a sharp, severely compressed fracture band. The trends of the fracture strain values (Fig. 6.) confirmed the above detailed effect. As the volume fraction of the ceramic GC hollow spheres increased, the fracture strain decreased significantly and the failure mode became brittle. The aspect ratio had similar effect on the fracture strain: the higher aspect ratio resulted in intensified shearing and due to this; the fracture occurred earlier. This effect was more emphasized in the case of higher GC content, because the sensitivity to shearing of the ceramic materials. The structural stiffness values changed at the contrary (Fig. 7.). The highest stiffness was measured in the case of H/D=2 in the case of the highest GC content. The aspect ratio had linear connection with the structural stiffness, but the increment of the GC hollow sphere fraction had an exponential effect on the stiffness.

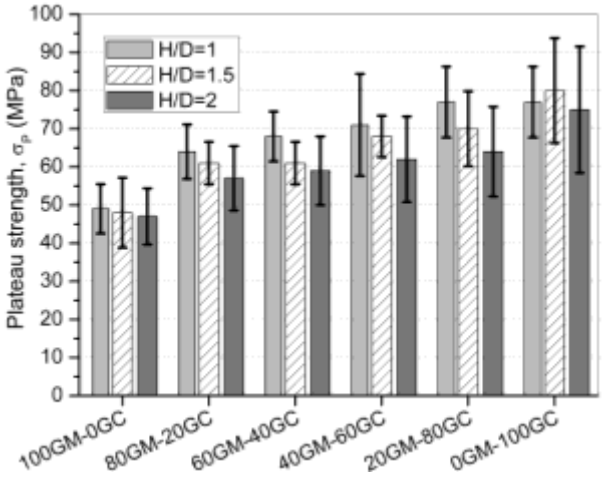

Figure 5. Plateau strength values

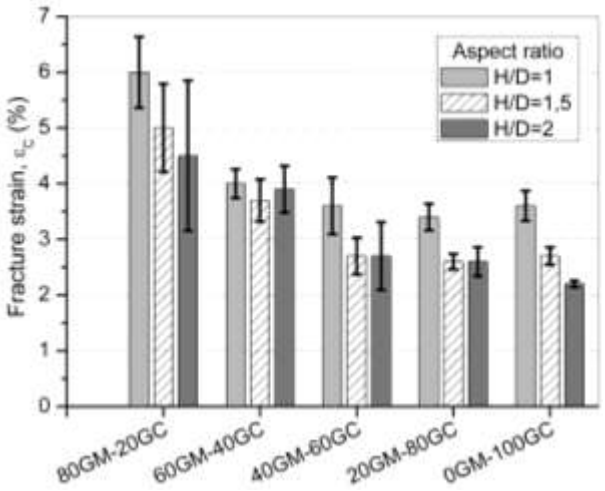

Figure 6. Fracture strain values

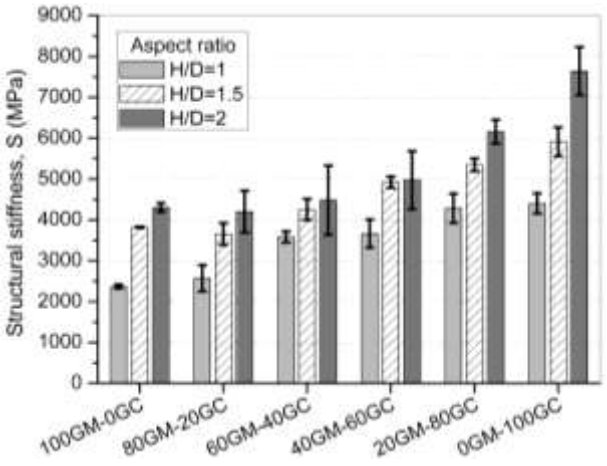

Figure 7. Structural stiffness values

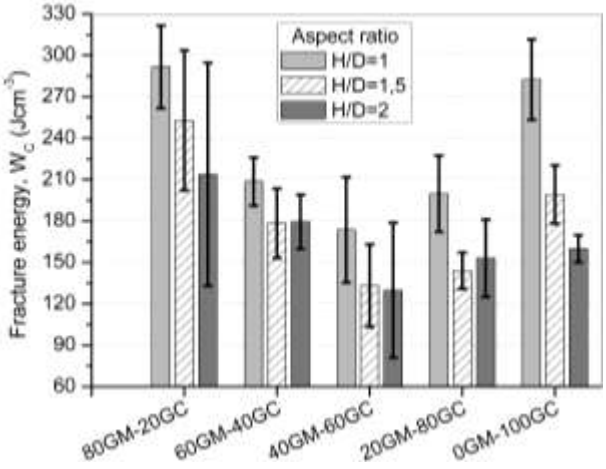

Figure 8. Fracture energy values

The fracture energy (Fig. 8) had a maximum in the case of pure GC reinforcement: the strong ceramic hollow spheres ensured high compressive and plateau stress levels; therefore the absorbed energy was high. As the weaker GM grade spheres were built in, the compressive strength and the fracture energy decreased. In the case of higher GM hollow sphere fraction (>40%) the fracture energy increased again: the decrement of the compressive strength was balanced by the plastic deformation capability, i. e. the higher fracture strain of the AMSFs (wider limits for the integration) and despite the lower compressive strength the fracture energy could become higher. Similar behaviour can be observed in the overall absorbed energy (calculated up to 25%, Fig. 9). The expected high energy absorption capacity could not be observed in the case of pure GM grade reinforcement due to their very low compressive and plateau strength.

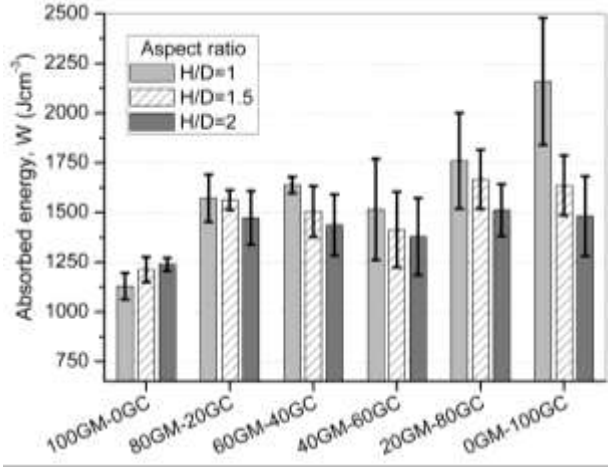

Figure 9. Overall absorbed mechanical energy values

Summary

From our investigations and results, the following statements can be concluded:

- Pressure infiltration is a reliable hybrid ASF production method. The process can ensure high hollow sphere content and low uninfiltrated porosity.

- The line EDS measurements indicated (i) solution of Fe from GM hollow spheres and (ii) an exchange reaction between the AlSi12 matrix and the GC hollow spheres into the AlSi12 matrix. Both process can cause damage to the wall and leads to infiltrated hollow spheres.
- The ratio of the GC and GM grade hollow spheres had strong influence on the mechanical properties of the produced AMSFs. The strengths and the stiffness increased by the increment of GC content.
- Both the fracture energy and the overall absorbed energy values had a local minimum in the case of 60GC+40GM reinforcement. Higher GC content resulted in higher compressive and plateau strengths and due to this the absorbed energies became higher. Lower GC content resulted in lower the strength values, but the ductility of iron GM hollow spheres could balance and overcome this effect.

Acknowledgements

This research was supported by the European Union and the State of Hungary, co-financed by the European Social Fund in the framework of TÁMOP 4.2.4. A/2-11-1-2012-0001 'National Excellence Program'. This paper was supported by the János Bolyai Research Scholarship of the Hungarian Academy of Sciences.

References

[1] L. Peroni, M .Scapin, M. Avalle, J. Weise, D. Lehmhus, Dynamic mechanical behavior of syntactic iron foams with glass microspheres, Mater Sci Eng A. 552(0) (2012) 364-375.
[2] L. Peroni, M .Scapin, M. Avalle, J. Weise, D. Lehmhus, J. Baumeister, M. Busse, Syntactic Iron Foams - On Deformation Mechanisms and Strain-Rate Dependence of Compressive Properties, Adv Eng Mater. 14(10) (2012) 909-918.
[3] A. Daoud, MT. Abou El-khair, M. Abdel-Aziz, P. Rohatgi, Fabrication, microstructure and compressive behavior of ZC63 Mg–microballoon foam composites, Compos Sci Technol. 67(9) (2007) 1842-1853.
[4] PK. Rohatgi, A. Daoud, BF. Schultz, T. Puri, Microstructure and mechanical behavior of die casting AZ91D-Fly ash cenosphere composites, Composites Part A. 40(6–7) (2009) 883-896.
[5] A. Daoud, Synthesis and characterization of novel ZnAl22 syntactic foam composites via casting, Mater Sci Eng A. 488(1–2) (2008) 281-295.
[6] A. Daoud, Effect of strain rate on compressive properties of novel Zn12Al based composite foams containing hybrid pores, Mater Sci Eng A. 525(1–2) (2009) 7-17.
[7] XF. Tao, YY. Zhao, Compressive failure of Al alloy matrix syntactic foams manufactured by melt infiltration, Mater Sci Eng A. 549 (2012) 228-232.
[8] PK. Rohatgi, N. Gupta, BF. Schultz, DD. Luong, The synthesis, compressive properties, and applications of metal matrix syntactic foams, JOM. 63(2) (2011) 36-42.
[9] JA. Santa Maria, BF. Schultz, JB. Ferguson, PK. Rohatgi, Al–Al2O3 syntactic foams – Part I: Effect of matrix strength and hollow sphere size on the quasi-static properties of Al-A206/Al2O3 syntactic foams, Mater Sci Eng A. 582 (2013) 415-422.
[10] JB. Ferguson, JA. Santa Maria, BF. Schultz, PK. Rohatgi, Al–Al2O3 syntactic foams—Part II: Predicting mechanical properties of metal matrix syntactic foams reinforced with ceramic spheres, Mater Sci Eng A. 582 (2013) 423-432.
[11] DD. Luong, OM. Strbik III, VH. Hammond, N. Gupta, K. Cho, Development of high performance lightweight aluminum alloy/SiC hollow sphere syntactic foams and compressive characterization at quasi-static and high strain rates, J Alloys Compounds. 550 (2013) 412-422.
[12] DD. Luong, N. Gupta, A. Daoud, PK. Rohatgi, High strain rate compressive characterization of aluminum alloy/fly ash cenosphere composites, JOM. 63(2) (2011) 53-56.
[13] DD. Luong, N. Gupta, PK. Rohatgi, The high strain rate compressive response of Mg-Al alloy/fly Ash cenosphere composites, JOM. 63(2) (2011) 48-52.
[14] XF. Tao, LP. Zhang, YY. Zhao, Al matrix syntactic foam fabricated with bimodal ceramic microspheres, Mater Des. 30(7) (2009) 2732-2736.

The modelling of crater wear in cutting with TiN coated high speed steel tool

Zoltán Pálmai

University of Miskolc, Institute of Manufacturing Science, Hungary
Alvinci u. 24, H-1022 Budapest, Hungary

palmayz@t-online.hu

Keywords: cutting, TiN-coated tool, crater wear model

Abstract. The flow zone of the chip in contact with the tool reaches a high temperature in cutting. According to chip hardening experiments α–γ transformation may occur in steel, so the tool is in contact with a high-temperature γ phase at high pressure. The microscopic examination of worn surfaces showed that the degradation of the tool is the result of adhesive/abrasive and thermally activated processes, therefore both friction length and temperature must be taken into consideration in the modelling of crater wear. Wear rate can be described by a non-linear autonomous equation. TiN coating, which increases tool life in high speed steel, changes and slows down the wear of the tool. The activation energy of wear can be calculated from the constants of the wear equation determined by cutting experiments. The deoxidation products to be found in the workpiece in cutting may form a protective layer on the TiN layer that blocks or slows down wear.

1. Introduction

The growing technological requirements in mechanical engineering have also enforced the enhanced wear and heat resistance of tool materials. One of the branches of this progress has focussed on applying a hard, heat-resistant coating on tools. Carbides with TiC, TiN, Al_2O_3 and combined or complex coating were brought into being, then by the appearance of the PVD (Physical Vapor Deposation) process, the TiN-coated high speed steels were developed [1]. The latter is characterised by a much smaller heat endurance of the material under the TiN layer than in the case of coated carbides. The purpose of the research presented here was to find out how the wear of this special tool material can be described by the mathematical model prepared for the crater wear of the cutting tool.

When steels are cut with carbide tools, the wear of the tool can be significantly influenced by a special phenomenon. The deoxidation products in steel may get smeared on the surface of the tool and may form a non-metallic protective layer preventing wear [2]. It was proven that such protective deposit may also develop on TiN-coated high speed steel tool [3], so the question what influence it has on the mathematical modelling of wear was raised.

2. The bearing force and wear of the cutting tool

The rake face of the tool is subject to a massive mechanical and thermal impact in cutting. The layer of the chip in contact with the tool, the so-called flow zone, is deformed rather significantly and gets heated. In these cases diffusion processes can also occur, as a result of which chips and the tool can even weld locally and temporarily. Fig. 1., which was obtained by suddenly withdrawing the tool downwards (quick stop technology), is a direct evidence of this. The chip and the tool got welded at some places, which is shown by the small pegs sticking out downwards from the chip.

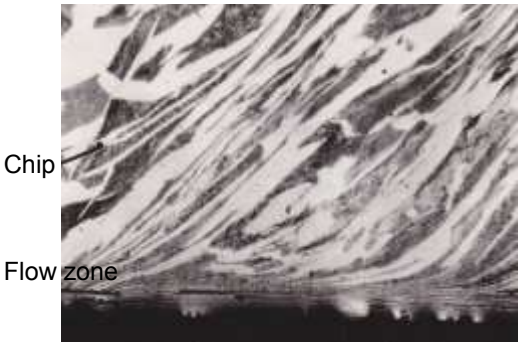

Fig. 1. Chip root in cutting C35 steel

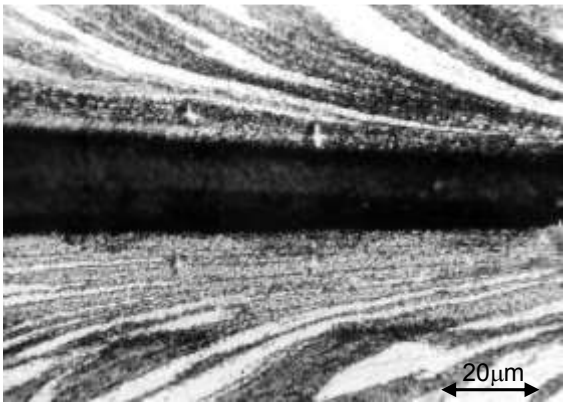

Fig. 2. The longitudinal section of chips cooling down in the air (above) and hardened in water (below)

The experiments conducted with hardened chips showed that α–γ transformation often occurs in the material of the flow zone as well. The C35 quality steel was turned at various speeds and the chips partly cooled down in the air, partly they were hardened in cold water. As shown by Fig. 2., the micro-hardness of the flow zone on the longitudinal section of chips increased when chips were hardened in water and the hardness was greater that in the case of chips cooling down in the air (Fig. 3.).

It is interesting that hardening could be shown even at a cutting speed of v=30m/min, when the temperature of the low surface of the chip certainly remained below the minimum A_{c1} temperature of α–γ transformation and even more below the A_{c3} temperature pertaining to C35 steel. This temperature was calculated with empirical function [4]

$$\theta = C_v v^x \qquad (1)$$

often used in cutting theory, where C_v is a constant depending on technological parameters. The fact that superscript x can only be regarded as constant in the temperature range characteristic of various tool materials was taken into consideration [5]. Thus, in this case, the constants of formula (1) within the v≤80m/min and the v≥80m/min ranges of cutting speed are C_v=210,2°C, x=0,33 and C_v=371,7°C, x=0,2, respectively.

The decrease of the transformation temperature in the chip material can be traced back to the massive fast deformation (≈50, ≈$10^4 s^{-1}$) occurring at a high surface pressure.

So it is a fact that the surface of the tool often gets in contact with high temperature γ-Fe in steel cutting.

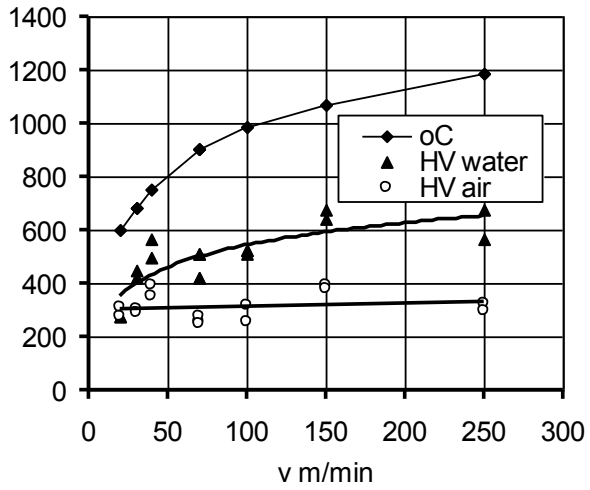

Fig. 3. The results of chip hardening experiments

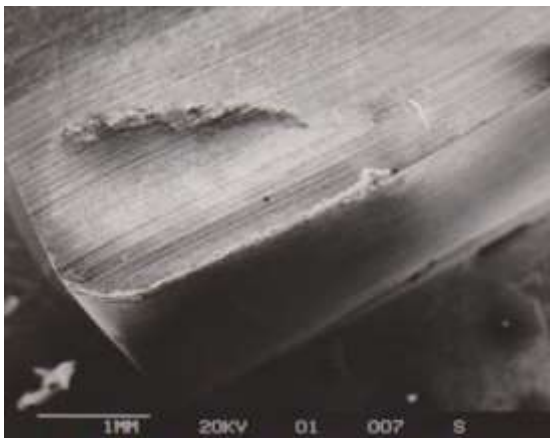

Fig. 4. The SEM picture of the TiN coated HSS tool after steel cutting

In spite of this it could be seen that steel did not get stuck on the TiN-coated high speed steel tool (Fig. 4.) until this coating got worn through. Then, however, as a result of the rather intensive exposure, the material of the plastic chip got smeared on the rake face of the tool, as shown by Fig. 5.

Under the metal smeared on the rake face, which is also in the move, the material of the tool is degraded as a result of thermally activated processes and gets shattered and worn as a result of massive mechanical exposure.

It is known that high wear resistance in high speed steel is caused by carbide grains embedded in a martensite structure (Fig. 6.). Martensite can transform easily at the temperature developing on the contact

surface of the chip and the tool, hardness decreases and the material of the matrix gets worn off. Fig. 7. was taken of a worn crater surface after etching. It can be seen that carbide grains behave like pebbles in a stream bed against wear. The direction of the flow is indicated by an arrow.

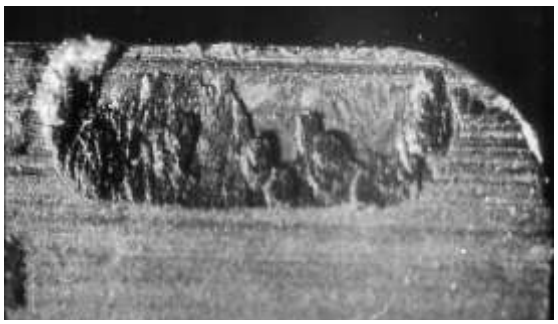

Fig. 5. Crater surface on coated HSS cutting tool after TiN has been worn off

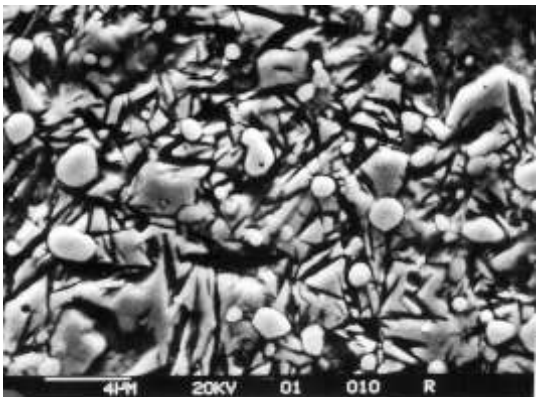

Fig. 6. Etched surface of an intact HSS tool

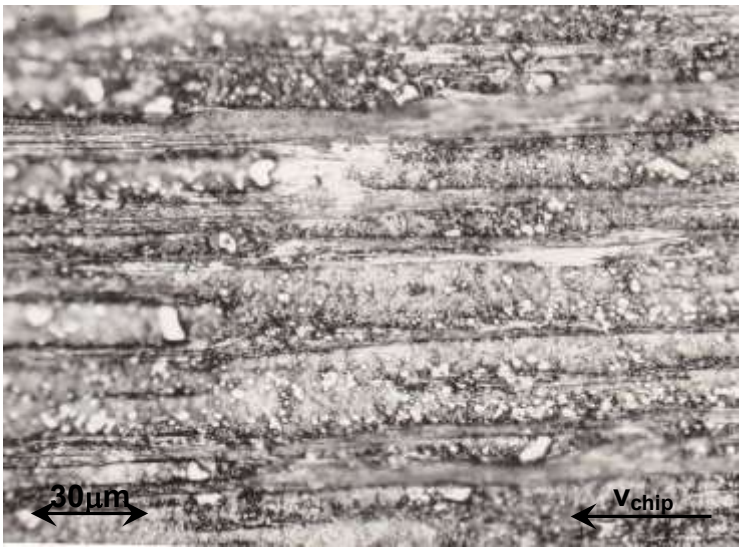

Fig. 7. The crater surface of HSS tool

So in summary we can conclude that the process of the crater wear of high speed steel happens as a joint impact of the thermally activated textural/structural transformation and adhesion/abrasion. So both the friction length and temperature need to be taken into consideration here.

3. The mathematical model of crater wear

The wear of the rake face of the tool can be characterised by two measures, the depth (KT) and width (KB) of the crater (Fig. 8.). Based on practical experiences, KT and KB are in a nearly linear relationship, which makes the description of the wear process easier, i.e.

$$KB \approx KB_o + C_{KB} KT, \qquad (2)$$

where K_{Bo} and C_{KB} are constants that can be simply determined by cutting measurements. For instance, according to measurements in C45 plain steel KB_o=1224µm, C_{KB}=3.36, if [KT]=µm (R^2=0.9363).
It must be taken into consideration in crater wear that

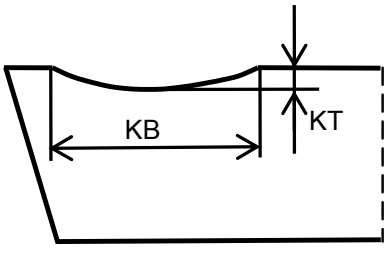

Fig. 8. Typical measures of crater wear

$v_{chip}<v$, because the thickness of the chip (h_{chip}) is mostly larger than undeformed chip thickness h, except for the cases of hard cutting and super high-speed cutting.
This is expressed by the ratio

$$\xi(v) = \frac{h_{chip}}{h} = \frac{v}{v_{chip}} \tag{3}$$

which depends of cutting speed and can easily be determined in practice, and can be written numerically by the empirical formula

$$\xi(v) \cong \xi_0 + C_f \exp -\alpha v \tag{4}$$

Here constants ξ_o, C_f and α can also be determined by simple technological experiments.
It must also be noted that the temperature developing on the boundary land of the chip and the tool also depends on wear, therefore, formula (1) must be extended with a term proportionate to wear. Thus, the amended form of (1) becomes

$$\theta \cong C_v v^x + C_{KT} KT = C_v \left(v^x + K_{KT} KT\right), \tag{5}$$

where C_{KT} and $K_{KT}= C_{KT}/C_v$ are constants.
According to the statement made about the nature of crater wear in the previous chapter, friction length and thermal impact jointly determine wear rate. This complex model of wear could be successfully used in flank wear [6]. In this case, taking the geometrical characteristics of crater wear into consideration (Fig. 8.), using (4) and (5), the speed of crater wear can be described by differential equation

$$\frac{dKT}{dt} = \frac{v}{\xi(v)} \frac{A_a + A_{th} \exp\left[-B/(v^x + K_{KT} KT)\right]}{KB_0 + 2C_{KB} KT} \tag{6}$$

where

$$B = \frac{Q}{RC_v}. \tag{7}$$

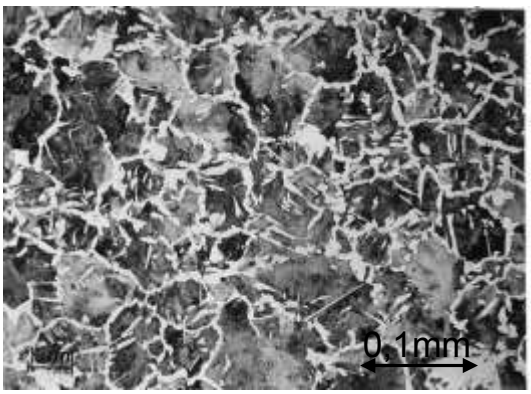

Fig. 9. Micrograph of the workpiece

Here t is time, R is the universal gas constant. x, C_{KB}, C_v, K_{KT}, KB_0 are constants and function $\xi(v)$ can be determined with a cutting examination. Wear is characterised by three constants, A_a is adhesive/abrasive, A_{th} is thermally activated wear whose activation energy is Q. These can also be calculated by measuring tool wear. The analytical solution of non-linear autonomous differential equation (6) is not possible but can be handled well numerically.
Cutting experiments were conducted with uncoated and TiN-coated high speed steel tool, which was used to cut C45 quality rolled steel. The chemical composition of the workpiece was C 0.42%, Mn 1.04%, Si 0.24%, P 0.016%, S 0.020%. The tool was HSS2 quality and rake angle was $\gamma_o=14^o$. The technological parameters of cutting were: cutting speed v=52m/min, feed f=0.25mm/rev, depth of cut a=2.5mm. The average thickness of TiN layer was 4μm. The micrographs of the tool and the workpiece are shown by Fig. 6 and 9, respectively.

The result of measurements are summarised by Fig. 10. The constants of equation (6) could be calculated from the data measured on the uncoated HSS tool: $A_a=5.5.10^9\mu m$, $A_{th}=5.2.10^{12}\mu m$, B=102, $K_{KT}=0.006$. Another valuable feature of this method is that the K_{KT} constant derived from the thermal characteristics of cutting could be calculated from the wear measurement results. The parameter showing the temperature excess developing as a result of wear in formula (5) is $C_{KT}=K_{KT}C_v=0.006x210.2=1.26^oC/\mu m$.

The wear of the TiN coated tool was naturally significantly slower initially, being only KT=6μm after a 7 minute cutting, so the coating was just broken through. The cutting quotient was ξ=2.93 at a speed of v=52m/min, thus, the wear distance was L=7*52/2,93=1067m, so the wear rate of the TiN layer as a function of the wear distance was KT/L≈6μm/1067m=0,0056μ m/m=5,6*10^{-9} m/m. Then the constants of equation (6) were nearly the same as those determined for the uncoated tool: $A_a=4.5x10^9\mu m$, $A_{th}=2.4x10^{12}$ μm. The value of B és K_{KT} remained the same. It can be seen that the constants that are related to adhesive/abrasive processes are a bit smaller in the case of the TiN-coated tool.

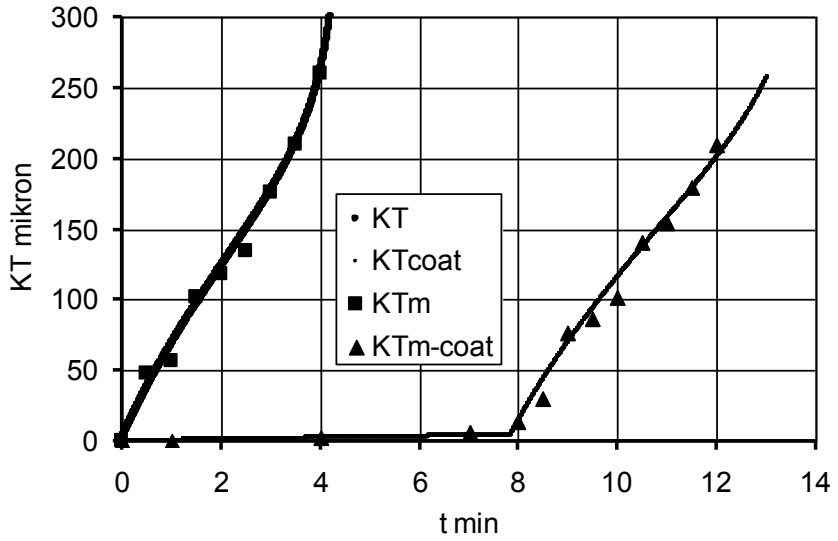

Fig.10. Calculated (KT) and measured (KT_m) crater wear in uncoated and coated HSS tool (v=52m/min, f.a=0.25x2.5mm^2)

Q activation energy of wear can also be calculated from formula (8), considering the fact that that the constant of formula (1) in this technology is $C_v=269.2^oC$ [6]:

$$Q=C_vRB=269.2x8.314x102=228.3kJ/mol$$

According to Friberg és Torndhal [7] the self-diffusion of Fe in ferrite and in austenite is Q=240kJ/mol and Q=286 kJ/mol, respectively. So according to the chip hardening experiment, in spite of the fact that the tool gets in contact with a material partially turned into austenite, the presence of ferrite is dominant. According to a later source [8], in the case of γ-Fe, Q=284,1kJmol^{-1} in self-diffusion occurring in crystal lattice, while Q=180,5 kJmol^{-1} in grain boundary self-diffusion. So this is a mixed process.

TiN coating does not only decrease wear rate with its high wear resistance but also with the characteristic that the plastic deoxidation products in the steel workpiece may form a protective layer on it [3]. As a result tool life may increase significantly. Figure 11 shows a tool that was used for cutting another C45 steel workpiece containing plastic oxide inclusions at a speed of v=70m/min for 29 minutes. Such speed resulted in the wear of the tool in 2 minutes in the cutting of the original material.

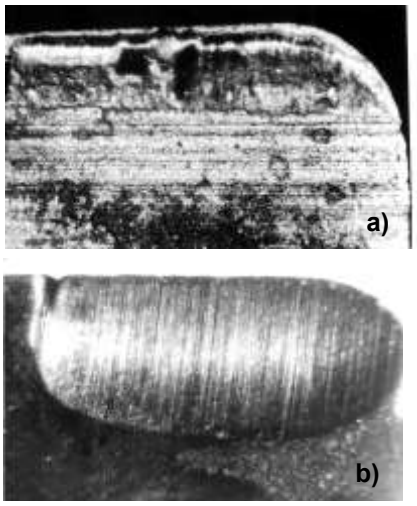

Figure 11 The cutting of two C45 steel type at a speed of v=70m/min
(a) t=29min, b) t=2min)

This is an extreme case as the material of the second workpiece was deliberately manufactured to facilitate the formation of such a protective non-metallic layer, therefore, enhance high machinability. Naturally, equation (6) may not be used in these cases as the tool is not destroyed because of crater wear but because of e.g. flank wear. Whenever this non-metallic oxide protective layer develops only partially, A_a and A_{th} adhesive/abrasive constants are expected to decrease. This assumption, however, is yet to be confirmed all the more so since the deoxidation products are modified in modern steel manufacturing processes, and therefore, their plasticity may also change in the temperature range that develops on the tool in the chip formation phase.

Summary

TiN and other hard layers produced with the PVD process significantly slow down wear in high speed steel tools. $\alpha-\gamma$ transformation may occur in the flow zone of the steel workpiece that is in contact with the tool under high mechanical and thermal impact, even below A_{c1} temperature. As a result, diffusion processes may also occur on the boundary land of the chip and the tool. By studying the microgeometry of worn surfaces it could be concluded that the friction distance and cutting temperature must be jointly considered in the modelling of the tool's degradation. Thus, wear rate can be described by a non-linear autonomous differential equation, which can be solved numerically. The constants of the equation can be determined by cutting measurements. The activation energy of the wear process can be calculated by using these constants. The TiN layer mainly slows down adhesive/abrasive processes. After this layer gets worn through, degradation continues similarly to uncoated HSS tools. In steel cutting, the deoxidation products in the workpiece may form a deposit on the surface of the TiN-coated tool and may slow down crater wear significantly.

Acknowledgement.

This research was carried out in the framework of the Center of Excellence of Innovative Engineering Design and Technologies at the University of Miskolc, and as part of Hungarian Scientific Research Fund OTKA K 84177.

Irodalom

[1] Pálmai, Z., Formation of non-metallic protective layers on high-speed steel tools. Metals Technology Jan 1984 Vol. 11:34-37

[2] Pálmai, Z., The effect of deoxidation of steel on machinability. Wear 38 (1976) 1-16.

[3] Pálmai, Z. The effect of a non-metallic material deposit in decreasing the wea of TiN-coated high speed steel cuting tool. Wear, 95 (1984) 1-7.

[4] Shaw, M.C.: Metal Cutting Principles, Oxford University Press, Oxford, 2nd Edition, 2005. p.672

[5] Pálmai, Z., Cutting temperature in increment cutting. Int. J. Mach. Tool Manufact. Vol. 27 (1987) No. 2. 261-274.

[6] Pálmai, Z., Proposal for a new theoretical model of the cutting tools flank wear. Wear 303 (2013) 437-445.

[7] Fridberg and Törndhalr, Diffusion in Iron, Jernkontorets Annaler Vol. 153. (1969) No. 6. 263-276.

[8] Murch, G.E., Ferrite and Austenit: Diffusion, Bulk and Interfacial. Encyclopedia of Materials: Science and technology. Elsevier 2001. pp. 3009-3012.

Examination of bone like materials

Dávid Pammer[1,a], Eszter Bognár[1,2,b]

[1]Department of Materials Science and Engineering, Faculty of Mechanical Engineering, Budapest University of Technology and Economics, Bertalan Lajos utca 7, H-1111 Budapest, Hungary

[2] MTA–BME Research Group for Composite Science and Technology, Műegyetem rkp. 3, H-1111 Budapest, Hungary

[a]dav.pammer@eik.bme.hu, [b]eszter@eik.bme.hu

Keywords: dental implant, bone, wood, polyurethane, torque, rotational work, insertion

Abstract. The aim of this research is to develop a new minimally invasive measurement procedure. With this method implantologist could determine the local mechanical and structural properties of the cellular solids materials (e.g. bones) into which implants are placed. The currently applied methods are based on image measurement procedures (CT, Hounsfield scale etc.). The dentists, with the knowledge of the determined mechanical properties of the bone, can choose the ideal surgical parameters (flap size, diameter of drill, hole-depth, healing time, etc.) and the ideal implant type for the patients. During the development of the measuring procedure, was used bone modeling materials ("bone-like materials") instead of bone. With these materials it is easier to do tests, than with living tissues. The bone like materials needs to have the same mechanical and structural properties as the given bone. The following bone like materials was used during the measurement: woods (Amaranth, Alnus, Ipe, Iroko, Robinia, Pyrus, Zebrano), and on the market available polyurethane solid foams (Sawbones D1 and D2). Among the literatures are summaries, which include the biomechanical assessments for implant stability. These technics are good to determine the implant stability in different bones and bone like materials after the implantation. In this work torsional test were used. This test is based on the determination of the insertion torque as a function of the implant displacement. Used the insertion torque functions and the screw geometrical parameters, the rotational work was determined. The different materials insertion torque functions have different slope values. The slopes and the rotational work results show which bone like material has similar insertion parameters (insertion torque function, rotational work) as a mandible during the insertion of an implant. With this torsional test and the knowledge of the bone like materials insertion torque functions and the rotational works it is possible to find the best material for the modeling of an implantation. Using this material, medical students can practice and improved the surgical techniques.

Introduction

Nowadays for dental implantation it is useful, if the dentist has information about the patient's bones, such as mechanical properties, structure and density. To get these parameters the current applied methods are based on the imaging technology (CT, Cone Beam CT, Hounsfield scale, Dual Energy X-ray absorptiometry, etc.) [1,2]. The results of these bone examinations helped the implantologists to classify the bones into 5 classes, which are D1-D5. These classes depend on the bone structure and density. D1 is a very dense cortical bone with small spongy part, and D5 is a very spongy bone with small cortical layer. [3]. On an industrial CT record of the mandible the regions with different structures and densities are clearly visible. In the practice, the used CBCT records have less information compared to the industrial CT records. On the CBCT records the bone structures, the spongy bone regions are not clean. The regions of the osteoporosis are detectable, but it is not possible to determine the quality of osteoporosis. In a biomechanical laboratory destructive and non-destructive test methods are used which are suitable to determine the mechanical parameters (E, G, ν) of the bone [4,5]. In the operating theatre there are no possibilities to use these

measurement methods; due to this the applied technics are the non-invasive imaging technologies, which are good to approximate some mechanical and structural parameters.
Figure 1 is a high power 3D CT record of a cadaver mandible (we used the high power industrial 3D CT of the Széchenyi István University, Department of Material Sciences and Technology). Figure 2 and Figure 3 shows the cross sections of the mandible at different planes (A, B). The discrete regions of interest (ROIs: D_1, D_2, D_3, D_4, D_5) shows that the changes of the mandible structure and densities are depend on the geometrical directions (x, y, z). That means, each region (where the dental implant can be placed) has individually mechanical and structural properties.

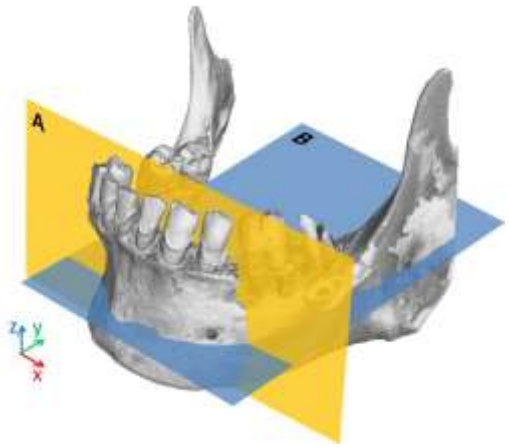

Figure 1. Two main planes (A, B) of the CT scanning

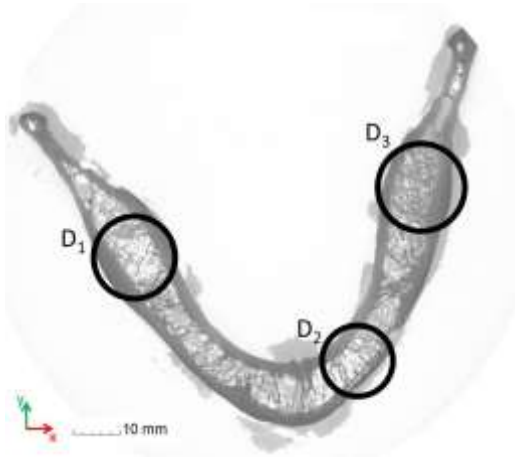

Figure 2. Cross section A of the mandible, with the ROIs

Figure 3. Cross section B of the mandible, with the ROIs

The dentists use CBCT records to analyze the patient's mandible (Figure 4 – made by SchindlerDent, Kiskunhalas). CBCT has a lower radiation doses compared to a normal CT or radiography [6]. On the CBCT record the teeth, implants and the mandible's geometry (high, width, etc.) are clearly visible. The spongy structure and density of the mandible are not well visible on the records.

Figure 4. CBCT „One Shot" image of a mandible

The imaging analyses of the mandibles are non-destructive, but biomechanical destructive tests are also needed to get information about the dental implant – bone interface, and the primary and secondary stability. Biomechanical tests are the pull-out test, push out test, removal torque test, RFA (Resonance Frequency Analysis), periotest, micro-motion test, cutting resistance torque. To the simulation of the biomechanical tests, FEM (Finite Element Method) can be used [7,8,9,10,11]. For the examination of the secondary stability, living bones (animal or human) are necessary, because there is no osseointergration between implants and bone like materials. The modeling methods of osseointegration between bone like materials and implants are now under developing. The bone like materials (also cadaver bones) are good to model the primary stability of the implants. The stability of an implant depends on the implant geometry, the surface treatment, the implant's material, the bone structure, and the osseointegration [12].

Materials and methods

Materials. Bone like materials has nearly the same mechanical and structural properties as the bone [13]. Each bones of the human body have different properties. These properties are influenced by the function of the bones. Due to this, one type of bone like materials are not adequate to use as a general bone like material.

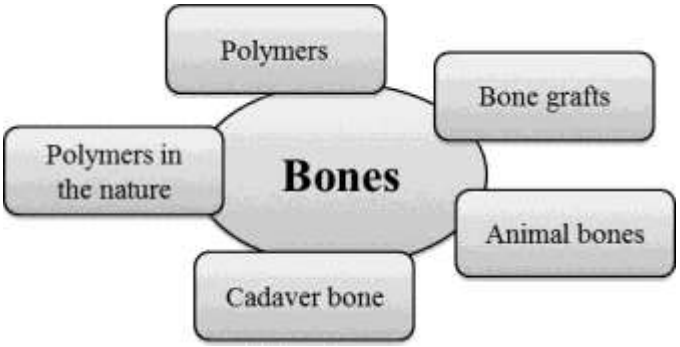

Figure 5. Bone like material groups

Figure 5 shows five main classes of bone like materials. The typically used bone like material is polyurethane. Some company has a wide product list of polyurethanes with different geometry and density. On the market available products have different densities (ASTM 1839) [14] to model the different mechanical and structural properties of living bones.

In this study the following bone like materials were used: Sawbones D1-PUR, Sawbones D2-PUR, 7 different wood types (Zebrano, Alnus, Pyrus, Robinia, Iroko, Amaranth, Ipe) and beef rib.

Methods. Torsional tests were used to find that material type of the listed bone like materials, which is the best for modeling an implantation process (insertion and stability). Modeling in this case means to get the same mechanical and tactile parameters as the bone. The test is based on the clinical used implantation surgery processes, without the medical steps (Figure 6) [15].

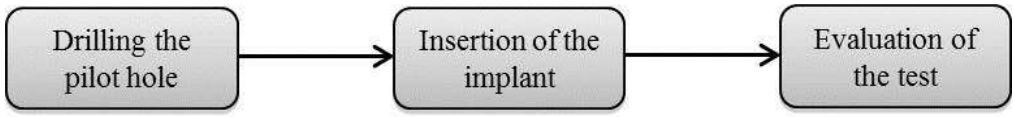

Figure 6. Main implant insertion steps

In case of all the used bone like materials the implant model screw (ISO 4.2×22) core diameter was drilled into them. The screw was "inserted" with a torque screwdriver (Wera 7440 0,30-1,20 Nm). The torque values (0.3→1.15 Nm; increment: 0.05 Nm) for each step of the screw displacement (the distance of the screw head position and the reference positon, Figure 7) were measured with a tensile test machine (Instron 5965). In each type of bone like materials 8 pilot holes were drilled and each insertion had 17 torque measuring points.

The geometrical parameters of the screw (Figure 8); Pitch=1.42; and the insertion torque function are known, due to this the rotational work was calculated.

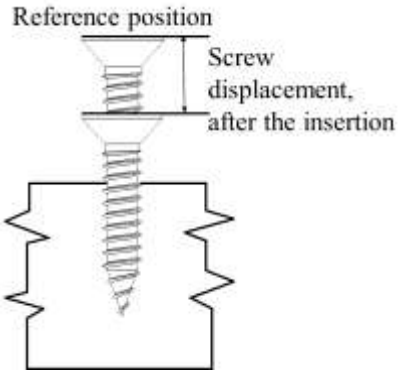

Figure 7. The screw displacement

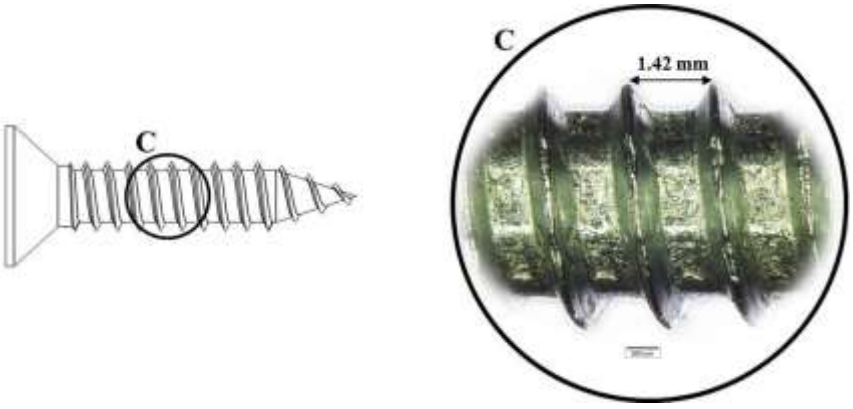

Figure 8. The implant model screw geometry and the pitch

Results

The insertion torque functions of the different bone like materials (Figure 9) shows, which material's function converge to the beef rib function. The Sawbones D1 had just 11 insertion torque measuring points (instead of woods 17 points), because with 0.9 Nm the implant model screw was easily screwed into the bone like material. The Sawbones D2 had also less torque measurement points, just 6, because with 0.65 Nm the implant model screw was screwed into the bone like material. Used the implant model screw geometry parameter (P) it was possible to determine the screwing function (Eq. 1) (screw displacement – screw rotational angle, Figure 10).

$$\varphi(s) = \frac{2 \cdot \pi}{p} \cdot s \tag{1}$$

Where φ is the rotational angle and s is the displacement of the screw.
The rotational angle to each torque value are known, due to this the rotational work was calculated. To get the total rotational work of an insertion (in one hole) the discrete rotational works were summarized (Eq. 2).

$$W_\tau = \sum_{i=1}^{n} \tau_i \varphi_i \tag{2}$$

Where W_τ is the total rotational work, τ_i is the discrete screwing torque, φ_i is the discrete rotational angle and n=17.
The insertion torque functions slopes were also calculated.

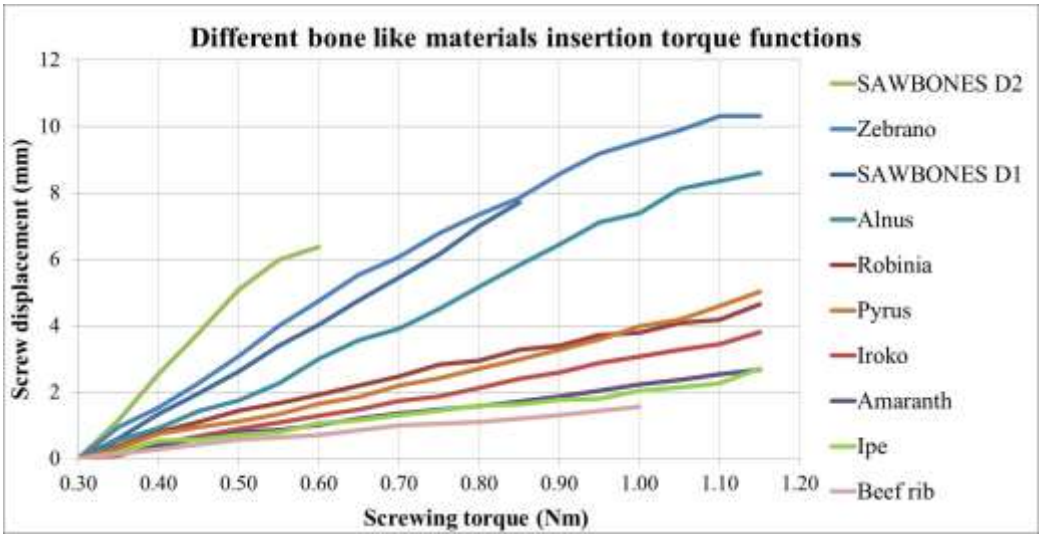

Figure 9. The insertion torque functions of the bone like materials

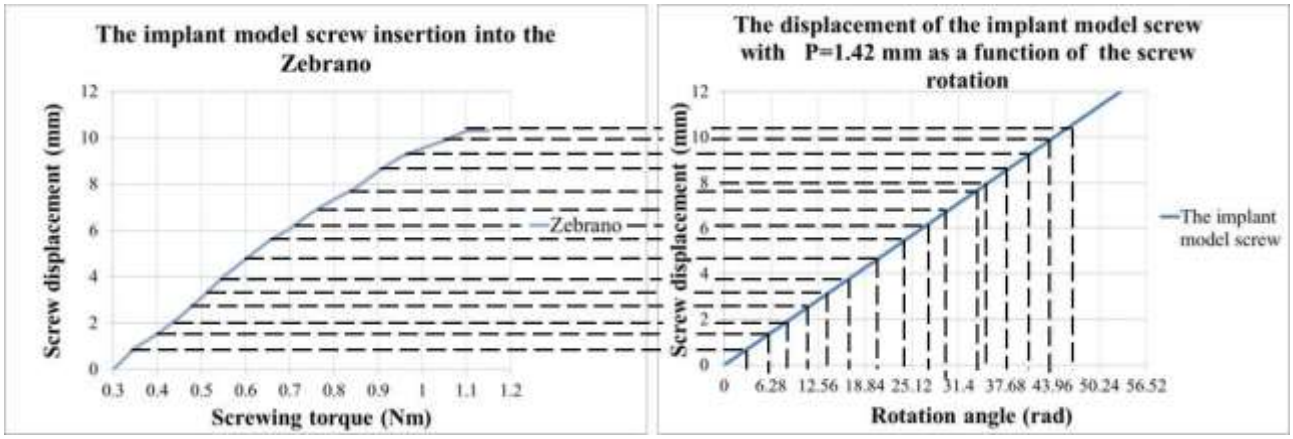

Figure 10. The calculation method of the rotational angles to each torque values

Table 1 and Figure 11 show all calculated results.

Bone like materials	Slope of screwing torque functions (-)	Rotational work (J)
Sawbones D2-Pur	22.37	12.81
Sawbones D1-Pur	14.03	19.67
Zebrano	12.65	30.87
Alnus	10.72	28.20
Pyrus	5.64	17.17
Robinia	5.16	14.74
Iroko	4.42	12.89
Amaranth	3.02	8.71
Ipe	2.78	9.11
Beef rib	2.14	4.39

Table 1. The calculated results of bone like materials

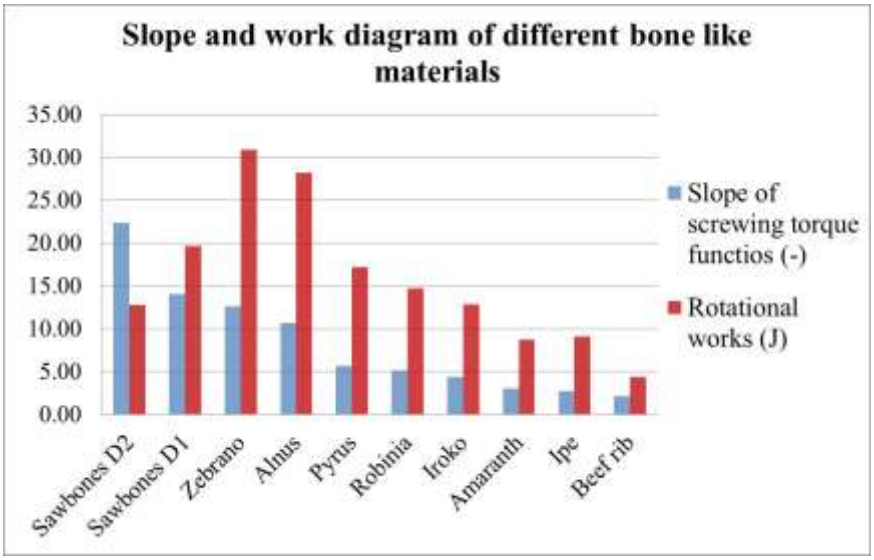

Figure 11. The summarized rotational work and the slopes of bone like materials

Conclusion

By modeling the implant insertion, the results shows that hard woods (Ipe, Amaranth, Iroko, Pyrus, Robinia) insertion torque functions converge to the beef rib function. The soft woods and the polyurethane bone like materials (Sawbones D1 and D2) insertion torque functions do not converge to the beef rib function. These results mean that on the market available D1 and D2 types of

polyurethane (the hardest blocks) bone like materials (Sawbones) are not recommended to use for modeling an implant insertion procedure. Thanks to the torsional test and the insertion torque functions different implant geometries and different bone like materials are possible to compare with each other, and find the ideal implant geometries and bone modeling material.

Acknowledgement

This work is connected to the scientific program of the " Development of quality-oriented and harmonized R+D+I strategy and functional model at BME" project. This project is supported by the New Hungary Development Plan (Project ID: TÁMOP-4.2.1/B-09/1/KMR-2010-0002).

References

[1] D. G. Pandurić et al., Current Concept of Densitometry in Dental Implantology, in Prof. Ilser Turkyilmaz (Eds.), Implant Dentistry - The Most Promising Discipline of Dentistry, Rijeka, 2011, pp. 453-477

[2] F. Koppány, Á. F. Joób, Gy. Szabó A csontsűrűség meghatározásának lehetőségei a maxillofaciális régióban (Irodalmi áttekintés) Fogorvosi Szemle 100. (2007) 77-81.

[3] Misch C. E.: Contemporary Implant Dentistry, Mosby Inc., 3rd ed. (2007)

[4] A.M. O'Mahony, J.L. Williams, P. Spencer, Anisotropic elasticity of cortical and cancellous bone in the posterior mandible increases peri-implant stress and strain under oblique loading. Clin Oral Implants Res.6 (2001) 648-657.

[5] I. Bagi, Finite element study of some parameters of bone fractures fixed with screws. Periodica Polytechnica Mechanical Engineering 55/1 (2011) 57–61

[6] L. Sennerby et al., Evaluation of a Novel Cone Beam Computed Tomography Scanner for Bone Density Examinations in Preoperative 3D Reconstructions and Correlation with Primary Implant Stability. Clin. Impl. Dent. and Related Research, 2013

[7] Jr. A.C. Freitas et al., The effect of implant design on insertion torque and immediate micromotion. Clin. Oral Impl. (2011)

[8] R.C. Van Staden et al. Application of the finite element method in dental implant research. Comput Methods Biomech Biomed Engin. 4 (2006) 257-70.

[9] Degidi M, Daprile G, Piattelli A. Determination of Primary Stability: A Comparison of the Surgeon's Perception and Objective Measurements. Int J Oral Maxillofac Implants. 3 (2010) 558-61.

[10] www.osstell.com/$-1/25038-03-en-osstell-isq-brochure-lr.pdf (2014.01.10)

[11] Szűcs A. et al. Problems of the biomechanical investigation of dental implants. Proceedings of the First Hungarian Conference of Biomechanics. (2004) 448-457

[12] V. Mathieu et al. Biomechanical determinants of the stability of dental implants: Influence of the bone–implant interface properties. Journal of Biomechanics. 47 (2014) 3–13

[13] N. F. Oliscovicz et al. Analysis of Primary Stability of Dental Implants Inserted in Different Substrates Using the Pullout Test and Insertion Torque. Hindawi Publishing Corporation International Journal of Dentistry. (2013) 5 pages

[14] ASTM International Standard Specification for Rigid Polyurethane Foam for Use as a Standard Material for Testing Orthopaedic Devices and Instruments F1839 - 2004, American Society for Testing and Materials. (2004).

[15] I. Vajdovich: Dentális implantológia. Semmelweis Kiadó, Budapest, 2008.

The effect of the severe plastic deformation on the artificial aging of the AlMgSi1 alloy

Judit Pázmán[1,a], Péter Bereczki[1,b], Balázs Verő[1,c], Ibolya Kardos[2,d], Jánosné Fehér[3,e]

[1]College of Dunaújváros, Institute of Technology, 2400 Dunaújváros, Táncsics Mihály street 1/A.; Hungary

[2] ISD Dunaferr Zrt., Innovation Directorate, 2400 Dunaújváros, Vasmű tér 1-3., Hungary

[3] Alcoa-EMP-European Mill Products-Köfém Kft., 8000 Székesfehérvár, Verseci street 1-15.; Hungary

[a]pazman@mail.duf.hu (corresponding author); [b]BERECZKIP@mail.duf.hu; [c]VEROB@mail.duf.hu; [d]iszalai@rt.dunaferr.hu; [e]janosne.feher@alcoa.com

Keywords: multiple forging, aging, aluminium alloys, hardening mechanism, additivity.

Abstract. The AlMgSi1 alloy is generally used in automotive industry owing to its excellent mechanical properties, which can be further improved by applying severe plastic deformation and heat treatment. The dislocation density in the material increases significantly during severe plastic deformation due to the characteristic intensive shear strain. Therefore the motion of dislocations becomes more and more retarded, consequently the strength improves. In addition, the motion of dislocations can be prevented by aging due to formation of coherent precipitations in the metal matrix in order to realize further increasing in strength. In this paper the combined effect of severe plastic deformation and artificial aging treatment on the evolution of mechanical properties was investigated. The samples were subjected to multiple forging (MF) process at room and enhanced temperature. One part of the deformed samples were heat treated at 150°C for different times. The deformed as well as deformed and heat treated samples were investigated by micro hardness testing and X-ray profile analysis.

Introduction

Application of lightweight metals have a growing trend in automotive industry, including the aluminium alloys. Its mechanical properties can be improved by different methods. The first and the most obvious solution is the alloying. The alloying elements placed into the crystal lattice distort it. Due to this distorting effect the mobility of dislocations is supressed, in consequence the strength behaviour of aluminium alloys improve. Respect to the Al6082 alloy, magnesium, silicon and manganese as alloying elements cause the distortion of crystal lattice. This effect can be explained by the disparate atomic diameters of these elements. Namely, the atomic diameter of silicon and manganese is smaller than the aluminium's, but the magnesium has bigger one. According to these facts, the lattice parameter marked with "a" is increased by adding magnesium and decreased by alloying silicon and manganese in homogenized state (Fig.1).

The other method for increasing the strength is plastic forming. The discontinuity faults in the material, especially the number of edge dislocations increases during plastic deformation particularly by severe plastic deformation (SPD) processes. Due to the intensive plastic deformation, the saturation state can be obtained by metals, whereby the dislocation density reaches its maximum level. In this state the formation and annihilation of dislocations are in balance due to the interactions of mobile and immobile dislocations. This was studied by Csanadi et al, who improved the model of Kubin-Estrin using his experiments on the pure Al, Cu and Ni at room temperature.

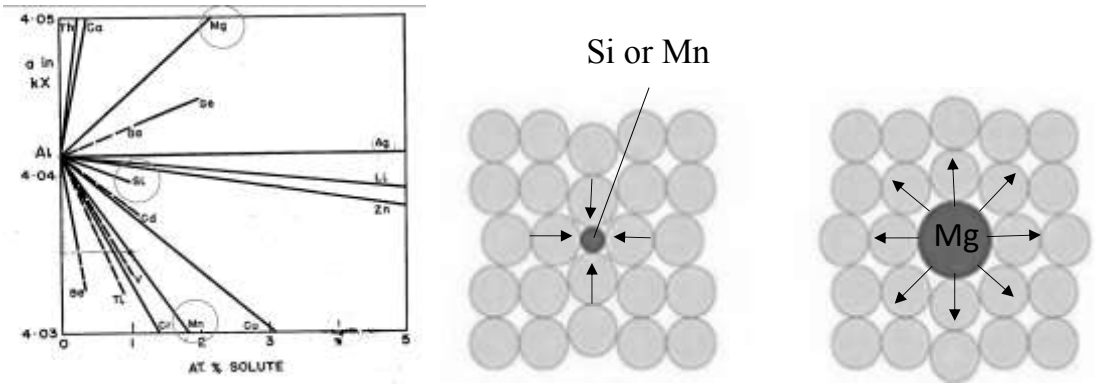

a) **b)**

Fig.1. Effect of alloying elements on the crystal lattice of aluminium

a) lattice parameter of aluminium as function of dissolved alloying elements
b) lattice distortion effect caused by substituted alloying elements

According to their results, the interactions between immobile and mobile dislocations in the range of large strains increase the density of immobile dislocations less than the interaction of mobile dislocations. Consequently, the occurrence of saturation state is attributable to the interaction of mobile dislocations [2-3].

Further increase in strength can be achieved by the coherent precipitations formed during the aging treatment in the metal matrix of precipitation hardening aluminium alloys before plastic forming. Namely, the moving of dislocations in the material is inhibited even more by formation of these precipitations, because the dislocations have to cross or evitate them (Fig. 2). The internal stress takes place in both cases and explains the increase in strength. Although, the presence of precipitations requires before applying the severe plastic deformation.

The other possibility to combine severe plastic deformation and aging is to applying first the deformation pass then performing the artificial aging treatment. It is not clear that these processes with respect to the resultant mechanical properties - eg. hardness and yield strength - are additive or not. Furthermore, applying the severe plastic deformation at aging temperature the effect of dynamic precipitation process can be investigated. In our experiments the AlMgSi1 samples were homogenized at 540°C for 4h. After homogenization the serve plastic deformation was realized by multiple forging with different accumulated strains, followed by aging treatment at 150°C for different times.

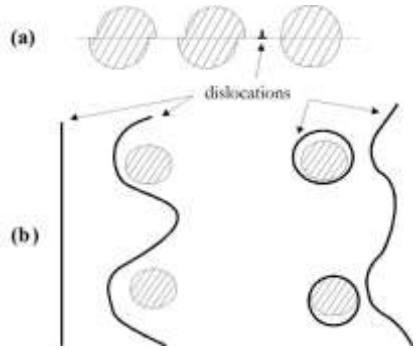

Fig. 2. The motion of dislocations regarding to the presence of hard and rigid phase [4].

a) cutting of precipitations
b) evitating of precipitations

Our investigation targeted on the determination of optimal process parameters whereby the characteristic strain applied by severe plastic deformation combined with the aging temperature results the maximum increase in strength.

The multiple forging experiments were carried out on a Gleeble 3800 physical simulator with MAXStrain System. Micro hardness were measured along the middle line of the cross sections as well as the hardness distribution were recorded in gridded layout also on the cross sections by the forged as well as the forged and heat treated samples in order to study the homogeneity of the formed microstructure and the additivity of hardening mechanisms. The dislocation structure was characterized after the deformed specimens was investigated by X-ray profile analysis.

Experimental

Applied alloy. Extruded AlMgSi1 raw material was used in our research work. Its chemical composition can be seen in Table 1. This commercial AlMgSi1 alloy is given in precipitation hardened state, so the strength is relatively high, but the ductility is lower. Generally, the precipitation hardening aluminium alloys show lower strength and higher ductility in homogenized state. In order to improve the formability before applying large-scale plastic deformation by multiple forging the specimens were homogenized at temperature of 540°C for 4 hours obtained from data in literature [5-9]. Using this prior heat treatment, cracks or any visible degradation were not occurred even after applying 10 forging pass.

Table 1 The chemical composition of AlMgSi1 alloy used in this research work.

Chemical composition	Si	Fe	Cu	Mn	Mg	Cr	Zn	Ti	Ni	V	Be	Al
Data sheet	**0.72**	0.25	0.06	**0.42**	**0.61**	0.02	0.03	0.02	-	-	-	**97.87**
For industrial heat treatment	0.75	0.22	0.065	0.42	0.66	0.019	0.042	0.021			0.00002	97.8

Severe plastic deformation. The multiple forging experiments were carried out on Gleeble 3800 thermo-mechanical simulator, equipped with MaxStrain multiaxial forging System. A photo from the experimental setup of multiaxial forging simulation is shown in Fig. 3. The specimen is mounted in the manipulator in order to restrain the axial deformation. The specimen is rotated between the deformations back and forth by the manipulator with 90°. A cubic part of the specimen with dimensions of 10×10×10mm is deformed between two tungsten carbide anvils, which are moved by an integrated hydraulic system in a fully enclosed, digital PID-control loop. Before the deformations, the anvils approach and contact the specimen according to the specified force-criterion. During the deformations, the amount of logarithmic strain and the strain rate are also controlled by the signals of longitudinal strain gauge, attached to the hydraulic pistons. In these tests, the specimens were deformed in each forging step with true strain of 0.5 at strain rate of 0.1 $^{1}/_{s}$.

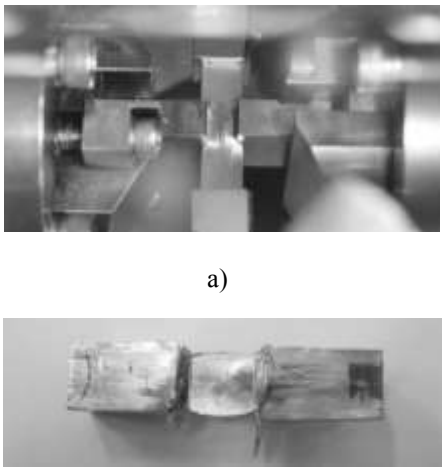

a)

b)

Fig. 3. Multiple forging with Gleeble 3800 thermo-mechanical simulator:
a) photo of experimental setup.
b) deformed sample (φ = 10).

Testing methods. The two-dimensional hardness maps in the deformed zone and the hardness profiles along the longitudinal symmetry axis of samples – included the deformed and non-deformed zones – were recorded by micro hardness tester (Wilson Wolpert 401MVD). The loading force was 0.2 kgf in order to study the distribution of strain in the deformed volume. Furthermore, the formed dislocation structure formed was investigated by X-ray profile analysis. One part of the deformed samples were aged at 150°C for different times from 15 minutes to 5 hours. The above mentioned hardness profiles were recorded on the deformed as well as heat treated samples in order to study the interaction of strengthening and precipitation hardening mechanism in regarding to the different accumulated strains.

Results

Natural and artificial aging. After homogenization the samples from the extruded raw material were naturally as well as artificially aged in order to study the increasing in strength by measuring the hardness increment, which caused by the formed coherent and semi-coherent precipitations. The hardness values increased after two days of natural aging from the range of 48.5-54.5 to 72.5-82.5 HV compared to the homogenized state, while the hardness reached the range of 85-97 HV after artificial aging at 150°C for 5 hours. The heat treatment experiments were reproduced in industrial conditions. The results of macro hardness tests showed that the hardness of homogenized samples increased from 60±2 HB to 64 HB after 7 days of natural aging, but the hardness does not exceed 68.5 HB after 30 days of natural aging. Regarding to the results of natural aging tests the hardness changes after homogenization significantly on first week, consequently the samples must be stored in most advertent conditions to prevent the onset of natural aging. The hardness can be further improved by applying artificial aging. The two-step artificial aging treatment (140°C 4h + 180°C 4h) after 30 days of natural aging resulted the highest hardness values concerning the industrial experiments. Tensile tests were performed on these heat treated samples and the highest yield stress ($R_{p0,2}$ = 284 MPa) as well as tensile strength (R_m = 306 MPa) were measured after the above mentioned two-step heat treatment. The yield stress increased by 446% compared to the homogenized state, while the tensile strength doubled. Regarding to the industrial measurements it can be summarized that the hardness improves significantly using natural or artificial aging, particularly if the two-step artificial aging follows the natural aging.

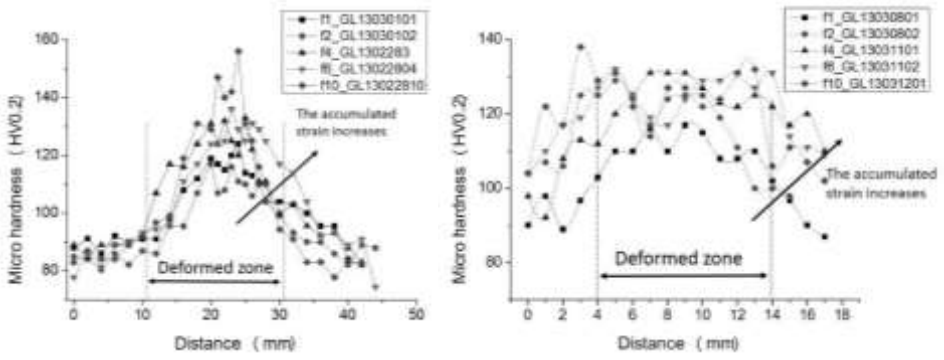

a) b)

Fig. 4. Hardness profiles of MF samples:
a) deformation at room temperature.
b) deformation at elevated temperature (150°C).

Multiple forging. Beside the aging experiments, the evolution of hardness was also studied on the forged samples regarding to the different applied strains. Fig. 4 shows the evolution of hardness values along the longitudinal symmetry axis of samples. Different symbols represent the amount of applied deformation. Continuously increasing in micro hardness at room temperature can be identified in Fig. 4/a. as the accumulated strain increases. It can be explained by the accumulation of dislocations as the number of deformation cycles increases. Namely, if the dislocations accumulate the mobile dislocations inhibit the movement of each other [10]. The dislocation density was measured by X-ray profile analysis on the 20 times deformed sample and it reaches a critical value ($0.8*10^{14}$ m^{-2}) that represents the saturated state for this material. This is clearly indicated also on the hardness map of its deformed zone in Fig. 5/b. Furthermore, the degree of inhomogeneity in hardness is observed as the accumulated strain increase until the material reaches its saturated state (Fig. 5).

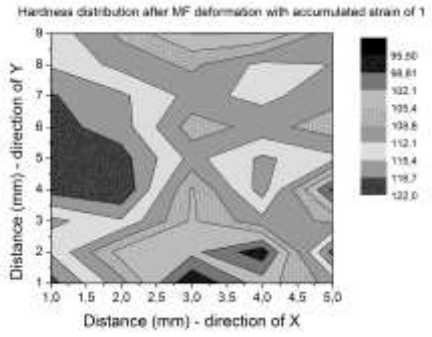

a)

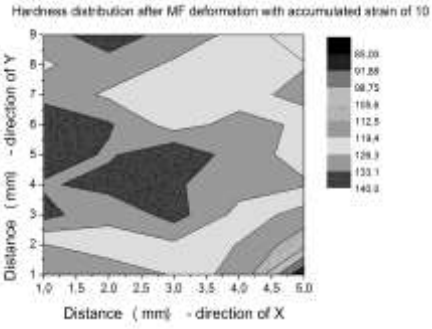

b)

Fig. 5 The hardness map of deformed samples:
a) accumulated strain is about 1.
b) accumulated strain is about 10.

Hardness profiles of the samples after forging at elevated temperature in Fig. 4 b) show significant differences compared to the profiles recorded after deformation at room temperature. Namely, in both case the hardness in deformed zones rises with increasing the number of deformation passes, while the values show higher homogeneity (curve with a plateau) concerning the experiments at enhanced temperature at room temperature, where the highest hardness value can be measured at the centre of deformed zone. This can be explained by occurrence of two processes, the accumulation of dislocations and the formation of precipitations at the same time. Usually the precipitations form on the grain boundaries, where the energetic conditions are optimal. As the microstructure refines, the volume fraction of grain boundaries increases, so more and more potential nucleation sites appear for precipitation. Moreover the grain refinement and the formation of sub-grains increases the strength. The average grain size weighted by the area is given about 84 nm after the accumulated strain reaches the value of about 10. Consequently, the main advantage of two strengthening mechanisms is the homogeneity of the deformed zone. This was observed concerning the hardness values in terms of accumulated strain, as shown Fig. 6. It can be seen that the maximum hardness values rises significantly as the accumulated strain reaches the value of 1 and 2 then by further deformation the increasing becomes slower (Fig. 6).

Artificial aging after multiple forging. The diagram of Fig. 7 shows the evolution of mean hardness values by the samples aged at 150°C after multiple forging at room temperature. The aim of these experiments was to study the effect of precipitation's formation on the motion of dislocations and vice versa in terms of time. According to Fig. 7, if the alloy has not reached its saturated state due to severe plastic deformation (for ex. at φ = 1), then further increase in hardness can be realized by formation of precipitations. Nevertheless, if the alloy approaches the saturated state due to severe plastic deformation (φ =2), then the strength cannot be improved further, but the obtained hardness remains constant. In contrary, if the accumulated strain exceeds the value dedicated to the saturated state (φ = 10), a surprising effect can be identified concerning the heat treatment, the deformation induced increasing in hardness decreases significantly.

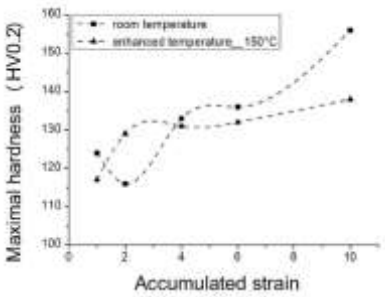

Fig. 6 The maximum hardness values in terms of accumulated strain.

Conclusion

The strength of pure aluminium can be improved by alloying as well as severe plastic deformation and precipitation hardening. The aim of our experiments was to study the interactions between these strengthening mechanism (Fig. 8.). Regarding to our research work and results the following conclusions can be drawn:

i. The effect of natural aging on hardness by homogenized AlMgSi1 alloy is very intensive for the first week, consequently the alloy requires a special storage to suppress it.

ii. Higher increase in strength can be reached by applying artificial aging after the natural aging than using each aging treatment separately.
iii. At the beginning the multiple forging eventuates an inhomogeneous microstructure, which becomes more homogenous after the saturated state is reached.
iv. The strengthening mechanisms of dislocation moving and formation of precipitation take place at same time during multiple forging at aging temperature. Consequently, the hardness distribution in deformed zone is more homogeneous than after multiple forging at room temperature.
v. The mechanism of precipitation hardening can be combined with dislocation hardening. If the saturated state has not reached due to multiple forging, then the hardness can be improved by the aging treatment. Nevertheless, if the saturated state is proved by deformation, then the aging decreases the deformation induced increasing in hardness due to multiple forging.

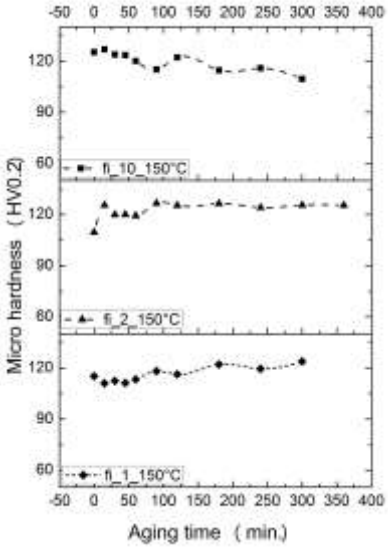

Fig. 7 The evolution of hardness by the samples after forged at RT and aged at the 150°C in terms of aging time

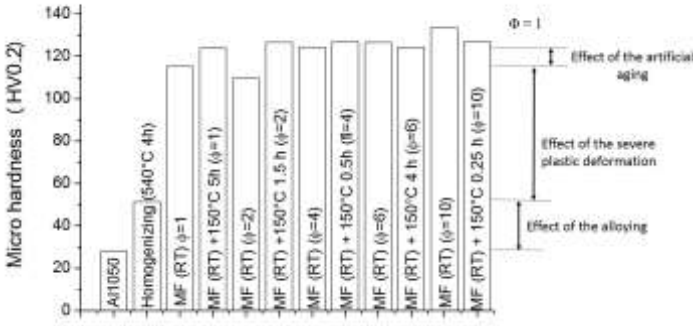

Fig. 8. The additivity of strengthening mechanisms.

Acknowledgements

The authors give thanks to Prof. Dr. Tamás Ungár and Bertalan Jóni at the Department of the Materials Physics at Eötvös University for the X-ray profile analysis results. The work/publication is supported by the TÁMOP-4.2.2.A-11/1/KONV-2012-0027 project. The project is co-financed by the European Union and the European Social Fund.

References

[1] Csanádi, T., Chinh, N. Q., Gubicza, J., & Langdon, T. G. (2011.). Plastic behavior of fcc metals over a wide range of strain: Macroscopic and microscopic descriptions and their relationship. Acta Materialia 59 , 2385–2391.
[2] Kubin, L., & Estrin, Y. (1990.). Acta Metallurgia 38, 697
[3] Estrin, Y., Tóth, L., Molinari, A., & Brechet, Y. (1998.). A dislocation-based model for all hardening stages in large strain deformation. Acta Materialia, Volume 46, 5509-5522.
[4] Gácsi, Z. (2008-2009.). Treatment of the metal alloys. Gácsi Zoltán, Miskolc, Hungary.
[5] Copley, S. M., & Langer, E. L. (1991.). Volume 4 - Heat treatment. In S. M. Copley, & E. L. Langer, ASM Metal Handbook, (old.: 1871-1875.). United States of America: ASM International.
[6] Mrówka-Nowotnik, G., Sieniawski, J., & Nowotnik, A. (2009.). Effect of heat treatment on tensile and fracture toughness properties of 6082 alloy. Journal of Achievements in Material and Manufacturing Engineering, Vol. 32, Issue 2, 162-170.
[7] Anjabin , N., & Karimi Taheri, A. (2010.). The effect of aging treatment on mechanical properties of AA6082 alloy: modelling and experiment. Iranian Journal of Materials Science & Engineering Vol. 7, Number 2, , 14-21.
[8] Biroli, G., Caglioti, G., Martini, L., & Riontino, G. (1998.). Precipitation kinetics of AA4032 and AA6082: A comparison based on DSC and TEM. Scipta Materialia, Vol. 39, No. 2,, 197-203.

[9] Mrówka-Nowotnik, G. (2010). Influence of chemical composition variation and heat treatment on microstructure and mechanical properties of 6xxx alloys. Archives of Materials Science and Engineering Vol. 46, (2), 98-107.
[10] Tóth, L., Molinari, A., & Estrin, Y. (2002.). Strain Hardening at Large Strains as Predicted by Dislocation Based Polycrystal Plasticity Model. Journal of Engineering Materials and Technology, Volume 124., 71-77.

Alternative, new method for predicting polymer waste stream contents

Dobrovszky K.[1,a], Csergő V.[1], Ronkay F.[1,b]

[1]Department of Polymer Engineering, Faculty of Mechanical Engineering, Budapest University of Technology and Economics, H-1111 Budapest, Műegyetem rkp. 3, Hungary

[a]e-mail: dobrovszky@pt.bme.hu

[b]e-mail address: ronkay@pt.bme.hu (corresponding author)

Keywords: polymer separation; melt stated separation; waste stream; content estimating

Abstract:

In order to achieve the desired polymer recycling standards, precise estimations are needed about the composition of the polymer waste streams. The technologies that are currently used for this purpose, such as the infrared spectroscopy and the pyrolysis are neither time nor energy efficient as the processes may take up to hours, moreover the results are usually concluded by only analyzing small fractions of the waste streams. Meanwhile, as the polymer consumption of the world is increasing, the recycling and recovery rates demanded by numerous laws and restrictions are getting higher as well. The aim of this paper is to introduce a new technology that utilizes centrifugal force to separate the different polymer components of a sample in a melted state, containing the most common polymers found in a regular waste stream. After the separation, using the calculation method that is described, the exact ratio of the different materials can be given as well. In order to show the possibilities hidden in this technology, two samples, containing PA/PS/PP and PET/PA/PS/PP respectively, were separated and analyzed. The promising results were verified using optical microscopy as well as Raman spectroscopy.

1. Introduction

The recycling of polymer wastes is an ever existing problem, as the different polymer materials are usually collected together, resulting in an extremely heterogeneous waste stream. Since the polymers are usually not compatible with each other, this waste stream must be separated in order to make it suitable for processing [1]. The recycling of the wastes is currently a multi-step process, combining different technologies [2], but in order to achieve the desired quality of the products and to optimize the process, the composition of the waste stream has to be known. The aim of this research was to provide a feasible solution to this problem.

The polymer consumption of the world is increasing 5% annually causing the growth of the waste stream as well, which is accompanied by strictening government laws. Concerning the automotive industry, the pressure from the European Community comes in the form of the 2000/53/EC Directive, which states that 85% of a car's total mass has to be recycled by the end of its lifetime. This is currently achieved by recycling the metal parts of the car which still correspond for the greater part of the vehicle's mass. After the shredding and metal recovery the remaining materials, called the automotive shredded residue (ASR) or car fluff, which accounts for almost one third of a vehicle, is currently sent to landfills [3]. Besides contaminating substances, such as glass fiber or textiles, ASR may contain up to 20 different polymer materials, but the most common ones are (i) polypropylene (PP); (ii) polyamide (PA); (iii) acrylonitrile butadiene styrene (ABS); (iv) polycarbonate (PC); (v) polyoxymethylene (POM); (vi) poly butylenes terephthalate (PBT) and

others, from which the PP, PA and ABS give nearly two third of all polymer parts [4]. As a result of this high diversity, recycling car fluff properly yet remains unsolved, which is even greater problem considering the fact that the recovery rate targeted in the above mentioned directive will change from 85% to 95% by 2015, including a 5% growth in the recycling rate as well. This means that recovering the metal parts of the vehicles will no longer satisfy the demands, therefore a new, cost efficient and environmentally sustainable system is needed, which is capable of recycling not only the metal parts, but the ASR as well [5].

Although the waste stream produced by the automotive industry is not negligible, the communal waste that is originated mainly from the households is more responsible for the environmental pollution. As a response to the problem, the EU legislatives issued several regulations, for example the Directive 2004/12/EC, which applies to the packaging wastes and similarly to the previously mentioned directive on end of life vehicles, it fixes certain recovery and recycling rates that are to be achieved. This is not an effortless task either, mainly because communal waste, just like the ASR, contains several different polymer materials, such as (i) polyethylene terephthalate (PET) from soft drink bottles; (ii) polypropylene (PP); (iii) polyethylene (PE) with high (HDPE) or low density (LDPE) from packaging and bottles; (iv) polystyrene (PS) from drinking cups and pots; and (v) polyvinyl chloride (PVC) from pipes and interior furnishings [6]. In order to meet the recycling standards, both the communal and the automotive waste stream have to be analyzed to gain more knowledge about their components.

However, there are some technologies that are currently used for waste stream analysis, such as Raman spectroscopy [7] and pyrolysis [8], their results are not satisfying. Using infrared spectroscopy [9], the samples from the waste stream are exposed to electromagnetic radiation and by measuring the changes of the trespassing and reflected waves that are caused by each material's unique molecular structure; the different polymers can be identified. Besides the many advantages of this technology, such as high output and the chance to automate, it struggles with analysing the black coloured ASR, which simply absorbs the radiation. Another widespread technology is the pyrolysis, which estimates the composition of the waste stream by examining the decomposition product of the samples. Sadly this technology is neither time nor energy efficient as the heating process may take up to hours. Moreover, the estimation is concluded by only analysing a small fraction of the waste stream which makes it inaccurate.

For all the reasons mentioned above, it would be desirable to develop a new technology. The aim of this paper is to present a new technology that uses centrifugal force to separate the previously melted components of a sample according to their difference in density. By examining the separated zones, estimation can be given for the original waste stream's composition.

2. Experimental

2.1 Materials

During the research, the samples were a mixture of primary polymer granules to represent the composition of a regular waste stream. Four different types of polymers were chosen, which also greatly differ in density: (i) PP (type: Tipplen R359, density: 0.90 g/cm^3) from TVK Nyrt (Hungary); (ii) PS (type: ENI Edistir N1840, density: 1.05 g/cm^3); (iii) PA (type: Lanxess Durethan B30S, density: 1.14 g/cm^3) and (iv) PET (type: NeoPet 80, density: 1.34 g/cm^3).

2.2 Equipment

In the preparation step, a CAS MWP-1500 scale was used to weight the samples. To melt the samples, a Nabertherm L9/11/C6 furnace was applied. To verify the separation and to measure the width of the zones, an Olympus BX 51M optical microscope was used, preceded by the polishing of the samples which was carried out by a Struers LaboPol-5 automatic polishing machine. For the Raman spectroscopy, a Horiba Jobin-Yvon LabRAM system was used.

2.3 Description of the technology

In order to carry out the experiments, a centrifuge device was developed (Fig. 1). The process started by weighting each component of the sample and then mixing them up and loading them into the centrifuge. In the melting phase, the centrifuge with the samples in its three tanks was put into the furnace for 1 hour at 290°C. After all the components were melted, the shaft of the centrifuge and thus the tanks with the samples inside, were rotated for 10 minutes in the furnace with an AC motor at 2900 rpm. As a result of the generated centrifugal force field, the components of the samples created distinct zones according to their density. In order to preserve the zones, the device was rotated for another 10 minutes outside the furnace, at room temperature which caused the solidification of the structure.

The polymer materials for the samples were chosen so that they represent the most common components of a regular waste stream. In both cases 50 grams of material was loaded into the tanks of the device.

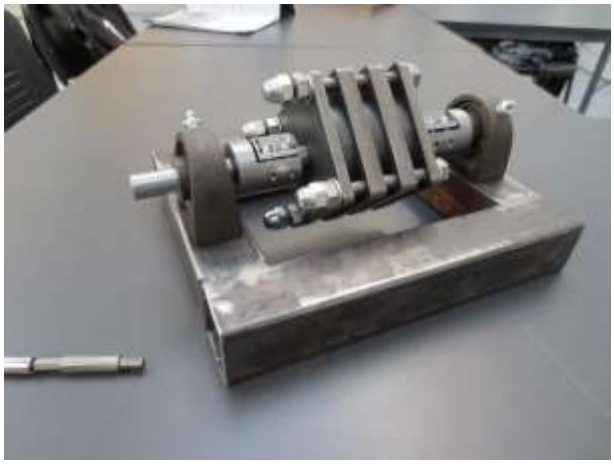

Figure 1. The centrifuge device, designed for the experiment

3. Results and discussion

3.1 Experiments with the PA/PS/PP mixture

Fig. 2 shows the separation results of the mixture. Since coloured granules were used, the separation can be observed with the naked eye (Fig. 2(a)). The 3 different materials formed nearly hundred percent pure zones, with the PA in the outer, the PS in the middle and the PP in the inner zone. The results were also verified by an optical microscope, showing the clear boundaries between the three phases (Fig. 2(b,c)).

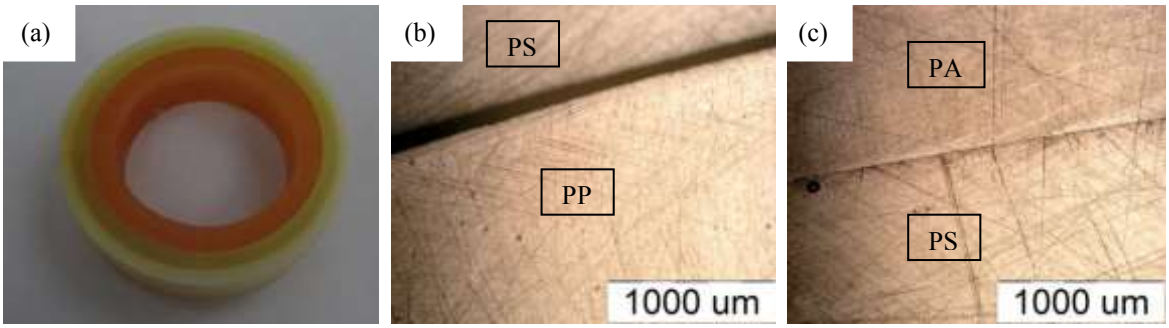

Figure 2. Separation results of the PA/PS/PP mixture: (a) the three different zones, (b) boundary between the PS and PP zones, (c) boundary between the PA and PS zones

As the aim of this research was to estimate the proportion of the components in the mixture, both the inner and the outer diameters of the rings were measure, containing the three different polymer materials, by the microscope, and also the height of the sample in order to calculate the volume of the rings using the following (Eq. 1):

$$V_i = \frac{1}{4}(D_{i,Out}^2 - D_{i,Inn}^2) \cdot \pi \cdot H \quad (1)$$

where: $D_{i,Out}$ is the outer diameter of the ring [mm], $D_{i,Inn}$ is the inner diameter of the ring, i = PA, PS, PP [mm], H is the height of the sample [mm]

By knowing the volume of each ring and the density of the materials the mass of the rings could also be calculated (Eq. 2):

$$m = V_i \cdot \rho_i \quad (2)$$

where: V_i the volume of the rings [cm^3], ρ_i the density of the polymer in the rings [g/cm^3], i = PA, PS, PP

As a result of knowing the mass of each polymer, the proportion of the different materials could be gives as well. Table 1 shows the results and the estimated composition of the sample, as well as the proportion of the materials loaded into the mixture.

Table 1. Results of the calculations compared to the actual values

Material	Density (ρ) [g/cm^3]	Calculated volume (V_i) [cm^3]	**Calculated mass (m) [g]**	**Original mass [g]**	**Agreement [%]**
PA	1.14	14.9	**16.99**	**17.0**	**99.9**
PS	1.05	15.6	**16.38**	**16.5**	**99.3**
PP	0.90	18.4	**16.56**	**16.5**	**99.6**
Total			49.93	50.0	

In this particular case, there was an opportunity to compare the estimated composition of the sample to the actual proportions that had been measured before the experiment, in order to draw conclusions about the efficiency of the method. As there were no significant differences concerning the values, it can be stated that the results are more than satisfying.

3.2 Experiments with the PET/PA/PS/PP mixture

In order to prove that increasing the number of components does not affect the effectiveness of the method, a four phase mixture, containing PET, PA, PS and PP (Fig. 3), was also analyzed. The

results, similarly to the previous experiment were convincing, the four different polymers formed four segregated zones, which was confirmed by the optical microscope as well (Fig. 3(b, c)).

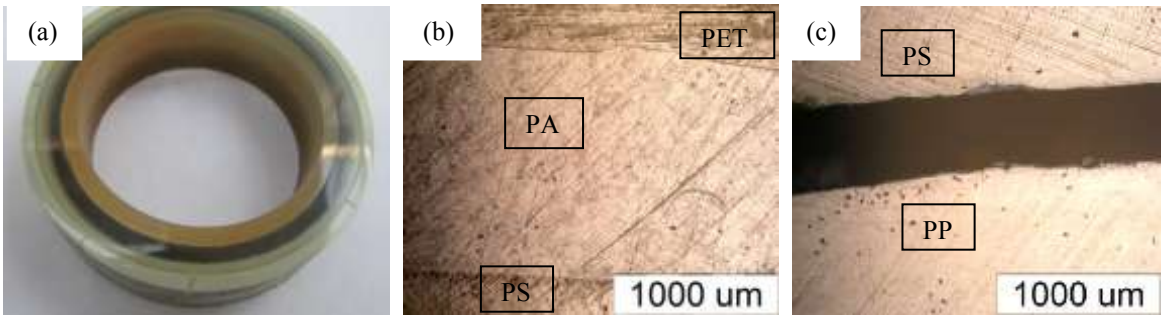

Figure 3. (a) Separated PET, PA, PS and PP zones, from the outer layers respectively, (b) the separated PET, PA, PS phases, (c) boundary between the PS/PP zones

Finally, to verify the purity of the phases, samples from each zone were analyzed using Raman spectroscopy. Fig. 4 shows the results, where the lower curves indicate the reference spectra, while the upper curves stand for the samples from the zones.

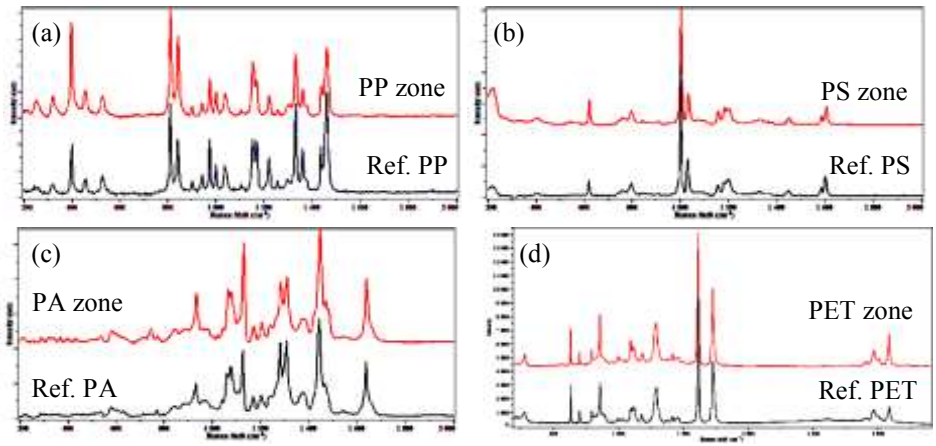

Figure 4. Raman spectra of the zones (a) PP zone, (b) PS zone, (c) PA zone, (d) PET zone

It is visible, that the characteristic peaks of the samples from the zones do not differ from the reference peaks of the supposed materials, therefore it can be concluded that the zones contain pure polymers.

4. Conclusion

The aim of this paper was to introduce a unique technology that may be a feasible solution for the pressing matter of waste stream analysis. In order to test the effectiveness of the technology, a new device was developed, which is capable of producing a centrifugal force field that separates the different polymer materials of a multi-component sample according to their difference in density. The efficiency of the technology was tested by examining PP/PS/PA and PET/PA/PS/PP mixtures and in both cases the device has proven to be capable of separating the different materials. Moreover by the presented calculation method, an almost perfect estimation can be given about the proportion of the components as well. Compared to the currently used technologies, this method is more economical, time efficient and last but not least, it is more precise, as it concludes to the composition of the waste stream by analyzing larger fractions of it.

Acknowledgement

This research was supported by the European Union and the State of Hungary, co-financed by the European Social Fund in the framework of TÁMOP 4.2.4. A/1-11-1-2012-0001 "National Excellence Program". The infrastructure of the research project was supported by the Hungarian Scientific Research Fund (OTKA K109224).

References

[1] A.L. Andrady, Plastics and the Environment, John Wiley & Sons, New Jersey (USA), 2003.

[2] S. Pongstabodee, N. Kunachitpimol, S. Damronglerd, Combination of three-stage sink–float method and selective flotation technique for separation of mixed post-consumer plastic waste, Waste Manage. 28 (2008) 475-483.

[3] I. Vermeulen, J. Van Caneghem, C. Block, J. Baeyens, C. Vandecasteele, Automotive shredder residue (ASR): Reviewing its production from end-of-life vehicles (ELVs) and its recycling, energy or chemicals' valorisation, J. Hazard Mater. 190 (2011) 8-27.

[4] M.S. Reddy, K. Kurose, T. Okuda, W. Nishijima, M. Okada, Selective recovery of PVC-free polymers from ASR polymers by ozonation and froth flotation, Resour. Conserv. Recy. 52 (2008) 941-946.

[5] B. Ruffino, S. Fiore, M.C. Zanetti, Strategies for the enhancement of automobile shredder residues (ASRs) recycling: Results and cost assessment, Waste Manage. 34 (2014) 148-155.

[6] F. Bezati, D. Froelich, V. Massardier, E. Maris, Addition of X-ray fluorescent tracers into polymers, new technology for automatic sorting of plastics: Proposal for selecting some relevant tracers, Resour. Conserv. Recy. 55 (2011), 1214-1221.

[7] B. Vajna, B. Bodzay, A. Toldy, I. Farkas, T. Igricz, Gy. Marosi, Analysis of car shredder polymer waste with Raman mapping and chemometrics, Express Polym. Lett. 6 (2012), 107-119.

[8] B. Bodzay, B.B. Marosfoi, T. Igricz, K. Bocz, Gy. Marosi, Polymer degradation studies using Laser pyrolysis-FTIR microanalysis, J. Anal. Appl. Pyrol. 85 (2009) 313-320.

[9] J. Beigbeder, D. Perrin, J-F. Mascaro, J-M. Lopez-Cuesta, Study of the physico-chemical properties of recycled polymers from waste electrical and electronic equipment (WEEE) sorted by high resolution near infrared devices, Resour. Conserv. Recy. 78 (2013) 105-114.

Surface layers produced by modified Floe ferritic nitrocarburising

Andrea Szilagyine Biro[1, a], Endre Szabo[1,b] Dr. Miklos Tisza[1,c]

[1]H-3515, Miskolc-Egyetemváros, Hungary

[a]biro.andrea@uni-miskolc.hu, [b]metsze@uni-miskolc.hu, [c]tisza.miklos@uni-miskolc.hu

Keywords: ferritic nitrocarburising, Floe process, white layer, porosity

Abstract. Ferritic nitrocarburising is a surface alloying heat treatment, which can provide to components high surface hardness, thus improved wear resistance. In structural steels the porosity of white layer has a key role in wear resistance: the porosity is undesirable. For tool steels the absence of white layer is undesirable. Floe process is one way to decrease the porosity of white layer. During our experiments we applied a modified Floe process on two different steels. The acontol of this process is simpler than conventional process. We measured the micro-hardness as a function of depth from the surface, and we made microscopic examination to analyse the structure of nitrided layer.

Introduction

Nitriding and ferritic nitrocarburising are surface modification technologies: nitrogen (and carbon) diffuse into the surface. The formed nitrides and complex carbonitrides increase the hardness of the surface, and thus the wear resistance, too. The surface treatments have important role in life time management of components: usually the loads on the surface are more complex than in the components **Hiba! A hivatkozási forrás nem található.**[2].

The nitrided layer consists of two parts. Directly on the surface there is a white/compound layer: it has high hardness and a few tens of micrometers in depth); it ensures the wear (and also the corrosion) resistance of the parts. Below the white layer there is a diffusion zone:, it has lower hardness (but the depth can be from few tenths of millimeter up to a few millimeter), furthermore, it supports the very hard white layer and provide good fatigue resistance [3][4].

About Gas Nitriding and Ferritic Nitrocarburising

In gas nitriding, ammonia gas provides the alloying nitrogen. On the surface of the components ammonia dissolves and the nitrogen diffuses into the surface. The nitrogen content of the surface layer can be controlled by the dissociation of ammonia. In most cases we can describe the nitriding effect by the nitriding potential, as given by Eq. (1)

$$N_P = \frac{p_{NH_3}}{p_{H_2}^{3/2}}. \tag{1}$$

When the nitriding potential is high, there is a high amount of ammonia in the chamber, thus more nitrogen can adsorb on the surface. In certain cases, there are specific demands against surface layers in nitriding/nitrocarburising. There are two distinct groups of these requirements. In tool steels, no need for the presence of white layer: the hardness of diffusion layer is sufficient to ensure the appropriate wear properties. In other cases, the presence of the white layer is required, but it is not possible to produce it without porosity in the required depth. It is caused by the porosity in the white layer. Porosity is present in the white layer, when the nitrogen absorption is much faster than the diffusion. When nitrogen concentration is too high two nitrogen atoms create a nitrogen molecule. This molecule is not diffusible - because of its size – and it forms porosity near the surface. The porosity in the white layer reduces the hardness of it, and consequently the wear resistance [5][6].

There are two ways to control the porosity. One of them is the increase of the decomposition of ammonia, and thus decreasing the absorption. This way we decrease the depth of nitrided layer. The

Floe process is regarded the other way; it contains two stages: absorption and diffusion stage – it does not decrease the depth of diffusion zone significantly [1].

Floe process. The application of the Floe process is one of the possible ways to reduce the depth or just the porosity of white layer. The Floe process is carried out as a two stage process (Figure 1). The first part is accomplished as a normal nitriding cycle at a temperature about 500°C with 15 to 30% dissociation of the ammonia (the atmosphere contains 70 to 85% ammonia). This will produce the nitrogen-rich compound zone at the surface. In the second stage the furnace temperature is increased to approximately 560 °C and gas dissociation also increased to 75 to 85% (the atmosphere contains 15 to 25% ammonia). The result of this two-stage process is a reduced depth and/or reduced porosity of the compound zone [1].

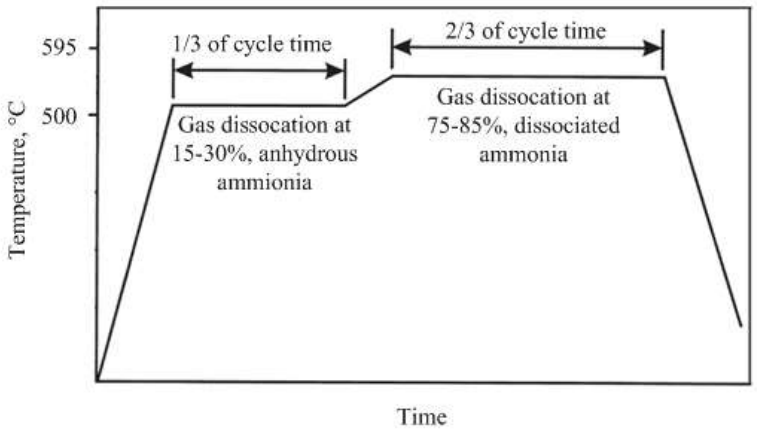

Figure 1. Typical Floe process [1]

Experiments

Parameters. There is a problem with application of the Floe process: in industrial furnaces the sudden increase of the temperature and dissociation of ammonia is not possible. Thus, it could be problematic to apply the Floe process. During our experiments we applied a modified Floe process as follows: nitriding is the first stage (at higher temperature than recommended in the normal Floe process); diffusion is the second stage , meanwhile there is no ammonia (and carbon-dioxide) in the gas mix, only nitrogen gas. The other modification was: we applied the two stages periodically during one nitriding process. We assume that after shorter diffusion stage it is easier to prevent the porosity in the white layer. The applied cycle is shown in Figure 2.

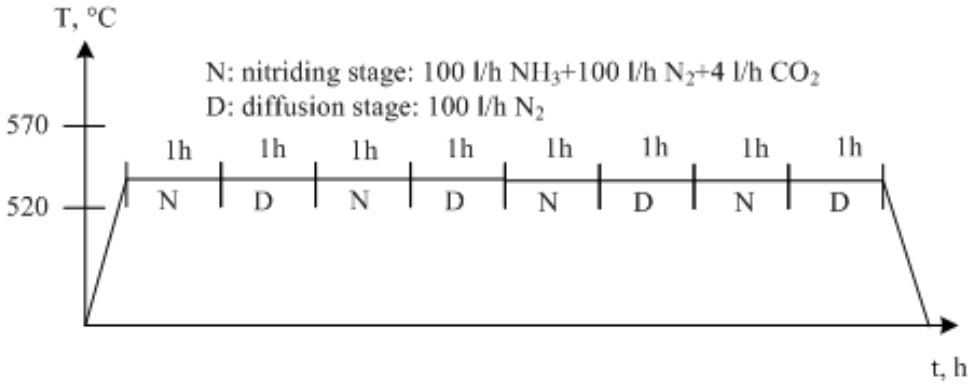

Figure 2. Modified Floe Process

We applied this process on two steel grades: C45 (1.1191) and 16MnCr5 (1.7131); the standard chemical composition for these steels are shown in Table 1. The C45 steel was hardened and tempered, the 16MnCr5 was normalized.

Table 1. Standard chemical composition

	C	Si	Mn	Cr	Other
C45	0.45	0.3	0.7	-	-/S=0.03
16MnCr5	0.17	0.3	1.2	0.9	-/S=0.03

The applied technological parameters are shown in Table 2.

Table 2. Applied heat treatment parameters

Code	Temperature, °C	Time, h	Technology
N1	560	10	gas ferritic nitrocarburising
N2	525	8	gas ferritic nitrocarburising
F1	560	4x(1+1)=8	modified Floe gas ferritic nitrocarburising
F2	525	4x(1+1)=8	modified Floe gas ferritic nitrocarburising

Specimens were ground, polished and etched to observe the microstructure and measure micro-hardness (HV0.1).

Results. The hardness profiles obtained by the above described surface treatment can be seen in Figure 3 and Figure 4.

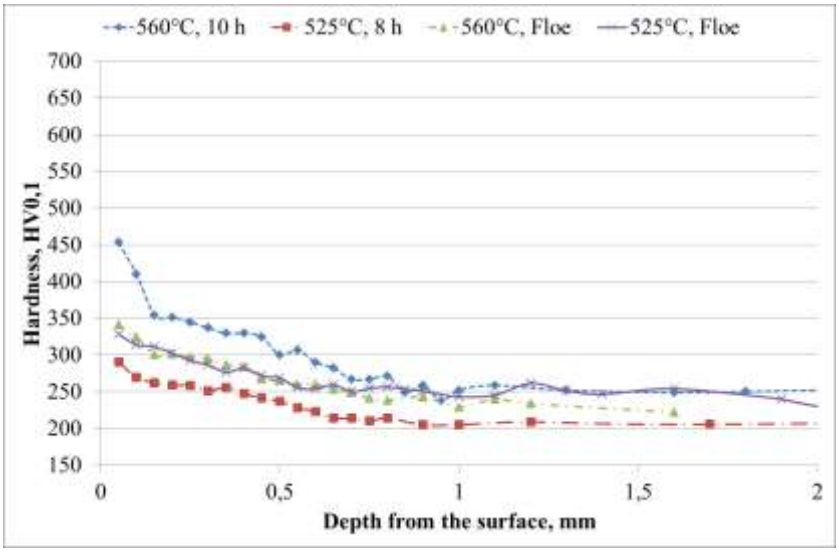

Figure 3. Hardness profiles for C45 plain carbon steel

The main difference between the two steels can be seen clearly: C45 is plain carbon steel which does not contains nitride-forming elements, thus the maximum hardness is about 500 HV0.1. 16MnCr5 is low alloyed case hardening steel, which contains strong nitride-forming element, therefore the maximum hardness is higher, i.e. 670 HV0.1.

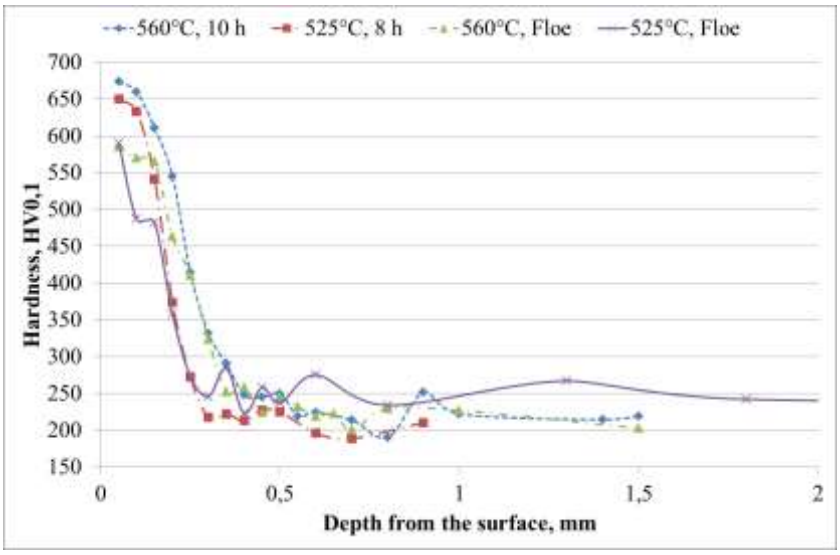

Figure 4. Hardness profiles for 16MnCr5 low-alloyed steel

The depth of the diffusion zone is one of the most important information concerning the results of nitriding; it can be seen in Figure 5. We defined the depth of diffusion zone as usual: the limit of hardness was 50HV0.1 higher than the base material. The higher content of nitride forming (alloying) elements results in thicker diffusion zone: the Nitrogen is bonded by the alloying elements and this reduces the amount of nitrogen which can diffuse into the inner layer; furthermore, the alloying elements decrease the diffusion rate of the nitrogen.

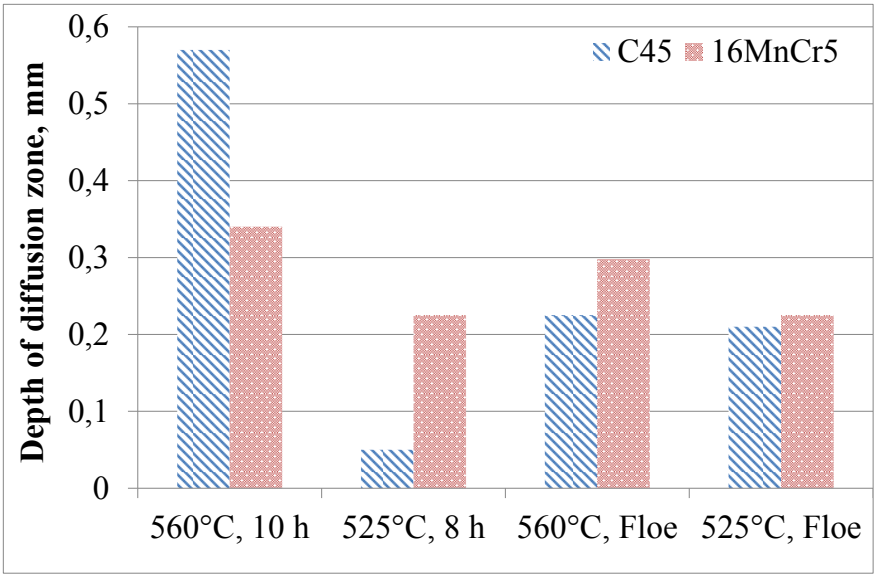

Figure 5. Depth of diffusion zone

Further important information about the nitrided layer is the depth of the white layer, since this ensures the wear resistance of the surface. The depth of the diffusion zone as a function of temperature and time can be seen in Figure 6. The diffusion rate is higher for C45 steel, since there are no alloying elements that can bond the nitrogen: that is the reason of thinner compound zone at higher temperatures. At lower temperatures, the alloying elements in 16MnCr5 steel bond the nitrogen near to the surface. At lower temperatures, the diffusion-rate is lower, but for C45 plain carbon steel the absence of alloying elements means higher diffusion depth.

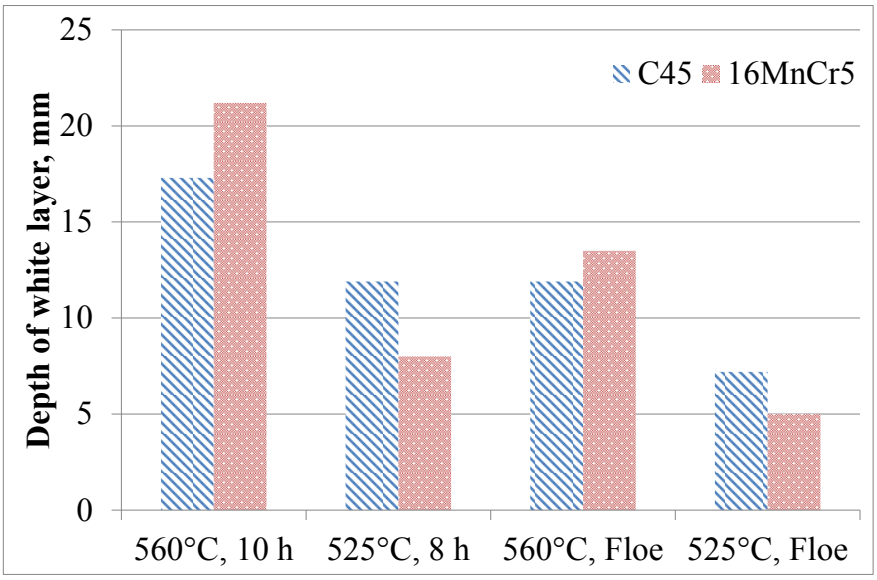

Figure 6. Depth of white layer

The main purpose of our experiments was to investigate the effect of modified Floe process on the depth of white layer. We measured not only the depth of white layer, but we also investigated the depth of the porosity of white layer, and we calculated the rate of porosity according to Eq. (2)

$$\text{rate of porosity} = \frac{\text{depth of porosity in white layer}}{\text{total depth of white layer}}. \quad (2)$$

It can be seen clearly, that the porosity decreased by applying the modified Floe process (Figure 7). If we compare the depth of diffusion zone, we can conclude that the nitrided depth did not change significantly. The amount of adsorbed nitrogen atoms during the modified Floe process was the half of that for conventional process. The microstructure of white layer can be seen in Figure 8.

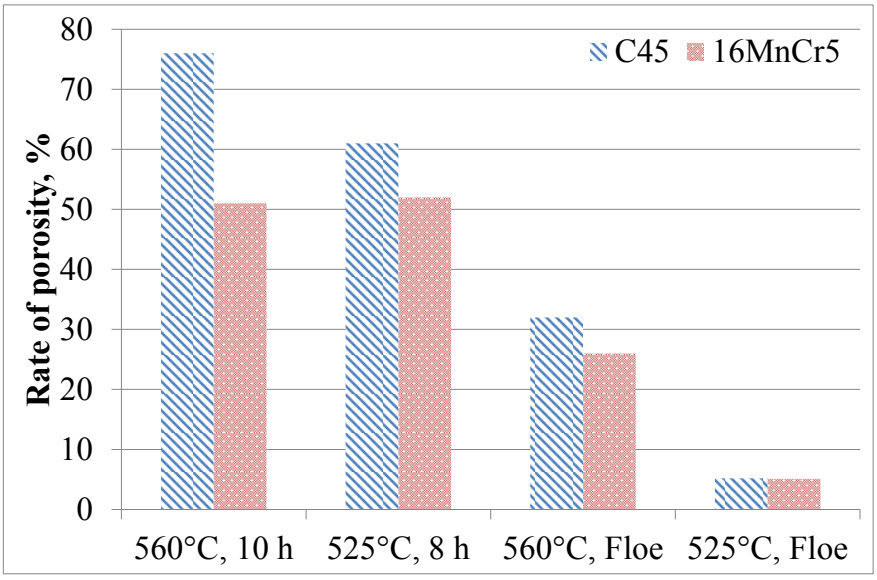

Figure 7. Porosity rate of white layer

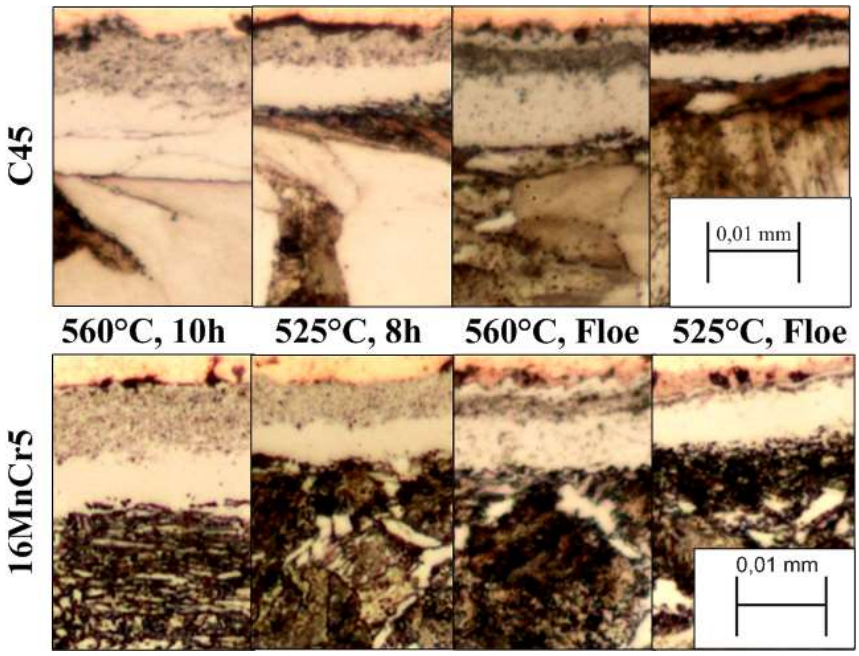

Figure 8. Optical microstructure of white layers

Summary

The Floe process is a method to reduce the porosity/depth of white layer, but under industrial circumstances it is difficult to apply: the sudden changing of temperature and ammonia dissociation not always resoluble.

We performed experiments with a modified Floe process: it is not needed to change the temperature, only to stop the flow of ammonia. The experimental results showed that this process can be applied effectively:

- the porosity of white layer is minimal;
- the change of depth of diffusion layer is not significant.

The porosity of white layer in most cases is not desirable: it decreases the hardness, and thus the wear resistance of the surface. The Floe and the modified Floe process are practical, efficient way to reduce the porosity in the white layer.

Acknowledgement

„The research work presented in this paper based on the results achieved within the TÁMOP-4.2.1.B-10/2/KONV-2010-0001 project and carried out as part of the TÁMOP-4.2.2/A-11/1-KONV-2012-0029 project in the framework of the New Széchenyi Plan. The realization of this project is supported by the European Union, and co-financed by the European Social Fund."

References

[1] David Pye: Practical Nitriding and Ferritic Nitrocarburizing, ASM International, December 1, 2003., ISBN: 978-0871707918
[2] LUKÁCS, J.: Dimensions of lifetime management. Materials Science Forum, Vols. 473-474, (2005) pp. 361-368. (Ed.: GYULAI, J.) Trans Tech Publications, Switzerland, 2005. ISSN 0255-5476.
[3] G. Krauss: Steels: Heat Treatment and Processing Principles, ASM International, 1997. ISBN: 0-87170-370-X, p. 305-315
[4] Karl-Erik Thelning: Steel And Its Heat Treatment, Second edition, Butterworths, 1984, ISBN 0-408-01424-5, p.492-544.
[5] Dr. V. Läpple: Wärembehandlund des Stahls, Grundlagen, Verfahren und Werkstoffe mit Aufgabensammlung, VerlagEuropa-Lehrmittel, 2010, ISBN 978-3-8085-1310-1
[6] George E. Totten: Steel Heat Treatment, ISBN: 9780824797508

Fabrication of nanopatterns in a-AlO_x thin films by a single laser pulse

János Szívós[1,2,a], M. Serényi[1], E. Gergely-Fülöp[1], G. Sáfrán[1]

[1]Institute of Technical Physics and Materials Science, Research Centre for Natural Sciences, Hungarian Academy of Sciences, H-1121 Budapest, Konkoly-Thege Miklós út 29–33.

[2]Doctoral School of Molecular- and Nanotechnologies, University of Pannonia, H-8200 Veszprém, Egyetem utca 10.

[a]szivos.janos@ttk.mta.hu

Keywords: nanopatterning, UV laser, LB film, ordered nanostructure

Abstract. Large area ordered nanopatterning of RF sputter deposited amorphous AlO_x films has been carried out. The technique involves UV laser treatment of the samples through LB films of silica nanospheres. The hexagonal, close packed arrangement of the spheres was projected to the surface due to the laser treatment resulting in ordered structure of pits of ~200 nm diameter and 1,3 nm depth. The samples were caracterized by means of AFM and XTEM. The experimental results are in good agreement with the simulations.

Introduction

Nano-scale modification of materials received wide research interest recently. This includes nanopatterning i.e. the preparation of nano size ordered structures. Nanopatterning is applicable in the fields of tissue engineering [1], nanoelectromechanical systems (NEMS) [2], photonic crystals e.g. [3], [4], self-cleaning structures [5], and meta-materials [6], [7]. New type semiconductor devices can be developed and the performance of conventional semiconductor devices can be improved with the help of nanopatterning [8]. One of the most promising fields of nanopatterning is the development of bit patterned magnetic media (BPM). There are several techniques for the fabrication of ordered nanostructures [9], such as e-beam lithography [10], nanoimprinting [11], focused ion beam lithography (FIB) [12], extreme ultraviolet lithography [13], or X-ray lithography [14]. Beside the above top-down techniques the bottom-up techniques are mainly based on nanosphere lithography [15] and molecular self-assembly [16]. The feature size has been decreased below 10 nm. However most of these methods suffer from the disadventages of low throughput and high costs.

In this paper a fast and low-cost method is proposed that is suitable to obtain ordered nanopatterns directly, or via preparation of masks and imprint molds for nanolithography. We apply a monolayer of self-assembled silica nanospheres prepared by the Langmuir-Blodgett (LB) technique [17], [18]. That is a template for a single pulse UV-laser treatment of the surface of the sample. This technique can be applied under atmospheric conditions and the treatment of relatively large areas requires only a short time.

In this work amorphous AlO_x layers have been nanostructured. Aluminium-oxide is a hard, durable non-reactive, high-melting point material that can be applied as (negative or positive) mask for nanolithography, and as mold for nanoimprinting [19].

Experimental

Amorphous AlO_x layers of 25 nm thickness were RF sputter deposited from an Al_2O_3 target onto single crystal Si substrates. The films were deposited at room temperature at a rate of 0.25 Å/s. The sputtering gas was an $Ar - O_2$ mixture with the partial pressures of $1.6*10^{-2}$ mbar and $4*10^{-3}$ mbar, respectively. Subsequently, the aluminium-oxide films were covered with a monolayer of silica nanospheres of 300 nm diameter arranged in a hexagonal structure by the LB technique. The 300 nm silica nanoparticles and their LB films were prepared as reported earlier [20, 21]. LB-films of the nanoparticles were prepared in a KSV 2000 film balance. The LB films were prepared by

vertical deposition (5 mm/min) at cca. 80% of the collapse pressure, which was determined prior to the LB-film deposition in a separate experimental run.
After drying at 50 °C in air the samples covered with LB film were exposed to pulses of a Kr-F UV excimer laser (λ=248 nm).
The laser spot of about 50x12 mm^2 size was mapped before the treatments in order to reveal the intensity distribution. It was carried out with a GaP UV-photodiode, indirectly, by using a plan-parallel quartz plate that reflects ~4 % of the incoming intensity. The intensity distribution was measured by scanning the board in 1 mm steps and recording the response voltage by an oscilloscope that was synchronized to the laser.
The energy of the laser pulse was adjusted to 100±6 mJ, the pulse length was 30 ns, so the total power of each pulse was 3.33±0.2 MW. The current response of the photodiode is proportional to the power of the pulse; therefore the response signal integrated for the entire spot gives the total power of the mapped pulse.
During the treatments the total energy of the laser pulse varied between 75-105 mJ/pulse. A single pulse with a pulse length of 30 ns was applied for the treatment of each sample. This way, we assume that the silica nanospheres themselves don't change during the laser treatment.
After the laser treatment the LB films were removed by acetone in an ultrasonic bath. The structure and morphology of the samples were characterized by Atomic Force - (AFM, by an AIST-NT SmartSPM 1010), and Transmission Electron Microscopy (TEM, by a JEOL 3010 (300kV; 0.17 nm point resolution)). Samples for TEM were prepared by mechanical and ion beam thinning.
The phenomena occuring at our experimental conditions were computer simulated with the help of Crystalwave [22]. The refractive index (n) and absorption coefficient ($\alpha=4\pi k/\lambda$, where k is the extinction coefficient) of our AlO_x layers were determined by a Woollam M2000DI rotating compensator spectroscopic ellipsometer.

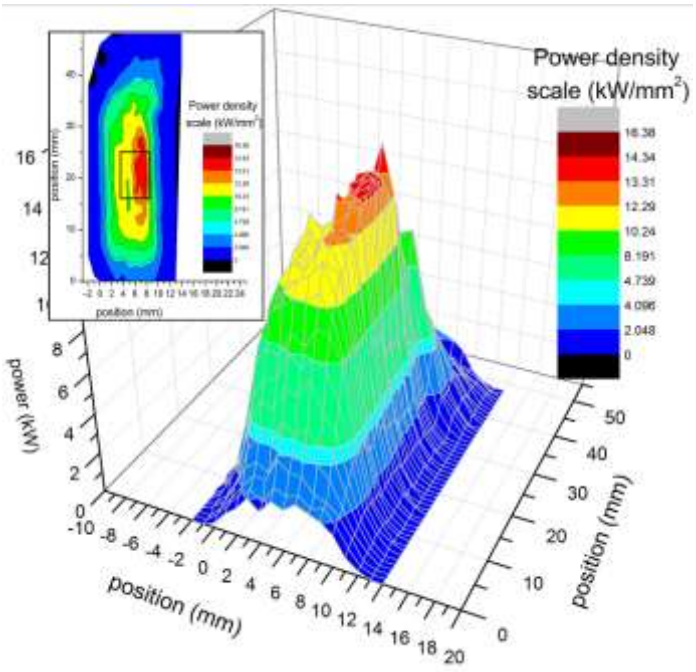

Fig. 1: 3D image of the measured intensity-distribution of the laser spot. Inset: top view color map of the spot. The black rectangle marks the part of the spot that passes through the aperture.

Results

The intensity distribution of the spot of the laser is roughly Gaussian-like as it is plotted in Fig. 1. Obviously, more than 14 kW is distributed in an area of 1 mm^2 at the most intense part of the spot while the power rapidly drops to 1-2 kW/mm^2 at the outer regions. In order to obtain reasonably uniform patterns in the AlO_x samples the inner part (5x9 mm^2) of the spot, marked with a rectangle in the color map of the spot (inset of Fig. 1), was chosen for the treatment, while the outer regions were masked out.
The intensity of the actual area of the laser spot was estimated to be uniform in our computer simulations. The two parameters at 248 nm wavelength (n=1.681±0.005 and $\alpha=(3.86\pm0.15)*10^4$ cm^{-1} as shown in Fig. 2 a) were taken from the data obtained by ellipsometry.
The computer simulations have shown that the silica nanospheres of the LB film can act as individual lenses that focus the incoming laser light (Fig. 2 b). According to the calculations the energy density of the laser light increases with an order of magnitude at the focus of the silica nanolenses (inset of Fig. 2 b). This way local increase of intensity occurs beneath every single silica

nanosphere that enables the modification of the sample, and the preparation of ordered nano-scale patterns.

The total energy of the laser pulse was set to 75±2 mJ, 84±2 mJ 99±2 mJ and 105±2 mJ. These correspond to fluences of 27±0.7 mJ/cm^2, 30±0.7 mJ/cm^2, 35±0.7 mJ/cm^2 and 38±0.7 mJ/cm^2 respectively. Here the Gaussian distribution of the entire spot was taken into account.

AFM investigation of the laser-treated samples revealed uniform, hexagonally structured pattern of shallow pits within the alumina films. The images and corresponding depth profiles are shown in Fig. 3.

The fluence of the laser shots was 27 mJ/cm^2, 30 mJ/cm^2 and 38 mJ/cm^2 as depicted in Fig. 3 a, b, and c, respectively. The lateral size of the pits is 220±30 nm. The depth of the pits is 0.8±0.3 nm at a fluence of 27 mJ/cm^2 while the patterned surface and the wall of the holes is quite rugged (Fig. 3 a).

The sample treated with 30 mJ/cm^2 fluence shows deeper (1.3±0.2 nm) pits and the wall of the holes and the surface is flat and uniform (Fig. 3 b).

At the highest fluence of 38 mJ/cm^2 a poor quality pattern shows up (Fig. 3 c). The pits are non-uniform most of them show coalescence and their depth decreases to less than 1 nm.

The cross-sectional TEM (XTEM) image of the sample treated with 35 mJ/cm^2 fluence, near to optimum, is shown in Fig. 4. A typical pit is seen here that exhibits ~210 nm diameter and ~3 nm depth.

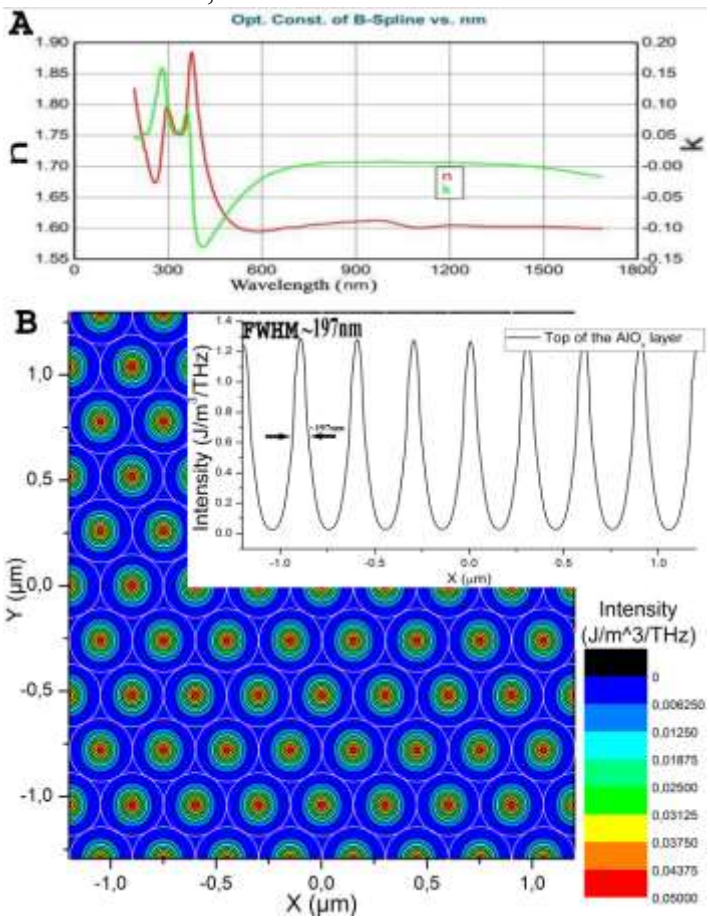

Fig. 2: (a) Refractive index and absorption coefficient of the a-AlO_x layers as a function of wavelength. (b) Focusing effect of the LB film of silica spheres: simulated lateral intensity map. The intensity scales up from blue to red color. Inset: Simulated intensity profile at the top of the AlO_x layer.

A 15-20 nm wide crystallized region is recognised at the bottom of the pit that may indicate remarkable heating effect of the pulse.

Discussion

We observed regular patterns of nano-pits formed in AlO_x due to the focusing effect of self-assembled silica nanospheres on the laser light. In the present experiments the size of the nanospheres (~300 nm) is larger than the wavelength (~248 nm). Therefore the spheres act as individual spherical lenses that focus the laser light beneath themselves. This phenomenon was revealed also by simulations (Fig. 2. b).

Since the full width at half maximum of the simulated intensity distribution beneath a nanosphere is around 200 nm (Fig. 2. b) the simulations are in a good agreement with the experiments. The size (~220 nm) of the pits observed by AFM confirms the focusing effect, as well. The AFM results help us to find the optimum fluence. It is suggested that the fluence of 38 mJ/cm^2 was too high (Fig. 3 c), since, the surface was modified not only below the nanospheres, it was roughened everywhere else as well. This resulted in the coalescence of the pits associated with a decrease of depth and increase

of width. The most regular pit pattern was found in samples treated with a fluence about 30 mJ/cm^2 (Fig 3 b).

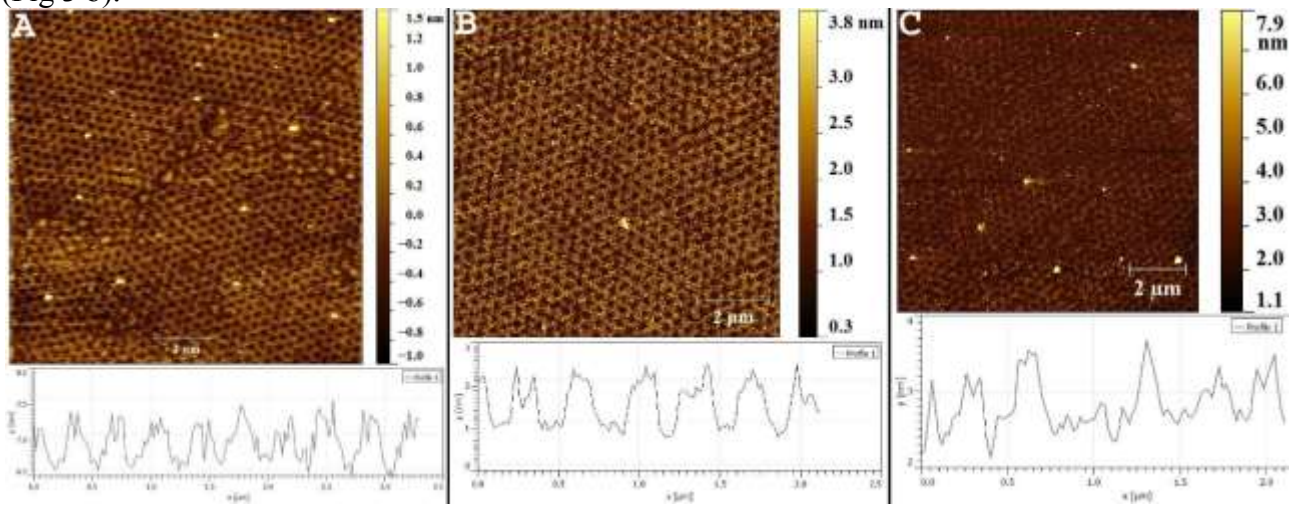

Fig. 3: AFM results of the patterns obtained at various laser energy densities (~6x6 µm^2 area). The images and depth profiles of the samples prepared at fluence of 27±0.7 mJ/cm^2, 30±0.7 mJ/cm^2, and 38±0.7 mJ/cm^2 (~5x5 µm^2 area) are shown in (a,) (b), and (c), respectively.

The low depth of the pits may be the consequence of the relatively low absorption coefficient of the amorphous AlO_x (α= (3.86±0.15)*10^4 cm^{-1}). The calculated intensity drop of the passing light is only 9.2±0.7 %, therefore the energy deposited in the layer is relatively low. According to XTEM it evokes only crystallization of the AlO_x at the bottom of the pits i.e. at the focus area (Fig. 4). The pit formation, however, cannot be explained by only the volume change due to crystallization localized to 10-20 nm area. We suggest a mechanism with the role of nanovoids typical in amorphous materials [23]: their inner surfaces are decorated and stabilized by electrically active dangling bonds. Due to a shock wave of the electromagnetic field of the laser pulse the nanovoids collapse that result in a volume decrease and the formation of the shallow pits.

The optimum laser fluence for our amorphous AlO_x films was 32±2 mJ/cm^2. At these conditions uniform patterns were prepared in domains that extend at least to 250x250 µm^2 area (Fig. 5). It is worth to mention that domains present in the LB film are replicated to the created pit patterns of the alumina films.

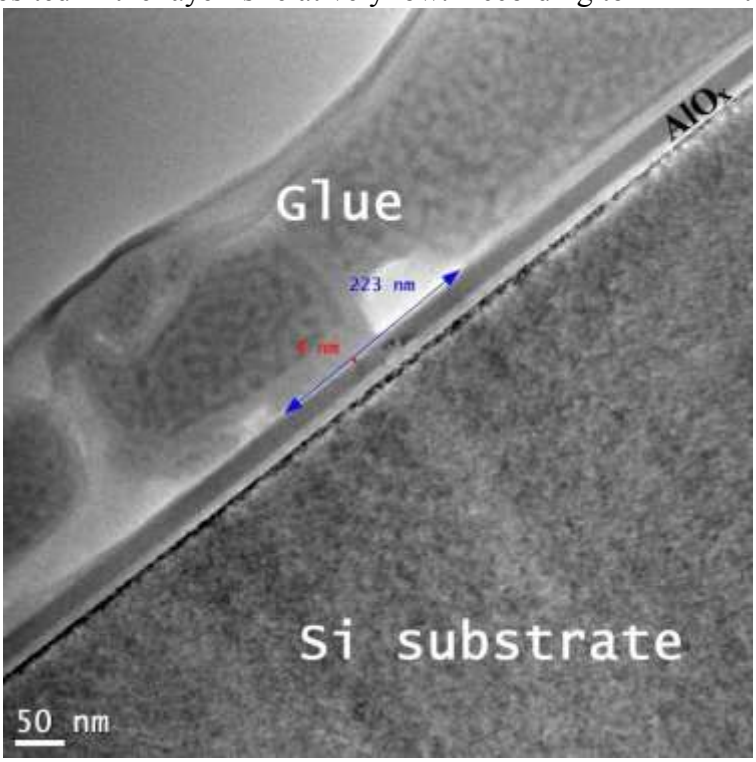

Fig. 4: Cross-sectional TEM image of a sample treated with 35±0.7 mJ/cm^2 fluence. A typical pit is seen here, showing ~200 nm width and 3-4 nm depth. A crystallized area is recognized in the AlO_x beneath the centre of the pit.

Summary

Nanoscale patterning of amorphous AlO_x films was succesfully carried out by treating the samples with laser pulses via a layer of self-assembled silica nanospheres. Areas as large as 250x250 μm^2 were pit-patterned uniformly, in domains (Fig. 5).
The focussing effect of the nanospheres was confirmed by both simulations and experiments. XTEM investigations have shown 10-20 nm area of crystallization of the a-AlO_x beneath the bottom of the fabricated nanopits. The formation of ~200 nm wide pits, however, cannot be explained by only the localized crystallization. We suggest that nanovoids collapsing due to the intense electromagnetic field of the UV laser pulse contribute to the local volume decrease.

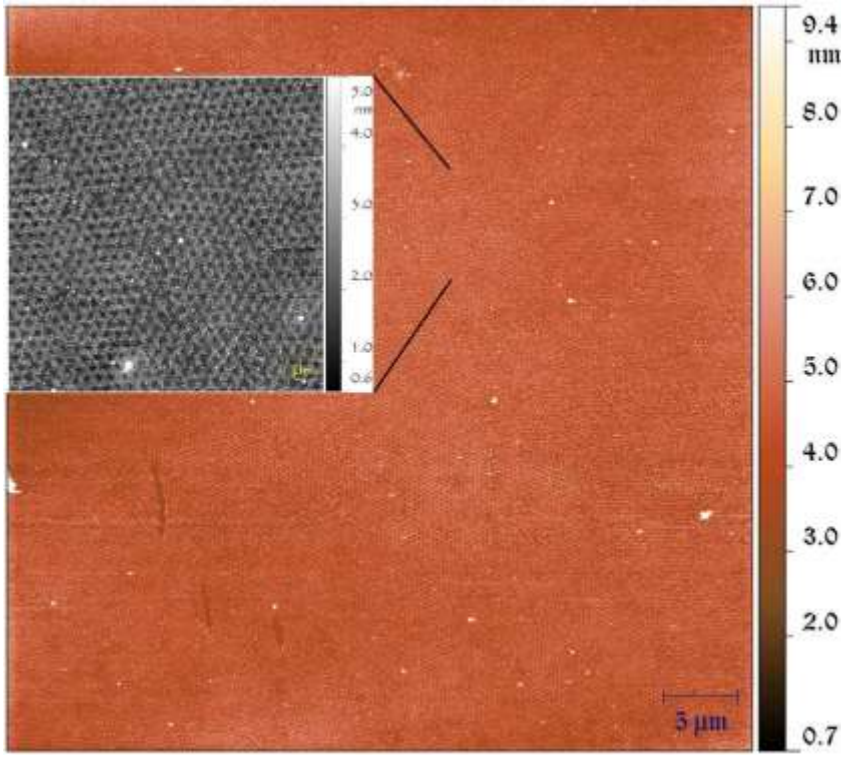

Fig. 5: AFM image of the sample prepared at 30±0.7 mJ/cm^2 laser fluence, demonstrating the size (at least 80x80 µm^2) of a patterned area. The arrangement and perfection of the pit-pattern is directly related to that of the applied layer of silica nanospheres. Inset: magnified ~9x9 µm^2 area.

Acknowledgement

The contributions of Z. Szabó and B. Fodor are acknowledged in the simulations and ellipsometry. This work was supported by the National Development Agency grant TÁMOP-4.2.2/B-10/1-2010-0025.

References

[1] H. N. Kim, A. Jiao, N. S. Hwang, M. S. Kim, D. H. Kang, D.-H. Kim, K.-Y. Suh, Nanotopography-guided tissue engineering and regenerative medicine, Adv. Drug Deliv. Rev. Vol. 65 Issue 4 (2013) 536–558.

[2] B. Bhushan, Nanotribology and nanomechanics of MEMS/NEMS and BioMEMS/BioNEMS materials and devices, Microelectronic Engineering Vol. 84 Issue 3 (2007) 387–412.

[3] I. Tamáska, G. Dobrik, P. Nemes-Incze, K. Kertész, E. Horváth, G.I. Márk, T. Jászi, P. Neumann, Z.E. Horváth, L.P. Biró, Bioinspired photonic nanoarchitectures from graphitic thin films, Thin Solid Films Vol. 519 Issue 12 (2011) 4078–4081.

[4] X. Meng, G. Gomard, O. El Daif, E. Drouard, R. Orobtchouk, A. Kaminski, A. Fave, M. Lemiti, A. Abramov, P. R. Cabarrocas, C. Seassal, Absorbing photonic crystals for silicon thin-film solar cells: Design, fabrication and experimental investigation, Solar Energy Mat. & Solar Cells Vol. 95 (2011) S32–S38.
[5] R. Fürstner, W. Barthlott, C. Neinhuis, P. Walzel, Langmuir Vol. 21 (2005) 956-961.
[6] A. Sihvola, Metamaterials in electromagnetics, Metamaterials 1 Vol. 1 Issue 1 (2007) 2–11.
[7] A. Boltasseva, V. M. Shalaev, Fabrication of optical negative-index metamaterials: Recent advances and outlook, Metamaterials 2 Vol. 2 Issue 1 (2008) 1–17.
[8] Q. T. Zhao, F. Klinkhammer, M. Dolle, L. Kappius, S. Mantl, A novel silicide nanopatterning method for the fabrication of ultra-short channel Schottky-tunneling MOSFETs, Microelectronic Engineering Vol. 50 Issues 1–4 (2000) 133–138.
[9] B. D. Terris and T. Thomson, Nanofabricated and self-assembled magnetic structures as data storage media, J. Phys. D: Appl. Phys. Vol. 38 (2005) R199-R222.
[10] J.-S. Noh, H. Kim, D. W. Chun, W. Y. Jeong, W. Lee, Hyperfine FePt patterned media for terabit data storage, Current Appl. Phys. Vol. 11 Issue 4 Suppl. (2011) S33–S35.
[11] S. Y. Chou, P. R. Krauss, P. J. Renstrom, Imprint of sub-25 nm vias and trenches in polymers, Appl. Phys. Lett. **67** (1995) 3114-3116.
[12] J. A. van Kan, J.L. Sanchez, B. Xu, T. Osipowicz, F. Watt, Micromachining using focused high energy ion beams: Deep Ion Beam Lithography, Nucl. Instr. and Methods in Phys. Research B Vol. 148 Issues 1–4 (1999) 1085-1089.
[13] C. W. Gwyn, R. Stulen, D. Sweeney, D. Attwood, Extreme ultraviolet lithography, J. Vac. Sci. Technol. B 16 (1998) 3142-3149.
[14] A. Heuberger, X-ray lithography, Microel. Engineering Vol. 5 Issues 1–4 (1986) 3–38.
[15] C. L. Haynes, R. P. Van Duyne, Nanosphere lithography: A versatile nanofabrication tool for studies of size-dependent nanoparticle optics, J. Phys. Chem. B Vol. 105 (2001) 5599-5611.
[16] G. M. Whitesides, J. P. Mathias, C.T. Seto, Molecular self-assembly and nanochemistry: a chemical strategy for the synthesis of nanostructures, Science Vol. 254 No. 5036 (1991) 1312-1319.
[17] W. Stöber, A. Fink, E. Bohn, Controlled growth of monodisperse silica spheres in the micron size range, J. of Colloid and Interface Sci. 26 (1968) 62-69.
[18] D. K. Schwartz, Langmuir-Blodgett film structure, Surface Science Reports Vol. 27 Issues 7–8 (1997) 245–334.
[19] L. Jay Guo, Nanoimprint lithography: methods and material requirements, Adv. Materials Vol. 19 Issue 4 (2007) 495-513.
[20] A. Deák, E. Hild, A. L. Kovács, Z. Hórvölgyi, Contact angle determination of nanoparticles: film balance and scanning angle reflectometry studies, Physical Chemistry Chemical Physics 9 (2007) 6359-6370.
[21] A. Deák, B. Bancsi, A. L. Tóth, A. L. Kovács, Z. Hórvölgyi, Complex Langmuir–Blodgett Films from Silica Nanoparticles: An Optical Spectroscopy Study, Colloids and Surfaces A: Physicochemical and Engineering Aspects Vol. 278 Issues 1-3 (2006) 10-16.
[22] http://www.photond.com/products/crystalwave.htm
[23] Z. Xia, L. Riester, B. W. Sheldon, W. A. Curtin, J. Liang, A. Yin and J. M. Xu, Mechanical properties of highly ordered nanoporous anodic alumina membranes, Rev. Adv. Mater. Sci. 6 (2004) 131-139.

Chemical Etching of Ultrafine Grained Titanium Surfaces to Optimise Cell Attachment

Attila Terdik[1,a], Péter Nagy[1,b], Eszter Bognár[1,2,c], Árpád Joób-Fancsaly[3,d], József Piffkó[4,e]

[1]Budapest University of Technology and Economics, Faculty of Mechanical Engineering, Department of Materials Science and Engineering, H-1111 Budapest, Bertalan Lajos u. 7, Hungary

[2]MTA-BME Research Group for Composite Science and Technology, H-1111 Budapest, Műegyetem rkp. 3, Hungary

[3]Semmelweis University, Faculty of Dentistry, Department of Oral and Maxillofacial Surgery and Stomatology, H-1085 Budapest, Mária u. 52, Hungary

[4]University of Szeged, Albert Szent-Györgyi Clinical Center, Faculty of Medicine, Department of Oral and Maxillofacial Surgery, H-6725 Szeged, Kálvária sgt. 57, Hungary

[a]attilat@gmail.com, [b]npeter@eik.bme.hu, [c]eszter@eik.bme.hu, [d]joobarpad@gmail.com, [e]office.maxillo@med.u-szeged.hu

Keywords: ultrafine-grained titanium, micromorphology, implant, surface roughness, osseointegration

Abstract. The goal of this research was to create a surface topography that would promote cell attachment onto Ultrafine-grained Grade 2 Titanium. Morphologies that assist the deposition of bone tissue and reduce colonisation by unwelcome bacteria onto dental implant surfaces are created most often by sand-blasting, chemical etching, or these two in combination. Discs of thickness 2 mm from the machined base material were prepared for this study. After machining, the samples were chemically etched. Three etchants were used: 30 % HCl and 85% H_3PO_4, and the two in combination. The etching temperatures were 20 °C, 40 °C, and 60 °C, the etching times were 5 minutes and 120 minutes. The surface morphologies of the discs were examined by confocal microscope and scanning electron microscope (SEM), and compared to the machined-only samples as reference values. Samples treated in the 30% HCl solution at 40 °C for 120 minutes and then in the 85 % H_3PO_4 solution at the same temperature and time altered macro and micromorphology together in ways which assist the attaching of bone.

1.0 Introduction

The goal of this research was to find the parameters for chemical surface treatment of a relatively 'new' material Ultrafine-grained Grade 2 Titanium (UFG-Ti) that create surface roughness and topography favouring biological cell adhesion [1].

2 acids – 30% HCl, 85% H_3PO_4 – were used as three etchants (the two acids used alone, and a third regime where 30% HCl was followed by 85% H_3PO_4), with two etching times of 5 minutes and 120 minutes, and temperature was controlled by maintaining the ultrasound water baths at 20 °C, 40 °C, and 60 °C.

All the micro-surface terrains created by each etching regime were investigated with confocal microscope and scanning electron microscope (SEM).

2.0 Research Literature

A wide range of treatments to titanium have been investigated and tested for their effects on surface morphology and specifically their promoting osseointegration, and thereby stability, of medical implants at the bone-metal interface. Treatments tested include acid-etching methods, physical surface abrasion (for example with sandblasting), laser-assisted modification, and anodisation [2]. Reviewing research in the early 21st century into modifying surface roughness of titanium to

promote integration of implant with bone tissue, it's helpful to first consider in section 2.1 immediately below a couple of typical studies into roughness and bone adhesion. Some researchers approach is to pair the effects of varying acid-etching regimes with either osseointegration in vivo tests or other existing measures of roughness as in the following three papers.

2.1 Relating roughness to bone integration (macro assessments). In a study separating out scales where roughness promotes better osseointegration, titanium beads were sintered to a titanium cylindrical surface. In 2003 Hacking, Harvey and colleagues [3] carried out the research on six dogs with extraction after 12 weeks so as to test bone attachment to acid-etched, and unetched surfaces.

Another 2003 study attempted a purely acid-etched surface on sample discs of Grade 5 titanium to create a surface resembling those made by combining sand-blasting and acid-etching. The study, reported by Juodzbalys and colleagues [4], also compared these to the surfaces of commercially available screw-type titanium dental implants. A range of surface results emerged from a variety of acid-etching protocols. The control group (machined surface) had regular uni-directional grooves with some irregular shallow roughness. The first category of acid-treated samples (etched with HCl) had a microtexture lacking micropits. The second category (etched with HCl and H_2SO_4) had a fairly rough surface but microtexture was poor with few micro pits and smooth waviness.

The third category (etched with H_2SO_4, HCl and H_3PO_4) created a surface showing distinct waviness without microtexture, by application of different acids alone. The fourth group (etched with H_2SO_4 and HCl) showed significant surface roughness with micro pits of 1-10 μm and large valleys of 20-30 μm with peaks of different sizes. The waviness and roughness of this fourth surface was regular and without intact areas.

It's clear from the work by the Juodzbalys team that studies aiming to compare etching treatments to in vivo bone-attachment assessments have a large space of potential variables to investigate – time of etching, composition of etchant, temperature, and these in combination. Viewed as a process that can be optimised, definitive results are difficult to find without exhausting a large number of processes and parameters. A group in 2008 led by Daugaard and Elmengaard [5] compared implants with a nonparticulate texture made by chemical milling (HF, HNO_3) (control) with implants that had a dual acid etched (HF, HCl) microtexture surface superimposed on the primary chemically milled texture. They used a joint replacement model in 8 dogs and after 4 weeks checked the surfaces for bone-cell adhesion. The dual-acid-textured implants had twice the median bone ongrowth (36.1% versus 18.4%) when compared to the control surfaces. At the same time, fibroblast growth was significantly lower for the dual-acid implant surfaces than the controls. Achieving both higher osseointegration and lower fibrous growth at implant interfaces is the elusive twin goal of many research investigations. Moving towards a theory of how and why various micro-topographies osseointegrate better than others, some researchers focus on relating surface scale features and dimensions more closely to the bone-cell attachment process.

2.2 Relating roughness to bone integration (micro processes & biology). Yang and colleagues in 2011 [6] modelled filopodia investigation of surfaces, paying special attention to whether filopodia react like the classic model of a flexing beam encountering surface topographical features of known stiffness. Yang's team remarks that surfaces with features of between "several hundred nanometers and a few microns" encourage colonisation by attaching cells, due to size compatibility with cell filopodia. Two earlier Dalby studies offer more biological guidelines for optimal nano-roughness to stimulate osseointegration.

Dalby, Gadegaard et al in 2003 [7] created test surfaces with regular pocking or pitting with laser beams of known diameter and spacing or pitch. For example, 20 nm-wide beams spaced 100 nm apart produced, by melting, regular craters or pits (of final diameter 35 nm) which were transferred by nickel dies to a polymer substrate. With the test surfaces in three sizes of pit spaced apart at different pitches, observations could be made of colonisation by fibroblast cells. The emphasis was on how filopodia reacted to the varying diameter of pit (35 nm pits turned out to be hard to observe and only to stimulate mild "interest" in the 100 nm-wide filopodia tips, but the 75 nm craters and 120 nm craters both stimulated substantial activity from the fibroblast filopodia).

A later paper in 2006 by Dalby, McCloy and colleagues [8] instead considered crater depth, and osteoprogenitor response by primary human mesenchymal bone marrow stromal cells (HBMSCs). Here a central research concern was whether surface structure could assist in differentiating between soft-tissue cell colonisation and bone-forming cells. The researchers found that along with conforming to a preferred size scale for filopodial attachment, depth of nano-pitting could also influence cytoskeletal development in the growing cells.

Even if cell-specific designed nano-surfaces still remain uneconomic for most implant technologies, these investigations throw a new light on general statements that certain measures of nano or micro-roughness promote integration with bone. Roughness-average-based measures such as Ra or Sa must be combined with metrics that more sensitively express size ranges for major surface features. Two surfaces can have the same Ra measure yet one could be suitable for colonisation by osteoblasts and the other completely unsuitable. Measures like Ra blur features of the surface such as vertical and horizontal amplitude between major peaks or troughs. Assessments of rival acid-etching protocols must involve attaching-cell size in measures of surface roughness.

2.3 Roughness, Cell-Attachment, and Ultrafine-grained Grade 2 Titanium. In the present study, the challenge is to match microscope images of implant surfaces known in macro-studies to osseointegrate well with etching methods that produce those surfaces, to find an etching regime for Ultrafine-grained Grade 2 Titanium. Reduced grain size enables pure UFG-Ti to mimic titanium alloys with aluminium and vanadium in strength and lightness, but without toxicity concerns. Meanwhile, reduced grain size of UFG-Ti also creates denser arrays of 3-point surface grain boundaries – shown to give habitats that encourage denser cell colonisation [9]. The missing piece of the puzzle is to use earlier in vivo studies on other forms of titanium to see which micro-terrains help osteoblast attachment best, then systematically test etching protocols to find etchants, times, and temperatures to recreate this micro-surface on UFG-Ti. That was the goal of the present study.

3.0 Methods

A billet of caliber-rolled Grade 2 titanium (a form of UFG-Ti which reduces crystal size and increases strength) was machined into 2 mm-thick, 8 mm-diameter, 1g-weight discs. These were ultrasonically cleaned before the experiment with acetone and then alcohol and after etching, in both cases at the same water bath temperatures as the experiments. After cleaning, the discs were placed into test tubes of etching solution, and test tubes were returned to the ultrasonic water bath. The two acids – 30% HCl, 85% H_3PO_4 – were used as three etchants (the two acids used alone, and a third regime of 30% HCl followed by 85% H_3PO_4), with two etching times of 5 minutes and 120 minutes, and temperature was controlled by maintaining the ultrasound water baths at 20 °C, 40 °C, and 60 °C. The rationale for these times was to compare the effects of two distinctly different exposures to etchants, and enable more sensitive comparison of roughness measures obtained when varying the etches by temperature. Values of Ra and Rz were established for each disc surface using an Alicona InfiniteFocusSL confocal microscope across a measuring length of 1,500 μm at 5× magnification. The data were tabulated into spreadsheets to allow statistical analysis. SEM (Philips XL30) photos were taken at magnifications of 500×, 2000×, and 5000×.

4.0 Discussion

Three major areas of comparison emerge out of the raw data that was collected, and in each of these some measurements are omitted so as to aid clearer comparisons between highs and lows. Figure 1 and 2 show the Ra and Rz values calculated for each etching regimen.

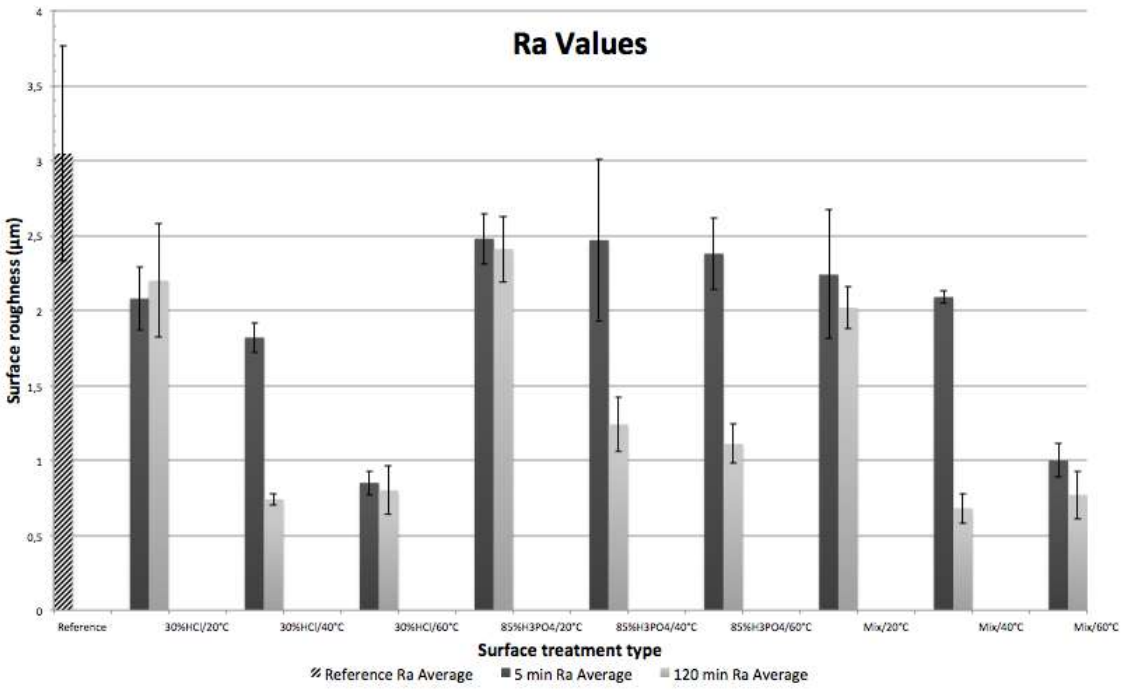

Figure 1 Ra surface roughness values for three acid etch regimens on UFG-Ti: 30% HCl, 85% H_3PO_4 and a third regime of 30% HCl followed by 85% H3PO4; with two etching times of 5 minutes and 120 minutes; and the temperature was 20 °C, 40 °C, and 60 °C.

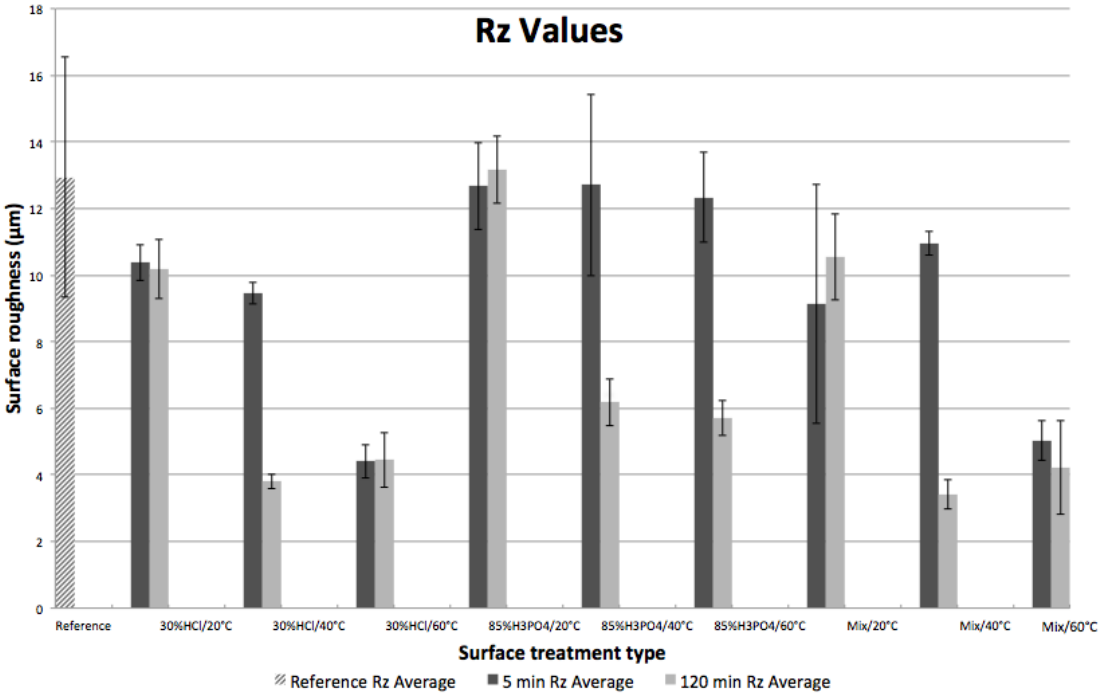

Figure 2 Rz surface roughness values for three acid etch regimens on UFG-Ti: 30% HCl, 85% H_3PO_4 and a third regime of 30% HCl followed by 85% H_3PO_4; with two etching times of 5 minutes and 120 minutes; and the temperature was 20 °C, 40 °C, and 60 °C.

4.1 The first is surface roughness plotted against temperature. With the 30% HCl exposure for only 5 minutes, the 40 °C treatment did not significantly cut surface roughness from the freshly-machined state, but the 60 °C treatment did. With the HCl wash at 120 minutes the 40 °C treatment significantly reduced surface roughness whereas the 60 °C treatment did not significantly reduce it

further (Fig. 3). The 85% H_3PO_4, after 5 minutes gave no significant change. With the same 85% H_3PO_4 etchant, after 120 minutes, the 40 °C treatment reduced the surface roughness and the 60 °C treatment was not significantly different.

For the exposure first to one acid and then to the other for 5 minutes each – the 40 °C treatment did not, but the 60 °C treatment did, significantly cut surface roughness. ”Mixing” at 120 minutes, already the 40 °C treatment significantly reduced the surface roughness and the 60 °C treatment did not differ significantly.

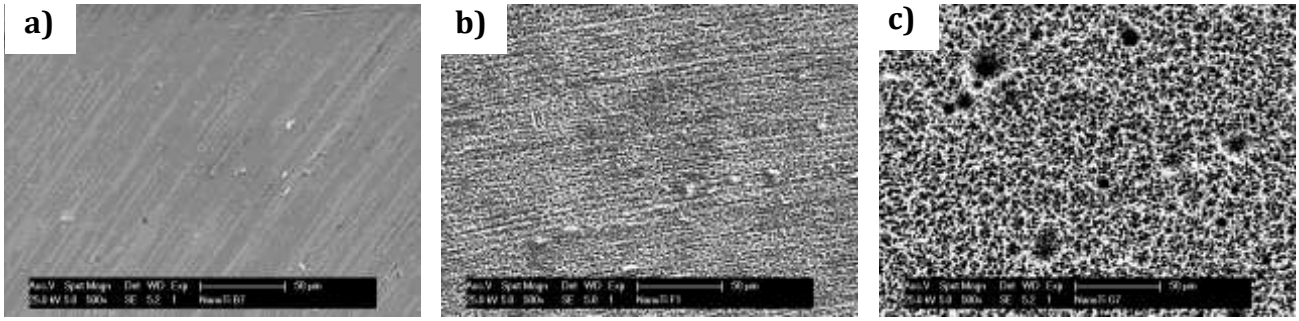

Figure 3 SEM images of UFG-Ti at 500× magnification a) HCl 60 °C 5 mins, b) HCl 40 °C 120 mins, c) HCl 60 °C 120 mins

4.2 The second plots surface roughness against time. For 30% HCl, the 40 °C treatment reduced surface roughness significantly, but between the 40 °C and 60 °C treatments there was no significant difference. For 85% H_3PO_4 the 40 °C and the 60 °C treatments did significantly reduce surface roughness, the effect increasing with time, but at 20 °C there was no major effect. ”Mixing” the two at 20 °C yielded no effect, but the 40 °C and 60°C treatments did significantly reduce surface roughness, the effect increasing with time (Fig. 4). However, with the 60 °C treatment the Rz value did not change significantly, only the Ra value, deviating from the rule of thumb that dictates Rz is usually some multiple of Ra.

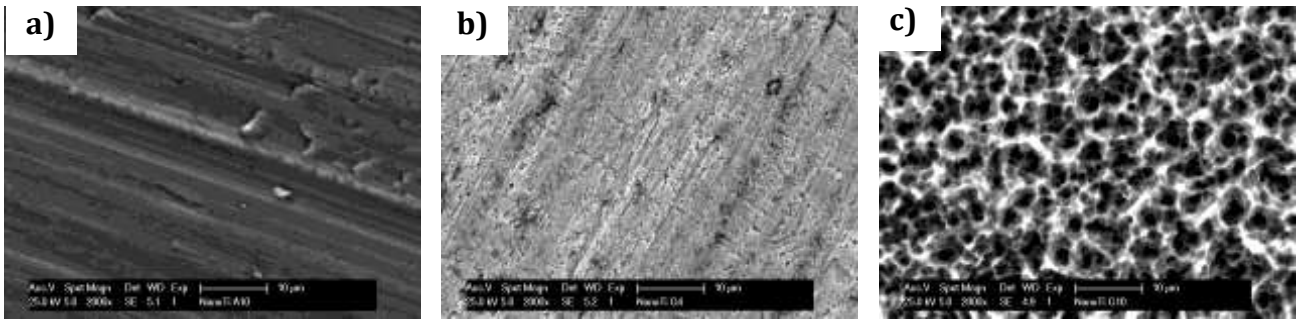

Figure 4 SEM images of UFG-Ti at 2000× magnification a) Mix 20 °C 120 mins, b) Mix 60 °C 5 mins, c) Mix 60 °C 120 mins

4.3 Plotting surface roughness against etchant effect gives the third group. For 20 °C treatments, at 5 minutes there was no significant change, whereas at 120 minutes the Rz value for the 85% H_3PO_4 was notably greater. 40 °C etches showed significant differences. The weakest was 85% H_3PO_4. At a temperature of 60 °C there were significant differences: the weakest the 85% H_3PO_4, the other two etchant regimes similar for every treatment time. At 120 minutes the Rz values, as above, did not differ significantly – only the Ra values.

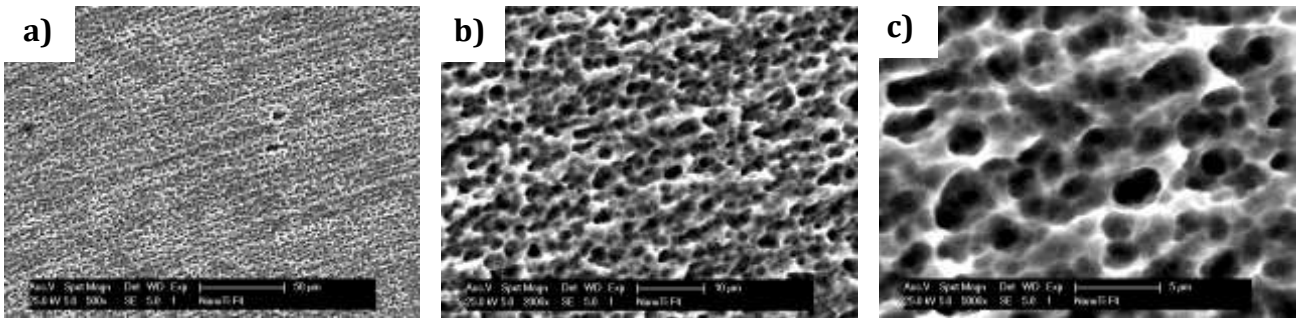

Figure 5 SEM images of UFG-Ti at different magnifications a) Mix 40 °C 120 mins, b) Mix 40 °C 120 mins, c) Mix 40 °C 120 mins,

Microscope inspection of etched surfaces picked out one etching treatment which both fell into desirable Ra and Rz ranges while showing visually the scale of featuring the literature convincingly links to cell colonisation of surfaces. This resulted from the mixed etch regime at 40 °C for 120 minutes for each of 30% HCl and 85% H_3PO_4 in turn (Fig. 5). This brings much closer successful deployment in dental implantology of a metal (ultrafine-grained Grade 2 titanium) of sufficient strength and stiffness to obviate the need for potentially toxic vanadium and aluminium alloying elements, yet brought to a near-optimal style of surface roughness for rapid and secure osseointegration.

Acknowledgment

This work is connected to the scientific program of the " Development of quality-oriented and harmonized R+D+I strategy and functional model at BME" project. This project is supported by the New Hungary Development Plan (Project ID: TÁMOP-4.2.1/B-09/1/KMR-2010-0002).

References

[1] J. Gubicza, Zs. Fogarassy, Gy. Krállics, J. Lábár, T. Törköly, Microstructure and Mechanical Behavior of Ultrafine-Grained Titanium, Mater. Sci. Forum 589 (2008) 99-104.

[2] E. Peláez-Abellán, L.T. Duarte, S.R. Biaggio, R.C. Rocha-Filho, N. Bocchi, Modification of the Titanium Oxide Morphology and Composition by a Combined Chemical-electrochemical Treatment on cp Ti, Materials Research. 15(1) 2012 159-165.

[3] S.A. Hacking, E.J. Harvey, M. Tanzer, J.J. Krygier, J.D. Bobyn, Acid-etched microtexture for enhancement of bone growth into porous-coated implants, J Bone Joint Surg Br. 85(8) (2003) 1182-1189.

[4] G. Juodzbalys, M. Sapragoniene, A. Wennerberg, New Acid Etched Titanium Dental Implant Surface, Stomatologija 5(3) (2003) 101-105.

[5] H. Daugaard, B. Elmengaard, J.E. Bechtold, K. Soballe, Bone growth enhancement in vivo on press-fit titanium alloy implants with acid etched microtexture, J Biomed Mater Res A. 87(2) (2008) 434-440.

[6] L Yang, V Chinthapenta, Q Li, D Stout, A Liang, B.W. Sheldon, T.J. Webster, Understanding osteoblast responses to stiff nanotopographies through experiments and computational simulations, J Biomed Mater Res A. 15;97(4) (2011) 375-82.

[7] M.J. Dalby, N. Gadegaard, M.O. Riehle, C.D.W. Wilkinson, A.S.G. Curtis, Investigating filopodia sensing using arrays of defined nano-pits down to 35 nm diameter in size, The International Journal of Biochemistry & Cell Biology 36 (2004) 2005–2015.

[8] M.J. Dalby, D. McCloy, M. Robertson, C.D.W. Wilkinson, R.O.C. Oreffo, Osteoprogenitor response to defined topographies with nanoscale depths, Biomaterials 27 (2006) 1306–1315.

[9] C.H. Park, C.S. Lee, Y.J. Kim, J.H. Jang, J.Y. Suh, J.W. Park, Improved Pre-Osteoblast Response and Mechanical Compatibility of Ultrafine-Grained Ti-13Nb-13Zr Alloy, Clin Oral Implants Res 22(7) 2011 735-42.

Formability of high strength sheet metals with special regard to the effect of the influential factors on the forming limit diagrams

Miklós Tisza[1,a], Péter Zoltán Kovács[2,b], Zsolt Lukács[3,c], Antal Kiss[4,d], Gaszton Gál[5,e]

[1,2,3,4,5] University of Miskolc, Institute of Materials Science and Materials Processing 3515 Miskolc-Egyetemváros, Hungary

[a]tisza.miklos@uni-miskolc.hu, [b]metkpz@uni-miskolc.hu, [c]lzsolt@kugli.met.uni-miskolc.hu, [d]metkis@uni-miskolc.hu, [e]metgalga@uni-miskolc.hu,

Keywords: sheet metal forming, forming limit diagram, high strength steels

Abstract: Car manufacturing is one of the main target fields of sheet metal forming: thus sheet metal forming is exposed to the same challenges as the automotive industry. The continuously increasing demand on lower consumption and lower CO_2 emission means the highest challenges on materials developments besides design and construction. As a general requirement, the weight reduction and light weight construction principles should be mentioned together with the increased safety prescriptions which require the application of high strength steels. However, the application of high strength steels often leads to formability problems. Forming Limit Diagrams (FLD) are the most appropriate tools to characterize the formability of sheet metals. Theoretical and experimental investigations of forming limit diagrams are in the forefront of todays' research activities.

Introduction

The sheet metal forming particularly in the vehicle industry, the computer aided technology and tool design, require more and more precisely characterized formability of the sheet materials to be processed. The Institute of Materials Science and Technology has been dealing with the sheet processing and formability for several years to meet the increasing demands of the domestic industry. In this paper, a new formability testing system introduced developed at the Institute of Materials Sciences and Technology (formerly the Department of Mechanical Technology) at the University of Miskolc. This is an integrated sheet metal formability system equipped with an optical strain measurement system. The realization of this system was financially supported by national and international projects won by the department. The overall view of the system can be seen in Fig.1. It consists of an electro-hydraulic, computer controlled sheet metal testing machine and an automatic optical measuring system.

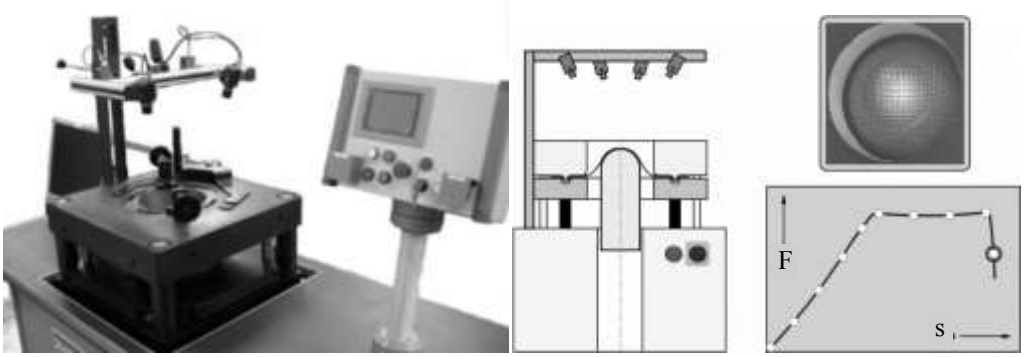

Figure 1. The universal sheet metal testing system with the optical measuring system

The system shown above is suitable for various formability tests. Among these tests, the determination of the Forming Limit Diagrams is one of the most important ones. Forming Limit Diagrams (shown in Fig.2) play a significant role in virtual sheet forming too. Not only the successsful or unsuccessful forming issue can be investigated by using them, but further useful information can be get to learn more and more complex parameters on forming processes. In Fig. 2. the typical parts of FLD determination are shown.

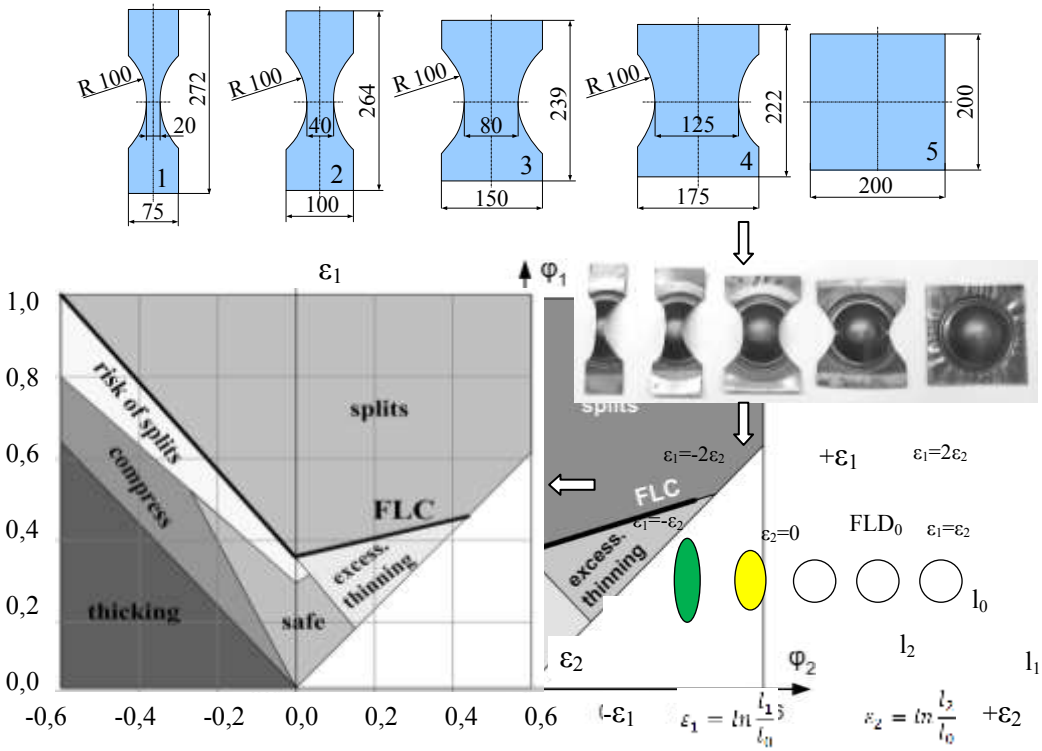

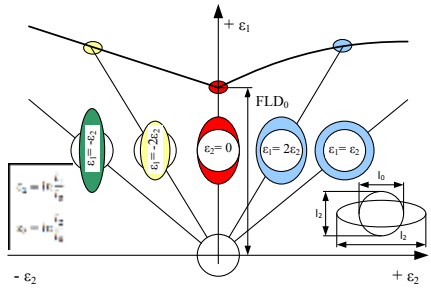

Figure 2. Forming Limit Diagram valid for the conventional sheet forming

Analyzing of the effects of various parameters on forming limit diagrams

Forming Limit Diagrams are very complex as the formability itself: when determining them we have to consider many parameters, which have significant effect on the forming limit value and thus on the reliability of the determined Forming Limit Diagrams, as well as on their practical application. We can classify the affecting parameters according to several points of view. The most significant parameters are summarized below:

- on of the most important parameter effecting the forming limits is the so-called deformation history, i.e. the strain path;
- further significant parameters are the material characteristics: the material quality, the mechanical properties, the anisotropy factor, the hardening exponent and the strain-rate exponent;
- the aging phenomena, the rolling process ratio and the effect of the scattering of material parameters, may also have significant effects,
- the sheet thickness is a very important issue as in general in formability,
- the effect of the workpiece shape and the applied measurement methods,
- the test circumstances (i.e. the type of the applied gridding, its size, its accuracy, the measuring mode of the grid shape changing, its accuracy, the friction, the lubrication conditions, the temperature, the effect of the investigation methods, etc.).

We have investigated mainly the effects of the rolling directions and the anisotropy. The aim of it was to define which direction will be the most adverse from the forming point of view. If it can be unambigously determined we can save significant work and time.

We wanted to study with a test series if it is possible to perform the same deformation history many times on a trial workpiece with one test, increasing the trial results reliability in this way. Accordingly we planned experiments and performed them with the forming called “star-shaped” specimen shown in the following figure.

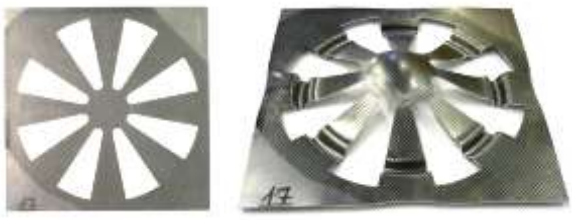

Figure 3. Star-shaped trial workpiece shape

The advantage of the trial workpiece shape shown in Figure 3, that the same deformation history can be realized many times during a test. Unfortunately, it

has some disadvantages, too, namely due to the bridge widths the formability limit can only be tested in the negative ε_2 interval. The more legs we form, the more we can separate. Naturally, increasing the number of legs leads to reducing the bridge width. We tested so-called 8-legged trial workpieces during our experiments. It results in two test possibilities along the rolling direction, two further tests in the perpendicular direction and four possibilities in the direction of 45° to the rolling direction. During these tests we could usually perform the experiments until 5 legs (bridges) were broken, which means, that the same – but at least almost same deformation history could be realized five times with one specimen. Figure 4. shows such experiment series results, for t = 1 mm sheet thickness, for DP600 material quality.

Material quality : DP600, wall thickness: 1 mm,
radius: 5mm, bridge width: ~10 mm

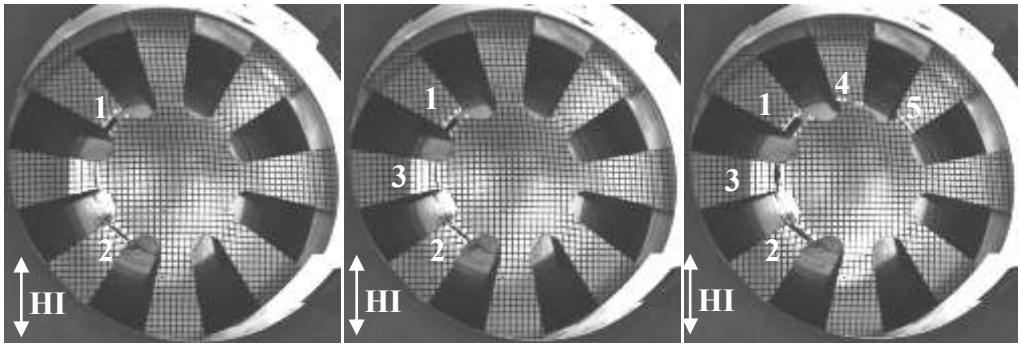

Figure 4. Forming experiments of star-shaped (8 legged) specimen
applied radius on workpiece were 5 mm- radius, and 10 mm- bridge width;
HI means the Rolling Direction

During the experiments in each case two legs of the four legs were broken, that stands in 45°.

A great advantage of this workpiece forming, that we have a possibility to study the effect of the rolling directions too. Only the first pair fracture can be considered as meaningful among the fractures to monitor the rolling directions, these will have effect on the further ones. From the fracture type and sequence of legs'fracture formed according to the rolling directions it can be stated, that which direction will be the most adverse from the forming point of view. Thus, there is no need to determine the forming diagram for the given material in every direction in the light of these results, but it is enough to do in the most adverse direction.

Applying these star specimen, the forming limit diagrams are determined. It can be seen in Figure 5. for several material grades of high strength steels.

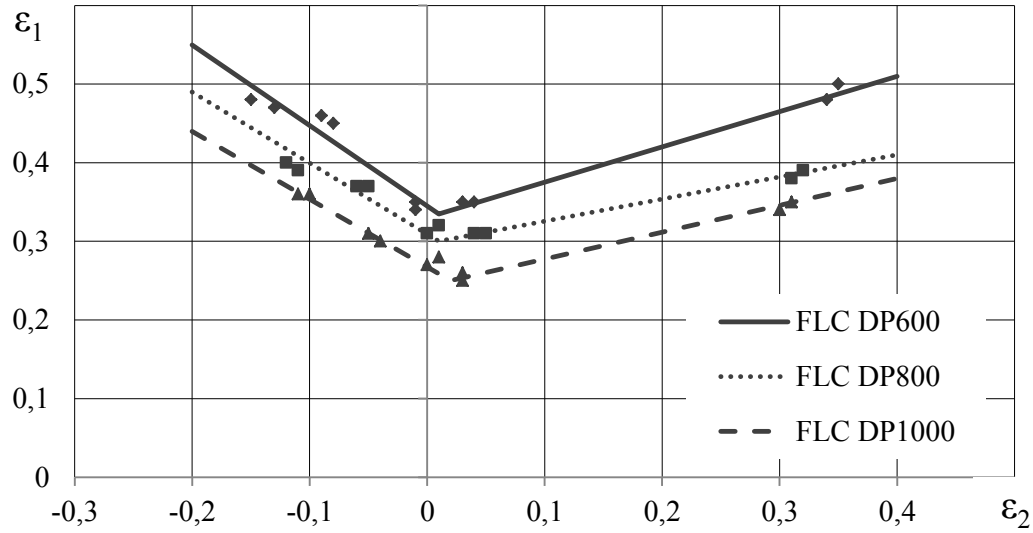

Figure 5. DP600, DP800, DP1000 forming limit diagram of high strength steels for t = 1 mm wall thickness

By using the determined anisotropy factors from sheet tensile test results, we can determine the expected fracture locations of the star-shaped pieces by modeling, too.

The simulation results show good agreement with the experiments performed on real workpieces from the same material grades.

We found from the simulation and experimental results (not detailed completely here), that the change of the anisotropy factors according to the directions has also effect on the fracture sequence of legs. Accordingly it can be stated, that the star shaped specimen is suitable for determining the most adverse direction.

Material grades tested

Generally it is valid that increasing the strength parameters the formability is reduced. The material qualities planned to be investigated within the project: DC01, DC04, DC05, DD14, and high strength steels, as DP600, DP800, DP1000, among AHSS and UHSS steels: TRIP steels, TWIP steels, and boron alloyed Manganese steels developed for hot forming: 22MnB5. We also plan to investigate some light Al and Mg alloys, too.

Summary

This paper deals with a special area of sheet metal forming, with the theoretical and experimental analysis of the Forming Limit Diagrams. The Forming Limit Diagrams are considered nowadays as the most generally applied and the most suitable qualifying tool in the evaluation of sheet metal formability .

Acknowledgement

The research work presented in this paper based on the results achieved within the TÁMOP-4.2.1.B-10/2/KONV-2010-0001 project and carried out as part of the TÁMOP-4.2.2/A-11/1-KONV-2012-0029 project in the framework of the New Széchenyi Plan. The realization of this project is supported by the European Union, and co-financed by the European Social Fund.

References

[1] Kovács P. Z., Tisza M.: Lemez alakíthatósági vizsgálatok optikai alakváltozás méréssel. Gépgyártástechnológia, 48 (2008) No.3. pp. 109-113.

[2] Tisza M., Kovács P.: Korszerű vizsgálati módszerek lemezanyagok alakíthatóságának elemzésére, Műszaki Tudomány az Észak-Kelet Magyarországi Régióban 2012, Szolnok, pp. 163.-172.

[3] Tisza M.., Kovács, P. .Z: Forming Limit Curves – A Practical Guide to AutoGrid, Miskolci Egyetem, Mechanikai Technológiai Tanszék, 2006.

[4] Banabic, D., Pöhlandt, K., Bunge, H-J., Tekkaya, A. E.: Formability of Metallic Materials, Springer, Berlin, 2000.

[5] Tisza, M., Gál, G., Kiss, A., Sárvári, J.: Metal Forming (in Hungarian), Nemzeti Tankönyvkiadó, Budapest. 1998.

[6] Ziaja György: Alakítási folyamatok határállapotai, MTA doktori értekezés, Budapesti Műszaki Egyetem, Mechanikai Technológiai Tanszék, 1994.

[7] Kiss A.: Lemezek alakíthatóságának átfogó értékelése, az n – r vizsgálat alkalmazásai. Research Report made within the OTKA T-037437 project, Miskolci Egyetem, Mechanikai Technológiai Tanszék, 2003.